GDAŃSK UNIVERSITY OF TECHNOLOGY

The author of the doctoral dissertation: Szymon Dudziak
Scientific discipline: Chemical Sciences

DOCTORAL DISSERTATION

Title of doctoral dissertation: Crystal facet effects in photocatalytic degradation of organic pollutants over anatase TiO_2

Title of doctoral dissertation (in Polish): Wpływ eksponowanej płaszczyzny krystalicznej TiO_2 o strukturze anatazu na efektywność fotokatalitycznej degradacji zanieczyszczeń organicznych

Supervisor
signature
Assoc Prof. Anna Zielińska-Jurek, PhD. DSc. Eng.

Gdańsk, year 2023

POLITECHNIKA GDAŃSKA

STATEMENT

The author of the doctoral dissertation: Szymon Dudziak

I, the undersigned, declare that I am aware that in accordance with the provisions of Art. 27 (1) and (2) of the Act of 4th February 1994 on Copyright and Related Rights (Journal of Laws of 2021, item 1062), the university may use my doctoral dissertation entitled:
Crystal facet effects in photocatalytic degradation of organic pollutants over anatase TiO_2
for scientific or didactic purposes.[1]

Gdańsk,_____   _____

signature of the PhD student

Aware of criminal liability for violations of the Act of 4th February 1994 on Copyright and Related Rights and disciplinary actions set out in the Law on Higher Education and Science (Journal of Laws 2021, item 478), as well as civil liability, I declare, that the submitted doctoral dissertation is my own work.

I declare, that the submitted doctoral dissertation is my own work performed under and in cooperation with the supervision of Assoc Prof. Anna Zielińska-Jurek, PhD. DSc. Eng.

This submitted doctoral dissertation has never before been the basis of an official procedure associated with the awarding of a PhD degree.

All the information contained in the above thesis which is derived from written and electronic sources is documented in a list of relevant literature in accordance with Art. 34 of the Copyright and Related Rights Act.

I confirm that this doctoral dissertation is identical to the attached electronic version.

Gdańsk,_____   _____

signature of the PhD student

I, the undersigned, agree to include an electronic version of the above doctoral dissertation in the open, institutional, digital repository of Gdańsk University of Technology.

Gdańsk,_____   _____

signature of the PhD student

---

[1] Art 27. 1. Educational institutions and entities referred to in art. 7 sec. 1 points 1, 2 and 4–8 of the Act of 20 July 2018 – Law on Higher Education and Science, may use the disseminated works in the original and in translation for the purposes of illustrating the content provided for didactic purposes or in order to conduct research activities, and to reproduce for this purpose disseminated minor works or fragments of larger works.

2. If the works are made available to the public in such a way that everyone can have access to them at the place and time selected by them, as referred to in para. 1, is allowed only for a limited group of people learning, teaching or conducting research, identified by the entities listed in paragraph 1.

GDAŃSK UNIVERSITY OF TECHNOLOGY

DESCRIPTION OF DOCTORAL DISSERTATION

The Author of the doctoral dissertation: Szymon Dudziak

Title of doctoral dissertation: Crystal facet effects in photocatalytic degradation of organic pollutants over anatase TiO_2

Title of doctoral dissertation in Polish: Wpływ eksponowanej płaszczyzny krystalicznej TiO_2 o strukturze anatazu na efektywność fotokatalicznej degradacji zanieczyszczeń organicznych

Language of doctoral dissertation: English

Supervisor: Anna Zielińska-Jurek

Date of doctoral defense:

Keywords of doctoral dissertation in Polish: Fotokataliza, oczyszczanie wody, płaszczyzny krystaliczne, domieszkowanie, anataz

Keywords of doctoral dissertation in English: Photocatalysis, water treatment, crystal facets, doping, anatase

Summary of doctoral dissertation in Polish: W pracy omówiono wyniki badań nad wpływem eksponowanych płaszczyzn krystalicznych tlenku tytanu(IV) na efektywność fotokatalitycznej degradacji związków organicznych. Omówiono najważniejsze istniejące informacje na temat geometrii i właściwości elektronowych nisko-indeksowych płaszczyzn krystalicznych TiO_2 o strukturze anatazu. W ramach przeprowadzonych badań otrzymano nanocząstki anatazu eksponujące płaszczyzny z rodzin {0 0 1}, {1 0 0} lub {1 0 1}, które następnie poddano badaniom aktywności fotokatalitycznej. Zaobserwowano wpływ eksponowanej rodziny płaszczyzn na efektywność degradacji oraz mineralizacji związków takich jak fenol, toluen, ibuprofen, karbamazepina oraz acetaminofen. W szczególności, stechiometryczne płaszczyzny {1 0 1} wykazały najwyższą efektywność degradacji i mineralizacji wszystkich badanych zanieczyszczeń, ze stałą prędkości degradacji około 2-3 razy wyższą niż dla pozostałych struktur. Połączenie otrzymanych cząstek z ferrytem $BaFe_{12}O_{19}$ wykazało dalsze różnice w końcowej aktywności jako efekt oddziaływań elektrycznych i magnetycznych między obiema fazami oraz eksponowanej płaszczyzny TiO_2. Ponadto, domieszkowanie otrzymanych struktur pozwoliło dodatkowo zwiększyć aktywność płaszczyzn {1 0 1} jednocześnie wskazując, że wpływ tej samej domieszki może być zupełnie różny, zależnie od powierzchniowej struktury elektronowej półprzewodnika.

Summary of doctoral dissertation in English: Presented work show detailed effect of the exposed crystal facets of anatase TiO_2 on the photocatalytic degradation of organic pollutants. The most important existing information about the geometry and electronic properties of the low index anatase facets are summarised. During the performed works, anatase nanoparticles with the dominant exposition of either {0 0 1}, {1 0 0} or {1 0 1} crystal facets were prepared and their photocatalytic activity was tested. A significant effect of the exposed crystal facets was observed for the degradation and mineralisation of compounds, such as phenol, toluene, ibuprofen, carbamazepine and acetaminophen. Overall results have indicated significant effect of the exposed facet, with stoichiometric {1 0 1} being the most suitable for both degradation and mineralisation of all studied compounds, with the observed degradation rate constant being approximately 2-3 higher than other nanostructures. Furthermore, after combining with the $BaFe_{12}O_{19}$ ferrite, different effects of both electronic and magnetic interactions between both phases were observed, depending on the exposed TiO_2 facets. Finally, doping of the obtained structures allowed to maximise activity of the {1 0 1} facets, simultaneously showing different effect of the same dopant, depending on the surface electronic structure of the material.

ACKNOWLEGMENTS

At the start of this work, I would like to express my thanks to numerous people who have helped me through all of these years. Although the detailed list would probably be too long to fir here, the special mentions goes to:

Prof. Anna Zielińska-Jurek, for all the patience, supervision and help with my scientific work, which ultimately resulted in this thesis,

My beloved Marta, for all the personal and scientific help provided every day for all these years,

My parents, grandparents and closets friends for all their help in everyday life, sincere curiosity about my work and not exaggerating the number of "Are you PhD yet?" questions. A special additional thanks to my brother, Łukasz, for all the help with the problematic computer-chemist interactions that I have encountered,

All the people who shared with me the burdens of a scientific works and who helped me with my studies. Some of them are (randomly): Zuza Bielan, Iza Wysocka, Ania Grzegórska, Agnieszka Sulowska, Agnieszka Fiszka Borzyszkowska, prof. Jakub Karczewski, Laura Cervera-Gabalda, prof. Cristina Gómez-Polo and other people from UPNA, Kuba Smoliński, Elvana Cako and prof. Marcin Pisarek.

ACKNOWLEGMENTS

TABLE OF CONTENT

SYMBOLS AND ABBREVIATIONS

Latin

C – concentration

C_0 – initial concentration

$d_{[h\,k\,l]}$ – crystallites size along the specific crystallographic direction [h k l]

E – energy

E_{Fermi} – Fermi energy

E_{Trap} – the energy of charge carriers trapping (sum of e^- and h^+ parts)

I – photon power flux

k – degradation rate constant

k_B – Boltzmann constant ($1.380649 \cdot 10^{-23}$ m^2·kg·s^{-2}·K^{-1})

n – quantity

n_P – quantity of the pollutant molecules

n_{Trap} – quantity of the surface trapping sites

N – Avogadro number ($6.02214076 \cdot 10^{23}$)

N_D – density of donor states

t – time

T – temperature

Greek

θ – glancing angle (between beam and surface tangent)

ζ – photonic efficiency (the ratio between reacted molecules and introduced photons)

λ – wavelength

γ – surface energy

η – chemical hardness

ρ – density of surface species

Abbreviations

ACT   – acetaminophen (*N*-(4-hydroxyphenyl)acetamide)

ADM   – ad-molecule model of surface reconstruction

B3LYP   – hybrid functional, based on the Becke and Lee-Yang-Parr functionals

BET   – Brunauer-Emmet-Teller (isotherm)

CBZ   – carbamazepine (5*H*-dibenzo[*b,f*]azepine-5-carboxamide)

DFT   – density functional theory

DR-UV/vis   – diffuse reflectance (spectroscopy) in the UV and visible light regions

EDS   – energy-dispersive X-ray spectroscopy

EPR   – electron paramagnetic resonance (spectroscopy)

GGA   – generalized gradient approximation

GGA+U   – generalized gradient approximation with Hubbard correction

ICP-OES – inductively coupled plasma-optical emission spectroscopy

IBU – ibuprofen ((*RS*)-2-(4-(2-methylpropyl)phenyl)propanoic acid)

IR – infrared light (photon wavelength range above 780 nm)

NIR – near-infrared light (photon wavelength range between 780-20 000 nm)

P25 – commercial TiO_2 powder, composed of approximately 79% of anatase and 16% of rutile polymorphs (wt. %, remaining part is amorphous), with mean surface area and crystallites size of approximately 55 $m^2 \cdot g^{-1}$ and 25 nm, respectively

PBE – Perdew-Burke-Ernzerhof exchange-correlation functional

PBE0 – hybrid functional, based on the Perdew-Burke-Ernzerhof functional

RDB-PAS – reverse double-beam photoacoustic spectroscopy

PHE – phenol

ROS – reactive oxygen species

SEM – scanning electron microscope

SHE – standard hydrogen electrode

TBT – titanium n-butoxide (titanium(IV) butan-1-olate)

SEM – scanning electron microscope

TEM – transmission electron microscope

TOC – total organic carbon

TPA – terephthalic acid (benzene-1,4-dicarboxylic acid)

UV – ultraviolet light (photon wavelength range between 100-400 nm)

UVA – type A of ultraviolet light (photon wavelength range between 315-400 nm)

vis – visible light (photon wavelength range between 400-780 nm)

XPS – X-ray photoelectron spectroscopy

XRD – X-ray diffraction

INTRODUCTION

1. PHOTOCATALYSIS IN THE SCOPE OF CURRENT ENVIRONMENTAL ISSUES

Throughout the last years, the growing human population and consumption have significantly impacted the environment. The major issues are associated with increased greenhouse gases emission, pollution of water with persistent organic compounds and heavy metals, as well as ongoing land industrialization and energy demand of the society. Accumulation of these problems has forced a response on the international level, resulting in the development of rules and strategies aimed at reduction of our environmental impact. In 2019, the European Union approved the European Green Deal, which includes net-zero emission of greenhouse gases and zero chemical pollution goals by 2050. Moreover, the circular economy action plan was developed in order to reduce waste and extend the life cycle of the products. This includes materials like plastics and batteries, but also wastewater, being regarded as "untapped resource" by the United Nations. More recently, analogical pledges of net-zero emission, reversed deforestation and reduced coal consumption were made by numerous countries, including China, India and Brazil, during the 26th United Nations Climate Change Conference in Glasgow. In order to put these goals into reality, combined technological, social and political efforts are necessary, which has become one of the biggest challenges for modern societies.

In this regard, development of new technologies that might help to reduce our impact on the environment are especially important for the near future. Both solutions that can provide more efficient utilisation of the existing resources, limit energy consumption and emissions, as well as help to reduce existing levels of pollution and greenhouse gasses are pursued worldwide. Following the need for such solutions, photocatalysis has gathered significant attention, as a way to promote chemical reactions, or initiate them, as a result of light introduction to the system containing photocatalyst. Depending on the reaction details, such an idea presents few contributions to the environmentally-relevant problems of chemical technology, schematically presented in Figure 1.1. First of all, suitably designed photocatalytic systems can utilize solar light irradiation, enhancing the reaction without the need for an artificial source of heat or photons. Therefore, the energy cost of a process might be significantly reduced. For example, Cheruvathoor Poulose and co-workers have shown an efficient and selective reduction of nitroarenes to amines under visible light irradiation using the $CuFeS_2$/hydrazine system [1]. As presented, the cost-normalised efficiency of the proposed reaction was calculated to be approximately 30 times higher than the state-of-the-art approach based on the catalytic process. Secondly, photocatalytic reactions can induce changes in otherwise very stable compounds. This is commonly used for water and air stream treatment from pollutants not susceptible to other purification processes. For example, carbamazepine has been recently recognized as a water micropollutant which is not susceptible to biological treatment in wastewater treatment
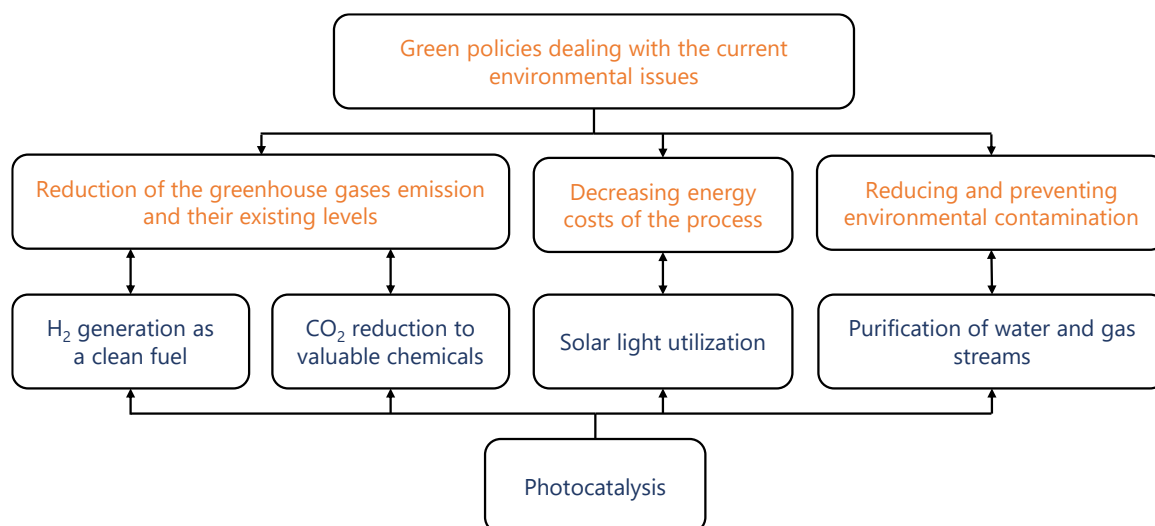
```
            ┌─────────────────────────────────────┐
            │   Green policies dealing with the    │
            │        current environmental issues  │
            └─────────────────────────────────────┘
```

Figure 1.1. Scheme of the possible application of photocatalysis and its connection with some of the green policies present in the field of chemical technology.

plants [2]; but can be effectively degraded during the photocatalytic process [3]. Although such photodegradation reactions usually deal with low efficiencies, they may help to fill the technological gap present in the existing solutions. Besides the degradation of organic pollutants, other purification processes might include the reduction of heavy metals in water [4] and NO_X reduction in the air [5]. Finally, photocatalysis might help to reduce the carbon footprint associated with energy production. Specifically, the photocatalytic generation of H_2 has been studied in detail by numerous authors, including the splitting of H-bearing molecules like water [6], ammonia [7] and ammonia borane [8], or dehydrogenation of organic molecules [9], [10]. Moreover, photocatalysis has been recently intensively studied for carbon dioxide (CO_2) reduction to valuable chemical compounds, such as methane, methanol, ethanol or formic acid [11]–[14]. Both of these approaches might help to prevent rising levels of atmospheric CO_2.

However, there are still some challenges in the application of photocatalysis related to the relatively low efficiency observed in most photocatalytic reactions. This connects with the complexity of the elementary steps involved in the photocatalytic reactions, most of which contribute to the final yield. As a result, even if a specific system has been reported as efficient for a particular application, the overall problem with the design of the photocatalytic process is still under intense investigation.

In this regard, the main goal of this work was to study the effect of photocatalyst design based on crystal facet engineering, especially for the efficient degradation of organic compounds in water. Detailed studies were planned in order to investigate if the exposition of different crystal facets and their possible modifications is a promising approach to optimizing photocatalytic activity, as well as to discuss the main features decisive for the activity of a specific surface structure.

2. ELEMENTARY STEPS IN HETEROGENEOUS PHOTOCATALYSIS

At the very heart of photocatalytic processes lies the conversion of the photon energy to chemical energy, providing a driving force for any further physicochemical phenomena. In heterogeneous systems, the basics of this conversion are usually described using general band structure theory, with semiconductors acting as photocatalysts. In such a case, the whole process is initiated by photon absorption, which excites the valence band electrons to their higher energy state, associated with the conduction band of the photocatalyst. These excited electrons (e^-) represent energy excess introduced to the system together with light. As a consequence of their high-energy nature, they can be seen as relatively reactive and can induce a reduction of other chemical species as long as the total energy of the system is decreased as a consequence. Simultaneously, the low-energy state, which is left unoccupied due to the excitation, can act as an electron acceptor and is described as a positively charged electron-hole (h^+). Analogically, these low-energy states can become occupied again due to electron transfer from the substrate to the valence band of the photocatalyst. Collectively, generated e^- and h^+ are known as charge carriers and their corresponding transfers give no change in the net charge inside the photocatalyst structure. Ideally, this allows its stable operation over long periods. A graphical representation of these processes, named photooxidation and photoreduction, is presented in Figure 2.1.

However, it is noteworthy that this description presents only a simplified idea of a photocatalytic reaction, while it is now well-known that multiple, different elementary steps can occur between photogenerated charge carriers and their transfer to substrates. Important steps especially include recombination or dissociation of the excitons, migration of free charge carriers within the crystal structure, their separation between different crystal phases (if present), thermalization and finally trapping at bulk or surface sites. Each of these steps makes its contribution to the final reaction efficiency, with corresponding energy changes, timeframes and limitations being subject to both previous and current studies. Noteworthy, the details of these processes and resulting activities depend heavily on the
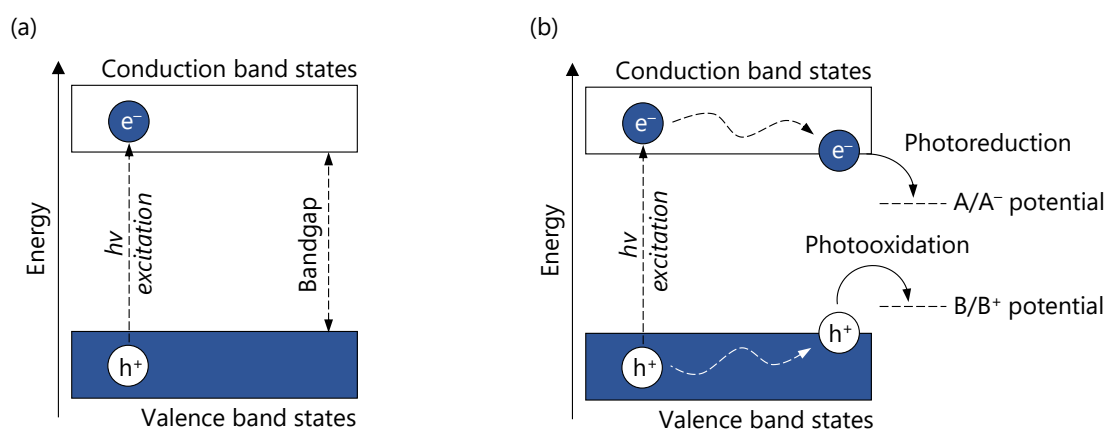

Figure 2.1. Scheme of the energy effects associated with the photocatalyst excitation (a) and possible reactions between the e^-/h^+ and hypothetical substrates A/B (b).

semiconductor composition and crystal structure, which results in a lot of attention being devoted to looking for new photocatalytic materials and optimizing their performance for a specific application. Focusing on the anatase polymorph of titanium dioxide (TiO_2), which is a main material investigated during the experimental part of this work, current information about the details of these elementary steps is summarized in the following sections for the clarity of the following discussion.

2.1. CHARGE CARRIERS GENERATION AND TRAPPING IN BULK ANATASE TIO_2

The anatase polymorph of TiO_2 is one of the most studied photocatalysts, especially considering its application in water treatment technology. It crystallizes in a tetragonal structure, assigned to the $I4_1/amd$ space group, which is composed of the TiO_6 octahedra connected via four edges and four corners [15], as presented schematically in Figure 2.2. Such a structure exhibits an indirect bandgap between the $\sim$X and Γ high symmetry points, with the reported energy being usually between 3.1-3.4 eV at room temperature [16]–[19], based on the diffuse-reflectance measurements. This allows it to absorb photons with maximum wavelengths of approximately 390 nm, leading to the observed photocatalytic activity in the UVA light range. The corresponding flatband potential of electrons within the anatase conduction band was reported approximately between -0.1 and -0.2 V
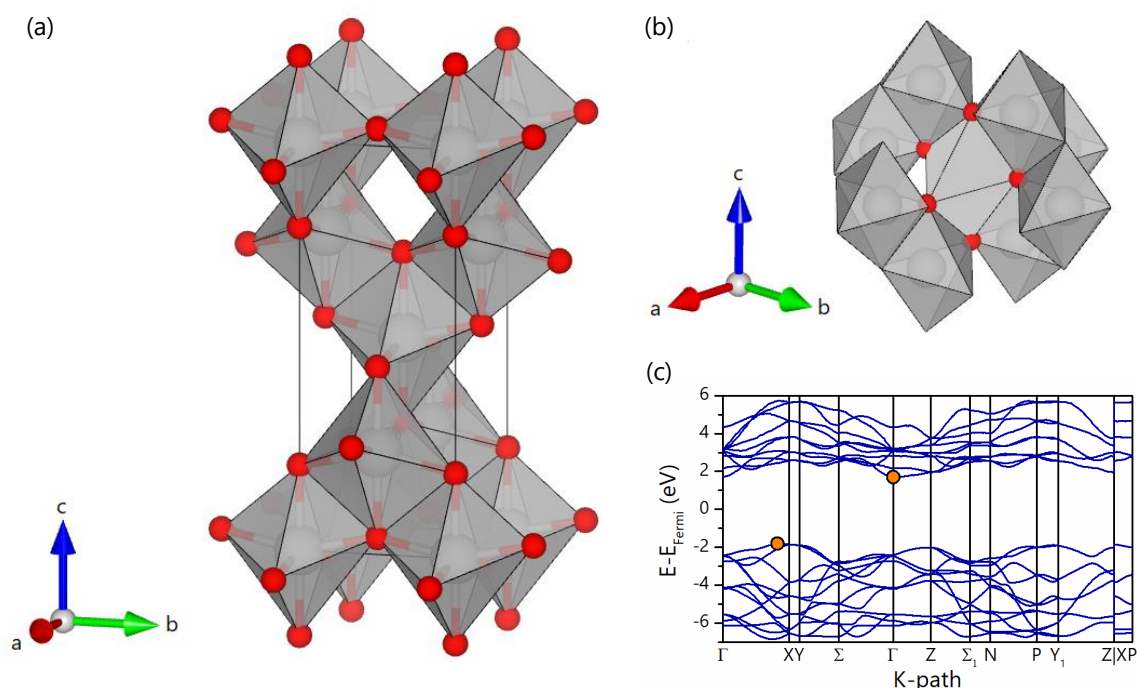
Figure 2.2. Visualization of the anatase TiO_2 unit cell with TiO_6 octahedra highlighted (a), as well as the local structure around selected TiO_6, showing bonding oxygens of the central unit (b). Panel (c) shows the simulated band structure of the presented structure. Throughout this work. titanium and oxygen atoms are grey and red spheres respectively. All visualizations of crystal structures and shapes are done with VESTA. Simulation of the band structure was performed with the Quantum Espresso software package including general gradient approximation with Hubbard correction (GGA+U), just to show its general characteristics.

for single crystals [20], [21], relative to a standard hydrogen electrode (SHE), however, even values as low as -0.8 V were reported for nanoparticles [22], [23].

Furthermore, various authors have discussed in detail anatase electronic structure and observed exciton generation. For example, Tang and co-workers have studied the optical absorption of an anatase single crystal, including a detailed description of the observed Urbach tail and its temperature dependence between 4.2 and 300 K [24]. They found that the absorption edge of the sample followed Urbach behaviour in the full temperature range and the T-independent optical gap was estimated to be approximately 3.420/3.460 eV, depending on the light polarization. Moreover, they noted strong exciton-phonon coupling inside the structure, which should contribute to the immediate exciton self-trapping in the TiO_6 octahedra and its weak intersite transfer. More recently, a detailed description of such an exciton behaviour inside the anatase crystals was reported by Baldini and co-workers [25], [26]. They observed relatively strong binding of the excitons as the result of excitation via a direct electronic gap with an energy of 3.98 eV (approximately the upper energy limit of the UVA light range). These excitons formed a 2-dimensional (2D) wave, confined to the (0 0 1) crystal plane, with an intermediate character between strongly-bound Frenkel excitons and weakly-bound Wannier-Mott excitons [25]. Importantly, the presented analysis concluded that this is also representative of the indirect excitation since the phonon contribution was found to be negligible beyond the appearance of the Urbach tail. Furthermore, such 2D excitons were found to be remarkably robust, resulting in their dissociation, connected with Mott transition, happening only for the densities higher than $5 \cdot 10^{19}$ cm^{-3} [26]. As noted in the original discussion, this is the highest Mott density reported so far for the semiconducting material. Visualization of such an excited anatase state is presented in Figure 2.3.

The relatively strong exciton-phonon coupling and high Mott density result in relatively fast thermalization and self-trapping of the photogenerated charge carriers at the TiO_6 octahedra, with low delocalisation. As shown by Park and co-workers, the
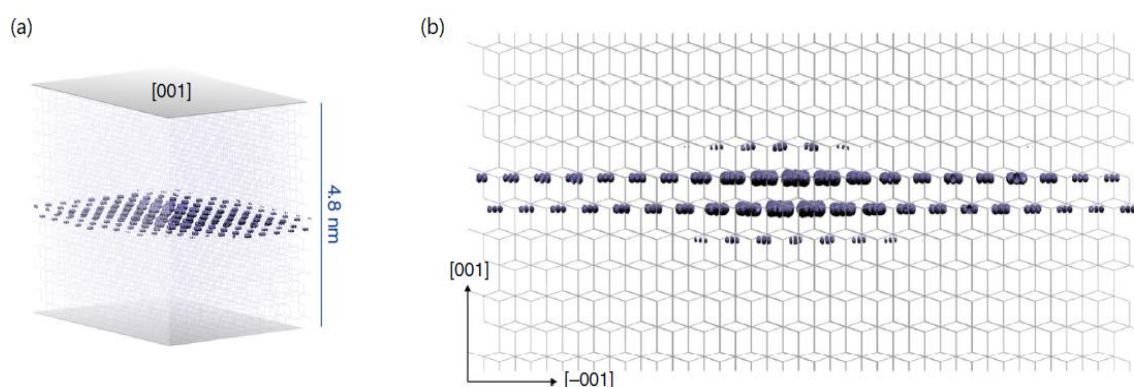

Figure 2.3. Perspective (a) and side (b) view of the 2D exciton isosurface, formed inside anatase crystal structure as the result of excitation via a direct electronic gap with the energy of 3.98 eV. Reproduced from [25] under the Creative Commons Attribution 4.0 CC BY license.

timeframe of e^-/h^+ cooling and self-trapping to form the final Ti^{3+}/O^- polaronic states is less than 0.7 and 0.32 ps, respectively [27]. As a comparison, the same study reports exciton recombination to occur between 0.8 and 10 ps, and decay of the polaronic states within the <320 ps for electrons and 8 ps for holes. These results show great insight into the importance of exciton trapping in anatase TiO_2, which was also reported by various other studies. It also explains well the anisotropy of the electron effective mass and thermal conductivity observed in different crystallographic directions [28], [29], which agrees that the [0 0 1] direction, perpendicular to the exciton plane, is unreferred for electron transport.

However, although these results describe precisely the initial steps of charge carriers generation and exciton trapping, they fail to predict in detail possible charge transfer from the crystal structure to the environment. For example, as shown by Liu and co-workers, the current passed through the sample along the [0 0 1] is even 60 times higher than along the [1 0 0], although the effective electron mass in anatase nanocrystals is 52 times larger in the [0 0 1] direction [28]. This difference was explained by the detailed interface structure between the analysed sample and the tungsten (W) probes used to provide current through the material. Specifically, the authors have shown that the potential of electron transfer from W to anatase is lower at the interface with the (0 0 1) crystal plane than with the (1 0 0), determining the observed current flow. Therefore, the overall performance of the sample was dominated by the surface structure and electronic interaction at the interface rather than charge carriers behaviour within the bulk material. This conclusion has fundamental meaning for the TiO_2 application in photocatalysis, as the occurrence of any chemical reaction requires the transfer of the generated charge carriers from the photocatalyst to the reacting substrates.

3. CRYSTAL FACETS

Following the highlighted discrepancy between the detailed description of bulk exciton inside the anatase TiO_2 and reported interfacial charge transfer, it is known that photocatalyst surface structure and its interactions with the other species are especially important for the final photocatalytic performance. Indeed, the importance of surface processes was realized very early in photocatalytic studies. For example, Gerischer, Heller and Wang have highlighted surface polarisation with trapped electrons as an efficiency-limiting problem of TiO_2-based degradation of organic pollutants; and proposed palladium deposition to remove excess electrons and catalyse dioxygen (O_2) reduction [30], [31]. Similarly, Moser and co-workers have suggested surface complexation of anatase nanoparticles with mono and bidentate benzene derivatives to promote the analogical transfer of photoexcited electrons [32]. Ever since, modification of the photocatalyst surface with noble and transition metals, defects, ions and molecules has become an important topic of photocatalyst design [33]–[40]. However, most of these studies have initially dealt with isotropic (spherical) particles, which offer only limited control over the detailed interface structure. This has changed recently since remarkable progress in the synthesis of nanocrystalline materials has been made, and an atomic-scale control over the final photocatalyst surface structure can be achieved as the result of the energetic

stabilisation of the specific crystal planes. Ultimately, this leads to an anisotropic growth in different crystalline directions and various, well-defined crystal shapes can be obtained due to the preferred exposition of one or more crystal planes to the environment. These exposed planes, forming a flat termination of the crystal structure, are known as crystal facets.

Due to the symmetry of the crystal structure, usually, a set of equivalent crystal facets is observed, which correspond to the set of equivalent crystal planes of the bulk structure. For example, the (1 0 0) crystal plane of anatase TiO_2 has 3 other equivalent planes: the (0 1 0), ($\bar{1}$ 0 0) and (0 $\bar{1}$ 0). Such a family of the equivalent planes is denoted using corresponding Miller indices and brackets {$h\ k\ l$}, which is also commonly used to index observed crystal facets. However, especially during the computational studies, some authors use notation corresponding to the specific crystal plane ($h\ k\ l$). During this work, the latter will be used as long as the discussion refers to the model of a specific crystal plane (therefore, not strictly a family of different planes), while the former will be used for a set of facets observed in the analysed sample. Visualization of such a faceted structure, compared to the spherical particle, is presented in Figure 3.1. using anatase TiO_2 as an example.

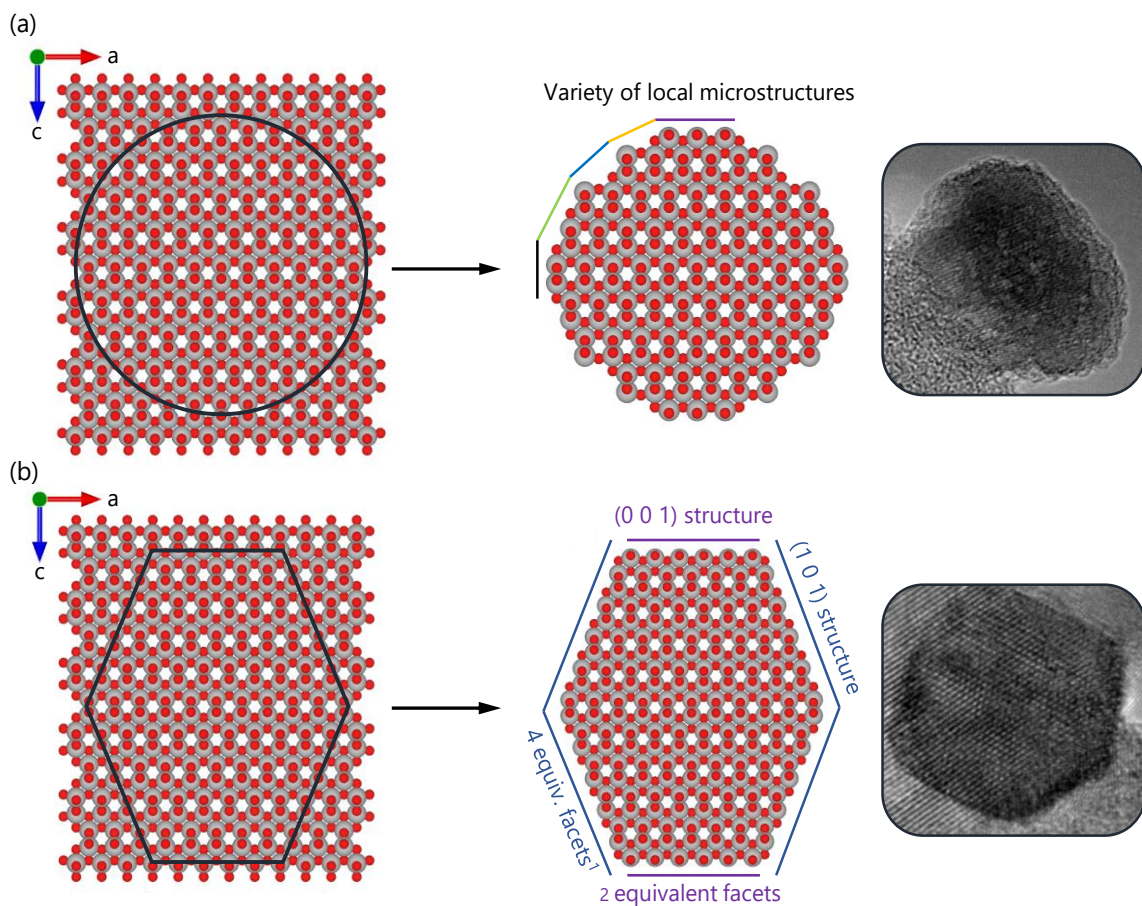**Figure 3.1.** Schematic comparison between spherical (a) and faceted (b) crystals of the anatase TiO_2 and the resulting differences in the surface structure; together with the exemplary images from the transmission electron microscope (TEM). [1]Please note that for the 3-dimensional structure, (1 0 1) crystal plane will form 8 equivalent facets, however only four are shown in a cross-section.

Compared to the isotropic particles, the faceted ones allow detailed control over the interface structure and simultaneous analysis of the reaction steps at the atomic scale. Moreover, different arrangement of the surface atoms results in the anisotropy of the surface properties such as surface energy, electronic structure and interactions with other chemical entities. In this regard, crystal facet engineering has recently gained increasing attention from the scientific community working on photocatalyst design. For example, some of the recent state-of-the-art photocatalysts were reported based on the facet-engineering approach, including strontium titanate ($SrTiO_3$) for water splitting [41], cadmium(II) sulphide for CO_2 reduction [42] or zinc oxide for NO oxidation [43]. Simultaneously, a detailed description of the charge carriers behaviour inside different photocatalysts is expanded from the bulk structure to specific facets, proving, i.e. their preferable separation and trapping at different surface sites [44]. In this regard, my dissertation was specifically focused on the exposed crystal facets of anatase TiO_2 and their photocatalytic activity. Noteworthy, since it is possible to achieve exposition of very different anatase facets, planned works were generally constrained to the most stable ones, which are also commonly observed. This includes facets such as the {0 0 1}, {1 0 0} and {1 0 1} ones, commonly referred to as "low index" facets. Information about their known structures, properties and stabilisation strategies is quickly summarized in the following sections.

3.1. GEOMETRIES AND ENERGIES OF THE LOW INDEX ANATASE FACETS

Recently, atomic structures of the possible crystal terminations have been studied using a computational approach based on the density functional theory (DFT). This allows to optimize the arrangement of atoms and calculate the corresponding energy of the system with almost non-constrained freedom. Then, by comparing the results obtained for the 2-dimensional surface models to the bulk structure calculation, the energy of the modelled surface can be easily extracted. Although the obtained values depend heavily on the computational details and should not be treated as absolute, they allow for relative comparison of the stability between different structures with good accuracy. Ultimately, the lowest-energy structures can be good representations of the actual surface geometry [45].

Regarding anatase TiO_2, the geometries and energies of its different crystal facets were studied in detail by multiple authors [46]–[51]. Concerning the (0 0 1), (1 0 0) and (1 0 1) surface structures, these reports are generally consensual about their relative stability, highlighting the (1 0 1) as the most stable one and the (0 0 1) as the least stable when analysing stoichiometric models in a vacuum. The high surface energy (γ) of the (0 0 1) plane results strictly from the high density of undercoordinated species (ρ) that appear as the result of crystal termination in a corresponding direction. As shown in Figure 3.2.a, in such a structure, all of the surface Ti atoms break one of their bulk-structure bonds and become 5-fold coordinated (5c-Ti), which is followed by half of the O being 2-fold coordinated (2c-O), after analogical bond breaking. Ultimately, both these species form chains of a [5c-Ti]-[2c-O]-[5c-Ti] bridges along the [0 1 0] direction. It is noteworthy that

(a) Anatase (0 0 1) surface

Crystal shape assuming dominant expositon

γ_{vacuum} = 0.90-1.38 J·m^{-2}
ρ_{5c-Ti} = 7.0 nm^{-2}
ρ_{2c-O} = 7.0 nm^{-2}
No. of equivalent planes = 2
Angle with {0 0 1} = Parallel
Angle with {1 0 0} = 90°
Angle with {1 0 1} = 111.7°

(b) Anatase (1 0 0) surface

γ_{vacuum} = 0.53-0.96 J·m^{-2}
ρ_{5c-Ti} = 5.4 nm^{-2}
ρ_{2c-O} = 5.4 nm^{-2}
No. of equivalent planes = 4
Angle with {0 0 1} = 90°
Angle with {1 0 0} = 90°
Angle with {1 0 1} = 158.3°

(c) Anatase (1 0 1) surface

γ_{vacuum} = 0.44-0.84 J·m^{-2}
ρ_{5c-Ti} = 5.1 nm^{-2}
ρ_{2c-O} = 5.1 nm^{-2}
No. of equivalent planes = 8
Angle with {0 0 1} = 111.7°
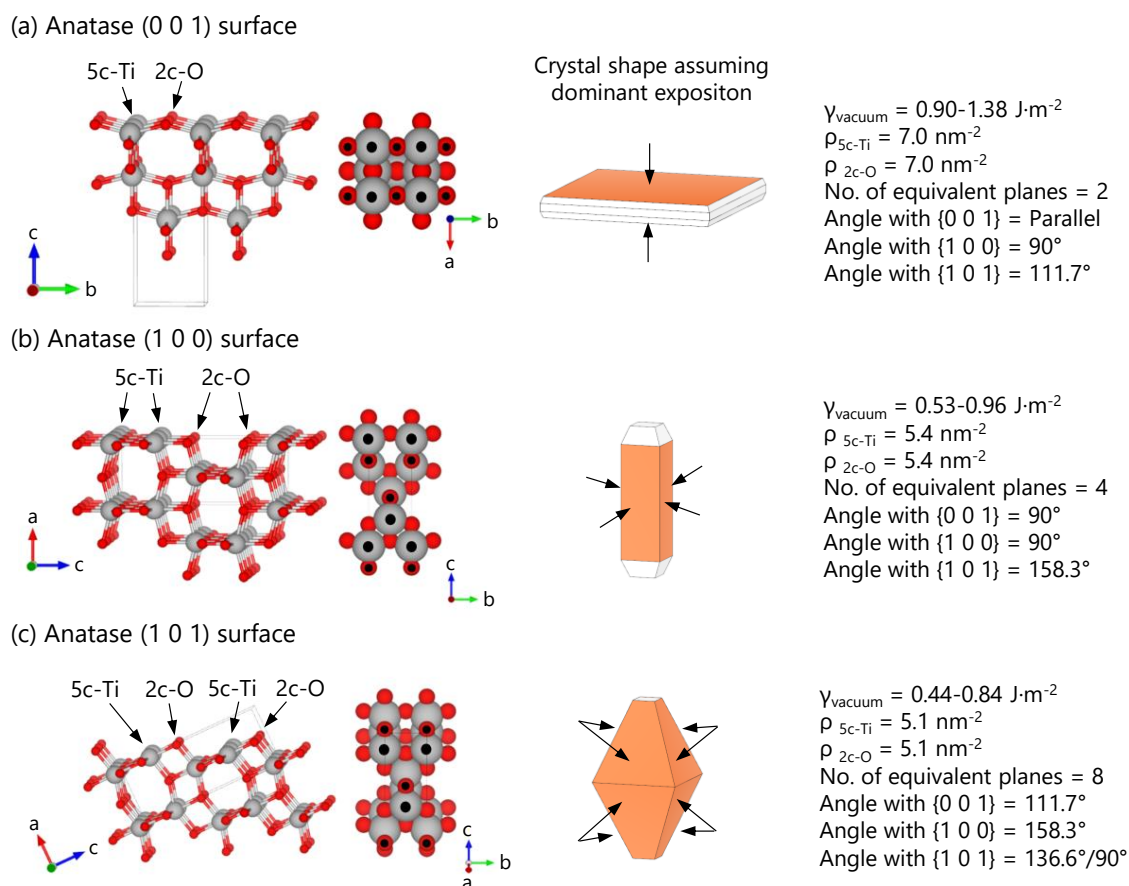Angle with {1 0 0} = 158.3°
Angle with {1 0 1} = 136.6°/90°

Figure 3.2. Isomeric (ball-and-stick) and top (space-filling) views of the perfect low index anatase TiO$_2$ surfaces, together with the crystal shape resulting from the dominant exposition of the corresponding facets. The Figure includes basic information about simulated surface energy (including different values, reported using different computational details [46]–[51]), the density of undercoordinated species, number of equivalent planes and expected angles between other, co-exposed facets. Bulk-structure unit cells are shown to help navigate between the models. In a top-view image, undercoordinated atoms are marked with black dots. In the crystal shape models, corresponding dominant facets are orange and are marked with arrows, including the ones behind the plane. Presented surface energy values (γ) correspond to the relaxed structures.

after geometry optimization (relaxation), one of these bridging bonds becomes shorter, leading to the situation when 2c-O is not equivalently bonded to the 5c-Ti. Analogical shifts along the [0 1 0] direction are also observed for the fully-coordinated O (3c-O) bonded to the 5c-Ti. Corresponding surface energies are often in the range of 0.90-1.00 J·m^{-2} when computed using Perdew-Burke-Ernzerhof (PBE) functionals [47]–[50], however, even a value as large as 1.38 J·m^{-2} was reported when using local density approximation (LDA) [50].

Compared to the (0 0 1) surface, both (1 0 0) and (1 0 1) have a less dense distribution of the 5c-Ti and 2c-O species and lower γ, as shown in panels (b) and (c) of Figure 3.2. Focusing on the (1 0 0) surface, its structure shows characteristic terrace-like steps along the [0 0 1] direction that exposes 5c-Ti/3c-O atoms in the middle and 2c-O at the edges, followed by a cavity that gives access to fully coordinated 6c-Ti and 3c-O. In the relaxed structure, the 3c-O atoms, exposed at the terraces, shift significantly outward the crystal

structure, followed by the 6c-Ti in a second atomic layer. On the contrary, the exposed 5c-Ti atoms relax inward the crystal structure, resulting in a situation where the most exposed part of the surface is relatively oxygen-rich. The corresponding energy values are commonly reported in the range of 0.53-0.75 J·m^{-2} using PBE functionals [47]–[50] and 0.96 J·m^{-2} using LDA [50]. Finally, the (1 0 1) surface shows a characteristic sawtooth-like profile with the 2c-O edges along the [0 1 0] direction, always bonded to the single 5c-Ti. The relaxation pattern of this surface includes shifts in the 6c-Ti/3c-O and 5c-Ti positions, analogical to the (1 0 0) surface. Simultaneously, the exposed 2c-O shortens its distances to the neighbouring Ti atoms leading to its stronger bonding. Corresponding γ values are usually in the range of 0.44-0.65 J·m^{-2} (PBE [47]–[50]) and 0.84 J·m^{-2} (LDA [50]), making it one of the most stable TiO$_2$ surfaces in general [52].

Noteworthy, while the (1 0 0) and (1 0 1) can be described as low-energetic, the (0 0 1) has high surface energy and therefore, reconstruction of its surface atoms might occur to minimize the final energy. This problem was especially observed during the ultra-high vacuum experiments with simultaneous Ne$^+$ sputtering of the anatase single crystal and further heating it to 900 K to restore the initial structure, as reported by Hengerer and co-workers [53]. After such treatment, they observed that the (0 0 1) surface formed a superstructure with (1 x 4) periodicity, which became thermodynamically stable. This was further investigated computationally by Lazzeri and Selloni, who suggested an "ad-molecule" model (AMD) of such a reconstructed surface [54]. This model includes rows of the TiO$_3$ bridges that develop above the perfect surface every fourth of the [5c-Ti]-[2c-O]-[5c-Ti] periodic units presented in Figure 3.2.a. Noteworthy, they proved that such structures exhibit energy minimum specifically for the (1 x 4) periodicity, which was connected with the favourable [5c-Ti]-[2c-O] bond shortening and corresponding stress relief. However, despite reported energetic stability (γ = 0.51 J·m^{-2} for the AMD geometry, vs 0.90 J·m^{-2} for the perfect surface), the suggested model was not completely in accordance with some of the experimental observations, especially connected with relatively low activity observed for the reconstructed (0 0 1) surface. This has led to the refinement of the proposed model by Wang and co-workers, who suggested that the TiO$_3$ bridges are further oxidized [55]. Therefore, the 4-fold coordinated Ti atoms introduced in the AMD model were transformed to the 6c-Ti, forming a chemically inert structure as long as no point defects were present. Visualization of this oxidized (1 x 4) reconstruction of the (0 0 1) surface is presented in Figure 3.3.

Nevertheless, although the (1 x 4) reconstruction should be minded, it is still possible that the (0 0 1) remains in its bulk-like form after the preparation. This results from the fact that the (0 0 1) surface must be stabilized during the growth (usually using fluorine, as discussed in the following parts), which would later require overcoming an energy barrier to induce reconstruction. For example, the stability of the unreconstructed (0 0 1) surface was confirmed experimentally by DeBenedetti and co-workers in the aqueous benzoate solution [56]. Generally, it is expected that fluorine-stabilised {0 0 1} facets should remain the geometry of a perfect (0 0 1) surface up to 400-600 °C [57], [58].
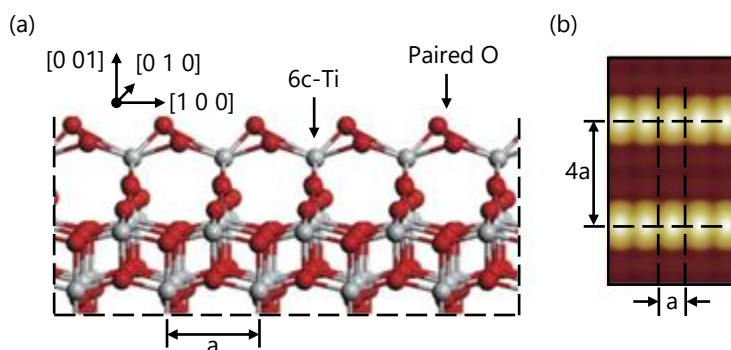
Figure 3.3. Visualization of the oxidized (1 x 4) reconstruction of the anatase (0 0 1) surface, proposed by Wang and co-workers (a), together with the simulated scanning tunnelling microscope image (b). Reproduced from [55] under the Creative Commons Attribution 3.0 CC BY licence.

3.2. ELECTRONIC PROPERTIES OF THE LOW INDEX ANATASE FACETS

Following the geometry description of the possible anatase terminations, analogical discussion about their electronic properties is also present in the existing literature. For example, Zhao and co-workers reported band structures, work functions, electron affinities and dipole moments of the different anatase surfaces in detail [49]. Focusing on the described low index facets, they have found that the relaxed (0 0 1) surface forms additional, surface-specific states above the valence band edge. Therefore, local reduction of the bandgap at this surface might be expected without the introduction of additional defects, which was not observed for the (1 0 0) and (1 0 1) models. Moreover, following calculated work functions, they highlighted that the ability to extract electrons from the analysed surfaces showed the order of (0 0 1) $\lesssim$ (1 0 0) < (1 0 1), which was generally in accordance with the electron affinity values being (1 0 0) $\lesssim$ (0 0 1) < (1 0 1). Based on these results, it can be assumed that the {1 0 1} facets should possess a high oxidizing ability compared to the {0 0 1} and {1 0 0} ones. However, it should be noted that this description was made strictly for the ground state of the system, while experimental observations show that during the photocatalytic processes, the {1 0 1} are preferred photoreduction sites rather than photooxidation. For example, this is observed as the selective deposition of the reduced species (Au^0, Pt^0), which preferentially occurs on these facets [59]–[62].

In this regard, a more detailed description of the surface electronic properties can be achieved by analysing the behaviour of the excited e^-/h^+, which is commonly achieved by arbitrarily changing the number of electrons inside the simulated model. Although these $n+1$ and $n−1$ electron states are not exactly equivalent to the actual excitation, where both e^- and h^+ are generated simultaneously, they do adopt energy levels analogical to the photogenerated charge carriers, which allow for their relative comparison. For example, using such an approach, Ma and co-workers have studied the trapping of both electrons and holes on the (0 0 1), (1 0 0) and (1 0 1) surfaces and their corresponding energy effects [63]. They have found that the (1 0 1) surface has the highest ability to trap conduction band electrons at surface 5c-Ti sites and is the only one of these three surfaces that prefers to trap e^- over h^+ (Figure 3.4a.). Following previous results by Zhao and co-workers [49], it

is in good agreement with the highlighted high electron affinity of this surface, simultaneously clarifying that this observation can be connected with the preference to localise excited electrons rather than their withdrawal from the possible substrates. It also explains the experimentally observed reductive character of the corresponding facets. Furthermore, in the same study, Ma and co-workers have observed that electrons do not trap strictly on the (0 0 1) surface atoms but instead can form a subsurface state [63].This is in good agreement with the described exciton behaviour in the bulk anatase crystal, which has shown its preferred delocalisation over the (0 0 1) plane [25]. Therefore, the {0 0 1} facets can be seen as poor electron-trapping sites with a low preference to localise excited electrons compared to other surface structures. Focusing back on the work of Ma and co-workers, a similar observation was also made for h^+, showing its relatively low preference to trap at the (0 0 1) surface, although in this case, the hole indeed localises at the interface 2c-O atom [63]. Ultimately, the described study concluded that the (1 0 1) surface shows the highest overall trapping ability with a preference to localise electrons, followed by the (1 0 0) one with a preference to trap holes, and finally, the (0 0 1) show the lowest trapping ability of both charge carriers with electrons not localising at the surface.
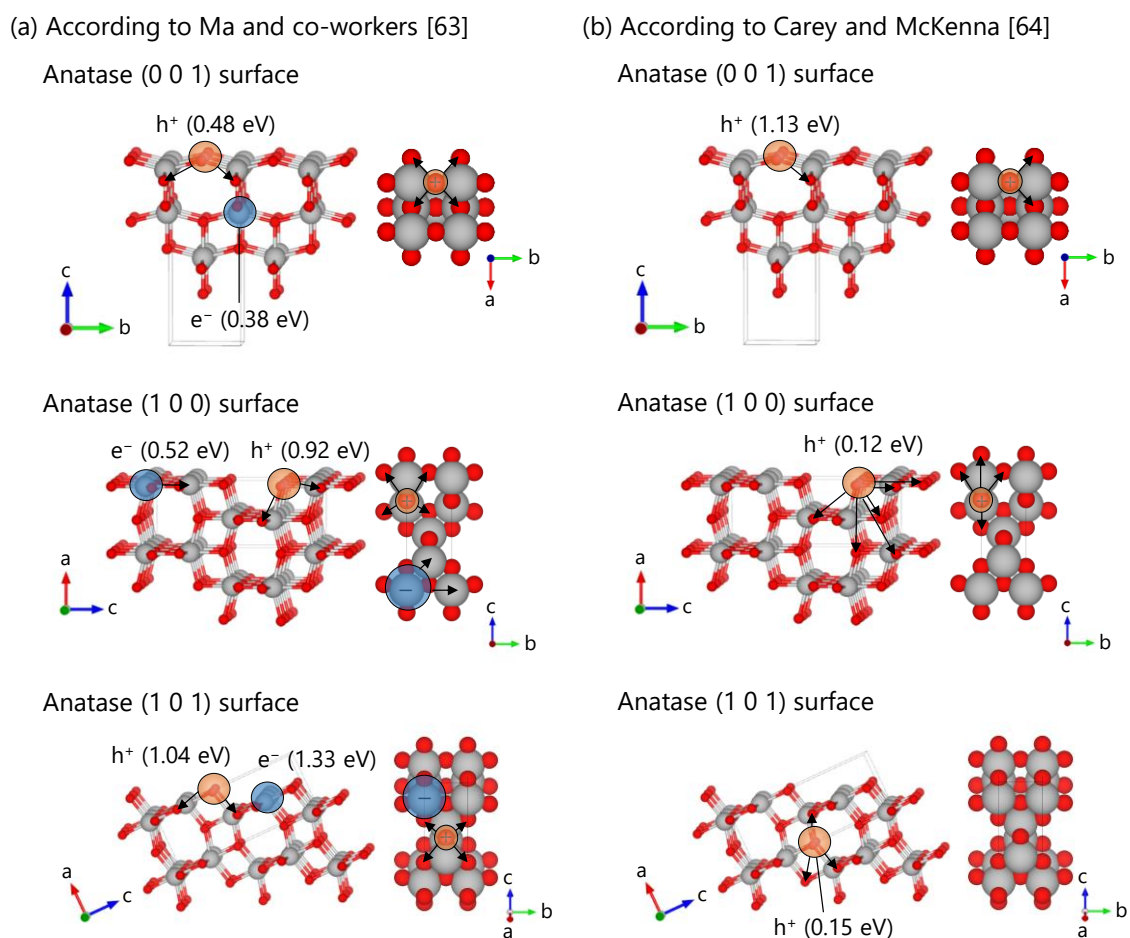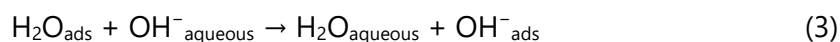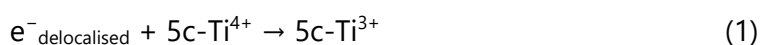

Figure 3.4. Presentation of the possible trapping sites of photogenerated charge carriers on the low index anatase surfaces in vacuum. Arrows indicate partial delocalisation. Values in parentheses show energy gain associated with the trapping. For clarity, possible equivalent sites are not marked.

On the other hand, different results were presented by Carey and McKenna (Figure 3.4b.), who have concluded that analogical electron trapping should not occur on any of these three facets but can occur on high-index surfaces such as a (1 0 3) or (1 0 5) [64]. Visual representations of the possible trapping sites, discussed in the described studies in vacuum conditions, are compared in Figure 3.4. Noteworthy, these results stand in visible contrast to each other, leading to the situation, where electron trapping on the commonly observed anatase facets might be questioned. In this regard, it is especially important to further consider possible interactions between the charge carriers and possible substrates, as their presence will affect the details of the possible elementary steps at the surface.
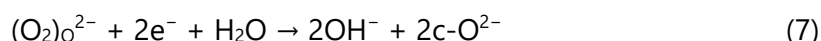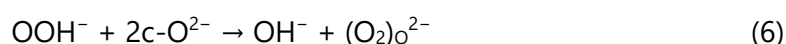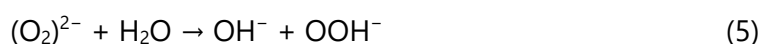
3.3. INTERACTIONS WITH WATER AND OXYGEN

Interactions between the photocatalyst surface and reacting species are considered the centre of photocatalytic reaction, making it an important topic of previous and current studies. However, it makes the overall description case-specific since every surface-substrate combination might be seen as a unique problem. Focusing on the photocatalytic reactions occurring in the aqueous phase, the main possible substrates are H_2O and O_2. These can act as sources of the reactive oxygen species (ROS) generated *in situ* during the photocatalytic water treatment from organic pollutants, which is the central problem of further experimental work or can undergo a chain of reactions to generate free H_2 and O_2 from the solution. In view of this, interactions between possible charge carriers and H_2O/O_2 molecules on the anatase facets received considerable attention in the previous studies, which are summarized below.

Following the presented charge carriers behaviour at different crystal planes, it is especially important to consider how H_2O presence can influence their possible localisation. It was discussed by Selcuk and Selloni, who compared e^- trapping on the (0 0 1) and (1 0 1) surfaces in a vacuum and at the interface with water [65]. They observed that H_2O presence supports e^- localisation on the surface 5c-Ti atoms of the (1 0 1) model, which was connected with H_2O dissociation and formation of the stable $[5c\text{-}Ti^{3+}]$-$[2c\text{-}O^-]$-H polaron state at the interface. Noteworthy, analogical electron trapping at the surface Ti was questionable without the stabilizing effect of the neighbouring $[2c\text{-}O^-]$-H; being either slightly favourable or unfavourable on the energy scale, depending on the computational details. On the other hand, the formation of the $[2c\text{-}O^-]$-H was also dependent on the $5c\text{-}Ti^{3+}$ presence. Without it, the proton attached to the 2c-O would rapidly rebuild the H_2O molecule from which it originated. The overall process can be summarized with the following reactions (1-3), which ultimately involve two different H_2O molecules and two subsequent proton transfers [65]:

$$e^-_{delocalised} + 5c\text{-}Ti^{4+} \rightarrow 5c\text{-}Ti^{3+} \tag{1}$$

$$2c\text{-}O^{2-}\cdots H_2O \rightarrow [2c\text{-}O^-]\text{-}H + OH^-_{aqueous} \tag{2}$$

$$H_2O_{ads} + OH^-_{aqueous} \rightarrow H_2O_{aqueous} + OH^-_{ads} \tag{3}$$

where the dotted line denotes hydrogen bonding, "aqueous" means that this species is not adsorbed on the surface and "ads" means that it is adsorbed. Please note that in reactions (1-3), the charge of the stoichiometric 5c-Ti and 2c-O sites was marked to keep up with the reaction charge balance, but for clarity, it is not presented within the text body. Furthermore, in the same study, it was reported that analogical e^-/H_2O interactions are not observed on the (0 0 1) surface, where introduced electrons always localise in the subsurface region of the model [65]. These findings support differences in electron trapping at the low index anatase facets, simultaneously highlighting the importance of the interface on the simulation results. The latter is especially noteworthy since photocatalytic reactions are not performed in a vacuum and interactions between substrates and the photocatalyst are always expected.

The second important finding of the work by Selcuk and Selloni is that, due to the reactions (1-3), one of the water molecules became dissociated, forming stable OH^- groups at the (1 0 1) surface [65]. This is even though, in contrast to the (0 0 1) and (1 0 0), dissociation of H_2O is not occurring completely on the perfect (1 0 1) plane [66]. Such an electron-induced water dissociation on the (1 0 1) surface was further investigated by Setvin and co-workers, with oxygen reduction as the starting point [67]. Based on the combination of DFT calculations and scanning tunnelling microscopy (STM), they observed the formation of the metastable OOH^- and H_2O_2 species at the surface, which decompose to the terminal -OH groups at room temperature. The step-by-step reaction was shown computationally to occur through the O_2 reaction with H_2O, which was especially favourable when two excess electrons were present inside the model. Possible surface steps involving OOH^-, are described in the following reactions (4-7) [67]:

$$O_2 + 2e^- \rightarrow (O_2)^{2-} \tag{4}$$

$$(O_2)^{2-} + H_2O \rightarrow OH^- + OOH^- \tag{5}$$

$$OOH^- + 2c\text{-}O^{2-} \rightarrow OH^- + (O_2)_O^{2-} \tag{6}$$

$$(O_2)_O^{2-} + 2e^- + H_2O \rightarrow 2OH^- + 2c\text{-}O^{2-} \tag{7}$$

where $(O_2)_O$ is an oxygen molecule replacing 2c-O at the surface, originating either due to reaction (6) or due to O_2 dissociation. Moreover, alternatively to reaction (6), OOH^- can form H_2O_2 that dissociates with the involvement of two further electrons (8-9) [67]:

$$OOH^- + H_2O \rightarrow OH^- + H_2O_2 \tag{8}$$

$$H_2O_2 + 2e^- \rightarrow 2OH^- \tag{9}$$
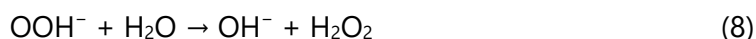
Noteworthy, all of these pathways were found to depend heavily on the presence of excess electrons and became more favoured when the number of e^- increased. However, in contrast to the OOH^-, dissociation of the H_2O_2 (9) was found to occur almost without an activation barrier. In this regard, the decomposition of the OOH^- (6) is a limiting step of

such an electron-induced water dissociation. The details of this process have shown that, outside of the e^- presence, reaction (6) also depends on the local surface configuration, with an important stabilizing role of the adjusting OH^-, generated in the previous step (5). Specifically, the removal of the OH^- group from the model decreased the calculated activation barrier of the OOH^- dissociation from 1.4 eV to 0.5 eV, in the presence of two excess electrons, which is a value reasonable with the observed OH^- formation at room temperature [67].

In the scope of the above findings, it is especially evident that O_2/H_2O reduction is crucial for the hydroxylation of the (1 0 1) surface. This problem has fundamental significance for its potential photocatalytic application, since H_2O and -OH species interact differently with the photogenerated charge carriers. For example, Chen and co-workers reported that h^+ transfer to the H_2O molecule on the (1 0 1) surface is preferably proceeded by the proton transfer, creating surface -OH in the first place [68]. Only then is the hole transferred from the surface 3c-O atom, according to the general reaction (10):

$$H_2O + h^+ \rightarrow \cdot OH + H^+ \tag{10}$$

This observation leads to the conclusion that water itself is rather a poor substrate for h^+ transfer, and its dissociation to -OH increases affinity to generated holes. A similar conclusion was also reported by Shirai and co-workers, who analysed in detail the water-assisted hole trapping at the anatase {0 0 1} and {1 0 1} facets and compared them to the spherical particles [69]. They observed that effective hole trapping occurs only at the surface -OH, but it also needs further stabilisation by co-adsorbed H_2O molecules to increase electron density at adsorbed hydroxyl. A favourable structure was found specifically at the spherical surface, where the exposition of four-coordinated Ti atoms (4c-Ti) and curvature facilitated H_2O adsorption and H-bonding with -OH [69]. These observations show that the h^+ transfer during water oxidation depends mostly on the exact electron density of the accepting species, which will be affected by the exact structure and possible H-bonding within the first shell of water coordination, which also agrees with other reports. For example, Panarelli and co-workers presented similar conclusions based on electron paramagnetic resonance (EPR) studies [70]. Noteworthy, the results obtained by Shirai and co-workers suggest that H_2O does not form hole-trapped states on the faceted particles, which was evidenced by the water vapour pressure having no effect on the time profiles of the transient absorption spectra, measured for the particles exposing {1 0 1} and {0 0 1} facets [69]. Therefore, for these particles, the water vapour does not influence the lifetime of the generated charge carriers, and the H_2O role in h^+ trapping and stabilisation on these surfaces was questioned. This observation was attributed to the unfavoured structure of the adsorbed H_2O, being either in its undissociated form on the (1 0 1) surface or forming two H-bonded -OH groups after dissociation on the (0 0 1). In the latter case, the hole localisation at the -OH resulted specifically in the breaking of the -OH·····OH- bond and destabilization of the system [69].

However, there seems to be no consensus between different studies about the possibility of such H_2O-assisted hole trapping at the anatase surfaces. For example, the above-mentioned work by Chen and co-workers has shown that after the proton transfer, localisation of h^+ at the surface -OH is possible on the (1 0 1) plane [68]. Moreover, the study by Zhang and co-workers have showed that h^+ trapping can occur at the H_2O molecule H-bonded to the -OH group at the (0 0 1) [71]. Schematic visualisation of the different h^+ trapped states discussed in these works is presented in Figure 3.5.

Despite differences in a detailed picture, all of these studies agree that the final state of the water-trapped hole involves hydrogen bonding with a surrounding species. Since this problem will depend on the exact number of H_2O molecules present in the system, some differences between the studies are not unexpected, and the formulation of the general conclusions might be seen as a challenging problem. It is also noteworthy that Setvin and co-workers observed that the hydroxyls generated via reactions (4-9) are negatively charged (basic hydroxyls) and therefore might act as better h^+ trapping centres [67]. This suggestion is also in accordance with the recent work by Hwang and co-workers, who observed that a noticeable amount of the free ·OH, generated by the anatase photocatalyst, is formed from the dissolved O_2 [72]. Although in this study, the authors used a photocatalyst that exposed a variety of very different crystal facets (anatase phase separated from the commercial TiO_2 P25 [73]), the {1 0 1} facets are also present in this case, and the overall discussion matches the mechanism that could be suggested from reactions (4-9), followed by oxidation of the generated -OH to ·OH.

Compared to the (1 0 1) and (0 0 1), the (1 0 0) surface is not studied to the same extent. Especially, the detailed interactions between the charge carriers and O_2/H_2O are far less investigated. Nevertheless, it was shown by Wahab and co-workers that H_2O should adsorb dissociatively on the (1 0 0), forming two hydroxyl groups at the surface, similar to the (0 0 1) one [74]. However, in the case of (1 0 0) surface, the formed -OH are not bonded to each other via a hydrogen bond, and one of them forms an H-bond with a neighbouring 3c-O instead. Furthermore, they also observed that O_2 adsorption is generally favourable on the (1 0 0) surface, with the preferred structure adopting peroxo geometry on the
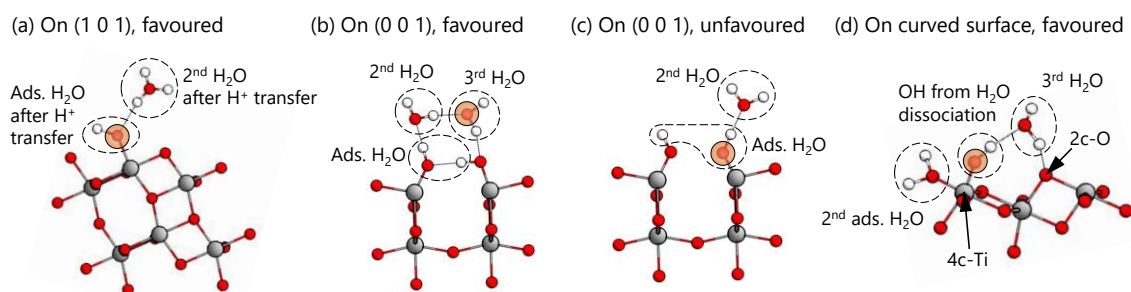
Figure 3.5. Schematic representation of the different h^+ trapped states at the (0 0 1) and (1 0 1) anatase surfaces, as discussed in the existing studies including possible interaction with surrounding H_2O/OH species: (a) according to Chen and co-workers [68]; (b) according to Zhang and co-workers [71]; (c) and (d) according to Shirai and co-workers [69]. Grey, red and white spheres are Ti, O and H atoms, respectively. The preferred trapping site is marked with an orange circle, without highlighting possible delocalisation. Thin, black lines between atoms are H-bonds, and dashed lines outline species originating from the environment.

surface 5c-Ti atom [74]. The same configuration of oxygen adsorption was reported by Bonapasta and Filippone, who have shown that such species are strong electron acceptors and will easily react with photogenerated electrons to form $\cdot O_2^-$ radicals [75]. However, they noted that on the perfect (1 0 0) surface, these $\cdot O_2^-$ radicals are tightly bound to the surface atoms and their possible release to the environment should be limited as long as no oxygen vacancies are present.

3.4. STABILISATION AND GROWTH OF THE LOW INDEX ANATASE FACETS

According to general thermodynamics, any growing crystal will tend to minimize its surface energy to achieve the energy minimum of the whole system. Therefore, some of the crystal planes are energetically more preferred to be exposed, while some might not form in the prepared sample. To predict such low-energy, equilibrium crystal shape, the so-called Wulff construction might be analysed based on the known values of surface energies and orientation of the specific crystal planes [76], [77]. Focusing on the anatase TiO_2, its Wulff construction predicts almost complete exposition of the {1 0 1} facets, with only a minority of the {0 0 1} exposed at the top/bottom of the crystal (~5% of the surface [50]). In this regard, the dominant exposition of facets other than {1 0 1} requires additional stabilisation by the environment.

The first thing to consider for possible stabilisation of the different facets might be their termination with O/H moieties, which should be present in most real situations. Such effect was studied in detail in the work by Barnard, Zapol and Curtiss, where they analysed different TiO_2 surfaces covered with a monolayer of hydrogens, hydroxyls and/or water molecules, as a representative case of crystal termination in the acidic and basic conditions [78]. Notably, they showed that the {1 0 1} achieve their highest stability when covered with hydrogens (H atoms adsorbed on every undercoordinated O and Ti), and their dominant exposition is changed only in the oxygenated conditions, where all 5c-Ti atoms are capped with a single O, as representative of a highly basic environment [78]. Under such conditions, {1 0 0} became the most stable, as shown in Figure 3.6.

The results presented by Barnard, Zapol and Curtiss explain experimentally observed formation of the {1 0 0} exposing particles, prepared using concentrated NaOH solutions [79], [80]. During such process, existing TiO_2 powder is firstly etched with NaOH to form corresponding sodium titanate, which is then rebuilt to the TiO_2 in the second reaction in H_2O. During this second reaction, Na atoms are released from the titanate structure, leading to TiO_2 growth in basic conditions, which indeed results in the increased exposition of the {1 0 0} facets. Noteworthy, high exposition of the {1 0 0} facets was also reported to form in the early stage of anatase growth from the aqueous solution of the $TiOSO_4 \cdot xH_2O$ in the presence of HF [81]. However, details of their stabilisation were not discussed. Furthermore, a similar preparation route based on the titanate treatment is commonly used to obtain nanocrystals with high {1 0 1} exposition. However, in such a case, KOH is used instead of NaOH. As shown by Amano and co-workers, hydrothermal treatment of analogical potassium titanate resulted in the formation of a product consisting of 70% of
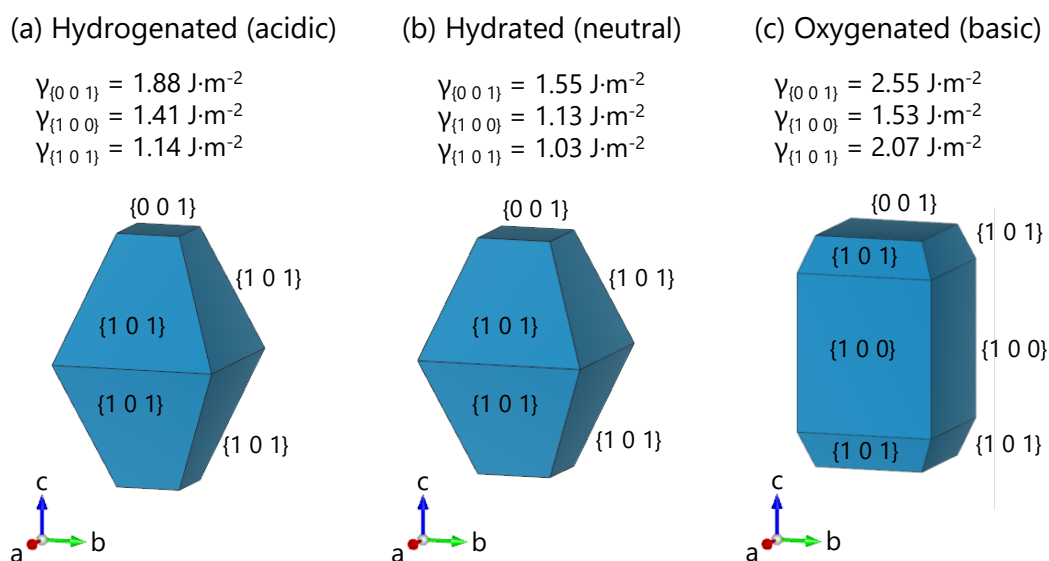
(a) Hydrogenated (acidic)	(b) Hydrated (neutral)	(c) Oxygenated (basic)
$\gamma_{\{0\,0\,1\}} = 1.88\ J \cdot m^{-2}$	$\gamma_{\{0\,0\,1\}} = 1.55\ J \cdot m^{-2}$	$\gamma_{\{0\,0\,1\}} = 2.55\ J \cdot m^{-2}$
$\gamma_{\{1\,0\,0\}} = 1.41\ J \cdot m^{-2}$	$\gamma_{\{1\,0\,0\}} = 1.13\ J \cdot m^{-2}$	$\gamma_{\{1\,0\,0\}} = 1.53\ J \cdot m^{-2}$
$\gamma_{\{1\,0\,1\}} = 1.14\ J \cdot m^{-2}$	$\gamma_{\{1\,0\,1\}} = 1.03\ J \cdot m^{-2}$	$\gamma_{\{1\,0\,1\}} = 2.07\ J \cdot m^{-2}$

Figure 3.6. Surface energies of different anatase facets and corresponding equilibrium crystal shapes, resulting from the adsorption of different H/O species, as reported by Barnard, Zapol and Curtiss [78]. Panels (a), (b) and (c) correspond to the hydrogenated, hydrated and oxyganated surfaces, as a representation of either acidic, neutral or basic environment, respectively.

the anatase octahedrons with the almost complete exposition of the {1 0 1} facets [82]. Further works by Wei and co-workers, as well as Li and co-workers, have shown that increased control over the final morphology can be achieved by exchanging K^+ ions within the titanate structure with H^+ or NH_4^+, ultrasonication and introduction of additional capping agents [83], [84].

Another preparation route to achieve dominant exposition of the {1 0 1} facets was reported by Gai and co-workers from the $Ti(SO_4)_2$ solution, using $N_2H_4 \cdot H_2O$ as the morphology-controlling agent [85]. Due to the reducing character of hydrazine, this is in accordance with the predicted {1 0 1} stability after the hydrogenation of the surface [78]. However, other ammonium-bearing compounds, as well as chloride presence, were also reported to increase {1 0 1} exposition. Gordon and co-workers have observed competition between the {1 0 1} and {0 0 1} exposition during the non-aqueous synthesis as the result of the introduced Ti precursor (TiF_4 vs. $TiCl_4$) and the organic capping agents with either -OH or $-NH_2$ moieties present [86]. Following their results, preferred exposition of the {1 0 1} over the {0 0 1} show order of $TiCl_4+R-OH \approx TiCl_4+TiF_4+R-NH_2 > TiF_4+R-NH_2 > TiF_4+TiCl_4+R-OH > TiF_4+R-OH$. Noteworthy, a combination of TiF_4 with $R-NH_2$ resulted in the formation of nanoparticles with the brookite crystal structure.

Focusing on the {0 0 1} facets, their energetic stabilisation can be achieved due to fluorine adsorption. This was shown in detail by Yang and co-workers, who have predicted and proved increased stability of the {0 0 1} facets prepared in the presence of hydrofluoric acid [58]. Specifically, they observed that F adsorption on the 5c-Ti atoms present at the (0 0 1) and (1 0 1) surfaces leads to the higher stability of the (0 0 1) over the (1 0 1), heavily affecting the equilibrium crystal shape. Based on their results, the formation of the anatase nanosheets with {0 0 1} exposition of almost 100% was predicted as possible to achieve.

However, their experimentally obtained single crystals, prepared from the HCl-stabilised, aqueous solution of TiF₄ and HF, showed a maximum {0 0 1} exposition of approximately 50% [58]. Furthermore, Yang and co-workers achieved higher {0 0 1} exposition by the addition of alcohol molecules as co-stabilising agents [87], also in accordance with the above-mentioned work by Gordon and co-workers [86]. Ultimately, various authors have reported the formation of anatase plates with the {0 0 1} presence of over 90%, when prepared in the presence of HF in an alcohol solution instead of water [88]–[90]. Noteworthy, the exposition of the {0 0 1} facets is sometimes expressed as the truncation ratio, where the length of the top edge of the crystal is compared to the middle one. This is schematically presented in Figure 3.7., together with the exemplary images of the real samples obtained during further works and approximated expositions of the {0 0 1} facets.

A few alternative strategies to stabilize the {0 0 1} facets, which do not include fluorine-bearing compounds, were also reported in the literature. For example, Hen and co-workers have reported {0 0 1} stabilization due to urea/CO₃²⁻ adsorption, resulting in their
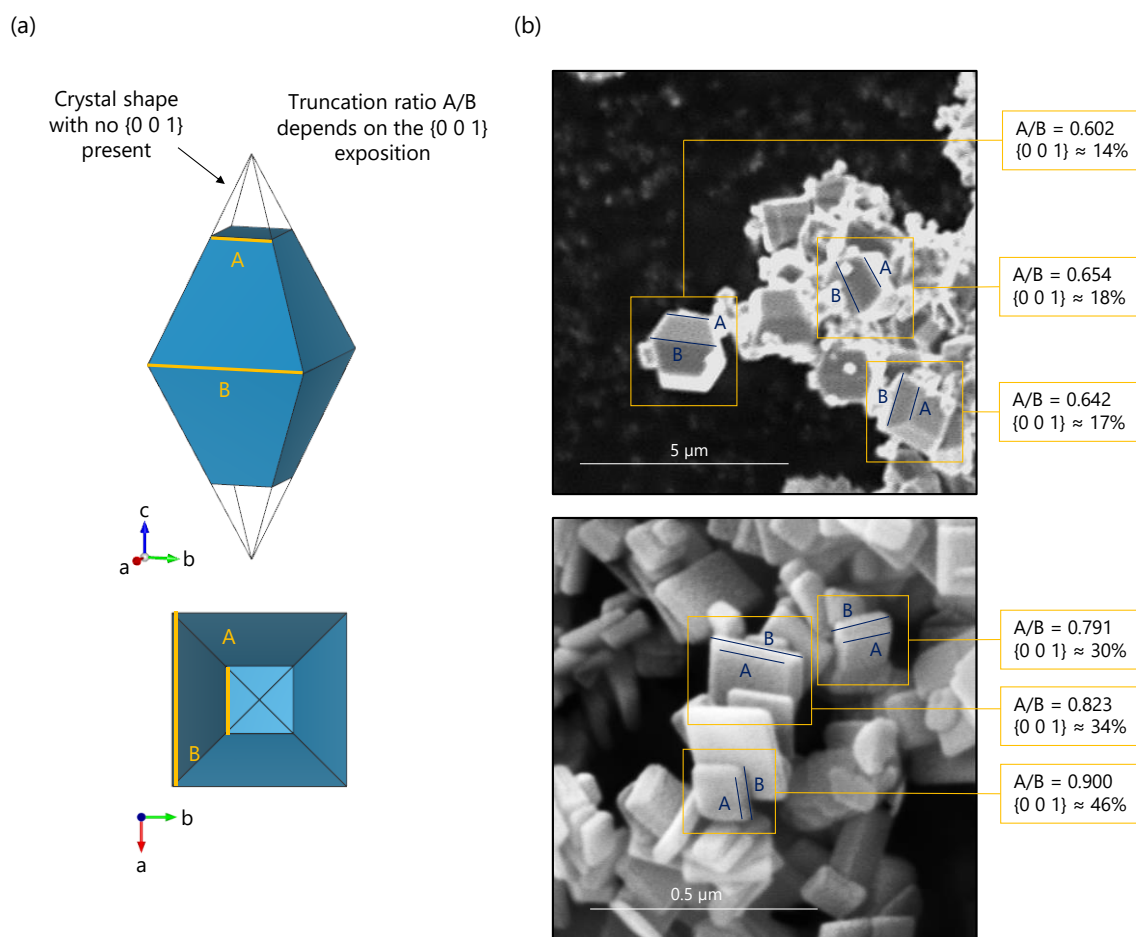
Figure 3.7. Scheme of the truncation of the anatase crystal (a), used to represent competition between the {0 0 1} and {1 0 1} exposition, defined as the ratio between its top and middle lengths; together with the exemplary scanning electron microscope images of the actual samples with different truncation levels (b). Exposition of the {0 0 1} facets is than calculated assuming perfect symmetry of the particle, basing on the known orientation between the (0 0 1) and (1 0 1) crystal planes.

Page | 32

exposition of over 90% [91]. Chen and co-workers have also achieved high {0 0 1} exposition as the result of hydrothermal growth from titanium n-butoxide (TBT), when TBT was dissolved in the organic phase deposited over the HCl-rich aqueous solution, and the reaction was performed without mixing both phases [92]. Relatively high exposition of the {0 0 1} facets was also achieved by Janczarek, Kowalska and Ohtani as the result of $TiCl_4$ oxidation with O_2 in the coaxial-flow gas phase reactor [93]. However, the detailed mechanism of their stabilisation was not discussed.

Following described strategies to stabilize the low index anatase facets, it is worth highlighting that the preparation route also needs to provide a suitable timeframe for the growth of the stabilised structure. It connects with the low solubility of the anatase structures in most solvents, especially in neutral conditions, which leads to a situation where most of the used Ti precursors form TiO_2 nuclei very quickly. Under such conditions, the control over their growth and final morphology is significantly reduced. Ultimately, in the simple aqueous or alcohol environment, condensation of the compounds such as $TiCl_4$, $TiOSO_4$ or TBT commonly results in the formation of ultrafine TiO_2 particles; without well-defined morphology and often with low crystallinity [94]–[97].

This problem of fast TiO_2 nucleation is usually dealt with using the dissolution-recrystallization processes, where nucleated seeds can be partially dissolved and dynamically recrystallised into the refined structure. Therefore, as the reaction time is increased, systematic growth of the particles can be observed [58], [98], with the most stable structures adopting minimum-energy equilibrium shape. Interestingly, HF is a good compound for TiO_2 dissolution, since very strong interactions between the F and Ti enable the exchange of O atoms within the TiO_6 octahedra of the anatase crystal structure [58]. In this regard, many different F-bearing compounds can be effectively used for stimulating TiO_2 growth, as most of them will either form some amount of equilibrium HF or will possibly bond to the Ti via available F atom. The scheme of such HF-assisted dissolution-recrystallisation process of the TiO_2 is presented in Figure 3.8.

However, strong Ti-F interactions might also lead to a low yield of the reaction and partial destruction of the growing particles. For example, Wang and co-workers have observed that together with increasing the initial TiF_4 concentration, the {0 0 1} facets of the prepared microcrystals became selectively etched during the reaction, while the {1 0 1} ones were stable [99]. This phenomenon was explained based on the preferable formation of the $TiOF_2$-like structure on the completely fluorinated (0 0 1) surface, which was further easily detached from the crystal structure after additional action of HF molecules. The same process was not favoured on the (1 0 1) surface. Indeed, the presence of the metastable cubic $TiOF_2$ phase was also observed as the intermediate product of TiF_4 hydrolysis in the presence of n-butanol, where only increased temperature and/or reaction time completed the further transformation to anatase [88], [100]. This observation correlates well with the F^- effect on the stability of the {0 0 1} facets, since the (1 0 0) plane of the $TiOF_2$ possesses a structure analogical to the (0 0 1) plane of anatase. In this regard, an easy transformation between the $TiOF_2$ structure and the {0 0 1} anatase facets might be seen as both the source
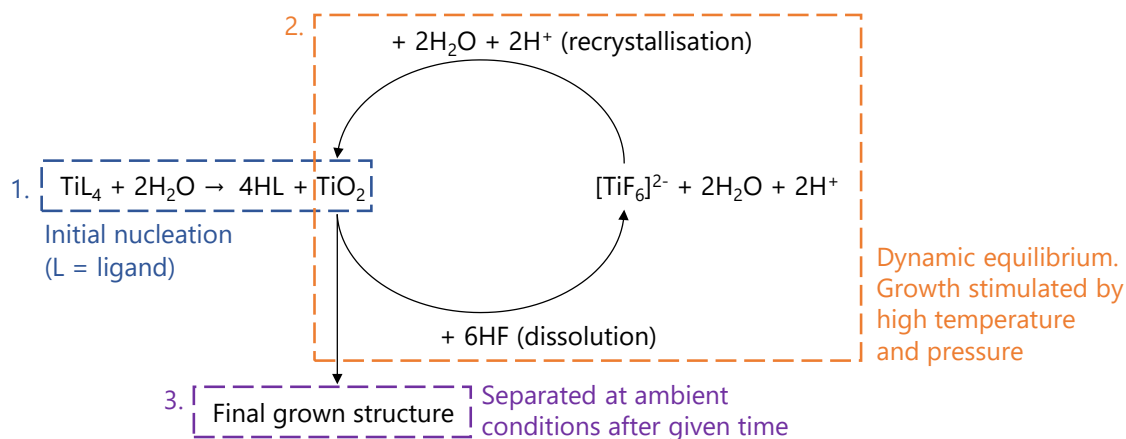
Figure 3.8. Scheme of the initial nucleation of the hypothetical TiL_4 compound (L = ligand) to TiO_2, and further dissolution-recrystallisation process in the presence of HF, as commonly used during the hydrothermal/solvothermal reactions. Please note that $[TiF_6]^{2-}$ anion is presented only schematically, and in the real solutions mixed-ligand anions are commonly observed [94], [128].

of the preferred {0 0 1} exposition, as well as the source of their selective degradation, depending on the environment details. Schematic visualisation of these transformations is shown in Figure 3.9.

On the other hand, utilization of the Ti-precursors that transform slower into TiO_2 can also be used to obtain well-faceted products. For example, during the $TiO_2 \rightarrow$ titanate $\rightarrow TiO_2$ route, the transformation between both phases depends on the K^+/Na^+ insertion and withdrawal from the crystal structure [101], rather than its condensation from the solution. Therefore, the additional presence of an aggressive environment, like HF, is not needed in this case. Other solid precursors of Ti were also used by various authors, including metallic
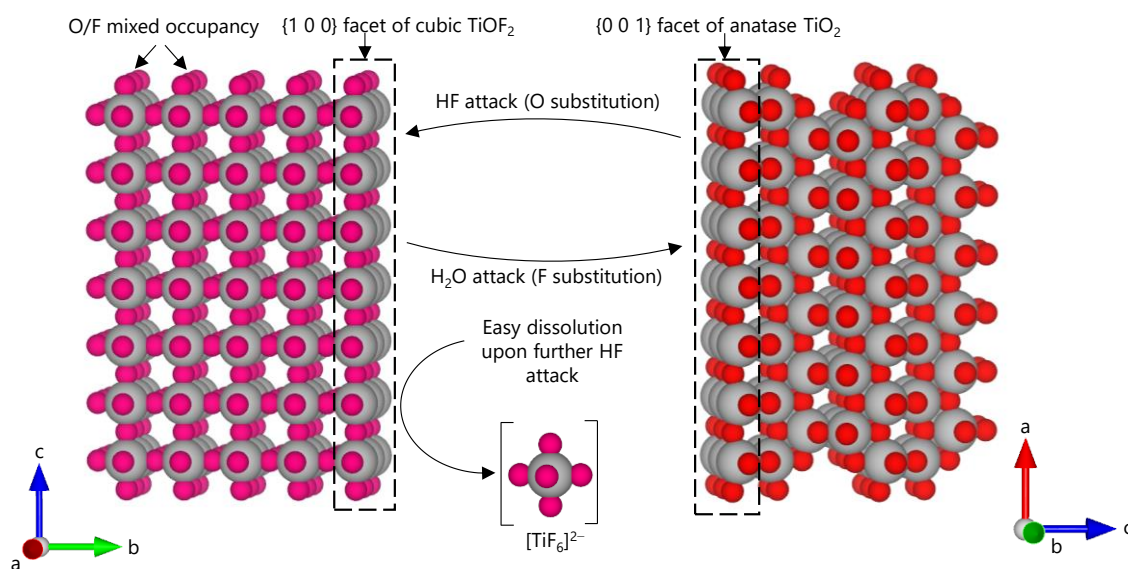
Figure 3.9. Scheme of the possible transformation between the cubic $TiOF_2$ structure and {0 0 1} crystal facet of anatase TiO_2, promoted by geometrical similarities between the exposed crystal planes. Similar configuration the exposed $Ti(O_XF_{6-X})$ octahedra in both phases might also promote selective etching of the anatase {0 0 1} facet for higher HF concentration [99]. The magenta spheres in the $TiOF_2$ structure show equivalent sites with mixed occupancy (0.66 of O and 0.33 of F).

Ti, TiSi$_2$, TiB$_2$ and Ti$_3$C$_2$ [102]–[105], however, it is noteworthy that in many of these cases, HF is still used to promote efficient transformation of such compounds to TiO$_2$, due to their high stability. Furthermore, obtained titanium oxyfluoride might also be used as the solid-state precursor of the TiO$_2$. For example, as shown by Xie and co-workers, simple calcination of the TiOF$_2$ cubes is enough to obtain anatase plates with well-defined {0 0 1} facets, without the need to introduce any solvents [106]. Similarly, Hu and co-workers have used NH$_4$TiOF$_3$ as the analogical substrate during calcination [107]. Finally, Gordon and co-workers used a seeded approach order to obtain a set of faceted TiO$_2$ nanocrystals [86]. During their work, they did not introduce additional solvent to etch obtained TiO$_2$ nuclei, but instead used them as the seeds for further crystallization under continuous addition of the Ti-containing solution. Such an approach allowed them to obtain ultrafine, monodisperse TiO$_2$ nanocrystals with various facet exposition, however, compared to other methods, it remains relatively complex.

Ultimately, the information stressed in this part underlines the most important aspects of the stabilisation and growth of the anatase crystals with low index facets exposed. Specifically, thermodynamic and kinetic considerations are highlighted as necessary to achieve well-defined morphology of the final particles. However, as the final note, it is worth mentioning that in many cases, the actual role of the specific compound might be more complex than the simple facet-stabilising effect or etching agent. For example, HF stabilise the {0 0 1} facets, etch the TiO$_2$ structure, and in some studies, it is also mentioned to hinder its nucleation. However, compared to the HF, detailed interactions between Ti and a variety of other compounds used during the preparation routes are not investigated to the same extent. In this regard, presented information should not be seen as a systematic description of all possible interactions and mechanisms involved in such processes but rather a summation of the existing strategies and differences between them, as shown schematically in Figure 3.10.
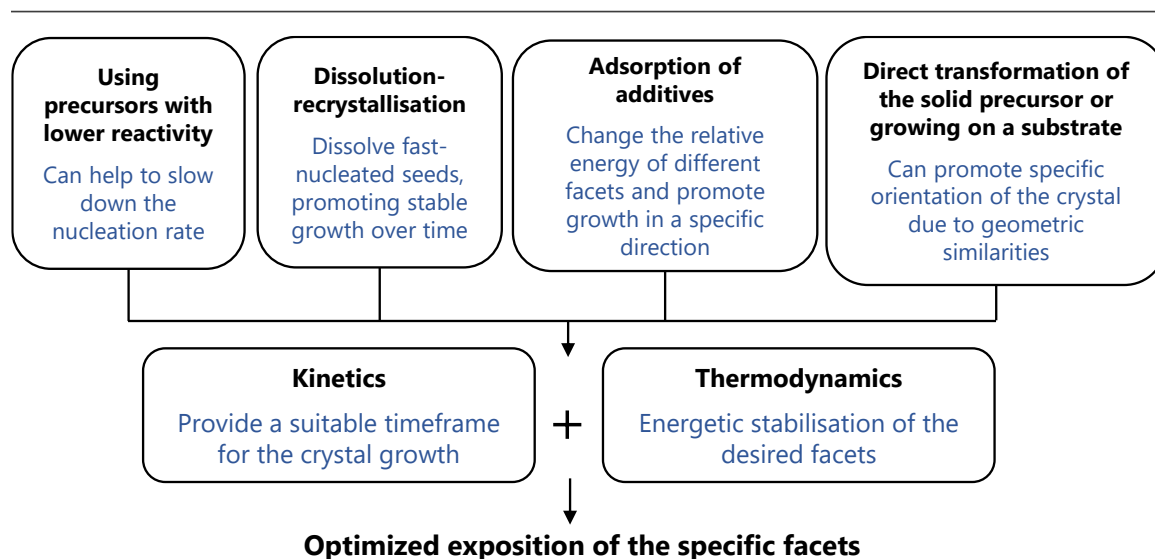

Figure 3.10. Summary of the most important aspects and strategies used for the preparation of faceted TiO$_2$ nanostructures. Reproduced from [52] under the Creative Commons Attribution 3.0 CC BY license.

3.5. KEY FINDINGS ABOUT THE PHOTOCATALYTIC ACTIVITY

Following the progress in the preparation of the faceted anatase particles, numerous authors have studied and discussed their photocatalytic activity. These works can be roughly categorised into 3 main topics: (1) comparison of the particles that expose specific crystal facets in the majority and discussing mechanisms of the process on the specific surface; (2) preparation of the particles that expose two or more different crystal facets and optimizing their presence for a specific reaction; and (3) studying interactions between the facets and introduced surface modifications (e.g. defects, single atoms, molecules, clusters, particles).

Focusing on the straightforward comparison of the different facets and their reactivity, the so-called activity orders were reported in the literature. Interestingly, different orders are commonly observed, depending on the process details. For example, Ye and co-workers have reported photocatalytic activities of the anatase nanoparticles with ≥90% exposition of either {0 0 1}, {1 0 0} or {1 0 1} facets, including rhodamine B degradation, generation of reactive oxygen species ($\cdot O_2^-$ and $\cdot OH$), as well as CO_2 photoreduction to CH_4 [80]. They observed that the {0 0 1} exposing particles, prepared from potassium titanate with $(NH_4)_2CO_3$ as the stabilising agent, revealed the highest activity towards the generation of both radicals and degradation of rhodamine B. On the other hand, particles exposing the majority of the {1 0 0} facets were found to be the most active towards CO_2 reduction. Similar, high activity of the {1 0 0} facets towards CO_2 reduction was also reported by other authors [14], [108]. On the other hand, focusing on the ROS generation and degradation of organic compounds, the described results of Ye and co-workers stand in some conflict with other studies. For example, multiple works have highlighted the efficient generation of the $\cdot OH$ radicals by the {1 0 0} facets, based on the oxidation of the terephthalic acid (TPA) as a probe molecule [79], [81], [109]. However, this high activity of the {1 0 0} facets towards $\cdot OH$ generation is not followed by reports showing efficient degradation of different organic compounds. For example, the work by Günnemann and co-workers reported that although the (1 0 0) surface, cut from the single crystal, showed the highest $\cdot OH$ generation in the TPA presence, its activity in the methanol oxidation was approximately two times lower than that of (1 0 1) and (0 0 1) [109]. In this regard, the preferred applicability of the {1 0 0} exposing particles towards water treatment is not obvious.

Furthermore, focusing on the {1 0 1} comparison with {0 0 1} during the oxidation/degradation reactions, different conclusions were also reported by various authors. In the above-mentioned work, Günnemann and co-workers reported that (1 0 1) is more active towards both $\cdot OH$ generation (TPA-based) and methanol oxidation [109]. This is in contrast to the works by Ye and co-workers but is in line with the results by Pan and co-workers [81], as well as Mino and co-workers, who have shown higher phenol removal over the {1 0 1} facets than {0 0 1} [110]. On the other hand, Wu and co-workers have shown that for anatase single crystals with similar sizes, an increase of the {0 0 1} content leads to a higher activity towards methylene blue removal [102]. Finally, Lu and

co-workers have also shown that {0 0 1} exposing particles perform better in both water oxidation and phenol degradation when used as a photoanode [111].

Noteworthy, these differences observed between different oxidation/degradation reactions might result from the experimental details. First of all, oxidation of alcohols in the presence of TiO_2 is known to occur also due to the direct h^+ transfer to the alcohol molecule [112], which is different from the reaction with *a priori* generated ·OH. Similarly, the degradation of colourful compounds, like methylene blue, might also involve the reactivity of the dye itself rather than the photocatalyst [113], [114]. Moreover, in the case of the TPA oxidation as the probe to detect generated ·OH, it is mostly performed in the basic environment to enhance its dissolution. As highlighted in the previous parts, possible h^+ localisation in the aqueous environment strongly depends on the electron density of the surface species. Therefore, the introduction of the basic conditions might lead to different results than e.g. in a neutral or acidic environment, simply due to the enhanced adsorption of the negatively charged OH^- ions. Noteworthy, the study by Zhou and co-workers has shown that the preferred oxidation/reduction of Mn and Fe species over the {0 0 1} and {1 0 1} facets might even change, depending on the pH [115].

Finally, the actual exposition of the discussed surfaces can change quite visibly, and co-exposition of the multiple facets might also influence the results. This is due to the known separation of the generated charge carriers, which can occur when multiple facets with different electronic structures are exposed. Right now, the authors have studied such a problem and reported that a specific ratio between exposed facets allows for optimisation of the efficiency during different photocatalytic reactions. For example, Yu and co-workers have shown maximum CO_2 conversion to CH_4 when {0 0 1}/{1 0 1} exposition ratio was ~58/42% [116]. Analogical results were also presented by Cao and co-workers [117]. Furthermore, Zhao and co-workers have shown that co-exposition of the {0 0 1} and {1 0 0} facets in the form of anatase cuboids allowed to achieve significantly higher TPA oxidation rate, compared to the particles with dominant {0 0 1} exposition and P25 standard [118]. However, it can be noted that in this case, overall results did not include particles with a majority of the {1 0 0} facets, which show high activity towards TPA oxidation on their own, as highlighted earlier. Ultimately, the work of Roy, Sohn and Pradhan have shown that co-exposition of all three low index facets with a similar share in the surface area achieved a maximum degradation rate of methyl orange [119] (the highest variance within the prepared samples, between the 0-32% , was observed in the {1 0 1} presence and the lowest one, between 35-42%, for the {0 0 1}).

Based on these exemplary studies, it can be noticed that co-exposition of different crystal facets might be a promising strategy for increasing photocatalytic activity. This is reasonably connected with the possible e^-/h^+ separation between different surfaces, which should decrease recombination of the photogenerated charge carriers.

In this regard, the effect is similar to the surface modification with co-catalysts and formation of junctions, which are long-time used strategies to achieve an analogical effect. In fact, combining both the exposition of specific facets and their further modification

might be considered the state-of-the-art approach to the complex problem of photocatalyst design. First, suitable selection of the exposed facets and surface species should straightforwardly promote separation and "withdrawal" of the charge carriers from the bulk structure [41], as shown schematically in Figure 3.11. Therefore, their lifetime and resulting efficiency might be increased. However, it should be noted that in such a case, charge transfer to modifying species might completely change the mechanism of reaction since their physicochemical properties can be significantly different from the photocatalyst itself. For example, it is known that the deposition of different co-catalysts on the TiO_2 surface can promote either holes or electrons separation, therefore changing their potential [120].

In this regard, considerable attention has been recently focused on studying interactions between the different facets and other materials, including either the dominant exposition of a selected facet or the co-exposition of multiple ones. For example, Mao and co-workers reported that deposition of Pt co-catalyst shows a different effect on the CO_2 reduction ability of the anatase nanoparticles exposing either {1 0 0} or {0 0 1} facets in the majority [108]. Specifically, they observed that after the modification with 1% wt. of Pt, {0 0 1} exposing nanoplates achieved almost 50% higher efficiency than the {1 0 0} rods (~0.045 $\mu mol \cdot g^{-1} \cdot m^{-2}$ of CH_4 production over the {1 0 0} vs. ~0.085 $\mu mol \cdot g^{-1} \cdot m^{-2}$ over the {0 0 1}), which was opposite than before the Pt loading (~0.105 $\mu mol \cdot g^{-1} \cdot m^{-2}$ vs. ~0.035 $\mu mol \cdot g^{-1} \cdot m^{-2}$ respectively). Therefore, the Pt presence has exactly the opposite effect on the activity of both facets. It was explained based on the specific structure and electronic properties of the facets itself, as well as differences in Pt dispersion on both surfaces. Interestingly, it can be noted that the highest activity (after surface normalisation) was observed for the unmodified {1 0 0}, which agrees with other studies showing their
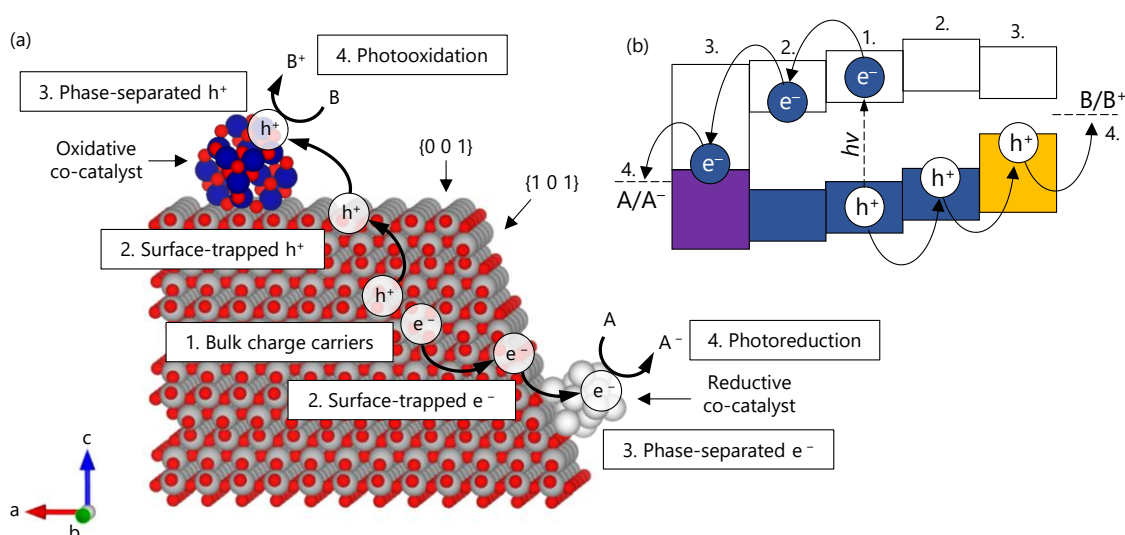
Figure 3.11. Scheme of the charge carriers separation between the co-exposed {0 0 1} and {1 0 1} facets, followed by transfer to selecteviely deposited co-catalysts and subsequent reactions (a); as well as associated energy chages of both h+ and e− (b). In panel b, electronic structure of the reductive co-catalyst is assumed to be metallic, with a contineous distribution of states filled up to the hypothetical Fermi level.

preference for CO_2 reduction, as mentioned before. In this regard, the modification strategy of the {1 0 0} facets for CO_2 reduction is not obvious at the moment.

On the other hand, photocatalytic generation of H_2 over TiO_2 generally requires modification of its surface with co-catalysts, due to the relatively low activity of the TiO_2 itself. In this regard, interactions between anatase facets and different co-catalysts are commonly studied. Concerning the simple case of the dominant exposition, various authors have compared their activity. Interestingly, performance seems to vary between the studies. For example, when modified with 1% wt. Pt, the {1 0 1} facets were reported as more active for H_2 generation from methanol/water solution than {0 0 1}, [86]. Similar conclusions were also presented by Wang and co-workers (ethanol/water, modified with Mo_XC [121]) and Liu and co-workers (methanol/water, modified with graphene [122]), however, in the later, the overall highest activity was observed for the sample exposing {1 0 0} facets. On the other hand, the results presented by Wei and co-workers have shown the opposite trend, with {0 0 1} achieving up to ~10 times higher H_2 evolution rate from water/methanol than {1 0 1}, when modified with both Pt, Au and their bi-metallic combinations [123]. Analogically, Liu and co-workers have shown higher activity of the {0 0 1} facets over both {1 0 0} and {1 0 1}, when modified with CuO_X (methanol/water [124]). Interestingly, it can be noted that in the case when {1 0 1} achieves visibly higher efficiency, prepared samples show the visible presence of excess electrons in their structure, which was not observed to the same extent in other studies. Therefore, different concentrations of defects might be possible sources of variation between these studies and their presence seems beneficial for the activity of the {1 0 1}.

Following studies with a dominant presence of a selected facet, the co-exposition of multiple ones seems to be a general strategy for improving H_2 generation. For example, Wei and co-workers compared the performance of the {1 0 1} exposing octahedrons with the {0 0 1}/{1 0 1} co-exposing decahedral anatase particles, after modification with either Cu, Ag or Au [60]. As presented, co-exposition of both facets allowed to achieve similar (Au) or 2-times better performance (Cu), despite the surface area of the TiO_2 particles being almost 10 times lower than in the case of the {1 0 1} octahedrons. Among others, this was attributed to the efficient charge separation between the {0 0 1} and {1 0 1} facets, as evidenced by time-resolved microwave conductivity measurements. Analogically, Zhang and co-workers have shown optimized {0 0 1}/{1 0 1} junction for H_2 evolution when modified with Pt [125]. Furthermore, as shown by Meng and co-workers, selective modification of the {0 0 1} with Co_3O_4 and {1 0 1} with Pt allowed to further boost H_2 production, compared to the single co-catalyst, as well as samples with a random distribution of either cobalt oxide or platinum [126]. Specifically, this work might be seen as a straightforward application of the strategy presented previously in Figure 3.11. Analogical structure of {0 0 1}-MnO_X/{1 0 1}-Pt was also proposed for CO_2 reduction [127].

4. RESEARCH GOALS

Summarising, the exposition of the different crystal facets significantly affects the photocatalytic activity of TiO_2, due to the differences in their geometries, energies and electronic properties. However, based on the presented literature overview, numerous white spots are still present within the existing information. Specifically, there seems to be no consensus about the most suitable crystal facet(s) for the degradation of organic pollutants. Furthermore, this problem is even more underexplored when taking into consideration different structures of the possible pollutants, their degradation pathways, mineralisation and generation of different reactive species under irradiation. Therefore, it is challenging to decide if crystal facet engineering is a suitable approach for optimizing TiO_2 activity for such reactions as well as to what extent conclusions from some studies could be generalised for different organic pollutants.

In this regard, systematic studies were planned within the PhD work in order to investigate in detail the effect of different crystal facets of anatase TiO_2 exposition on the efficiency of photocatalytic degradation of selected persistent organic pollutants in water. Specifically, the main focus was directed at the exposition of low index anatase facets and analysing their application for the degradation of aromatic pollutants; with phenol acting as the model pollutant and followed by other environmentally relevant compounds. The specific problems, such as:

i. Determination which crystal facets are the most suitable for the degradation of organic compounds (Is there any? Does it depend on the pollutant type?),

ii. Investigation of the relation between exposed crystal facet and possible degradation pathway and mineralisation efficiency (Does the degradation pathway depend on the exposed facet? Does mineralisation correlate with the degradation efficiency of the parent compound or some observed by-products?),

iii. Finding factors that might be seen as the most decisive for a particular facet-pollutant combination and establishing a specific relation between them and observed degradation rate (What determines the activity of the specific facet and what is the contribution of the pollutant electronic structure? Is it possible to find such dominant factors?),

iv. Investigation of the interactions between different faceted TiO_2 nanoparticles and ferrimagnetic semiconductor when combined as a composite (Are these interactions the same or differ, depending on the exposed crystal facet? Can the magnetic properties of the second phase significantly affect observed degradation rate?),

v. Investigation interactions between introduced dopants (point defects) and exposed crystal facets (Is the effect of the same dopant always the same,

indecently on the exposed facet? Can we optimize reaction rate by introducing specific species to the TiO_2 lattice?),

are all underexplored in the existing studies and were especially important for the planned works. Noteworthy, the main aim of this work is not connected strictly with the fundamental studies of the possible anatase crystal facets, which to a great extent have already been reported, but rather to create a link between their basic information and actual performance observed during the photocatalytic water treatment.

Following identified white spots and raised questions, the hypotheses can be presented, either based on the straightforward analyses of the existing studies or as a result of the progressing works. The most important of these hypotheses might be formulated as:

H1. Alternation of the exposed crystal facet will significantly affect the observed efficiency of the pollutant degradation over anatase TiO_2,

H2. Efficient degradation will lead to proportionally efficient mineralisation, measured as total organic carbon removal,

H3. Different exposed facets will lead to different degradation pathways of the same pollutant,

H4. There is a specific feature of the analysed facets that might be seen as decisive for the efficiency of the water treatment process and a specific relation between them might be established,

H5. Different facets will achieve higher degradation/mineralisation, depending on the structure and properties of the pollutant,

H6. When combined as a composite, interactions between TiO_2 and other materials might have a different effect on activity, depending on the exposed crystal facet,

H7. Different exposed facets will react differently to the same point defects and the associated change in the density of charge carriers at the ground state,

H8. The same exposed crystal facet will achieve maximum activity for a different ground state density of charge carriers (connected with point defects), depending on the investigated reaction.

Ultimately, a specific workplan was designed to systematically investigate possible effects. As presented schematically in Figure 4.1., the research issues of the PhD dissertation were studied and discussed in detail in a series of 6 directly related publications [P1-P6]. The first study [P1] was aimed at the initial analysis of the possible crystal facet effect on phenol degradation, its pathway and mineralisation, when using particles prepared at relatively similar conditions. This was followed by preparation of the TiO_2 particles with a dominant exposition of either {0 0 1}, {1 0 0} or {1 0 1} facets, which included a detailed study on the growth of the {0 0 1} exposing particles in different alcohol
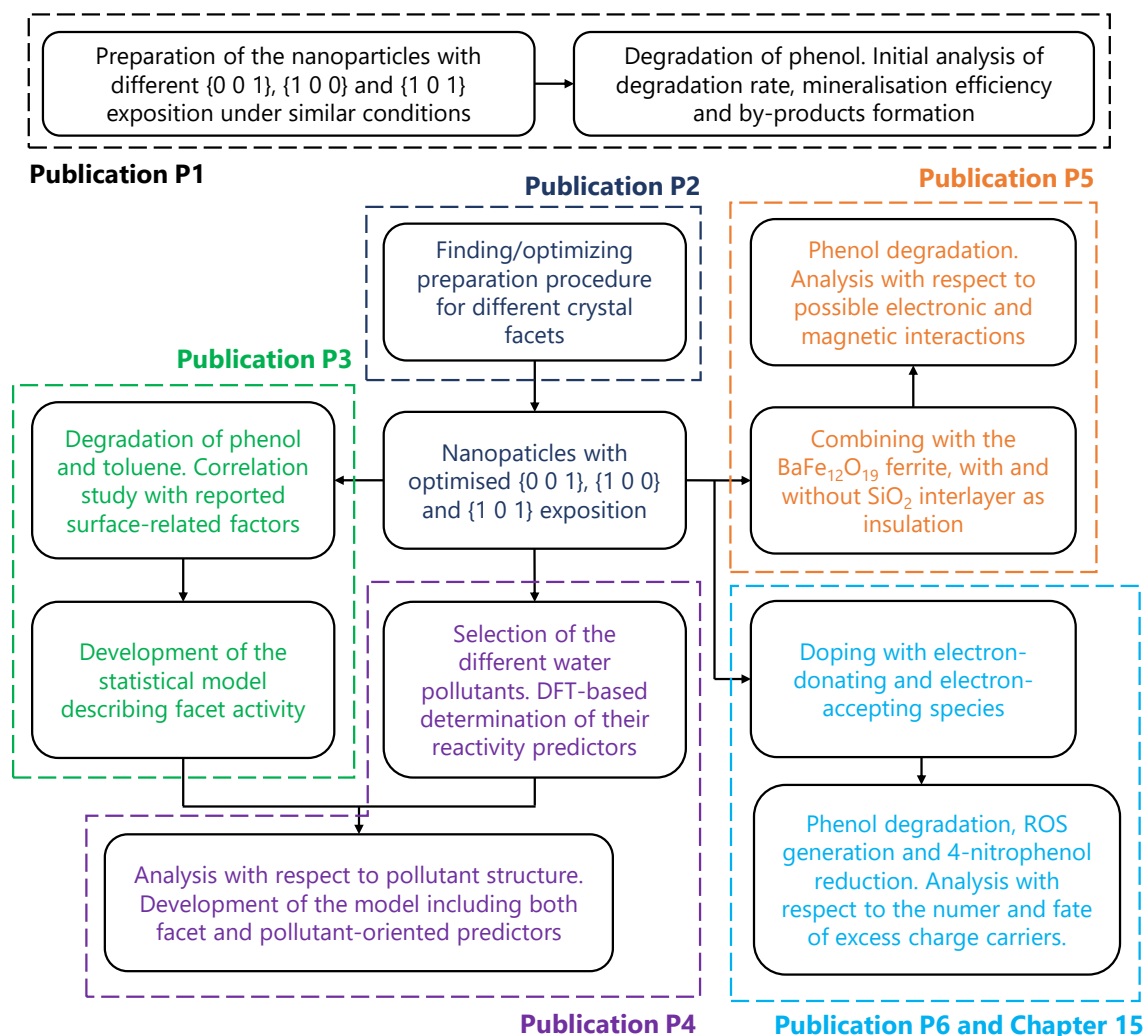
Figure 4.1. Scheme of the perfomed works and problems investigated within the presented PhD thesis. Publication number defined the order of the following chapters.

environment [P2]. Obtained particles with optimised exposition of each facets were further used in studies on identifying the most important factors deciding observed degradation ability, focused either on the facets themselves [P3] or both exposed facets and structure of the pollutant [P4]. Following studies on the unmodified TiO_2, analogical particles were combined with the $BaFe_{12}O_{19}$ to study their performance when combined with other crystal phases, which in this case included both electronic and magnetic interactions [P5]. As the last part of the PhD study, analogical TiO_2 structures were also doped with the Nb^{5+} ions in order to study the effect of excess electrons on the photocatalytic activity, when different crystal facets are exposed. The most important information and findings of these studies [P1-P6] are briefly summarised in the following sections. The detailed publications [P1-P6] are presented at the end, after the references. Finally, chapter 15 describes unpublished results (currently under review), which are a direct continuation of the relations observed in the publication [P6], therefore completing the works associated with the research goals.

EXPERIMENTAL PART

5. PREPARATION OF THE PHOTOCATALYSTS

The photocatalysts were prepared using hydro/solvothermal methods exclusively, with 200 cm^3 Teflon-lined reactors placed in a laboratory oven. Temperature, time, substrates and environment varied depending on the work and designed material. All presented reaction times include heating of the oven, to 210 °C. In the case of the TiO_2 P25 etching with NaOH or KOH solutions in 100 cm^3 reactors was used. After the reaction reactors were taken out and left to cool down naturally. If not stated otherwise, prepared powders were centrifuged, washed with water 3-4 times, dried at 80-90 °C and grounded in agate mortar. The detailed descriptions of the preparation methods are presented in publications [P1-P6].

6. CHARACTERIZATION OF THE PHOTOCATALYSTS

Typical characterization of the prepared materials included analysis of the crystal structure, absorbance spectra, development of the surface area, elemental composition, morphology of the materials, surface composition and chemical states, as well as analysis of the valence band edge.

The crystal structure was analysed based on the powder X-ray diffraction (XRD) measurements, performed using the Rigaku MiniFlex 600 diffractometer with Cu Kα radiation. Qualitative analysis was performed based on the available cards of the standard compounds in the International Centre for Diffraction Data (ICDD) database. Quantitative analysis was made using the reference intensity ratio (RIR) method. Alternatively, if Rietveld refinement of the profile was performed, crystallographic information files (.cif) were obtained from the Crystallography Open Database (COD), and the refinement was made using X'Pert HighScorePlus 2006 software.

Absorption properties of the samples were analysed based on the diffusive reflectance spectroscopy measurements using the Thermo Fisher Scientific Evolution 220 spectrophotometer in the wavelength range between 200-1100 nm (DR-UV/vis). For the reflectance standard, $BaSO_4$ was used throughout the works. Detailed estimation of the bandgap energy was made using the Tauc method, following the exact procedure suggested by Makuła, Pacia and Macyk [19].

Development of the surface area was estimated based on the analysis of the N_2 adsorption isotherm in the temperature of liquid nitrogen, within the range of partial pressures between 0.05 and 0.30 (Brunauer-Emmet-Teller isotherm, BET). Measurements were performed with the Micromeritics Gemini V apparatus. Prior to measurements, samples were degassed in the flow of N_2, either at 200 °C for 2 h or 140 °C for 4 h.

Morphology and elemental composition of the samples were analysed using the scanning electron microscope (SEM), combined with the energy dispersive X-ray electron

spectroscopy (EDS) measurements. Measurements were made using the FEI Quanta FEG 250 microscope, equipped with an Apollo-X SDD spectrometer. The EDS data were obtained as the average over the large, possibly uniform area of the samples using an accelerating voltage of 30 kV with a scanning resolution of 132 eV. The detection level for the analysed elements, except for oxygen, was determined as 0.1 at %. Prior to the observations, samples were coated with a thin layer of Au to help remove excess charge introduced during the analysis. Depending on the study, statistical analysis of the observed nanoparticles' dimensions was made based on at least 100-200 measurements.

The chemical states of the elements on the surface were determined by X-ray photoelectron spectroscopy (XPS) in cooperation with various researchers, depending on the study. In each case, high-resolution spectra were collected and deconvoluted in order to determine the chemical states of the elements. Measurement details, such as the source of radiation, pass energy and the number of scans, varied depending on the equipment. Peak positions were generally corrected by treating carbon signal C 1s = 284.8 eV as the internal standard. Depending on the study, XPS analysis included scanning of the valence band in order to investigate the possible formation of the surface defect states above the band's edge.

7. DENSITY FUNCTIONAL THEORY CALCULATIONS

Depending on the study, experimental results were supported by density functional theory calculations to get better insight into possible explanation of the observed effects. Two types of calculations were performed, either in the periodic systems or for the molecular models. Calculations for molecules were performed using Orca software [128], [129] with hybrid functionals (either PBE0 or B3LYP [130], [131]), combined with possible D3BJ correction [132] and different basis sets, depending on the study. The geometry of each structure was always optimized, which was controlled by the analysis of the vibrational frequencies (no negative frequencies). All Orca calculations included conductor-like polarizable continuum model of solvation (CPMC) to account for possible effects of the water matrix [133].

Calculations in periodic systems were performed with the Quantum Espresso software package [134], [135], using PBE functionals [136] with additional introduction of the Hubbard U parameter to account for the on-site coulombic interactions. Crystal structures of the analysed phases were modelled based on the available .cif files and their geometry was always optimized to the convergence threshold of 10^{-3} Ry·Bohr^{-1} using the BFGS algorithm. For the 3D dimensional crystal structures, optimization included both atom position and cell parameters. For the simulation of the surfaces, 2D slab models were constructed from the optimized structure of the bulk phase and further optimization was performed only for the positions of atoms. For these models, minimum 10 Å of vacuum was added between the repeating surfaces. Further details, including model sizes, surface types, possible defects and number of introduced K-points varied between the studies.

Lastly, different details of the periodic calculations were used in the publication [P3], in cooperation with José R. B. Gomes and José Daniel Gouveia from University of Aveiro.

8. PHOTOCATALYTIC ANALYSES

Majority of the photocatalytic tests were performed using 25 cm^3 reactor, equipped with a cooling jacket, magnetic stirrer, hoses for the sample collection and airflow introduction, as well as a quartz window as the light's entry. The scheme of the reactor is presented in Figure 8.1a. The reactor was irradiated from one side using 300 W xenon lamp with water filter to cut-off IR irradiation, and the light's beam was concentrated at the reactor centre. If not stated otherwise, reactor position was adjusted to achieve maximum UVA flux intensity (I_{Centre}) of 30 ±1 mW·cm^{-2}, controlled using Hamamatsu C9536-1 UV power meter, equipped with a H9958 head. Detailed emission spectrum of the lamp and distribution of the UVA flux at the reactor border for I_{Centre} = 30 mW·cm^{-2} are presented in Figure 8.1b.

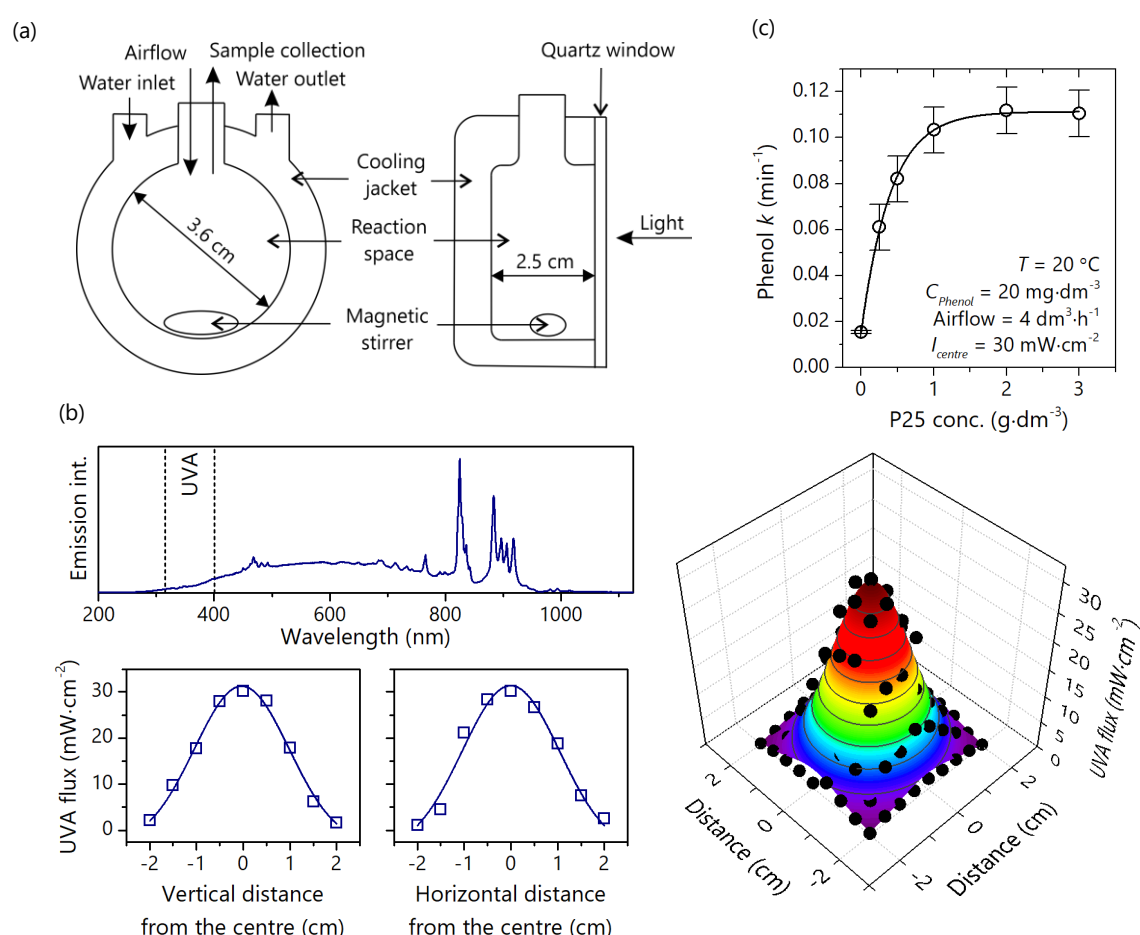**Figure 8.1.** Scheme of the photocatalytic reactor used during most of the performed processes (a), together with the emission spectrum of the utilized Xe lamp and measured UVA flux around the centre of reactor for I_{Centre} = 30 mW·cm^{-2} (b), as well as observed change in the phenol degradation rate with increasing concentration of commercial P25, performed in order to initially estimate optimal degradation conditions (c).

For a typical degradation process, phenol solution with a concentration of 20 ±1 mg·dm^{-3} (approx. 0.2 mmol·dm^{-3}) was prepared from the 500 mg·dm^{-3} stock solution and was mixed with a photocatalyst to achieve powder concentration of 2 g·dm^{-3}. Such suspensions were left to achieve equilibrium for 30 min (600 rpm stirring, 20 ±1 °C and 4.5 ±0.5 dm^3·h^{-1} of airflow), during which the lamp flux was stabilizing. Adopted conditions were based on the general IUPAC recommendations [137], as well as control measurement of the degradation rate over commercial P25, which showed maximum rate constant (k) for concentration ≥ 2 g·dm^{-3} (Figure 8.1c). Analogical relations between the observed k and photocatalyst concentration were verified for different prepared materials, which always agreed that 2 g·dm^{-3} is a suitable amount for comparing their maximum activity. Depending on the study, concentration of the phenol solution was changed to achieve different amount of pollutant molecules per surface unit of the introduced photocatalyst, under otherwise the same optical properties of the suspension.

For the degradation of compounds other than phenol, their maximum concentrations varied between ~14-20 mg·dm^{-3}, depending on the solubility. In the case of 4-nitrophenol, its reduction was carried out in the methanol solution, which was purged with Ar during the stabilisation (no airflow was introduced during the process). In this case, 0.50 ±0.05 mmol·dm^{-3} solution was prepared from the 12.5 mmol·dm^{-3} stock solution before each process.

In the case of toluene degradation in the gas phase, samples were tested as layers deposited on the glass substrates with different size. Degradation process was performed in a flat stainless-steel reactor with a working volume of 30 cm^3, equipped with a quartz window, two valves, a septum and 25 light-emitting diodes (LEDs) acting as the UV light source (λ_{max} = 375 nm). The intensity of the incident UVA light above the photocatalyst layer was 5 ±0.5 mW·cm^{-2}. In a typical experiment, the prepared substrate was placed in the centre of the reactor, and the reactor was filled with the mixture of toluene (approximately 40 mg·dm^{-3}) and synthetic air at a flow rate of 0.17 m^3·h^{-1} for 1 min. After this time, the flow was stopped, the reactor was closed with the valves and kept in the dark for 40 min to achieve equilibrium before the introduction of light.

Degradation kinetics were always analysed with a I-order reaction model, with a determined rate constant (k) as $k = \ln(C_0/C)$, where C is concentration and C_0 is a concentration at the start of the photocatalytic process.

9. ANALYTICAL PROCEDURES

All collected liquid samples were passed through the Chromil PET syringe filters with 0.2 μm pore size in order to remove photocatalyst particles. The efficiency of the processes was monitored using a Shimadzu high-pressure liquid chromatography system equipped with a diode array detector and Phenomenex Gemini 5 μm C18 column (HPLC-DAD).

Quantitative analyses, including phenol, *para*-hydroxyphenol, *ortho*-hydroxyphenol, benzoquinone, ibuprofen, acetaminophen, carbamazepine, 4-nitrophenol and

4-aminophenol were performed after calibration with commercially available pure compounds. Details of the separation conditions varied, depending on the target compound.

Removal of the organic carbon from the solution was monitored after the degradation processes as the change in the concentration of the total organic carbon (TOC), compared to the initial solution of the pollutant. Measurements were performed with the Shimadzu TOC-L analyser.

The degradation of toluene was monitored chromatographically after calibration with toluene samples of known concentration by collecting gas samples from the reactor through the septum using a gastight syringe. Analysis was performed using a PerkinElmer Clarus 500 gas chromatograph equipped with a flame ionization detector and a DB-1 capillary column (30 m × 0.32 mm, film thickness 3.0 μm).

RESEARCH DESCRIPTION

The following part summarizes the most important aspects and results obtained during the PhD dissertation. The order of the chapters follows the logical order of the published works, with the corresponding publications highlighted in the titles. Please note that for clarity, some figures originally present in these publications were rearranged to better fit the summation. Nevertheless, at their core, they always present the same data and conclusions. Finally, additional comments that were not included in the original publications are occasionally present in order to help discuss the results presented in the overall works all-together.

10. INITIAL STUDY ON THE POSSIBLE FACET EFFECT [P1]

The initial study on the possible effect of the exposed crystal facet on photocatalytic degradation of organic pollutants was performed using phenol as a model pollutant. In this work, a special focus was on obtaining different facet exposition as a result of a similar preparation route to minimise the number of possible factors affecting final properties. In this regard, the original approach was proposed, treating metastable cubic $TiOF_2$ as a universal precursor for different anatase morphologies. The exact procedure involved the preparation of $TiOF_2$ from TiF_4 in the presence of n-butanol, and further transformation of the $TiOF_2$ to anatase in an aqueous environment, with different amounts of HF, HCl, N_2H_4 and NH_4OH introduced as morphology-controlling agents. In such a way, the amount of fluorine that is naturally introduced to the system together with the Ti precursor was limited compared to the commonly used TiF_4. This especially increased the yield of the final TiO_2 product and enabled (relatively) easy control over its morphology in the aqueous environment. Noteworthy, in the case of the N_2H_4 and NH_4OH, their molar concentration in both reactions was equal and they were introduced in a visible excess to Ti, in order to change environment to basic.

The single-phase character of both anatase and $TiOF_2$ as a precursor was confirmed with the powder XRD, without any noticeable features in the patterns. Furthermore, SEM observations confirmed differences in the TiO_2 morphology associated with the exposed crystal facets, as presented in Figure 10.1a.

Briefly, hydrolysis of $TiOF_2$ in pure water produced ultrafine particles in the form of truncated octahedrons, as expected from the Wulff construction (sample labelled as H_2O). Further introduction of HF, HCl or HCl/HF mixture generally stimulated the growth of the particles and exposition of the {0 0 1} facets, in accordance with the increased fluorine presence and enhanced dissolution-recrystallisation reaction (possibly with the formation of hypothetical $[TiCl_xF_{6-x}]^{2-}$ species). On the other hand, particles prepared in the presence of N_2H_4 show well-defined octahedral morphology, with an almost complete exposition of the {1 0 1}, which agrees with the known role of hydrazine in promoting their presence [85]. Noteworthy, in this case, orientation between the exposed {1 0 1} and the facets that appear at the top of octahedrons does not match the co-exposition of the {1 0 1} with {0

Page | 48

0 1}, suggesting that these minority facets might adopt the structure of other crystal planes, possibly (1 0 3) or (1 0 5). Nevertheless, their content is strictly limited to approximately 1.5% of the total exposed surface, making it unlikely that their presence would be decisive for the properties of the sample. In this regard, after simplifying that sample N_2H_4 is enclosed with the {1 0 1} facets, samples HF, HF/HCl, HCl, H_2O and N_2H_4 form a series of materials with competing {0 0 1}/{1 0 1} exposition, which was described as a truncation ratio A/B.

Interestingly, changing N_2H_4 to NH_4OH with the same concentration formed a unique morphology, which can be described as aggregates of elongated, tetragonal particles that would match increased exposition of the {1 0 0} facets. Possibly, this could be a result of the NH_4OH being a stronger base than N_2H_4, which might increase oxygenation of the surface, analogical to the known case of {1 0 0} stabilisation from Na-titanates.

Outside of the morphological differences, important observations were made based on the XPS analysis. As presented in Figure 10.1b., all of the prepared samples show some amount of non-stoichiometric Ti states, which is attributed to the formation of the TiO_{2-x} structure. The concentration of these defects states generally follows the acidity/HF presence of the solution, with some exceptions in the case of the sample prepared with the addition of HCl. It was proposed that for this sample, the presence of HCl promoted recrystallization of the initially defected structures, but in contrast to HF it was not aggressive enough to etch the stoichiometric surface with similar efficiency.

Following characterization, all samples were studied towards phenol degradation, as described in detail in the chapter 8. In each case, prepared materials were able to degrade phenol, with *ortho*-hydroxyphenol (catechol) and *para*-hydroxyphenol (hydroquinone) observed as the initial aromatic by-products and subjected to quantitative analysis. Interestingly, as presented in Figure 10.1c., *ortho*-hydroxyphenol formation was greatly suppressed in the presence of the NH_4OH and N_2H_4 samples.

Detailed analysis of the degradation kinetics revealed that all materials show a relatively random activity order of phenol degradation as HCl > N_2H_4 >H_2O > NH_4OH > HF > HF/HCl. However, it was not followed by the TOC removal. As highlighted in Figure 10.2a., the removal of organic carbon has shown a remarkable trend with the calculated truncation ratio, where more truncated particles achieved less efficiencies, independently on the removal of phenol itself. In this regard, obtained results present an important conclusion that efficient removal of the parent compound will not always correlate with possible mineralisation, which was presented for the first time considering different exposed facets. In this regard, a strong correlation between the {1 0 1} presence and increased TOC removal can be seen as an important observation for their possible application in water treatment processes.
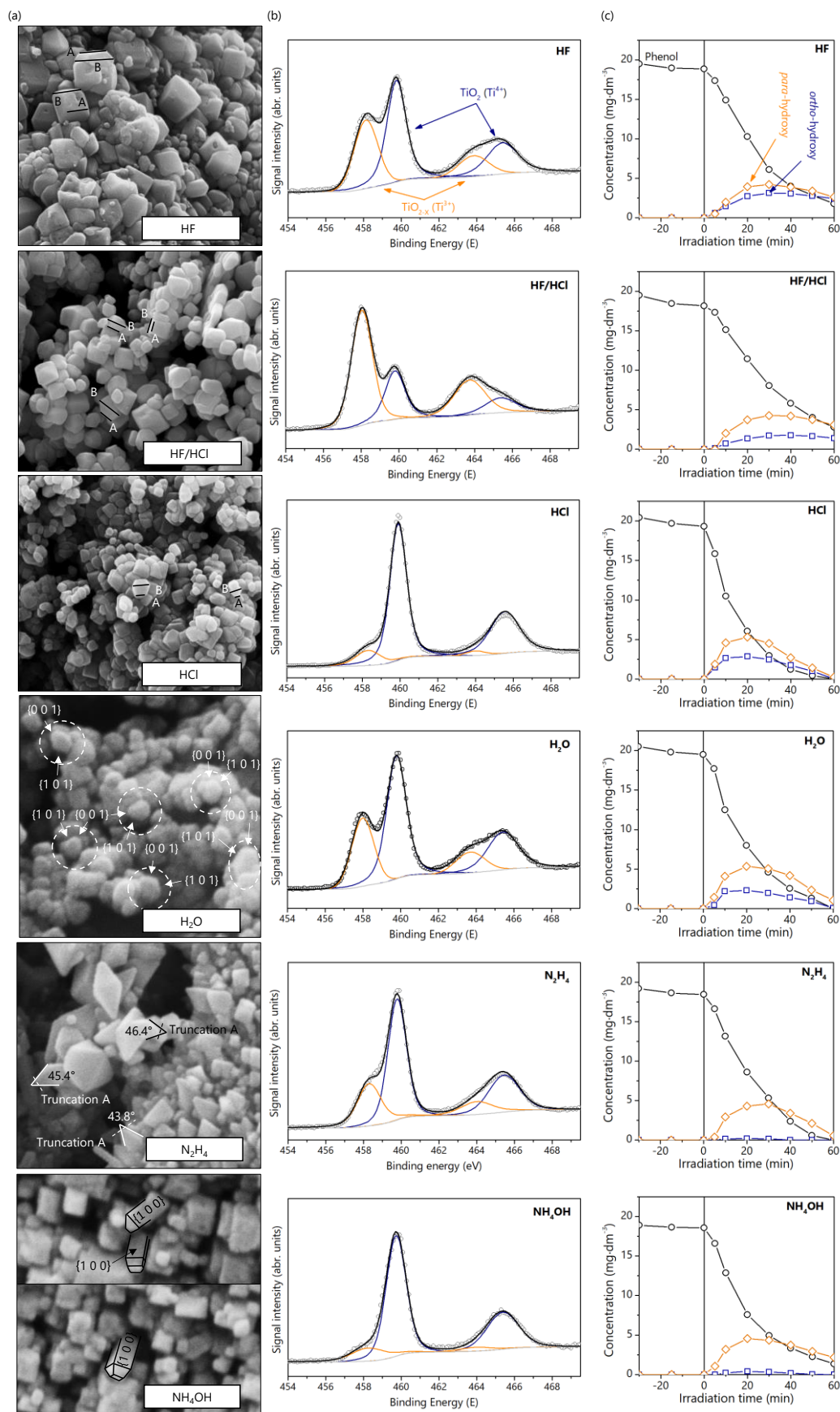
Figure 10.1. Exemplary SEM images (a), deconvoluted XPS signals of the Ti 2p states (b) and phenol degradation curves (c) of the anatase samples prepared from the TiOF$_2$ in the presence of selected stabilising agents.

Finally, a more detailed analysis was also performed concerning observed differences in the created by-products (*para* and *ortho*-hydroxyphenols). As presented in detail in Figure 10.2b., in the case of samples NH_4OH and N_2H_4, the formation of *ortho*-hydroxyphenol was greatly suppressed, with its *para*-substituted analogue achieving approximately 11 and 27 times higher concentrations, respectively. Noteworthy, compared to other materials, both these samples were not characterised the formation of the well-defined {0 0 1} facets, suggesting that their presence was important for the formation of *ortho*-substituted product. In this regard, two possibilities were considered to influence the reaction pathway: either the specific interactions between the exposed facet and the phenol are responsible for the observed substitution pattern, or it results from the different reactive species generated by different materials. To investigate these possibilities further, simple calculations of the minimum energy path were performed for both ·OH and ·O_2^- addition at *ortho* and *para* positions as the initial degradation steps, using the nudged elastic band (NEB) method implemented in the Orca software. Interestingly, as presented in Figure 10.2c., obtained results have indicated that in both cases, addition at the *ortho* position is energetically more favoured, which cannot explain the absence of this by-product during the reaction. In this regard, it was concluded that some facet-dependent surface processes must be responsible for the observed selective formation of *para*-hydroxyphenol.

In summary, the initial study confirmed important differences in the activity of TiO_2 with alternated facet exposition. Specifically, the obtained results disproved hypothesis [H2], showing that photocatalysts with slower degradation of phenol itself might achieve higher removal of total organic carbon. In this regard, increased exposition of the {1 0 1} facets promotes TOC removal, independently of the degradation rate. This fact can be connected with the preferred reductive character of the {1 0 1} that might stimulate the
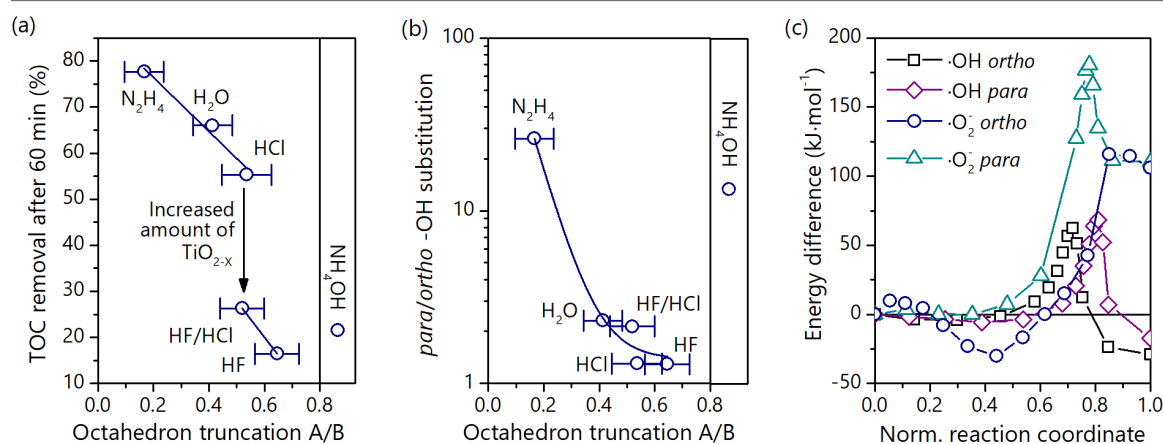
Figure 10.2. Observer removal of the total organic carbon (TOC) after the 60 min of phenol degradation over the samples prepared from the $TiOF_2$, with respect to the observed octahedron truncation (a); corresponding ratio between observed amount of *para* and *ortho*-hydroxyphenol, calculated for the 30% of phenol degradation (b); and calculated energy barrier for the ·OH and ·O_2^- addition at both positions in the phenol ring, obtained from the NEB calculations (c). In panel (a) and (b), sample prepared in the presence of NH_4OH is shown separately, since analogical A/B value does not apply for this morphology.

formation of the $\cdot O_2^-$ radicals, a species that are commonly reported to form and react slower than $\cdot OH$ (also supported by the NEB results) [138], [139], but are good ring-opening agents [140]. Furthermore, the presence of *ortho*-hydroxyphenol was found to depend on the {0 0 1} presence, which cannot result from the differences in the ROS generation. Therefore, the selectivity of the degradation pathway was also suggested to depend on the facet-dependent surface processes, initially suggesting hypothesis [H3] to be true, however, a detailed mechanism was not possible to present at this point.

11. OPTIMIZATION OF THE {0 0 1} EXPOSITION [P2]

Following the initial study, {1 0 1} facets were proposed as most suitable for the water treatment, especially showing better TOC removal than {0 0 1} and {1 0 0}. However, it must be noted that in all cases, samples prepared from the $TiOF_2$ precursor had defected surface structure, as confirmed by the XPS analysis. Moreover, during this study, both {0 0 1} and {1 0 0} achieved only limited exposition in the analysed samples, in contrast to the {1 0 1}. For example, the highest exposition of the {0 0 1} facets, observed for the sample prepared with the addition of HF and with truncation ratio of A/B $\approx$ 0.65, can be estimated only as ~17%. In this regard, further works were focused on obtaining stoichiometric materials, with the maximised exposition of all three facets, in order to confirm initial observations.

While, in the case of the {1 0 1} and {1 0 0}, preparation of the defect-free particles with their dominant exposition was relatively straightforward, as summarized in the next part, preparation of the analogical {0 0 1} structure was found to be more challenging. Specifically, initial trials have highlighted significant variation in the final morphology and properties, depending on the reaction environment, temperature, stabilising agent, its amount, titanium concentration and others. For example, these failed trials include the formation of the {0 0 1} exposing plates in the K-titanate/CO_3^{2-} system, as proposed by Han and co-workers [91]. Ultimately, solvothermal condensation of titanium *tert*-butoxide (TBT) in the presence of alcohols with concentrated HF was found to be the most reliable method, when performed at 210 °C. Following this observation, a systematic study was made in order to optimize the final product. Specifically, different types and amounts of alcohols were tested as an environment since this problem was not investigated in detail in the existing literature. Detailed preparation procedure included condensation of 17 cm^3 TBT, together with 3.4 cm^3 of HF solution (48% wt.) at 210 °C. Furthermore, various alcohols (methanol, ethanol, n-butanol and n-hexanol) were added in different amounts (10, 30 or 60 cm^3), and the reaction was carried out between 8 and 24 h.

After each reaction, nanoparticles were centrifuged and washed several times with ethanol, followed by water. During the second part of the washing, approximately 10 cm^3 of 0.1 M solution of NaOH was introduced once per sample to help remove adsorbed fluorine ions. Obtained samples were denoted as "SolventX-Yh", where the solvent is methanol (Me), ethanol (Et), n-butanol (But) or n-hexanol (Hex), X is the volume of the solvent, and Y is the reaction time. For example, But30-8h is a photocatalyst prepared with 30 cm^3 of n-butanol during 8 h reaction.

Overall, the obtained results have shown a significant effect of the alcohol environments on the final properties of the materials. For example, this includes stabilisation of the $TiOF_2$ for syntheses prepared with a low amount of n-butanol and n-hexanol, as observed based on XRD analysis. Furthermore, increased reaction time allowed to obtain larger, more crystalline particles with a lower surface area, in accordance with the prolonging dissolution-recrystallisation reactions. Summation of the XRD analysis, including Rietveld refinement and BET measurements for all obtained samples, is presented in Table 11.1. Estimation of the amorphous phase content was based on the XRD measurements with NiO acting as the internal standard. Crystallite size was estimated using the Sherrer equation.

Samples obtained in the presence of short-chained alcohols (methanol and ethanol) exhibited less platelet morphology compared to the n-butanol and n-hexanol. SEM images of the materials are presented in Figure 11.1a. Based on the combined XRD and SEM

Table 11.1. Summation of the XRD analysis and measured BET surface area of the samples prepared solvothermally from TBT in the presence of HF and different alcohols. Crystallites size were estimated using Sherrer equation, based on the refined patterns. Amorphous phase content was determined using NiO as internal standard.

Sample	Anatase crystallite size along the [0 0 1] direction (nm)	$TiOF_2$ content (% wt.)	Amorphous phase content (% wt.)	BET surface area ($m^2 \cdot g^{-1}$)
Me10-8h	14	0	37.5	85
Me10-24h	23	0	18	54
Me30-8h	13	0	24	94
Me30-24h	15	0	35	85
Et10-8h	13	0	39	100
Et10-24h	17	0	16	68
Et30-8h	16	0	32	83
Et30-24h	30	0	14	34
But10-8h	9	**13**	51	Not analysed
But10-13h	14	**9**	39	Not analysed
But10-24h	12	**51**	33	Not analysed
But30-6h	10	**23**	64	Not analysed
But30-8h	12	0	66	99
But30-13h	17	0	58	62
But30-18h	21	0	46	47
But30-24h	33	0	19	19
But60-8h	15	0	33.5	80
But60-13h	22.5	0	25.5	47
But60-24h	21	0	23	Not analysed
Hex10-8h	11	**15**	39	73
Hex10-24h	16.5	**3**	58	52
Hex30-8h	12	**6**	54	79
Hex30-24h	27	0	21	42

analyses, it was concluded that the length of the alcohol chain affects the nucleation of the TiO_2 particles and possible dissolution-recrystallisation. The reason for this might be connected with possible nucleation via ether-elimination reaction (11), as proposed by Pina and co-workers for the general formation of metal oxides (M-O-M) from the corresponding alkoxides [141]:

$$2M\text{-}OR \rightarrow M\text{-}O\text{-}M + R\text{-}O\text{-}R \tag{11}$$

For such a process, a longer carbon chain of the alkyl group (R) might slow down the process, for example, due to the larger steric hindrance. While it is noteworthy that in case of the investigated system mixed ligand species $[TiF_{6-x}(OR)_x]^{2-}$ should form [142], therefore possibly enabling condensation via analogical elimination of the alkyl fluoride (RF), the general conclusion of the slower nucleation for the system with longer R chain seems equally valid, as long as alcohol species are the predominant source of oxygen in the system (which is true since the initial amount of H_2O in the system is limited to the added HF solution, which is in the minority to the alcohol environment and TBT itself). On the other hand, it is also possible that for higher amounts of ROH introduced to the synthesis, condensation of the free alcohol molecules might lead to the formation of additional H_2O [100], further stimulating condensation of the TiO_2. Interestingly, this is in agreement with the observation that for the highest molar amounts of introduced alcohol, produced particles form less platelet morphology (series Met30, But60 and Et30), which might be due to increased preference to expose {1 0 1} facets in the water environment [87]. A summation of the relation between the molar amount of introduced alcohol and the observed purity/morphology of the nanoparticles is presented in Figure 4 in the publication [P2].

Ultimately, based on the overall XRD and SEM analyses, moderate amounts of n-butanol (here 30 cm^3) were found to be the most suitable for controlled growth of the 2D anatase plates with high {0 0 1} exposition. As presented in Figure 11.1b., particles prepared in such a way posses well-defined platelet morphology with rectangular shape, as well as pronounced selective broadening of the (0 0 4) and (1 0 5) reflections in the XRD pattern, in accordance with the expected size reduction along the [0 0 1] direction (Figure 11.1c.). Noteworthy, calculated crystallite size from the (0 0 4) reflection ($d_{[0\ 0\ 1]}$) is in general accordance with the observed height of the nanoplates (Figure 11.1d.), proving exposed facets to be perpendicular to the [0 0 1]. Finally, detailed observations for sample But30-24h have indicated the formation of the ~136.6° and ~111.7° angles on the side of the particles, proving co-exposition of the dominant {0 0 1} facets with {1 0 1} at the sides (136.6° is the theoretical angle between the (1 0 1) and ($\bar{1}$ 0 1) planes and 111.7° is the angle between the (1 0 1) and (0 0 1) ones), as presented in Figure 11.1e.
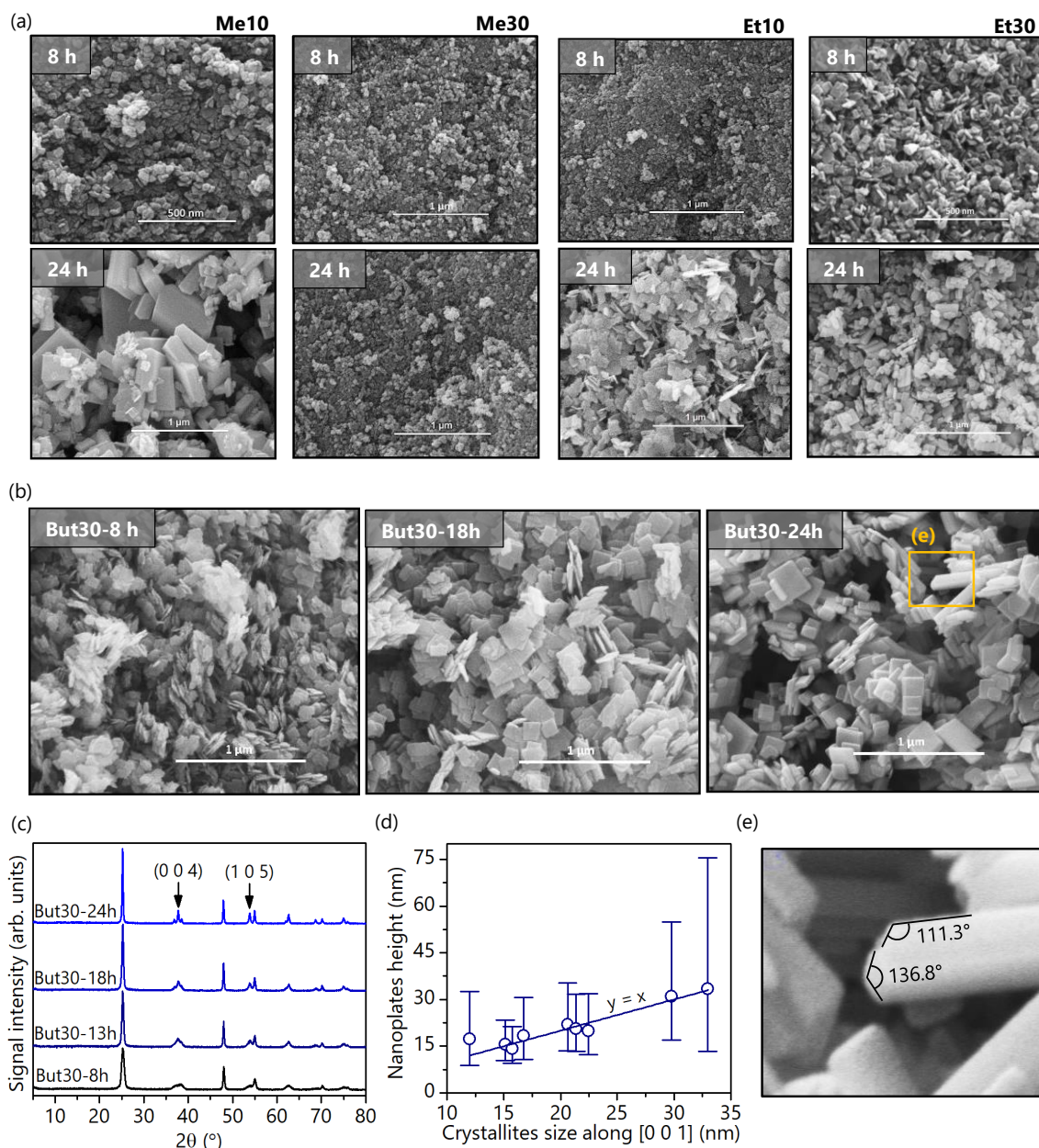
Figure 11.1. Exemplary SEM images of the anatase samples prepared in the presence of short-chained alcohols, indicating formaton of smaller/less platelet particles than in case of n-butanol and n-hexanol (a). Exemplary SEM images of the samples prepared in the presence of 30 cm³ n-butanol, presenting stable, controlled growth of the well-defined 2D plates (b) with corresponding XRD patterns of the series (c). Overall relation between the crystallites size obtained from the (0 0 4) reflection and observed height of the nanoplates, considering all samples with well-defined platelet morphology (d) and observed characteristic angles between the co-exposed {1 0 1} and {0 0 1} facets for sample But30-24h (e).

Prepared samples were studied for phenol degradation, analogically to the previous work, with the only exception being the maximum flux value at the reactor centre increased to 40 mW·cm⁻². Furthermore, to verify the possible effect of different BET surface areas, initial phenol concentration was changed between 20-100 mg·dm⁻³ to achieve multiple degradation curves for the same material. Photodegradation analyses were followed by physicochemical characteristics of the semiconductor materials. Outside of the described

SEM and XRD data, this particularly includes XPS measurements performed for the selected samples. Noteworthy, this detailed analysis was not performed for samples with $TiOF_2$ impurities, since their degradation ability was analogical or worse than other materials, suggesting no positive effect of the $TiOF_2$ presence. Interestingly, overall results allowed samples to be grouped into three different-behaving groups. Specifically:

Group A. The samples show relatively fast degradation of phenol with simultaneous formation of both *para* and *ortho*-hydroxyphenol with TOC removal being almost linearly dependent on the available surface area. Based on the described SEM/XRD analysis and additional XPS data, these samples have 2D morphology, with relatively high surface fluorination mostly as adsorbed species (F signal with binding energy < 685 eV, with observed ratio between F and Ti at the surface approximately between 0.11 and 0.24 at.), no Ti^{3+} species at the surface, with possible defects in the bulk structure (based on pale-blue colour of some samples). Samples: Et10-24h, all anatase samples from But30 series, But60-8h and Hex30-24h,

Group B. Samples show slow phenol degradation, with highly hindered formation of *ortho*-hydroxyphenol and low TOC removal. Overall data show that this behaviour correlates with less platelet character, but is still quite 2-dimensional, with an especially lower amount of surface fluorine (F/Ti below 0.10 at.) and possible excess of electrons on the surface, observed for sample Et30-24h as a surface Ti^{3+} states and tailing of the valence band edge. Samples: Et30-8h, Et30-24h, But60-13h and But60-24h,

Group C. Samples show slower phenol degradation than Group A, with very little amount of *ortho*-hydroxyphenol formed but with relatively high removal of the organic carbon. Materials from this Group mostly show ultrafine morphology without well-defined platelet shapes and heavily defected structure (greyish colour of most samples and lack of metal oxide Ti^{4+} states at the surface for sample Me30-8h). Samples: all prepared in the presence of methanol and Et10-8h.

Mean degradation curves for each group are shown in Figure 11.2a for an initial phenol concentration of 20 mg·dm^{-3}, together with the observed TOC removal in the function of available surface area in Figure 11.2b. (data for all degradation processes, expressed as the ratio between hypothetical surface oxygen sites, calculated from BET areas assuming (0 0 1) structure, and the total number of carbon at the start of the process). Finally, in Figure 11.2c., exemplary results of the XPS measurements are presented, highlighting the most significant differences between the samples from different groups.

Ultimately, systematic study on the formation of the {0 0 1} exposing nanoparticles in the presence of different alcohols and their amounts allowed for optimization of both desired facet exposition and their performance for phenol degradation. Furthermore, excessive data gathered allowed us to define the features most important for the observed

activity. Specifically, highly platelet shape, visible surface fluorination and no surface defects are desired for the possibly high activity of {0 0 1}. Interestingly, TOC removal seems to be linearly dependent on the {0 0 1} area, however, even for the highest surface developments obtained (approximately 100 $m^2 \cdot g^{-1}$), observed TOC removal was still lower than control experiments with TiO_2 P25 and isotropic TiO_2, prepared from simple condensation of $TiCl_4$. Similarly to the previous study, this is despite the fact that phenol itself can be removed faster with {0 0 1} exposing nanoplates. Therefore, overall results support the initial conclusion that {0 0 1} might not be best suited for water treatment from organic pollutants.
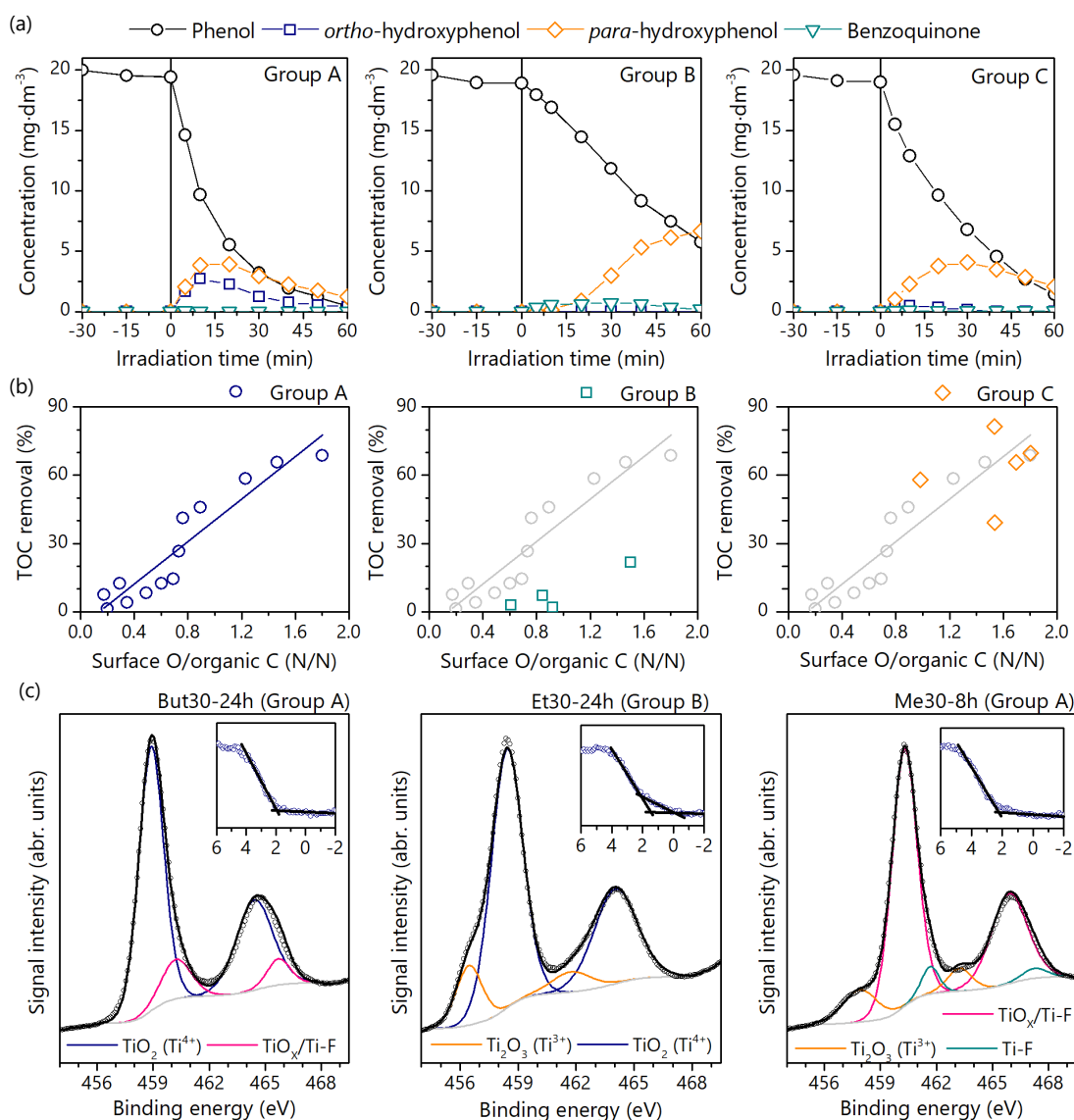
Figure 11.2. Mean phenol degradation curves for initial concentration of 20 mg·dm^{-3} over analysed samples, after grouping them according to the observed features (a), together with the observed TOC removal vs. available surface area per amount of pollutant (expressed as the O/C ratio, more details in text) for all processes performed (b). High-resolution XPS spectra of the deconvoluted Ti 2p signals for the exemplary sample from each Group, with corresponding scans of the valence band edge in the inset (c).

12. ANALYSIS OF THE MAIN FEATURES AFFECTING OBSERVED ACTIVITY

12.1. ANALYSIS WITH RESPECT TO THE EXPOSED FACET [P3]

Following the optimized procedure for the preparation of the {0 0 1} exposing nanoparticles, further works were focused on finding the correlation between the observed activity and features specific to the exposed facet. In this regard, samples with the dominant exposition of either {0 0 1}, {1 0 0} or {1 0 1} were prepared, following existing information and previous studies. Specifically, a sample analogical to the But30-18h was prepared to represent the {0 0 1}, while for the {1 0 0}, the procedure suggested by Li and co-workers was applied [79]. Finally, in the case of the {1 0 1} exposing particles, a procedure analogical to the one reported by Amano and co-workers was used [82], with the additional introduction of the NH_4OH/NH_4Cl buffer in the second reaction. Detailed procedures to obtain each sample are summarised in Table 12.1.

Prepared samples were thoroughly analysed to confirm their possibly high quality. As presented in Figure 12.1.1., each sample possesses the expected shape, specific for the dominant exposition of the designed facets. Statistical analysis of the observed dimensions suggested that corresponding expositions of each facet are approximately 80% for {0 0 1}, 82% for {1 0 0} and almost 100% for {1 0 1}. Furthermore, XRD patterns have confirmed the single-phase character of all three materials, with the observed crystallite size along different directions following the expected trends (for example, the largest size along the [0 0 1] for the {1 0 0} exposing structures and the lowest for the {0 0 1} ones). Finally, the combination of both UV/vis absorption spectra and XPS analyses have indicated a possibly defect-free structure of all samples, with a single chemical state of titanium on the surface, similar bandgap values and positions of the valence band edge, as well as without noticeable absorption increase above $\lambda \approx 400$ nm. In this regard, prepared samples were considered as suitable for future analyses.

Table 12.1.1. Summation of the preparation routes adopted to obtain dominant exposition of all three investigated crystal facets. In the table "M" stands for "$mol \cdot dm^{-3}$".

| Sample	First step			Second step		
	Substrates	Parameters	Post-reaction	Substrates	Parameters	Post-reaction
{0 0 1}	Not performed			17 cm^3 TBT 30cm^3 n-butanol 3.4 cm^3 HF (48% wt.)	200 cm^3 reactor, 210 °C, 18 h	Wash 3x with ethanol, 2x water, 1x with 0.1 M NaOH, 3x water, dry
{1 0 0}	1 g P25, 40cm^3 NaOH 10 M	100 cm^3 reactor, 120 °C, 20 h	Wash with water unit pH ≈ 10.5, don't dry	Half of the wet product from 1st step, 100 cm^3 H_2O	200 cm^3 reactor, 210 °C, 24 h	Wash with water 4-5 times, dry
{1 0 1}	1 g P25, 40cm^3 KOH 8.5 M	100 cm^3 reactor, 200 °C, 16 h	Wash with water unit pH ≈ 7-8, dry	0.4 g of the dried product from 1st step, 100 cm^3 of the NH_4OH/NH_4Cl (0.3/0.3 M)	200 cm^3 reactor, 210 °C, 16 h	Wash with water 4-5 times, dry
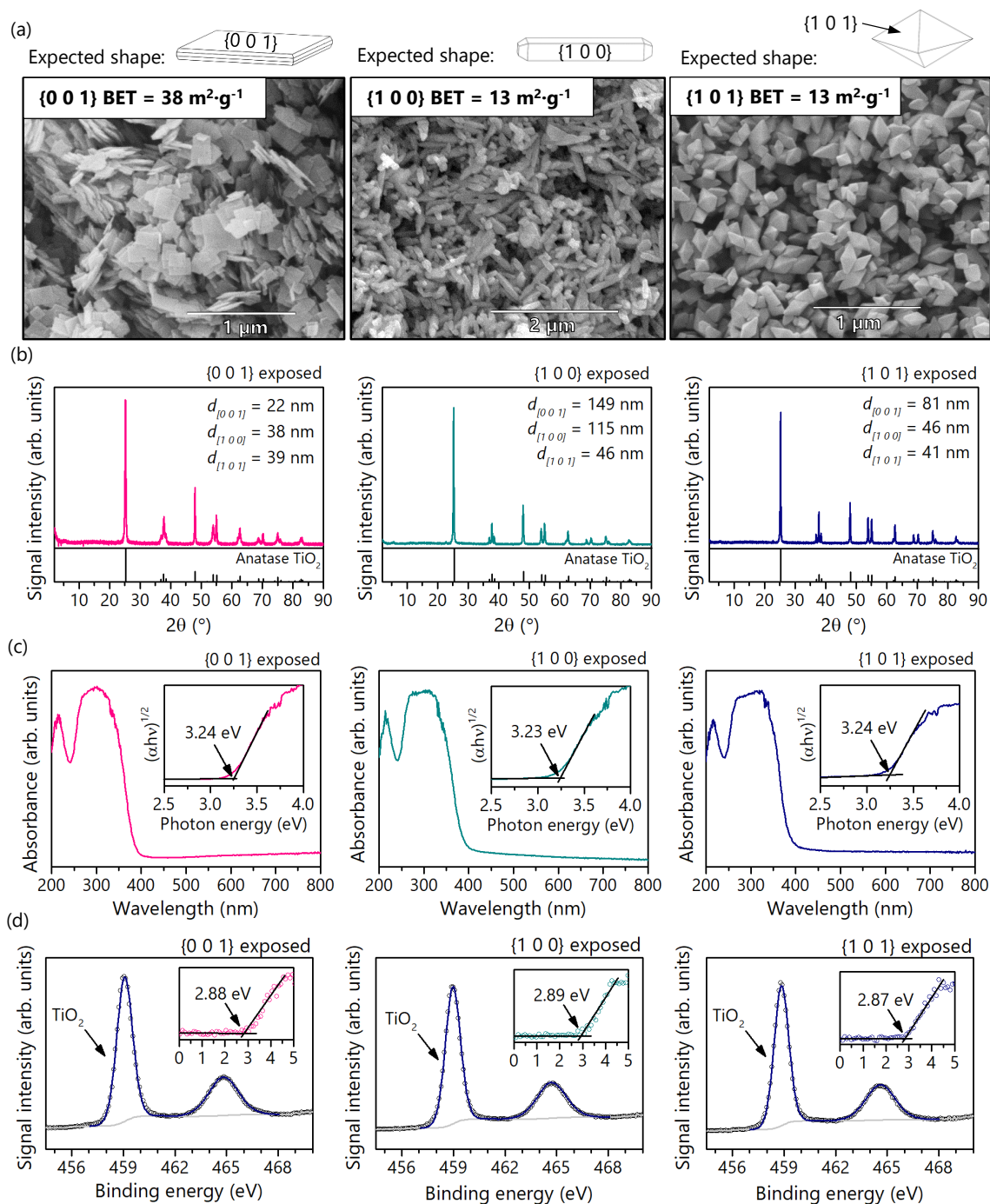
Figure 12.1.1. Summarized results of the physicochemical characterization of the anatase samples exposing majority of the {0 0 1}, {1 0 0} or {1 0 1} facets: SEM images and measured surface development (a), corresponding XRD patterns and calculated crystallites size in different crystallographic directions (b), absorbance spectra with bandgap estimation using Tauc method in the inset (c), and deconvoluted Ti 2p signals with scans of the valence band edge in the inset (d). In panel (b) the standard pattern is shown in the box below the recorded signal.

Following characterization, prepared samples were analysed towards phenol and toluene degradation. In both reactions, three different levels of pollutant-per-surface-area ratios were investigated, either by changing initial phenol concentration (10, 20 or 30 mg·dm^{-3}) or increasing glass substrate area for TiO$_2$ deposition in case of toluene

degradation. All degradation data was transformed to the $\ln(C_0/C)$ and corresponding rate constant of the I-order reaction (k) was determined as the slope of the linear function vs. time (Figure 12.1.2a.). Noteworthy, in the case of phenol degradation, simultaneous monitoring of the created by-products confirmed that the degradation rate is always proportional to the formation of the hydroxyphenols, proving that it is strictly related to its chemical transformation.

Determined k were used to create a correlation model between their experimental values and different properties of the prepared materials. Analysis was started by plotting k vs. $S \cdot n_P^{-1}$ ratio, which is the amount of available surface area (S) per absolute amount of pollutant molecules at the start of the process (n_P). During this transformation, the surface area of the deposited TiO_2 layer was roughly estimated from its weighted mass and BET surface area of the photocatalyst. As presented in Figure 12.1.2b., such an approach resulted in grouping of all data into the facet-dependent series, with k increasing fairly linear with the $S \cdot n_P^{-1}$, as expected due to higher amount of "free" surface active sites in the system. Starting from this point, the slope of the fitted k vs. $S \cdot n_P^{-1}$ relations, denoted as "a", was assumed to be factor depending purely on the properties of the exposed dominant facet, and the actual analysis was focused on finding best expression to define a with parameters describing properties of the corresponding surface.

Ultimately, a very strong correlation was found between the a and summarised value of the trapping energy of both h^+ and e^- at the surface atoms (E_{Trap}), as reported by Ma and co-workers using surface models in vacuum [63]. The value of this energy is associated with the energy gain of the system, when delocalised charge carrier became trapped at the surface as a polaron state (that is, it includes deformation of the crystal lattice in the proximity of the trapping site), therefore influencing the probability of forming long-lived electron states at the surface. Noteworthy, during this approach, energy of e^- trapping on the {0 0 1} facets was treated as 0, since electron localisation is more favoured at the subsurface atoms in this case, which also agrees with other studies. The relation between fitted a and E_{Trap} is not linear but shows exponential character, which is in accordance with the expected distribution of the electron states. Ultimately, fitting a to the Boltzmann distribution was found to give an excellent correlation in both cases, as presented in Figure 12.1.2c., with the final expression being (12):
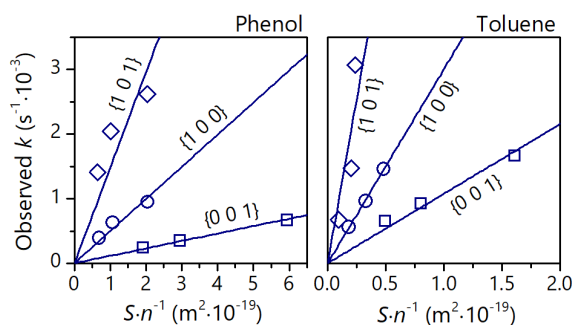
$$a = b \cdot (e^{(c \cdot ETrap/(kB \cdot T))} - 1) \tag{12}$$

where b and c are fitted parameters, k_B is Boltzmann constant and T is temperature. Please note, that during this fitting, artificial point (0, 0) was introduced to avoid fitting exponential function to 3 points.

(a) Slope of the fitted line = k (I-order reaction, $\ln(C_0/C) = k \cdot t$)
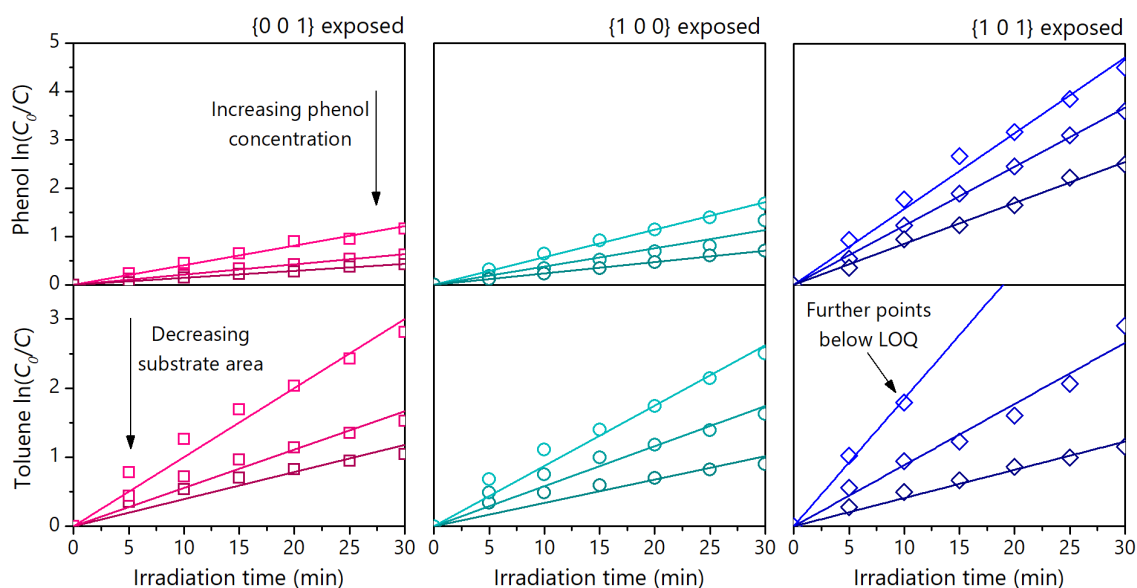
(b) $k = a \cdot S \cdot n^{-1}$

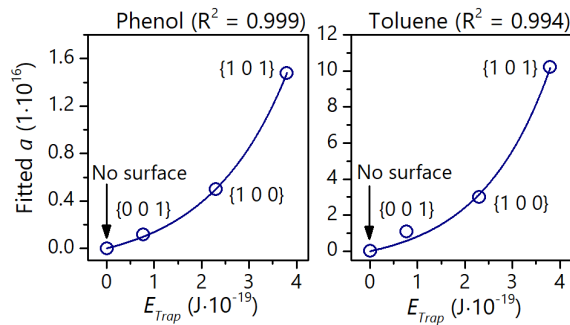(c) $a = b \cdot (e^{(c \cdot E_{Trap} \cdot k_B^{-1} \cdot T^{-1})} - 1)$

Figure 12.1.2. Determination of the rate constants k for all performed photocatalytic reactions, including I-order reaction model (a), with further linear fitting of the determined k value vs. calculated $S \cdot n_P^{-1}$ ratio (b) and final expression of the a (slope from panel (b)) with respect to the reported trapping energy E_{Trap} (c). Corresponding equations are shown above each panel. More details in the text. "LOQ" stands for "limit of quantification".

In the end, the combination of equation (12) with the k vs. $S \cdot n_P^{-1}$ relation allowed us to express k with a simple model of only two parameters (upon treating $S \cdot n_P^{-1}$ as a single parameter that describes the possible number of available surface active sites). Although it must be highlighted that the presented approach is purely statistical and, for example, the appearance of the b and c parameters results strictly from the model regression, it is interesting to notice its possible physical interpretation, which is relatively straightforward. Specifically, the final model can be seen as a combination of the probability of the charge carriers' localisation at the surface (exponential relation with E_{Trap}), with a number of available reaction centres (linear relation with $S \cdot n_P^{-1}$). Noteworthy, the final model is very similar to other, historically-presented expressions for k, such as Arrhenius and Eyring equations or collision theory. Furthermore, the appearance of the c parameter in the fitted exponent, which always adopts low values of approximately 0.02-0.05, might also be reasoned as necessary to "slow down" the actual process. This is due to the fact that

between charge carriers trapping and actual transformation of the pollutant, multiple other elementary steps are also necessary, which are unlikely to occur with 100% efficiency (for example, carriers transfer to the O_2/H_2O and further reaction between ROS and pollutant). Therefore, it is reasonable that the absolute difference in modelled trapping energy in a vacuum will not lead to equally high differences in the actual reaction rate, and E_{Trap} must be weighted with additional parameter. However, it must be noted that strict interpretation of both b and c cannot be presented at the moment.

Based on this simple model of $k(S \cdot n_P^{-1}, E_{Trap})$, it could be suggested that the probability of charge carriers localisation at the surface, expressed through E_{Trap}, is the most decisive factor for the observed degradation ability of the specific facet. Therefore, it agrees with hypothesis [H4], presenting for the first time a quantitative description of the observed photocatalytic activity of the surface with respect to its fundamental physical properties. As presented in Figure 12.1.3a., such an approach reproduced the observed activity order quite well, especially for the phenol degradation, with random, heteroscedastic distribution of the residuals clearly observed in both cases.

Following these general findings, both models were further refined based on the systematic alternation of the $S \cdot n^{-1}$ ratio to other expressions, as well as the introduction of the surface energy (γ) to the equation. As presented in Figure 12.1.3b., both predictions can be visibly improved, however the final models start to depend on the reaction. In this regard, it is not expected that these optimized expressions are universal and probably depend on the system details (e.g. distribution of light's flux, mass transfer in the system, structure of the pollutant etc.). Nevertheless, the optimised model for phenol degradation, including the introduction of γ and number of possible trapping centres (n_{Trap}) instead of

(a)
$$k = b \cdot S \cdot n^{-1} \cdot (e^{(c \cdot E_{Trap} \cdot k_B^{-1} \cdot T^{-1})} - 1)$$

(b)
Phenol: $k = b \cdot \gamma \cdot (n_{Trap} \cdot n^{-1})^{0.5} \cdot (e^{(c \cdot E_{Trap} \cdot k_B^{-1} \cdot T^{-1})} - 1)$
Toluene: $k = b \cdot \gamma^2 \cdot S \cdot n^{-1} \cdot (e^{(c \cdot E_{Trap} \cdot k_B^{-1} \cdot T^{-1})} - 1)$

Phenol: $c = 0.02275$, $b = 1.93387 \cdot 10^{15}$
Toluene: $c = 0.02581$, $b = 9.66209 \cdot 10^{15}$

Phenol: $c = 0.02842$, $b = 3.0841 \cdot 10^{-4}$
Toluene: $c = 0.03972$, $b = 1.26703 \cdot 10^{16}$
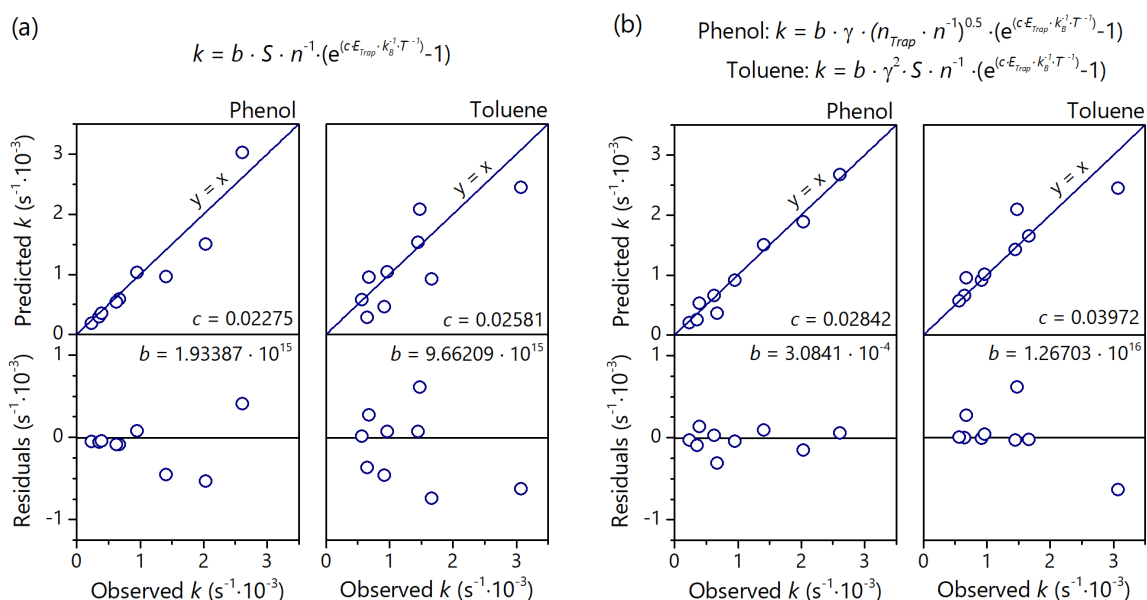
Figure 12.1.3. The simplest (a) and the most accurate (b) models of the observed rate constant k, developed with respect to different parameters describing properties of the exposed crystal facet. Lower panels show corresponding distribution of the residuals. Fitted parameters b and c are presented withitn the graphs. See text for a detailed description of the symbols.

S, shows excellent correlation with experimental data and will be used as the starting point for further analysis (here, n_{Trap} is roughly equal to the density of undercoordinated species on the surface, with detailed discussion presented in the publication [P3]).

Finally, it is noted that overall models show little change when considering possible fluorination of the {0 0 1} facets, which was tested by checking the effect of different post-treatment procedures on their activity and refitting of the models. Also, the introduction of the different γ values reported in the literature had minimal effect on the accuracy. On the other hand, to the best knowledge of the Author, the work by Ma and co-workers [63] is the only one that reports trapping energy for both charge carriers on all three investigated facets, allowing for their quantitative comparison. Therefore, it is hard to discuss accuracy with respect to the detailed values of E_{Trap}. However, since it is known that DFT methods allow for a good comparison between energies obtained under the same computational details (in contrast to the absolute value, which might change between different procedures [50]), there seems to be no obvious reason why adopted values of E_{Trap} should not be suitable for comparison of the analysed facets.

12.2. ANALYSIS WITH RESPECT TO THE POLLUTANT STRUCTURE IN WATER [P4]

Based on the previous study on the effect of exposed crystal facets, the optimized model for phenol degradation was adapted as the starting point for further analysis of the possible effect of the pollutant structure. Specifically, analogical TiO_2 materials were studied in the degradation process of acetaminophen (ACT), carbamazepine (CBZ) and ibuprofen (IBU), all being pharmaceutically active compounds recently recognised as possible threats to the environment [143], [144]. Moreover, in order to confirm if previous results are sensitive to the details of the reaction setup, an alternative setup with no airflow, different reactor geometry (15 cm^3 of reaction space) and different light source (high-pressure Hg lamp with 15 mW·cm^{-2} UVA flux reaching reactor border) was used. In this regard, additional analyses of phenol (PHE) degradation were performed as a control to previous studies, and overall results were compared to the photocatalytic activity of TiO_2 P25.

Obtained degradation results are visualised in Figure 12.2.1., generally presenting high activity of the {1 0 1} exposing particles, in accordance with the previous findings. Noteworthy, in the case of this sample, significant differences in the calculated rate constant were observed between the initial and late parts of the ACT and CBZ degradations. This indicates that after initial degradation, the reaction is hindered, probably due to the increased stability of the generated by-products. In this regard, the final value of *k* was determined as a mean between both time-regions, as highlighted with the two fitted lines. In all cases, the final values of *k* were controlled by calculating corresponding $t_{1/2}$ and comparing them to the experimental data. For example, for the ACT degradation over {1 0 1}, experimental $t_{1/2}$ is approximately 8.55 min, the $t_{1/2}$ calculated from the mean *k* value is 8.67 min, while $t_{1/2}$ calculated only from initial points would be
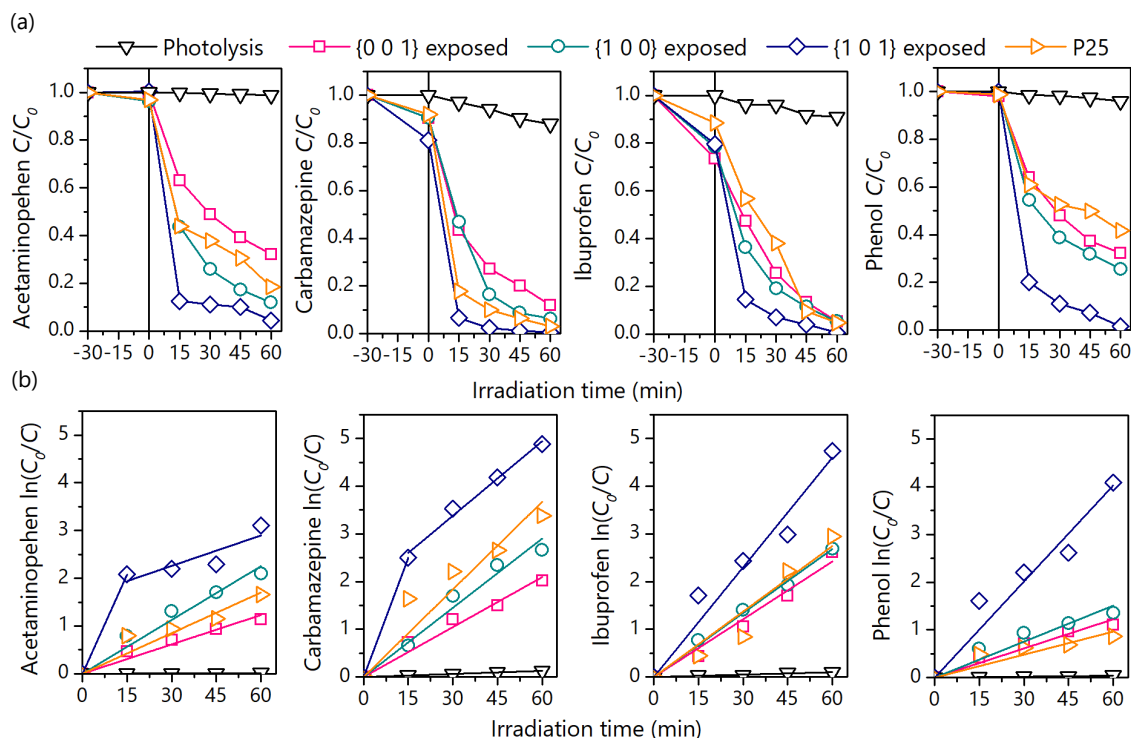
Figure 12.2.1. Observed degradation curves of all tested water pollutants (a) with the corresponding data fitting to the model of I-order reaction (b). For the acetaminophen and carbamazepine, final rate constant is expressed as a mean between both fitted regions highlighted in panel "b".

5.00 min. Simultaneously, the removal of organic carbon from the solution generally followed degradation rates.

Determined rate constants were compared with the ones predicted with previously-optimized model for phenol degradation after additional consideration of the photolysis rate k_0, as presented in equation (13):

$$k = b \cdot \gamma \cdot (n_{Trap} \cdot n_P^{-1})^{0.5} \cdot (e^{(c \cdot ETrap/(kB \cdot T))} - 1) + k_0 \qquad (13)$$

where $b = 3.327 \cdot 10^{-4}$ and $c = 0.02766$, based on the initial fitting. Noteworthy, the general activity order was reproduced well, however, different accuracy was observed depending on the pollutant (more accurate prediction for phenol and acetaminophen, with less accurate for carbamazepine and ibuprofen) and the overall results followed the trend $k \approx (k_{Model})^{0.5}$. Therefore, further refinement of the model was performed in order to extract the possible effect of the pollutant structure. In this regard, the focus was placed on the $(n_{Trap} \cdot n_P^{-1})^{0.5}$ term of the equation (13), since every other parameter describe a strictly exposed facet (E_{Trap} and γ) or is independent from the pollutant-photocatalyst interactions (k_0). Therefore, the analysed relation was (14):

$$(k - k_0) \cdot (\gamma \cdot (e^{(0.02766 \cdot ETrap/(kB \cdot T))} - 1))^{-1} = B \cdot (n_{Trap} \cdot n_P^{-1})^D \qquad (14)$$

where left part of the equation is known, while *B* and *D* are new parameters. The analysis was started by considering different exponents *D* (*D* = 0.5, 1 or 2) and determining *B* for each pollutant independently. This have shown that the overall highest accuracy was observed when *D* = 1, suggesting that previously found value of *D* = 0.5 was not universal. Following this observation, actual pollutant-oriented analysis was started by finding best way to describe newly-found, pollutant-dependent *B* value, using possibly simple descriptors of their molecular properties. Ten different parameters were analysed as possible predictors for *B*, namely: Gibbs energy, dipole moment, energy level of the highest occupied molecular orbital (HOMO), energy level of the lowest unoccupied molecular orbital (LUMO), LUMO−HUMO difference (ΔE), chemical potential, electronegativity, chemical hardness (η), chemical softness and electrophilicity index. All values were obtained from the DFT-based simulations of the pollutants molecules, using Orca software as specified in the experimental section and with further details presented in the publication [P4]. Overall correlation analysis included expression of *B* as linearly-depended on each predictor separately, on all possible combinations of two predictors (I-order interactions) and on the squared value of each predictor.

Performed analyses have indicated that *B* can be predicted very well using either ΔE^2, η^2 or their combination $\Delta E \cdot \eta$. However, since the $\Delta E \cdot \eta$ term does not provide better accuracy and requires knowing both ΔE and η values, this relation might be seen as redundant and was not analysed in detail. Ultimately, both ΔE^2 and η^2 were proposed as useful to predict *B*. Noteworthy, it can be seen that for compounds with possibly low values of ΔE or η, the relation fitted within the investigated region would result in a meaningless, negative value of *B*. In this regard, the below investigated range, linear relation down to (0, 0) was proposed as more accurate, which is presented in Figure 12.2.2a. This was further justified by the control experiments of methyl orange (MO) degradation, which agreed that visibly lower ΔE and η result in a significantly slower degradation rate, and in such case negative value of *B* must be avoided (Figure 12.2.2b.). Finally, pollutant-refined model showed better accuracy than the initial approach, proving that statistically, possible effect of the pollutant structure can be extracted from the overall data. As presented in Figure 12.2.2c., only one point significantly stands out from the y = x relation, which is a process of ibuprofen degradation over the {1 0 1} facets. However, it is noteworthy that this combination is a special case, since under accepted conditions ibuprofen is in anionic form and {1 0 1} facets are expected to accumulate photogenerated electrons under irradiation. In this regard, this particular combination might suffer from the increase in repulsive interactions during the photocatalytic process, significantly decreasing observed *k*.

Ultimately, the final model included three main terms, that represent either charge carriers trapping and a number of available surface sites, analogically to the previous study, and predictor of the pollutant reactivity (η or ΔE). Interestingly, it is worth noting that from all molecular predictors considered in this work, the correlation was observed only for those that include both the stability of the oxidised and reduced molecule simultaneously. It agrees with some general observations that usually it is not possible to identify single, well-defined way to initiate the degradation process, and most of the time multiple reactive
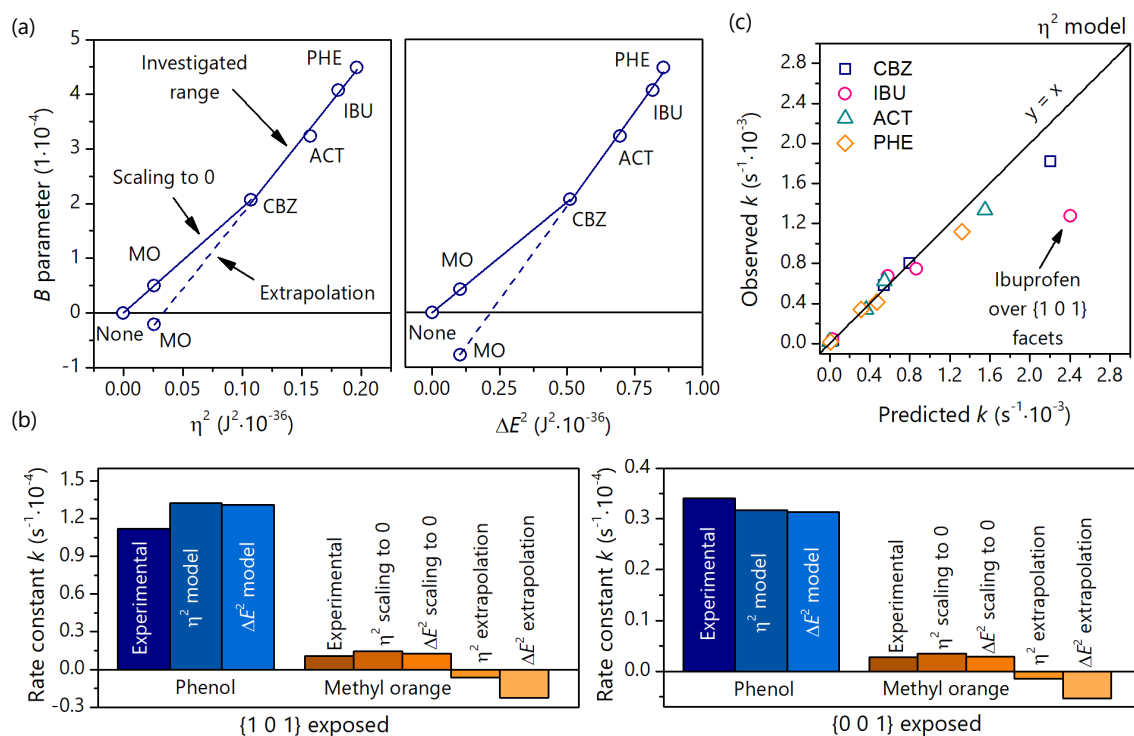
Figure 12.2.2. Results of B fitting to the η^2 and ΔE^2 predictors, including original investigated range and scaling/extrapolation to lower values. In case of methyl orange (MO), two estimated B values are shown, depending on the adopted approach (a). Comparison of the degradation rates for phenol and methyl orange degradation over the {1 0 1} and {0 0 1} facets, including values predicted with different model details and experimentally observed. Outside of the pollutant structure, both these processes were identical (b). Visualisation of the final model accuracy within the originally investigated range of η^2 (c).

species are found to be important for the reaction efficiency [145], [146]. Especially, the stability of the oxidised molecule ($n-1$ electrons), which is often considered as a very initial species formed during photocatalytic degradation (due to h^+ or $\cdot$OH action) [140], [147], was not found to be a universal predictor of the degradation rate. Furthermore, it was presented that pollutants with lower stability of both $n-1$ and $n+1$ electron states react faster during the TiO$_2$-assisted degradation.

12.3. DEGRADATION OF THE PHARMACEUTICALS MIXTURE [P4]

Following the presented analyses of the pollutant-photocatalyst interactions, additional experiments were performed to study the behaviour of the prepared materials when all three pharmaceuticals were present simultaneously. During these processes, the ratio between CBZ, IBU and ACT was always approximately 1:1:0.5 (mg$\cdot$dm^{-3}), while the total concentration varied between 5 and 50 mg$\cdot$dm^{-3}. As presented in Figure 12.3.1., a noticeable effect of total concentration on the degradation rate of different pollutants can be observed. Specifically, ibuprofen degrades visibly faster for the highest concentration, while acetaminophen degradation is enhanced only for the lowest one. This trend suggests that there is a strong preference about which compound reacts in the first place, independently of the previous analysis. Interestingly, this degradation preference of
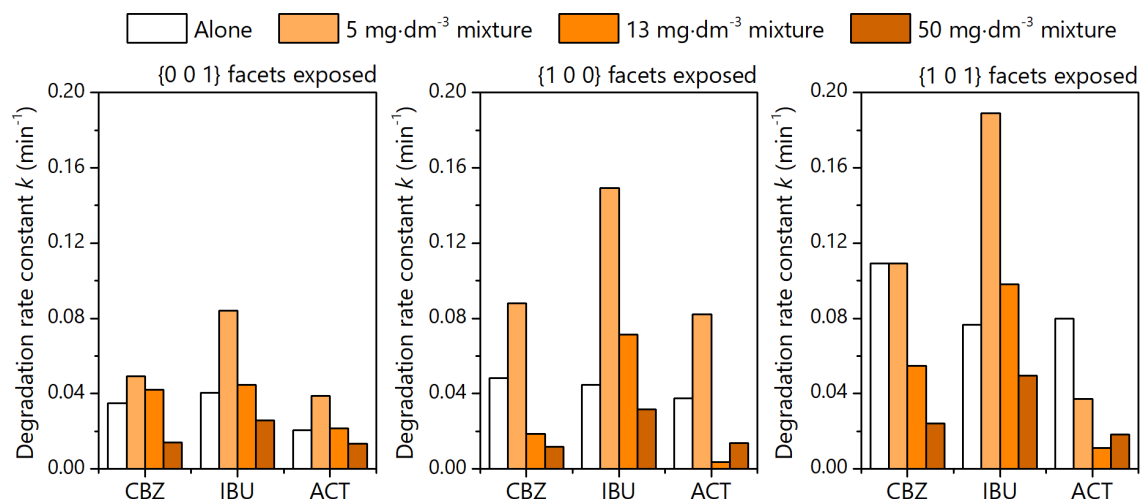
Figure 12.3.1. Rate constants obtained from the degradation testes of pharmaceuticals mixture over the different anatase crystal facets, compared to single-compound studies. Each mixture was composed respectively of 1:1:0.5 carbamazepine (CBZ), ibuprofen (IBU) and acetaminophen (ACT).

ibuprofen > carbamazepine > acetaminophen is in accordance with the possible adsorption of each compound during the stabilisation period, as can be observed in Figure 12.2.1. for the case of single-compound degradation. In this regard, for the combination of multiple compounds, preferred adsorption might be seen as an additional factor, decisive for the final degradation rate.

Finally, it is also noteworthy that during these experiments, all three TiO$_2$ samples were analysed in the three consecutive cycles of degradation for the 5 mg·dm^{-3} mixture, showing no visible signs of activity loss. Simultaneously, the {1 0 1} facets achieved the highest removal of organic carbon, analogically to previous results. As the last experiment, results obtained in the alternative reaction setup with Hg lamp (degradation of 5 mg·dm^{-3} mixture) were completed with the control process under Xe lamp illumination, using setup from previous studies. This has shown that under UV-vis light, degradation order was almost identical to the case of single-pollutant studies using UVA light (including both type of the exposed facet and structure of pollutant). Although the exact reason for this observation cannot be suggested at the moment, it does confirm that the final degradation rate will further depend on the technical details of the reaction setup, which generally is a known issue of photocatalytic reactions [148].

12.4. SUMMATION OF THE RESULTS FOR OPTIMISED FACET EXPOSITION

Information stressed to this point (publications [P1-P4]) closes the first part of the work, focusing on the dominant exposition of the low index anatase facet and in-depth analysis of their performance during water treatment from organic pollutants. In this regard, additional comments are made in this section to highlight most important findings of all these works together. Specifically:

1. Effect of the exposed facet is significant and {1 0 1} are best-suited for the degradation processes: As systematically observed, the {1 0 1} facets can achieve visibly higher degradation rates and TOC removal than both {1 0 0} and {0 0 1}. While the final values of both k and TOC removal can change depending on other factors, the overall conclusions are almost always the same, which confirms hypothesis [H1],

2. TOC removal is not always proportional to the degradation rate of the parent compound: Although ultimately, the sample with non-defected {1 0 1} facets achieved the best results of both these responses, the overall data clearly show that photocatalysts with faster degradation rates failed to remove organic carbon with proportional efficiency on multiple occasions. Therefore, the relation between these two problems is not strict and should always be considered separately (disproving hypothesis [H2]),

3. Degradation pathway does not depend on the exposed facet, but can depend on the surface defects: Although initial results have suggested that different by-products of phenol are formed, depending on the exposed facet, the results obtained for the non-defected surface structures always showed similar formation of hydroxyphenols (detailed results are presented e.g. in Figure 7 in publication [P3]). Analogically, for these samples, no significant changes in the chromatographs were observed during the degradation of pharmaceuticals. Therefore, hypothesis [H3] was not confirmed for the stoichiometric surfaces. However, it can be noticed that two cases when the absence of *ortho*-hydroxyphenol was observed are both connected with possible presence of Ti^{3+}/TiO_{2-x} defects at the surface (samples NH_4OH and N_2H_4 from publication [P1] and Group B from publication [P2]). In this regard, degradation pathway seems more dependent on the possible surface defects than the exposed facet itself, which can be investigated deeper in further works,

4. Degradation rate is proportional to the available surface active sites and probability of charge carriers trapping on the surface: As presented in publications [P3] and [P4], the per-surface activity of the stoichiometric facets follow mostly ratio between the number of surface active sites and pollutant concentration, further completed with the probability of charge carriers trapping. Specifically, combination of linear relation with the first term and exponential relation with the trapping energy allowed to recreate general trends in all degradation tests of single compounds. This was observed independently on the two reactor geometries, two different light sources and five different pollutants investigated in the water and gas phases. Therefore, it confirms that trapping energy is probably the most important parameter of the exposed TiO_2 facet during degradation of organic pollutants, in accordance with hypothesis [H3],

5. Activity order for the investigated facets does not change for different water pollutants, but the final rate scales with the chemical hardness/ LUMO−HOMO gap of the pollutant: The per-surface activity order of {1 0 1} > {1 0 0} > {0 0 1} was observed for all investigated compounds, disproving hypothesis that it can be affected by the structure of pollutant [H4]. On the other hand, the final rate over all facets was found to increase proportionally to the $\eta^2/\Delta E^2$ of the pollutant, showing that compounds which form less stable intermediate states (both oxidised and reduced together) react faster during the process. The final model predicts well order-of-magnitude differences between rate constants obtained for compounds like phenol and methyl orange,

6. Other important parameters might be identified and possibly introduced to improve prediction of the degradation rate, but the observed relations are less universal: Surface energy, utilized setup (different light source, flux intensity and reactor geometry), presence of pollutants mixture and the exact expression for the number of available surface active sites were all found to further influence predicted degradation rate. However, no universal relation between these parameters and overall data can be established. For example, compared to the single-compound studies, the degradation order of ACT, CBZ and IBU in mixture over the {1 0 1} was different when studied using UVA light, but was the when same using UV-vis light.

13. INTERACTIONS WITH THE FERRIMAGNETIC BARIUM HEXAFERRITE [P5]

Following analysis of the unmodified materials, further experiments were focused on combining analogical anatase nanoparticles with other, well-defined semiconducting phases. Since the main focus of the performed works was aimed at water treatment application, studied TiO_2 was specifically combined with the ferrimagnetic materials, as such composites were recently proposed to enhance possible separation of the photocatalyst after the degradation process [149]. However, although the magnetic photocatalysts have been studied for a while now, there are no information in the existing literature that discusses their possible interactions with respect to the exposed crystal facet. Moreover, there is no in-depth information that would discuss both electron transfer and the possible effect of the built-in magnetic field of the ferrimagnetic phase on the final photocatalytic performance.

In this regard, the TiO_2 photocatalysts were combined with the $BaFe_{12}O_{19}$ hexagonal ferrite, which is a well-known ferrimagnetic material. Selection of the $BaFe_{12}O_{19}$ was based on its known semi-hard magnetic character with high remanent magnetization, strong uniaxial magnetic anisotropy, relatively low Curie point of approx. 450 °C and preference to growth into two-dimensional microparticles under hydrothermal conditions [150], [151]. Therefore, after successful $BaFe_{12}O_{19}$ preparation, TiO_2 could be deposited on the same, preferentially exposed facet of the ferrite, leading to a relatively fixed orientation between both phases. In such geometry, photocatalytic activity can be analysed either after

magnetization of the ferrite in the external field or in its demagnetized state, after crossing Curie point, without inducing significant changes in the phase structure of both materials (e.g. without transition of anatase to rutile). Finally, coating of the $BaFe_{12}O_{19}$ with SiO_2 layer before deposition of the TiO_2 was also made as the control experiments, when electron transfer between the ferrite and photocatalyst was hindered.

Preparation of the $BaFe_{12}O_{19}$ was confirmed with the XRD, SEM and measurements of the magnetic properties. As presented briefly in Figure 15.1a., the final prepared ferrite revealed 1.8% (wt.) of the α-Fe_2O_3, probably as the result of the CO_2 capture from the atmosphere during the preparation, which is a known problem [152]. Despite several preparation attempts, the total elimination of the α-Fe_2O_3 from the final structure was unsuccessful (details are discussed in the publication). Nevertheless, as presented in the Figure 15.1b. and Figure 15.1c., such material already exhibits both uniform micro-platelet morphology and uniform magnetic response (smooth magnetization hysteresis, without visible steps, as presented in Figure 15.1c.), which was suitable enough for further study.

Deposition of the silica on the ferrite surface (sample $BaFe_{12}O_{19}@SiO_2$) was further studied with the combination of Fourier transform infrared spectroscopy (FTIR), zeta potential (ζ) measurements and XPS analyses, as summarized in Figure 15.2. All three measurements indicated the appearance of the features characteristic for the SiO_2 presence, being either ~1100 cm^{-1} peak in the FTIR spectrum [153], ζ potential shift to the negative values [154] and Si 2p signal in the XPS. Interestingly, XPS results showed that deposited Si exist as a highly non-stoichiometric structure, with a visible contribution of the metallic species, originating either from the Si-Si bonds or, alternatively, from the possible Ba-Si and Fe-Si bonds at the interface with ferrite (nevertheless, it will be still referred to as "SiO_2" for clarity of discussion). Noteworthy, detailed XRD, SEM and EDS results have not indicated any noticeable differences between the unmodified and SiO_2-
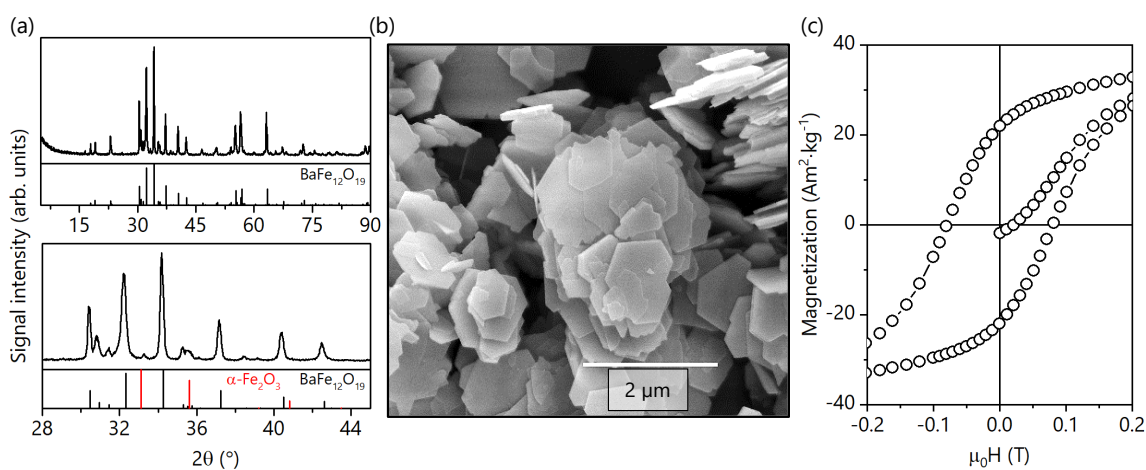

Figure 15.1. XRD pattern of the final $BaFe_{12}O_{19}$ sample (a), together with the exemplary SEM image (b) and closeup to irreversible part of the magnetic hysteresis loop of the material (c). Detailed results of the magnetic properties measurements are presented in the publication [P5].
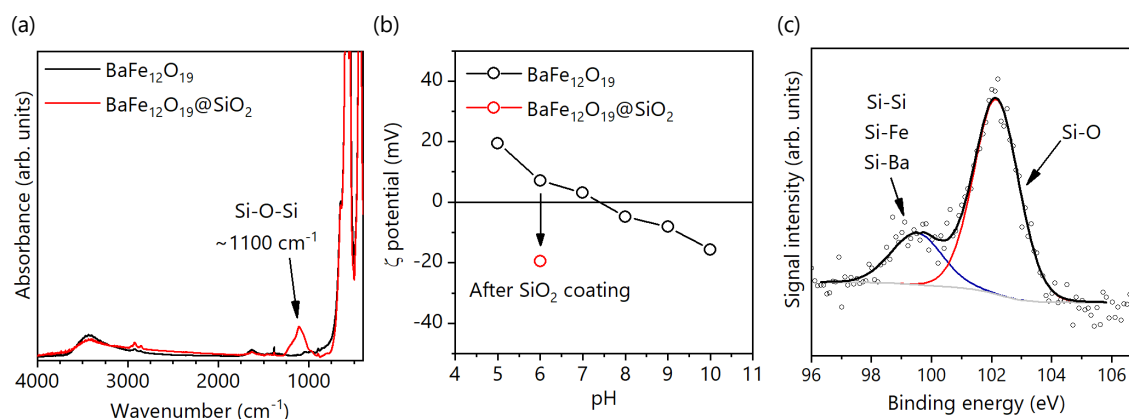
Figure 15.2. FTIR spectra of the $BaFe_{12}O_{19}$ sample before and after surface modification with SiO_2 (a), together with the corresponding shift in the ζ potential value due to the SiO_2 presence (b) and deconvoluted Si 2p signal observed in the XPS spectrum of the modified sample (c).

modified samples, which prove SiO_2 to be strictly at the surface without forming any largerr, independent entities.

The prepared $BaFe_{12}O_{19}$ and $BaFe_{12}O_{19}@SiO_2$ samples were further combined with the three types of TiO_2 particles, with different facets exposed in the majority, by a simple physical mixing of the dispersions with possibly suitable pH. This was followed by evaporation of the solvent under constant mechanical stirring and calcination of the composite at 500 °C for 2 h. For each TiO_2 crystal facet, composites were prepared in three combinations: (I) with 25% wt. of TiO_2 deposited on the unmodified $BaFe_{12}O_{19}$, (II) with 50% wt. of TiO_2 deposited on the unmodified $BaFe_{12}O_{19}$ and (III) with 50% wt. of TiO_2 deposited on the $BaFe_{12}O_{19}@SiO_2$. Noteworthy, higher TiO_2 contents were not designed since relatively large particles of the $BaFe_{12}O_{19}$ offer only limited surface for creation of the well-defined interface. Therefore, for the smaller fraction of $BaFe_{12}O_{19}$, the interactions between both phases might be more difficult to observe. Morphology and crystal phase composition of all composites were checked with the XRD and SEM analyses, which in each case confirmed the formation of the designed structures. As presented in Figure 15.3., TiO_2 particles can be easily observed on the surface of the $BaFe_{12}O_{19}$, with their characteristic morphological features highlighted. Noteworthy, some differences between observed TiO_2 morphology and previous studies might especially result from additional calcination, performed to strengthen the connection between both phases in the composite.

As-prepared materials were studied in reaction of phenol degradation as the model pollutant, performed with a slightly alternated setup, in order to eliminate the need for magnetic stirring during the process. Specifically, photocatalysts dispersions were mechanically mixed with the customized 3-D printed stirrer, without airflow introduction and under reduced light flux. The light source (Xe lamp) and photocatalytic reactor were analogical to the general setup (Figure 8.1). Phenol degradation was monitored spectrophotometrically after conjugation reaction with the 4-nitroaniline. Figure 15.4. show overall results of the phenol degradation, including control TiO_2 samples (calcined at 500 °C, analogically to the composites) and $BaFe_{12}O_{19}$ alone. In this figure, straight lines connecting end points of each series represent activity level expected from the simple

TiO$_2$ {0 0 1} exposed
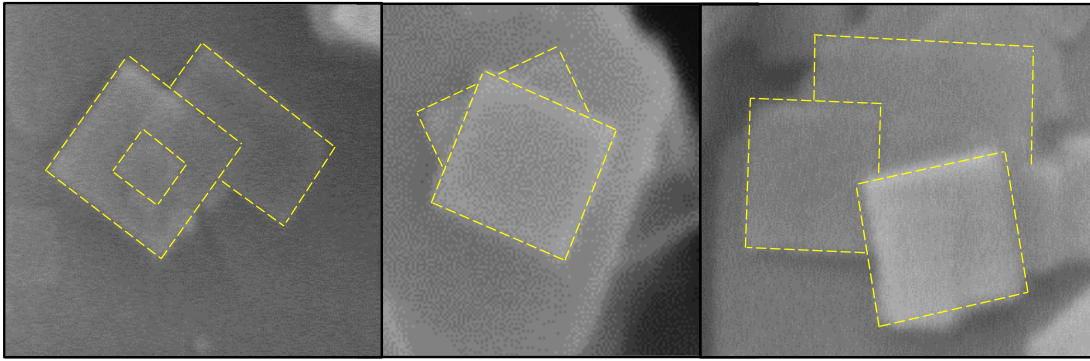
TiO$_2$ {1 0 0} exposed
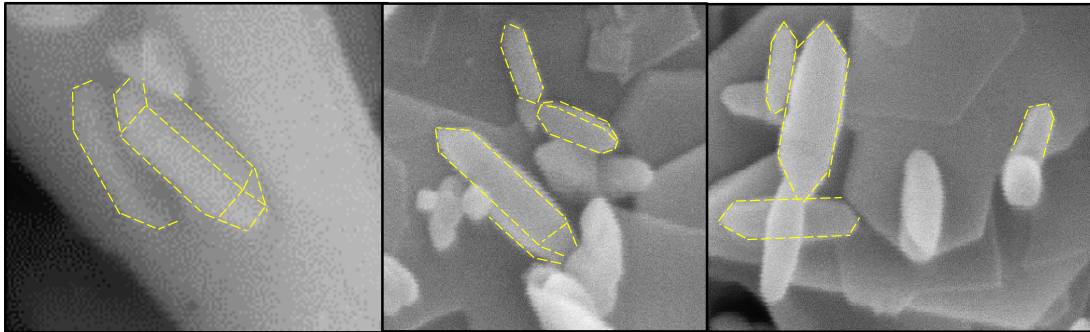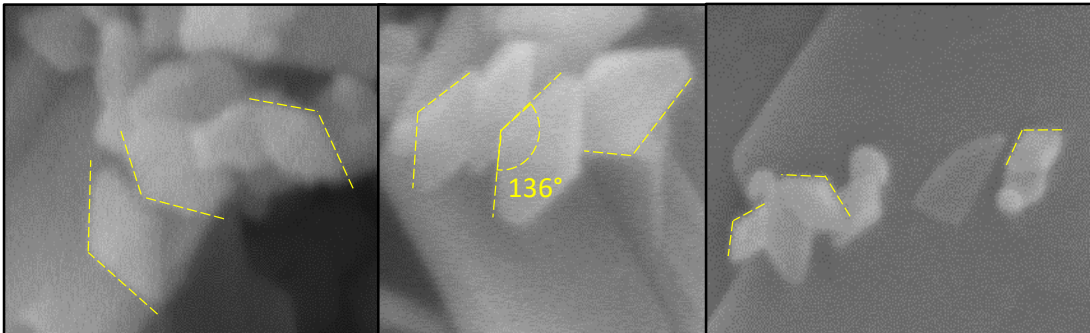

TiO$_2$ {1 0 1} exposed

Figure 15.3. Closeups of the SEM images, highlighting TiO$_2$ particles deposited on the ferrite surface for all three low index facets investigated.

fraction of each phase in the composite. Therefore, if the experimental activity agrees with this line, it can indicate that effectively no significant interaction affect final degradation. Noteworthy, this is the case for the combination of the SiO$_2$-covered ferrite with all TiO$_2$ materials, being in accordance with the expected inhibition of the electron transfer in the presence of insulating interlayer. Furthermore, for the non-modified BaFe$_{12}$O$_{19}$, two significant effects can be noticed. First is reduction of the degradation ability of the sample with 50% of the {1 0 1} TiO$_2$, as well as a significant improvement of the 25% {1 0 0} performance after magnetization of the ferrite.

Obtained results show two important conclusions. First of all, electron transport to the ferrite is especially undesirable for the activity of TiO$_2$ with {1 0 1} facets exposed. As presented in Figure 15.5a., these observations were further completed with the Mott-Schottky analysis, which confirmed band alignment suitable for the possible electron
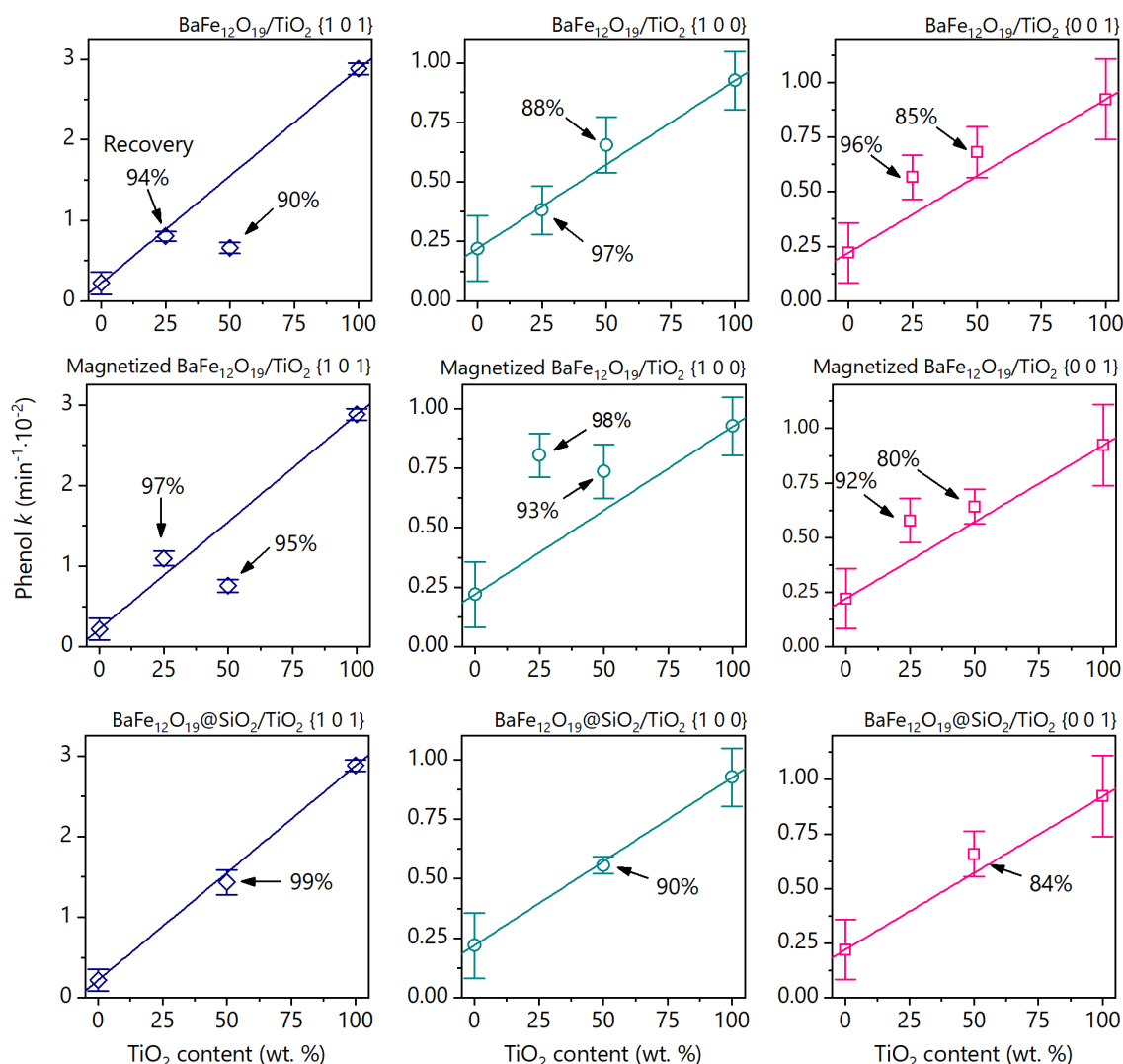
Figure 15.4. Results of the photocatalytic phenol degradation over the prepared composites, including (from top) demagnetized ferrite after the calcination above Curie point, ferrite magnetized with the laboratory magnet and demagnetized ferrite with surface covered with SiO_2. Lines represent activity level expected from the simple fraction of both phases. Control TiO_2 samples included calcination, analogical to the composites

transfer in order of $BaFe_{12}O_{19}@SiO_2 \rightarrow TiO_2 \rightarrow BaFe_{12}O_{19}$. This suggests that excited electrons are especially decisive for the activity of the {1 0 1}, however, the same is not happening for the {0 0 1} and {1 0 0} facets. This is in accordance with the fact that on both of these facets, electrons, which remain as the majority carriers in all materials, are not needed to dissociate water, and generation of the ·OH might occur efficiently simply through the h^+ oxidation at the interface. Therefore, it is presented that the effect of the same junction can be very different, depending on the exposed crystal facet, and the final results can be tracked down to the existing information about the fate of both h^+ and e^- on each surface, respectively.

Secondly, the effect of the built-in magnetic field can stimulate reaction efficiency, but the observed effect is not isotropic and depends on the orientation between TiO_2 and $BaFe_{12}O_{19}$. These results were further completed with the photoluminescence studies,

which have indicated that particularly for the sample 25% {1 0 0}, magnetization prior to the measurements reduces observed emission, therefore affecting recombination of the charge carriers, as presented in Figure 15.5b. While it must be highlighted that at this point, it is not possible to distinguish if this effect results strictly from the orientation of both phases in their bulk form or due to the surface-specific states on each facet, it is interesting to notice that specifically for the {1 0 0} exposing sample deposited on the $BaFe_{12}O_{19}$, the
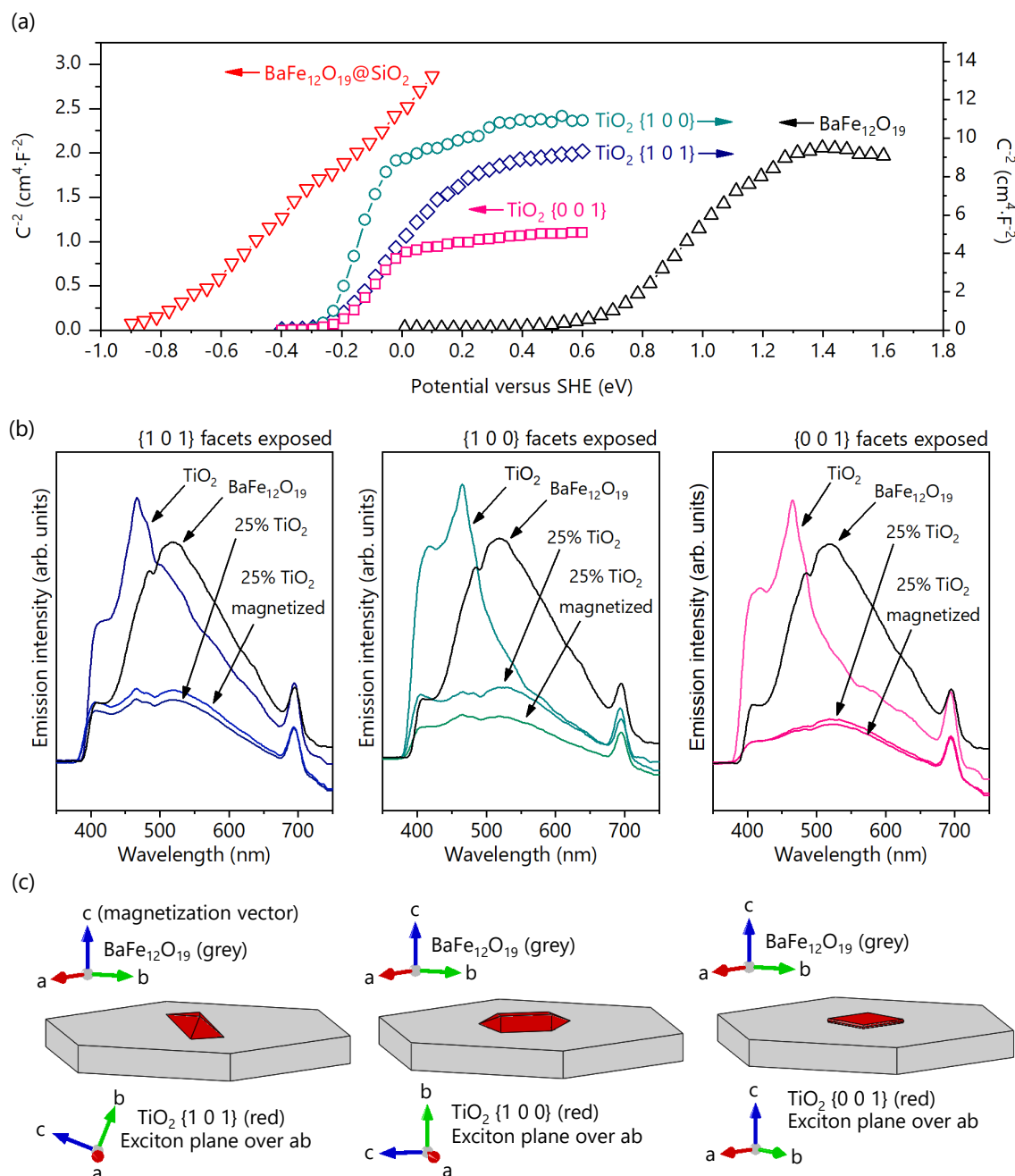
Figure 15.5. Mott-Shottky plots of all single-phase components of the prepared composites (a). Photoluminescence spectra of the single-phase TiO_2 and $BaFe_{12}O_{19}$, together with the magnetized and demagnetized composite with 25% of each TiO_2 (b). Idealized orientation between both phases within the prepared composites, due to the different geometry of the deposited TiO_2 particles (c). Arrows in panel (a) categorize each data to the OY axis.

Lorentz force generated by the ferrite magnetic field should act perpendicular to the exciton plane within anatase structure [25] (idealized orientation within each composite is presented schematically in Figure 15.5c.). Therefore, especially for this combination, generated Lorentz force might influence the exciton dissociation, being a possible source of the observed differences. This would also explain the almost zero effect of the magnetic field on the activity of the {0 0 1} facets, where Lorentz force should act perpendicularly to the exciton plane.

Overall, the main conclusions support the initial hypothesis [H6], showing very different effects of both electronic and magnetic interactions between the faceted TiO_2 and ferrimagnetic $BaFe_{12}O_{19}$. Noteworthy, this is the first time when such detailed interactions were extracted and discussed from the overall performance of such composites.

14. INCREASING ELECTRON DENSITY AT THE GROUND STATE [P6]

Based on the described studies [P1-P5], the high activity of the {1 0 1} facets was attributed mostly to the high probability of charge carriers trapping at their surface, while especially preference to trap electrons might also stimulate braking of the benzene ring of aromatic compounds through increased involvement of $\cdot O_2^-$. Interestingly, another possibility to manipulate the number of reacting charge carriers might be connected with their ground state density, strictly related to the point defects of the crystal structure. In this regard, introduction of e.g. dopants might further influence the number of holes or electrons reacting on a specific facet. Noteworthy, experimental investigation of this interplay between charge introduced with a dopant and exposed crystal facets has not been presented so far, even though computational studies usually analyse exactly analogical case of $n+1$ and $n-1$ surface models to describe the possible behaviour of both charge carriers.

In this regard, samples with the optimised exposition of the investigated crystal facets were doped with Nb^{5+} to increase ground state density of electrons for each nanostructure and investigate resulting properties. The selection of Nb was based on its known electron-donating character when introduced as a dopant into TiO_2 as well as its limited effect on the density of states distribution when substituting Ti within bulk anatase structure [155], [156]. Therefore, the possible formation of surface-specific electron states could be easier to observe.

Obtained materials were analysed with XRD, SEM and EDS for the crystalline structure, morphology and Nb presence, with additional control measurements of Nb concentration obtained from the inductively coupled plasma atomic emission spectroscopy (ICP-OES). Both elemental analyses confirmed that Nb concentration increased systematically in each series, with only limited deviations from the designed Nb/Ti ratios. Furthermore, the introduction of Nb has not resulted in the presence of any NbO_X phase in the XRD pattern, as well as has not induced any visible change in the particles morphology (exemplary images of the most doped samples are presented in Figure 13.1a.). On the other hand, in

the case of the nanoparticles exposing {1 0 0} and {1 0 1} facets, the unit cell of the anatase structure is expanding systematically with the increase of Nb concentration, as presented in the inset of Figure 13.1a based on the Rietveld-refined XRD patterns. This is in agreement with a slightly bigger ionic radius of Nb^{5+} when substituting Ti^{4+} in octahedral coordination [157]. The same trend was not observed for the {0 0 1} exposing nanoparticles, however it is noteworthy that in this case, the introduction of HF during the synthesis might result in a simultaneous increase of the oxygen vacancies (V_O) concentration. Since the formation of V_O leads to the appearance of Ti^{3+} states, it might also result in the expansion of the anatase unit cell due to a bigger radius of Ti^{3+} than Ti^{4+}, as reported in the literature [158] (the actual size order of the ions is $Ti^{3+} > Nb^{5+} > Ti^{4+}$). Therefore, for this particular case, competition between Nb^{5+} incorporation and possible etching of the oxygen atoms by HF might lead to the non-linear change of the unit cell volume.

Following structural and elemental characterization, the effect of Nb presence for each exposed facet was thoroughly investigated using a series of spectroscopic techniques. The most important findings are presented in Figure 13.1b. and 13.1c., based on the combined absorbance spectroscopy (DR-UV/vis), low-temperature electron paramagnetic resonance spectroscopy (EPR) and reverse double-beam photoacoustic spectroscopy (RDB-PAS). Specifically, DR-UV/vis results have indicated that in the case of the {1 0 1} facets, the introduction of Nb significantly increased absorbance up to the NIR range, which is characteristic for the presence of excess electrons within TiO_2 structure [159], [160]. However, significant differences in the absorbance between the series showed that exposed crystal facet affect the fate of the Nb-introduced electrons. The low-temperature (liquid N_2) EPR results have further proved that in the case of both {0 0 1} and {1 0 0} facets exposed, electrons get trapped strictly as the bulk Ti^{3+} states, forming well-defined doublet with g = 1.989 and g = 1.955 [161]. However, this was not observed for the {1 0 1} facets. Instead, in this case, a slight distortion of the EPR spectrum was noticed, especially for the lower g values (higher magnetic field). This suggests that for the {1 0 1} facets, electrons might localise at the surface sites since broad, distorted EPR signals in this region are characteristic for the surface-trapped e^- [161], [162]. Nevertheless, this effect in the EPR spectrum is not explicit and therefore, the surface presence of electrons was confirmed with the RDB-PAS measurements. RDB-PAS is a relatively new method developed strictly to determine the density of electron traps in the powdered photocatalyst samples [163]. During these measurements, electrons from the valence band are excited directly to the trapping states using wavelength-scanned continuous light irradiation, with methanol acting as the scavenger of photogenerated holes. As presented in Figure 13.1c, these measurements confirmed that upon doping with Nb^{5+}, the measured density of electron traps for the {1 0 1} exposing nanoparticles practically disappeared, proving that these states became occupied with introduced electrons. As RDB-PAS is known to be especially sensitive towards surface trapping sites, showing a clear correlation of the observed trap density with surface development [163], these results ultimately prove that for the Nb-doped particles with {1 0 1}, electrons will tend to localise at the surface. Such effect was

not observed for the {0 0 1} and {1 0 0} facets, in accordance with absorbance and EPR results. Noteworthy, described features of the Nb-doped {1 0 1} facets were not sensitive to the O_3 treatment and H_2O_2 washing, proving that these states are not easily oxidised.

Interestingly, it is worth noting that these results were not straightforwardly supported by the XPS analysis. This is mostly due to the fact that Nb presence was not found to increase the fraction of the Ti^{3+} states on the {1 0 1} facets, which might have been expected as the result of electron accumulation on the surface. Instead, for each nanostructure, a significant fraction of the Nb^{4+} states were observed in the Nb $3d_{5/2}$ signal. The reason for this might be connected with the alternated presence of the surface species during the XPS measurements in high vacuum conditions. As presented in the introduction, it is expected that charge localisation on the surface will be affected by even up-to-few layers
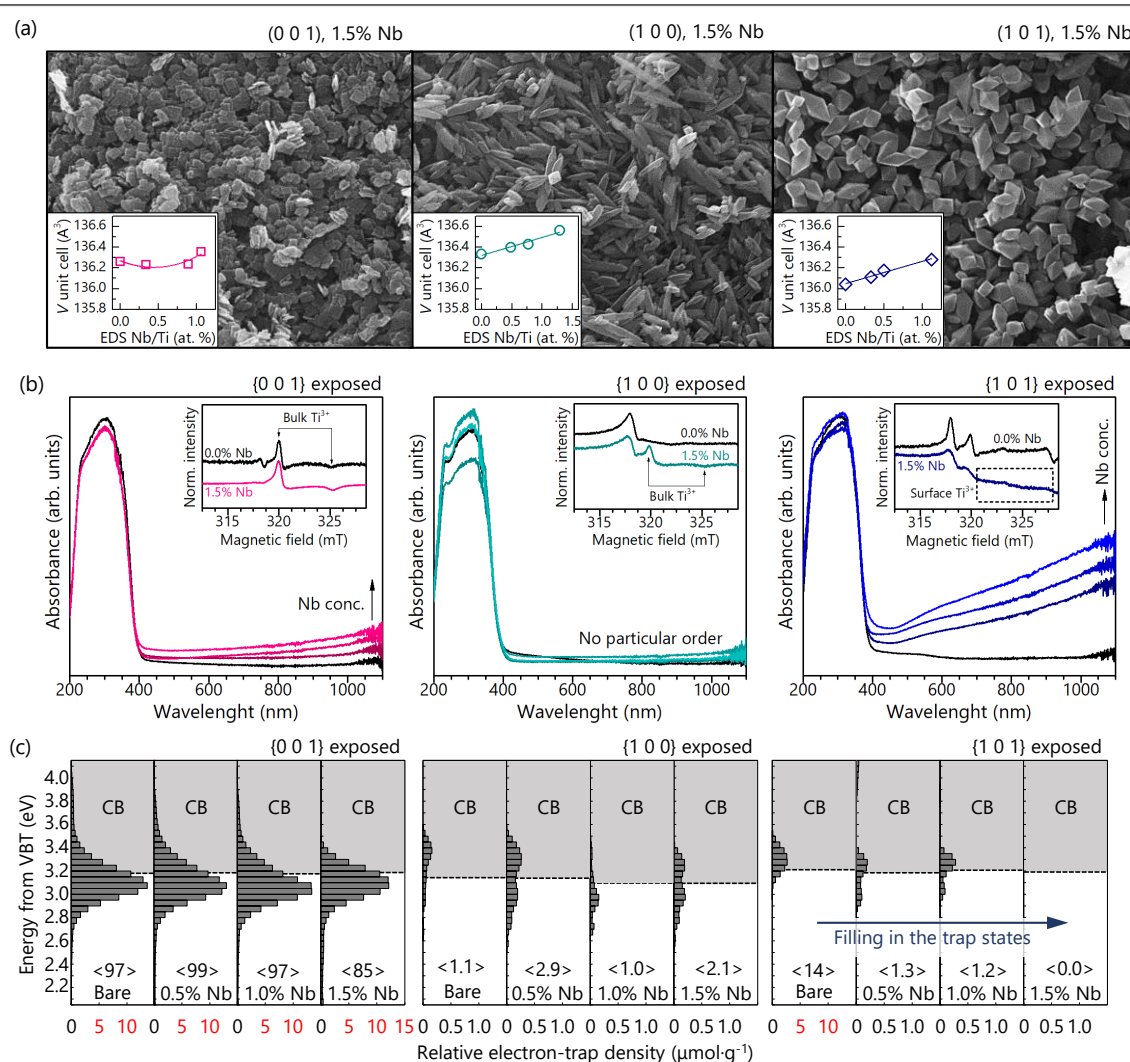
Figure 13.1. Exemplary SEM images of the TiO_2 nanoparticles doped with 1.5% atomic of Nb (relative to Ti), with observed evolution of the anatase unit cell volume for each series in the inset (a). Absorbance spectra of all obtained Nd-doped samples, together with the EPR spectra (77 K) of the corresponding unmodified and most-doped samples in each series shown in the inset (b). Distribution of the electron-trap density obtained for all samples from the RDB-PAS measurements. Please note different values on the X scales. Total trap densities are given in chevrons within each individual graph (c). The "VBT" stands for "valence band top" and "CB" stands for "conduction band".

of possible H_2O/O_2 species adsorbed and detailed bonding between them, which might differ between vacuum and non-vacuum measurement conditions. In this regard, results obtained from the DR-UV/vis, EPR and RDB-PAS measurements are treated as closer to the actual conditions of the photocatalytic reactions. Nevertheless, the exact structure of the electrons localised on the Nb-doped {1 0 1} facets might be described more precisely in the future.

Following characterization, prepared materials were studied in the reactions of photocatalytic phenol degradation and 4-nitrophenol (4-NPH) reduction to 4-aminophenol in methanol. Especially, the second one was performed specifically to investigate the effect of introduced electrons on the reaction that strictly requires e^- transfer to the substrate. Interestingly, as presented in Figure 13.2., the effect of Nb presence can be completely different, depending on the exposed crystal facet, which is observed independently on the possible surface normalisation. In the case of both reactions, the highest efficiency was observed for the unmodified {1 0 1} facets and Nb introduction always significantly decreased their activity. On the other hand, the reduction ability of the {0 0 1} and {1 0 0} can be visibly enhanced due to the presence of Nb, achieving respectively 64% and 600% increase of 4-aminophenol formation, relative to the
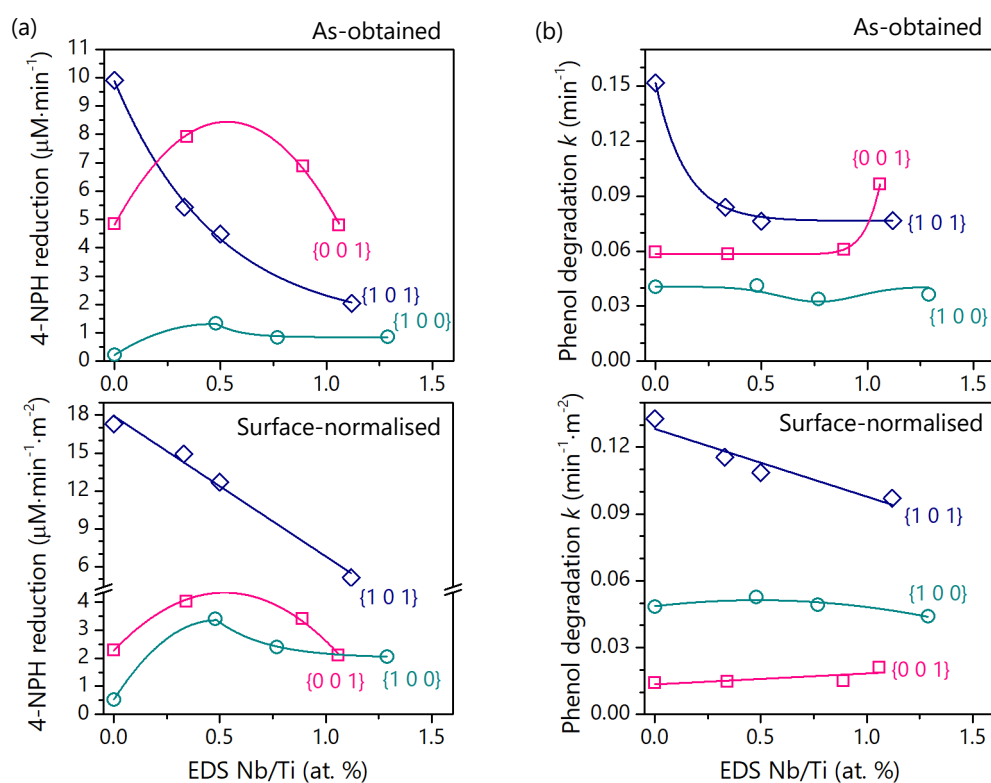
Figure 13.2. Summation of the observed photocatalytic activity of all Nb-doped samples in the reactions of 4-nitrophenol (4-NPH) reduction to 4-aminophenol (a) and phenol degradation (b). Data is presented both directly as-obtained and after the normalisation of the results with the surface area of the photocatalyst, calculated from BET isotherms. Detailed change in the concentration of the monitored compounds is presented in the Supporting Information of the Publication [P6].

unmodified samples. These results clearly support hypothesis [H7], proving that the effect of the same dopant can be opposite, depending on the structure of the exposed facet. Interestingly, it could be noted that the negative effect of Nb presence is observed only for the "reductive" {1 0 1} facets, which have a preference to trap electrons, while it can be positive (4-nitrophenol reduction) or is minimal (phenol) in case of both "oxidative" {0 0 1} and {1 0 0}. Nevertheless, it is also visible that in both cases, the unmodified {1 0 1} achieves the best performance, leading to the conclusion that overall, the introduction of Nb is not beneficial for maximising observed photocatalytic activity.

REDUCING ELECTRON DENSITY FOR THE {1 0 1} FACETS

Following the results obtained for the materials doped with Nb^{5+}, it was concluded that excess electrons indeed tend to localise at the surface of the {1 0 1} facets, in accordance with computational predictions. However, as the consequence, the resulting photocatalytic activity is significantly hindered. Interestingly, this is despite existing information clearly highlight multi-electron oxygen reduction as critical for the activity of these facets during ROS generation, and this reduction should be enhanced when excess electrons are present within the material [67], [72]. Possibly, this effect might be connected with the fact that too high concentration of the excess electrons will hinder the subsequent h^+ transfer, which must also occur during the overall reaction. In this regard, the activity of the {1 0 1} facets was further investigated upon systematic introduction of the electron-accepting dopant, in order to obtain data in the broader range of ground state concentration of free e^-. As a suitable dopant, Gd^{3+} was used due to its stable 3+ oxidation state, the possibility to substitute Ti^{4+} within the anatase structure without the formation of the additional states deep within the bandgap, as well as its limited solubility in the alkaline environment (used during the synthesis of the {1 0 1} exposing particles) [164]. Preparation procedure was analogical to the Nb^{5+} case, with $Gd(NO_3)_3 \cdot 9H_2O$ used as the Gd^{3+} source and with the designed Gd/Ti concentrations being 0.00%, 0.25%, 0.50%, 0.75%, 1.00% and 1.50% (at.).

Similar to the previous studies, combination of the XRD, SEM and BET adsorption studies revealed all prepared samples to be single phase anatase with well-defined octahedral morphology, clean facets and very similar surface areas (overall 16.5 ± 2 $m^2 \cdot g^{-1}$), as presented briefly in Figure 15.1. Furthermore, the Gd presence was analysed with the combination of EDS and ICP-OES studies, which both confirmed increasing Gd concentration within the series, with a slightly lower value obtained from the EDS, as presented in Table 15.1.

Following the initial characterization of the prepared samples, a detailed analysis of their electronic structure was performed based on the combined EPR, XPS and DR-UV/vis measurements. Similarly to the Nb-doped samples, XPS results clearly confirmed surface enrichment in Gd, compared to the designed Gd/Ti concentration, as presented in Table
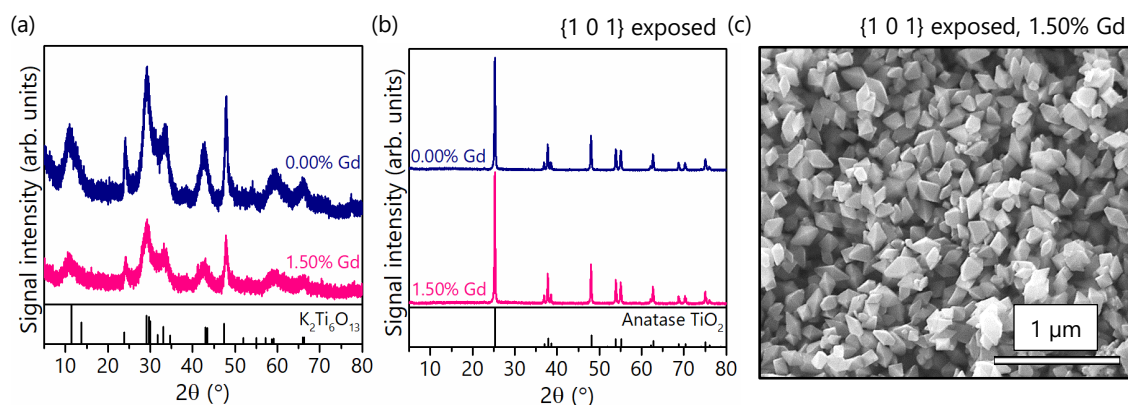
Figure 15.1. Exemplary XRD patterns of the prepared, undoped and Gd-doped $K_2Ti_6O_{13}$ precursors (a), resulting single-phase anatase products (b) and exemplary SEM image of the anatase with 1.50% addition of the Gd (c).

15.1, together with other XPS results. Furthermore, analysis of the Gd 4d and Gd 3d states indicated that their maxima are systematically shifted, compared to the reported values for the Gd_2O_3, $Gd(OH)_3$ and metallic $Gd/Gd-O_x$ [165]–[169]. This is followed by the detailed deconvolution of the Gd $4d_{5/2}$ states, supported by the existing information about their multiplet splitting [170], [171]. As observed, the Gd $4d_{5/2}$ signals can be easily deconvoluted using five expected bands (magenta lines in Figure 15.2a.), however their relative intensities change between the samples and generally differ from the existing reports for the high-quality Gd compounds, with low-energy bands being greatly supressed. Both these observations strongly indicate that the local environment of Gd^{3+} ions is different in case of the prepared samples, which is in accordance with its role as a dopant within the TiO_2 lattice. Beside the Gd states, XPS analysis of other elements have not indicated other significant differences, with exemplary Ti 2p, C 1s and O 1s signals presented in Figure 15.2b.

Interestingly, as presented in Figure 15.2c., low temperature X-band EPR spectra have suggested more complex structure than XPS, as beyond the Gd presence, it also indicated

Table 15.1. Summation of the EDS, ICP-OES and XPS results concerning Gd presence in the prepared samples. Presented values of Gd 4d and Gd 3d states correspond to the observed maxima.

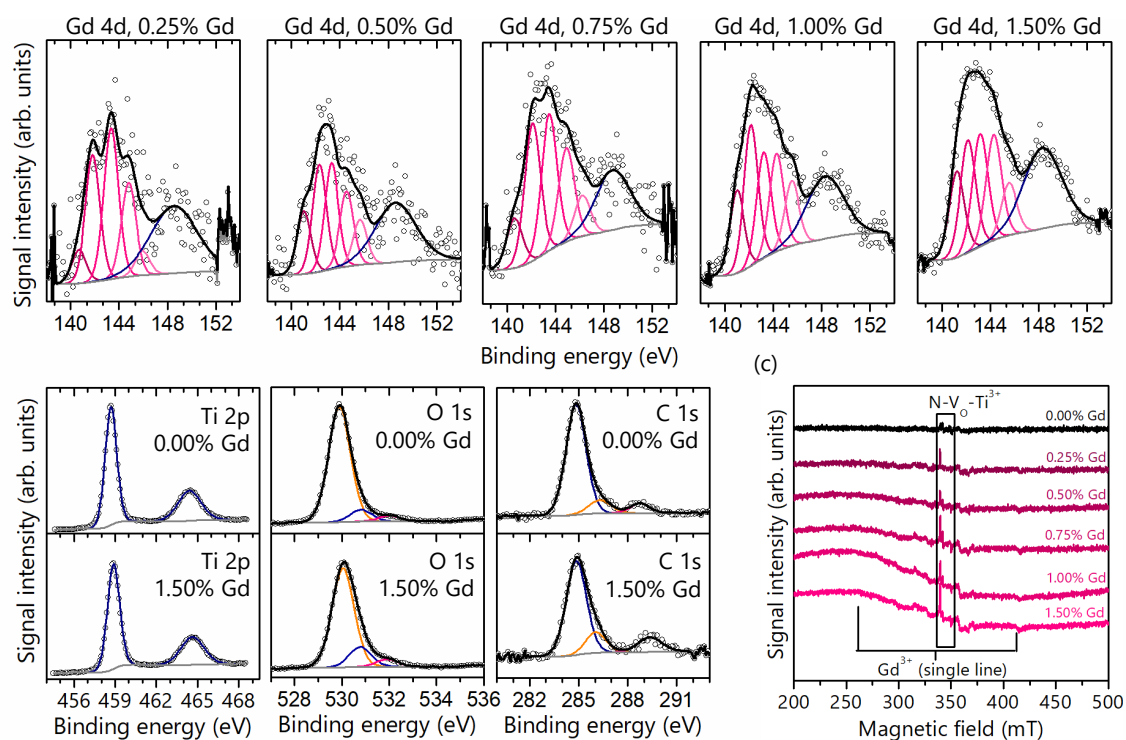| Sample	EDS Gd/Ti (at. %)	ICP-OES Gd/Ti (at. %)	XPS Gd/Ti (at. %)	Gd 4d (eV)	Gd 3d (eV)	Refs.
0.00% Gd	0.0	-	0.00	-	-	
0.25% Gd	0.2 ±0.2	0.24 ±0.01	1.75	143.0	1187.9	
0.25% Gd	0.4 ±0.2	0.48 ±0.01	4.76	142.8	1187,6	
0.75% Gd	0.5 ±0.2	0.65 ±0.01	4.43	142.9	1187.7	
1.00% Gd	0.8 ±0.2	0.82 ±0.01	6.68	142.8	1187.7	
1.50% Gd	1.0 ±0.2	1.45 ±0.01	8.91	142.7	1187.7	
Gd_2O_3				142-142.5	1187-1187.0	[165]–[169]
$Gd(OH)_3$				141.7	n.d.	
Gd				140-141	n.d.	

Figure 15.2. Deconvolution of the XPS Gd 4d signals, including multiplet splitting of the $4d_{5/2}$ states (magenta lines) for all Gd-modified samples (a), as well as exemplary Ti 2p, O 1s and C 1s signals for unmodified and 1.50% doped samples (b). Only single Ti state was observed for all samples, without noticeable, Gd effect on the O 1s and C 1s states. The X-band EPR spectra of all samples from the Gd-doped series recorded at 120 K (c), with the highlighted regions corresponding to the Gd^{3+} presence and possible $N-VO-Ti^{3+}$ defects. Additional signals in the recorded spectra (not marked) suggest ppm level presence of the transition metal ions impurities, possibly V^{5+}.

that other additional defects are always present within the samples. However, no clear correlation between their presence and amount of introduced Gd can be noticed, suggesting their origin as the random effect of the adapted preparation procedure. These signals can be roughly identified to originate from the complex $N-V_O-Ti^{3+}$ defects [172], [173], as well as the additional presence of other transition metals, possibly V^{5+} [174], [175]. Nevertheless, it should be noted that their concentration is very low and their possible contribution to the final photocatalytic activity is not obvious. Moreover, the lack of the observed/attributable XPS signals makes their detailed identification not possible at the moment.

Following the elemental analysis, XPS scanning of the valence band states have shown appearance of the additional signals below the lower edge of the TiO_2 band, as presented in Figure 15.3a., which origin from the Gd 4f electrons [166], [170]. Further DFT-based simulation of the Ti substitution by Gd within the (1 0 1) surface model (GGA+U) supports this observation to result from such doping, with additional states clearly formed below the lower edge of the simulated valence band (Figure 15.3b.). This is also followed by the formation of additional O 2p states slightly above the valence band edge. Indeed, a relative increase of the absorbance around the main valence-to-conduction band transition was also noticed for the Gd-doped samples during the DR-UV/vis measurements after
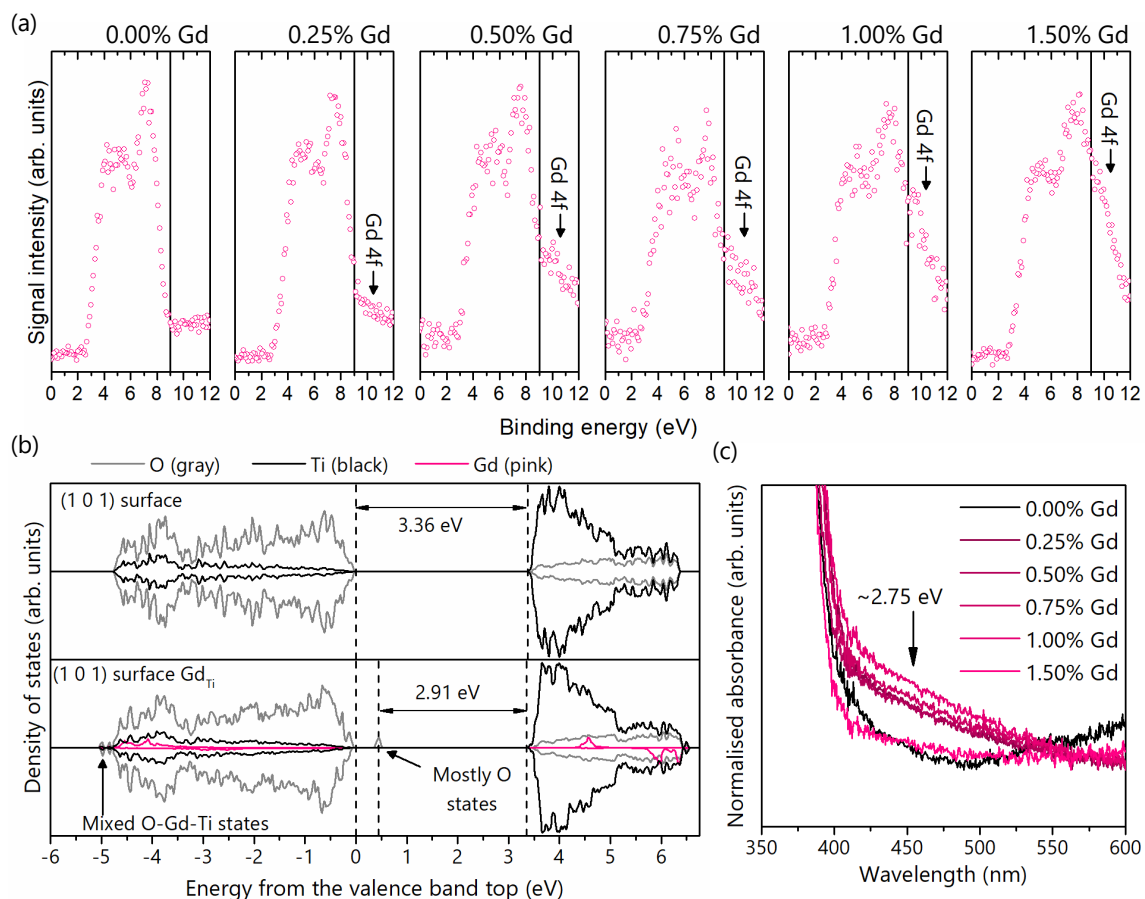
Figure 15.3. XPS-based scan of the valence band for all Gd-doped samples and prepared control (a), together with the simulated density of states distribution for the 96-atom models of anatase (1 0 1) surface with and without Gd atom substituting Ti (b) and with the experimental absorbance spectra around the main valence-to-conduction band transition (c).

normalisation of the spectra, which is presented in Figure 15.3c. However, it must be noted that in this case the effect is not explicit.

Finally, detailed electron-accepting character of the Gd^{3+} was investigated electrochemically, which also included control measurements of the 1% Nb-doped sample (preparation and characteristics of this sample were analogical to publication [P6]). As presented in Figure 15.4a., the increase of the Gd^{3+} concentration clearly reduces the net density of donor states N_D, connected also with spontaneous defects, which is observed as the increase of the fitted lines slope. Although it should be noted that calculated N_D values are likely overestimated in this case, e.g. due to the approximation of the interface area simply as the area of the deposited layer, both morphological similarities of the materials and additional error estimation from two separate electrodes (error as absolute difference) supports conclusions that Gd presence is significant for the N_D reduction, as presented in the Figure 15.4b.

Prepared samples were further studied in four independent reactions: phenol degradation, 4-nitrophenol reduction, O_2 reduction to H_2O_2 and ·OH generation. Formation of H_2O_2 was monitored using iodometric method and the process was
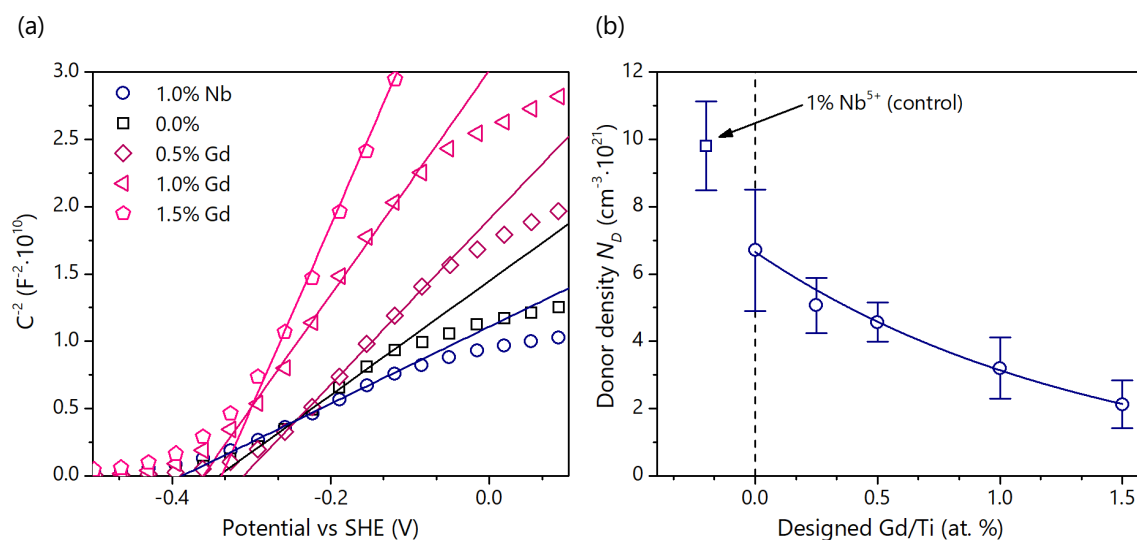
Figure 15.4. The Mott-Schottky plots of the selected samples (a) and corresponding donor states densities N_D (b). Electrochemical measurements were completed by the control measurements of the sample doped with 1% at. Nb^{5+}, and are presented as mean from two separate electrodes. In panel (a) both error and detailed data for the 0.25% doped samples are not presented for clarity.

conducted under increased aeration (10 $dm^3 \cdot h^{-1}$) with 10% vol. isopropanol acting as a hole scavenger. Generation of ·OH was estimated from the initial formation of the 7-hydroxycoumarin, as a known indicator of ·OH generation by TiO_2 photocatalysts [176].

As presented in Figure 15.5., phenol degradation connects strictly with the ·OH generation rate and achieves a clear maximum concerning the determined N_D value. Analogical maxima were also observed for both H_2O_2 generation and 4-nitrophenol reduction however, in this case they are systematically shifted to the higher N_D. This is in accordance with the expected number of electrons needed for each reaction to occur, where 4-nitrophenol reduction require 6 electrons to transform to 4-aminophenol, O_2 reduction to H_2O_2 require 2 electrons, while generation of ·OH/phenol degradation is most likely a mixed effect of both single and double electron processes. Therefore, these results clearly support hypothesis [H8], indicating that different reaction will require different amount of excess charge (defects) when occurring over the same exposed facet. Noteworthy, this is despite the fact that all materials remain as the n-type semiconductors (positive slope of the fitted lines during Mott-Schottky analysis), which indicates that some excess e^- are always present.

Focusing on the possible water treatment application, the 0.50% doped sample achieved the highest degradation of phenol, in accordance with the ·OH generation rate. The observed $k(N_D)$ maximum confirms that observed degradation rate does not depend strictly on one of the charge carriers but rather on their cooperation, achieving maximum when both h^+ and e^- react with some optimal rates, here fine-tuned by their ground-state density. Interestingly, these observations are in a very good agreement with the reduction-induced water dissociation on the {1 0 1} facets, as highlighted in the recent literature, which can be further oxidised by the generated holes, in accordance with the simplified reactions (15) and (16):

$$\frac{1}{2}O_2 + 2e^- + H_2O \rightarrow 2OH^- \qquad (15)$$

$$2OH^- + 2h^+ \rightarrow 2HO\cdot \qquad (16)$$

However, this maximum is observed independently on the possible O_2 reduction to H_2O_2, which achieved clear maximum for the 0.25% doped sample. This probably results from the competition between dissociation of the intermediate OOH^- to OH^- (15) or its further transformation to H_2O_2 (reaction (8) in the literature description) [67]. In this regard, mechanism of ROS generation through the OOH^- dissociation is suggested to be mainly responsible for stimulating activity of the {1 0 1} facets during the degradation of compounds such as phenol. Finally, it is worth noting that the highest degradation rate leads also to the highest mineralisation, measured as the TOC removal, however in this case, the Gd effect is much smaller and overall within the possible error.
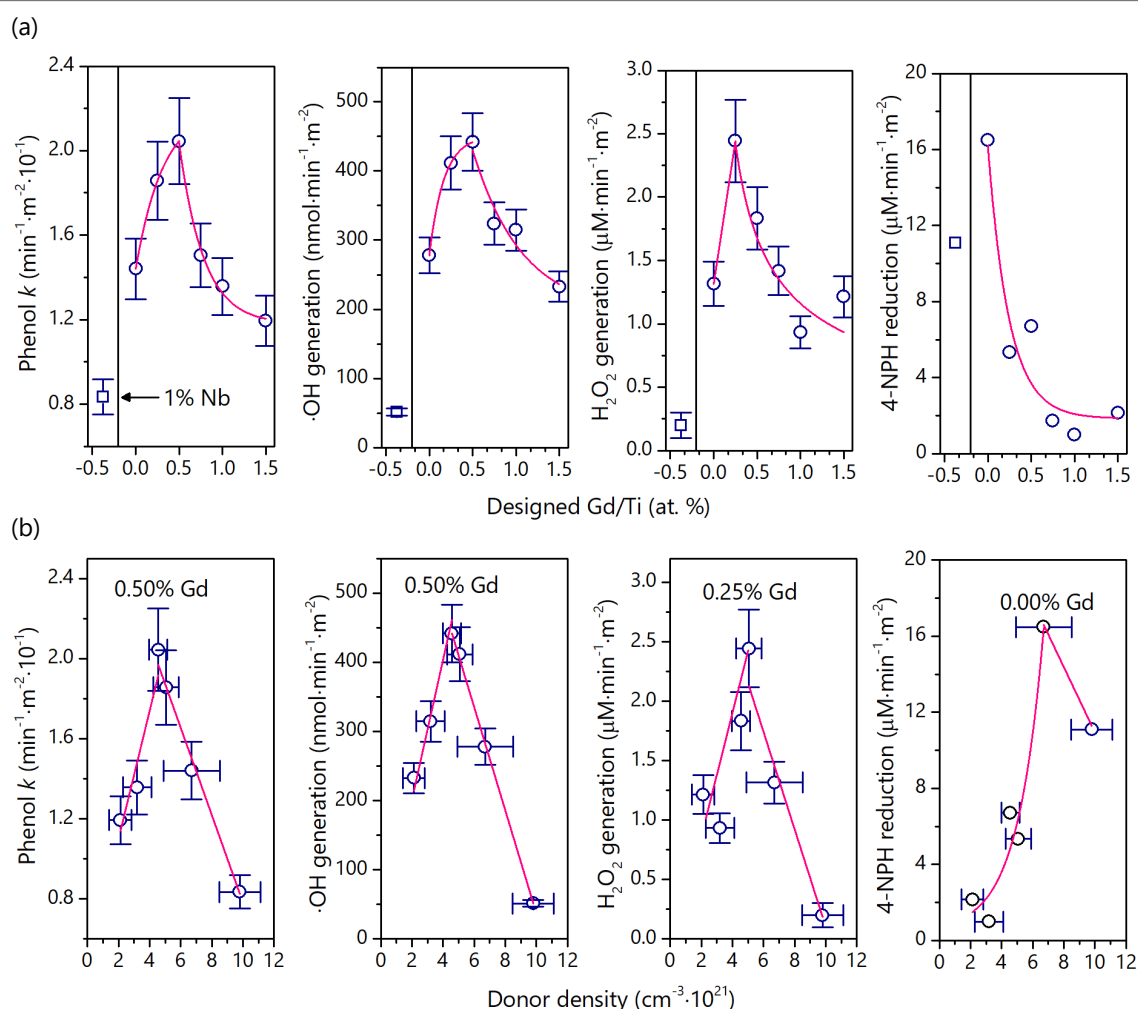
Figure 15.5. Observed activity of the prepared Gd and Nb doped samples in a photocatalytic reactions of phenol degradation, ·OH generation (detection with 7-hydroxycoumarin), H_2O_2 generation (detection with iodometric method) and 4-nitrophenol reduction to 4-aminophenol. Panel (a) show results as a function of designed Gd concentration and panel (b) show them in function of calculated donor density from Mott-Schottky analysis.

CONCLUSIONS

The PhD dissertation presents systematic insight into the photocatalytic activity of the low index anatase crystal facets in degradation of the aromatic organic pollutants. In accordance with hypothesis [H1], obtained results clearly show that activity of the anatase nanoparticles can be significantly optimized due to the alternation of the exposed facet; and the {1 0 1} appear as the best suited for the degradation of compounds such as phenol, toluene, carbamazepine, ibuprofen and acetaminophen. For the first time, it was shown that high degradation rate observed for the nanostructures that expose these facets in majority connect with efficient mineralisation of the organic carbon, measured as the removal of TOC. Noteworthy, while during the [P1] and [P2] studies nanostructures with higher {0 0 1} exposition achieved higher degradation rates, their ability to mineralise target pollutant was lower than {1 0 1}. Therefore, these responses are not strictly connected and hypothesis [H2] was not proved

Interestingly, the type of exposed facet seems not to influence on the degradation pathway of the pollutants over stoichiometric surfaces, but a combination of specific facet with further defects on the surface can inhibit the formation of some by-products, such as an *ortho*-hydroxyphenol. In this regard, hypothesis [H3] was not straightforward supported. However, this observation opens a promising approach for further studies on the selectivity of the degradation process, where the focus can be placed on the specific interactions between the exposed facet and arbitrarily introduced surface species. This is specifically a topic of ongoing studies, where some initial results confirmed that unique products of diclofenac degradation can be observed over surface-modified samples.

Furthermore, for the stoichiometric surfaces, the regression model of the observed activity has indicated that the final degradation rate over each low index facet is exponentially proportional to the reported energy of charge carriers trapping at corresponding surface models, with further significant contribution of the surface area development. This leads to the conclusion that the degradation rate depends on the number of possible trapping centres at the surface and the probability of the e^- and h^+ localisation at them. For the first time, such a relation was presented as the most decisive for the activity of the investigated nanostructures, reproducing general activity trends for different compounds and reaction setups alike, proving the hypothesis [H4].

Excluding known cases of the possible sensibilisation of TiO_2 by some photoactive compounds, no effect of the pollutant structure on the activity order of the stoichiometric facets was observed, disproving the hypothesis [H5]. However, it was found that pollutants which form less stable products after the charge transfer will react faster during the overall process. Importantly, this includes the stability of both oxidised and reduced molecules together, showing that simple oxidation by the h^+, which is often highlighted in the literature as an initial step of the degradation process, is not always decisive for the degradation efficiency of different compounds. For the first time, specific interactions between different pollutants and different exposed facets were investigated in detail,

providing both qualitative and quantitative insight into the parameters most decisive for the observed kinetics.

When degrading a mixture of different pharmaceuticals, compounds that are preferentially adsorbed on the surface will react faster. This is especially observed for the higher total concentrations of pollutants, as well as smaller surface areas of the photocatalysts. Therefore, for such systems, conclusions made for a single-pollutant case might not be valid. In this regard, further investigations in this direction are especially planned for future works.

Finally, in accordance with hypothesis [H6], the results obtained for the $BaFe_{12}O_{19}/TiO_2$ composites have shown that different effects of both electronic and magnetic interactions between both phases can be expected, depending on the exposed facet of TiO_2. In analogy to previous conclusions, electron transfer from TiO_2 to the $BaFe_{12}O_{19}$ was found to be hindering the activity of the {1 0 1} facets, but not the {0 0 1} and {1 0 0} ones. Moreover, the built-in magnetic field of the ferrite was shown to possibly hinder the recombination rate of the generated charge carriers, however the significant effect was observed only for the {1 0 0} exposing sample. It is suggested that this anisotropy might result from the 2-dimensional nature of the excitons generated within the anatase structure and the uniaxial vector of the $BaFe_{12}O_{19}$ magnetic field. However, the additional contribution of the surface electron states cannot be ruled out at this point, opening a problem for further, more detailed studies.

Finally, following-up the observed relation between degradation rate and probability of charge carriers trapping at the surface, further optimization of the activity can be achieved by manipulating ground-state concentration of the electrons within the materials. However, as shown by the in-depth investigation of the Nb^{5+} doped samples, the behaviour of the dopant-introduced charge can be completely different, depending on the electronic structure of the exposed crystal facet, in accordance with the hypothesis [H7]. Interestingly, an increase of the electron density is particularly undesired for the {1 0 1} facets, which was clearly observed both phenol degradation and 4-nitrophenol reduction, making it a poor approach for the application in water treatment.

Following the negative effect of the Nb^{5+} doping on the photocatalytic activity of the {1 0 1} facets, further investigation clearly shows that a slight reduction of the spontaneously present donor states with Gd^{3+} ions maximises their ability to generate reactive species, creating a highly active material for this particular reaction. Interestingly, maximum activity for the 4-nitrophenol reduction, ·OH generation and H_2O_2 formation were all observed for different donor densities, supporting hypothesis [H8] that for a particular facet-reaction case, maximum activity will require different density of excess charge at the ground state.

Overall, the obtained results confirm the importance of the exposed facet of the anatase photocatalysts on the resulting activity, influencing the performance of the unmodified materials, as well as its further interactions with defects, dopants and other

crystal phases. As a general observation, it is worth noting that the behaviour of the analysed samples generally follows predictions obtained from the DFT simulations, providing a good insight into the possible fate of both charge carriers on different surfaces. However, a straightforward prediction of the photocatalytic activity from such simulations is still challenging. This is mostly due to the simplicity of the arbitrary designed models, compared to the real reactions systems, which include problems like the simultaneous presence of holes and electrons during the process, formation of spontaneous defects within crystal structure and a vast number of possible species and intermediate products at the surface, which in most cases are not simulated in detail. In this regard, experimental optimization of the photocatalytic performance seems still needed. Based on the performed works, a general approach for such optimization might be suggested as (I) finding a suitable crystal structure for a particular reaction, (II) optimizing the presence of a most-active crystal facets, and (III) optimizing ground state density of charge carriers for a particular facet-reaction case. Such optimized single-phase materials might be further subjected to studies regarding surface modifications/junctions/reaction environment to obtain photocatalytic systems with boost efficiencies.

REFERENCES

[1] A. Cheruvathoor Poulose *et al.*, "Fast and selective reduction of nitroarenes under visible light with an earth-abundant plasmonic photocatalyst," *Nat Nanotechnol*, vol. 17, no. 5, pp. 485–492, May 2022, doi: 10.1038/s41565-022-01087-3.

[2] E. Archer, B. Petrie, B. Kasprzyk-Hordern, and G. M. Wolfaardt, "The fate of pharmaceuticals and personal care products (PPCPs), endocrine disrupting contaminants (EDCs), metabolites and illicit drugs in a WWTW and environmental waters," *Chemosphere*, vol. 174, pp. 437–446, 2017, doi: 10.1016/j.chemosphere.2017.01.101.

[3] C. Martínez, M. Canle L, M. I. Fernández, J. A. Santaballa, and J. Faria, "Kinetics and mechanism of aqueous degradation of carbamazepine by heterogeneous photocatalysis using nanocrystalline TiO2, ZnO and multi-walled carbon nanotubes-anatase composites," *Appl Catal B*, vol. 102, no. 3–4, pp. 563–571, 2011, doi: 10.1016/j.apcatb.2010.12.039.

[4] H. Alshaikh, L. A. Al-Hajji, M. H. H. Mahmoud, and A. A. Ismail, "Visible-light-driven S-scheme mesoporous Ag3VO4 /C3N4 heterojunction with promoted photocatalytic performances," *Sep Purif Technol*, vol. 272, Oct. 2021, doi: 10.1016/j.seppur.2021.118914.

[5] T. Maggos, J. G. Bartzis, M. Liakou, and C. Gobin, "Photocatalytic degradation of NOx gases using TiO2-containing paint: A real scale study," *J Hazard Mater*, vol. 146, no. 3, pp. 668–673, Jul. 2007, doi: 10.1016/j.jhazmat.2007.04.079.

[6] P. Zhou *et al.*, "Solar-to-hydrogen efficiency of more than 9% in photocatalytic water splitting," *Nature*, vol. 613, no. 7942, pp. 66–70, 2023, doi: 10.1038/s41586-022-05399-1.

[7] Y. Yuan *et al.*, "Earth-abundant photocatalyst for H 2 generation from NH 3 with light-emitting diode illumination." [Online]. Available: https://www.science.org

[8] R. Tahawy *et al.*, "Exceptionally stable green rust, a mixed-valent iron-layered double hydroxide, as an efficient solar photocatalyst for H2 production from ammonia borane," *Appl Catal B*, vol. 286, Jun. 2021, doi: 10.1016/j.apcatb.2020.119854.

[9] T. Chen *et al.*, "Photocatalytic Anaerobic Dehydrogenation of Alcohols over Metal Halide Perovskites: A New Acid-Free Scheme for H2Production," *Journal of Physical Chemistry Letters*, vol. 13, no. 28, pp. 6559–6565, Jul. 2022, doi: 10.1021/acs.jpclett.2c01501.

[10] H. Issa Hamoud *et al.*, "Selective Photocatalytic Dehydrogenation of Formic Acid by an in Situ-Restructured Copper-Postmetalated Metal-Organic Framework under Visible Light," *J Am Chem Soc*, vol. 144, no. 36, pp. 16433–16446, Sep. 2022, doi: 10.1021/jacs.2c04905.

[11] F. He, B. Zhu, B. Cheng, J. Yu, W. Ho, and W. Macyk, "2D/2D/0D TiO2/C3N4/Ti3C2 MXene composite S-scheme photocatalyst with enhanced CO2 reduction activity," *Appl Catal B*, vol. 272, Sep. 2020, doi: 10.1016/j.apcatb.2020.119006.

[12] A. Adamu, M. Isaacs, K. Boodhoo, and F. R. Abegão, "Investigation of Cu/TiO2 synthesis methods and conditions for CO2 photocatalytic reduction via conversion of bicarbonate/carbonate to formate," *Journal of CO2 Utilization*, vol. 70, p. 102428, Apr. 2023, doi: 10.1016/j.jcou.2023.102428.

[13] M. Ma *et al.*, "Ultrahigh surface density of Co-N2C single-atom-sites for boosting photocatalytic CO2 reduction to methanol," *Appl Catal B*, vol. 300, Jan. 2022, doi: 10.1016/j.apcatb.2021.120695.

[14] M. P. Jiang *et al.*, "Magnetic-Field-Regulated TiO2 {100} Facets: A Strategy for C-C Coupling in CO2 Photocatalytic Conversion," *Chem*, vol. 6, no. 9, pp. 2335–2346, 2020, doi: 10.1016/j.chempr.2020.06.033.

[15] C. J. Howard, T. M. Sabine, and F. Dickson, "Structural and thermal parameters for rutile and anatase," *Acta Crystallogr B*, vol. 47, no. 4, pp. 462–468, Aug. 1991, doi: 10.1107/S010876819100335X.

[16] M. B. Poudel, C. Yu, and H. J. Kim, "Synthesis of conducting bifunctional polyaniline@mn-TiO2 nanocomposites for supercapacitor electrode and visible light driven photocatalysis," *Catalysts*, vol. 10, no. 5, May 2020, doi: 10.3390/catal10050546.

[17] S. Prathapani, V. More, S. Bohm, P. Bhargava, A. Yella, and S. Mallick, "TiO2colloid-based compact layers for hybrid lead halide perovskite solar cells," *Appl Mater Today*, vol. 7, pp. 112–119, Jun. 2017, doi: 10.1016/j.apmt.2017.01.009.

[18] A. Hamrouni, H. Azzouzi, A. Rayes, L. Palmisano, R. Ceccato, and F. Parrino, "Enhanced solar light photocatalytic activity of ag doped tio2-ag3po4 composites," *Nanomaterials*, vol. 10, no. 4, Apr. 2020, doi: 10.3390/nano10040795.

[19] P. Makuła, M. Pacia, and W. Macyk, "How To Correctly Determine the Band Gap Energy of Modified Semiconductor Photocatalysts Based on UV-Vis Spectra," *Journal of Physical Chemistry Letters*, vol. 9, no. 23, pp. 6814–6817, 2018, doi: 10.1021/acs.jpclett.8b02892.

[20] R. Hengerer, L. Kavan, P. Krtil, and M. Grätzel, "Orientation Dependence of Charge-Transfer Processes on TiO2 (Anatase) Single Crystals," *J Electrochem Soc*, vol. 147, no. 4, pp. 1467–1472, 2000.

[21] L. Kavan, M. Grätzel, S. E. Gilbert, C. Klemenz, and J. Scheel, "Electrochemical and Photoelectrochemical Investigation of Single-Crystal Anatase," *Journal of the American Chemical Society*, vol. 118, pp. 6716–6723, 1996.

[22] Y. Yang *et al.*, "Efficient Charge Separation from F- Selective Etching and Doping of Anatase-TiO2{001} for Enhanced Photocatalytic Hydrogen Production," *ACS Appl Mater Interfaces*, vol. 10, no. 23, pp. 19633–19638, Jun. 2018, doi: 10.1021/acsami.8b02804.

[23] M. Kunnamareddy, R. Rajendran, M. Sivagnanam, R. Rajendran, and B. Diravidamani, "Nickel and sulfur codoped TiO2 nanoparticles for efficient visible light photocatalytic activity," *J Inorg Organomet Polym Mater*, vol. 31, no. 6, pp. 2615–2626, Jun. 2021, doi: 10.1007/s10904-021-01914-5.

[24] H. Tang, F. Levy, H. Berger, and P. E. Schmid, "Urbach tail of anatase TiO2," *Phys Rev B*, vol. 52, pp. 7771–7774, 1995.

[25] E. Baldini *et al.*, "Strongly bound excitons in anatase TiO2 single crystals and nanoparticles," *Nat Commun*, vol. 8, no. 1, Dec. 2017, doi: 10.1038/s41467-017-00016-6.

[26] E. Baldini, T. Palmieri, A. Dominguez, A. Rubio, and M. Chergui, "Giant Exciton Mott Density in Anatase TiO2," *Phys Rev Lett*, vol. 125, no. 11, Sep. 2020, doi: 10.1103/PHYSREVLETT.125.116403.

[27] S. H. Park *et al.*, "Direct and real-time observation of hole transport dynamics in anatase TiO2 using X-ray free-electron laser," *Nat Commun*, vol. 13, no. 1, Dec. 2022, doi: 10.1038/s41467-022-30336-1.

[28] G. Liu *et al.*, "Greatly Enhanced Electronic Conduction and Lithium Storage of Faceted TiO2 Crystals Supported on Metallic Substrates by Tuning Crystallographic Orientation of TiO2," *Advanced Materials*, vol. 27, no. 23, pp. 3507–3512, 2015, doi: 10.1002/adma.201500198.

[29] P. Torres and R. Rurali, "Thermal Conductivity of Rutile and Anatase TiO2 from First-Principles," *Journal of Physical Chemistry C*, vol. 123, no. 51, pp. 30851–30855, Dec. 2019, doi: 10.1021/acs.jpcc.9b09299.

[30] H. Gerischer and A. Heller, "The role of oxygen in photooxidation of organic molecules on semiconductor particles," *Journal of Physical Chemistry*, vol. 95, no. 13, pp. 5261–5267, 1991, doi: 10.1021/j100166a063.

[31] C. M. Wang, A. Heller, and H. Gerischer, "Palladium Catalysis of O2 Reduction by Electrons Accumulated on TiO2 Particles during Photoassisted Oxidation of Organic Compounds," *J Am Chem Soc*, vol. 114, no. 13, pp. 5230–5234, 1992, doi: 10.1021/ja00039a039.

[32] J. Moser, S. Punchihewa, P. P. Infelta, and M. Grätzel, "Surface Complexation of Colloidal Semiconductors Strongly Enhances Interfacial Electron-Transfer Rates," *Langmuir*, vol. 7, no. 12, pp. 3012–3018, 1991, doi: 10.1021/la00060a018.

[33]   O. Nasr, O. Mohamed, A. S. Al-Shirbini, and A. M. Abdel-Wahab, "Photocatalytic degradation of acetaminophen over Ag, Au and Pt loaded TiO2 using solar light," *J Photochem Photobiol A Chem*, vol. 374, no. October 2018, pp. 185–193, 2019, doi: 10.1016/j.jphotochem.2019.01.032.

[34]   M. Chen *et al.*, "High-performance of Cu-TiO2 for photocatalytic oxidation of formaldehyde under visible light and the mechanism study," *Chemical Engineering Journal*, vol. 390, no. November 2019, p. 124481, 2020, doi: 10.1016/j.cej.2020.124481.

[35]   M. Kong *et al.*, "Tuning the relative concentration ratio of bulk defects to surface defects in TiO2 nanocrystals leads to high photocatalytic efficiency," *Journal of Americal Chemical Society*, vol. 133, pp. 16414–16417, 2011.

[36]   E. Kowalska, H. Remita, C. Colbeau-Justin, J. Hupka, and J. Belloni, "Modification of Titanium Dioxide with Platinum Ions and Clusters: Application in Photocatalysis," *Journal of Physical Chemistry C*, vol. 112, pp. 1124–1131, 2008.

[37]   N. Wang, Z. Chen, L. Zhu, X. Jiang, B. Lv, and H. Tang, "Synergistic effects of cupric and fluoride ions on photocatalytic degradation of phenol," *J Photochem Photobiol A Chem*, vol. 191, no. 2–3, pp. 193–200, 2007, doi: 10.1016/j.jphotochem.2007.04.023.

[38]   H. Irie, S. Miura, K. Kamiya, and K. Hashimoto, "Efficient visible light-sensitive photocatalysts: Grafting Cu(II) ions onto TiO2 and WO3 photocatalysts," *Chem Phys Lett*, vol. 457, no. 1–3, pp. 202–205, 2008, doi: 10.1016/j.cplett.2008.04.006.

[39]   H. Hao, J. L. Shi, H. Xu, X. Li, and X. Lang, "N-hydroxyphthalimide-TiO2 complex visible light photocatalysis," *Appl Catal B*, vol. 246, pp. 149–155, Jun. 2019, doi: 10.1016/j.apcatb.2019.01.037.

[40]   N. O. Balayeva, N. Zheng, R. Dillert, and D. W. Bahnemann, "Visible-Light-Mediated Photocatalytic Aerobic Dehydrogenation of N-heterocycles by Surface-Grafted TiO2 and 4-amino-TEMPO," *ACS Catal*, pp. 10694–10704, 2019, doi: 10.1021/acscatal.9b03322.

[41]   T. Takata *et al.*, "Photocatalytic water splitting with a quantum efficiency of almost unity," *Nature*, vol. 581, no. 7809, pp. 411–414, 2020, doi: 10.1038/s41586-020-2278-9.

[42]   N. Wang *et al.*, "Efficient, Selective CO2Photoreduction Enabled by Facet-Resolved Redox-Active Sites on Colloidal CdS Nanosheets," *J Am Chem Soc*, vol. 144, no. 37, pp. 16974–16983, Sep. 2022, doi: 10.1021/jacs.2c06164.

[43]   Y. Wan, J. Li, J. Ni, C. Wang, C. Ni, and H. Chen, "Crystal-facet and microstructure engineering in ZnO for photocatalytic NO oxidation," *J Hazard Mater*, vol. 435, Aug. 2022, doi: 10.1016/j.jhazmat.2022.129073.

[44]   R. Chen *et al.*, "Spatiotemporal imaging of charge transfer in photocatalyst particles," *Nature*, vol. 610, no. 7931, pp. 296–301, 2022, doi: 10.1038/s41586-022-05183-1.

[45]   W. Yuan *et al.*, "Real-Time Observation of Reconstruction Dynamics on TiO2 (001) Surface under Oxygen via an Environmental Transmission Electron Microscope," *Nano Lett*, vol. 16, no. 1, pp. 132–137, 2016, doi: 10.1021/acs.nanolett.5b03277.

[46]   A. S. Barnard and P. Zapol, "Effects of particle morphology and surface hydrogenation on the phase stability of TiO2," *Phys Rev B Condens Matter Mater Phys*, vol. 70, no. 23, pp. 1–13, 2004, doi: 10.1103/PhysRevB.70.235403.

[47]   L. Mino, A. M. Ferrari, V. Lacivita, G. Spoto, S. Bordiga, and A. Zecchina, "CO adsorption on anatase nanocrystals: A combined experimental and periodic DFT study," *Journal of Physical Chemistry C*, vol. 115, no. 15, pp. 7694–7700, 2011, doi: 10.1021/jp2017049.

[48]   C. Arrouvel, M. Digne, M. Breysse, H. Toulhoat, and P. Raybaud, "Effects of morphology on surface hydroxyl concentration: A DFT comparison of anatase-TiO2 and γ-alumina catalytic supports," *J Catal*, vol. 222, no. 1, pp. 152–166, 2004, doi: 10.1016/j.jcat.2003.10.016.

[49]   Z. Zhao, Z. Li, and Z. Zou, "Surface properties and electronic structure of low-index stoichiometric anatase TiO2 surfaces," *Journal of Physics Condensed Matter*, vol. 22, no. 17, p. 175008, 2010, doi: 10.1088/0953-8984/22/17/175008.

[50]   M. Lazzeri, A. Vittadini, and A. Selloni, "Structure and energetics of stoichiometric TiO2 anatase surfaces," *Phys Rev B Condens Matter Mater Phys*, vol. 63, no. 15, pp. 1554091–1554099, 2001, doi: 10.1103/PhysRevB.63.155409.

[51]   F. Labat, P. Baranek, and C. Adamo, "Structural and electronic properties of selected rutile and anatase TiO2 surfaces: An ab initio investigation," *J Chem Theory Comput*, vol. 4, no. 2, pp. 341–352, 2008, doi: 10.1021/ct700221w.

[52]   S. Dudziak, M. Kowalkińska, and A. Zielińska-Jurek, "Crystal facet engineering of TiO2 from theory to application," in *Updates on titanium dioxide*, B. Bejaoui, Ed., IntechOpen, 2023. doi: 10.5772/intechopen.111565.

[53]   R. Hengerer, B. Bolliger, M. Erbudak, and M. Grätzel, "Structure and stability of the anatase TiO2 (101) and (001) surfaces," *Surf Sci*, vol. 460, no. 1–3, pp. 162–169, 2000, doi: 10.1016/S0039-6028(00)00527-6.

[54]   M. Lazzeri and A. Selloni, "Stress-driven reconstruction of an oxide surface: The anatase TiO2 (001)-(1×4) surface," *Phys Rev Lett*, vol. 87, no. 26, pp. 266105-1-266105–4, 2001, doi: 10.1103/PhysRevLett.87.266105.

[55]   Y. Wang *et al.*, "Role of point defects on the reactivity of reconstructed anatase titanium dioxide (001) surface," *Nat Commun*, vol. 4, pp. 1–8, 2013, doi: 10.1038/ncomms3214.

[56]   W. J. I. DeBenedetti, E. S. Skibinski, D. Jing, A. Song, and M. A. Hines, "Atomic-Scale Understanding of Catalyst Activation: Carboxylic Acid Solutions, but Not the Acid Itself, Increase the Reactivity of Anatase (001) Faceted Nanocatalysts," *Journal of Physical Chemistry C*, vol. 122, no. 8, pp. 4307–4314, 2018, doi: 10.1021/acs.jpcc.7b11054.

[57]   S. Selçuk and A. Selloni, "Surface structure and reactivity of anatase TiO2 crystals with dominant {001} facets," *Journal of Physical Chemistry C*, vol. 117, no. 12, pp. 6358–6362, 2013, doi: 10.1021/jp402100v.

[58]   H. G. Yang *et al.*, "Anatase TiO2 single crystals with a large percentage of reactive facets," *Nature*, vol. 453, no. 7195, pp. 638–641, 2008, doi: 10.1038/nature06964.

[59]   S. Gao, W. Wang, Y. Ni, C. Lu, and Z. Xu, "Facet-dependent photocatalytic mechanisms of anatase TiO2: A new sight on the self-adjusted surface heterojunction," *J Alloys Compd*, vol. 647, pp. 981–988, 2015, doi: 10.1016/j.jallcom.2015.06.204.

[60]   Z. Wei *et al.*, "Noble metal-modified faceted anatase titania photocatalysts: Octahedron versus decahedron," *Appl Catal B*, vol. 237, pp. 574–587, 2018, doi: 10.1016/j.apcatb.2018.06.027.

[61]   T. Butburee *et al.*, "New understanding of crystal control and facet selectivity of titanium dioxide ruling photocatalytic performance," *J Mater Chem A Mater*, vol. 7, no. 14, pp. 8156–8166, 2019, doi: 10.1039/c8ta11475g.

[62]   A. Meng, J. Zhang, D. Xu, B. Cheng, and J. Yu, "Enhanced photocatalytic H2-production activity of anatase TiO2 nanosheet by selectively depositing dual-cocatalysts on (101) and (001) facets," *Appl Catal B*, vol. 198, pp. 286–294, Dec. 2016, doi: 10.1016/j.apcatb.2016.05.074.

[63]   X. Ma, Y. Dai, M. Guo, and B. Huang, "Relative photooxidation and photoreduction activities of the {100}, {101}, and {001} Surfaces of Anatase TiO2," *Langmuir*, vol. 29, no. 44, pp. 13647–13654, 2013, doi: 10.1021/la403351v.

[64]   J. J. Carey and K. P. McKenna, "Does Polaronic Self-Trapping Occur at Anatase TiO2 Surfaces?," *Journal of Physical Chemistry C*, vol. 122, no. 48, pp. 27540–27553, 2018, doi: 10.1021/acs.jpcc.8b09437.

[65]   S. Selcuk and A. Selloni, "Facet-dependent trapping and dynamics of excess electrons at anatase TiO2 surfaces and aqueous interfaces," *Nat Mater*, vol. 15, no. 10, pp. 1107–1112, 2016, doi: 10.1038/nmat4672.

[66]   F. Fasulo, G. Piccini, A. B. Muñoz-García, M. Pavone, and M. Parrinello, "Dynamics of Water Dissociative Adsorption on TiO2Anatase (101) at Monolayer Coverage and below," *Journal of Physical Chemistry C*, vol. 126, no. 37, pp. 15752–15758, 2022, doi: 10.1021/acs.jpcc.2c03077.

[67]   M. Setvin *et al.*, "Following the Reduction of Oxygen on TiO2 Anatase (101) Step by Step," *J Am Chem Soc*, vol. 138, no. 30, pp. 9565–9571, 2016, doi: 10.1021/jacs.6b04004.

[68]   J. Chen, Y. F. Li, P. Sit, and A. Selloni, "Chemical dynamics of the first proton-coupled electron transfer of water oxidation on TiO2 anatase," *J Am Chem Soc*, vol. 135, no. 50, pp. 18774–18777, 2013, doi: 10.1021/ja410685m.

[69]   K. Shirai *et al.*, "Water-Assisted Hole Trapping at the Highly Curved Surface of Nano-TiO2 Photocatalyst," *J Am Chem Soc*, vol. 140, no. 4, pp. 1415–1422, 2018, doi: 10.1021/jacs.7b11061.

[70]   E. G. Panarelli, S. Livraghi, S. Maurelli, V. Polliotto, M. Chiesa, and E. Giamello, "Role of surface water molecules in stabilizing trapped hole centres in titanium dioxide (anatase) as monitored by electron paramagnetic resonance," *J Photochem Photobiol A Chem*, vol. 322–323, pp. 27–34, May 2016, doi: 10.1016/j.jphotochem.2016.02.015.

[71]   H. Zhang *et al.*, "Hydrogen-Bond Bridged Water Oxidation on {001} Surfaces of Anatase TiO2," *Journal of Physical Chemistry C*, vol. 121, no. 4, pp. 2251–2257, Feb. 2017, doi: 10.1021/acs.jpcc.6b11900.

[72]   J. Y. Hwang *et al.*, "Crystal phase-dependent generation of mobile OH radicals on TiO2: Revisiting the photocatalytic oxidation mechanism of anatase and rutile," *Appl Catal B*, vol. 286, no. November 2020, p. 119905, 2021, doi: 10.1016/j.apcatb.2021.119905.

[73]   L. Mino, G. Spoto, S. Bordiga, and A. Zecchina, "Particles morphology and surface properties as investigated by HRTEM, FTIR, and periodic DFT calculations: From pyrogenic TiO 2 (P25) to nanoanatase," *Journal of Physical Chemistry C*, vol. 116, no. 32, pp. 17008–17018, Aug. 2012, doi: 10.1021/jp303942h.

[74]   H. S. Wahab, T. Bredow, and S. M. Aliwi, "Computational investigation of water and oxygen adsorption on the anatase TiO2 (1 0 0) surface," *Journal of Molecular Structure: THEOCHEM*, vol. 868, no. 1–3, pp. 101–108, Nov. 2008, doi: 10.1016/j.theochem.2008.08.010.

[75]   A. A. Bonapasta and F. Filippone, "Photocatalytic reduction of oxygen molecules at the (1 0 0) TiO2 anatase surface," *Surf Sci*, vol. 577, no. 1, pp. 59–68, Feb. 2005, doi: 10.1016/j.susc.2004.12.019.

[76]   G. Wulff, "XXY . Zur Frage der Geschwindigkeit des Wachs-," *Z Kristallogr Cryst Mater*, pp. 449–530, 1901.

[77]   G. D. Barmparis, Z. Lodziana, N. Lopez, and I. N. Remediakis, "Nanoparticle shapes by using Wulff constructions and first-principles calculations," *Beilstein Journal of Nanotechnology*, vol. 6, no. 1, pp. 361–368, 2015, doi: 10.3762/bjnano.6.35.

[78]   A. S. Barnard, P. Zapol, and L. A. Curtiss, "Anatase and rutile surfaces with adsorbates representative of acidic and basic conditions," *Surf Sci*, vol. 582, no. 1–3, pp. 173–188, 2005, doi: 10.1016/j.susc.2005.03.014.

[79]   J. Li and D. Xu, "Tetragonal faceted-nanorods of anatase TiO2 single crystals with a large percentage of active {100} facets," *Chemical Communications*, vol. 46, no. 13, pp. 2301–2303, 2010, doi: 10.1039/b923755k.

[80]   L. Ye, J. Mao, J. Liu, Z. Jiang, T. Peng, and L. Zan, "Synthesis of anatase TiO2 nanocrystals with {101}, {001} or {010} single facets of 90% level exposure and liquid-phase photocatalytic reduction and oxidation activity orders," *J Mater Chem A Mater*, vol. 1, no. 35, pp. 10532–10537, Sep. 2013, doi: 10.1039/c3ta11791j.

[81]   J. Pan, G. Liu, G. Q. Lu, and H. M. Cheng, "On the true photoreactivity order of {001}, {010}, and {101} facets of anatase TiO2 crystals," *Angewandte Chemie - International Edition*, vol. 50, no. 9, pp. 2133–2137, 2011, doi: 10.1002/anie.201006057.

[82]   F. Amano, T. Yasumoto, O. O. Prieto-Mahaney, S. Uchida, T. Shibayama, and B. Ohtani, "Photocatalytic activity of octahedral single-crystalline mesoparticles of anatase titanium(IV) oxide," *Chemical Communications*, no. 17, pp. 2311–2313, 2009, doi: 10.1039/b822634b.

[83]   Z. Wei, E. Kowalska, J. Verrett, C. Colbeau-Justin, H. Remita, and B. Ohtani, "Morphology-dependent photocatalytic activity of octahedral anatase particles prepared by ultrasonication-hydrothermal reaction of titanates," *Nanoscale*, vol. 7, no. 29, pp. 12392–12404, 2015, doi: 10.1039/c5nr02386f.

[84]   J. Li, Y. Yu, Q. Chen, J. Li, and D. Xu, "Controllable synthesis of TiO2 single crystals with tunable shapes using ammonium-exchanged titanate nanowires as precursors," *Cryst Growth Des*, vol. 10, no. 5, pp. 2111–2115, 2010, doi: 10.1021/cg9012087.

[85]   L. Gai, Q. Mei, X. Qin, W. Li, H. Jiang, and X. Duan, "Controlled synthesis of anatase TiO2 octahedra with enhanced photocatalytic activity," *Mater Res Bull*, vol. 48, pp. 4469–4475, 2013, doi: 10.1016/j.materresbull.2013.07.057.

[86]   T. R. Gordon *et al.*, "Nonaqueous synthesis of TiO2 nanocrystals using TiF4 to engineer morphology, oxygen vacancy concentration, and photocatalytic activity," *J Am Chem Soc*, vol. 134, no. 15, pp. 6751–6761, 2012, doi: 10.1021/ja300823a.

[87]   H. G. Yang *et al.*, "Solvothermal synthesis and photoreactivity of anatase TiO2 nanosheets with dominant {001} facets," *J Am Chem Soc*, vol. 131, no. 11, pp. 4078–4083, 2009, doi: 10.1021/ja808790p.

[88]   C. Z. Wen, J. Z. Zhou, H. B. Jiang, Q. H. Hu, S. Z. Qiao, and H. G. Yang, "Synthesis of micro-sized titanium dioxide nanosheets wholly exposed with high-energy {001} and {100} facets," *Chemical Communications*, vol. 47, pp. 4400–4402, 2011, doi: 10.1039/c0cc05798c.

[89]   M. Li *et al.*, "Ultrathin anatase TiO2 nanosheets for high-performance photocatalytic hydrogen production," *Small*, vol. 13, no. 16, p. 1604115, 2017, doi: 10.1002/smll.201604115.

[90]   W. Q. Fang *et al.*, "Hierarchical structures of single-crystalline anatase TiO2 nanosheets dominated by {001} facets," *Chemistry - A European Journal*, vol. 17, no. 5, pp. 1423–1427, 2011, doi: 10.1002/chem.201002582.

[91]   X. Han *et al.*, "Carbonate ions-assisted syntheses of anatase TiO 2 nanoparticles exposed with high energy (001) facets," *RSC Adv*, vol. 2, no. 8, pp. 3251–3253, Apr. 2012, doi: 10.1039/c2ra00834c.

[92]   X. L. Cheng, M. Hu, R. Huang, and J. Sen Jiang, "HF-free synthesis of anatase TiO2 nanosheets with largely exposed and clean {001} facets and their enhanced rate performance as anodes of lithium-ion battery," *ACS Appl Mater Interfaces*, vol. 6, no. 21, pp. 19176–19183, Nov. 2014, doi: 10.1021/am504971h.

[93]   M. Janczarek, E. Kowalska, and B. Ohtani, "Decahedral-shaped anatase titania photocatalyst particles: Synthesis in a newly developed coaxial-flow gas-phase reactor," *Chemical Engineering Journal*, vol. 289, pp. 502–512, 2016, doi: 10.1016/j.cej.2016.01.008.

[94]   A. Vioux, "Nonhydrolytic sol-gel routes to oxides," *Chemistry of Materials*, vol. 9, no. 11, pp. 2292–2299, 1997, doi: 10.1016/S0022-3093(98)00789-3.

[95]   K. Kozma, M. Wang, P. I. Molina, N. P. Martin, Z. Feng, and M. Nyman, "The role of titanium-oxo clusters in the sulfate process for TiO2 production," *Dalton Transactions*, vol. 48, no. 29, pp. 11086–11093, 2019, doi: 10.1039/c9dt01337g.

[96]   S. Ngamta, N. Boonprakob, N. Wetchakun, K. Ounnunkad, S. Phanichphant, and B. Inceesungvorn, "A facile synthesis of nanocrystalline anatase TiO2 from TiOSO4 aqueous solution," *Mater Lett*, vol. 105, pp. 76–79, 2013, doi: 10.1016/j.matlet.2013.04.064.

[97]   M. Addamo *et al.*, "Preparation and photoactivity of nanostructured TiO2 particles obtained by hydrolysis of TiCl4," in *Colloids and Surfaces A: Physicochemical and Engineering Aspects*, Elsevier, Sep. 2005, pp. 23–31. doi: 10.1016/j.colsurfa.2004.11.048.

[98]   Z. Huang, Z. Wang, K. Lv, Y. Zheng, and K. Deng, "Transformation of TiOF2 cube to a hollow nanobox assembly from anatase TiO2 nanosheets with exposed {001} facets via solvothermal strategy," *ACS Appl Mater Interfaces*, vol. 5, no. 17, pp. 8663–8669, 2013, doi: 10.1021/am4023048.

[99]   Y. Wang, H. Zhang, Y. Han, P. Liu, X. Yao, and H. Zhao, "A selective etching phenomenon on {001} faceted anatase titanium dioxide single crystal surfaces by hydrofluoric acid," *Chemical Communications*, vol. 47, no. 10, pp. 2829–2831, 2011, doi: 10.1039/c0cc04848h.

[100]   J. Wang, F. Cao, Z. Bian, M. K. H. Leung, and H. Li, "Ultrafine single-crystal TiOF2 nanocubes with mesoporous structure, high activity and durability in visible light driven photocatalysis," *Nanoscale*, vol. 6, no. 2, pp. 897–902, 2014, doi: 10.1039/c3nr04489k.

[101]   H. Y. Zhu *et al.*, "Phase transition between nanostructures of titanate and titanium dioxides via simple wet-chemical reactions," *J Am Chem Soc*, vol. 127, no. 18, pp. 6730–6736, 2005, doi: 10.1021/ja044689+.

[102]   Q. Wu, M. Liu, Z. Wu, Y. Li, and L. Piao, "Is photooxidation activity of {001} facets truly lower than that of {101} facets for anatase TiO2 crystals?," *Journal of Physical Chemistry C*, vol. 116, no. 51, pp. 26800–26804, 2012, doi: 10.1021/jp3087495.

[103]   L. Wu, H. B. Jiang, F. Tian, Z. Chen, C. Sun, and H. G. Yang, "Ti0.89Si0.11O2 single crystals bound by high-index {201} facets showing enhanced visible-light photocatalytic hydrogen evolution," *Chemical Communications*, vol. 49, no. 20, pp. 2016–2018, 2013, doi: 10.1039/c3cc38105f.

[104]   G. Liu *et al.*, "Enhanced photoactivity of oxygen-deficient anatase TiO2 sheets with dominant {001} facets," *Journal of Physical Chemistry C*, vol. 113, no. 52, pp. 21784–21788, 2009, doi: 10.1021/jp907749r.

[105]   A. Grzegórska *et al.*, "Enhanced photocatalytic activity of accordion-like layered Ti3C2 (MXene) coupled with Fe-modified decahedral anatase particles exposing {1 0 1} and {0 0 1} facets," *Chemical Engineering Journal*, vol. 426, no. June, p. 130801, 2021, doi: 10.1016/j.cej.2021.130801.

[106]   S. Xie *et al.*, "Solid state precursor strategy for synthesizing hollow TiO2 boxes with a high percentage of reactive {001} facets exposed," *Chemical Communications*, vol. 47, no. 23, pp. 6722–6724, 2011, doi: 10.1039/c1cc11542a.

[107]   J. Hu, Y. Cao, K. Wang, and D. Jia, "Green solid-state synthesis and photocatalytic hydrogen production activity of anatase TiO2 nanoplates with super heat-stability," *RSC Adv*, vol. 7, no. 20, pp. 11827–11833, 2017, doi: 10.1039/c6ra27160j.

[108]   J. Mao *et al.*, "Pt-loading reverses the photocatalytic activity order of anatase TiO2 {001} and {010} facets for photoreduction of CO2 to CH4," *Appl Catal B*, vol. 144, pp. 855–862, 2014, doi: 10.1016/j.apcatb.2013.08.027.

[109]   C. Günnemann, C. Haisch, M. Fleisch, J. Schneider, A. V. Emeline, and D. W. Bahnemann, "Insights into Different Photocatalytic Oxidation Activities of Anatase, Brookite, and Rutile Single-Crystal Facets," *ACS Catal*, vol. 9, no. 2, pp. 1001–1012, 2019, doi: 10.1021/acscatal.8b04115.

[110]   L. Mino *et al.*, "Beyond Shape Engineering of TiO2 Nanoparticles: Post-Synthesis Treatment Dependence of Surface Hydration, Hydroxylation, Lewis Acidity and Photocatalytic Activity of TiO2 Anatase Nanoparticles with Dominant {001} or {101} Facets," *ACS Appl Nano Mater*, vol. 1, no. 9, pp. 5355–5365, 2018, doi: 10.1021/acsanm.8b01477.

[111]   Y. Lu, Y. Zang, H. Zhang, Y. Zhang, G. Wang, and H. Zhao, "Meaningful comparison of photocatalytic properties of {001} and {101} faceted anatase TiO2 nanocrystals," *Sci Bull (Beijing)*, vol. 61, no. 13, pp. 1003–1012, 2016, doi: 10.1007/s11434-016-1109-8.

[112]   W. T. Chen, Y. Dong, P. Yadav, R. D. Aughterson, D. Sun-Waterhouse, and G. I. N. Waterhouse, "Effect of alcohol sacrificial agent on the performance of Cu/TiO2 photocatalysts for UV-driven hydrogen production," *Appl Catal A Gen*, vol. 602, no. April, p. 117703, 2020, doi: 10.1016/j.apcata.2020.117703.

[113]   F. R. Amalia, M. Takashima, and B. Ohtani, "Are you still using organic dyes? Colorimetric formaldehyde analysis for true photocatalytic-activity evaluation," *Chemical Communications*, no. Ddl, pp. 11721–11724, 2022, doi: 10.1039/d2cc04291f.

[114]   N. Barbero and D. Vione, "Why Dyes Should Not Be Used to Test the Photocatalytic Activity of Semiconductor Oxides," *Environ Sci Technol*, vol. 50, no. 5, pp. 2130–2131, 2016, doi: 10.1021/acs.est.6b00213.

[115]   P. Zhou, H. Zhang, H. Ji, W. Ma, C. Chen, and J. Zhao, "Modulating the photocatalytic redox preferences between anatase TiO2 {001} and {101} surfaces," *Chemical Communications*, vol. 53, no. 4, pp. 787–790, 2017, doi: 10.1039/c6cc08785j.

[116]   J. Yu, J. Low, W. Xiao, P. Zhou, and M. Jaroniec, "Enhanced Photocatalytic CO2-Reduction Activity of Anatase TiO2 by Co-exposed {001} and {101} Facets," *Journal of the Americal Chemical Society*, vol. 136, p. 8839, 2014.

[117]   Y. Cao, Q. Li, C. Li, J. Li, and J. Yang, "Surface heterojunction between (001) and (101) facets of ultrafine anatase TiO2 nanocrystals for highly efficient photoreduction CO2 to CH4," *Appl Catal B*, vol. 198, pp. 378–388, 2016, doi: 10.1016/j.apcatb.2016.05.071.

[118]   X. Zhao *et al.*, "Shape- and size-controlled synthesis of uniform anatase TiO2 nanocuboids enclosed by active {100} and {001} facets," *Adv Funct Mater*, vol. 21, no. 18, pp. 3554–3563, 2011, doi: 10.1002/adfm.201100629.

[119]   N. Roy, Y. Sohn, and D. Pradhan, "Synergy of low-energy {101} and high-energy {001} TiO2 crystal facets for enhanced photocatalysis," *ACS Nano*, vol. 7, no. 3, pp. 2532–2540, 2013, doi: 10.1021/nn305877v.

[120]   A. Meng, L. Zhang, B. Cheng, and J. Yu, "Dual Cocatalysts in TiO2 Photocatalysis," *Advanced Materials*, vol. 31, no. 30. Wiley-VCH Verlag, Jul. 26, 2019. doi: 10.1002/adma.201807660.

[121]   Y. Wang, L. Mino, F. Pellegrino, N. Homs, and P. Ramírez de la Piscina, "Engineered MoxC /TiO2 interfaces for efficient noble metal-free photocatalytic hydrogen production," *Appl Catal B*, vol. 318, p. 121783, 2022.

[122]   L. Liu *et al.*, "Engineering the TiO2-graphene interface to enhance photocatalytic H2 production," *ChemSusChem*, vol. 7, no. 2, pp. 618–626, 2014, doi: 10.1002/cssc.201300941.

[123]   T. Wei, P. Ding, T. Wang, L. M. Liu, X. An, and X. Yu, "Facet-Regulating Local Coordination of Dual-Atom Cocatalyzed TiO2for Photocatalytic Water Splitting," *ACS Catal*, vol. 11, no. 23, pp. 14669–14676, Dec. 2021, doi: 10.1021/acscatal.1c03703.

[124]   Y. Liu, Z. Ye, D. Li, M. Wang, Y. Zhang, and W. Huang, "Tuning CuO x -TiO 2 interaction and photocatalytic hydrogen production of CuO x /TiO 2 photocatalysts via TiO 2 morphology engineering," *Appl Surf Sci*, vol. 473, pp. 500–510, Apr. 2019, doi: 10.1016/j.apsusc.2018.12.177.

[125]   A. Y. Zhang *et al.*, "Epitaxial facet junctions on TiO2 single crystals for efficient photocatalytic water splitting," *Energy Environ Sci*, vol. 11, no. 6, pp. 1444–1448, Jun. 2018, doi: 10.1039/c7ee03482b.

[126]   A. Meng, J. Zhang, D. Xu, B. Cheng, and J. Yu, "Enhanced photocatalytic H2-production activity of anatase TiO2 nanosheet by selectively depositing dual-cocatalysts on (101) and (001) facets," *Appl Catal B*, vol. 198, pp. 286–294, Dec. 2016, doi: 10.1016/j.apcatb.2016.05.074.

[127]   A. Meng, L. Zhang, B. Cheng, and J. Yu, "TiO 2 -MnO x -Pt Hybrid Multiheterojunction Film Photocatalyst with Enhanced Photocatalytic CO 2 -Reduction Activity," *ACS Appl Mater Interfaces*, vol. 11, no. 6, pp. 5581–5589, Feb. 2019, doi: 10.1021/acsami.8b02552.

[128]   F. Neese, F. Wennmohs, U. Becker, and C. Riplinger, "The ORCA quantum chemistry program package," *Journal of Chemical Physics*, vol. 152, no. 22, 2020, doi: 10.1063/5.0004608.

[129]   F. Neese, "Software update: The ORCA program system—Version 5.0," *Wiley Interdiscip Rev Comput Mol Sci*, no. February, pp. 1–15, 2022, doi: 10.1002/wcms.1606.

[130]   C. Adamo and V. Barone, "Toward reliable density functional methods without adjustable parameters: The PBE0 model," *Journal of Chemical Physics*, vol. 110, no. 13, pp. 6158–6170, 1999, doi: 10.1063/1.478522.

[131] P. J. Stephens, F. J. Devlin, C. F. Chabalowski, and M. J. Frisch, "Ab Initio Calculation of Vibrational Absorption and Circular Dichroism Spectra Using Density Functional Force Fields," 1994.

[132] S. Grimme, S. Ehrlich, and L. Goerigk, "Effect of the damping function in dispersion corrected density functional theory," *J Comput Chem*, vol. 32, no. 7, pp. 1456–1465, May 2011, doi: 10.1002/jcc.21759.

[133] V. Barone and M. Cossi, "Quantum Calculation of Molecular Energies and Energy Gradients in Solution by a Conductor Solvent Model," 1998.

[134] P. Giannozzi *et al.*, "QUANTUM ESPRESSO: A modular and open-source software project for quantum simulations of materials," *Journal of Physics Condensed Matter*, vol. 21, no. 39, 2009, doi: 10.1088/0953-8984/21/39/395502.

[135] P. Giannozzi *et al.*, "Advanced capabilities for materials modelling with Quantum Espresso," *Journal of Physics: Condensed Matter*, vol. 29, p. 465901, 2017.

[136] J. P. Perdew, M. Ernzerhof, and K. Burke, "Rationale for mixing exact exchange with density functional approximations Rationale for mixing exact exchange with density functional approximations," *Journal of Physical Chemistry*, vol. 105, no. 22, pp. 9982–9985, 1996, doi: 10.1063/1.472933.

[137] N. Serpone and A. Salinaro, "Terminology, relative photonic efficiencies and quantum yields in heterogeneous photocatalysis. Part I: Suggested protocol (Technical Report)," *Pure and Applied Chemistry*, vol. 71, no. 2, pp. 303–320, 1999, doi: 10.1351/pac199971020303.

[138] D. W. Bahnemann, M. Hilgendorff, and R. Memming, "Charge Carrier Dynamics at TiO2 Particles: Reactivity of Free and Trapped Holes," *Journal of Physical Chemistry A*, vol. 101, no. 21, pp. 4265–4275, 1997.

[139] Y. Nosaka and A. Y. Nosaka, "Generation and Detection of Reactive Oxygen Species in Photocatalysis," *Chem Rev*, vol. 117, no. 17, pp. 11302–11336, 2017, doi: 10.1021/acs.chemrev.7b00161.

[140] C. S. A. Antunes, M. Bietti, M. Salamone, and N. Scione, "Early stages in the TiO2-photocatalyzed degradation of simple phenolic and non-phenolic lignin model compounds," *J Photochem Photobiol A Chem*, vol. 163, no. 3, pp. 453–462, 2004, doi: 10.1016/j.jphotochem.2004.01.018.

[141] N. Pinna, G. Garnweitner, M. Antonietti, and M. Niederberger, "Non-aqueous synthesis of high-purity metal oxide nanopowders using an ether elimination process," *Advanced Materials*, vol. 16, no. 23–24, pp. 2196–2200, 2004, doi: 10.1002/adma.200400460.

[142] R. O. Ragsdale and B. B. Stewart, "Fluorine-19 Nuclear Magnetic Resonance Study of Some Pentafluorotitanate Complexes," *Inorg Chem*, vol. 2, no. 5, pp. 1002–1004, 1963, doi: 10.1021/ic50009a029.

[143] P. Paíga and C. Delerue-Matos, "Determination of pharmaceuticals in groundwater collected in five cemeteries' areas (Portugal)," *Science of the Total Environment*, vol. 569–570, pp. 16–22, 2016, doi: 10.1016/j.scitotenv.2016.06.090.

[144] J. Liu, G. Lu, Z. Xie, Z. Zhang, S. Li, and Z. Yan, "Occurrence, bioaccumulation and risk assessment of lipophilic pharmaceutically active compounds in the downstream rivers of sewage treatment plants," *Science of the Total Environment*, vol. 511, pp. 54–62, 2015, doi: 10.1016/j.scitotenv.2014.12.033.

[145] S. Moradi, A. A. Isari, F. Hayati, R. Rezaei Kalantary, and B. Kakavandi, "Co-implanting of TiO2 and liquid-phase-delaminated g-C3N4 on multi-functional graphene nanobridges for enhancing photocatalytic degradation of acetaminophen," *Chemical Engineering Journal*, vol. 414, no. January, p. 128618, 2021, doi: 10.1016/j.cej.2021.128618.

[146] T. Hathway and W. S. Jenks, "Effects of sintering of TiO2 particles on the mechanisms of photocatalytic degradation of organic molecules in water," *J Photochem Photobiol A Chem*, vol. 200, no. 2–3, pp. 216–224, 2008, doi: 10.1016/j.jphotochem.2008.07.010.

[147] K. Lv *et al.*, "Photocatalytic selective oxidation of phenol to produce dihydroxybenzenes in a TiO2/UV system: Hydroxyl radical versus hole," *Appl Catal B*, vol. 199, pp. 405–411, 2016, doi: 10.1016/j.apcatb.2016.06.049.

[148] F. Matter and M. Niederberger, "The Importance of the Macroscopic Geometry in Gas-Phase Photocatalysis," *Advanced Science*, vol. 9, no. 13, pp. 1–15, 2022, doi: 10.1002/advs.202105363.

[149] Z. Bielan, S. Dudziak, A. Kubiak, and E. Kowalska, "Application of spinel and hexagonal ferrites in heterogeneous photocatalysis," *Applied Sciences (Switzerland)*, vol. 11, no. 21, 2021, doi: 10.3390/app112110160.

[150] R. C. Pullar, "Hexagonal ferrites: A review of the synthesis, properties and applications of hexaferrite ceramics," *Prog Mater Sci*, vol. 57, no. 7, pp. 1191–1334, 2012, doi: 10.1016/j.pmatsci.2012.04.001.

[151] M. Drofenik, M. Kristl, A. Žnidaršič, D. Hanžel, and D. Lisjak, "Hydrothermal synthesis of Ba-hexaferrite nanoparticles," *Journal of the American Ceramic Society*, vol. 90, no. 7, pp. 2057–2061, 2007, doi: 10.1111/j.1551-2916.2007.01740.x.

[152] D. Lisjak and M. Drofenik, "The mechanism of the low-temperature formation of barium hexaferrite," *J Eur Ceram Soc*, vol. 27, no. 16, pp. 4515–4520, 2007, doi: 10.1016/j.jeurceramsoc.2007.02.202.

[153] R. Dong, L. Wang, J. Zhu, L. Liu, and Y. Qian, "A novel SiO2–GO/acrylic resin nanocomposite: fabrication, characterization and properties," *Appl Phys A Mater Sci Process*, vol. 125, no. 8, pp. 1–11, 2019, doi: 10.1007/s00339-019-2847-7.

[154] A. Zielińska-Jurek *et al.*, "Design and application of magnetic photocatalysts for water treatment . The effect of particle charge on surface functionality," *Catalysts*, no. 7, p. 360, 2017, doi: 10.3390/catal7120360.

[155] S. Khan *et al.*, "Defect engineering toward strong photocatalysis of Nb-doped anatase TiO2: Computational predictions and experimental verifications," *Appl Catal B*, vol. 206, pp. 520–530, 2017, doi: 10.1016/j.apcatb.2017.01.039.

[156] H. Y. Lee and J. Robertson, "Doping and compensation in Nb-doped anatase and rutile TiO2," *J Appl Phys*, vol. 113, no. 21, 2013, doi: 10.1063/1.4808475.

[157] D. S. Bhachu *et al.*, "Solution processing route to multifunctional titania thin films: Highly conductive and photcatalytically active Nb:TiO2," *Adv Funct Mater*, vol. 24, no. 32, pp. 5075–5085, 2014, doi: 10.1002/adfm.201400338.

[158] S. T. Myung *et al.*, "Black anatase titania enabling ultra high cycling rates for rechargeable lithium batteries," *Energy Environ Sci*, vol. 6, no. 9, pp. 2609–2614, 2013, doi: 10.1039/c3ee41960f.

[159] G. Zhu *et al.*, "Hydrogenated blue titania with high solar absorption and greatly improved photocatalysis," *Nanoscale*, vol. 8, no. 8, pp. 4705–4712, 2016, doi: 10.1039/c5nr07953e.

[160] S. Zhang, S. Cao, T. Zhang, and J. Y. Lee, "Plasmonic Oxygen-Deficient TiO2-x Nanocrystals for Dual-Band Electrochromic Smart Windows with Efficient Energy Recycling," *Advanced Materials*, vol. 32, no. 43, 2020, doi: 10.1002/adma.202004686.

[161] M. Chiesa, M. C. Paganini, S. Livraghi, and E. Giamello, "Charge trapping in TiO2 polymorphs as seen by Electron Paramagnetic Resonance spectroscopy," *Physical Chemistry Chemical Physics*, vol. 15, no. 24, pp. 9435–9447, 2013, doi: 10.1039/c3cp50658d.

[162] J. Biedrzycki, S. Livraghi, E. Giamello, S. Agnoli, and G. Granozzi, "Fluorine- and niobium-doped TiO2: Chemical and spectroscopic properties of polycrystalline n-type-doped anatase," *Journal of Physical Chemistry C*, vol. 118, no. 16, pp. 8462–8473, 2014, doi: 10.1021/jp501203h.

[163] A. Nitta, M. Takashima, N. Murakami, M. Takase, and B. Ohtani, "Reversed double-beam photoacoustic spectroscopy of metal-oxide powders for estimation of their energy-resolved distribution of electron traps and electronic-band structure," *Electrochim Acta*, vol. 264, pp. 83–90, 2018, doi: 10.1016/j.electacta.2017.12.160.

[164] W. Chen, P. Yuan, S. Zhang, Q. Sun, E. Liang, and Y. Jia, "Electronic properties of anatase TiO 2 doped by lanthanides: A DFTU study," *Physica B Condens Matter*, vol. 407, no. 6, pp. 1038–1043, 2012, doi: 10.1016/j.physb.2012.01.085.

[165] N. Ullah *et al.*, "Highly dispersed ultra-small Pd nanoparticles on gadolinium hydroxide nanorods for efficient hydrogenation reactions," *Nanoscale*, vol. 9, no. 36, pp. 13800–13807, Sep. 2017, doi: 10.1039/c7nr05096h.

[166] D. A. Zatsepin *et al.*, "Electronic structure, charge transfer, and intrinsic luminescence of gadolinium oxide nanoparticles: Experiment and theory," *Appl Surf Sci*, vol. 436, pp. 697–707, Apr. 2018, doi: 10.1016/j.apsusc.2017.12.086.

[167] J. A. Gupta *et al.*, "Interfacial layer formation in Gd2O3 films deposited directly on Si(0 0 1)," *Appl Surf Sci*, vol. 173, p. 318, 2001.

[168] D. Raiser and J. P. Deville, "Study of XPS photoemission of some gadolinium compounds," *J Electron Spectros Relat Phenomena*, vol. 57, p. 91, 1991.

[169] D. Barreca, A. Gasparotto, A. Milanov, E. Tondello, A. Devi, and R. A. Fischer, "Gd2O3 Nanostructured Thin Films Analyzed by XPS," *Surface Science Spectra*, vol. 14, no. 1, pp. 60–67, Dec. 2007, doi: 10.1116/11.20080703.

[170] W. J. Lademan, A. K. See, L. E. Klebanoff, and G. Van Der Laan, "Multiplet structure in high-resolution and spin-resolved x-ray photoemission from gadolinium," *Phys Rev B*, 1996.

[171] G. Van Der Laan, E. Arenholz, E. Navas, A. Bauer, and G. Kaindl, "Magnetic dichroism and orbital momentum coumpling in 4d photoemission from Gd(0001)," *Phys Rev B*, vol. 53, p. R5998, 1996.

[172] C. Chen, M. Wu, C. Ma, M. Song, and G. Jiang, "Efficient Photo-Assisted Thermal Selective Oxidation of Toluene Using N-Doped TiO2," *ACS Omega*, vol. 8, no. 23, pp. 21026–21031, Jun. 2023, doi: 10.1021/acsomega.3c01887.

[173] C. Chen *et al.*, "Electron-donating N−−Ti3+−Ov interfacial sites with high selectivity for the oxidation of primary C–H bonds," *Cell Rep Phys Sci*, vol. 3, no. 7, Jul. 2022, doi: 10.1016/j.xcrp.2022.100936.

[174] M. Grätzel and R. F. Howe, "Electron Paramagnetic Resonance Studies of Doped TiO2 Colloids," *J. Phys. Chem*, vol. 94, pp. 2566–2572, 1990, [Online]. Available: https://pubs.acs.org/sharingguidelines

[175] R. Gallay, J. J. Van Der Klink, and J. Moser, "EPR study of vanadium (4+) in the anatase and rutile phases of TiO2," *Phys Rev B*, vol. 34, no. 5, pp. 3060–3068, 1986.

[176] J. Zhang and Y. Nosaka, "Photocatalytic oxidation mechanism of methanol and the other reactants in irradiated TiO2 aqueous suspension investigated by OH radical detection," *Appl Catal B*, vol. 166–167, pp. 32–36, 2015, doi: 10.1016/j.apcatb.2014.11.006.

PUBLICATION [P1]

Facet effect of TiO$_2$ nanostructures from TiOF$_2$ and their photocatalytic activity

Marta Kowalkińska[a], Szymon Dudziak[a], Jakub Karczewski[b], Jacek Ryl[c], Grzegorz Trykowski[d], Anna Zielińska-Jurek[a,*]

[a] *Department of Process Engineering and Chemical Technology, Faculty of Chemistry, Gdansk University of Technology (GUT), G. Narutowicza 11/12, 80-233 Gdansk, Poland*
[b] *Department of Solid State Physics, Faculty of Applied Physics and Mathematics, Gdansk University of Technology (GUT), 80-233 Gdansk, Poland*
[c] *Department of Electrochemistry, Corrosion and Materials Engineering, Gdansk University of Technology (GUT), 80-233 Gdansk, Poland*
[d] *Faculty of Chemistry, Nicolaus Copernicus University, Gagarina 7, 87-100 Toruń, Poland*

HIGHLIGHTS

- Different TiO$_2$ nanostructures were prepared from TiOF$_2$ precursor.
- The effect of the particles shape on phenol mineralization was investigated.
- The (1 0 1) anatase surface was found to be more suitable for TOC removal than (0 0 1).
- HF induced surface formation of TiO$_{2-x}$ additionally lowered TOC mineralization.
- Formation of *ortho*-hydroxylated phenol was found to depend on the (0 0 1) presence.

ARTICLE INFO

ABSTRACT

In this study, special attention is focused on the design of TiO$_2$ morphology and microstructure in the two-step preparation procedure using TiOF$_2$ as a precursor to study their photodegradation mineralization efficiency. Firstly, TiOF$_2$ was synthesized by a simple solvothermal method using titanium(IV) tetrafluoride, which was further used as a precursor in preparation of anatase 2D nanosheets, octahedral, decahedral, and rectangular prisms shape structures. The as-obtained nanostructures were characterized by X-ray diffraction (XRD), scanning electron microscopy (SEM), Brunauer-Emmett-Teller surface area analysis (BET), X-ray photoelectron spectroscopy (XPS), UV–vis diffuse reflectance spectroscopy and photoluminescence spectroscopy. It was assumed that TiOF$_2$ could be applied as a useful precursor for the preparation of nanostructured TiO$_2$ with defined morphology. Simple controlling of the reaction environment, together with the stabilizing effect of the introduced substrates, resulted in the formation of TiO$_2$ particles with different morphologies and consequently exposed crystal facets. The presence of {0 0 1}, {1 0 1} and {1 0 0} facets influence on their photocatalytic activity but mostly on their mineralization efficiency and the pathway of phenol degradation. From the obtained series, the TiO$_2$ octahedra exposing {1 0 1} facets exhibited the highest photoactivity and mineralization efficiency under UV–Vis light irradiation, which decreases as the other facets appear and become more exposed. The obtained results were compared with a computational study on the ·OH and ·O$_2^-$ attack on the phenyl ring. Overall results showed that the surface effects of the photocatalyst could be an influencing factor in both mineralization efficiency and photodegradation products formation.

1. Introduction

Through the last years, titanium(IV) oxide has established itself as one of the most important wide-gap semiconducting material with numerous applications. Due to its excellent chemical stability, electron transport properties and overall availability it is being studied as a pure or modified material for sensors development [1], electronic devices [2], self-cleaning materials [3] and photoanodes preparation [4]. Moreover, it remains as one of the most important material that is continuously used in the field of photocatalysis. Although a great effort

* Corresponding author.
E-mail address: annjurek@pg.edu.pl (A. Zielińska-Jurek).

was made to understand and utilize TiO_2 properties as a photocatalyst, some questions and unknown details are still present, mostly regarding interactions between TiO_2 and reacting substrates. More recently, this has led to significant attention being given to preparation and studying activity of nanostructured TiO_2 particles, exposing specific crystal facets, to describe the photocatalytic process on its fundamental level [5–8]. Reported findings have shown that surface structure can remarkably influence on reactivity towards H_2 generation and storage [9,10], oxidation of organic compounds [11,12], generation of reactive radicals [13], CO_2 photoconversion to methane [14] and gas sensing ability of TiO_2 [15]. It can be controlled by growing TiO_2 particles in a specific environment, from which HF, ammonium-bearing compounds (amines, hydrazine), alcohols and pH regulators were found to influence significantly on particles morphology [16–22]. However, it is still challenging to find a preparation method that would limit the chemicals required to control TiO_2 crystallization without compromising a variety of its possible structures.

In this regard, titanium-fluorine compounds can be seen as useful precursors, as they naturally introduce fluorine ions inside the reaction system. Moreover, compounds like $(NH_4)_2TiF_6$ or TiF_4 can be easily obtained from the processing of $Fe_2O_3 \cdot TiO_2$ minerals [23–25]. Within this group, TiF_4 was already introduced, with great success, as a substrate in the preparation of anatase decahedrons and platelets [16], however, their direct synthesis results in the formation of large, microsized particles, which is unfavourable for their application in photocatalysis. As an alternative approach, Gordon et al. have obtained series of TiO_2 nanostructures from TiF_4 by dissolving and subsequent crystal growing in mixtures of organic surfactants [6], which remain as a rather complex and waste-generating method. On the other hand, $(NH_4)_2TiF_6$ was used in a solid-state reaction, where final TiO_2 morphology results from coalescence of calcined particles, which were obtained only in the form of nanosheets [26].

However, an alternative way can be emerged from solvothermal processing of titanium oxyfluoride $TiOF_2$, utilizing fact of its easy degradation to TiO_2. Titanium oxyfluoride is a metastable phase which exists in two known polymorphs, the first one with cubic structure (space group Pm-3 m) and the second with hexagonal (space group R-3c). Both of them are composed of titanium atoms octahedrally coordinated by randomly distributed oxygen and fluorine, which are then connected differently. The unit cells of both structures, visualized by the VESTA program, are presented in Fig. 1. Usually, $TiOF_2$ with cubic structure is synthesized through partial hydrolysis/oxidation of titanium butoxide or TiF_4 [27–30]. However, it can also be obtained through the fluorination of TiO_2 [31]. Although pure $TiOF_2$ was found to be active under visible light [32,33], its possible photocatalytic activity under a broad spectrum is rather low, comparing to TiO_2 [34]. In this regard, it was applied as a precursor for the synthesis of TiO_2 or $TiO_2/TiOF_2$. At present, only $(0\,0\,1)$ plane-exposing anatase was formed from $TiOF_2$, which is not always desired [11,12]. Therefore, in this study, the possibility to create a variety of TiO_2 structures, followed by

their activity analysis, starting from $TiOF_2$ precursor and with the addition of possibly simple growth-controlling agents, was investigated. The effect of octahedral, decahedral, and rectangular prisms shape of TiO_2 on the ability to mineralize organic pollutants was further investigated. The correlation between anatase $(0\,0\,1)$ and $(1\,0\,1)$ surfaces ratio, and mineralization efficiency was studied in detail. Moreover, computationally analysis by calculating the minimum energy path (MEP) of radical addition at the *ortho* and *para* positions was applied to study the participation of ·OH and ·O_2^- radicals in phenol molecule degradation. The initial and final structures were geometry optimized using DFT calculations with PBE0 hybrid functional and the D3BJ dispersion correction.

2. Experimental section

The synthesis of titanium oxyfluoride and titanium(IV) oxide nanostructures were proceeded by a facile solvothermal method. Titanium (IV) tetrafluoride, 1-butanol, hydrofluoric acid (48%), hydrochloric acid (35%), hydrazine hydrate (60%) and ammonia water (25%) were used as received from Sigma-Aldrich without any purification.

2.1. Fabrication of TiOF₂ precursor

In the preparation of $TiOF_2$ precursor, 10 g of TiF_4 powder was added into a 200 cm^3 Teflon reactor with 120 cm^3 of 1-butanol (without introducing any HF). Obtained mixture was stirred for 15 min to form stable suspension using a Teflon-coated magnetic stirrer bar. After that, the reactor was transferred into a stainless-steel autoclave immediately and was heated at 210℃ for 24 h. The obtained product was separated through centrifugation and was washed thoroughly with absolute ethanol and deionized water to remove the residual contamination and fluorine species. After drying at 80 ℃, the $TiOF_2$ grey precursor was harvested.

2.2. The synthesis of TiO₂ nanostructures

In the second step, the obtained $TiOF_2$ precursor was hydrothermally treated to form nanostructured TiO_2. Different capping agents (hydrochloric acid, hydrofluoric acid, hydrazine, and ammonia) were selected as growth-controlling species, based on the previous reports [35–37]. In a typical synthesis, 0.25 g of as-synthesized $TiOF_2$ was dissolved in a 100 cm^3 mixture of deionized water and stabilizing agent and was transferred into a 200 cm^3 autoclave after 15 min of stirring. The prepared suspension was heated at 210 ℃ for 24 h, then cooled down naturally. Obtained precipitates were centrifuged, washed, and dried the same way as during fabrication of the precursor, to obtain white powders of TiO_2. Moreover, $TiO_2\_H_2O$ sample was synthesized as previously described in 100 cm^3 of deionized water as a medium, without introducing any growth-controlling agent. Detailed information regarding the synthesis conditions of the obtained samples and
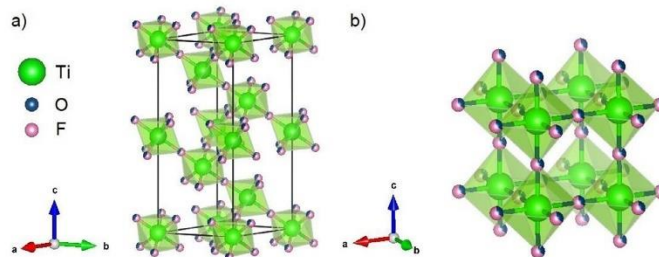

Fig. 1. Visualization of a) hexagonal $TiOF_2$ unit cell, b) cubic $TiOF_2$ unit cell. The probability of distribution in lattice is 1/3 for oxygen and 2/3 for fluorine.

Table 1
Synthesis conditions of the obtained samples.

Sample name	Precursor	Precursor amount [g]	Medium		Volume [cm³]	
			Solvent	Capping agent	Solvent	Capping agent
TiOF₂	TiF₄	10	1-butanol	–	120	–
TiO₂_HCl	TiOF₂	0.25	water	HCl	98	2
TiO₂_HF/HCl				HF and HCl	99	0.25/0.75
TiO₂_HF				HF	99.75	0.25
TiO₂_H₂O				–	100	–
TiO₂_N₂H₄				N₂H₄·H₂O	75	25
TiO₂_NH₃				NH₃·H₂O	47	53

their description is presented in Table 1.

To show the critical effect of the size change on the activity of the obtained photocatalyst the comparison of nanosheets prepared directly from TiF_4 to structures obtained from $TiOF_2$ was performed.

Briefly, anatase sheets were solvothermally synthesised directly from TiF_4 in the presence of 1-butanol and with addition of hydrofluoric acid. For a synthesis a 3.06 g of TiF_4 was introduced to the 120 cm^3 of 1-butanol inside a 200 cm^3 Teflon lined reactor and 0.68 cm^3 of HF (48%) was subsequently added. Then, the mixture was transferred to an oven and was kept in 210 °C for 24 h. Obtained TiO_2 particles were centrifuged, washed with water, dried at 80 °C and finally calcined at 500 °C to remove residual F^-.

2.3. Material characterization

The structure of the samples and phase composition were investigated by X-ray powder diffraction (Cu Kα radiation, Rigaku MiniFlex 600 X-Ray diffractometer). The analysis and Rietveld refinements were performed with the HighScorePlus software package (PANalytical, 2006) and the ICDD database with data fitting based on the pseudo-Voigt profile function. The specimen displacement, lattice parameters, polynomial coefficients for the background function, profile parameters, and Gaussian and Lorentzian profile coefficients were refined. The amorphous phase content was analyzed using an internal standard (NiO, Aldrich, Germany).

The morphologies of the nanostructures were characterized by field emission scanning electron microscope (SEM, FEI Quanta FEG 250). The selected area electron diffraction (SAED) analysis were performed using the transmission electron microscope (TEM) Tecnai 20F X-Twin, an electron source, cathode with field emission gun (FEG), EHT = 200 keV, camera for TEM Orius, Gatan Inc. The Brunauer-Emmett-Teller (BET) surface area of the powders was analysed by nitrogen adsorption using a Micromeritics Gemini V instrument. All samples were degassed at 200 °C prior to nitrogen adsorption measurements. The BET surface area was determined by a multipoint BET method. The chemical states on the surface of nanostructures were determined by X-ray photoelectron spectroscopy (XPS) using Escalab 250Xi (Thermo Fisher Scientific, Waltham, USA) with Al Kα radiation and pass energy 20 eV. The optical properties were studied by a UV–Vis spectrophotometer (Thermo Fisher Scientific Evolution 220) for the measurement of diffuse reflectance (DRS), using $BaSO_4$ as a standard. Based on the obtained data, the bandgap energy calculations were performed using Tauc's method. The photoluminescence (PL) spectra were recorded on a Perkin-Elmer LS 55 spectrophotometer with a Xe discharge lamp as the excitation source. The samples were excited at 250 nm in the air at room temperature. During measurements, a 290 nm cut-off filter was used.

2.4. Determination of photocatalytic activity

Photocatalytic activity of obtained samples was tested in a model reaction of phenol degradation, performed in the black-box. All

mentioned chemicals were used as delivered by the provider and were used without any purification.

In a typical experiment of phenol degradation, 25 cm^3 of pollutant solution (20 mg·dm^{-3}, diluted from the concentrated stock solution) and 50 mg of photocatalyst were put into a 25 cm^3 quartz reactor under stirring. A Xe lamp (model 6271H, Oriel, USA) with a water IR filter, emitting light from the UV–Vis range, was used as a light source and the system was set up to obtain the measured UV-spectrum flux intensity at the reactor border equal to 30 mW·cm^{-2}. During the reaction, a constant air flow of 5 dm^3·h^{-1} was introduced through suspension, which was magnetically stirred and thermostated at 20 °C. Before irradiation, the whole system was kept in the dark for 30 min to achieve the adsorption–desorption equilibrium. After that, the process was initiated by turning on the Xe lamp. All the experiments were studied for 60 min of irradiation. Samples were collected at −30, -15, 0, 5, 10, 20, 30, 40, 50, and 60 min of the process, where 0 is the point of light introduction. Degradation efficiency was monitored using a high-performance liquid chromatography system (HPLC, model Shimadzu LC-6A), combined with a photodiode array detector (SPD-M20A) and C18 column (Phenomenex Gemini 5 μm; 150x4.6 mm) working at 45 °C. During HPLC measurements mobile phase composed of (v/v) 70% acetonitrile, 29.5% water and 0.5% orthophosphoric acid (85% w/w solution) was used at the flow rate of 0.3 cm^3·min^{-1}. Moreover, mineralization efficiency was analysed after the process as the difference in total organic carbon (TOC) concentration. TOC measurements were performed using Shimadzu TOC-L apparat.

Quantitative analysis of all observed species was performed utilizing the external calibration method using standard compounds, all purchased from Sigma-Aldrich. An HPLC grade acetonitrile and ortho-phosphoric acid solution were provided by Merck.

2.5. Computational details

The attack of ·OH and ·O_2^- radicals on the phenol molecule was studied computationally by calculating the minimum energy path (MEP) of radical addition at the *ortho* and *para* positions. Before MEP calculations, initial and final structures were geometry optimized using DFT calculations with PBE0 hybrid functional and the D3BJ dispersion correction to a convergence threshold of 10^{-8} Ha [38–40]. The MEP calculations were performed using the Nudged Elastic Band (NEB) method with an energy weighted spring constant and L-BFGS optimization method, as implemented in the Orca 4.2.1 software package [41]. In the presented results, the relative 0 energy is a sum of reactants energy obtained in separate runs. Throughout the calculations, the CPMC model of continuum solvation was introduced to account for the solvent effect during model reactions.

3. Results and discussion

3.1. Structural and morphological analysis

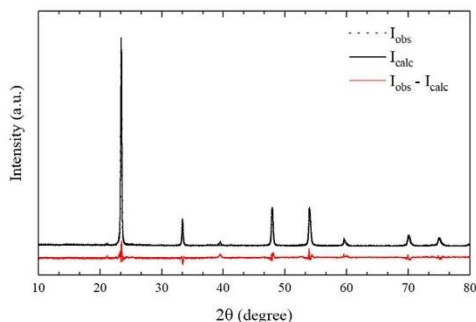The phase structure and crystallinity of $TiOF_2$ precursor and TiO_2

3

Fig. 2. Rietveld refinement of the XRD pattern of the $TiOF_2$ precursor.

Fig. 4. SEM image of $TiOF_2$ precursor.

nanostructures are significant for their morphologies. Fig. 2 shows the XRD patterns of titanium oxyfluoride compared with the calculated model. All the diffraction peaks corresponding to $TiOF_2$ were observed, which indicates that the $TiOF_2$ with high purity was obtained. The Rietveld refinement was necessary to confirm the presence of titanium oxyfluoride. Therefore, fitting experimental data with the calculated model was performed. The results of Rietveld refinement for the as-obtained TiO_2 nanostructures are presented in Fig. S1 and Table S1 in the Supporting Materials.

The broad reflection at $2\theta = 24.3°$ with the highest intensity corresponds to the (1 0 0) plane diffraction of $TiOF_2$. As presented in Fig. 3, in the second step of the synthesis, the peaks of $TiOF_2$ vanished, and the peak intensity of (1 0 1) plane at $2\theta = 25.3°$ of anatase increased, indicating the complete phase transformation of $TiOF_2$ to anatase. The different environments (1-butanol, hydrofluoric acid, hydrochloric acid, hydrazine hydrate, ammonia water, and water) influenced the shapes of diffraction peak parameters, especially in the range of $2\theta = 53-56°$. The sample $TiO_2\_N_2H_4$ had the higher reflection at $53.9°$ than $55°$ and similar intensities of peaks at $37.8°$ and $48.1°$, which are typical for octahedral TiO_2 nanostructures [6]. The difference between their intensities disappeared in other samples. Titanium(IV) oxide samples prepared by reaction in the presence of acids were more crystallized than obtained in basic conditions. As presented in Table S2 (in the Supporting Materials) the highest amorphous phase content was
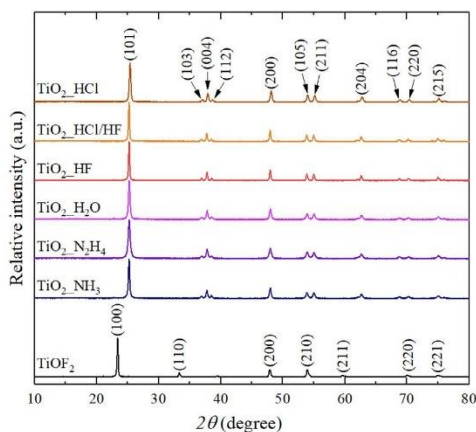
observed for sample $TiO_2\_N_2H_4$, and the lowest for TiO_2_HF/HCl photocatalyst. No other reflections were detected, suggesting the high purity of the as-synthesized photocatalysts.

The XRD pattern of the obtained nanosheets with an observed anatase structure is presented in Fig. S2 in the Supporting Materials. The enhancement of the (2 1 1) signal, comparing to the (1 0 5) one, at approximately 53-55° indicates size reduction along the c direction of the anatase structure. It is consistent with reported patterns for anatase nanosheets exposing (0 0 1) facets and the effect of HF addition in the alcohol environment [6,18].

The morphologies of $TiOF_2$ precursor and TiO_2 nanostructures were further studied by scanning microscopy analysis. Fig. 4 showed SEM images of the as-prepared $TiOF_2$ powders. It was found that the obtained precursor consists of a mixture of cubic and spherical particles, with a mean size of 260 ± 138 nm (this corresponds to a sphere diameter or a cube side). Comparing to some other results of $TiOF_2$ preparation [27–29,33] the morphology of the obtained precursor is not uniform, which could result from high amounts of TiF_4 used during synthesis. As reported by Wang et al., nanocubic titanium oxyfluoride can be obtained from TiF_4 during the solvothermal alcoholysis process [33]. The final oxidation from fluoride to oxyfluoride results from alcohol condensation and subsequent hydrolysis of initially formed $(RO)_xTiF_{4-x}$ structure. Obtained $TiOF_2$ was observed to form spheres in the first place and was subsequently transformed into cubes as the process was prolonged. Since the kinetics of the described process was reported to depend mostly on H_2O production during alcohol condensation, the conclusion is that a higher amount of TiF_4 to alcohol, would hinder the hydrolysis process, resulting in the formation of both spheres and cubes, as observed. It could probably be managed by increasing reaction time and the introduction of HF, which both include H_2O as a solvent and catalyses alcohol condensation [33]. Nevertheless, in this study, the obtained $TiOF_2$ particles were used as a precursor for the fabrication of TiO_2 nanostructures.

Figs. 5 and 6 showed SEM images of the obtained TiO_2, resulting from $TiOF_2$ processing in the presence of different capping agents. In most cases, the formation of clearly defined nanostructures with a size smaller than the original precursor was observed. These primary particles can be freely observed in the sample or are aggregated, forming a representation of the original $TiOF_2$ macroparticle, in a way similar to already observed for TiO_2 hollow boxes obtained from $TiOF_2$ (see in Fig. S3 in the Supporting Materials) [27–29]. It suggests that the initial nucleation of TiO_2 was mostly observed as a surface process, and

Fig. 3. X-ray diffraction patterns of TiO_2 in comparison to the precursor.
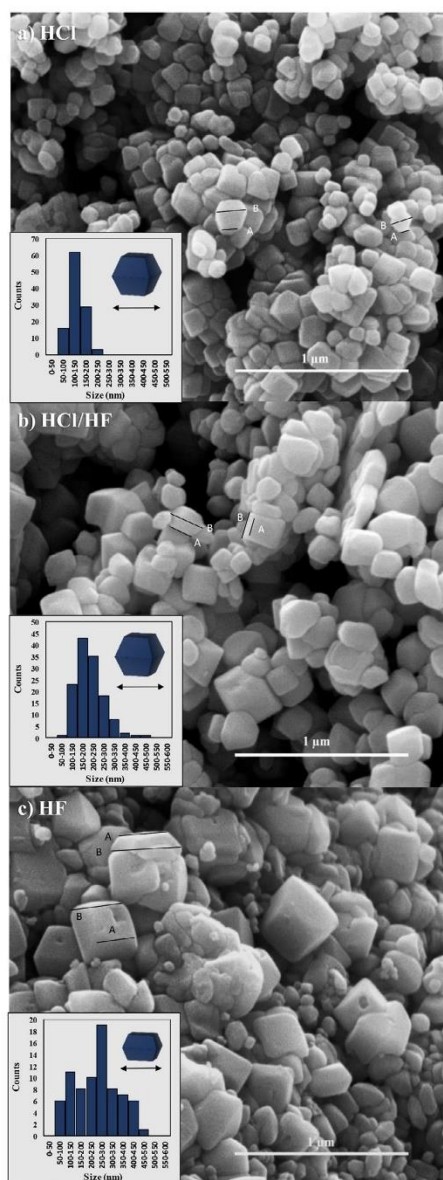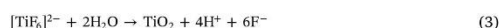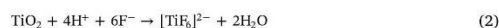
4

Fig. 5. SEM images of TiO₂ samples obtained with addition of a) HCl, b) a mixture of HF and HCl and c) only HF.

possible aggregation of the final particles can be controlled by the size reduction of the precursor particles. For fluorinated compounds, the original process is known to result from their hydrolysis, accompanied by HF formation [42], and is followed by a growth of nucleated seeds.

The TiO₂ growing is usually described in terms of the rapid dissolution–recrystallization processes [43], in which Ti atoms are reversibly transferred between their solid oxide form and octahedral ions, giving rise to a gradual growth of the specified and most stable crystal structure.

For a TiOF₂ system, without additional substrates, it could be described by a series of following equations (however formation of different octahedrally coordinated Ti species is generally possible [36,37]):

$$TiOF_2 + H_2O \rightarrow TiO_2 + 2HF \tag{1}$$

$$TiO_2 + 4H^+ + 6F^- \rightarrow [TiF_6]^{2-} + 2H_2O \tag{2}$$

$$[TiF_6]^{2-} + 2H_2O \rightarrow TiO_2 + 4H^+ + 6F^- \tag{3}$$

For samples prepared in pure water or acidic environment of HCl or HF, this has led to a formation of anatase decahedrons, enclosed with {001} and {101} facets. These particles can be characterized by a truncation level, defined as a ratio between their top and a middle side (A/B), as highlighted in Fig. 5. The final shape of the obtained particles results from competitive growth along both [001] and [101] directions, which depends on their relative surface energy [44]. It is well known that HF presence is crucial for stabilizing {001} surface of anatase [9,16,18], and that is the reason for the highest truncation observed for a sample obtained with the addition of HF during preparation. The observed particles became more enclosed with {101} surface as the environment was changed to HCl/HF and HCl only. For both of these samples, similar morphologies were observed, showing that both acidity and fluorine or chloride presence influenced on the growth behaviour of anatase. It probably results from a mixed effect of a surface protonation [17], increased amounts of molecular HF in the attendance of HCl [45], and their competitive adsorption on the surface of growing particles (HCl is a stronger acid than HF, although also promotes stabilization of {101} surface [6,16]). Moreover, it was observed that increased HF concentration promotes the growth of larger particles, regardless of their truncation.

Comparing with samples obtained at acidic conditions, TiO₂ prepared in pure water was only little truncated and its particles were much smaller. It would be changed when both N₂H₄·H₂O and NH₃·H₂O are introduced to the reaction system, resulting in the formation of well-defined anatase octahedrons and prisms enclosed with {101} pyramids, respectively (see in Fig. 6). Hydrazine was already proved to be an effecting agent for a {101} surface capping and promotes the formation of the octahedral particles when combined with other species stabilizing {001} surface [36]. In this study, the system composed of N₂H₄ and HF could be obtained through hydrazine introduction and initial TiOF₂ hydrolysis resulting in the formation of almost completely enclosed octahedrons. These particles can be characterized by some truncation, in a way similar to the previously described HCl/HF samples; however, they are not uniformly enclosed by {001} surface at the top.

In many cases, a curve, as well as facet, not parallel to a B side, was observed. These could be ascribed to {103} surfaces or a series of microfacets that result in a top curvature [45]. Therefore their nature could differ from these observed in acidic samples [46]. Nevertheless, their content in the total particle's surface was negligible, and they were not analysed in detail. Instead, a simple fact of octahedrons truncation was minded. Finally, a unique morphology was obtained in the presence of NH₃. The formation of elongated rods, with their sides enclosed with anatase {100} and {010} facets was observed, which were topped off with irregular pyramids, composed with a {101}, {001} and possibly other, higher-index facets. Comparing to N₂H₄, ammonium is a stronger base (pK_b = 4.75 for NH₃ versus 5.9 for hydrazine), therefore {100} formation could be explained as the increased basicity of the solution and more oxygenated surface of the growing particles [17]. From SEM images, it was confirmed that simple hydrothermal
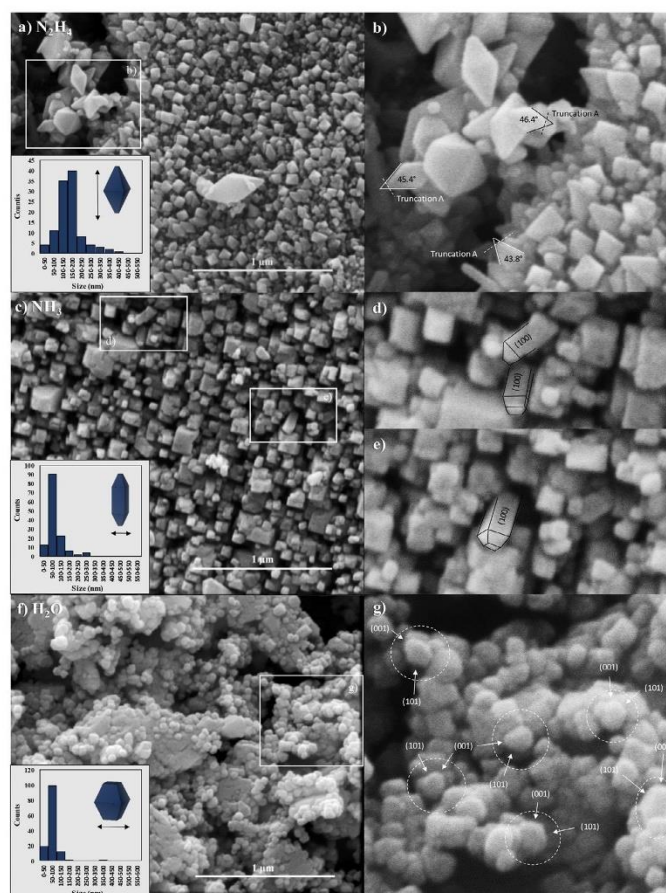
Page | 103

Fig. 6. SEM images of TiO$_2$ samples obtained with addition of a) N$_2$H$_4$, c) NH$_3$ and f) in pure H$_2$O; b), d), e), g) magnifications of selected areas of a), c), f).

processing of TiOF$_2$ particles has resulted in the formation of a series of anatase nanostructures, mostly with different ratios of {0 0 1} and {1 0 1} facets exposition. Moreover, the two-step synthesis starting from TiF$_4$ enables the formation of fine anatase nanoparticles (mean size between 50 and 250 nm) rather than macro-sized ones, which are usually obtained from growing directly from titanium fluoride. Nevertheless, particles are mostly aggregated, probably due to the growth on the surface of the precursor (see also in Fig. S4 for a macro-sized sample), indicating the critical role of the precursor morphology on the final product. Additionally, the selected area electron diffraction measurements for selected samples were performed, and the results are presented in Fig. S5 in the Supporting Materials. The obtained results indicate the presence of all (0 0 1), (1 0 0) and (1 0 1) lattice planes. The (0 0 1) and (1 0 0) are visible as (0 0 4) and (2 0 0) reflections due to the extinction rules. However, the observed from SAED analysis patterns were mostly polycrystalline, as shown in Fig. S5 with 1, 2 and 3 reflexes corresponding to (1 0 1), (0 0 4) and (2 0 0) respectively.

The performed two-step synthesis from TiF$_4$ to TiOF$_2$ and subsequently to TiO$_2$ resulted in a significant size reduction than reported for direct TiF$_4$ processing [16]. To show a critical effect of the size change on the activity of the obtained photocatalyst the comparison of nanosheets prepared directly from TiF$_4$ to structures obtained from TiOF$_2$ was performed. The morphology of 2D nanosheets obtained from TiF$_4$ is shown in Fig. S4 in the Supplementary Materials. As expected, the synthesised TiO$_2$ nanostructures resulted in the formation of a thin macro-sized sheets with highly exposed {0 0 1} facets. These particles were partially aggregated forming a flower-like structures.

Measured surface areas of TiO$_2$ nanostructures are presented in Table 2, together with a summation of the SEM observations. The surface area of the precursor was relatively small, and during the second step of the reaction, this parameter increased for each sample. When the transformation from TiOF$_2$ to TiO$_2$ occurred, crystal growth started on the surface, and nanocrystals became more textured, smaller, and partially disaggregated in comparison with a precursor, which resulted in the surface development. It is generally followed by an increase in the total pore volume, as shown in Table 2. The specific surface area of TiO$_2$ nanosheets (see its characteristic in the Supplementary Materials) was 18.1 m^2·g^{-1}, which is generally comparable or higher than TiO$_2$

6

M. Kowalkińska, et al.

Table 2

The representation of the specific surface area and morphology summation of obtained samples. Presented size corresponds to the crystal side highlighted in Figs. 5 and 7.

Sample	Surface area [$m^2 \cdot g^{-1}$]	Pore volume [$cm^3 \cdot g^{-1}$]	Mean size [nm]	Crystal shape	Identified facets	Truncation level (A/B)
$TiOF_2$	5.2	0.003	260 ± 138	Spheres and cubes	–	–
TiO_2_HCl	13.8	0.007	132 ± 32	Decahedral	{001}, {101}	0.54 ± 0.09
TiO_2_HCl/HF	9.4	0.006	209 ± 68	Decahedral	{001}, {101}	0.52 ± 0.08
TiO_2_HF	6.1	0.004	250 ± 104	Decahedral	{001}, {101}	0.65 ± 0.08
TiO_2_H_2O	17.2	0.009	74 ± 34	Decahedral	{001}, {101}	0.41 ± 0.07
TiO_2_N_2H_4	33.9	0.017	156 ± 69	Octahedral	{101}	0.17 ± 0.07
TiO_2_NH_3	12.6	0.006	88 ± 32	Rectangular prisms with pyramids on top	{100}, {010}, {101}	–

nanostructures obtained from $TiOF_2$ to TiO_2 transformation.

3.2. X-ray photoelectron spectroscopy

To study the surface composition of the obtained samples X-ray induced photoelectron spectroscopy (XPS) analyses were performed. The survey scans of all samples (Fig. S8) confirmed low content of F^- ions (less than 1%) in comparison with other elements, implying their successful removal during post-synthesis treatment and their limited effect on the observed photoactivity. For all samples, the O and Ti signals were dominant. The observed O1s spectra can be resolved into three peaks, which are ascribed to lattice oxygen, bridging oxygen and hydroxyl groups bound to titanium at ~529.2 eV, ~531 eV and ~532.9 eV, respectively [47,48]. Based on the Ti2p XPS spectra (Fig. 7), all photocatalysts showed a right shift, which indicates the presence of nonstoichiometric TiO_{2-x} next to TiO_2 compound. The Ti^{3+} sites were not found directly in any sample, which resulted from the oxidizing conditions [49,50].

The content of individual elements was different for the TiO_2 nanostructures. There was observed an overall tendency that the amount of stoichiometric TiO_2 on the surface of the particles decreased at acidic conditions, especially for HF and HF/HCl samples. It followed by the changes in the oxygen species observed at the surface, especially in an increase of Ti-OH and lattice oxygen signals. Observed results correspond with H^+ and HF presence and could be explained as the basis of the HF-induced surface etching. It is known that molecular HF can induce surface decomposition of anatase particles (especially (001) surface), initiated by the substitution of the bridging oxygen by F^- [45]. As the surface bounding of fluorine to titanium is supposed to be occurring in the first place, this process is strongly dependent on the HF amount possible to react with the forming TiO_2. Generally, F^- amounts can be considered as a limiting factor for both particle growth (dissolution/recrystallization reactions (2) and (3)) and possible etching. For samples prepared without the addition of HF, it was limited to the F^- introduced through $TiOF_2$ hydrolysis. Therefore, sample TiO_2_H_2O was obtained in the form of ultrafine particles, which growth was limited due to the small amounts of F^- possible to react with forming TiO_2. However, the HF formed during the $TiOF_2$ hydrolysis was still able to induce some surface decomposition observed for this sample. Comparing to TiO_2_H_2O, neutralization of HF with hydrazine or ammonia have led to more stoichiometric surface composition and less visible TiO_{2-x} signal. It was changed when HCl was introduced to the system, as the particle growth can be enhanced through the involvement of additional H^+ and Cl^- ions to create $[TiCl_6]^{2-}$. Moreover, in the case of TiO_2_HCl, the F^- amount was still relatively low compared with the Ti presence, which would limit the surface decomposition. It is concluded that such increase in recrystallization efficiency, enabled by the introduction of HCl, together with low content of F^- resulted in the enhancement of particles crystallinity and more stoichiometric surface composition for this sample. Later this is changed when HF was introduced during the synthesis and for samples TiO_2_HF and TiO_2_HCl/HF, enhanced surface etching began with the increase of the TiO_{2-x} signal. Ultimately, the TiO_2_HCl/HF sample was characterized by the

highest TiO_{2-x} presence as the hydrochloric acid, having lower pK_a than hydrofluoric acid, enhanced the formation of molecular HF, which is consistent with the observations of Wang et al. [45]. Presented surface etching and the relative absence of F^- resulted in the enhanced amount of the surface oxygen, which was introduced to compensate under-coordination of the titanium atoms (e.g., as the oxygen add atoms [51–53]). As shown in Fig. 8, the overall ratio of the observed Ti/O changed between approx. 0.35 and 0.24 throughout the samples. The highest values were observed for TiO_2_N_2H_4 and TiO_2_HCl samples and were very close to the expected value of 0.33 (that is, a typical TiO_2 structure with one –OH group attached to every surface Ti atom, with a hypothetical surface formula of TiO_3), while the lowest was observed for both TiO_2_HF and TiO_2_HF/HCl samples, suggesting bounding of the additional oxygens at the surface.

3.3. Absorption and photoluminescence spectroscopy analysis

Fig. 9-a presents the DR-UV–Vis spectra of titanium oxyfluoride. The sample exhibited a considerable absorption below 380 nm range. However, a small band in the range of visible light appears, which vanished for TiO_2 (see Fig. 9-b). This spectrum explains the discrepancy in the literature. Titanium oxyfluoride is shown as a poor photocatalyst [34]. On the other side, Wang et al. [33] presented the small-sized $TiOF_2$ nanocubes with mesoporous structure, which exhibited high activity in the visible light in the reaction of Rhodamine B and 4-chlorophenol degradation. Through the UV-vis spectra, the bandgap of $TiOF_2$ value was (3.15 ± 0.06) eV was calculated by Tauc method [54]. Energy band gaps for anatase nanostructures are presented in Fig. S9 in Supporting Materials.

The photoluminescence (PL) spectra of TiO_2 nanostructures, which were synthesized from $TiOF_2$ were measured at room temperature. The PL spectra of photocatalysts in comparison with the precursor with an excitation wavelength of 250 nm are shown in Fig. 10. Four main visible emissions peaks at ~398 nm, ~486 nm, ~528 nm, and ~596 nm were observed. The emission in the UV range describes the band edge emission of the anatase and titanium oxyfluoride, which also explain the bandgap of these materials. The calculated band gaps from the Tauc method were ~3.15 eV for all samples, which correlate with DR-UV–Vis analysis. This band overlaps with bands at ~418 nm and ~443 nm, which originated from the self-trapped excitons localized on the TiO_6 octahedral. Due to the splitting of the conduction band, these types of trapped sites were found below the conduction band edge [55]. The bands at ~486 nm and 596 nm were variously attributed to oxygen vacancies [56]. The 2.55 eV vacancy level, which corresponds to 0.6 eV below the conduction band, has been attributed to Ti^{4+} ions adjacent to oxygen vacancies (intragap surface states). The presence of shallow electron trapping levels located about 0.6–1.6 eV below the conduction band edge is typical for anatase nanostructures [57]. The band at ~528 nm is related to non-stoichiometric TiO_2 [55].

3.4. Photocatalytic activity measurements

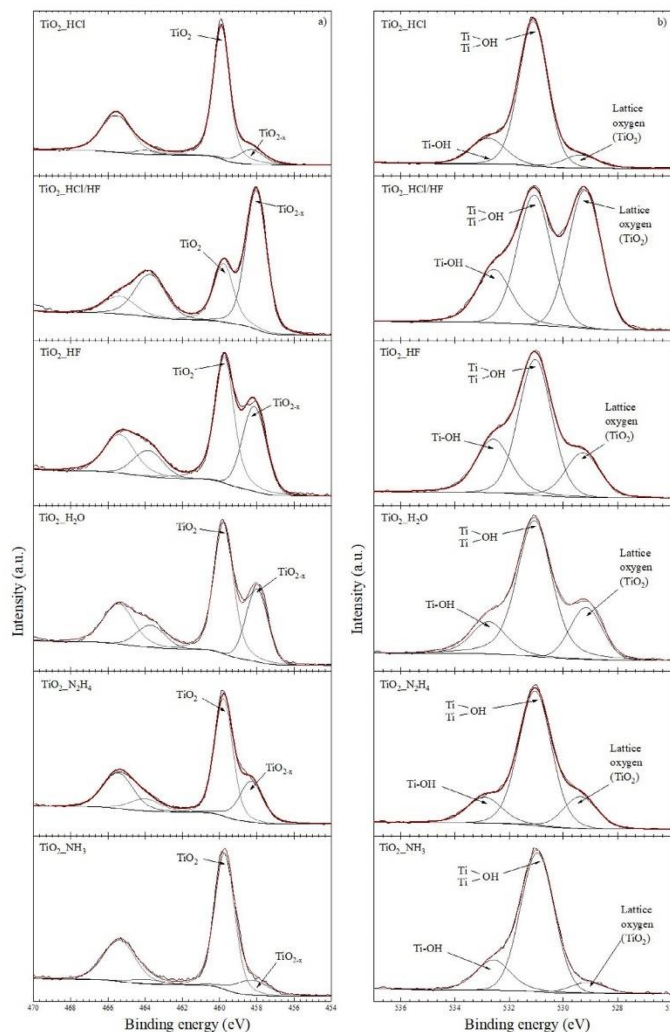The photocatalytic activity of TiO_2 nanostructures was studied in a

7

Fig. 7. XPS spectra of samples showing a) Ti2p and b) O1s signals with Gaussian fits, respectively.

model reaction of phenol degradation. Briefly, photocatalytic oxidation of phenol is known to go through catechol (CT) and hydroquinone (HQ) formation in the first step, followed by their subsequent breaking into series of organic acids (e.g., maleic, fumaric, and oxalic [58–60]), which are finally mineralized to CO_2 and H_2O (see in Fig. 11). Formation of benzoquinone (BQ), being in possible equilibrium with hydroquinone is also mentioned in some works [59–62].

The results of phenol degradation are presented in Fig. 12. All samples possessed similar activity, achieving results between 86 and 100% of degradation, while synthesised precursor showed only 13% of phenol disappearance. No clear correlation between their morphology or synthesis conditions alone was found. However, a slight trend to

decrease the efficiency for the sample obtained in the presence of HF can be noticed. It can result from a decrease of the surface area and surface defectivity which was observed for these samples. Significantly lower than for the samples prepared from $TiOF_2$ at the same process conditions, phenol degradation efficiency (65% after 1 h of irradiation) was noticed in the presence of the TiO_2 nanosheets obtained from TiF_4, as shown in Fig. S10 in the Supporting Materials. Despite rather similar results of phenol removal, obtained materials showed significant differences in mineralization efficiency and formation of oxidation products. Fig. 13 show observed phenol removal together with the monitored formation of catechol and hydroquinone for the obtained samples.
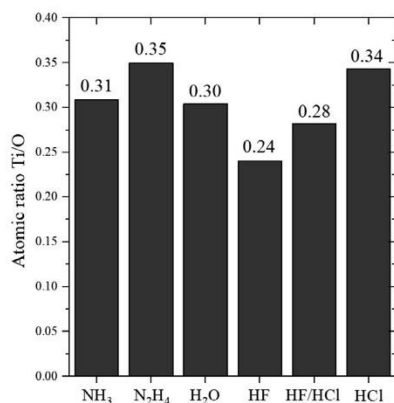
8

Fig. 8. The diagram of atomic ratio Ti/O on the surface for each sample.

Fig. 10. The PL spectra of TiO_2 nanostructures in comparison with $TiOF_2$.

Within the results, a significant difference in the concentration of *ortho*-hydroxyphenol (catechol) can be observed, while the concentration of hydroquinone is rather similar for all samples. Notably, the lack of defined {001} facets observed for samples $TiO_2\_NH_3$ and $TiO_2\_N_2H_4$ can be correlated to almost the complete disappearance of catechol during the process. After the exclusion of samples TiO_NH_3 (rectangular prisms), the amount of observed CT and HQ was recalculated concerning the amount of decomposed phenol and the results are presented in Fig. 14, showing a visible dependence on the {001}/{101} ratio. For photocatalysts with decahedral shape, constant change was observed, and a significant decrease in catechol concentration was noticed only for octahedrons. It shows the importance of {001} facet presence on the formation of *ortho*-hydroxylated phenol.

Moreover, the formation of another aromatic derivative was observed, which was found to be a possible product from BQ ↔ HQ equilibrium. It was analysed by additional irradiation of hydroquinone and benzoquinone solutions in the presence of $TiO_2\_N_2H_4$ and TiO_2_HF samples, both giving rise to a spectrum with characteristic 253 and 374 nm signals. Between them, the TiO_2_HF sample showed a higher formation rate, especially when starting from BQ solution, which is in agreement with the results obtained during phenol runs (see Fig. 15-a). Moreover, for BQ stock solution, small amounts of HQ and the described compound were observed already at the start of the process. It can give an idea of the structure of the observed compound. As reported by Kurien and Robins [63], the benzoquinone solutions can
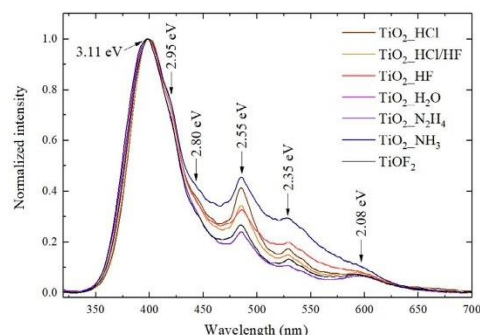
spontaneously degrade to 1,2,4-hydroxybenzene or a mixture of 2-hydroxybenzoquinone with HQ. Since, in this study, BQ irradiation gives almost immediate raise to HQ and 253 nm signal, it is concluded that the observed compound is 2-hydroxybenzoquinone (2-HBQ). Described equilibrium is shown in Fig. 15-b, and detailed results of the additional irradiations are shown in Fig. S11 in the Supporting Materials.

A significant difference follows the observed differences in by-products formation and phenol removal in mineralization efficiency. As presented in Fig. 16-a, the particles with octahedral shape achieved the highest TOC removal of 78%, while the lowest was observed for the TiO2_HF sample, characterized by the highest truncation ratio. A visible difference between samples $TiO_2\_N_2H_4$ and TiO_2_HCl can be observed, in favour of N_2H_4, suggesting that sample morphology is a more important factor contributing to TOC removal than the simple degradation rate of phenol.

The overall trend of mineralization decreased together with more platelet morphology is well-observed, as shown in Fig. 16-b. Analogically to catechol's formation, obtained results create a visible dependence concerning a measured truncation, clearly indicating that nanostructures with less exposed {101} facets are less suitable for phenol mineralization. This change seems to be linear for the obtained samples when grouped in connection with the HF introduction during synthesis and corresponds well with a surface defectivity revealed by the XPS analyses. It is well known that defect type and location can influence TiO_2 activity [64,65], mostly through promoting charge carriers separation or recombination, and generally, one can expect that defects concentration should have some optimal level that supports photocatalyst performance [66–68]. Therefore, it was concluded that increased TiO_{2-x} concentration for HF and HCl/HF samples was mostly
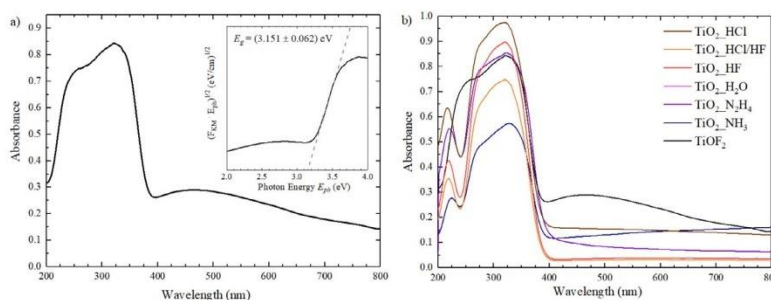

Fig. 9. UV–Vis diffuse reflectance spectra of a) $TiOF_2$ and b) TiO_2 nanostructures in comparison with $TiOF_2$. The inset in 9a shows the transformation of Kubelka-Munk function versus photon energy.
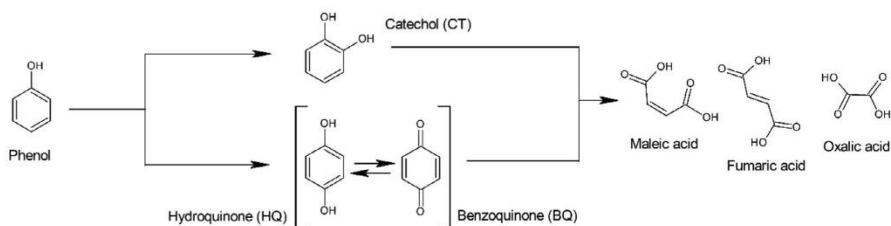
9

Fig. 11. Main mechanism of phenol oxidation during photocatalytic process.

responsible for the observed decrease in mineralization efficiency, comparing to other samples. For TiO$_2$_HCl/HF sample, the morphology is almost the same as for TiO$_2$_HCl, so the effect of particles shape can be excluded. Moreover, since the sample TiO$_2$_H$_2$O also showed considerable amounts of TiO$_{2-x}$, it could be concluded that the defect formation results in different effect, depending on the surface structure of the sample.

3.5. Degradation mechanism discussion

During the phenol oxidation, the initial reaction provides to form three possible hydroxyl derivatives, distinguished by a type of substitution (*meta, ortho,* and *para*). Only compounds in *ortho* (catechol), and *para* (hydroquinone) substitution were observed during degradation experiments. As the first possible factor affecting their formation, generation of different reactive oxygen species (ROS) was considered. In the photocatalytic reactions, ·OH and ·O$_2^-$ radicals are most commonly reported to be primary ROS generated at the photocatalyst surface [69–73], so their reactivity with phenol was computationally investigated, as presented in Fig. S12 in the Supporting Materials. Fig. 17 shows the calculated minimum energy paths of their initial addition to the phenol molecule. The ·OH attack preferentially occurs at the ortho position with an energy barrier difference of 10.9 kJ·mol[1] between both isomers. These results correspond well with the electrophilic nature of ·OH and the charge distribution inside phenol molecule, which shows alpha carbons to be more electronegative than *para*-substitution (partial charge of 0.25 versus 0.19, according to Mulliken charge distribution). On the other hand, the ·O$_2^-$ attack was also found to occur preferentially at *ortho*-substitution, with a formation of the energetically favourable intermediate state. Moreover, its addition is characterized by a high energy barrier, which could explain existing reports, showing ·O$_2^-$ to

react slower than ·OH [74].

The obtained computational results can support the experimental observations of increased catechol formation for samples more exposed with {0 0 1} facets. As shown by Ma et al., the photogenerated holes tend to localize at the bridging oxygens of (0 0 1) surface, while electrons remain in bulk-localized Ti atoms [75]. Moreover, the (0 0 1) surface in comparison with (1 0 1) and (1 0 0) is the only one with a high density of low energy O 2 s states above the valence band edge of the TiO$_2$ [76]. Therefore, it is suitable for the oxidation of H$_2$O to ·OH. The preference of {0 0 1} facets to create ·OH though hole trapping on the surface bridging O would also explain the significant effect of TiO$_{2-x}$ formation on the activity of more truncated samples (HF and HF/HCl). On the other hand, the (1 0 1) surface is adequate for electrons accumulation and should promote oxygen reduction to ·O$_2^-$. It is in accordance with our study, as the superoxide radicals were reported to be very effective ring-opening agents [77]. Therefore, their enhanced generation could explain high TOC removal by the {1 0 1} exposing particles, while observed phenol removal rate is similar, because of the high energy barrier of their initial addition.

Nevertheless, the obtained results cannot fully explain experimental observations, mostly regarding the disappearance of catechol for the particles exposed only with {1 0 1} facets. It suggests that surface effects must also influence on the degradation mechanism. In this case, some geometric consideration can be taken into account. As shown in Fig. 18, the phenol adsorption at the TiO$_2$ surface should occur between –OH moiety and the Ti sites, acting as the Lewis acid, which for (0 0 1) leaves four twofold-coordinated oxygens in the direct neighbourhood of the adsorbed phenol. Such increase of the density of surface oxygens, close to Ti (1.98 Å away) should promote ·OH attack at *ortho* substitution and can also explain the increased formation of the 2hydroxybenzoquinone, resulting from further hydroxylation of BQ or HQ.
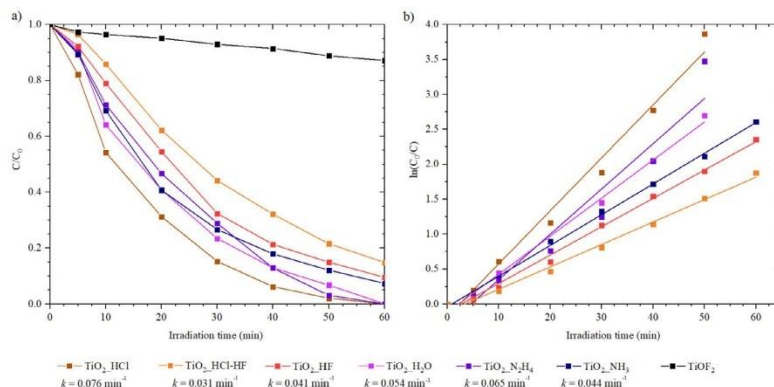

Fig. 12. Obtained results of a) phenol degradation for obtained samples and b) their transformation to determine rate constant (assuming first order).
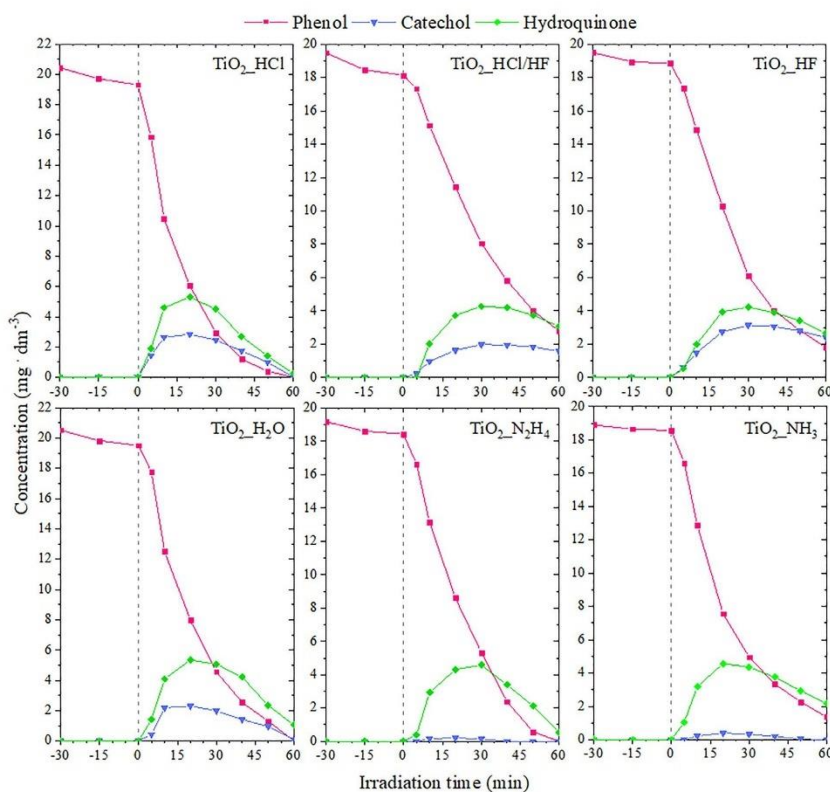
Fig. 13. Obtained results of phenol degradation for TiO_2 nanostructures.
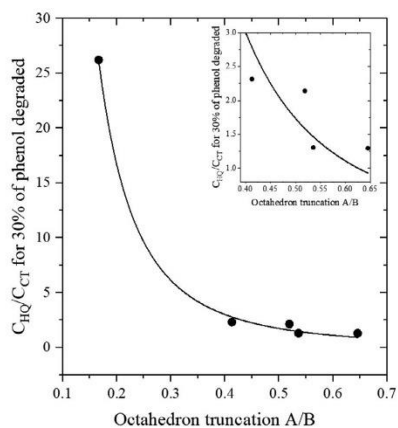

Fig. 14. The observed ratio of hydroquinone (HQ) to catechol (CT) formation at the first part of the process with respect to a truncation level.

On the other hand, the oxygen reduction at the TiO_2 surface, preferentially (101), should also occur at the Ti site, which results in a higher distance between both reactants. Starting from the phenol-adsorbed Ti atom, the closest Ti site is 3.79 Å away, while the bond length between *ipso* and *ortho* carbons is 1.39 Å. Therefore, it is suggested that the increased Ti-Ti distance at the surface could prevent *ortho* substitution of $\cdot O_{2-}$, which could be especially valid for (101) surface due to its preference to accumulate electrons on the surface Ti atoms. These results suggest that photocatalyst structure can promote a specific pathway of the degradation of the pollutants and could be an important factor considering the oxidation of more complex compounds, such as pharmaceuticals, pesticides or dyes.

4. Conclusions

To summarize, a simple synthetic method for the synthesis of TiO_2 nanostructures by a solvothermal route from the $TiOF_2$ precursor was developed. Different environments of reactions (acidic/basic) and capping agents were studied, showing that the application of titanium oxyfluoride allows obtaining TiO_2 nanostructures with various morphologies (decahedral, octahedral, rectangular prisms). Shapes of nanostructures were related to exposed facets, which were crucial concerning the mineralization efficiency and the pathway of phenol degradation. The TiO_2 octahedral particles exposing {101} facets
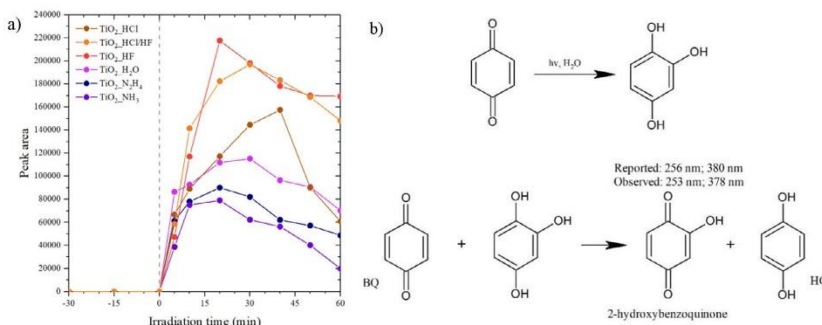
11

Fig. 15. The observed peak area for signal with 253 nm maximum (a) and mechanism of 2hydroxybenzoquinone formation, as reported by Kurien and Robins [63] (b).

exhibited the highest TOC removal efficiency under UV light irradiation, which decreased as the other facets appeared and became more exposed to the surface of the particles. Experimental results were confronted with simulated ·OH and ·O_2^- attack on a phenol molecule, showing that the ·OH addition at the *ortho* substitution is energetically favoured. It explains the importance of {001} facet for the enhanced formation of catechol as the photogenerated holes, as opposed to electrons, are expected to preferential localize on this plane. On the other hand, the increased formation of ·O_2^- on the {101} facet was expected because of the significant effect of {101} exposition on TOC reduction and favoured electron localization on the surface. However, the direct attack of ·O_2^- on the phenol molecule cannot provide a mechanism for occurring reaction and cannot explain the formation of *para*-substituted products. Based on the increased distance between neighbouring sites that could promote superoxide radical attack at the *para* position, it was suggested that surface structure might be another factor contributing to the creation of the products.

Funding

Declaration of Competing Interest

The authors declare that they have no known competing financial interests or personal relationships that could have appeared to influence the work reported in this paper.

Fig. 17. Results of performed NEB calculations of initial ·OH and ·O_2^- attack on different patterns in phenol molecule.
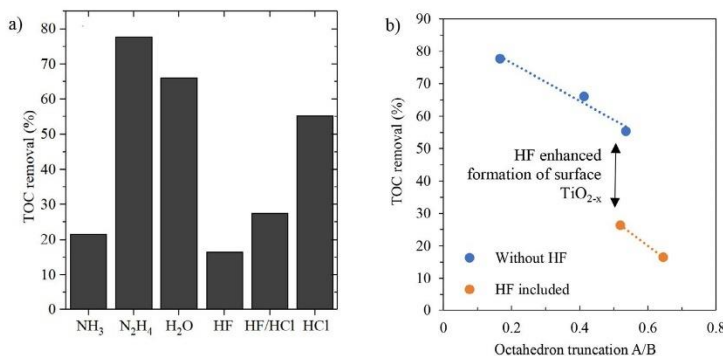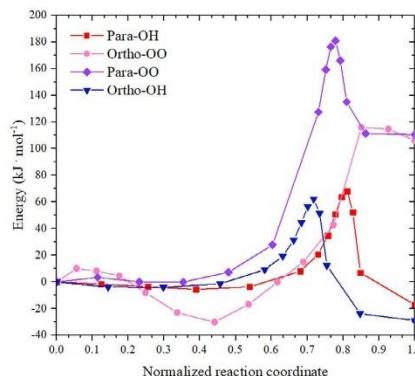
Acknowledgements

Fig. 16. The efficiency of TOC removal for the obtained samples a) and its dependence on the observed truncation level b).
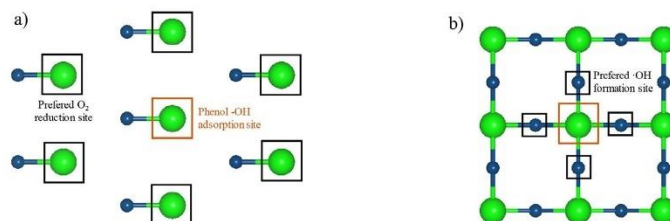
Fig. 18. Simplified view on the top of anatase surface, showing undercoordinated Ti and O atoms around hypothetical site of phenol –OH adsorption: a) (1 0 1) and b) (0 0 1) surface. In the squares, there are highlighted sites which are expected to be especially active for this surface.

Appendix A. Supplementary data

Supplementary data to this article can be found online at https://doi.org/10.1016/j.cej.2020.126493.

References

[1] A. Umar, F.A. Harraz, A.A. Ibrahim, T. Almas, R. Kumar, M.S. Al-Assiri, S. Baskoutas, Coatings 10 (2020) 182.
[2] A. Umar, M.S. Akhtar, R.I. Badran, M. Abaker, S.H. Kim, A. Al-Hajry, S. Baskoutas, Appl. Phys. Lett. (2013) 103.
[3] J. Li, Y. Lu, Z. Wu, Y. Bao, R. Xiao, H. Yu, Y. Chen, Ceram. Int. 42 (2016) 9621.
[4] G. Xiang, Z. Yu, Y. Hou, Y. Chen, Z. Peng, L. Sun, L. Sun, Sep. Purif. Technol. 161 (2016) 144.
[5] C. Günnemann, C. Haisch, M. Fleisch, J. Schneider, A.V. Emeline, D.W. Bahnemann, ACS Catal. 9 (2019) 1001.
[6] T.R. Gordon, M. Cargnello, T. Paik, F. Mangolini, R.T. Weber, P. Fornasiero, C.B. Murray, J. Am. Chem. Soc. 134 (2012) 6751.
[7] W.J.I. DeBenedetti, E.S. Skibinski, D. Jing, A. Song, M.A. Hines, J. Phys. Chem. C 122 (2018) 4307.
[8] Y. Wang, H. Sun, S. Tan, H. Feng, Z. Cheng, J. Zhao, A. Zhao, B. Wang, Y. Luo, J. Yang, J.G. Hou, Nat. Commun. 4 (2013) 1.
[9] C.Z. Wen, J.Z. Zhou, H.B. Jiang, Q.H. Hu, S.Z. Qiao, H.G. Yang, Chem. Commun. 47 (2011) 4400.
[10] M. Zhang, X. Xiao, X. Wang, M. Chen, Y. Lu, M. Liu, L. Chen, Nanoscale 11 (2019) 7465.
[11] Z. Wei, M. Janczarek, M. Endo, K. Wang, A. Balčytis, A. Nitta, M.G. Méndez-Medrano, C. Colbeau-Justin, S. Juodkazis, B. Ohtani, E. Kowalska, Appl. Catal. B 237 (2018) 574.
[12] Y. Lu, Y. Zang, H. Zhang, Y. Zhang, G. Wang, H. Zhao, Sci. Bull. 61 (2016) 1003.
[13] X. Zhao, W. Jin, J. Cai, J. Ye, Z. Li, Y. Ma, J. Xie, L. Qi, Adv. Funct. Mater. 21 (2011) 3554.
[14] J. Mao, L. Ye, K. Li, X. Zhang, J. Liu, T. Peng, L. Zan, Appl. Catal. B 144 (2014) 855.
[15] Y. Liang, Y. Yang, H. Zhou, C. Zou, K. Xu, X. Luo, T. Yu, W. Zhang, Y. Liu, C. Yuan, Ceram. Int. 45 (2019) 6282.
[16] H.G. Yang, C.H. Sun, S.Z. Qiao, J. Zou, G. Liu, S.C. Smith, H.M. Cheng, G.Q. Lu, Nature 453 (2008) 638.
[17] A.S. Barnard, L.A. Curtiss, Nano Lett. 5 (2005) 1261.
[18] M. Li, Y. Chen, W. Li, X. Li, H. Tian, X. Wei, Z. Ren, G. Han, Small (2017) 13.
[19] Y. Zheng, J. Wang, P. Yang, J. Nanosci. Nanotechnol. 17 (2017) 1204.
[20] N. Wu, J. Wang, D.N. Tafen, H. Wang, J. Zheng, J.P. Lewis, X. Liu, S.S. Leonard, J. Am. Chem. Soc. 2 (2010) 6679.
[21] D. Wang, J. Liu, Q. Huo, Z. Nie, W. Lu, R.E. Williford, Y.B. Jiang, J. Am. Chem. Soc. 128 (2006) 13670.
[22] J. Li, Y. Yu, Q. Chen, J. Li, D. Xu, Cryst. Growth Des. 10 (2010) 2111.
[23] N.M. Laptash, I.G. Maslennikova, Adv. Mater. Phys. Chem. 02 (2012) 21.
[24] A.A. Andreev, A.N. Diachenko, Theor. Found. Chem. Eng. 43 (2009) 707.
[25] V.I. Sachkov, R.A. Nefedov, V.V. Orlov, R.O. Medvedev, A.S. Sachkova, Minerals 8 (2018) 1.
[26] J. Hu, Y. Cao, K. Wang, D. Jia, RSC Adv. 7 (2017) 11827.
[27] Y. Zheng, X. Hu, P. Yang, CrystEngComm 20 (2018) 4485.
[28] C.Z. Wen, Q.H. Hu, Y.N. Guo, X.Q. Gong, S.Z. Qiao, H.G. Yang, Chem. Commun. 47 (2011) 6138.
[29] Z. Huang, Z. Wang, K. Lv, Y. Zheng, K. Deng, ACS Appl. Mater. Interfaces 5 (2013) 8663.
[30] B. Li, D. Wang, Y. Wang, B. Zhu, Z. Gao, Q. Hao, Y. Wang, K. Tang, Electrochim. Acta 180 (2015) 894.
[31] N. Louvain, Z. Karkar, M. El-Ghozzi, P. Bonnet, K. Guérin, P. Willmann, J. Mater. Chem. A 2 (2014) 15308.
[32] J. Zhu, F. Lv, S. Xiao, Z. Bian, G. Buntkowsky, C. Nuckolls, H. Li, Nanoscale 6 (2014) 14648.
[33] J. Wang, F. Cao, Z. Bian, M.K.H. Leung, H. Li, Nanoscale 6 (2014) 897.
[34] Z. Wang, K. Lv, G. Wang, K. Deng, D. Tang, Appl. Catal. B 100 (2010) 378.
[35] A. Ballestas-Barrientos, X. Li, S. Yick, A.F. Masters, T. Maschmeyer, Sustainable Energy Fuels 2 (2018) 1463.
[36] I. Gai, Q. Mei, X. Qin, W. Li, H. Jiang, X. Duan, Mater. Res. Bull. 48 (2013) 4469.
[37] P. Leidich, O. Linker, M. Panthöfer, W. Tremel, CrystEngComm 16 (2014) 8486.
[38] S. Grimme, J. Antony, S. Ehrlich, H. Krieg, J. Chem. Phys. (2010) 132.
[39] C. Adamo, V. Barone, J. Chem. Phys. 110 (1999) 6158.
[40] J.P. Perdew, M. Ernzerhof, K. Burke, J.P. Perdew, M. Ernzerhof, K. Burke 9982 (2010) 9982.
[41] F. Neese, Wiley Interdisciplinary Reviews: Computational Molecular Science, 2012, 2, 73.
[42] J.C. Lytle, H. Yan, R.T. Turgeon, A. Stein, Chem. Mater. 16 (2004) 3829.
[43] Y. Chen, W. Li, J. Wang, Y. Gan, L. Liu, M. Ju, Appl. Catal. B 191 (2016) 94.
[44] R. Li, X. Zhang, H. Dong, Q. Li, Z. Shuai, W. Hu, Adv. Mater. 28 (2016) 1697.
[45] Y. Wang, H. Zhang, Y. Han, P. Liu, X. Yao, H. Zhao, Chem. Commun. 47 (2011) 2829.
[46] G. Fazio, D. Selli, L. Ferraro, G. Seifert, C. Di Valentin, ACS Appl. Mater. Interfaces 10 (2018) 29943.
[47] X. Chen, Y. Cui, X. Yan, L. Tian, and X. Chen, Black TiO 2 Nanomaterials for Energy Applications, 2017, 5.
[48] T. Leshuk, R. Parviz, P. Everett, H. Krishnakumar, R.A. Varin, F. Gu, ACS Appl. Mater. Interfaces 2013 (1892) 5.
[49] Y. Zhang, X. Wang, P. Dong, Z. Huang, X. Nie, X. Zhang, Green Chem. 20 (2018) 2084.
[50] A. Zielińska-jurek, Z. Wei, M. Janczarek, I. Wysocka, E. Kowalska, Catalysts 9 (2019) 1.
[51] J. P. C. C, Y. Du, Z. Dohna, and I. Lyubinetsky, J. Phys. Chem. C, 2008, 2, 2649.
[52] Y. Wang, D. Pillay, G.S. Hwang, Phys. Rev. B – Condensed Matter Mater. Phys. 70 (2004) 1.
[53] Q. Zhang, Y.J. Li, H.F. Wen, Y. Adachi, M. Miyazaki, Y. Sugawara, R. Xu, Z.H. Cheng, J. Brndiar, L. Kantorovich, I. Štich, J. Am. Chem. Soc. 140 (2018) 15668.
[54] J. Tauc, R. Grigorovici, A. Vancu, Phys. Status Solidi (B) Basic Res. 627 (1966) 363.
[55] G. Nabi, W. Raza, M.B. Tahir, J. Inorg. Organomet. Polym Mater. 30 (2019) 1425.
[56] M.M. Kumar, S. Badrinarayanan, M. Sastry, Thin Solid Films 358 (2000) 122.
[57] A. Fujishima, X. Zhang, D.A. Tryk, Surf. Sci. Rep. 63 (2008) 515.
[58] A. Turki, C. Guillard, F. Dappozze, Z. Ksibi, G. Berhault, H. Kochkar, Appl. Catal. B 163 (2015) 404.
[59] A. Sobczyński, L. Duczmal, W. Zmudziński, J. Mol. Catal. A: Chem. 213 (2004) 225.
[60] I.G. Devi, K.E. Rajashekhar, J. Mol. Catal. A: Chem. 334 (2011) 65.
[61] T.T.T. Dang, S.T.T. Le, D. Channei, W. Khanitchaidecha, A. Nakaruk, Res. Chem. Intermed. 42 (2016) 5961.
[62] I. Wysocka, E. Kowalska, K. Trzciński, M. Łapiński, G. Nowaczyk, A. Zielińska-Jurek, Nanomaterials (2018) 8.
[63] K.C. Kurien, P.A. Robins, J. Chem. Soc. B 855 (1970).
[64] Y. Nam, L. Li, J.Y. Lee, O.V. Prezhdo, J. Phys. Chem. Lett. 10 (2019) 2676.
[65] M. Kong, Y. Li, X. Chen, T. Tian, P. Fang, F. Zheng, X. Zhao, J. Am. 133 (2011) 16414.
[66] C. Liu, A.Y. Zhang, D.N. Pei, H.Q. Yu, Environ. Sci. Technol. 50 (2016) 5234.
[67] M. Liu, H. Li, W. Wang, Catal. Today 264 (2016) 236.
[68] T. Nakano, R. Ito, S. Kogoshi, N. Katayama, J. Phys. Chem. Solids 98 (2016) 136.
[69] E. Jimenez-Relinque, M. Castellote, Appl. Catal. A 565 (2018) 20.
[70] F. Dong, T. Xiong, Y. Sun, L. Lu, Y. Zhang, H. Zhang, H. Huang, Y. Zhou, Z. Wu, Appl. Catal. B 219 (2017) 450.
[71] R. Nakamura, T. Okamura, N. Ohashi, A. Imanishi, Y. Nakato, J. Am. Chem. Soc. 127 (2005) 12975.
[72] W. Jiang, J.A. Joens, D.D. Dionysiou, K.E. O'Shea, J. Photochem. Photobiol., A 262 (2013) 7.
[73] K. Lv, X. Guo, X. Wu, Q. Li, W. Ho, M. Li, H. Ye, D. Du, Appl. Catal. B 199 (2016) 405.
[74] D.W. Bahnemann, M. Hilgendorff, R. Memming, J. Phys. Chem. A 101 (1997) 4265.
[75] X. Ma, Y. Dai, M. Guo, B. Huang, Langmuir 29 (2013) 13647.
[76] Z. Zhao, Z. Li, Z. Zou, J. Phys.: Condens. Matter (2010) 22.
[77] C.S.A. Antunes, M. Bietti, M. Salamone, N. Scione, J. Photochem. Photobiol., A 163 (2004) 453.

13
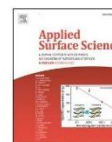
Full Length Article

Solvothermal growth of {001} exposed anatase nanosheets and their ability to mineralize organic pollutants. The effect of alcohol type and content on the nucleation and growth of TiO$_2$ nanostructures

Szymon Dudziak [a], Marta Kowalkińska [a], Jakub Karczewski [c], Marcin Pisarek [d], Katarzyna Siuzdak [e], Adam Kubiak [f], Katarzyna Siwińska-Ciesielczyk [f], Anna Zielińska-Jurek [a,b,*]

[a] Department of Process Engineering and Chemical Technology, Faculty of Chemistry, Gdańsk University of Technology, G. Narutowicza 11/12, 80 233 Gdańsk, Poland
[b] EcoTech Center, Gdańsk University of Technology, G. Narutowicza 11/12, 80-233 Gdańsk, Poland
[c] Institute of Nanotechnology and Materials Engineering, Faculty of Applied Physics and Mathematics, Gdańsk University of Technology, G. Narutowicza 11/12, 80-233 Gdańsk, Poland
[d] Institute of Physical Chemistry, Polish Academy of Sciences, Kasprzaka 44/52, 01–224 Warsaw, Poland
[e] Centre for Plasma and Laser Engineering, The Szewalski Institute of Fluid-Flow Machinery Polish Academy of Sciences, Fiszera 14, 80-231 Gdańsk, Poland
[f] Institute of Chemical Technology and Engineering, Faculty of Chemical Technology, Poznań University of Technology, Berdychowo 4, 60-965 Poznań, Poland

ABSTRACT

Herein, the series of {001} exposed anatase nanosheets from HF-assisted solvothermal growth synthesis were obtained. The two-dimensional TiO$_2$ were characterized, including both bulk (XRD, DR-UV–Vis, Mott-Schottky) and surface characteristics (N$_2$ sorption, XPS, SEM) with experimental results compiled with Density Functional Theory (DFT) calculations. The effect of alcohol amount and type was studied, demonstrating the crucial role of nucleation rate on the final material properties, which was connected with the possible ligand exchange between F$^-$ and ROH in the $[TiF_6]^{2-}$ octahedra, leading to further TiO$_2$ condensation through an ether elimination reaction. Highly active 2D nanoparticles were easily obtained for different reaction times when a moderate amount of n-butanol or n-hexanol was introduced to the synthesis. The photoactivity of 2D TiO$_2$ with exposed {001} facet strongly depended on the photocatalytic available surface area with an increased amount of *ortho*–hydroxyphenol (catechol) formed as a by-product. Meanwhile, the rise of n-butanol or n-hexanol content during solvothermal reaction or changing it to ethanol allowed to form smaller and more crystalline anatase particles, but their activity was hindered. For these samples, the slow phenol disappearance and no catechol formation occurred due to (i) a lower amount of adsorbed fluorine, (ii) band position shifting towards lower values, and (iii) the surface presence of Ti^{3+}, which prevented the generation of ˙OH radicals. It was also found that changing the nucleation rate by modifying the reaction environment influences the fluorine ions distribution, determining the final properties of 2D structure photocatalyst.

1. Introduction

Over the past years, photocatalytic degradation of persistent organic pollutants became one of the most studied technological issues. In photocatalytic reaction, the ability to generate reactive oxygen species or induce charge transfer directly to a contaminant during irradiation has been examined extensively for various materials [1–3]. Within them, TiO$_2$ is presented as one of the most chemically stable photocatalysts, with much attention being given to describe the mechanism responsible for its photocatalytic activity in both pure and modified form [4].

The correlation between morphological properties of semiconductor materials and their photocatalytic activity is crucial for design new and more efficient photocatalytic systems. The possibility of using the knowledge of crystallography of single crystals in the research of nanocrystals with facet exposition is a key to understand crystal growth and surface chemistry at nanoscale. In this regard, understanding the formation of anatase materials with exposed specific crystal facets

allows studying their interactions with chemical species at the atomic level and may contribute to the improved photocatalytic activity. The surface energy of {0 0 1} facets is significantly higher than other low-index crystal planes (0.90 J·m^{-2}). Therefore, they are not supposed to be exposed in anatase nanocrystals [5]. Initially, such particles' crystal growth was confined within the kinetically controlled regime under nonequilibrium conditions, e.g., the gas-phase thermal oxidation of TiCl$_4$ at high temperature or rapid heating and quenching of Ti(OC$_4$H$_9$)$_4$ [6]. However, Yang et al. have shown that fluorine ions can stabilize the {0 0 1} structure, promoting its exposition instead of the thermodynamically favored {1 0 1} facet [7]. The {0 0 1} facet of TiO$_2$ particles is described as more active than TiO$_2$ enclosed by other facets [7–8]. Notably, a positive influence of the {0 0 1} facet exposition on acetaldehyde, coumarin, methyl orange, and terephthalic acid photodegradation was reported, however, without considering their detailed study of transformation products formation and mineralization [9–12]. In this regard, some aspects of the photocatalytic activity of {0 0 1} exposed particles require further investigation.

In this regard, the photocatalytic activity and mineralization ability of the 2D structure anatase with exposed {0 0 1} facet was investigated using phenol as a model pollutant. Phenol and its derivatives are the commonly encountered organic contaminants in industrial effluents that have caused severe environmental problems [13]. Phenolic compounds are persistent and have acute toxicity with carcinogenic and mutagenic character. The US Environmental Protection Agency (EPA) and the European Union (EU) have classified phenolic compounds as priority pollutants since they are harmful to organisms even at low concentrations. The discharge limits of phenols in surface water must not exceed a concentration of 1 mg·dm^{-3}.

Therefore, phenol removal from wastewater using heterogeneous photocatalysis is intensively studied. The mechanism of phenol photocatalytic degradation proceeds by the attack of photogenerated radicals on the benzene ring [14–18]. The created phenoxy radical initiates further transformations to form dihydroxylated products, such as commonly reported *ortho*-hydroxyphenol (catechol) and *para*-hydroxyphenol (hydroquinone). Further oxidation of these compounds leads to (i) formation of more hydroxylated intermediate products, (ii) opening of the phenyl ring and the formation of short aliphatic compounds, and (iv) final mineralization to carbon(IV) oxide and water [19–20].

Furthermore, a clear identification of different intermediates and photodegradation pathways of phenol degradation is essential because some of the by-products formed, e.g., hydroquinone and benzoquinone, are much more toxic than phenol itself. Therefore, the oxidation route of phenol has been the subject of studies in the last two decades. The mechanism of phenol degradation is strictly dependent on photodegradation reaction parameters, including solution pH, photocatalyst loading and type, ionic composition of wastewater, oxidant concentration, as well as light intensity and range [21–24]. Krivec et al. studied the effect of different process parameters, including residence time, initial phenol concentration, pH value, and UV light irradiation intensity on phenol photodegradation in a microreactor with a TiO$_2$ layer immobilized on the reactor inner walls [25]. They reported that selective oxidation of phenol to catechol proceeds very slow and that the generation of benzoquinone was completely suppressed. The total organic carbon analysis showed that phenol mineralization did not occur at any of the performed experimental conditions, possibly due to the strong adsorption of intermediates during laminar flow conditions in the microreactor. The reaction pathway of phenol degradation, involving only hydroquinone as the reaction intermediate, was probably related to anatase crystallite size [25].

Emeline et al. reported that the surface active sites responsible for the formation of catechol were less active in phenol photodegradation over six commercial TiO$_2$ samples (Degussa P-25, Hombikat UV100, ST-41, ST-21, FTL-200), which differed in polymorphic phase composition, crystallite size, and surface area. Simultaneously, within the series of analyzed TiO$_2$ samples, a positive correlation between selectivity and

photocatalytic activity was observed for hydroquinone produced by both oxidation and reduction pathways [26]. On the contrary, Suhadolnik et al. reported that most of the phenol was converted to benzoquinone during photodegradation in TiO$_2$-nanotubes-based, coil-type photo-electrocatalytic microreactor [27]. Phenol degradation and mineralization were inefficient due to the increased electron-hole recombination. The complete degradation and mineralization were observed only after applying electrical potential [27]. Wang et al. have shown that crystallites/nanoparticles size is crucial to achieving high photocatalytic activities [28]. Moreover, it is known that different photocatalyst types could result in a degradation pathway to different intermediates [29], which might affect on mineralization degree [25].

Furthermore, it is also expected that the photocatalyst morphology should affect a phenol photocatalytic degradation mechanism [30]. The observed correlations between the activity and selectivity of TiO$_2$ photocatalysts toward primary phenol by-products can result from the difference in surface concentration of charge carriers and corresponding surface active sites, which might depend on the types of dominating surface faces [26–31]. Therefore, the role of the surface structure of photocatalyst is crucial in the photodegradation processes. Gao et al. observed that phenol removal is a facet-dependent process concerning Pt-modified TiO$_2$; however, only microcrystals with a single morphology were studied [32]. Also, in the previous work, we have reported that {1 0 1} exposed particles are suitable for the mineralization of phenol under UV–Vis irradiation, and the efficiency declines with the rise of {0 0 1} facets content in decahedral nanostructures [33]. However, due to the limited exposition of the {0 0 1} surface (up to ~ 17%) and relatively small sample set, the in-depth analysis with respect to the surface structure and other physicochemical features, such as nanoparticles size, was severely straitened during this work [33]. Therefore, there is still a lack of detailed information about the correlation between the individual exposed facet, size of the nanoparticles, their crystallinity, and composition on the photocatalytic degradation of organic pollutants, including phenol.

Therefore, the ability of the 2D structured anatase with a majority of exposed highly energetic {0 0 1} facets to mineralize organic pollutants was studied in detail. To best understand their influence on the photocatalytic process, series of {0 0 1} exposed TiO$_2$ nanoparticles differing in their physicochemical parameters have been prepared. The preparation procedure included TiO$_2$ hydrolysis from the titanium *tert*-butoxide in the presence of HF and different alcohols as additional reagents. This allowed us to obtain anatase particles with (i) high {0 0 1} facet exposition, (ii) different size, (iii) shape and (iv) crystallinity. Yang et al. have emphasized that the addition of aliphatic alcohol can strengthen the stabilization effect associated with fluorine adsorption over (0 0 1) surface and thus stimulate its preferred growth [34]. However, outside of this, information about the exact alcohol role in the crystallization process is rather limited. Therefore, we have discussed our results to give more detailed insight into alcohol's role in this synthesis procedure and how it helps to achieve different morphological features of the 2D anatase nanoparticles. Additionally, to better understand the obtained samples' morphological properties, the electronic structure of anatase and its {0 0 1} surface slab models were investigated computationally using density functional theory calculations.

2. Experimental section

The synthesis of 2D structure titanium(IV) oxide nanosheets was carried out by a facile solvothermal method. Tetrabutyltitanate (TBT), n-hexanol, n-butanol, ethanol, methanol, and hydrofluoric acid (48%) were used as received from Sigma-Aldrich without further purification.

2.1. Fabrication of TiO$_2$ nanosheets

During a typical preparation of 2D TiO$_2$, 17 cm^3 of TBT was introduced to the 200 cm^3 Teflon-lined stainless-steel reactor, together with

2

3.4 cm^3 of HF solution (48%) and was kept at 210 °C for various times to observe the growth of the nanocrystals (mentioned times include heating of the oven from room temperature to 210 °C, which takes approximately 1.5 h). Moreover, to achieve the highest possible control over the reaction, the addition of n-hexanol, n-butanol, ethanol, and methanol as solvents was investigated in different amounts: 10 cm^3, 30 cm^3, or 60 cm^3 of alcohol. After each reaction, nanoparticles were centrifuged and washed several times with ethanol, followed by water to remove residual organic species and ions. During the second part of the washing, 0.1 M solution of NaOH was introduced once per sample to help remove adsorbed fluorine ions. Separated nanosheets were then dried at 80 °C to gain the final material.

Obtained samples are denoted as SolventX-Yh, where X is the solvent volume (Me stands for methanol, Et for ethanol, But for n-butanol and Hex for n-hexanol), and Y is the reaction time. For example, But30-8h is an as-synthesized photocatalyst for which 30 cm^3 of n-butanol was used during the 8 h of the solvothermal process.

2.2. Material characterization

The samples and phase composition structure were investigated by X-ray powder diffraction (Cu Kα radiation, Rigaku MiniFlex 600 X-Ray diffractometer). The analyses and Rietveld refinements were performed with the HighScorePlus software package (PANalytical, 2006) and the ICDD database with data fitting based on the pseudo-Voigt profile function. The specimen displacement, lattice parameters, polynomial coefficients for the background function, profile parameters, and Gaussian and Lorentzian profile coefficients were refined. To determine the possible amorphous phase content in the samples, XRD analyses were carried out with crystalline NiO as an internal standard [35].

The nanostructures' morphology was characterized by field emission scanning electron microscopy (SEM, FEI Quanta FEG 250). Before the observations, all samples were coated with an Au layer to help discharge the excess electrons during the analysis. The observed particles' size was measured in two dimensions for the selected samples, and the obtained datasets were fitted with log-normal functions to obtain size probability distributions. The fitting details are presented in Supplementary Materials (Section 1), and the results were used to analyze the facet exposition observed under SEM.

An ASAP 2020 physisorption analyzer (Micromeritics Instrument Co., USA) was used to determine the surface parameters of the obtained nanoparticles, including Brunauer–Emmett–Teller (BET) surface area pore volume and pore size using low-temperature N$_2$ sorption. Before measurement, the analyzed materials were degassed at 120 °C for 4 h. The surface area was determined by the multipoint BET method using adsorption data for relative pressure (p/p_0) in the range 0.05–0.30.

A Microlab 350 (Thermo Electron) XPS spectrometer with non-monochromatic Al Kα radiation (hν = 1486.6 eV, power 300 W, voltage 15 kV) was used to determine the surface chemistry of the received materials. The analyzed area was 2x5 mm. The hemispherical analyzer was used for collecting the high-resolution (HR) XPS spectra with the following parameters: pass energy 40 eV, energy step size 0.1 eV. The collected XPS spectra were fitted using the Avantage software (version 5.9911, Thermo Fisher Scientific), where a Smart function of background subtraction was used to obtain XPS signal intensity, and an asymmetric Gaussian/Lorentzian mixed-function was applied. The carbon C1s peak position was assumed to be at 285.0 eV and used as an internal standard to determine other photoelectron peaks' binding energy.

The optical properties were studied in the range from 190 nm to 1100 nm (6.53 – 1.13 eV) by a UV–Vis spectrophotometer (Thermo Fisher Scientific Evolution 220) for the measurement of diffuse reflectance (DRS), using BaSO$_4$ as a standard.

2.3. Computational details

The electronic structure of bulk anatase and its (0 0 1) surface slab models were investigated computationally using density functional theory calculations within the generalized gradient approximation, as implemented in Quantum Espresso 6.5 software package [36,37]. All calculations were performed using ultrasoft pseudopotentials with Perdew-Burke-Ernzerhof (PBE [38]) exchange-corrected functionals, and the electronic wave functions were expanded to the energy cut-off of 500 eV. During the bulk calculations, the $2 \times 1 \times 1$ anatase supercell was used, while for the (0 0 1) surface, the 2×1 slab with 3-titanium layers along the *l* direction was created, separated by a 20 Å layer of vacuum. K-point grids of $4 \times 5 \times 3$ and $5 \times 5 \times 1$ were used for the bulk and slab models, respectively. Next to the pure structures, oxygen vacancy and fluorine doping were modeled by removing a single O atom, replacing an O atom with F, and inserting F atoms at the interstitial position. Before the final calculations, all structures were allowed to relax using Broyden–Fletcher–Goldfarb–Shanno method with the threshold of 10^{-3} Ry·Bohr^{-1}. In the (0 0 1) slab, one of the outermost Ti—O layers was kept fixed during the optimization. Optimized structures are shown in Supplementary Materials (Figure S3 and S4). During the calculations, Hubbard parameter $U = 4.6$ eV was applied for both Ti and O atoms to obtain reasonable bandgap values.

Moreover, to verify the alcohol chain length effect on the ligand exchange with [TiF$_6$]$^{2-}$ complex, additional energy calculations for the F$^-$ ion, methanol, ethanol, n-butanol, and n-hexanol molecules as well as for the [TiF$_6$]$^{2-}$, [TiF$_5$MeOH]$^-$, [TiF$_5$EtOH]$^-$, [TiF$_5$ButOH]$^-$ and [TiF$_5$HexOH]$^-$ complexes were performed using PBE functionals within the 20x24x19 Å unit cell to assure minimum 10 Å distance between neighboring molecules. For these calculations, $3 \times 3 \times 3$ k-points grid was used, and geometric optimization was carried out analogical to the crystal structure calculations for most of the structures. Only in the case of [TiF$_5$ButOH]$^-$ and [TiF$_5$HexOH]$^-$ their optimization was not entirely performed due to the significant computational times required. Instead, an optimized [TiF$_5$EtOH]$^-$ structure was taken, and additional —CH$_x$ groups were added based on the optimized n-butanol and n-hexanol geometries. For these structures, single energy calculations proceeded.

2.4. Electrochemical measurements

To perform Mott-Schottky analysis, 0.02 g of the synthesized nanoparticles were mixed with 0.2 cm^3 of deionized water in an agate mortar, and the obtained paste was applied on the clean fluorine-doped tin oxide (FTO) glass substrate using a doctor blade technique. The as-prepared electrodes were calcined at 450 °C for 2 h with a 5° · min^{-1} heating rate. To ensure that calcination does not affect the materials' morphology, additional SEM observation was performed for the selected sample after the whole procedure (see Fig. S9 in Supplementary Materials).

The electrochemical tests for the series of materials were performed in a three-electrode configuration. The FTO covered by the titania layer was the working electrode, Ag/AgCl/0.1 M KCl, and Pt served as reference and counter electrode, respectively, as the electrolyte 0.5 M Na$_2$SO$_4$ was used. The solution was 40 min deaerated with argon before measurements, while during the tests, the gas flow was maintained above the solution. The electrochemical impedance spectroscopy (EIS) data was recorded for 45 different potentials selected from the range from + 0.8 V to −1.0 V vs. Ag/AgCl/0.1 M KCl using 10 mV amplitude of the AC signal and 1000 Hz frequency. Those conditions were controlled by the potentiostat–galvanostat Biologic SP-150. The Mott-Schottky plot describing the relation Csc^{-2} vs. E was obtained using the following calculation of the space charge capacitance [39]: C$_{SC} = -1/(2\pi f Z_{im})$, where the imaginary part of the impedance Z_{im} was taken into account, f stands for the frequency of AC signal. The flat band potential position was determined based on the tangent's intersection to the Mott-Schottky plot with the potential (E) axis.

3

2.5. Determination of photocatalytic activity

The photocatalytic activity of the obtained samples was determined in a model reaction of phenol degradation. In a typical run, 0.05 g of the photocatalyst was dispersed inside a 25 cm^3 quartz reactor filled with phenol solution, with a pollutant concentration varying between 20 and 100 mg·dm^{-3} to achieve different phenol/photocatalyst ratios. The obtained suspension was kept in the dark for 30 min to achieve adsorption–desorption equilibrium, followed by 60 min of UV–Vis irradiation. During the whole process, an airflow of 4 dm^3·g^{-1} was passed through the suspension, and the whole system was thermostated

to 20 °C. A Xe lamp equipped with a water filter was used as a light source, and the distance between the reactor border and the lamp was adjusted to keep the measured UV-flux intensity equal to 40 mW·cm^{-2}.

Both phenol disappearance and the formation of aromatic by-products were monitored using a high-performance liquid chromatography system (HPLC, Shimadzu LC-6A). During the HPLC runs, an iso-cratic mobile phase consisting of acetonitrile (Merck), water, and H$_3$PO$_4$ (Merck, 85% solution) was used, with their volume fractions equal to 0.7/0.295/0.005, respectively. The C18 5 μm, 150 × 4.6 mm column was used for separation (Phenomenex). Simultaneously, the concentration of total organic carbon after each process was monitored using
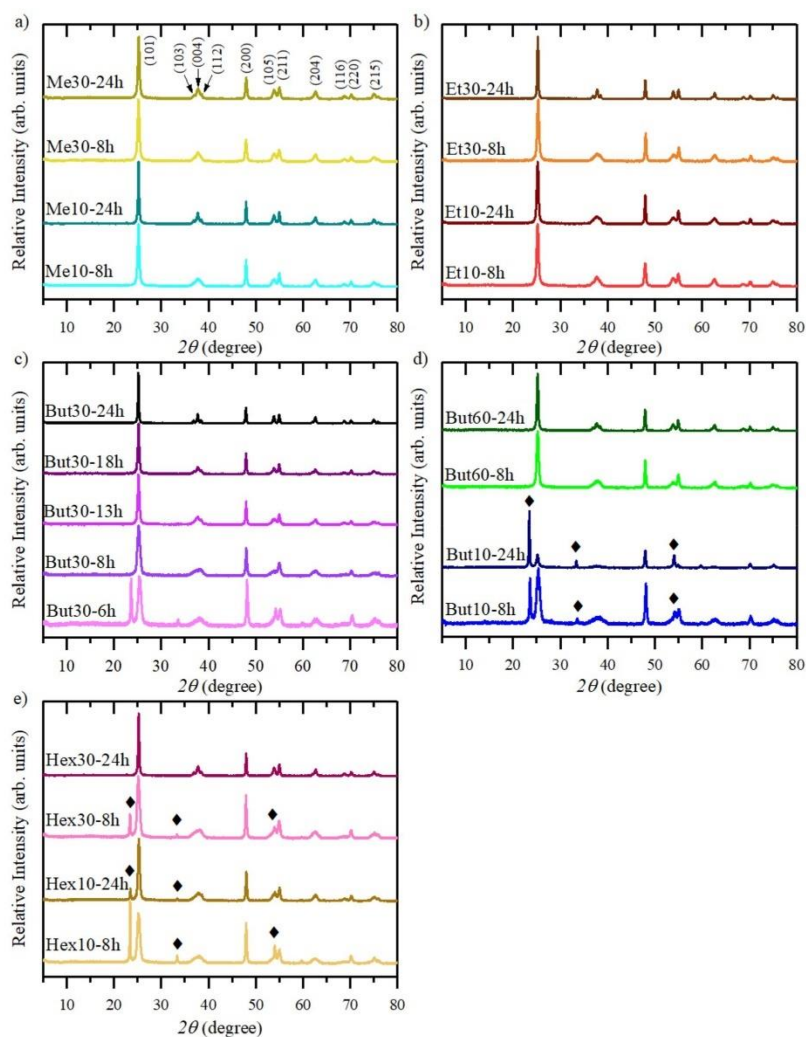

Fig. 1. XRD patterns of samples prepared in (a) methanol, (b) ethanol, (c) 30 cm^3 of n-butanol, (d) 10 and 60 cm^3 of n-butanol and (e) n-hexanol. Throughout the results, reflexes originating from anatase TiO$_2$ are not marked and are indexed in (a), while cubic TiOF$_2$ signals are marked with rhombus.

4

the Shimadzu TOC-L analyzer.

3. Results and discussion

3.1. Structural and morphological analyzes

Phase structure and crystallinity of the nanoparticles were analyzed with powder X-ray diffraction (XRD). All obtained results are presented in Fig. 1 and Table 1. Throughout the samples, a formation of anatase TiO_2 was observed and cubic $TiOF_2$ in the case of n-butanol and n-hexanol assisted processes. $TiOF_2$ is known to be an intermediate phase obtained in the presence of HF, which subsequently hydrolyze to TiO_2 [40]. The results showed that this transformation depended on both volume and the type of solvent. The lower content of long-chain alcohols (n-butanol and n-hexanol) stabilized the $TiOF_2$ phase and only increased their amount, promoting further conversion to TiO_2. Moreover, an additional effect of the alcohol was observed in terms of crystallite growth and the amount of amorphous phase presence inside obtained materials. In the case of pure TiO_2 particles, both increasing alcohol

amount and changing it to the shorter chain alcohol promoted the creation of more crystalline particles at the early stage of the process. On the other hand, the opposite approach resulted in a continuous crystallinity rise, which covered a broader parameter range. It is generally followed by the crystallites' growth, which is shown in Table 1, calculated for the size along the l crystallographic direction. A visible dependence of both factors on the type and the volume of alcohol suggests that its presence affected the growth rate of the TiO_2 nanocrystals. As a consequence, it further indicates that the alcohol role is not limited solely to co-stabilization of the {0 0 1} structure together with fluorine, as previously shown [34,41].

Furthermore, XRD patterns showed a characteristic broadening of the signals originating from the (0 0 4) and (1 0 5) planes of anatase, which suggested that the size of the nanoparticles was significantly reduced in the l direction [42]. That was further confirmed by the SEM observations, as shown in Fig. 2. The formation of 2D anatase nanoparticles resulted directly from the HF presence during the synthesis, which stabilizes the {0 0 1} facets and promotes growth in the hk directions, according to the Gibbs-Curie-Wulff theorem [5]. For the well-defined 2D nanoparticles, their observed heights are in agreement with the calculated crystallites size using the (0 0 4) reflection, proving that the obtained particles should be single crystalline with {0 0 1} facets exposed at the top/bottom (see Fig. S7 in the Supporting Materials). Nevertheless, some differences between samples were noticed. It can be seen that increasing alcohol content and changing it to shorter-chain alcohol produced smaller and less platelet materials. It was primarily observed for the 8 h reactions, while for the 24 h, increased alcohol amount inhibited the particles' further growth. Moreover, for the reactions involving methanol and 10 cm^3 of ethanol extremely fine particles, without expected 2D morphology were observed and formation of well-defined nanosheets occur only for the ethanol when prolonging the synthesis time. This effect was not observed for the *n*-butanol and *n*-hexanol series.

It is known that particles size is influenced by their nucleation rate [43] and therefore is dependent on both alcohol amount and its type, with the highest nucleation rate observed for the MeOH and EtOH series. On the other hand, subsequent TiO_2 growth in the HF-assisted synthesis is known to be a result of fluorine mediated dissolution-recrystallization process [40,44–45], which could be schematically described by the following equation:

$$TiO_2 + 6HF \leftrightarrow [TiF_6]^{2-} + 2H_2O + 2H^+$$

In this process, titanium is reversibly transferred between its solid oxide form and dissolved ion/molecule, preferably coordinated with 6 ligands in the form of bipyramid. The above reaction illustrates the behavior of samples Et10-8h and Et10-24h, showing fast nucleation of TiO_2 nanoparticles, which further rearranged to form well-defined nanosheets as the reaction time was prolonged. However, despite the necessity of HF presence to etch TiO_2 structure, formation of $[TiF_6]^{2-}$ is questionable, and the presence of other, less fluorinated Ti species was also reported [46]. An alcohol exchange with halide ligands is primarily known to be possible under solvothermal conditions [47–48]. Therefore, we have computationally verified if alcohol chain length could influence such process by replacing single fluorine from $[TiF_6]^{2-}$ octahedra with alcohol molecules.

$$[TiF_6]^{2-} + ROH \rightarrow [TiF_5ROH]^- + F^-$$
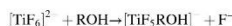
As shown in Fig. 3, a visible effect between the short and long-chain alcohols can be observed, with ethanol and methanol requiring lower energy for such reaction to occur. A possible exchange of F$^-$ with MeOH and EtOH at relatively mild conditions could especially promote further TiO_2 condensation through an ether elimination mechanism [49–50], which would increase its nucleation rate. Moreover, this seems especially possible while considering an increased steric hindrance together with the alcohol chain length, which, on the other hand, should slow

Table 1
Structural parameters of the obtained samples.

| Sample name	Anatase crystallite size along with the [0 0 1] direction (nm)	Anatase lattice parameters (Å)		Phase content (w/w %)		Amorphous phase content (w/w %)
		a,b	*c*	TiO_2 (anatase)	$TiOF_2$	
Me10-8h	14	3.787	9.512	100	–	37.5
Me10-24h	23	3.786	9.508	100	–	18
Me30-8h	13	3.788	9.504	100	–	24
Me30-24h	15	3.788	9.506	100	–	35
Et10-8h	13	3.789	9.513	100	–	39
Et10-24h	17	3.787	9.511	100	–	16
Et30-8h	16	3.790	9.522	100	–	32
Et30-24h	30	3.786	9.505	100	–	14
But10-8h	9	3.796	9.558	87	13	51
But10-13h	14	3.791	9.522	91	9	39
But10-24h	12	3.801	9.560	49	51	33
But30-6h	10	3.792	9.538	77	23	64
But30-8h	12	3.790	9.526	100	–	66
But30-13h	17	3.789	9.514	100	–	58
But30-18h	21	3.788	9.505	100	–	46
But30-24h	33	3.787	9.506	100	–	19
But60-8h	15	3.789	9.518	100	–	33.5
But60-13h	22.5	3.787	9.513	100	–	25.5
But60-24h	21	3.787	9.509	100	–	23
Hex10-8h	11	3.789	9.527	85	15	39
Hex10-24h	16.5	3.791	9.523	97	3	58
Hex30-8h	12	3.788	9.520	94	6	54
Hex30-24h	27	3.787	9.508	100	–	21
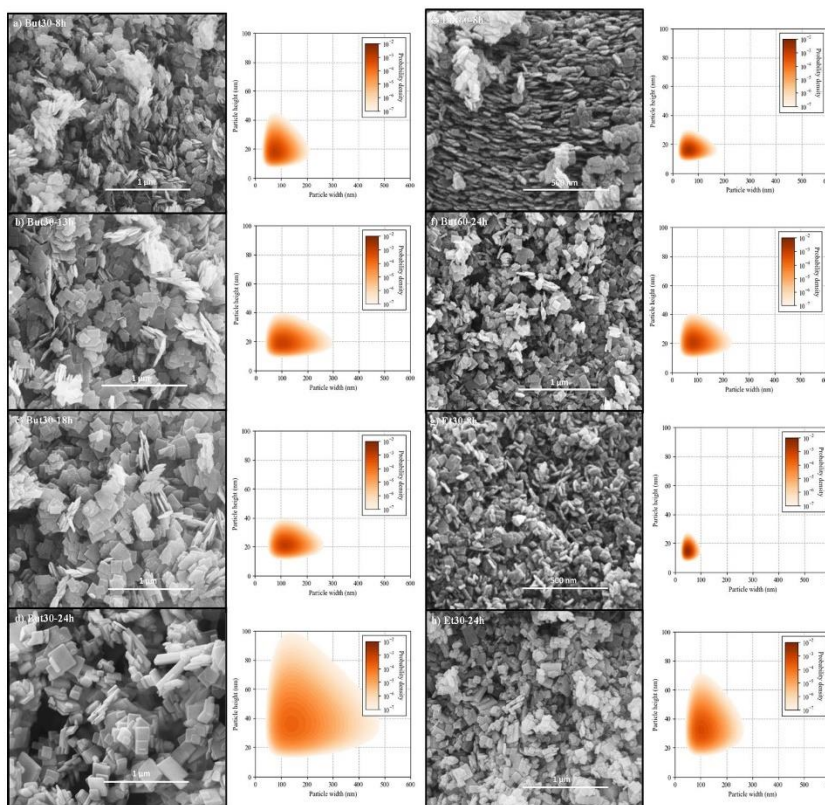
Fig. 2. SEM images of 2D TiO$_2$ nanosheets and graphs of their size distribution. Other SEM images are presented in Supporting Materials (Fig. S2).
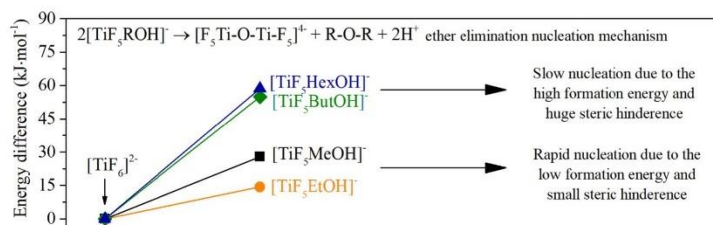

Fig. 3. Obtained energy difference due to the exchanging F$^-$ to ROH ligand in the [TiF$_6$]$^{2-}$ complex.

down such a process [51]. For the n-butanol and n-hexanol assisted processes, this could promote slower nucleation of the TiO$_2$ nanoparticles, which could grow into well-defined nanosheets. Therefore, low energy required to exchange the fluorine, together with small steric hindrance, could explain observed morphology differences, especially for the 8 h processes, as a result of increased nucleation rate through ether elimination (2D morphology for But30 and Hex30 series vs. ultrafine, but irregular particles for Met10 and Et10).

On the other hand, a significant increase in alcohol content (Met30, Et30, and But60) can promote subsequent alcohol condensation in the presence of HF to produce additional H$_2$O molecules [43].

Therefore, the TiO$_2$ structure became more stable, and the dissolution-recrystallization process became slowed down, as observed mainly for samples Met30-8h and Met30-24h. Moreover, increased H$_2$O content results in less platelet particles' formation due to gradual hydrolysis and condensation of fluorine-terminated TiO$_2$ facets in the aqueous environment [52].

Described results showed that alcohol effect is not limited to

6

influence on F$^-$ chemisorption and especially its volume is also affecting the kinetics of TiO$_2$ growth. Specifically, as shown in Fig. 4, the stable formation of highly platelet particles in the adapted conditions can be obtained when ROH/TBT ratio is between 3.5 and 6.5. Furthermore, for this reaction system, the kinetics of TiO$_2$ nucleation depends on the possible alcohol exchange with fluorine, which should promote faster nucleation through subsequent ether elimination. For the lower alcohol contents, TiOF$_2$ stabilization may occur mainly for samples prepared with n-butanol and n-hexanol. Moreover, less platelet particles are formed for the higher alcohol amounts through increased ROH condensation to give H$_2$O.

3.2. Surface properties

Since semiconductors' surface properties are critical in the context of their practical applications, the prepared TiO$_2$ samples were further analyzed in terms of their surface development and composition. Fig. 5 shows the isotherms of nitrogen adsorption-desorption for the synthesized nanoparticles in the range of p/p_0 from 0 to ~1.

The obtained isotherms showed characteristic features of the type IV family [53], with the reversible mono- and multilayer adsorption in the lower range of p/p_0, followed by the hysteresis loop for higher pressure values. For all samples, a visible decrease in the adsorbed volume with the reaction time was noticed, especially for the lower part of the isotherm, which is in agreement with the observed crystal growth and crystallinity increase of the material. Moreover, both H1 (adsorption limit for high p/p_0 values) and H3 (no limit) isotherm types are observed, with a significant effect of the introduced alcohol [54]. The type H3 loop is ascribed to materials with aggregates of plate-like particles giving rise to slit-shaped pores and therefore corresponds well with the 2D morphology observed, especially for the But30 and hexanol series [27]. Moreover, since the hysteresis were observed for high p/p_0 values for these samples (mostly > 0.85), it was found that most of the pores' volume was formed by the inter-aggregate macro/mesopores created between nanocrystalline platelets. On the other hand, an introduction of methanol results in the type H1 loop, which is in agreement with their ultrafine but less platelet morphology, as revealed by the SEM analysis. Furthermore, smaller pores' formation was observed for these samples with more narrow distribution (see Fig. S8 in the Supporting Materials for distribution graphs). The surface development and pore size distribution followed the SEM and XRD results,

Fig. 4. Schematic representation of the observed alcohol effect on the formation of {001} exposed anatase nanoparticles after arranging them in accordance with the ROH/Ti ratio.

showing an alcohol influence on the obtained samples' adsorption behavior. Detailed sorption measurements, including calculated BET surface area, total pore volume, and average pore size, are given in Table 2.

Simultaneously, selected samples were analyzed with XPS to determine their surface composition. Due to the strong Ti—F interactions, HF addition can affect the surface structure of the growing TiO$_2$ and, consequently, influence their final properties [56]. It can be observed even after initial washing with a basic solution, such as NaOH. The presence of both Ti and F on the surface was demonstrated in XPS spectra of all samples, and the summation of their characteristics is presented in Table 2.

As shown in Fig. 6, for most analyzed samples, well-defined Ti^{4+} doublet can be observed around the 458.5/464 eV, which corresponds to the TiO$_2$ surface structure. However, throughout the samples, both signals at the lower and higher energies can be observed, which can be ascribed to the Ti^{3+} states, as well as to the possible Ti—F bonds, respectively [57,58]. Concerning the solvent effect, it was found that alcohol type and its amount affect surface Ti—F bonding and possible Ti reduction. Mainly, methanol introduction resulted in a visible surface fluorination and little (or zero) presence of the stoichiometric TiO$_2$. This can be seen as a consequence of very fast nucleation, which further leaves the remaining HF to react and etch the particle's surface. On the other hand, most of the ethanol and n-butanol assisted samples showed clear TiO$_2$ surfaces with only some differences in their fluorination. For this series, it can be observed that an increase in the alcohol content decreases the amount of surface fluorine. It is known that fluorinated TiO$_2$ nanosheets undergo gradual hydrolysis and further condensation to the 3D particles due to the hydrothermal reaction in the H$_2$O environment [52]. Therefore, both less platelet character of the But60 and Et30 series and their less fluorinated surface should especially result from increased H$_2$O presence, comparing the But30 and Et10 series, respectively.

Furthermore, a significant amount of the Ti^{3+} species were observed in the case of sample Et30-24, which might result from the surface presence of oxygen vacancy induced by the free HF in the H$_2$O-rich environment [59]. It was followed by the visible valence band tailing observed for this sample, which is shown in Fig. 7. Finally, for the Hex30-24 sample, a series of additional Ti—F states is observed along with the TiO2 signal, which might inhibit TiO$_2$ hydrolysis and stabilization of the intermediate TiOF$_2$ structure for the longer chain alcohols, as revealed by the XRD analysis.

3.3. Optical properties and electronic structure

DR/UV–Vis spectra of the prepared TiO$_2$ nanosheets are presented in Fig. 8. For all samples, the main absorption around 3.2 eV was observed, ascribed to the electron transfer from the valence band to the conduction band in the pure anatase structure. No increase of absorbance, which would overlap with this transition was observed, indicating no additional bulk states directly above/below the valence/conduction band edge. However, a visible difference was noticed within the bandgap of the samples. Especially, samples that were found to possess higher amounts of Ti—F surface bonds (Met series, Et10-24h, and Hex30-24h) showed visible enhancement either around the 500 nm or in the whole visible-NIR regions of the spectrum. This is in agreement with other studies describing the TiOF$_2$ absorbance spectrum, with the characteristic band at approx. 480 nm [33]. A similar but smaller effect could be observed for the sample Et10-24h. On the other hand, the samples prepared with n-butanol and 30 cm^3 of ethanol showed a different behavior with a monotonous absorbance increase towards the longer wavelengths. Especially for the But30 series, the appearance of two bands at 2.2 and 1.1 eV was noted, while the far-UV absorbance was simultaneously decreasing, suggesting a change in the amount of O 2p bonding orbitals (these are defined as being within the Ti$_3$O plane [60]). In the case of series But60 and Et30, no well-defined band at 2.2 eV was
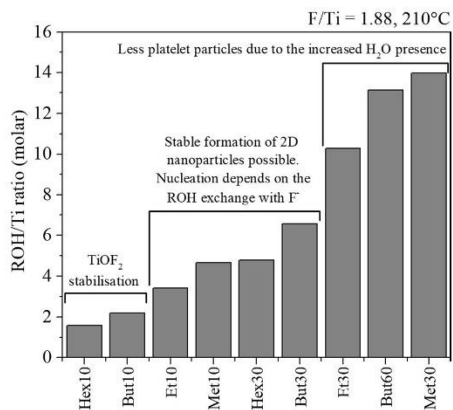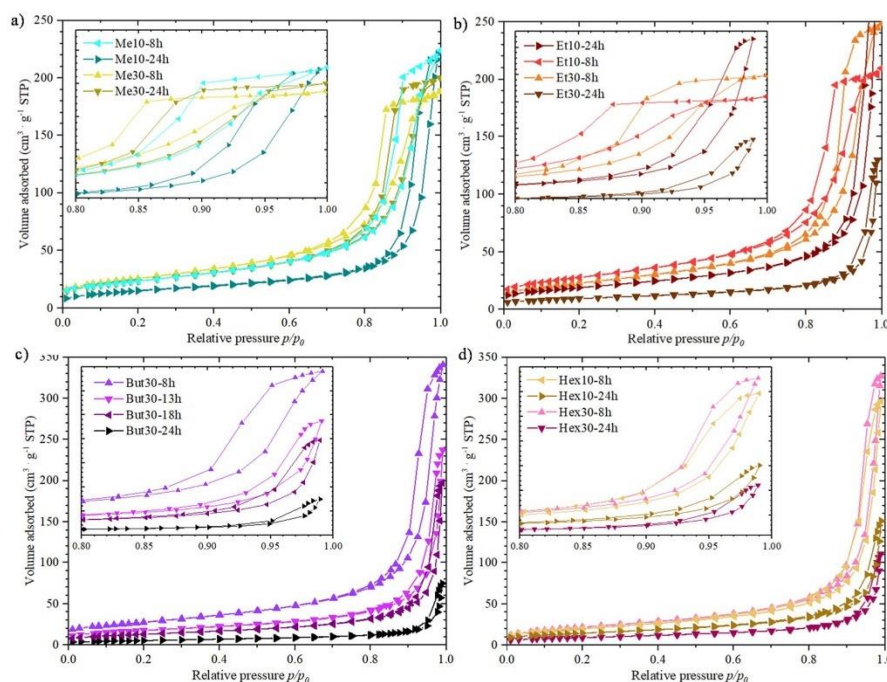
Fig. 5. Low-temperature N$_2$ sorption isotherms measured for the obtained samples. Inside are given the close-up views of the high p/p_0 regions.

Table 2
Surface characteristics obtained from the N$_2$ sorption and XPS analysis.

Sample name	Sorption			XPS			
	S$_{BET}$ (m$^2 \cdot$g^{-1})	V$_{pores}$ (cm$^3 \cdot$g^{-1})	d$_{Pores}$[1] (nm)	Ti^{3+}/Ti^{4+}	Ti-F/Ti-O	Total F/Ti	VB edge (eV)
Me10-8h	85	0.35	13.3	0	5.87	0.18	1.97
Me10-24h	54	0.34	21.8	n.d.	n.d.	n.d.	n.d.
Me30-8h	94	0.29	9.8	No TiO$_2$	6.3	0.11	2.22
Me30-24h	85	0.31	11.7	n.d.	n.d.	n.d.	n.d.
Et10-8h	100	0.33	10.6	0	0.32	0.12	1.84
Et10-24h	68	0.49	25.9	0	0.26	0.15	1.79
Et30-8h	83	0.39	14.6	0	0.06	0.075	2.08
Et30-24h	34	0.20	23.0	0.19	0	0.063	~0
But30-8h	99	0.53	17.8	0	0.13	0.15	2.12
But30-13h	62	0.37	22.5	n.d.	n.d.	n.d.	n.d.
But30-18h	47	0.31	23.2	n.d.	n.d.	n.d.	n.d.
But30-24h	19	0.12	22.7	0	0.18	0.13	1.89
But60-8h	80	0.37	15.4	0	0.17	0.24	2.01
But60-13h	47	0.37	27.3	0	0.10	0.066	1.74
Hex10-8h	73	0.46	19.6	n.d.	n.d.	n.d.	n.d.
Hex10-24h	52	0.24	17.0	n.d.	n.d.	n.d.	n.d.
Hex30-8h	79	0.51	20.9	n.d.	n.d.	n.d.	n.d.
Hex30-24h	42	0.17	20.3	0.05	0.52	0.11	1.93

[1] Average pore size is determined for all macro, meso, and micropores together to represent a change in the overall size distribution. For the detailed results of the observed pores' size, please see the Supporting Materials.

observed, while the absorbance change within the UV region was very limited, especially for the Et30 series. However, the absorbance rise was still observed up to $\lambda = 1100$ nm for these samples.

Since almost all samples obtained from ButOH and EtOH series were found to be pure 2D anatase, with the majority of the TiO$_2$ surface signals, their absorbance should be connected with the possible point defects in their crystal structure. Therefore, to better understand their behavior, possible electronic structures using Density Functional Theory (DFT) method have been simulated. The calculated density of state distributions is shown in Fig. 9, including bulk and (0 0 1) surface slab
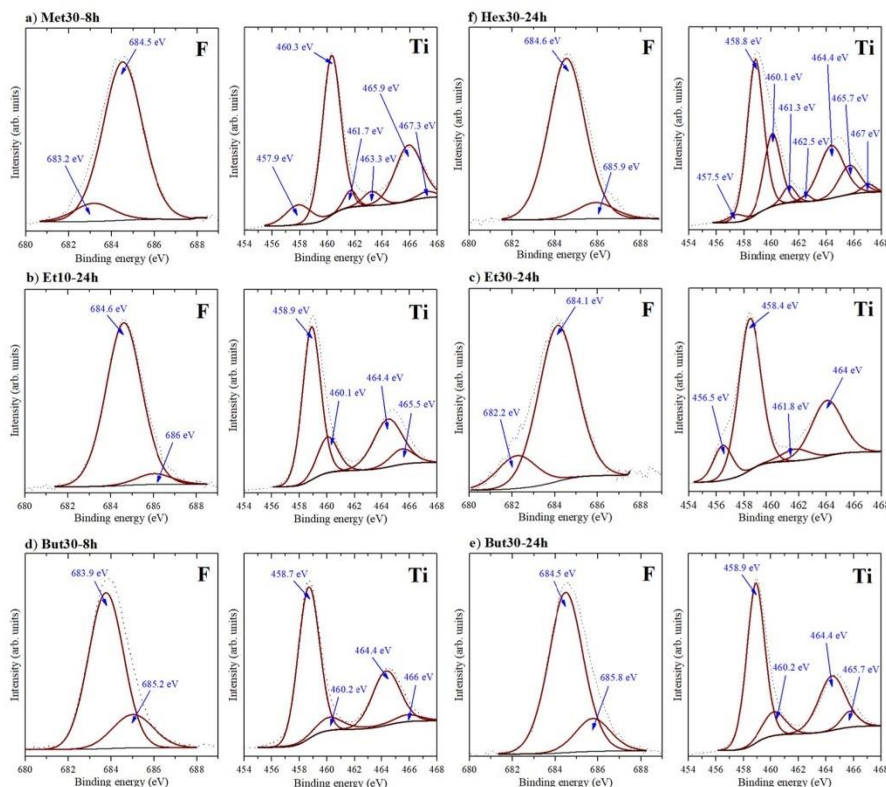
8

Fig. 6. The observed XPS signals originating from Ti and F atoms together with their deconvolution for selected anatase samples.

models, both pure and with possible defects considered. The obtained results showed a formation of well-defined midgap states resulting from the oxygen removal due to the presence of unpaired d electrons on the Ti atom, forming Ti^{3+} ions. For a bulk structure, these states are located approximately between 1 and 2 eV from the valence band edge and, therefore, would fit very well to the bands observed in the UV–Vis spectrum of the But30 series. The formation of oxygen vacancies inside the bulk structure can be further reasoned by the structural change around the vacancy, which would cause O atoms to displace themselves from the Ti_3O plane, therefore decreasing the number of highly bounded orbitals responsible for the UV absorption below 300 nm. Finally, no Ti^{3+} states observed in the XPS spectrum of this sample fit well the above description.

However, similar results were not observed in series But60 and Et30, suggesting that their structures differ from the But30 samples. Significantly, the lack of a band at 2.2 eV and strong light absorption at $\lambda = 250$ nm suggest that no oxygen vacancies are present in their bulk structure. None of the calculations considered in Fig. 9a could explain well the obtained XPS/UV–Vis results. Therefore, the effect of the {0 0 1} surface structure was taken into consideration. The performed calculations, especially the formation of surface oxygen vacancies, seem to be in good agreement with the obtained results for sample Et30-24h, which showed both the surface presence of Ti^{3+} and the valence band tailing. It also agrees with the study of Linh et al., who have shown that the mid-

gap states created as the result of oxygen vacancy at the (0 0 1) surface could shift according to the Ti-O interactions [61] (affected during calculations by the arbitrary applied *U*). Assuming the formation of a more continuous distribution of these mid-gap states in reality and the pinning of the Fermi energy at their level, this seems to be a reasonable interpretation of the observed valence band tail in the XPS spectra for Et30-24h. In this case, the absence of additional maxima on the UV–Vis spectrum could be due to the bandgap reduction on the surface and their relatively low amount compared to the whole structure.

On the contrary, But60 samples and sample Et30-8h did not show any significant valence band tailing or Ti^{3+} presence. Therefore, their characteristics should result from different features. As an alternative explanation, we focused on the F ions present in the sample's surface region. Fluorine enhanced the n-type properties of TiO_2 and could create additional electrons inside the anatase structure [62–63]. These electrons can be a reason for the rising absorbance up to the IR spectrum due to their localization inside the conduction band states [64]. The interplay between TiO_2 stoichiometry and F presence was studied by Seo et al., who have shown that fluorine passivates the defects states caused by O deficiency and could contribute to the conduction band electrons without changing the bandgap of anatase [63]. It seems to be a plausible explanation of the UV–Vis behavior of these samples and is in agreement with our calculations, showing that F_I presence below the (0 0 1) surface does not change the material's electronic structure significantly.
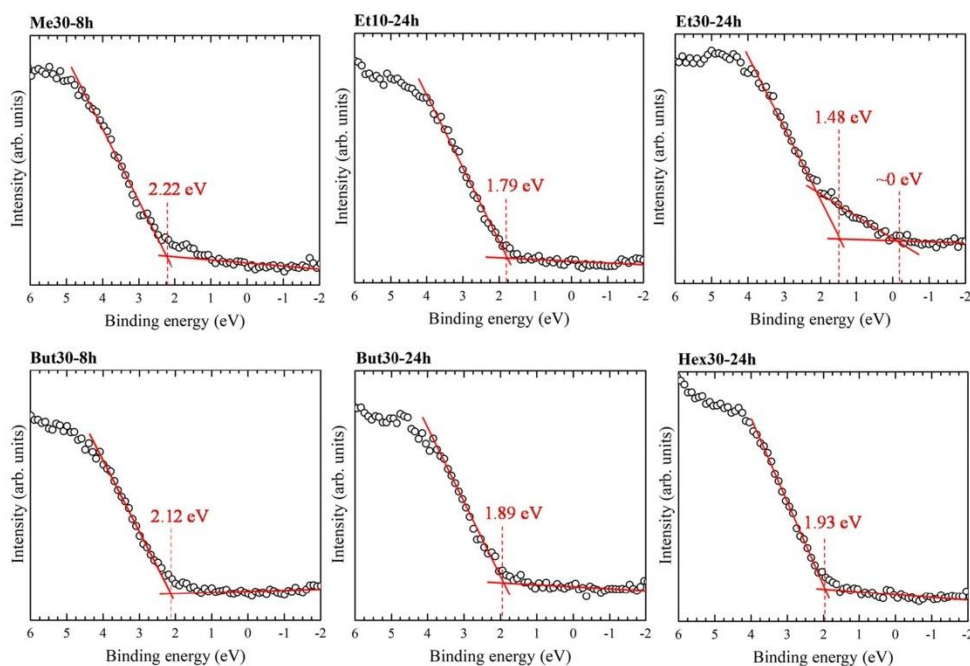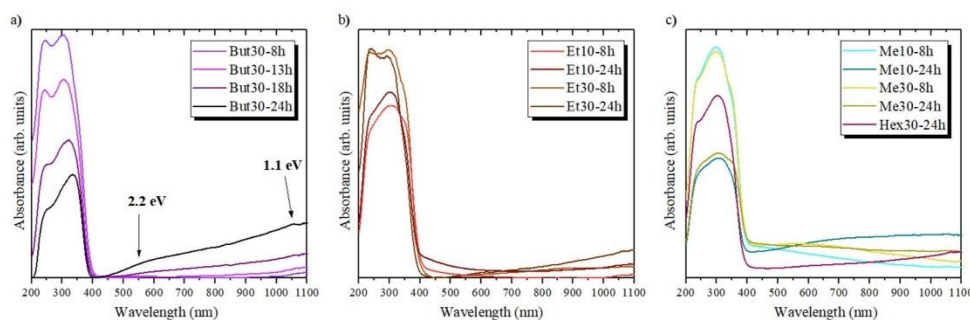
9

Fig. 7. Observed valence band edges for the selected anatase samples.

Fig. 8. DR/UV–Vis spectra of TiO$_2$ nanosheets obtained using (a) 30 cm^3 of n-butanol, (b) ethanol, (c) methanol, and 30 cm^3 of n-hexanol.

3.4. Electrochemical studies

Fig. 10 shows the band positions of pure TiO$_2$ samples, based on Mott-Schottky and UV–Vis analysis of the obtained nanosheets. The determined flat band potential is regarded as a significant quantity for semiconductor electrodes because it determines the position of band edges at the interface between the electrode material and electrolyte [65]. Consequently, the energy of conduction-band electrons, and taking into account bandgap energy, the valence band edge position can be estimated. It was found that for the Me10 and But30 series, no visible effect of the reaction time onto the location of energy bands was present, while for both But60 and Et30 series, a distinct change was observed,

with longer preparation time resulting in the negative shifting of the bands' edges. It can result from lowering the surface content of fluorine with a longer synthesis time for these series, while F ions are known to cause bending of the conduction band edge [66–67]. Indeed, the band positions seem to be fluorine-dependent, and a significant downshift of the conduction and valence bands was observed for the most fluorinated samples, name But60-8h, Me10-8h, or Et10-24h. Meanwhile, samples But30-8h and But30-24h possess almost the same band positions and similar fluorine content.

As it is known, the band position influence significantly the charge transfer between the photocatalyst and the reacting species. The degradation of organic pollutants is connected with the generation of
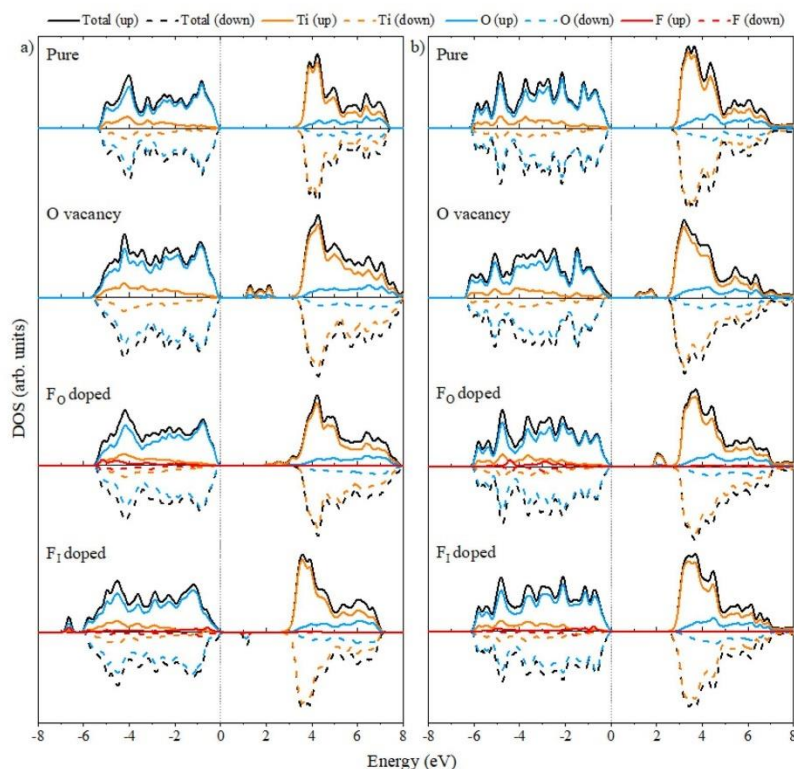
Fig. 9. The calculated density of states (DOS) distributions for (a) bulk and (b) (0 0 1) surface slab models of anatase. Shown results are for pure structures as well as oxygen-deficient anatase, structures with fluorine-doped in the place of oxygen (F_O), and anatase with fluorine-doped in interstitial position (F_I).
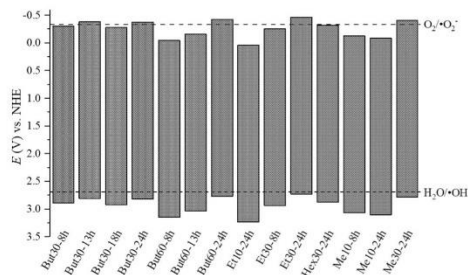

Fig. 10. Band edge positions of TiO_2 nanoparticles determined from the Mott-Schottky analysis and UV–Vis absorption. The length of the grey stripes corresponds to the bandgap energy values. Redox potentials for radicals formation are adapted from [68].

reactive oxygen species, especially ˙OH and ˙O_2^- through water oxidation and reduction of the adsorbed oxygen on the photocatalyst surface [69–70]. In this regard, it was found that depending on their morphology and surface characteristics, the solvothermal reaction conditions influenced the photocatalytic activity of these materials,

which will be discussed further.

3.5. Photocatalytic activity measurements

The photocatalytic activity of the obtained materials were tested in the reaction of phenol degradation. The results are shown in Fig. 11, in which sample But30-13 h was omitted due to all characteristics being analogical to the other three samples from this series. It was observed that the remarked rate of phenol disappearance exhibits an extreme variation between the samples, ranging from $k = 0.118$ min^{-1} to 0.019 min^{-1}. Considering performed characteristics and observed phenol removal efficiency, obtained samples can be classified into four categories: well defined 2D nanoparticles, which allow efficient phenol degradation (series A), 2D nanoparticles, which photocatalytic activity was compromised, and no formation of *ortho*-hydroxyphenol (catechol) was observed (series B), non-2D nanoparticles (series C) and $TiO_2/TiOF_2$ mixture samples (series D). Considering the $TiOF_2$ presence, it was reported that it could enhance the visible light activity of the TiO_2 materials [43,71]. However, when irradiated with UV–Vis light, its activity is poor, comparing with anatase [10,33]. It is in agreement with our previous study as well as with control measurements performed for samples But10-8h, But30-6h, Hex10-8h, and Hex10-24, which have shown no positive effect of the $TiOF_2$ presence on the photocatalytic performance (see SI Fig. S10 for more details). Therefore, these samples were not
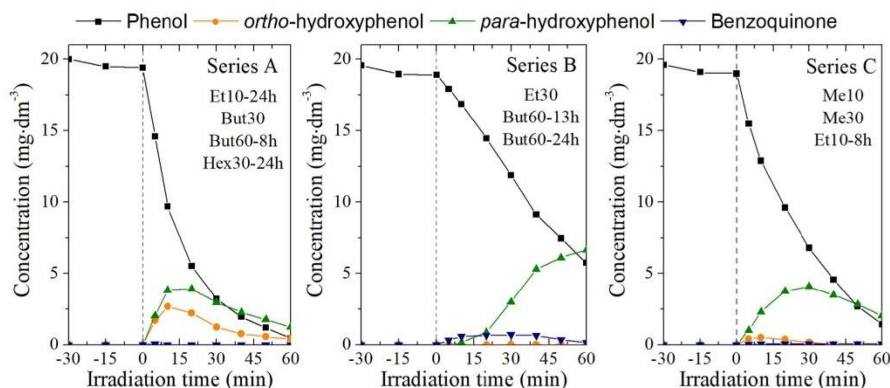
11

Fig. 11. Mean results of the degradation of $20 \, mg \cdot dm^{-3}$ phenol solution for the obtained samples after grouping them in similar-behaving series. Detailed results for each sample are presented in Supporting Materials (Fig. S11).

discussed in detail.

Focusing on the pure TiO_2 samples, series A seems to work "properly", and the obtained rate constants are comparable or higher than presented in the literature. For example, the photocatalytic activity in UV–Vis light of these 2D photocatalysts is similar to doped TiO_2 [18,72–73], or anatase nanosheets/bipyramids from the solvothermal synthesis in water [74]. Mino et al. have shown TiO_2 anatase nanostructures with dominant {0 0 1} or {1 0 1} facets obtained from solvothermal synthesis connected with lyophilization. The most efficient photocatalyst was bipyramidal nanoparticles; however, they achieved only ca. 10% phenol degradation after 60 min of the photodegradation reaction [74]. On the other hand, Sui et al. have presented Ti^{3+} self-doped TiO_2 single crystals with internal pores, which decomposed about 100% of phenol in 35 min when truncated octahedral bipyramid structured TiO_2 was used as the photocatalyst [75]. However, both studies do not present phenol mineralization efficiency.

Considering series B, its behavior was quite surprising both due to the markedly lower phenol degradation and significant change in the by-products formation. Moreover, a weak dependence between the rate constant and surface area of the photocatalyst was noted for this series. From the overall results, this effect seems to be connected with three previously noticed features (i) the low amount of surface fluorine observed for these samples, (ii) an upward shift of the band position for longer synthesis time, and (iii) the possible surface defectivity, especially connected with a surface excess of electrons (Ti^{4+} reduction on the surface of Et30-24h sample). Significantly, the latter could influence the formation of reactive oxygen species on the photocatalyst surface. As reported by Ma et al., the anatase {0 0 1} surface should preferentially localize photogenerated holes on the surface bridging O atoms [31], which is a position also suitable to generate ·OH from water [70]. In this case, both cathodic band shift and electron accumulation on the surface (Ti^{3+} states) could prevent h^+ from localization on the surface O and further H_2O oxidation. This can explain a distinct decrease of k since {0 0 1} surface should not be able to accumulate electrons directly on the surface Ti atoms [31]. Therefore, the whole process starts to be limited by the energy barrier of charge carrier transfer to the surface rather than further reactions with different species. This is in agreement with the minimal effect of the surface area on the activity of these samples. Moreover, inhibition of the ·OH formation would explain the absence of catechol since its creation should result from ·OH attack close to the phenol adsorption site [33].

Finally, samples from series C exhibit quite good photocatalytic performance; however, observed phenol removal was still visibly slower

than in series A. Moreover, no catechol formation was noticed for this series. These results suggest that samples from series C behave differently than series A and B, which should especially result from their different morphology. Comparing it with series A, it was observed that the situation is opposite to series B, and a relatively high amount of fluorine on the surface, together with the lack of defined surface defects, have led to high k values for this series.

All of the performed photocatalytic tests were followed by analyzing total organic carbon (TOC) to determine the obtained samples' mineralization ability. Concerning 2D nanostructures, it is known that reaction at the {0 0 1} facet is driven by photogenerated holes and further by ·OH attack to phenol molecule. Therefore samples from series A have shown a noticeable dependence on the available surface area (calculated as a ratio between undercoordinated surface O atoms, being active sites for ·OH formation, and the total amount of organic C at the start of the process). Furthermore, samples from series B achieved visibly lower per-surface mineralization, which agreed with their compromised activity, as observed before. On the other hand, series C showed good mineralization efficiency, especially when considering their lower rates of phenol removal, when compared to series A. These differences could especially result from the alternate surface structure of series C samples, which could enhance the formation of other reactive species, such as ·O_2^- radicals that could help mineralize aromatic compounds. The comparison between mineralization efficiency of described series is presented in Fig. 12.

From the overall results, it was found that a maximum TOC removal of 69% is observed for series A and 81% for series C. These results are promising considering the difficult and complex mechanism of phenol degradation and comparing to similar studies, which usually report photocatalytic phenol mineralization below 50% [72,74,76].

Furthermore, it is worth noting that quite different mineralization efficiency for all series clearly shows that the relationship between created phenol's by-products and TOC removal is morphology-dependent. Both samples from series B and C promoted the formation of hydroquinone as almost only intermediate, while their mineralization ability was significantly different. On the other hand, series A can achieve relatively high mineralization while the presence of catechol was observed during the process. In this study, no correlation between particle size and selective hydroquinone or catechol production was noticed since the smallest nanoparticles were obtained for series C, while both series A and B included samples with different sizes. Although Suhadolnik et al. and Turki et al. have presented phenol mineralization mechanism going through benzoquinone formation [27,77], the
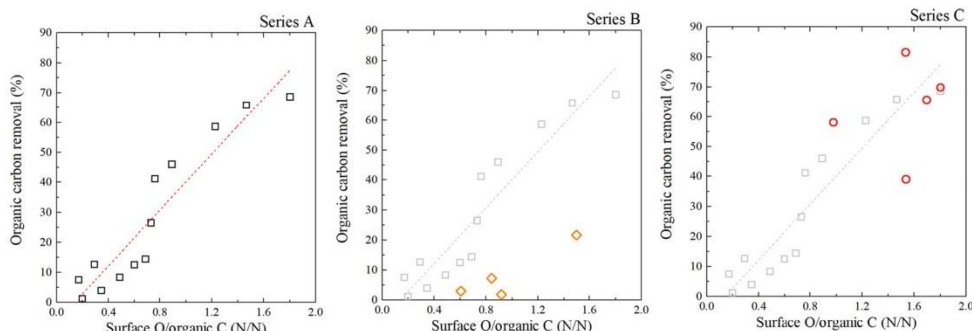
Fig. 12. The dependence between the observed mineralization ability and obtained samples on the surface area of the photocatalyst (recalculated as a ratio between undercoordinated surface O atoms and the total amount of organic C at the start of the process).

presence of benzoquinone was observed only for the series B, which was followed by significant inhibition of the mineralization process.

Therefore, it was assumed that facet exposition influence both of these processes. As highlighted before, it should especially result from differences in the generated reactive oxygen species and their further reaction with phenol. The {001} exposed particles are primarily reactive toward ˙OH generation, and therefore the formation of ˙O_2^- should be unfavored for these nanoparticles [31]. This allows to achieve a high phenol removal rate; however, mineralization is relatively lower since hydroxyl radicals are worse ring-opening agents than ˙O_2^-. For such materials, the final TOC removal depends strictly on the available surface area.

On the contrary, when h^+ transfer and further reaction at the surface became suppressed (series B) degradation process became significantly hindered for such materials. On the other hand, despite achieving quite good mineralization efficiency for the {001} exposed nanoparticles, the series C samples generally allow to obtain higher TOC removal, regardless of the simple phenol degradation rate. Specifically, sample Me10-8h, also with high surface area, achieved 81% of organic carbon removal while possessing less defined morphology, highly defected surface structure, and slower removal of phenol itself (see Fig. S11 in

Supporting Materials). Assuming that morphology change for these samples allowed to generate superoxide radicals effectively, it became reasonable that higher TOC removal could be obtained. Moreover, surface O defects might promote ˙O_2^- generation for such samples [78]. The defect-enhanced activity was not observed for series B, suggesting similar morphology dependence of such phenomenon. Analogically, this could be explained based on the different charge carriers' localization and further ROS generation between the series. As a final comparison, the activity of commercial P25 and other anatase nanoparticles obtained from $TiCl_4$ without any structure-defining additives was analyzed and compared to the most active 2D sample – But30-8h. As shown in Fig. 13, a higher phenol degradation rate constant was noticed for {001} nanosheets, with a higher amount of *para*-hydroxyphenol (hydroquinone) and lower mineralization ability measured as a TOC removal compared to commercial TiO_2 P25 and TiO_2 from $TiCl_4$.

3.6. Final remarks on the photocatalyst structure

Focusing on the photocatalytic activity of the obtained nanosheets, the overall results suggest that it depends on the {001} ability to produce ˙OH radicals involved in phenol degradation. In this regard, the
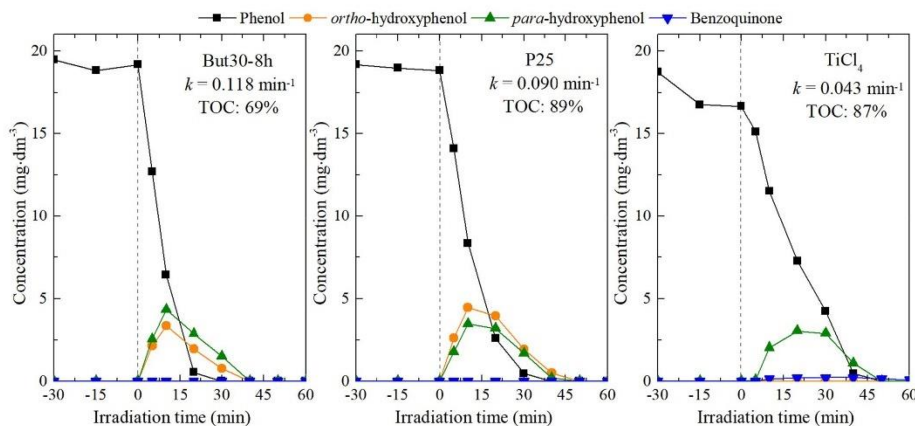

Fig. 13. A comparison of degradation and mineralization efficiency between the most active of the 2D nanoparticles, P25, and an additional control material prepared from $TiCl_4$. The preparation procedure and basic characteristics of the $TiCl_4$ sample are given in ESI.

13

observed enhancement of the degradation with a higher amount of surface fluorine is in agreement with the results of Mrowetz and Selli, who showed increased ˙OH generation with the fluorinated TiO_2 [79]. It could be observed as a result of F atoms influencing the surface charge distribution and raising charge separation. As presented in Fig. 14, an approximate 50% decrease of the F/Ti ratio was observed for the But30-24h sample, while Et30-24h kept its composition at a relatively constant level.

A similar reason is already well established for oxygen vacancies [80], and the different fluorine distributions/ratios between surface, subsurface, or bulk states could be a plausible explanation for some of the differences observed between samples. It could especially logically correlate with the observed differences with the synthesis environment and time (being the actual variables in the study) since the alcohol type can impact the nucleation rate of the anatase from the intermediate phase $TiOF_2$, influencing F ions distribution within the final structure.

4. Conclusions

Herein, the results of HF-assisted growth of anatase 2D nanoparticles, exposed with highly energetic {0 0 1} facets, using different alcohols as solvents were discussed in detail. The obtained results indicated that controlling both type and amount of alcohol could significantly influence the material's final properties. The morphological properties were associated with different nucleation rates, resulting from a possible ROH substitution to the $[TiF_6]^{2-}$ complex, promoting faster nucleation for short-chain alcohols through subsequent ether elimination reaction. It was found that the introduction of a low amount of n-butanol and n-hexanol can stabilize the $TiOF_2$ structure. Simultaneously, a significant increase in alcohol content promotes the formation of less platelet and less fluorinated particles due to increased H_2O produced through alcohol condensation. Moreover, the introduction of long-chain alcohols decreases TiO_2 nucleation and promotes the formation of the highly platelet nanoparticles at the early stage of the process, while ethanol and methanol produce ultrafine but more irregular-shaped particles. Compared to the control samples of commercial TiO_2 P25 and TiO_2 from $TiCl_4$ hydrolysis, the highest phenol removal efficiency was noticed for {0 0 1} nanosheets. However, the analyzed mineralization efficiency for anatase {0 0 1} facets showed lower organic carbon removal than the control sample of TiO_2 P25, which suggests their ability to break C-C bonds is relatively lower compared to other TiO_2 structures. The type of reactive species generated on the photocatalyst surface varies from different anatase structures that drive conversion to CO_2. Therefore, it can be assumed that other oxygen species are more efficient as ring-opening agents for the aromatic compounds than ˙OH radicals formed as a dominating species on the {0 0 1} facets. These results are significant regarding removing the persistent organic pollutants and studying their mineralization when discussing the surface properties of new design photocatalytic materials.

Author contributions

Anna Zielińska-Jurek: Conceptualization, Methodology, Supervision, Project administration, Writing—review and editing, Funding acquisition. **Marta Kowalkińska:** Investigation, Draft preparation. **Szymon Dudziak:** Formal analysis, Investigation, Validation, Visualization, Methodology, Draft preparation. **Jakub Karczewski:** Formal analysis. **Marcin Pisarek:** Investigation. **Adam Kubiak:** Investigation. **Katarzyna Siwińska-Ciesielczyk:** Formal analysis. **Katarzyna Siuzdak:** Formal analysis. **Anna Zielińska-Jurek:** Conceptualization, Methodology, Supervision, Project administration, Writing—review and editing, Funding acquisition. **Marta Kowalkińska:** Investigation, Draft preparation. **Szymon Dudziak:** Formal analysis, Investigation, Validation, Visualization, Methodology, Draft preparation. **Jakub Karczewski:** Formal analysis. **Marcin Pisarek:** Investigation. **Adam Kubiak:** Investigation. **Katarzyna Siwińska-Ciesielczyk:** Formal analysis.
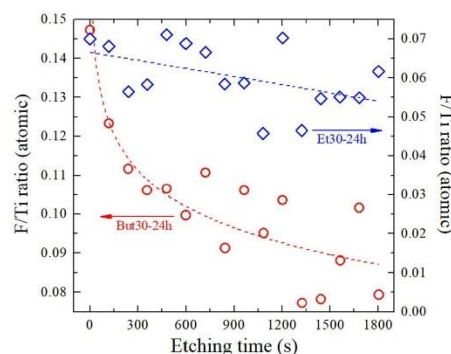

Fig. 14. The observed change in the total F/Ti ratio measured during XPS etching for samples But30-24 and Et30-24h. Presented ordinate axes have the same length.

Katarzyna Siuzdak: Formal analysis.

Declaration of Competing Interest

The authors declare that they have no known competing financial interests or personal relationships that could have appeared to influence the work reported in this paper.

Appendix A. Supplementary material

Supplementary data to this article can be found online at https://doi.org/10.1016/j.apsusc.2021.150360.

References

[1] S. Ahmed, M.G. Rasul, W.N. Martens, R. Brown, M.A. Hashib, Desalination 261 (2010) 3.
[2] P.V.L. Reddy, K.H. Kim, B. Kavitha, V. Kumar, N. Raza, S. Kalagara, J. Environ. Manage. 213 (2018) 189.
[3] F. Saadati, N. Keramati, M.M. Ghazi, Crit. Rev. Environ. Sci. Technol. 46 (2016) 757.
[4] L.G. Devi, R. Kavitha, Appl. Catal. B: Environ. 140–141 (2013) 559.
[5] R. Li, X. Zhang, H. Dong, Q. Li, Z. Shuai, W. Hu, Adv. Mater. 28 (2016) 1697.
[6] S. Liu, J. Yu, M. Jaroniec, Chem. Mater. 23 (2011) 4085.
[7] H.G. Yang, C.H. Sun, S.Z. Qiao, J. Zou, G. Liu, S.C. Smith, H.M. Cheng, G.Q. Lu, Nature 453 (2008) 638.
[8] C.Z. Wen, J.Z. Zhou, H.B. Jiang, Q.H. Hu, S.Z. Qiao, H.G. Yang, Chem. Commun. 47 (2011) 4400.
[9] X. Zhao, W. Jin, J. Cai, J. Ye, Z. Li, Y. Ma, J. Xie, L. Qi, Adv. Funct. Mater. 21 (2011) 3554.
[10] Z. Wang, K. Lv, G. Wang, K. Deng, D. Tang, Appl. Catal. B: Environ. 100 (2010) 378.
[11] M.V. Sofianou, V. Psycharis, N. Boukos, T. Vaimakis, J. Yu, R. Dillert, D. Bahnemann, C. Trapalis, Appl. Catal. B: Environ. 142–143 (2013) 761.
[12] W.S. Wang, D.H. Wang, W.G. Qu, L.Q. Lu, A.W. Xu, J. Phys. Chem. C 116 (2012) 19893.

14

[13] N.C. Saha, F. Bhunia, A. Kaviraj, Bull. Environ. Contamination Toxicol. 63 (1999) 195.
[14] L. Zhang, T. Kanki, N. Sano, A. Toyoda, Environ. Monit. Assess. 115 (2006) 395.
[15] C.S.A. Antunes, M. Bietti, M. Salamone, N. Scione, J. Photochem. Photobiol., A 163 (2004) 453.
[16] A.M. Peiró, J.A. Ayllón, J. Peral, X. Doménech, Appl. Catal. B: Environ. 30 (2001) 359.
[17] A. Sobczyński, L. Duczmal, W. Zmudziński, J. Mol. Catal: A: Chem. 213 (2004) 225.
[18] Z. Bielan, S. Dudziak, A. Sulowska, D. Pelczarski, J. Ryl, A. Zielińska Jurek, Materials 13 (2020) 1.
[19] T.T.T. Dang, S.T.T. Le, D. Channei, W. Khanitchaidecha, A. Nakaruk, Res. Chem. Intermed. 42 (2016) 5961.
[20] L.G. Devi, K.E. Rajashekhar, J. Mol. Catal: A: Chem. 334 (2011) 65.
[21] A. Blažková, I. Csöllecová, V. Brezová, J. Photochem. Photobiol., A 113 (1998) 251.
[22] Y. Zhang, R. Selvaraj, M. Sillanpää, Y. Kim, C.W. Tai, Chem. Eng. J. 245 (2014) 117.
[23] C.H. Chiou, C.Y. Wu, R.S. Juang, Chem. Eng. J. 139 (2008) 322.
[24] A.C. Mecha, M.S. Onyango, A. Ochieng, C.J.S. Fourie, M.N.B. Momba, J. Catal. 341 (2016) 116.
[25] M. Krivec, A. Pohar, B. Likazor, G. Drazic, AIChE J. 61 (2015) 572.
[26] A.V. Emeline, X. Zhang, T. Murakami, A. Fujishima, J. Hazard. Mater. 211–212 (2012) 154.
[27] L. Suhadolnik, A. Pohar, B. Likozar, M. Čeh, Chem. Eng. J. 303 (2016) 292.
[28] X. Wang, L. So, R. Su, S. Wendt, P. Hald, A. Mamakhel, C. Yang, Y. Huang, B. B. Iversen, F. Besenbacher, J. Catal. 310 (2014) 100.
[29] J. Moreira, B. Serrano, A. Ortiz, H. de Lasa, Chem. Eng. Sci. 78 (2012) 186.
[30] I. Wysocka, E. Kowalska, K. Trzciński, M. Łapiński, G. Nowaczyk, A. Zielińska-Jurek, Nanomaterials (2018) 8.
[31] X. Ma, Y. Dai, M. Guo, B. Huang, Langmuir 29 (2013) 13647.
[32] S. Gao, W. Wang, Y. Ni, C. Lu, Z. Xu, J. Alloy. Compd. 647 (2015) 981.
[33] M. Kowalkińska, S. Dudziak, J. Karczewski, J. Ryl, G. Trykowski, A. Zielińska-Jurek, Chem. Eng. J. 404 (2021), 126493.
[34] H.G. Yang, G. Liu, S.Z. Qiao, C.H. Sun, Y.G. Jin, S.C. Smith, J. Zou, H.M. Cheng, G. Q. Lu, J. Am. Chem. Soc. 131 (2009) 4078.
[35] V.A. Lebedev, D.A. Kozlov, I.V. Kolesnik, A.S. Poluboyarinov, A.E. Becerikli, W. Grünert, A.V. Garshev, Appl. Catal. B: Environ. 195 (2016) 39.
[36] P. Giannozzi, et al., J. Phys.: Condens. Matter 29 (2017), 465901.
[37] P. Giannozzi, et al., J. Phys.: Condens. Matter (2009) 21.
[38] J.P. Perdew, M. Ernzerhof, K. Burke, J.P. Perdew, M. Ernzerhof, K. Burke 9982 (2010) 9982.
[39] R. Beranek, Adv. Phys. Chem. 2011 (2011) 80.
[40] Z. Huang, Z. Wang, K. Lv, Y. Zheng, K. Deng, ACS Appl. Mater. Interfaces 5 (2013) 8663.
[41] M. Li, Y. Chen, W. Li, X. Li, H. Tian, X. Wei, Z. Ren, G. Han, Small (2017) 13.
[42] T.R. Gordon, M. Cargnello, T. Paik, F. Mangolini, R.T. Weber, P. Fornasiero, C. B. Murray, J. Am. Chem. Soc. 134 (2012) 6751.
[43] J. Wang, F. Cao, Z. Bian, M.K.H. Leung, H. Li, Nanoscale 6 (2014) 897.
[44] Y. Chen, W. Li, J. Wang, Y. Gan, L. Liu, M. Ju, Appl. Catal. B: Environ. 191 (2016) 94.
[45] J. Yu, J. Fan, K. Lv, Nanoscale 2 (2010) 2144.

[46] R.O. Ragsdale, B.B. Stewart, Inorg. Chem. 2 (1963) 1002.
[47] Z. Bian, J. Zhu, H. Li, J. Photochem. Photobiol., C 28 (2016) 72.
[48] A. Vioux, Chem. Mater. 9 (1997) 2292.
[49] N. Pinna, G. Garnweitner, M. Antonietti, M. Niederberger, Adv. Mater. 16 (2004) 2196.
[50] G. Garnweitner, M. Niederberger, J. Mater. Chem. 18 (2008) 1171.
[51] R. Pazik, R. Tekoriute, S. Hakansson, R. Wiglusz, W. Strek, G. A. Seisenbaeva, Y. K. Gun'ko, and V. G. Kessler, Chem. - A Eur. J. 15 (2009) 6820.
[52] X.H. Yang, Z. Li, C. Sun, H.G. Yang, C. Li, Chem. Mater. 23 (2011) 3486.
[53] K.S.W. Sing, D.H. Everett, R.A.W. Haul, L. Mascou, R.A. Pierotti, T. Siemieniewska, Pure Appl. Chem. 57 (1985) 603.
[54] J. Liu, P. Li, Z. Sun, Z. Lu, Z. Du, H. Liang, D. Lu, Fuel 210 (2017) 446.
[56] J.Y. Ruzicka, F.A. Bakar, L. Thomsen, B.C. Cowie, C. McNicoll, T. Kemmitt, H.E. A. Brand, B. Ingham, G.G. Andersson, V.B. Golovko, RSC Adv. 4 (2014) 20649.
[57] T. Shi, Y. Duan, K. Lv, Z. Hu, Q. Li, M. Li, X. Li, Front. Chem. 6 (2018) 1.
[58] Y. Wang, L. Li, X. Huang, Q. Li, G. Li, RSC Adv. 5 (2015) 34302.
[59] Y. Wang, H. Zhang, Y. Han, P. Liu, X. Yao, H. Zhao, Chem. Commun. 47 (2011) 2829.
[60] C. Maheu, L. Cardenas, E. Puzenat, P. Afanasiev, C. Geantet, Phys. Chem. Chem. Phys. 20 (2018) 25629.
[61] N.H. Linh, T.Q. Nguyen, W.A. Diño, H. Kasai, Surf. Sci. 633 (2015) 38.
[62] J. Biedrzycki, S. Livraghi, E. Giamello, S. Agnoli, G. Granozzi, J. Phys. Chem. C 118 (2014) 8462.
[63] H. Seo, L.R. Baker, A. Hervier, J. Kim, J.L. Whitten, G.A. Somorjai, Nano Lett. 11 (2011) 751.
[64] F. Pellegrino, E. Morra, L. Mino, G. Martra, M. Chiesa, V. Maurino, J. Phys. Chem. C 124 (2020) 3141.
[65] S. Al Hilli, M. Willander, Sensors 9 (2009) 7445.
[66] E.M. Samsudin, S.B. Abd Hamid, Appl. Surf. Sci. 391 (2017) 326.
[67] W.Q. Fang, X.L. Wang, H. Zhang, Y. Jia, Z. Huo, Z. Li, H. Zhao, H.G. Yang, X. Yao, J. Mater. Chem. A 2 (2014) 3513.
[68] X. Li, J. Yu, M. Jaroniec, Chem. Soc. Rev. 45 (2016) 2603.
[69] T. Hirakawa, K. Yawata, Y. Nosaka, Appl. Catal.: A: General 325 (2007) 105.
[70] Y. Nosaka, A. Nosaka, ACS Energy Lett. 1 (2016) 356.
[71] C. Hou, W. Liu, R. Soc. Open Sci. (2018) 5.
[72] C. Adán, A. Bahamonde, M. Fernández-García, A. Martínez-Arias, Appl. Catal. B: Environ. 72 (2007) 11.
[73] J.J. Murcia, M.C. Hidalgo, J.A. Navío, J. Araña, J.M. Doña Rodríguez, Appl. Catal. B: Environ. 179 (2015) 305.
[74] L. Mino, F. Pellegrino, S. Rades, J. Radnik, V.D. Hodoroaba, G. Spoto, V. Maurino, G. Martra, ACS Appl. Nano Mater. 1 (2018) 5355.
[75] Y. Sui, Q. Liu, T. Jiang, Y. Guo, Appl. Surf. Sci. 426 (2017) 116.
[76] R. Scotti, M. D'Arienzo, A. Testino, F. Morazzoni, Appl. Catal. B: Environ. 88 (2009) 497.
[77] A. Turki, C. Guillard, F. Dappozze, Z. Ksibi, G. Berhault, H. Kochkar, Appl. Catal. B: Environ. 163 (2015) 404.
[78] W. Yu, F. Chen, Y. Wang, L. Zhao, RSC Adv. 10 (2020) 29082.
[79] M. Mrowetz, E. Selli, Phys. Chem. Chem. Phys. 7 (2005) 1100.
[80] M. Kong, Y. Li, X. Chen, T. Tian, P. Fang, F. Zheng, X. Zhao, J. Am. Chem. Soc. 133 (2011) 16414.

15

PUBLICATION [P3]

Surface and Trapping Energies as Predictors for the Photocatalytic Degradation of Aromatic Organic Pollutants

Szymon Dudziak,* Marta Kowalkińska, Jakub Karczewski, Marcin Pisarek, José D. Gouveia, José R. B. Gomes, and Anna Zielińska-Jurek
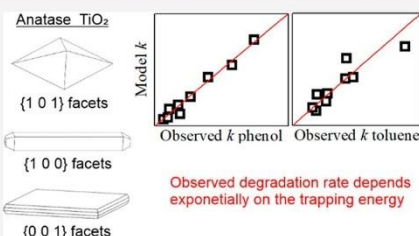
ACCESS | Metrics & More | Article Recommendations

ABSTRACT: In this study, anatase samples enclosed by the majority of three different crystal facets {0 0 1}, {1 0 0}, and {1 0 1} were successfully synthesized. These materials were further studied toward photocatalytic degradation of phenol and toluene as model organic pollutants in water and gas phases. The obtained results were analyzed concerning their surface structure, reaction type, and surface development. Moreover, the regression model was created to find the correlation between the possible predictors and the photodegradation rate constants (k). From the studied factors, the trapping energy of charge carriers at the surface was found to be the most significant one, exponentially affecting the observed k. This resulted in the overall per-surface activity between the samples being in the order {1 0 1} > {1 0 0} > {0 0 1}. Further introduction of the surface energy (E_{surf}) to the regression model and the number of possible trapping centers per number of pollutant's molecules ($n_{trap} \cdot n^{-1}$) improved the model accuracy, simultaneously showing the dependence on the reaction type. In the case of phenol photocatalytic degradation, the best accuracy was observed for the model including $E_{surf} \cdot (n_{trap} \cdot n^{-1})^{1/2}$ relation, while for the toluene degradation, it included E_{surf}^2 and the $S \cdot n^{-1}$ ratio, where S is the simple surface area. Concerning different surface features which influence photocatalytic performance and are commonly discussed in the literature, the results presented in this study suggest that trapping is of particular importance.

Anatase TiO$_2$

{1 0 1} facets

{1 0 0} facets

{0 0 1} facets

Model k — Observed k phenol — Observed k toluene

Observed degradation rate depends exponentially on the trapping energy

1. INTRODUCTION

Following early work on photo-induced reactions over semiconductor particles,[1−4] photocatalytic processes have been widely developed and proposed as a possible way to induce redox reactions inside the chemical systems.[5−7] Primarily, environmental and energy-related applications are extensively studied, including photocatalytic water splitting,[8,9] H$_2$ generation,[10,11] CO$_2$ and heavy metal reduction,[12−14] as well as degradation of organic pollutants from water and air streams.[15−18] Each of these processes is initiated by photon absorption and creation of electron−hole pairs, which can further undergo charge transfer to the substrate present at the surface, inducing its chemical transformation. The efficiency of such a transfer and the number of transferred charge carriers directly determine the final efficiency of the process and strictly depend on the nature of the photocatalyst. Because of this, many studies focus on designing new photocatalytic materials, which could provide the highest efficiency of such photo-to-chemical energy conversion,[19−22] therefore increasing their applicational potential. For an unmodified material, several factors are well known to be crucial in relation to photocatalytic performance in specific reactions, such as valence band/conduction band potentials, band gap type, and light

absorption efficiency.[23−27] Due to the suitable band edge alignment, TiO$_2$ is the most studied photocatalytic material and became almost a standard in the photocatalytic degradation processes of different organic pollutants.[28−33] However, significant differences in performance are observed depending on the synthesis conditions, which influence the structural and textural properties of the photocatalytic material.[34−37] This suggests that comprehensive studies are still needed to describe what makes a specific material an exceptional photocatalyst.

Since the desired charge transfer must occur strictly on the surface, one of the more recent approaches in this aspect is to develop photocatalytic materials with a strictly defined surface structure.[38−42] So far, the presented results have shown that the efficiency of the process strongly depends on the nature of the crystal facet exposed at the photocatalyst's surface.

However, the exact details on what surface features affect observed performance remain an open question. Different properties, including (i) high surface energy,[43,44] (ii) high number of the active sites,[45] (iii) efficient trapping and consumption of the charge carriers,[39] as well as (iv) efficient adsorption of the substrates,[46] are some of the commonly highlighted reasons behind the high photocatalytic activity of such materials. However, majority of the studies presented in the literature considered the above parameters separately, without attempts to indicate the dominant factor, which influence mostly the photocatalytic performance. Simultaneously, from the strictly material design-oriented point of view, it is desired to know which surface feature could be dominant for the considered reaction. Such an approach could help to further design, simulate, and optimize the photocatalyst surface without extensive experimental work. However, such a link between possible surface-related factors and observed activity is hardly found so far.

In this regard, the present study aimed to explain how the surface structure of the anatase affects the photodegradation efficiency of the aromatic organic compounds. Specifically, three questions were raised before this work:

1 Is there a surface structure-related factor that could be identified as the dominant one regarding the photocatalytic degradation of organic pollutants?

2 How this dominant factor affects the observed reaction rate (linearly, exponentially, or other)?

3 If the dominant factor can be recognized, what is the impact of the other factors? For example, can they be neglected?

To find answers for these questions, anatase nanoparticles exposing the majority of the $\{0\,0\,1\}$, $\{1\,0\,0\}$, and $\{1\,0\,1\}$ crystal facets were prepared and used for phenol and toluene photocatalytic degradation in the water and gas phases. Experimental results of degradation were further correlated with well-known factors that describe differences between the exposed facets, such as the surface energy, the number of trapping centers, and the trapping energy. The present work focuses primarily on the simple predictors that should be possible to obtain through computational studies as it might be helpful for further design of new photocatalytic materials without extensive experimental work.

2. METHODS

2.1. Chemicals. Commercial titanium(IV) oxide P25 (Evonik, Germany), ≥96% sodium and potassium hydroxides (POCH, Poland), ≥99% titanium tert-butoxide (Alfa Aesar, Germany), 50% hydrofluoric acid (w/w, Chempur, Poland), ≥99% n-butanol (Alfa Aesar, Germany), ≥99% ammonium chloride (Sigma Aldrich, Germany), and 25% ammonia solution (w/w, POCH, Poland) were used during the syntheses as received from the manufacturers. Phenol, ortho-hydroxyphenol, para-hydroxyphenol, para-benzoquinone (≥98%, Merck, Germany), and toluene (>99.5%, POCH, Poland) were used as model pollutants/byproducts and standards for calibration. High-pressure liquid chromatography (HPLC) grade acetonitrile and H_3PO_4 solution (85% w/w) were used for the mobile phase preparation and provided by Merck, Germany. During the gas-phase experiments, toluene was dispersed in the synthetic air (Air Liquid, Poland).

2.2. Preparation of the Photocatalysts. Anatase TiO_2 nanoparticle, exposing majority of $\{0\,0\,1\}$, $\{1\,0\,0\}$, and $\{1\,0\,1\}$ facets were synthesized in three different reaction systems based on previous reports.[42,47,48] All reactions were prepared under hydrothermal/solvothermal conditions using Teflon-lined reactors of given volume and the laboratory oven. Presented times include approximately 1−1.5 h of oven heating to the final temperature. Preparation of the $\{0\,0\,1\}$ exposed photocatalysts was conducted starting from 17 cm^3 of titanium tert-butoxide as the Ti source, which was mixed with 30 cm^3 of n-butanol and 3.4 cm^3 of 50% HF solution inside the 200 cm^3 reactor. The prepared mixture was heated up to 210 °C for 18 h. Synthesis of the nanoparticles enclosed with the $\{1\,0\,0\}$ facets was started by treating 1 g of commercial P25 titanium dioxide with 40 cm^3 of 10 M sodium hydroxide solution inside the 100 cm^3 reactor at 120 °C for 20 h. The obtained Na-titanate product was centrifuged and washed with water until the pH reached a level between 10 and 11, and half of the product was immediately placed inside the 200 cm^3 reactor without drying. The second synthesis step was carried out using 120 cm^3 of water, and the mixture was heated up to 210 °C for 16 h. Finally, preparation of the nanoparticles exposing $\{1\,0\,1\}$ facets was conducted similar to the $\{1\,0\,0\}$ ones using 40 cm^3 of 8.5 M potassium hydroxide solution in the first step and heating it to 200 °C for 16 h. The obtained analogical K-titanate product was washed with water until pH was between 7 and 8 and dried at 80 °C. The dried product was grounded, and 0.4 g of the final powder was taken for the second reaction using 100 cm^3 of NH_4Cl/NH_4OH buffer, with the concentration of both compounds being 0.3 M (the pH was around 9). The final reaction was conducted at 210 °C for 16 h. All final products were centrifuged and washed with water five times, then dried at 80 °C, and grounded before further characterization.

2.3. Characterization of the Photocatalysts. The obtained materials were analyzed using powder X-ray diffraction (XRD). Measurements were performed using a Rigaku MiniFlex diffractometer with the Cuα radiation source within the 2θ range between 2 and 90°. The scanning speed and step were $1°\cdot min^{-1}$ and 0.005°, respectively. The morphology of the obtained photocatalysts was observed under a FEI Quanta FEG 250 scanning electron microscope (SEM) after covering with the Au layer to help remove introduced excess electrons. Based on the observed morphology, the nature of the exposed facets was confirmed by comparing the symmetry of the nanoparticles with the characteristic shapes. Diffuse reflectance spectroscopy measurements in the UV and visible light range (DR-UV/vis) were performed using a Thermo Fisher Evolution 220 spectrophotometer. Absorption spectra were recorded using $BaSO_4$ as a standard in the incident light range of 200−800 nm. X-ray photoelectron spectroscopy (XPS) measurements were performed using a PHI 5000 VersaProbe (ULVAC-PHI) spectrometer with monochromatic Al Kα radiation (hν = 1486.6 eV) from an X-ray source operating at 100 μm spot size, 25 W, and 15 kV. The high-resolution (HR) XPS spectra were collected with the hemispherical analyzer at the pass energy of 117.4 and the energy step size of 0.1 eV. The X-ray beam was incident at the sample surface at the angle of 45° with respect to the surface normal, and the analyzer axis was located at 45° with respect to the surface. CasaXPS software was used to evaluate the XPS data. Deconvolution of all HR XPS spectra was performed using a Shirley background and a Gaussian peak shape with 30% Lorentzian character. The obtained powders' surface area was measured using the 10-

point Brunauer−Emmet−Teller (BET) isotherm method within the p/p_0 range of 0.05−0.3. Analyses were performed with the Micromeritics Gemini V apparatus at the temperature of 77 K using N_2 as the adsorbate. Before the measurements, each sample was degassed at 140 °C for 3 h under the N_2 flow.

2.4. Photocatalytic Degradation of Phenol. The photocatalyst activity was tested toward removing phenol from the aqueous phase as the model reaction for the water purification process. Each sample was analyzed using a 25 cm³ quartz reactor. Phenol solution was prepared from the stock solution (~500 mg·dm⁻³), and the first sample was analyzed using HPLC/diode array detector (DAD) after dilution and before introducing photocatalysts to check the actual concentration at the start of the process. The prepared suspension of the photocatalyst ((25 ± 0.5) mg in 25 cm³ of phenol solution) was mixed under a magnetic stirrer with 600 rpm, thermostated to (20 ± 1)°C and bubbled with (4 ± 0.5) dm³·h⁻¹ of airflow. The whole system was left for 30 min to achieve adsorption−desorption equilibrium and was further irradiated with the 300 W Xe lamp equipped with the water filter to cut off infrared light. Prior to the process, the reactor-lamp distance was set up to achieve (30 ± 1) mW·cm⁻² of the UV flux at the reactor border.

The collected samples were analyzed using a Shimadzu Prominence HPLC/DAD. Separation was performed using a Phenomenex C18 column operating at 45 °C and with a mobile phase consisting of (v/v) 0.7 acetonitrile, 0.295 water, and 0.05 H_3PO_4 solution (85% w/w). Analyses were performed after the external calibration with pure compounds.

2.5. Photocatalytic Degradation of Toluene. To study the efficiency of toluene degradation in the gas phase, approximately 0.1 g of each sample was dispersed in 5 cm³ of water overnight using a magnetic stirrer, and the prepared suspension was later drop-casted onto the clean glass substrate with the measured dimension to prepared the photocatalyst layer. After applying the suspension, the substrate was dried at 90 °C. For each sample, three substrate sizes were used to achieve a different surface area of the photocatalyst. Further degradation process was performed in a flat stainless-steel reactor with a working volume of 30 cm³. The reactor was equipped with a quartz window, two valves, and a septum, with 25 light-emitting diodes (LEDs) acting as the UV light source (λ_{max} = 375 nm). The intensity of the incident UV light above the photocatalyst layer was (5 ± 0.5) mW·cm⁻².

In a typical experiment, the prepared substrate was placed in the center of the reactor, and the reactor was filled with the mixture of toluene and synthetic air at a flow rate of 0.17 m³·h⁻¹ for 1 min (toluene concentration approx. 40 mg·dm⁻³). After this time, the flow was stopped, and the reactor was closed with the valves. Before the photocatalytic process, the system was kept in the dark for 40 min to achieve an adsorption−desorption equilibrium, followed by 30 min of LED irradiation. The concentration of toluene was measured chromatographically by collecting gas samples from the reactor through the septum using a gastight syringe. Analysis was performed using a gas chromatograph (Clarus 500, Perki-nElmer) equipped with a flame ionization detector and a DB-1 capillary column (30 m × 0.32 mm, film thickness 3.0 μm). Prior to the analysis, calibration was performed using toluene samples with known concentration.

2.6. Analysis of the Results concerning Surface Energy and Trapping Energy. The obtained degradation results were analyzed with respect to the reported values of

surface energy, as well as the trapping energy of e⁻ and h⁺ at the models of the (0 0 1), (1 0 0), and (1 0 1) surfaces.[49,50] The values of both predictors, presented in Table 1, were

Table 1. Reported Surface Energies and Trapping Energies of e⁻ and h⁺ on Different Anatase Surfaces. Presented Values Correspond to Models in Vacuum

surface model	surface energy (J·m⁻²)	trapping energy e⁻ (J·10⁻¹⁹)	trapping energy h⁺ (J·10⁻¹⁹)	refs.
(0 0 1)	0.90	0[a]	0.77	49,50
(1 0 0)	0.53	0.83	1.47	
(1 0 1)	0.44	2.13	1.67	

[a]Reported trapping does not occur at the surface atoms.

obtained from the works of Lazzeri et al. for the surface energy[49] as well as Ma et al. in the case of trapping energies.[50] Prior to the analysis, the results of toluene and phenol degradation were transformed from initial mg·dm⁻³ to mmol·dm⁻³, and the rate constant k was determined assuming I-order kinetics, as commonly observed during the photocatalytic reactions

$$k = d \ln(C_0/C) \cdot dt^{-1}$$

where C_0 is the pollutant concentration at the start of the irradiation, d is the derivative, and t is the time. For further analysis, the total number of pollutant molecules in the reaction system was also calculated to compare with the photocatalyst surface area.[51] Different phenol concentrations and different sizes of the photocatalyst layer were used to achieve different amounts of phenol/toluene molecules reacting per surface unit of each structure. The photocatalyst concentration was fixed for water-phase experiments to minimize its effect on each series' light scattering inside the slurry.[52] Furthermore, additional analysis was also performed upon considering the total number of undercoordinated species on each surface that could act as the trapping center for both charge carriers. In this case, the total surface area was replaced with the calculated number of "active" atoms.

The obtained experimental data were statistically modeled using regression analysis to find the correlation with all considered predictors. Analysis was started from the simple correlation between the available surface area (or the number of active sites) and the number of pollutant molecules. This arranged all results within three groups depending on the surface type. Further analysis considered the difference between these groups to be purely surface-type dependent. Ultimately, different models were analyzed, and their fit to the experimental data was monitored using the residual sum of squares (RSS) to find the best correlation.

2.7. Electron Localization on an F-Modified Anatase TiO₂ (0 0 1) Surface. To study possible electron trapping on the fluorinated {0 0 1} anatase facet, additional density functional theory calculations (DFT) of the (0 0 1) surface slab model were performed using the VASP code.[53−56] The DFT calculations considered dipole-corrections, spin polar-ization, and the Perdew−Burke−Ernzerhof (PBE[57]) ex-change−correlation functional, including D3 dispersion corrections[58,59] to correctly describe the van der Waals interactions. The wave function of valence electrons was expanded using a plane-wave basis set with an energy cutoff of 415 eV, with core electrons implicitly considered with the projector augmented wave method.[60] Orbital occupations were

set using Gaussian smearing with a width of 0.01. Convergence criteria for total energies and for atomic positions were 10^{-5} eV and 0.01 eV/Å, respectively. The Brillouin zone was sampled with a $4 \times 4 \times 1$ Monkhorst–Pack grid of special k-points.[61]

The prepared model consisted of the (0 0 1) surface of TiO_2 as a 3×3 periodically repeated slab with 18 TiO_2 layers (6 Ti layers), terminated by O on the one side (the "bulk" side of the slab) and by F on the other side (the "free" side of the slab). During atomic position optimizations, the nine bottom most TiO_2 units and the oxygen termination were fixed to mimic the bulk structure.[62] The width of the slab was approximately 16 Å, and the simulation box height was fixed at 28 Å, leaving 12 Å of vacuum width to avoid interaction between periodic replicas of the system in the direction perpendicular to the surface.

In order to force charge localization on the surface Ti site, two steps were performed.[63−65] First, the wavefunction of the selected Ti was changed to V, creating a singly negatively charged TiO_2 system since the neutral V atom contains one more electron than a neutral Ti. Also, the V atom contains one more proton in its nucleus than a Ti one, and it attracts electrons more strongly. The second step for localizing charge around a Ti atom consists of replacing the V atom with a Ti one again and using the wavefunction obtained in the first step as the starting point for calculating the electronic density of the TiO_2 system.

3. RESULTS AND DISCUSSION

3.1. Photocatalysts' Characterization. The crystal structure and morphology of the prepared photocatalysts were analyzed with powder XRD measurements and SEM observations to confirm their desired structure. The obtained XRD patterns and selected images from the electron microscope are presented in Figures 1 and 2, respectively.
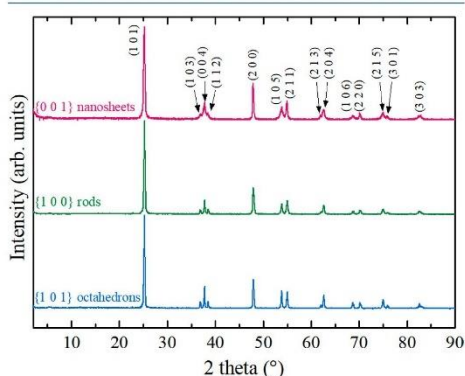

Figure 1. XRD patterns of the obtained samples. All reflections correspond to the anatase TiO_2 crystal structure.

The single-phase anatase structure was present for all samples, only with some differences in the relative intensity of selected signals. This is in agreement with the expected shape variance between the samples since the different sizes of the crystal in a specific direction and their orientation to the X-ray source should affect the width and intensity of the reflections.[40] In this regard, especially broadening of the (0 0 4) and (1 0 5) signals for the {0 0 1} sample is in agreement with the expected size

reduction along with the [0 0 1] direction, which by now is a well-documented effect.[66−72] Furthermore, similar features might also be noticed for the {1 0 0} sample, specifically a broadening of the (2 0 0) signal and the sharp (0 0 4) one. Moreover, for the {1 0 1} sample, no significant broadening of any reflections was noted, with a characteristic higher intensity of the (1 0 5) reflection, compared to the (2 1 1), around 55°.[73,74]

Furthermore, based on the observed width of the XRD reflections, the approximate size of the crystallites in different crystallographic directions was calculated, as shown in Table 2.

Table 2. Calculated Crystallite Size in Different Crystallographic Directions

sample	crystallite size (0 0 4) (nm)	crystallite size (2 0 0) (nm)	crystallite size (1 0 1) (nm)
{0 0 1}	22	38	39
{1 0 0}	149	115	46
{1 0 1}	81	46	41

As observed, the relative difference in the observed dimensions match quite well the expected trends. Especially, the crystallite size along the [0 0 1] direction, calculated from the (0 0 4) reflection, is the lowest for the sample exposing {0 0 1} and the highest for the {1 0 0} one. Moreover, the sample exposing {0 0 1} is the only one with the higher size observed along the [1 0 0] direction, based on the (2 0 0) reflection, than [0 0 1].

Nevertheless, since XRD analysis alone is not sufficient for the determination of exposed facets, it was further completed with the morphology observation for all samples. The expected shape of the nanocrystal in each case can be obtained based on the Wulff theorem and the known symmetry of the anatase structure.[75] The comparison between expected and observed morphologies is presented in Figure 2. As shown, the real samples match their theoretical constructs very well, with rectangular sheets, rectangular rods, and octahedrons being formed for the samples exposing the {0 0 1}, {1 0 0}, and {1 0 1} facets, respectively. The formation of each structure results directly from the combination of HF with n-butanol in the case of the {0 0 1} sample[76,77] as well as from the pH increase during the growth of the {1 0 1} structures (pH ~ 9) and the {1 0 0} ones (pH > 10).[78]

Furthermore, to study the possible defect formation inside the obtained nanoparticles, additional DR-UV/vis and XPS studies were performed. As shown in Figure 3, all of the samples possess similar surface composition, with Ti 2p and O 1s signals being typical for the stoichiometric TiO_2. Especially, no signs of Ti^{3+} states are visible for all samples, as well as the amount of non-lattice oxygen is both limited and similar between different structures. These additional O signals could be easily connected with the presence of adsorbed carbon species on the samples' surface, which is typical during the XPS analysis. The only noteworthy feature is the clearly visible presence of fluoride on the surface of the sample exposing {0 0 1} facets, which match reported signals for the fluorinated TiO_2 (approx. 684.5 eV). Fluorine presence resulted from the HF introduction during the synthesis and is typical for the HF-mediated stabilization of the {0 0 1} facets. No signs of a lattice O-substitution by F is observed (XPS signals for the binding energy ≥685 eV),[79−81] and therefore all of the observed fluoride is simply adsorbed on the surface Ti. The atomic F/Ti ratio is 0.25.
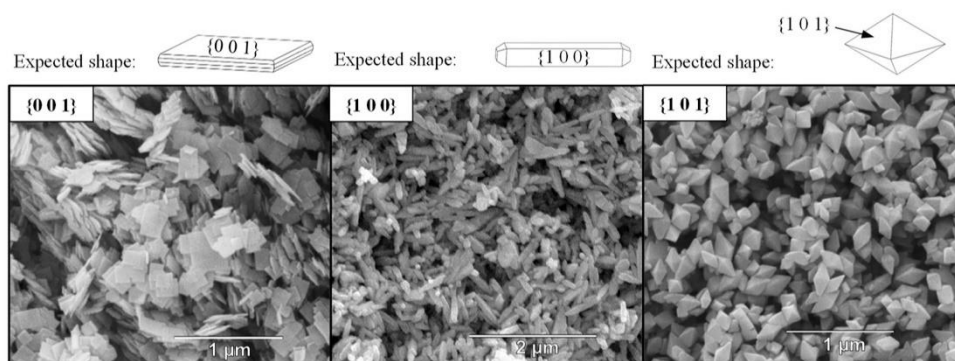
Figure 2. SEM images of the obtained samples and their expected shapes based on the designed facet exposition.
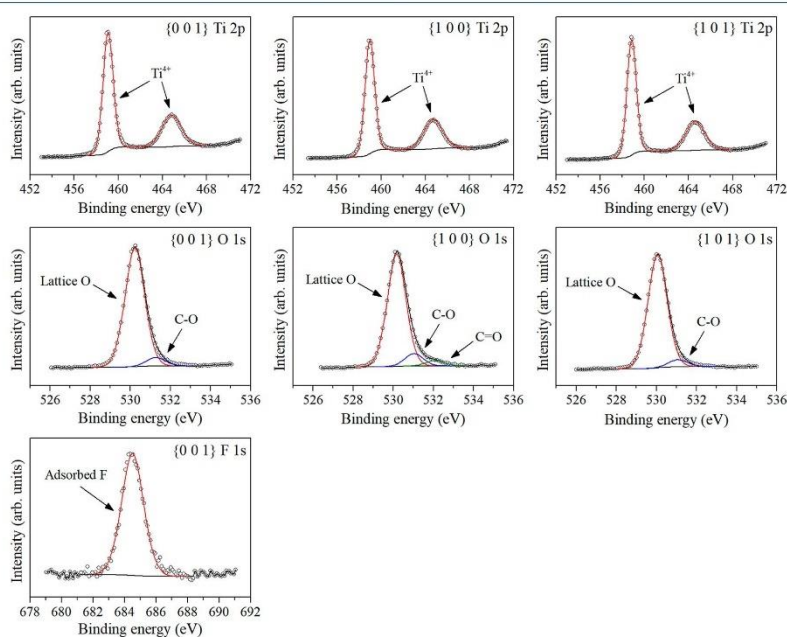
Figure 3. XPS signals observed for the Ti, O, and F states on the surface of each nanostructure.

Moreover, as shown in Figure 4, the energy of the valence band edge observed during the XPS studies is very consistent between the samples, showing that no shifts in the Fermi energy level are present. Especially, this shows that no acceptor defect states should be present above the valence band edge for each nanostructure.

Finally, the absorption spectra of the prepared samples are shown in Figure 5a. Similar to the XPS studies, no significant difference in the observed signals is noticed, and especially no defined peaks are present for $\lambda > 400$ nm. Furthermore, the absorption edge for the valence-to-conduction band excitation

is almost the same for all nanostructures, and the corresponding band gap values are very similar for all samples (Figure 5b). Comparing this with the position of the valence band edge from Figure 4, it can be seen that the Fermi level of all samples is also similar and lies approximately 0.35 eV below the conduction band edge. This is reasonable with the anatase being the n-type semiconductor and further proves that no significant concentration of defects should be present within each sample, as well as they do not alternate the surface states of the photocatalyst, as evidenced by XPS. In this regard, the surface structure of all samples is expected to closely represent

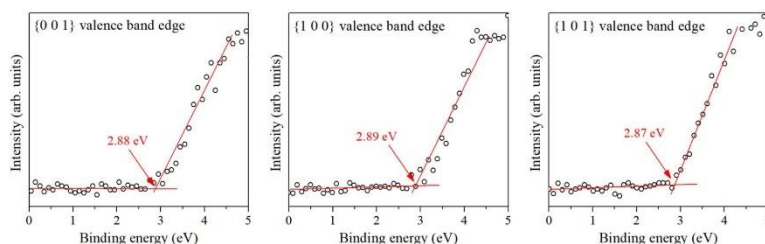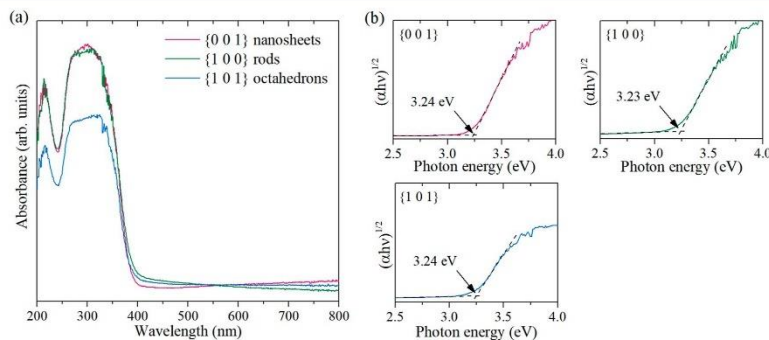**Figure 4.** Valence band edge observed for each sample during the XPS studies.

Figure 5. DR-UV/vis absorption spectra of the obtained TiO$_2$ samples, exposing different crystal facets (a), as well as the corresponding Tauc's plots and determined band gap values (b).

Table 3. Summation of the Experimental Factors Affecting the Observed Degradation Efficiency, as Measured Before the Photocatalytic Tests

sample	BET surface area ($m^2 \cdot g^{-1}$)	aqueous phase		gas phase
		photocatalyst mass (mg)	initial phenol concentration (mmol·dm^{-3})	photocatalyst's layer mass (mg)
{0 0 1}	38	24.99	0.332	10.02
		25.14	0.217	16.28
		25.41	0.108	32.65
{1 0 0}	13	25.41	0.323	10.59
		24.99	0.207	19.12
		25.05	0.108	28.08
{1 0 1}	13	24.57	0.319	5.74
		24.47	0.203	12.53
		24.59	0.101	14.71

their theoretical models, excluding F adsorbed on the {0 0 1} facets, which justify the analysis of their activity with respect to the different predictors presented in the computational studies.

3.2. Photocatalytic Degradation in Water and Gas Phases. Prior to testing the photocatalytic activity of the obtained materials, the surface area of the powders was measured using the BET method, and the masses of the photocatalyst's layer on the substrate were precisely determined. These data were summarized in Table 3, together with the exact photocatalyst mass introduced during the water-phase experiments and the initial concentration of phenol (to account for possible error during dilution). Regarding the gas-phase experiments, the toluene concentration was fixed

between the processes. Therefore, it was not considered to affect the observed differences between the samples.

Furthermore, Figure 6 presents the as-observed photo-catalytic degradation rates of phenol and toluene over the prepared samples, and the slope of the fitted line defines the reaction rate constant k. A visible effect of all three factors can be observed from the very start of the analysis (surface type, phenol concentration/layer area, and gaseous/aqueous environment). In each case, increasing the number of pollutant molecules reacting per surface of the photocatalyst lowered the observed rate constant. This is in agreement with the expected outcome since an increase in the surface area is known to promote faster reaction rates as it provides more active centers for the reaction to occur.[51] Similarly, changing the amount of
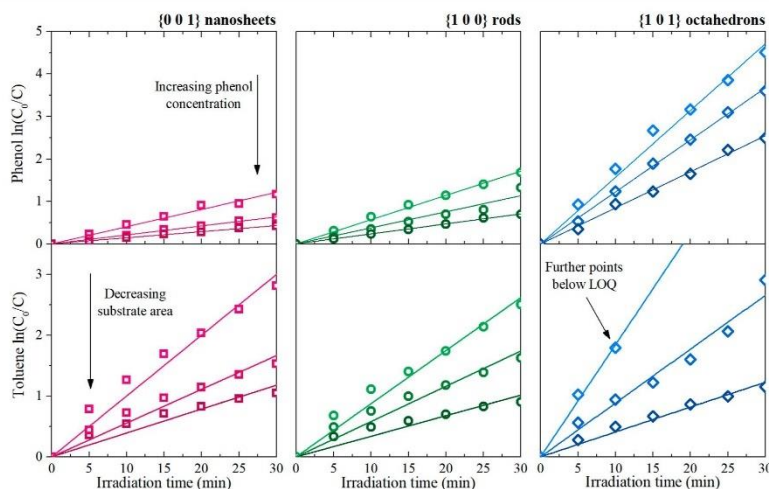
Figure 6. As-obtained phenol and toluene degradation results over the prepared samples, without accounting for possible factors (LOQ stands for "limit of quantification"). The slope of the fitted lines is the rate constant (k) for the I-order reaction $\ln(C_0/C) = k \cdot t$.

the reacting pollutant will give the same result, and the final reaction rate will increase proportionally to the $S \cdot n^{-1}$ ratio. This ratio should roughly represent the number of active centers that are "free" to react with a single pollutant's molecule (S is the total surface area and n is the number of pollutant molecules). The same relation was also observed previously for the series of different {0 0 1} exposed anatase nanosheets.[42]

Ultimately, Figure 7 presents the detailed results of the phenol degradation and formation of its aromatic byproducts, including *ortho* and *para*-hydroxylated species. As observed, the amount of degraded phenol strictly correlates with the amount of the oxidized species, proving that the observed kinetics of phenol removal represents its chemical transformation rather than a photo-stimulated adsorption. For the highest removal rates (the {1 0 1} samples), the rapid formation of the observed byproducts is followed by their further disappearance, which is expected in the case of step-by-step oxidation. For all series, increasing the initial phenol concentration results in higher amounts of formed byproducts and their slower subsequent removal. This would fit the expected results as the number of "free" active sites should be lower when the amount of initial pollutant increases; therefore, further reaction of byproducts became limited and their higher accumulation is observed.

Regarding the surface structure, high activity of the {1 0 1} enclosed octahedrons was noticed for both reactions, while it especially dominated in the aqueous phase. This is despite the lowest surface area of this sample. Therefore, the surface energy should not be a dominant factor for both reactions since the {1 0 1} surfaces possess the lowest surface energy. In the aqueous phase, all samples clearly followed the per-surface activity order of {1 0 1} > {1 0 0} > {0 0 1}, which is in agreement with some other studies that have shown relatively low activity of the {0 0 1} surfaces.[38,39] On the other hand, the

difference between the octahedrons and other structures is less visible in the gas phase.

Concerning the {0 0 1} nanosheets and {1 0 0} rods, they revealed similar activity in both reactions; however, the measured surface area of the {0 0 1} nanosheets was still 3 times larger than that of the {1 0 0} rods. However, the surface area exposed to the reaction system is hard to be accurately provided in the gas phase due to the unknown porosity of the prepared layer. In such a case, the facile measurement of the photocatalyst layer area may be inaccurate because particle geometry affects the roughness of the layer and further diffusion of the substrate through the film.[82] Therefore, an approach similar to the aqueous phase was applied, assuming the total possible area of the photocatalyst through measured mass and BET results. That should partially correct the effect of the particles' morphology on the actual area available for the reaction in the gas phase. By accepting this approach, the per-surface activity order in the gas phase became the same as in water due to the high surface area of the {0 0 1} samples. However, these differences are less noticeable than for phenol degradation. Ultimately, this suggests that surface energy might be a more important factor during the gas-phase process. These results are shown in Figure 8, in which observed k is presented concerning the $S \cdot n^{-1}$ ratio, clearly dividing the data into three series depending on the surface type. These could be described as

$$k = a \cdot S \cdot n^{-1}$$

where k is the rate constant defined by the slope in Figure 6, a is the fitted constant, S is the total surface area of the photocatalyst during the process, defined by its mass and BET surface area, and n denotes the amount of pollutant molecules at the start of the process. Specifically

$$n = \frac{C_{mmol} \cdot V \cdot N_A}{1000}$$

14865
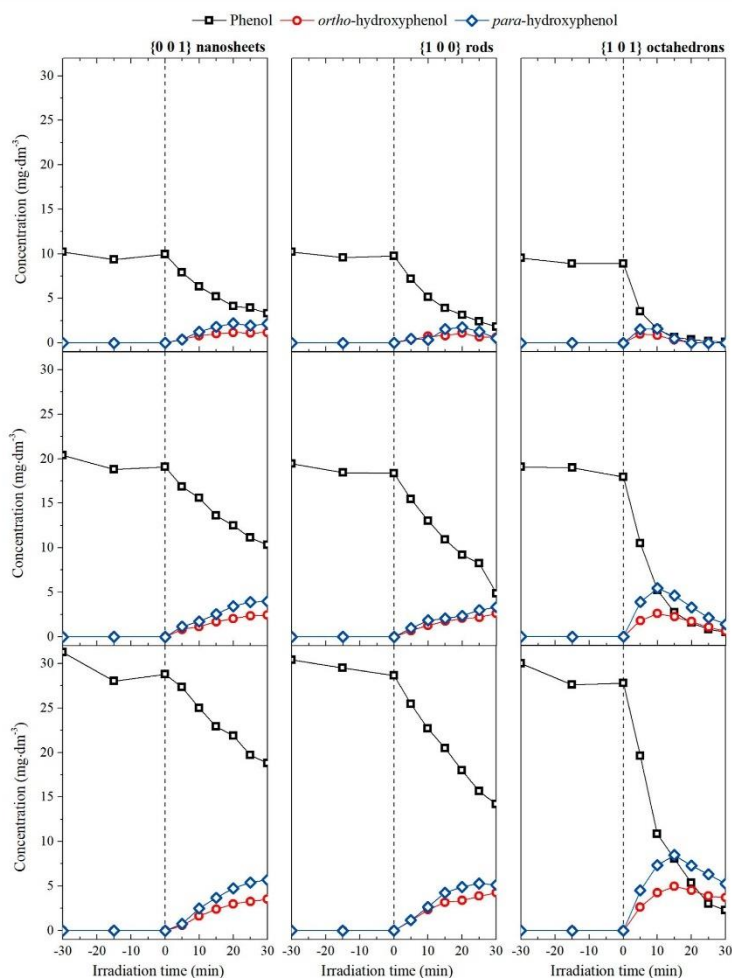
Figure 7. Detailed results of the photocatalytic phenol degradation in the aqueous phase.

where C_{mmol} is the pollutant's concentration in mmol·dm^{-3}, V is the reactor volume in dm^3, and N_A is the Avogadro number. Starting from this point, the slope of the fitted lines in Figure 8 (a parameter) should depend strictly on the nature of the exposed facet. Therefore, further analysis of the fitted a was performed with respect to the discussed predictors.

3.3. Analysis with Respect to Trapping Energy. Since octahedral particles, enclosed with the {1 0 1} facets, was found to be the most photocatalytic active in both reactions, analysis of the fitted a was started by finding its correlation with the trapping energy, which is the highest for this surface (see Table 1). Figure 9 shows a as a function of total trapping energy E_{trap} (simple sum of both electron and hole trapping

energies), together with an additional (0, 0) point, representing the hypothetical situation of no surface present.

In the case of both reactions, this relation follows the exponential character, which could be specially connected with the possible distribution of the trapped states. As suggested by Ma et al., the difference in the trapping energy should influence the distribution of the trapped states, following Boltzmann distribution.[50] Then, the concentration of these states should affect the actual performance observed during the photocatalytic reaction. Therefore, further analysis was performed assuming the general formula of

$$a = b \cdot \left(e^{c \cdot E_{trap} / k_B T} - 1 \right)$$

Figure 8. Obtained results of phenol and toluene degradation with respect to the ratio between the total surface area of the photocatalyst (S) and the number of the pollutant molecules at the start of the process (n).
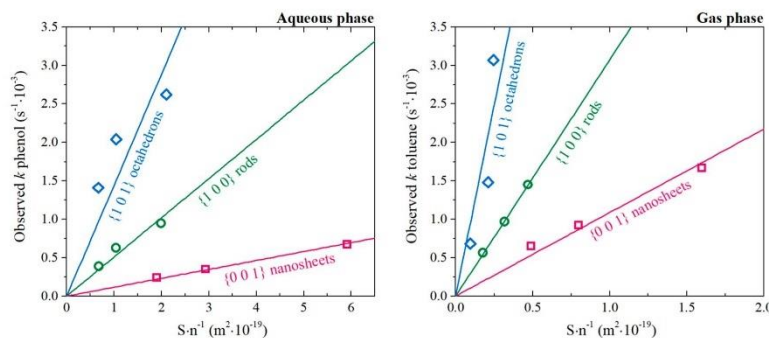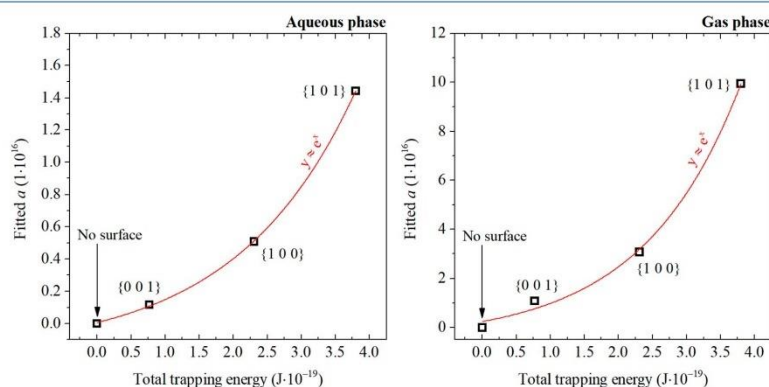

Figure 9. Correlation between the observed a parameter and the total trapping energy (sum of electron and hole trapping energies) reported for each surface. The presented $y = e^x$ line is drawn here only to highlight the general correlation.

Table 4. Results of a Fitting to the Expression $a = b \cdot (e^{E_{trap}/k_B T \cdot c} - 1)$

$a = b \cdot (e^{E_{trap}/k_B T \cdot c} - 1)$	R^2	fitted b	fitted c	reported photonic efficiency of •OH generation by TiO_2	ref.
aqueous phase	0.9998	$1.93387 \cdot 10^{15}$	0.02275	between 0.029 and 0.035	[86]
gas phase	0.9936	$9.66209 \cdot 10^{15}$	0.02581		

where a is the analyzed slope from Figure 8, E_{trap} is the total trapping energy, as defined before, k_B is the Boltzmann constant, T is the absolute temperature, and b, c are further fitted parameters. The summation of this analysis is presented in Table 4, showing an excellent correlation in both cases. Moreover, it could be further reasoned that the obtained c parameter probably indicates the fraction of the trapped charge carriers that effectively react at the surface. During the photocatalytic degradation of aromatic pollutants, the generation of different reactive oxygen species (ROS) is crucial, and the actual oxidation is often initiated by the attack of generated radicals.[29,83] Therefore, step-by-step illustration of the process could be divided into four consecutive processes, namely, (i) generation of charge carriers, (ii) their trapping at the surface, (iii) surface reaction to generate ROS, and (iv) reaction between ROS and the pollutant. Possible reactions

(eqs 1–7) are shown below for the photogenerated charge carriers[28,84,85]

$$TiO_2 + h\nu \rightarrow h^+ + e^- \tag{1}$$

$$h^+ \rightarrow h^+_{trapped} \tag{2}$$

$$e^- \rightarrow e^-_{trapped} \tag{3}$$

$$h^+_{trapped} + H_2O \rightarrow \bullet OH + H^+ \tag{4}$$

$$e^-_{trapped} + O_2 \rightarrow \bullet O_2^- \tag{5}$$

$$\bullet OH + A \rightarrow A-OH \tag{6}$$

$$\bullet O_2^- + AH \rightarrow \bullet A + HO_2^- \tag{7}$$

14867
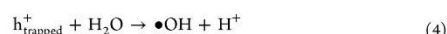
Figure 10. Predicted vs observed k and the residual plot for both reactions, obtained with the model considering only the trapping energy and the $S \cdot n^{-1}$ ratio. Parameters obtained from the regression analysis are presented in Table 4.
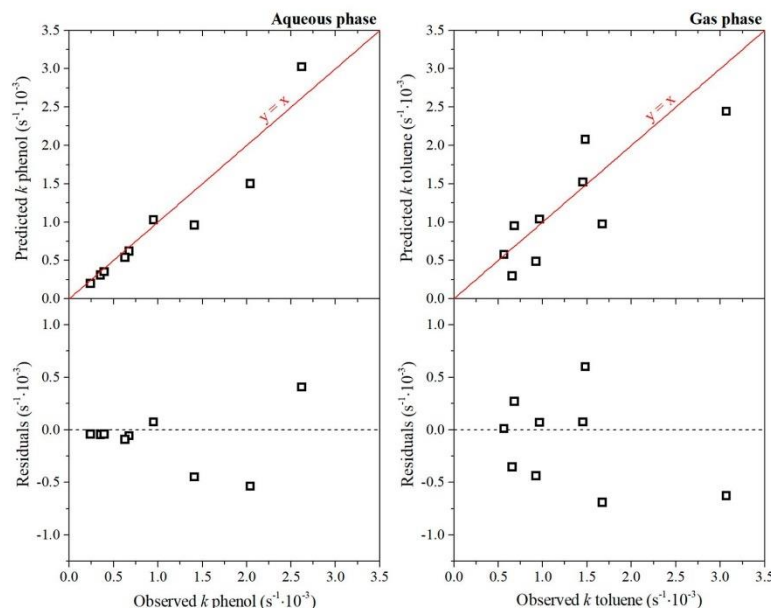
In this study, the rate constant of the final steps that leads to the chemical transformation of the pollutant using eqs 6 and 7 was calculated, while especially reactions 2 and 3 should be driven by the analyzed trapping energy. However, it seems not possible for all trapped states to effectively contribute to the final rate since it would imply that reactions 4 reactions −7 are occurring with 100% efficiency. Therefore, the c parameter must appear to "slow down" the process rate that could be expected from the simple increase of the trapping energy. Moreover, although the strict interpretation of the c parameter is not obvious, it could be noted that its values of approximately 0.02−0.03 are close to the reported photonic efficiency of •OH generation by TiO_2 (approx. 3%[86]). In this regard, it might be suggested that these parameters are somehow connected, for example, both will be affected by the possible surface recombination. Ultimately, it is shown that the observed rate should follow the trapping energy exponentially, with the exponent being $E_{trap}/k_B T \cdot c$, and c might be a fraction of maximum possible trapped states that will effectively influence the reaction.

At this point, straightforward prediction of k, based on the calculated $S \cdot n^{-1}$ ratio and analyzed trapping energy, reproduces the overall activity order well. This indicates that E_{trap} is probably the most important factor affecting the final rate. Although it is not possible to directly identify reaction steps through such an analysis, these results are in agreement with, for example, the general mechanism of •OH formation on the anatase TiO_2 surface presented by Nosaka and Nosaka, which includes h+ trapping on the surface O atom and the subsequent H_2O attack.[28] However, Shirai et al. reported that details of

such a process might differ between the spherical and faceted particles. In particular, the water-assisted hole trapping was not observed for the {0 0 1} and {1 0 1} anatase facets, and {1 0 0} was not considered.[87] In this regard, the detailed mechanism of possible reaction 4 might not be obvious for all nanostructures, and a more complex mechanism might be discussed. First of all, as shown by Chen et al., formation of the •OH radicals on the {1 0 1} facet might involve h+ trapping on the surface 3-fold coordinated O atom and subsequent transfer to the terminal −OH group, which was found to be an energetically favorable process.[88] This might be further reasoned since −OH groups are commonly observed on the TiO_2 surface, for example, on the FTIR spectrum.[89] Furthermore, other species are also expected to be present at the photocatalyst surface depending on the environment (gas/liquid, pH, O_2 concentration, and adsorbed pollutant), which could further affect charge carriers trapping and transfer.[90] As recently reported by Hwang et al., formation of •OH might also include the reductive path from O_2, which contributed to approximately one-third of the observed oxidation product of benzoic acid over anatase particles.[91] During such a reaction, H_2O is expected to react with the surface O_2 in the presence of excited electrons. As reported by Setvin et al., this specific process on the {1 0 1} facet induces dissociation of water to OOH^- and OH^-, which becomes almost a barrierless reaction.[92] Therefore, due to the reduction process on the {1 0 1} facet, generation of the •OH radicals might also be increased through the subsequent oxidation of OH^-, rather than H_2O itself. This might also be stimulated by the relatively high water

adsorption and Lewis acidity, previously reported for this surface.[89]

Unfortunately, due to the limited number of such detailed studies, similar cooperation between the reduction and oxidation of oxygen/water can be analyzed in detail only for the {1 0 1} facets. Therefore, more detailed studies on the reactivity of all these facets to generate different ROS, for example, in different environments, are planned to give better insight into the details of their possible formation. Nevertheless, the presented description of the possible reactions on the {1 0 1} combine both h⁺ and e⁻ processes to "cooperate" with one another due to (i) e⁻/O_2 induced dissociation of water and (ii) h⁺ reaction with the OH⁻ generated through this dissociation, and this fits the presented trend nicely, explaining why the high trapping energy of both charge carriers on the {1 0 1} facets resulted in its highest observed activity. Ultimately, Figure 10 shows the plots of predicted versus observed k for both reactions, when only the trapping energy was considered to determine a, as well as calculated residuals for both cases ($k_{model} - k_{obs}$). Specifically

$$k = b \cdot \frac{S}{n} \cdot \left(e^{c \cdot \frac{E_{trap}}{k_B T}} - 1\right)$$

As seen, especially in the case of phenol degradation, some points are predicted very well. However, the overall error might still achieve quite large values, especially for the high k (up to 40% of the observed rate constant), as well as predictions for toluene are generally erroneous, despite the overall trend being preserved. In this regard, other factors that might improve possible predictions were studied.

3.4. Further Analysis concerning the Surface Energy and the Number of Trapping Centers.

The analysis described in the previous section focused on the reported trapping energies of holes and electrons on the obtained anatase crystal surfaces. These energies should especially influence the probability of charge carriers' trapping at the surface, which could react with other substrates, as outlined in the previous section. However, to describe the whole process properly, this should be further connected with the number of trapping centers and the number of reacting molecules at the surface. Initially, it was assumed to be proportional to the $S \cdot n^{-1}$ ratio; however, further considerations might be made to improve this relationship. First of all, it is known that different surfaces have different numbers of different-coordinated atoms that could effectively trap both charge carriers. Although it was highlighted before that specific trapping behavior can change due to the presence of adsorbates, the details are not presented for all surfaces.[87,93] Therefore, at this point, we will follow the trapping description presented in the same study as adopted trapping energies (in vacuum) since they are strictly connected and still allow to relatively compare analyzed facets. Based on these results, the theoretical number of surface atoms that could effectively start the reaction was calculated. For the (1 0 0) and (1 0 1) surface models, this is equal to the number of both 5-fold coordinated Ti atoms (5f-Ti) and 2-fold coordinated O atoms (2f-O) as both electrons and holes should effectively localize on them.[50] However, in the case of the (1 0 0) surface, Ma et al. have shown that these electrons partially delocalize over the surface 5f-Ti atoms.[50] In this regard, it could be expected that not all Ti sites can effectively trap e⁻ for this surface. Therefore, the density of 5f-Ti atoms that could trap electrons on (1 0 0) was arbitrarily reduced to

represent only two-third of the total Ti atoms. Finally, surface localization of electrons is not occurring for the (0 0 1) model,[50,93,94] as highlighted before. Therefore, the possible number of active centers should correspond only to holes trapping on the 2f-O atoms. These values are presented in Table 5.

Table 5. Calculated Number of 5f-Ti Atoms and 2f-O Atoms That Could act as a Trapping Center for e⁻ and h⁺, Based on the Surface Structures and Trapping Process Described in the Literature

surface model	5f-Ti atoms available for e⁻ trapping ($10^{18} \cdot m^{-2}$)	2f-O atoms available for h⁺ trapping ($10^{18} \cdot m^{-2}$)	refs.
(0 0 1)	0[a]	6.96378	
(1 0 0)	3.70300[b]	5.55450	49,50
(1 0 1)	5.15191	5.15191	

[a]Reported trapping does not occur at the surface. [b]Arbitrarily reduced by one-third due to partial delocalization over adjusting 5f-Ti.

Based on the obtained number of "active" atoms on the surface, the initial $S \cdot n^{-1}$ ratio was rearranged to the actual number of possible trapping centers (n_{trap}) per number of pollutant molecules (n). Furthermore, the actual number of reacting molecules should differ depending on its adsorption rate from the fluid to the surface. This process should especially depend on the surface energy (E_{surf}) as it will influence the final energy of adsorption.[95] Therefore, the surface energy was introduced as a final factor in the considered model. Starting from this point, identical analysis was performed; however, the initial $S \cdot n^{-1}$ ratio was changed to the number of different expressions, including either the surface energy or the calculated $n_{trap} \cdot n^{-1}$ ratio. Therefore, the value on X-axis in Figure 8 was changed, which affected the obtained a parameter. Ultimately, the new a value was fitted to the trapping energy in the same way as before. To represent model consistency with the experimental results, the RSS was calculated for each considered model. As presented in Table 6, introduction of different terms either improved or worsened the model's fit depending on the reaction type. Nevertheless, a visibly better fit can be obtained when specific terms were introduced. Concerning the phenol degradation, introduction of both E_{surf} and the square root of $n_{trap} \cdot n^{-1}$ allowed to achieve the best model accuracy, which especially resulted from the better fit for the high k values.

For the toluene degradation reaction, mostly the presence of the second power of E_{surf} improves model accuracy when both $n_{trap} \cdot n^{-1}$ and $S \cdot n^{-1}$ ratios were considered. However, the best fit is still obtained when a simple surface area is considered instead of the number of the trapping sites. First of all, this shows that different contributions of the surface energy might be expected for different reaction systems. Especially, it might be suggested that surface energy contributes more to the mass transfer inside the system for the gas-phase process since this reaction was performed in static air. Second, it shows that estimation of the active sites present during the gas-phase process is less accurate than for the phenol degradation. This probably results from the difficulties to precisely determine the fraction of the prepared layer, which is freely exposed to the reaction system. Nevertheless, as shown in Figure 11, the general predictions of both models are good, especially in the case of phenol degradation. The highest error is observed mostly for the high k values in the case of toluene degradation,

Table 6. RSS Obtained for the Models Calculated Using Different Terms in the First Step of the Fitting

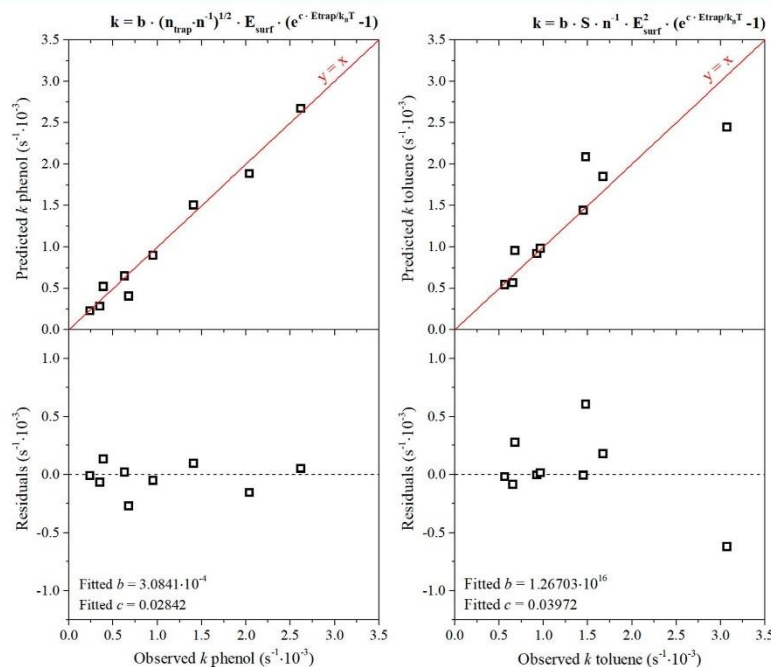| RSS·(10^{-6})	S·n−1	Esurf·S·n−1	Esurf2·S·n−1	ntrap·n−1	Esurf·ntrap·n−1	Esurf2·ntrap·n−1	Esurf·(n_{trap}·n^{-1})$^{1/2}$
phenol	0.68	0.71	1.08	0.71	0.67	0.82	**0.14**
toluene	1.64	1.09	**0.87**	1.90	1.37	**0.90**	2.45

Figure 11. Predicted versus observed k and the residual plot for both reactions, obtained with the best-fitting model for both cases.

and specifically, this is for the {1 0 1} enclosed octahedral nanoparticles. This suggests that samples enclosed with these facets might behave slightly different from the {1 0 0} and {0 0 1} ones in the gas phase.

Finally, it could be also noticed that similar behavior was observed for the phenol degradation process. In this case, the introduction of the E_{surf}·(n_{trap}·n^{-1})$^{1/2}$ term produced the best results overall. However, this mainly resulted from the best fit for the high k values (so, the octahedral samples), while actually for the low k, the relative error was the lowest for the E_{surf}·n_{trap}·n^{-1} term. In fact, the better fit exclusively for the low phenol k values is observed even in Figure 10 than in Figure 11. Ultimately, this suggests that there might be a significant difference in the effect of crucial factors for low and high surface-to-pollutant ratios.

3.5. Side Facets Effect and Variance with Different E_{surf} Values. The analysis performed so far was focused on the properties of facets that were found to be dominant for each sample. However, especially in the case of the {0 0 1} and {1 0 0} exposing nanostructures, additional facets must appear at the side/end of the particle to "close" its three-dimensional structure. These additional side facets are most likely to influence the final activity due to the different properties and

possible charge separation. Unfortunately, precise description of such facets is difficult when their content is reduced and formation of the strictly defined structures is often not observed. Instead, less defined structures, curvatures, and combinations of different facets and microfacets also appear, whose exact structure and properties are not precisely known. In this regard, their systematic introduction into the model is much more complicated than in the case of the dominant facets.

Nevertheless, some simplified approach can be introduced and analyzed, assuming that these side facets would have properties similar to the {1 0 1} one. This could be especially justified by noticing that most of the possible side facets, including structures like {1 0 1}, {1 0 3}, {1 0 5}, or {1 1 0}, can expose low-coordinated titanium atoms (4-fold) on the surface, which can especially promote electron trapping. Therefore, possible trapping of the charge carriers should be enhanced if such structures would appear along with the {0 0 1} or {1 0 0} facets. As a result, the E_{trap} value in the model should be increased. This effect can be partially corrected if we assume E_{trap} to be a weighted mean between the dominant facet and the {1 0 1} one, where weights are their approximate share in the particle's surface. Specifically
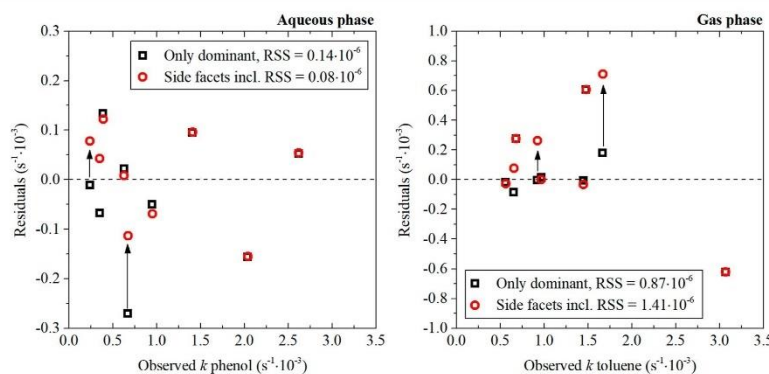
14870

Figure 12. Comparison of the models' accuracy with and without considering possible effects of the side facets for the {0 0 1} and {1 0 0} exposing nanoparticles. Arrows indicate changes most contributing to the total accuracy.

$$E_{trap} = E_{dominant} \cdot x_{dominant} + E_{\{1\ 0\ 1\}} \cdot x_{\{1\ 0\ 1\}}$$

where $E_{dominant}$ and $E_{\{101\}}$ are the trapping energies reported for the dominant facet and {1 0 1} one, respectively, and x is their corresponding share in the particle's surface ($x_{dominant} + x_{\{101\}} = 1$). To obtain x values, detailed analysis of the particles' morphology was performed based on the SEM images, and estimated share of the dominant facet was calculated following the observed lengths and theoretical orientation between the (0 0 1)/(1 0 0) and the (1 0 1) crystal planes of anatase (these could be easily obtained from the commonly accessible.cif files). Ultimately, the calculated share of the dominant facets is approximately 80% for the {0 0 1} exposing sample and 82% for the {1 0 0} one. The remainder of the particles is assumed to be enclosed by the {1 0 1} facets in both cases. Based on these values, the modified E_{trap} energy was introduced to the analysis for the best-fitting models, as well as E_{surf} and n_{trap}, recalculated analogically to the trapping energy.

As presented in Figure 12 based on the calculated residuals, such an approach gave only a moderate change to the model accuracy, mostly affecting individual points indicated with arrows. Moreover, the effect is opposite for the gas and aqueous phases, that is, for the phenol degradation, it improved accuracy, while it decreased for toluene. While this is in some consistency with the previous observations, showing generally that a more accurate model is possible to obtain when particles are dispersed in water, more details are probably needed to introduce a similar analysis with a significant effect. In this regard, especially more studies on the facet-to-facet junctions would be necessary to precisely describe their interactions in a quantitative way.

Finally, it was also studied how different values of E_{surf} reported in the literature could affect the accuracy of the developed model. To do so, different models were developed based on the surface energies summarized in Table 7.

The change in the model accuracy when developed with different E_{surf} values is presented in Figure 13 as the observed maximum, mean, and minimum absolute residual values. Noteworthy, the effect is quite small, with the error change between different models being generally $\leq 5 \cdot 10^{-5}$ s^{-1}. This is approximately 15% of the lowest rate constants and approximately 5% of the mean values for both reactions.

Table 7. Different Values of Surface Energies Reported in the Literature, Used for the Models' Comparison

Surface energy (J·m^{-2})	Lazzeri et al. PBE	Lazzeri et al. LDA	Mino et al. fixed cell	Mino et al. relaxed cell	Arrouvel et al.	Zhao et al.
{0 0 1}	0.90	1.38	1.275	1.12	0.98	1.08
{1 0 0}	0.53	0.96	0.79	0.76	0.53	0.71
{1 0 1}	0.44	0.84	0.67	0.64	0.44	0.61
ref.	49	49	96	96	97	98

Moreover, it could be observed that the highest and lowest errors in the gas phase are almost independent of the surface energy value. Therefore, compared to previous analysis, the effect is quite small, and models with analogical accuracy can be obtained with different E_{surf} values (e.g., changes indicated in Figure 12 are generally 1 order of magnitude higher than here). This is in some general agreement with the known accuracy of the DFT methods, which show that while the exact obtained values could differ between the studies/methods, the observed trends are more robust and the change is similar for all considered models. Therefore, as long as the analyzed values are obtained with the same computational details, their effect on the final model is nearly the same.

3.6. Fluorination of the {0 0 1} Facets and Model Limitations. The presented analysis shows that the activity of the TiO$_2$ nanostructures in the degradation process of organic compounds is mostly controlled by the charge carriers trapped on the photocatalyst surface. This process is heavily affected by the exposed crystal facet, and therefore, through computational analysis of such trapping behavior, it is possible to predict the activity of the final nanostructure. However, it should be noted that some limitations of such approach are still present. First of all, the performed studies are based on the models of ideal surfaces, which under the real conditions are not always expected. For example, fluorination of the {0 0 1} facets was observed during this study as a result of HF-mediated growth. Right now, the presence of different adsorbed species, and fluorine in particular,[99−101] is known to affect the chemical states on the TiO$_2$ surface. However, it is not arbitrarily known how exactly it will affect the distribution of the trapped charge carriers. For example, Mino et al. have observed that removal of the fluorine from the {0 0 1} facets by NaOH washing
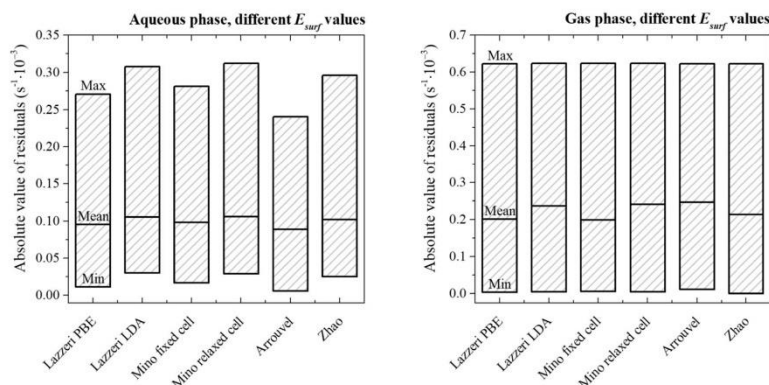
Figure 13. Comparison of absolute error values (maximum, mean, and minimum) for models developed with different reported values of surface energy for the dominant facets.
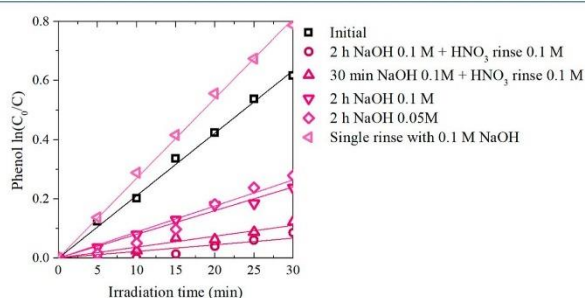

Figure 14. Effect of different washing procedures on the observed photocatalytic activity of the anatase particles with exposed {0 0 1} facets in the degradation of 20 mg·dm^{-3} phenol solution.

Table 8. Effect of Washing the {0 0 1} Nanosheets With NaOH Solution on the Details of the Best-Fitting Models for Both Reactions

	aqueous phase		gas phase	
	before wash	after wash	before wash	after wash
fitted a for {0 0 1} series	3.18858·10−4	4.0763·10^{-4}	1.34236·10^{16}	1.71608·10^{16}
R^2 exp fit of a for all series	0.9985	0.99495	0.99957	0.99993
fitted b	3.0841·10^{-4}	3.32709·10^{-4}	1.26703·10^{16}	1.29706·10^{16}
fitted c	0.02842	0.02766	0.03972	0.03948
RSS (10^{-6})	0.14	0.28	0.87	1.03

increased the phenol degradation rate.[89] On the other hand, it should be also noted that some surface fluorination is known to increase •OH generation through water oxidation by TiO$_2$, as shown by Chen et al.[102] or Mrowetz et al.[103] Therefore, at this point, it could be expected that some maximum activity of the {0 0 1} facets should be observed depending on the exact presence of the fluorine; however, the optimal conditions for each specific case are more complex. In this regard, to increase the observed activity of the prepared {0 0 1} nanosheets, different washing procedures were performed: (1) washing with a 0.1 M NaOH solution for 2 h at 300 K, with TiO$_2$ concentration of 10 mg·cm^{-3}, followed by rinsing with 0.1 M HNO$_3$ and water, as described by Mino et al.;[89] (2) analogical

procedure but only with 30 min of NaOH wash; (3) analogical to 1 but without HNO$_3$ washing; (4) analogical to 1 but without HNO$_3$ washing and with NaOH concentration reduced to 0.05 M; (5) only single-time rinsing with 0.1 M NaOH solution and then with water. Performed activity tests after the washing procedures are presented in Figure 14 for the degradation of 20 mg·dm^{-3} phenol solution (analogical effects was observed for other reactions).

It was found that the activity increases only in the case of procedure 5, that is, single-time rinsing with 0.1 M NaOH solution and then with water, while all other procedures lead to a reduction of the observed activity. This suggests that the exact surface states became alternated between different
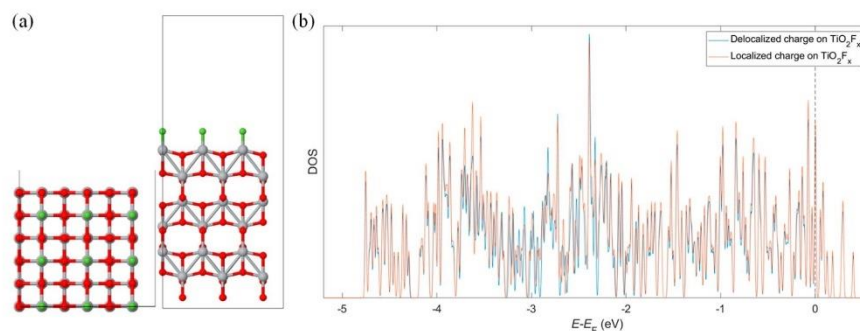
Figure 15. (a) Top and side views of the model of the F-covered anatase TiO$_2$ (0 0 1) surface. The rectangle represents the boundaries of the periodic simulation box, and circles represent atoms of titanium (gray), oxygen (red), or fluorine (green). (b) DOS plot of the TiO$_2$ system in its negatively charged state, with the charge of the extra electron localized or delocalized. The energies are relative to the Fermi level, represented by the dashed vertical line.

washing procedures. Nevertheless, the activity of the {0 0 1} facets could be indeed increased by eliminating some of the present fluorine, and the final activity is approximately 28% higher than initial, which is comparable with the effect observed by Mino et al.[89] This change affected the model details and generally resulted in lower accuracy of all considered models. Nevertheless, the change is not high enough to change the general observations. Specifically, the relative activity of different facets remains the same and still shows good exponential correlation with the trapping energy. Finally, the "best-fitting" models from Table 6 remain best fitting after the washing, and their comparison is shown in Table 8.

The second challenge of the presented model is that the performed analysis does not represent the total reactivity of the charge carriers since their direct transfer from the photocatalysts, without trapping, is still possible.[104] This leads to the problem that it is not possible to precisely determine the "limiting" current of the specific charge carrier,[105,106] for example, e$^-$ reacting on the {0 0 1} facet. This problem is observed both for pure as well as for the fluorinated (0 0 1) surfaces. The second one was specifically performed during this study, and the obtained results of the possible electron trapping on the F-terminated (0 0 1) model are presented in Figure 15 based on the density of states (DOS) distribution. As shown in Figure 15b, no change in the DOS position is observed after localizing the electron on the surface Ti, which shows that no additional states are formed. Moreover, the calculated Bader charge on the trapping Ti atom indicated only partial localization compared to the delocalized model (0.16e difference, where e is the electron charge unit). Finally, the trapping energy, defined analogical as in the work of Ma et al.,[50] resulted only in a value of 2 meV. Therefore, possible energetic stabilization due to charge localization is negligible and below DFT accuracy. In this regard, further studies are needed on the possible electron transfer and its reactivity on the (0 0 1) surface, as well as on the effect of fluorine or other adsorbates on this particular process. The presented approach allows only to predict relative reactivity of different surfaces based on their comparison, rather than arbitrarily model it from the single simulation.

Thus, it is expected that the specific details of the model should also depend on the exact nature of the pollutant. At this point, we can anticipate that pollutants which prefer to directly transfer an electron to the photocatalyst (e.g., some dyes) would show higher deviation from the model introduced in this work. Nevertheless, concerning pollutants that are photochemically stable themselves, phenol and toluene are suggested as good model representatives. Moreover, the presented analysis can still provide valuable information about the photocatalyst. It allows to show if trapped charge carriers are mostly responsible for inducing the degradation reaction. In such a case, the number of reacting species depends on the trapping energy (the energy gain of the system when the charge carrier became trapped on the surface) rather than the surface energy or even the number of active sites (undercoordinated atoms). Since design strategies of the possibly most active photocatalysts still present an extremely complex image, such findings might be a good guide for future studies. Above all, this directly links the observed photocatalytic activity to the specific surface features that could be designed, simulated, and optimized without extensive experimental work. So far, such an approach is generally missing in the literature.

4. CONCLUSIONS

Analyzed data showed that under the accepted experimental conditions, photocatalytic degradation of both toluene and phenol is mainly affected by the energy of charge carriers trapping at the photocatalysts' surface. This straightforwardly predicts the highest per-surface photocatalytic activity of the {1 0 1} enclosed anatase octahedrons due to their high trapping energy. Simultaneously, anatase nanosheets with the {0 0 1} exposed facets are the least active ones. The relation between the trapping energy and the observed rate constants is exponential, which is in accordance with the expected Boltzmann distribution of the trapped states. However, the exact value of the E_{trap}/kT exponent should be further weighted with the additional parameter c. It could be suggested that this parameter represents the fraction of the surface-trapped states that effectively induces the process since it is well known that not all excited/trapped charge carriers will contribute to the final reaction. Moreover, the c value obtained

14873

during analyses was always found to be in the range of 0.020–0.041, which would fit the value of, for example, the photonic efficiency of •OH generation (approx. 3%). Concerning other possible factors, their introduction might further improve the performed prediction. However, their contribution depends on the reaction system.

For the phenol degradation, the surface energy affects the rate constant linearly, while in the gas-phase reaction, it acts as a E_{surf}^2. Finally, depending on the reaction, the best model was obtained when the number of possible trapping centers was introduced (water phase) or it was estimated with the simple surface area of the photocatalyst (gas phase). These results might be beneficial for further design of the new photocatalyst structures, giving a clear insight on what effect might be expected for its different surfaces without performing extensive experimental studies.

■ AUTHOR INFORMATION

Corresponding Author

Szymon Dudziak — *Department of Process Engineering and Chemical Technology, Gdansk University of Technology, Gdansk 80-233, Poland;* ● orcid.org/0000-0002-9225-7748; Email: dudziakszy@gmail.com

Authors

Marta Kowalkińska — *Department of Process Engineering and Chemical Technology, Gdansk University of Technology, Gdansk 80-233, Poland;* ● orcid.org/0000-0003-0518-7508

Jakub Karczewski — *Institute of Nanotechnology and Materials Engineering, Gdansk University of Technology, Gdansk 80-233, Poland*

Marcin Pisarek — *Institute of Physical Chemistry, Polish Academy of Sciences, Warsaw 01-224, Poland;* ● orcid.org/0000-0002-7424-5954

José D. Gouveia — *Department of Chemistry CICECO-Aveiro Institute of Materials, University of Aveiro, Aveiro 3810-193, Portugal;* ● orcid.org/0000-0002-5099-7772

José R. B. Gomes — *Department of Chemistry CICECO-Aveiro Institute of Materials, University of Aveiro, Aveiro 3810-193, Portugal;* ● orcid.org/0000-0001-5993-1385

Anna Zielińska-Jurek — *Department of Process Engineering and Chemical Technology, Gdansk University of Technology, Gdansk 80-233, Poland;* ● orcid.org/0000-0002-9830-1797

Complete contact information is available at:
https://pubs.acs.org/10.1021/acs.jpcc.2c02775

Notes

The authors declare no competing financial interest.

■ ACKNOWLEDGMENTS

■ REFERENCES

(1) Fujishima, A.; Honda, K. Electrochemical Photolysis of Water at a Semiconductor Electrode. *Nature* 1972, 238, 37–38.

(2) Domen, K.; Naito, S.; Soma, M.; Onishi, T.; Tamaru, K. Photocatalytic Decomposition of Water Vapour on an NiO-SrTiO3 Catalyst. *J. Chem. Soc. Chem. Commun.* 1980, 543–544.

(3) Kraeutler, B.; Bard, A. J. Heterogeneous Photocatalytic Decomposition of Saturated Carboxylic Acids on TiO2 Powder. Decarboxylative Route to Alkanes. *J. Am. Chem. Soc.* 1978, 100, 5985–5992.

(4) Yoneyama, H.; Yamashita, Y.; Tamura, H. Heterogeneous Photocatalytic Reduction of Dichromate on N-Type Semiconductor Catalysts. *Nature* 1979, 282, 817–818.

(5) Pichat, P., Ed. *Photocatalysis: Fundamentals, Materials and Potential*; MDPI: Basel, 2016.

(6) Colmenares, J. C.; Xu, Y.-J., Eds. *Heterogeneous Photocatalysis. From Fundamentals to Green Applications*; Springer Berlin: Heidelberg, 2016.

(7) Pichat, P., Ed. *Photocatalysis and Water Purification. From Fundamentals to Recent Applic*; Viley-VCH: Weinheim, 2013.

(8) Takata, T.; Jiang, J.; Sakata, Y.; Nakabayashi, M.; Shibata, N.; Nandal, V.; Seki, K.; Hisatomi, T.; Domen, K. Photocatalytic Water Splitting with a Quantum Efficiency of Almost Unity. *Nature* 2020, 581, 411–414.

(9) Moniz, S. J. A.; Shevlin, S. A.; Martin, D. J.; Guo, Z. X.; Tang, J. Visible-Light Driven Heterojunction Photocatalysts for Water Splitting-a Critical Review. *Energy Environ. Sci.* 2015, 8, 731–759.

(10) Meng, A.; Zhang, J.; Xu, D.; Cheng, B.; Yu, J. Enhanced Photocatalytic H2-Production Activity of Anatase TiO2 Nanosheet by Selectively Depositing Dual-Cocatalysts on (101) and (001) Facets. *Appl. Catal. B Environ.* 2016, 198, 286–294.

(11) Simon, T.; Carlson, M. T.; Stolarczyk, J. K.; Feldmann, J. Electron Transfer Rate vs Recombination Losses in Photocatalytic H2 Generation on Pt- Decorated CdS Nanorods. *ACS Energy Lett* 2016, 1, 1137–1142.

(12) Xie, S.; Zhang, Q.; Liu, G.; Wang, Y. Photocatalytic and Photoelectrocatalytic Reduction of CO2 Using Heterogeneous Catalysts with Controlled Nanostructures. *Chem. Commun.* 2016, 52, 35–59.

(13) Liu, X.; Ye, L.; Liu, S.; Li, Y.; Ji, X. Photocatalytic Reduction of CO2 by ZnO Micro/Nanomaterials with Different Morphologies and Ratios of {0001} Facets. *Sci. Rep.* 2016, 6, 38474.

(14) Alshaikh, H.; Al-Hajji, L. A.; Mahmoud, M. H. H.; Ismail, A. A. Visible-Light-Driven S-Scheme Mesoporous Ag3VO4 /C3N4 Heterojunction with Promoted Photocatalytic Performances. *Sep. Purif. Technol.* 2021, 272, 118914.

(15) Grzegórska, A.; Gluchowski, P.; Karczewski, J.; Ryl, J.; Wysocka, I.; Siuzdak, K.; Trykowski, G.; Grochowska, K.; Zielińska-Jurek, A. Enhanced Photocatalytic Activity of Accordion-like Layered Ti3C2 (MXene) Coupled with Fe-Modified Decahedral Anatase Particles Exposing {1 0 1} and {0 0 1} Facets. *Chem. Eng. J.* 2021, 426, 130801.

(16) Sulowska, A.; Wysocka, I.; Pelczarski, D.; Karczewski, J.; Zielińska-Jurek, A. Hybrid TiO2-Polyaniline Photocatalysts and Their Application in Building Gypsum Plasters. *Materials (Basel)* 2020, 13, 1516.

(17) Wang, K.; Bielan, Z.; Endo-Kimura, M.; Janczarek, M.; Zhang, D.; Kowalski, D.; Zielińska-Jurek, A.; Markowska-Szczupak, A.; Ohtani, B.; Kowalska, E. On the Mechanism of Photocatalytic Reactions on CuxO@TiO2core-Shell Photocatalysts. *J. Mater. Chem. A* 2021, 9, 10135–10145.

(18) Kowalkińska, M.; Gluchowski, P.; Swebocki, T.; Ossowski, T.; Ostrowski, A.; Bednarski, W.; Karczewski, J.; Zielińska-Jurek, A. Scheelite-Type Wide-Bandgap ABO4Compounds (A = Ca, Sr, and Ba; B = Mo and W) as Potential Photocatalysts for Water Treatment. *J. Phys. Chem. C* 2021, 125, 25497–25513.

(19) Yang, J.; Yan, H.; Wang, X.; Wen, F.; Wang, Z.; Fan, D.; Shi, J.; Li, C. Roles of Cocatalysts in Pt-PdS/CdS with Exceptionally High Quantum Efficiency for Photocatalytic Hydrogen Production. *J. Catal.* 2012, 290, 151–157.

(20) She, X.; Wu, J.; Zhong, J.; Xu, H.; Yang, Y.; Vajtai, R.; Lou, J.; Liu, Y.; Du, D.; Li, H.; Ajayan, P. M. Oxygenated Monolayer Carbon

Nitride for Excellent Photocatalytic Hydrogen Evolution and External Quantum Efficiency. *Nano Energy* **2016**, *27*, 138−146.

(21) Hazra, C.; Samanta, T.; Asaithambi, A. V.; Mahalingam, V. Bilayer Stabilized Ln3+-Doped CaMoO4 Nanocrystals with High Luminescence Quantum Efficiency and Photocatalytic Properties. *Dalt. Trans.* **2014**, *43*, 6623−6630.

(22) Guo, H. L.; Du, H.; Jiang, Y. F.; Jiang, N.; Shen, C. C.; Zhou, X.; Liu, Y. N.; Xu, A. W. Artificial Photosynthetic Z-Scheme Photocatalyst for Hydrogen Evolution with High Quantum Efficiency. *J. Phys. Chem. C* **2017**, *121*, 107−114.

(23) Li, X.; Yu, J.; Jaroniec, M. Hierarchical photocatalysts. *Chem. Soc. Rev.* **2016**, *45*, 2603−2636.

(24) Idrees, M.; Din, H. U.; Rehman, S. U.; Shafiq, M.; Saeed, Y.; Bui, H. D.; Nguyen, C. V.; Amin, B. Electronic Properties and Enhanced Photocatalytic Performance of van Der Waals Heterostructures of ZnO and Janus Transition Metal Dichalcogenides. *Phys. Chem. Chem. Phys.* **2020**, *22*, 10351−10359.

(25) Schneider, J.; Matsuoka, M.; Takeuchi, M.; Zhang, J.; Horiuchi, Y.; Anpo, M.; Bahnemann, D. W. Understanding TiO2 Photocatalysis: Mechanisms and Materials. *Chem. Rev.* **2014**, *114*, 9919−9986.

(26) Zhang, J.; Zhou, P.; Liu, J.; Yu, J. New Understanding of the Difference of Photocatalytic Activity among Anatase, Rutile and Brookite TiO2. *Phys. Chem. Chem. Phys.* **2014**, *16*, 20382−20386.

(27) Radecka, M.; Rekas, M.; Trenczek-Zajac, A.; Zakrzewska, K. Importance of the Band Gap Energy and Flat Band Potential for Application of Modified TiO2 Photoanodes in Water Photolysis. *J. Power Sources* **2008**, *181*, 46−55.

(28) Nosaka, Y.; Nosaka, A. Y. Understanding Hydroxyl Radical (•OH) Generation Processes in Photocatalysis. *ACS Energy Lett* **2016**, *1*, 356−359.

(29) Wang, C.; Zhang, X.; Liu, Y. Promotion of Multi-Electron Transfer for Enhanced Photocatalysis: A Review Focused on Oxygen Reduction Reaction. *Appl. Surf. Sci.* **2015**, *358*, 28−45.

(30) Bianco Prevot, A.; Vincenti, M.; Bianciotto, A.; Pramauro, E. Photocatalytic and Photolyric Transformation of Chloramben in Aqueous Solutions. *Appl. Catal. B Environ.* **1999**, *22*, 149−158.

(31) Poulios, I.; Kositzi, M.; Kouras, A. Photocatalytic Decomposition of Triclopyr over Aqueous Semiconductor Suspensions. *J. Photochem. Photobiol. A Chem.* **1998**, *115*, 175−183.

(32) Lair, A.; Ferronato, C.; Chovelon, J. M.; Herrmann, J. M. Naphthalene Degradation in Water by Heterogeneous Photocatalysis: An Investigation of the Influence of Inorganic Anions. *J. Photochem. Photobiol. A Chem.* **2008**, *193*, 193−203.

(33) Dudziak, S.; Bielan, J.; Kubica, P.; Zielińska-Jurek, A. Optimization of Carbamazepine Photodegradation on Defective TiO2-Based Magnetic Photocatalyst. *J. Environ. Chem. Eng.* **2021**, *9*, 105782.

(34) Sun, L.; Shao, R.; Chen, Z.; Tang, L.; Dai, Y.; Ding, J. Alkali-Dependent Synthesis of Flower-like ZnO Structures with Enhanced Photocatalytic Activity via a Facile Hydrothermal Method. *Appl. Surf. Sci.* **2012**, *258*, 5455−5461.

(35) Chen, Y. J.; Chiang, Y. W.; Huang, M. H. Synthesis of Diverse Ag2O Crystals and Their Facet-Dependent Photocatalytic Activity Examination. *ACS Appl. Mater. Interfaces* **2016**, *8*, 19672−19679.

(36) Cho, C. H.; Kim, D. K.; Kim, D. H. Photocatalytic Activity of Monodispersed Spherical TiO2 Particles with Different Crystallization Routes. *J. Am. Ceram. Soc.* **2003**, *86*, 1138−1145.

(37) Wang, X.; Sø, L.; Su, R.; Wendt, S.; Hald, P.; Mamakhel, A.; Yang, C.; Huang, Y.; Iversen, B. B.; Besenbacher, F. The Influence of Crystallite Size and Crystallinity of Anatase Nanoparticles on the Photo-Degradation of Phenol. *J. Catal.* **2014**, *310*, 100−108.

(38) Kowalkińska, M.; Dudziak, S.; Karczewski, J.; Ryl, J.; Trykowski, G.; Zielińska-Jurek, A. Facet Effect of TiO2 Nanostructures from TiOF2 and Their Photocatalytic Activity. *Chem. Eng. J.* **2021**, *404*, 126493.

(39) Pan, J.; Liu, G.; Lu, G. Q.; Cheng, H. M. On the True Photoreactivity Order of {001}, {010}, and {101} Facets of Anatase TiO2 Crystals. *Angew. Chemie - Int. Ed.* **2011**, *50*, 2133−2137.

(40) Gordon, T. R.; Cargnello, M.; Paik, T.; Mangolini, F.; Weber, R. T.; Fornasiero, P.; Murray, C. B. Nonaqueous Synthesis of TiO2 Nanocrystals Using TiF4 to Engineer Morphology, Oxygen Vacancy Concentration, and Photocatalytic Activity. *J. Am. Chem. Soc.* **2012**, *134*, 6751−6761.

(41) Günnemann, C.; Haisch, C.; Fleisch, M.; Schneider, J.; Emeline, A. V.; Bahnemann, D. W. Insights into Different Photocatalytic Oxidation Activities of Anatase, Brookite, and Rutile Single-Crystal Facets. *ACS Catal.* **2019**, *9*, 1001−1012.

(42) Dudziak, S.; Kowalkińska, M.; Karczewski, J.; Pisarek, M.; Siuzdak, K.; Kubiak, A.; Siwińska-Ciesielczyk, K.; Zielińska-Jurek, A. Solvothermal Growth of {0 0 1} Exposed Anatase Nanosheets and Their Ability to Mineralize Organic Pollutants. The Effect of Alcohol Type and Content on the Nucleation and Growth of TiO2 Nanostructures. *Appl. Surf. Sci.* **2021**, *563*, 150360.

(43) Li, M.; Chen, Y.; Li, W.; Li, X.; Tian, H.; Wei, X.; Ren, Z.; Han, G. Ultrathin Anatase TiO2 Nanosheets for High-Performance Photocatalytic Hydrogen Production. *Small* **2017**, *13*, 1604115.

(44) Wen, C. Z.; Zhou, J. Z.; Jiang, H. B.; Hu, Q. H.; Qiao, S. Z.; Yang, H. G. Synthesis of Micro-Sized Titanium Dioxide Nanosheets Wholly Exposed with High-Energy {001} and {100} Facets. *Chem. Commun.* **2011**, *47*, 4400−4402.

(45) Yuan, Y. J.; Ye, Z. J.; Lu, H. W.; Hu, B.; Li, Y. H.; Chen, D. Q.; Zhong, J. S.; Yu, Z. T.; Zou, Z. G. Constructing Anatase TiO2 Nanosheets with Exposed (001) Facets/Layered MoS2 Two-Dimensional Nanojunctions for Enhanced Solar Hydrogen Generation. *ACS Catal.* **2016**, *6*, 532−541.

(46) Zhang, D.; Wang, S.; Zhu, J.; Li, H.; Lu, Y. WO3 Nanocrystals with Tunable Percentage of (001)-Facet Exposure. *Appl. Catal. B Environ.* **2012**, *123−124*, 398−404.

(47) Amano, F.; Yasumoto, T.; Prieto-Mahaney, O. O.; Uchida, S.; Shibayama, T.; Ohtani, B. Photocatalytic Activity of Octahedral Single-Crystalline Mesoparticles of Anatase Titanium(IV) Oxide. *Chem. Commun.* **2009**, *17*, 2311−2313.

(48) Li, J.; Xu, D. Tetragonal Faceted-Nanorods of Anatase TiO2 Single Crystals with a Large Percentage of Active {100} Facets. *Chem. Commun.* **2010**, *46*, 2301−2303.

(49) Lazzeri, M.; Vittadini, A.; Selloni, A. Structure and Energetics of Stoichiometric TiO2 Anatase Surfaces. *Phys. Rev. B - Condens. Matter Mater. Phys.* **2001**, *63*, 1554091−1554099.

(50) Ma, X.; Dai, Y.; Guo, M.; Huang, B. Relative Photooxidation and Photoreduction Activities of the {100}, {101}, and {001} Surfaces of Anatase TiO2. *Langmuir* **2013**, *29*, 13647−13654.

(51) Amano, F.; Nogami, K.; Tanaka, M.; Ohtani, B. Correlation between Surface Area and Photocatalytic Activity for Acetaldehyde Decomposition over Bismuth Tungstate Particles with a Hierarchical Structure. *Langmuir* **2010**, *26*, 7174−7180.

(52) Chiou, C. H.; Wu, C. Y.; Juang, R. S. Influence of Operating Parameters on Photocatalytic Degradation of Phenol in UV/TiO2 Process. *Chem. Eng. J.* **2008**, *139*, 322−329.

(53) Kresse, G.; Hafner, J. Ab initiomolecular dynamics for liquid metals. *Phys. Rev. B* **1993**, *47*, 558−561.

(54) Kresse, G.; Hafner, J. Ab Initio Molecular-Dynamics Simulation of the Liquid-Metalamorphous- Semiconductor Transition in Germanium. *Phys. Rev. B* **1994**, *49*, 14251−14269.

(55) Kresse, G.; Furthmüller, J. Efficient Iterative Schemes for Ab Initio Total-Energy Calculations Using a Plane-Wave Basis Set. *Phys. Rev. B - Condens. Matter Mater. Phys.* **1996**, *54*, 11169−11186.

(56) Kresse, G.; Furthmüller, J. Efficiency of Ab-Initio Total Energy Calculations for Metals and Semiconductors Using a Plane-Wave Basis Set. *Comput. Mater. Sci.* **1996**, *6*, 15−50.

(57) Perdew, J. P.; Burke, K.; Ernzerhof, M. Generalized Gradient Approximation Made Simple. *Phys. Rev. Lett.* **1996**, *77*, 3865−3868.

(58) Grimme, S.; Ehrlich, S.; Goerigk, L. Effect of Damping Function in Dispersion Corrected Density Functional Theory. *J. Comput. Chem.* **2011**, *32*, 1456−1465.

(59) Grimme, S.; Antony, J.; Ehrlich, S.; Krieg, H. A Consistent and Accurate Ab Initio Parametrization of Density Functional Dispersion

Correction (DFT-D) for the 94 Elements H-Pu. *J. Chem. Phys.* **2010**, *132*, 154104.

(60) Blöchl, P. E. Projector Augmented-Wave Method. *Phys. Rev. B* **1994**, *50*, 17953−17979.

(61) Monkhorst, H. J.; Pack, J. D. Special Points for Brillouin-Zone Integrations. *Phys. Rev. B* **1976**, *13*, 5188−5192.

(62) Zhang, C.; Hu, P.; Alavi, A. A General Mechanism for CO Oxidation on Close-Packed Transition Metal Surfaces. *J. Am. Chem. Soc.* **1999**, *121*, 7931−7932.

(63) Deskins, N. A.; Rousseau, R.; Dupuis, M. Localized Electronic States from Surface Hydroxyls and Polarons in TiO 2(110). *J. Phys. Chem. C* **2009**, *113*, 14583−14586.

(64) Deskins, N. A.; Dupuis, M. Intrinsic Hole Migration Rates in TiO 2 from Density Functional Theory. *J. Phys. Chem. C* **2009**, *113*, 346−358.

(65) Deskins, N. A.; Dupuis, M. Electron Transport via Polaron Hopping in Bulk Ti O2: A Density Functional Theory Characterization. *Phys. Rev. B* **2007**, *75*, 195212.

(66) Han, X.; Kuang, Q.; Jin, M.; Xie, Z.; Zheng, L. Synthesis of Titania Nanosheets with High Percentage of Exposed (001) Facets and Related Photocatalytic Properties. *J. Am. Chem. Soc.* **2009**, *131*, 3152−3153.

(67) Yu, J.; Fan, J.; Lv, K. Anatase TiO2 Nanosheets with Exposed (001) Facets: Improved Photoelectric Conversion Efficiency in Dye-Sensitized Solar Cells. *Nanoscale* **2010**, *2*, 2144−2149.

(68) Zhang, Y.; Li, C.; Pan, C. N + Ni Codoped Anatase TiO2 Nanocrystals with Exposed {001} Facets Through Two-Step Hydrothermal Route. *J. Am. Ceram. Soc.* **2012**, *95*, 2951−2956.

(69) Mao, J.; Ye, L.; Li, K.; Zhang, X.; Liu, J.; Peng, T.; Zan, L. Pt-Loading Reverses the Photocatalytic Activity Order of Anatase TiO2 {001} and {010} Facets for Photoreduction of CO2 to CH4. *Appl. Catal. B Environ.* **2014**, *144*, 855−862.

(70) Huang, Z.; Wang, Z.; Lv, K.; Zheng, Y.; Deng, K. Transformation of TiOF2 Cube to a Hollow Nanobox Assembly from Anatase TiO2 Nanosheets with Exposed {001} Facets via Solvothermal Strategy. *ACS Appl. Mater. Interfaces* **2013**, *5*, 8663−8669.

(71) Yu, J.; Qi, L.; Jaroniec, M. Hydrogen Production by Photocatalytic Water Splitting over Pt/TiO2 Nanosheets with Exposed (001) Facets. *J. Phys. Chem. C* **2010**, *114*, 13118−13125.

(72) Wang, Z.; Lv, K.; Wang, G.; Deng, K.; Tang, D. Study on the Shape Control and Photocatalytic Activity of High-Energy Anatase Titania. *Appl. Catal. B Environ.* **2010**, *100*, 378−385.

(73) Wei, Z.; Kowalska, E.; Verrett, J.; Colbeau-Justin, C.; Remita, H.; Ohtani, B. Morphology-Dependent Photocatalytic Activity of Octahedral Anatase Particles Prepared by Ultrasonication-Hydrothermal Reaction of Titanates. *Nanoscale* **2015**, *7*, 12392−12404.

(74) Gai, L.; Mei, Q.; Qin, X.; Li, W.; Jiang, H.; Duan, X. Controlled Synthesis of Anatase TiO2 Octahedra with Enhanced Photocatalytic Activity. *Mater. Res. Bull.* **2013**, *48*, 4469−4475.

(75) Li, R.; Zhang, X.; Dong, H.; Li, Q.; Shuai, Z.; Hu, W. Gibbs-Curie-Wulff Theorem in Organic Materials: A Case Study on the Relationship between Surface Energy and Crystal Growth. *Adv. Mater.* **2016**, *28*, 1697−1702.

(76) Yang, H. G.; Sun, C. H.; Qiao, S. Z.; Zou, J.; Liu, G.; Smith, S. C.; Cheng, H. M.; Lu, G. Q. Anatase TiO2 Single Crystals with a Large Percentage of Reactive Facets. *Nature* **2008**, *453*, 638−641.

(77) Yang, H. G.; Liu, G.; Qiao, S. Z.; Sun, C. H.; Jin, Y. G.; Smith, S. C.; Zou, J.; Cheng, H. M.; Lu, G. Q. Solvothermal Synthesis and Photoreactivity of Anatase TiO2 Nanosheets with Dominant {001} Facets. *J. Am. Chem. Soc.* **2009**, *131*, 4078−4083.

(78) Barnard, A. S.; Curtiss, L. A. Prediction of TiO2 Nanoparticle Phase and Shape Transitions Controlled by Surface Chemistry. *Nano Lett.* **2005**, *5*, 1261−1266.

(79) Zhu, J.; Lv, F.; Xiao, S.; Bian, Z.; Buntkowsky, G.; Nuckolls, C.; Li, H. Covalent Attachment and Growth of Nanocrystalline Films of Photocatalytic TiOF2. *Nanoscale* **2014**, *6*, 14648−14651.

(80) Yu, J. C.; Yu, J.; Ho, W.; Jiang, Z.; Zhang, L. Effects of F-Doping on the Photocatalytic Activity and Microstructures of Nanocrystalline TiO2 Powders. *Chem. Mater.* **2002**, *14*, 3808−3816.

(81) Ruzicka, J. Y.; Bakar, F. A.; Thomsen, L.; Cowie, B. C.; McNicoll, C.; Kemmitt, T.; Brand, H. E. A.; Ingham, B.; Andersson, G. G.; Golovko, V. B. XPS and NEXAFS Study of Fluorine Modified TiO2 Nano-Ovoids Reveals Dependence of Ti3+ Surface Population on the Modifying Agent. *RSC Adv.* **2014**, *4*, 20649−20658.

(82) Seo, M. H.; Yuasa, M.; Kida, T.; Huh, J. S.; Shimanoe, K.; Yamazoe, N. Gas Sensing Characteristics and Porosity Control of Nanostructured Films Composed of TiO2 Nanotubes. *Sensors Actuators, B Chem.* **2009**, *137*, 513−520.

(83) Nosaka, Y.; Nosaka, A. Y. Generation and Detection of Reactive Oxygen Species in Photocatalysis. *Chem. Rev.* **2017**, *117*, 11302−11336.

(84) Hirakawa, T.; Yawata, K.; Nosaka, Y. Photocatalytic Reactivity for •O2- and OH• Radical Formation in Anatase and Rutile TiO2 Suspension as the Effect of H2O2 Addition. *Appl. Catal. A Gen.* **2007**, *325*, 105−111.

(85) René, A.; Abasq, M. L.; Hauchard, D.; Hapiot, P. How Do Phenolic Compounds React toward Superoxide Ion? A Simple Electrochemical Method for Evaluating Antioxidant Capacity. *Anal. Chem.* **2010**, *82*, 8703−8710.

(86) Marugán, J.; Hufschmidt, D.; López-Muñoz, M. J.; Selzer, V.; Bahnemann, D. Photonic Efficiency for Methanol Photooxidation and Hydroxyl Radical Generation on Silica-Supported TiO2 Photocatalysts. *Appl. Catal. B Environ.* **2006**, *62*, 201−207.

(87) Shirai, K.; Fazio, G.; Sugimoto, T.; Selli, D.; Ferraro, L.; Watanabe, K.; Haruta, M.; Ohtani, B.; Kurata, H.; Di Valentin, C.; Matsumoto, Y. Water-Assisted Hole Trapping at the Highly Curved Surface of Nano-TiO2 Photocatalyst. *J. Am. Chem. Soc.* **2018**, *140*, 1415−1422.

(88) Chen, J.; Li, Y. F.; Sit, P.; Selloni, A. Chemical Dynamics of the First Proton-Coupled Electron Transfer of Water Oxidation on TiO2 Anatase. *J. Am. Chem. Soc.* **2013**, *135*, 18774−18777.

(89) Mino, L.; Pellegrino, F.; Rades, S.; Radnik, J.; Hodoroaba, V. D.; Spoto, G.; Maurino, V.; Martra, G. Beyond Shape Engineering of TiO2 Nanoparticles: Post-Synthesis Treatment Dependence of Surface Hydration, Hydroxylation, Lewis Acidity and Photocatalytic Activity of TiO2 Anatase Nanoparticles with Dominant {001} or {101} Facets. *ACS Appl. Nano Mater.* **2018**, *1*, 5355−5365.

(90) Litke, A.; Su, Y.; Tranca, I.; Weber, T.; Hensen, E. J. M.; Hofmann, J. P. Role of Adsorbed Water on Charge Carrier Dynamics in Photoexcited TiO2. *J. Phys. Chem. C* **2017**, *121*, 7514−7524.

(91) Hwang, J. Y.; Moon, G. h.; Kim, B.; Tachikawa, T.; Majima, T.; Hong, S.; Cho, K.; Kim, W.; Choi, W. Crystal Phase-Dependent Generation of Mobile OH Radicals on TiO2: Revisiting the Photocatalytic Oxidation Mechanism of Anatase and Rutile. *Appl. Catal. B Environ.* **2021**, *286*, 119905.

(92) Setvin, M.; Aschauer, U.; Hulva, J.; Simschitz, T.; Daniel, B.; Schmid, M.; Selloni, A.; Diebold, U. Following the Reduction of Oxygen on TiO2 Anatase (101) Step by Step. *J. Am. Chem. Soc.* **2016**, *138*, 9565−9571.

(93) Selcuk, S.; Selloni, A. Facet-Dependent Trapping and Dynamics of Excess Electrons at Anatase TiO2 Surfaces and Aqueous Interfaces. *Nat. Mater.* **2016**, *15*, 1107−1112.

(94) Carey, J. J.; McKenna, K. P. Does Polaronic Self-Trapping Occur at Anatase TiO2 Surfaces? *J. Phys. Chem. C* **2018**, *122*, 27540−27553.

(95) Bahamon, D.; Khalil, M.; Belabbes, A.; Alwahedi, Y.; Vega, L. F.; Polychronopoulou, K. A DFT Study of the Adsorption Energy and Electronic Interactions of the SO2molecule on a CoP Hydrotreating Catalyst. *RSC Adv.* **2021**, *11*, 2947−2957.

(96) Mino, L.; Ferrari, A. M.; Lacivita, V.; Spoto, G.; Bordiga, S.; Zecchina, A. CO Adsorption on Anatase Nanocrystals: A Combined Experimental and Periodic DFT Study. *J. Phys. Chem. C* **2011**, *115*, 7694−7700.

(97) Arrouvel, C.; Digne, M.; Breysse, M.; Toulhoat, H.; Raybaud, P. Effects of Morphology on Surface Hydroxyl Concentration: A DFT

Page | 144

Comparison of Anatase-TiO2 and γ-Alumina Catalytic Supports. *J. Catal.* **2004**, *222*, 152−166.

(98) Zhao, Z.; Li, Z.; Zou, Z. Surface Properties and Electronic Structure of Low-Index Stoichiometric Anatase TiO2 Surfaces. *J. Phys. Condens. Matter* **2010**, *22*, 175008.

(99) Seo, H.; Baker, L. R.; Hervier, A.; Kim, J.; Whitten, J. L.; Somorjai, G. A. Generation of Highly N-Type Titanium Oxide Using Plasma Fluorine Insertion. *Nano Lett.* **2011**, *11*, 751−756.

(100) Pellegrino, F.; Morra, E.; Mino, L.; Martra, G.; Chiesa, M.; Maurino, V. Surface and Bulk Distribution of Fluorides and Ti3+ Species in TiO2 Nanosheets: Implications on Charge Carrier Dynamics and Photocatalysis. *J. Phys. Chem. C* **2020**, *124*, 3141−3149.

(101) Peng, Y. K.; Keeling, B.; Li, Y.; Zheng, J.; Chen, T.; Chou, H. L.; Puchtler, T. J.; Taylor, R. A.; Tsang, S. C. E. Unravelling the Key Role of Surface Features behind Facet-Dependent Photocatalysis of Anatase TiO2. *Chem. Commun.* **2019**, *55*, 4415−4418.

(102) Chen, M.; Ma, J.; Zhang, B.; He, G.; Li, Y.; Zhang, C.; He, H. Remarkable Synergistic Effect between {001} Facets and Surface F Ions Promoting Hole Migration on Anatase TiO2. *Appl. Catal. B Environ.* **2017**, *207*, 397−403.

(103) Mrowetz, M.; Selli, E. Enhanced Photocatalytic Formation of Hydroxyl Radicals on Fluorinated TiO2. *Phys. Chem. Chem. Phys.* **2005**, *7*, 1100−1102.

(104) Moser, J.; Punchihewa, S.; Infelta, P. P.; Graetzel, M. Surface Complexation of Colloidal Semiconductors Strongly Enhances Interfacial Electron-Transfer Rates. *Langmuir* **1991**, *7*, 3012−3018.

(105) Wang, C. M.; Heller, A.; Gerischer, H. Palladium Catalysis of O2 Reduction by Electrons Accumulated on TiO2 Particles during Photoassisted Oxidation of Organic Compounds. *J. Am. Chem. Soc.* **1992**, *114*, 5230−5234.

(106) Gerischer, H.; Heller, A. The Role of Oxygen in Photo-oxidation of Organic Molecules on Semiconductor Particles. *J. Phys. Chem.* **1991**, *95*, 5261−5267.

PUBLICATION [P4]

Photocatalytic degradation and pollutant-oriented structure-activity analysis of carbamazepine, ibuprofen and acetaminophen over faceted TiO$_2$

Szymon Dudziak, Agnieszka Fiszka Borzyszkowska, Anna Zielińska-Jurek *

Department of Process Engineering and Chemical Technology, Gdańsk University of Technology, G. Narutowicza street 11/12, 80-233 Gdańsk, Poland

ABSTRACT

Photocatalytic degradation of carbamazepine, ibuprofen, acetaminophen and phenol was studied in the presence of anatase photocatalyst, exposing three different crystal facets in the majority of {0 0 1}, {1 0 0} or {1 0 1}. It was found that octahedral anatase particles exposing {1 0 1} facets allow to achieve the best degradation and mineralization of all persistent organic pollutants. This confirms that the previous findings, showing high {1 0 1} activity, are not limited to phenol and could be generalized for other water pollutants. Based on the obtained results, a correlation model including exposed TiO$_2$ crystal facet and chemical hardness of the pollutant was developed to predict the degradation rate of pollutants with a possibly diverse electronic structure. The structure-activity analyses, based on the reactivity predictors obtained from the DFT calculations for all tested compounds, have shown that pollutants with higher chemical hardness react faster with the photocatalyst. Alternatively, a similar effect was observed for the higher HOMO-LUMO energy gap of the compound. This relation indicates that for compounds with a low energy position of LUMO orbital, e.g., carbamazepine, process efficiency is not strictly dependent on the stability of h$^-$ generated organic radical, which is often pointed out as an initial reactive form. Based on these results, a correlation model was developed for the first time to quantitatively describe the effect of the facet-pollutant interactions based on their independent electronic properties. Finally, this was followed by the detailed degradation study of the pharmaceuticals mixture, showing the impact of the total concentration and role of active species on the degradation efficiency over facet-engineered TiO$_2$ photocatalysts.

1. Introduction

A growing human population has led to a significant increase in the consumption of pharmaceuticals. Commonly used pharmaceutical compounds such as carbamazepine (CBZ), ibuprofen (IBU) and acetaminophen (ACT, also known as paracetamol) are currently detected in the aqueous environment worldwide [1,2]. The occurrence of some pharmaceuticals in surface waters presents a global challenge considering their potential for bioaccumulation and biomagnification. For example, the removal efficiency of carbamazepine from wastewater treatment plant effluents is about 10% due to low sorption properties on activated sludge microorganisms. Therefore, compounds like carbamazepine are not susceptible to biodegradation using conventional water treatment processes [2,3]. For carbamazepine, the environmental concentrations are close to the threshold value affecting plasma 11-keto-testosterone concentration in male fish, while for ibuprofen, it exceeded the threshold for decreasing fish egg fertilization (about 100 ng•dm^{-3} for IBU [3] and 500 ng•dm^{-3} for CBZ [4]). Bioaccumulation of both

carbamazepine and ibuprofen is reported to easily occur in mussels, achieving 90 (CBZ) and 460-fold (IBU) concentration increase in the tissue [5]. Parolini et al. reported that even acetaminophen concentrations as low as 1.5 µg•dm^{-3} could induce a cyto-genotoxic effect on zebra mussels [6]. Furthermore, the study by Galus et al. has shown that chronic exposure to ACT and CBZ induces histopathological changes in zebrafish kidneys, as well as increases embryo mortality [4]. Finally, in the case of carbamazepine, toxic by-products, especially acridine, and acridone, can form during the photolysis process, which increases the toxicity of the aqueous phase [7,8]. In this regard, all these compounds are considered pharmaceutical active compounds (PhACs), belonging to the group of emerging pollutants of major concern. Therefore, there is a need to develop effective technologies that allow a more significant reduction of toxic PhACs, which are not susceptible to biodegradation, to solve the current water pollution problem.

Photocatalysis is one of the successful methods that remove persistent organic pollutants and is also classified as green technology. However, although a great effort was made in the field of photocatalytic

S. Dudziak et al.

water purification, including (i) photocatalyst composition [9–14], (ii) process optimization [15,16], and (iii) reactor design [17,18], there are still some challenges concerning detailed photocatalyst design for the particular application in photocatalytic process. This especially concerns the surface structure of the photocatalyst, which can be modified by the exposition of suitable crystal facets [19,20]. Furthermore, photocatalytic reactions are still difficult to describe precisely through model development due to the complexity of the involved reactions. More recently, computational simulations allowed to study elementary steps of these processes on a fundamental level, providing a general description of how the overall process could be initiated [21–23]. However, regarding photocatalytic water treatment from emerging contaminants, a relationship between observed process efficiency and the results obtained from the computational studies is generally not present in the literature so far. Recently, we have studied such an approach and observed that phenol and toluene degradation efficiency as model organic pollutants over the different anatase facets depend mostly on the probability of trapping electrons and holes on the surface atoms [24]. This probability is proportional to the reported "trapping energy" for these surface structures [25], which is the energy gain of the system when an electron or hole becomes localized on the surface atoms. Therefore, the degradation process over the TiO$_2$ photocatalyst is mostly controlled by the distribution of surface trapped states, specific for each crystal facet (highest density for the {1 0 1} facets and the lowest for {0 0 1} one). Following the previous findings for the phenol degradation, the observed per-second rate constant (k) can be described with the following Eq. (1) [24]:

$$k = A \cdot E_{surf} \cdot \left(\frac{n_{trap}}{n_{pollutant}} \right)^{1/2} \cdot \left(e^{\frac{B \cdot E_{trap}}{kT}} - 1 \right) + k_0 \qquad (1)$$

where A and B are fitted constants, E_{surf} is the surface energy of the dominant facet, n_{trap} is the number of the trapping centers on the surface of the photocatalyst (calculated from the photocatalyst's mass, BET surface and atomic model of the dominant facet [25]), $n_{pollutant}$ is a number of pollutant molecules at the start of the process, E_{trap} is a sum of trapping energies reported for both holes and electrons for the dominant facet [25], kT is a product of Boltzman constant and temperature and k_0 is spontaneous photolysis of the pollutant. This specific relation showed a very good correlation with the degradation rate of phenol, however, due to a large number of possible contaminants, it seems necessary to further investigate the accuracy of the model with respect to the different water-phase pollutants.

In this regard, in the present study, TiO$_2$ photocatalysts exposing the majority of {0 0 1}, {1 0 0}, and {1 0 1} crystal facets were synthesized and systematically studied in the degradation of carbamazepine, ibuprofen, and acetaminophen. The novelty of the present work is focused on three aspects: (i) cross-investigation of the facet-pollutant interactions, based on the electronic properties of both of them; (ii) quantitative description of these interactions through the development of the statistical model and (iii) degradation experiments of the pharmaceuticals mixture, using facet-engineered photocatalysts. The combination of real-life water pollutants with TiO$_2$ exposing specific crystal facets allowed us, for the first time to show and discuss the photocatalytic activity concerning both photocatalyst surface structure and chemical structure of the pollutant. Furthermore, photocatalytic studies were completed with the phenol (PHE) degradation analyses as a relative comparison with previous works. Finally, degradation tests of the pharmaceuticals mixture using facet-engineered photocatalysts were also performed to validate the results obtained for the single-pollutant case.

2. Experimental

2.1. Photocatalyst preparation

Photocatalyst preparation was performed under solvothermal conditions according to the previously reported procedures [20,27,28]. Briefly, synthesis of the {0 0 1} sample was made solvothermal from 17 cm^3 of titanium *tert*-butoxide in the presence of 3.4 cm^3 of 50% wt. HF solution and 30 cm^3 of *n*-butanol. All substrates were mixed and placed inside a 200 cm^3 Teflon-lined reactor at 210 °C for 18 h. Sample exposing {1 0 0} facets was prepared in a two-step reaction, starting from the 1 g of commercial TiO$_2$ P25, which was etched at 120 °C for 20 h using 40 cm^3 of 10 M NaOH solution inside the 100 cm^3 reactor. The obtained Na-titanate product was washed with water until pH equaled 10.5 and immediately separated into two equal parts. Each part was mixed with 100 cm^3 of water inside the 200 cm^3 reactor and was left to react at 210 °C for 24 h. Sample exposing {1 0 1} facets was prepared analogically to the {1 0 0}, except that 8.5 M solution of KOH was used in the first reaction, and the obtained K-titanate product was washed until pH reached approximately 7. In the second step, 0.4 g of the dried K-precursor was mixed with the 100 cm^3 of NH$_4$OH/NH$_4$Cl buffer with concentrations of 0.3/0.3 M (pH approximately 9) and left to react at 210 °C for 16 h. All prepared samples were centrifuged, washed with water 4 times, dried, and hand-grounded in the agate mortar before further characterization and photocatalytic studies.

2.2. Photocatalyst characterization

Obtained photocatalysts were investigated concerning their crystal structure, diffuse reflectance UV/Vis absorbance spectra (DR-UV/vis), Brunauer-Emmett-Teller surface area (BET), and morphology. The crystal structure was analyzed based on the X-ray diffraction pattern (XRD) in the 2Θ range 10–80°, collected using Rigaku MiniFlex diffractometer with the scan speed and step being 2°·min^{-1} and 0.05° respectively. The crystallinity of the prepared samples was analyzed using highly crystalline NiO as an internal standard. The DR-UV/vis absorbance spectra were recorded using ThermoFisherScientific Evolution 220 spectrophotometer with BaSO$_4$ as a standard in the λ range between 200 and 800 nm. The Fourier-transformed infrared (FTIR) absorption spectra were measured using a Thermo Fisher Scientific Nicolet iS10 spectrometer in the wavenumber from 1500 to 4000 cm^{-1}. Before measurements, the analyzed sample was mixed with the KBr, and the pellet was made using a hydraulic press. The BET surface area was analyzed based on the N$_2$ adsorption isotherm in the 77.15 K between the $p/p_0 = 0.05$ and 0.3, and the samples were degassed at 200 °C for 2 h prior to the measurement. The morphology of the samples was observed under the FEI Quanta FEG 250 scanning electron microscope (SEM). The surface composition of the samples was analyzed based on the X-ray photoelectron spectroscopy (XPS) measurements performed with the PHI 5000 VersaProbe (ULVAC-PHI) spectrometer.

2.3. Photocatalytic degradation analysis

Firstly, the photocatalytic degradation experiments in the presence of faceted TiO$_2$ were performed in 15 cm^3 reactors at constant temperature (25 °C), with magnetic stirring using a high-pressure Hg lamp as an irradiation source with 15 mW•cm^{-2} of UVA flux at the reactor border. Moreover, control experiments were made using commercial TiO$_2$ P25 as a standard material. These experiments were performed for a single solution of each pollutant (with the initial concentration of 20 mg·dm^{-3} for acetaminophen, ibuprofen, and phenol and 14 mg·dm^{-3} for carbamazepine), as well as for the mixture of examined pharmaceuticals. Before irradiation, each solution was stirred for 30 min in the dark to ensure adsorption equilibrium between the photocatalyst and the organic pollutant. After this time, irradiation with light was started, and samples were taken at given intervals and filtered

2

through syringe filters ($\varphi = 0.2\,\mu m$) for the removal of photocatalyst particles. Furthermore, the pharmaceuticals mixture degradation using facet-engineered photocatalysts was performed and the stability of the photocatalyst was analyzed in the subsequent cycles of degradation. Moreover, the trapping experiments in the presence of the active species scavengers were performed to discuss their role in the degradation process (5 mmol•dm^{-3} of isopropanol as •OH scavenger, 1 mmol•dm^{-3} of benzoquinone as •O$_2$ scavenger or 5 mmol•dm^{-3} of ammonium oxalate as h$^+$ scavenger). Additionally, the relative •OH generation ability was tested using 50 μmol•dm^{-3} coumarin solution and determined the initial formation rate of 7-hydroxycoumarin for the obtained photocatalyst samples. Quantification of the 7-hydroxycoumarin was performed based on the calibrated emission intensity at 454 nm after exciting solution with the 332 nm wavelength using a Shimadzu RF-6000 spectrofluorometer. Finally, degradation experiments using an alternative set-up with a 300 W Xe lamp were performed to discuss the possible effect of light. During these experiments, the measured UVA flux at the reactor border was 25 mW•cm^{-2}. Besides the coumarin-based tests, the concentration of all pollutants was evaluated with the high-pressure liquid chromatography method using a Shimadzu LC-6A system equipped with a pump (LC-20 CE), autosampler (SIL-20AHT) and diode array detector (SPD-M20A). During all measurements, the Phenomenex Kinetex C-18 column (150 × 4.6 mm, 2.6 μm) was used for separation. An isocratic method was used for every examined pharmaceutical, but flow rate, the composition of the eluents and wavelengths of detection varied depending on the compound; details are presented in Table 1. Mineralization of the pharmaceuticals was determined as a removal of the total organic carbon (TOC) and measured using a Shimadzu TOC-L analyzer. Degradation rate constants were calculated assuming a first-order reactions model. In the case of a visible change in the observed rate in the initial and late part of the process, the final rate constant was calculated as a mean between different linear regions.

2.4. Computational details and structure-activity relationship

Computational studies of the analyzed pharmaceutical molecules were performed with the density functional theory (DFT) calculations using Orca 5.0.3 software [29,30]. All calculations were performed using the hybrid exchange-correlation B3LYP functional [31] with aug-cc-PVDZ basis set. Such a combination was recently reported to be reliable in predicting some molecule parameters, such as a dipole moment, under a reasonable computational time [32]. Each molecule was optimized to its relaxed geometry, and the true energy minimum was confirmed with the vibrational frequencies (no negative frequencies) analysis. Geometry optimization was followed with the analysis of HOMO and LUMO orbitals for each molecule. All computations were performed using the CMCP model of continuum solvation.

Based on the performed calculations, a set of parameters representing each molecule was obtained and used for further structure-activity

Table 1
HPLC methods parameters.

Parameter	Acetaminophen	Carbamazepine	Ibuprofen	Phenol
Wavelength (nm)	244	285	219	272
Flow rate (cm^3·min^{-1})	0.8	1.5	0.5	0.3
Injection volume (μL)	10	10	10	10
Temperature (°C)	45	45	45	45
Mobile phase (v/v)	MeOH/H$_2$O/ HCOOH 30/69.9/0.1	H$_2$O/ACN/H$_3$PO$_4$ 68/31.6/0.4	ACN/ H$_2$O/ H$_3$PO$_4$ 70/29.5/ 0.5	ACN/ H$_2$O/ H$_3$PO$_4$ 70/ 29.5/ 0.5

analysis. Specifically, the HOMO and LUMO energies, HOMO-LUMO gap, dipole moment, total Gibbs energy, chemical potential, electronegativity, chemical hardness, softness, and electrophilicity index were selected to represent each pollutant. The values of HOMO and LUMO energies (E_{HOMO} and E_{LUMO}), HOMO-LUMO gap (ΔE), dipole moments (d), and total single-point energies (G) were obtained directly from the computed results. The chemical potentials (μ), electronegativities (χ), absolute hardness (η), softness (S), and electrophilicity indices (ω) were calculated for each molecule based on the original definitions by Parr and Pearson [33,34] under the assumptions of Koopman theorem [35] with further improvement by Tozer and De Proft concerning the exact η value [36]. The final equations are:

$$\mu = \frac{(E_{LUMO} + E_{HOMO})}{2} = -\chi \tag{2}$$

$$\eta = \frac{(E_{LUMO} - E_{HOMO})}{2} + E_{HOMO} + I = \frac{1}{S} \tag{3}$$

$$I = E_{N-1} - E_N \tag{4}$$

$$\omega = \frac{\mu^2}{2\eta} \tag{5}$$

where I is vertical ionization potential, E_N is the energy of the considered molecule and E_{N-1} is the energy of the same molecule with one less electron.

3. Results and discussion

3.1. Photocatalyst structure and properties

Characterization of the prepared photocatalysts was started from the analysis of their crystal structure and UV–vis absorption properties, as presented in Fig. 1. All samples are single-phase TiO$_2$ with the reflections corresponding to the anatase crystal structure. Moreover, in the case of sample {0 0 1} prepared with the addition of HF as a stabilizing agent, visible broadening of the (0 0 4) and (1 0 5) reflections can be observed, which results from the thickening of the nanocrystals along the c crystallographic direction.

Simultaneously, this sample had about 20% wt. of the amorphous phase, as shown in Table 2, based on the additional measurements with NiO as the internal standard. Noteworthy, the crystallinity of the TiO$_2$ can influence its photocatalytic activity, however it was shown previously that its effect is not significant in phenol degradation (crystallinity between ~10–85%) [37]. Furthermore, our recent study has also shown that particularly in the case of different samples with exposed {0 0 1} facets, their ability to degrade phenol is not connected with the presence of amorphous phase content (crystallinity between ~34–81%), but depend mostly on the surface development and surface defects [20]. In this regard, the determined 20% presence of the amorphous phase is not expected to be decisive for the comparison of the samples. Comparing to the {0 0 1} exposed one, samples {1 0 0} and {1 0 1} did not show visible amorphous phase content.

Furthermore, as shown in Fig. 1b, the absorbance spectra of all samples are similar and negligible below 400 nm. The bandgap energies are shown in Fig. 1c and were about 3.22 eV for all samples, which is a value characteristic of the pure anatase structure. Finally, the SEM images presented in Fig. 1d confirmed morphology differences, characteristic for each exposed facet (rectangular plates in the case of {0 0 1} exposition, rectangular rods for {1 0 0} and octahedrons in the case of {1 0 1}). Corresponding BET surface areas are shown inset of SEM images.

Furthermore, the surface hydroxylation of the samples was analyzed based on the performed FTIR analysis, as presented in Fig. 2. The presence of adsorbed water is observed for all samples, with a broad peak in the range of 3650–3000 cm^{-1} and a sharp one at 1635 cm^{-1}, corresponding to the stretching and bending vibrations of the H$_2$O [38].
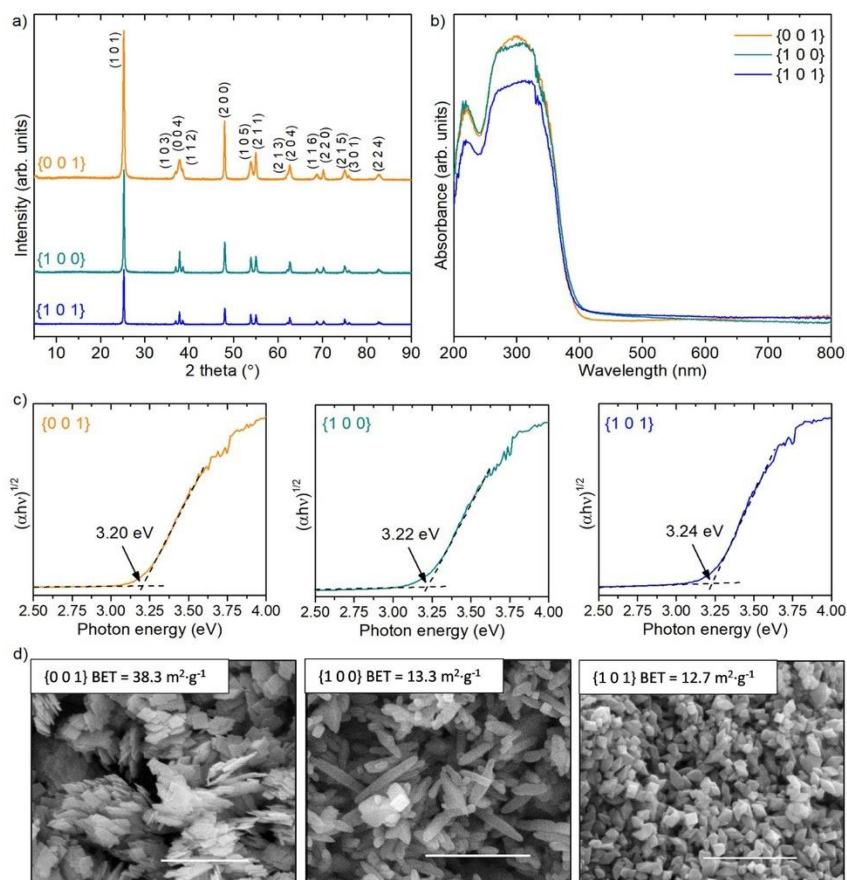
3

Fig. 1. Basic characteristics of the obtained photocatalysts, including XRD patterns (a), UV–vis absorption spectra (b), calculated bandgap values (c), and SEM morphology of the samples with obtained BET surface areas (d). Scale bars are 1 μm.

Table 2
Summation of the XPS results and crystallinity of the prepared samples (LOD stands for "*limit of detection*").

Sample	Ti^{4+} (485.5 eV)	Ti^{3+} (486.5 eV)	F_{ads} (684.5 eV)	F/Ti	Amorphous content
{0 0 1}	100%	Below LOD	100%	0.19 at.	20%
{1 0 0}	100%	Below LOD	Below LOD	-	Below LOD
{1 0 1}	100%	Below LOD	Below LOD	-	Below LOD

Noteworthy, sample {1 0 0} showed visible enhancement of the absorption near 3100 cm^{-1}, suggesting that some amount of H$_2$O is bound stronger to the surface [39].

This is in some agreement with the known stabilization of the {1 0 0} facets through increased hydroxylation [40], which might suggest stronger TiO$_2$-H$_2$O interactions. Nevertheless, the overall amount of adsorbed H$_2$O is similar for {1 0 0} and {1 0 1} samples and is only slightly higher for the {0 0 1} one, as observed for the 1635 cm^{-1} signal.

Since the analysis was performed for the controlled, similar amount of samples, this is in agreement with the determined surface development, which should affect the number of possible adsorption sites. Therefore, surface hydroxylation seems similar between the samples, with absorption proportional to the surface development.

Considering the possible surface defects, XPS analyses were performed, and the results are summarized in Table 2. As observed, no surface Ti^{3+} was noticed for the prepared samples, suggesting the absence of structural surface defects. Combined with the UV–vis spectra presented in Fig. 1, this shows that the overall structure is defect-free. Moreover, in the case of samples {1 0 0} and {1 0 1}, their overall characteristics are very similar, and therefore, differences in the exposed facets are expected to be the main factor affecting their photocatalytic performance. Some differences are observed only in the case of the sample with exposed {0 0 1} facets. However, it should be noted that the preparation route of this sample is based on the previously optimized procedure [20]. In this regard, it should be a good representative of the material exposing the majority of the {0 0 1} facets. The final
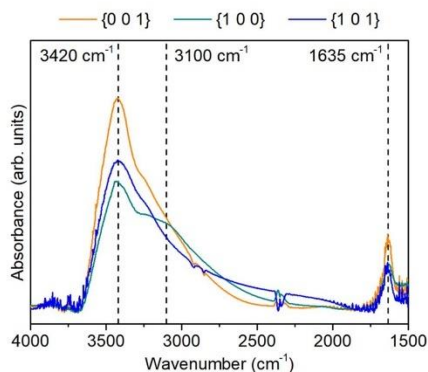
4

Fig. 2. FTIR spectra of the prepared TiO₂ samples.

noteworthy observation for this sample is the presence of surface-adsorbed fluorine, which is typical for the materials prepared in the presence of HF. The calculated atomic ratio between F/Ti is 0.19, which might influence the electronic structure of the (0 0 1) surface. However, it is expected that partial fluorination of the {0 0 1} facets is inhibiting to their photocatalytic activity [41–43]. Particularly, 2D samples prepared at very analogical conditions have not shown a negative effect of surface fluorination between F/Ti = 0.13 and 0.18 [20]. Moreover, the final activity of these samples could be improved with a suitable post-treatment. However, these effects are reported to be within the range of a 20% activity increase [24,44]. As it will be shown

later, differences in the activity observed between prepared samples are a few times larger than this, suggesting the predominant effect of the exposed facet.

3.2. Degradation study of single pharmaceutical compounds

Obtained materials were analyzed for photocatalytic degradation of selected pharmaceuticals; carbamazepine (CBZ), ibuprofen (IBU) and acetaminophen (ACT) in water to determine possible interactions between their structure and the exposed facet of the photocatalyst. Furthermore, the degradation of phenol (PHE), a widely used model organic pollutant, as well as TiO₂ P25 as a standard photocatalytic material, were performed as control experiments for other analyses. As shown in Fig. 3 and Table 3, all of the TiO₂ nanostructures can induce degradation of the tested compounds, while the spontaneous photolysis is low. Furthermore, visible differences between specific pollutant-photocatalyst reactions are noticeable. First of all, carbamazepine and ibuprofen appear to be more prone to adsorb on the photocatalyst surface in the absence of light. This is especially visible for ibuprofen and is in agreement with its expected anionic form in neutral conditions (pKa = 5.2), which can promote its interactions with the TiO₂ surface.

These differences, observed without light, are generally followed by the degradation efficiency under the UV–vis light, with the highest rates observed for carbamazepine and ibuprofen, followed by acetaminophen and lastly phenol photodegradation. In all cases, sample exposing {1 0 1} facets exhibit the highest activity, while nanosheets exposing {0 0 1} revealed the lowest photoactivity. The weak performance of the sample with exposed {0 0 1} facets is even more noticeable when considering its relatively large surface area compared to the remaining two (approx. 3 times larger). This is in agreement with our recent studies, showing higher activity of the {1 0 1} facets than {0 0 1} for phenol degradation [19,20]. However, it especially confirms that this
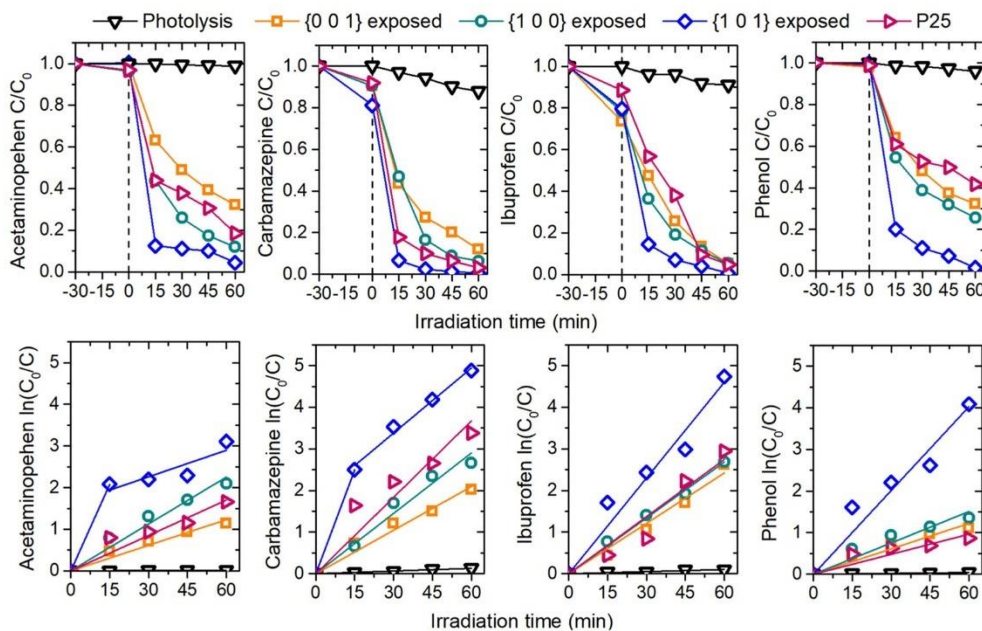

Fig. 3. Observed photocatalytic degradation of the acetaminophen (ACT), carbamazepine (CBZ), ibuprofen (IBU) and phenol (PHE) over prepared TiO₂ samples.

5

Table 3
Detailed values of the observed rate constants and initial concentrations.

Compound	Carbamazepine	Ibuprofen	Acetaminophen	Phenol
C_0 (mg•dm^{-3})	13.0	20.6	19.5	18.9
k_0 (s^{-1})	0.36•10^{-4}	0.28•10^{-4}	0.03•10^{-4}	0.11•10^{-4}
$k_{\{0\ 0\ 1\}}$ (s^{-1})	5.82•10^{-4}	6.73•10^{-4}	3.42•10^{-4}	3.40•10^{-4}
$k_{\{1\ 0\ 0\}}$ (s^{-1})	8.06•10^{-4}	7.45•10^{-4}	6.26•10^{-4}	4.19•10^{-4}
$k_{\{1\ 0\ 1\}}$ (s^{-1})	18.20•10^{-4}	12.78•10^{-4}	13.33•10^{-4}	11.19•10^{-4}
k_{P25} (s^{-1})	10.20•10^{-4}	7.62•10^{-4}	4.73•10^{-4}	2.68•10^{-4}

observation is not limited to phenolic compounds and could also be expected for other water pollutants. Furthermore, it is also in agreement with the control experiments of the •OH radicals generation, using 7-hydroxycoumarin (7-OHC) as the fluorescent probe [45], directly connecting observed pharmaceutical degradation rates with the ability to generate hydroxyl radicals (7-OHC generation rates were 36 nM•min^{-1} for {0 0 1} sample, 52 nM•min^{-1} for the {1 0 0} and 74 nM•min^{-1} for the {1 0 1} one). Noteworthy, the sample exposing{1 0 1} facets revealed higher photocatalytic activity than commercial TiO$_2$ P25, despite a few times lower surface area.

Degradation tests were followed by the measurements of total organic carbon (TOC) before and after 60 min of the process to verify the possible mineralization of the target compound. As shown in Fig. 4, the observed removal of the organic carbon between the samples is in general agreement with their degradation rates and follows the order {1 0 1} > {1 0 0} > {0 0 1}. The only exception is carbamazepine degradation over the {1 0 0} facets, which achieved the highest TOC removal.

However, the value is very close to the {1 0 1} one. Regarding the pollutant type, some discrepancy might be seen between the observed degradation rate and final TOC removal, which generally is quite high for phenol and acetaminophen. This might result from the fact that their molecules are relatively smaller than carbamazepine and ibuprofen, which might promote their faster breaking into CO$_2$, despite relatively slow transformation at the beginning of the process (number of carbon atoms per one molecule is 15 for CBZ, 13 for IBU, 8 for ACT and 6 for PHE).

Finally, it is also visible that the mineralization of ibuprofen is visibly slower than other pollutants, suggesting that the degradation rates of further transformation products are low for this compound. Relatively low TOC removal during the ibuprofen degradation by TiO$_2$ was reported previously [46,47], and generally, additional reagents such as ozone are known to enhance the degradation of possible intermediates [48]. Compared to the facet-engineered TiO$_2$ samples, commercial TiO$_2$ P25 revealed higher TOC reduction efficiency only for IBU degradation. This suggests that either higher surface development or charge carriers separation might be crucial for IBU mineralization (P25 is composed of both rutile and anatase phases and therefore, improved separation of the generated e$^-$ and h$^+$ between both components is possible in this case).

3.3. Analysis of facet-pollutant interactions with respect to pollutant structure

Obtained results showed that regardless of the pollutant structure, the {1 0 1} facets are the most active, in each case recreating the same trend as previously observed for phenol [24]. Therefore, the activity order of the exposed facets is not dependent on the exact pollutant structure. Moreover, since ibuprofen is present in its anionic form during the process (pKa = 4.91), even a specific charge on the pollutant molecule seems to be less important, not influencing the overall trend. In this regard, experimental data was compared with the modeled results obtained using a previously optimized Eq. (1). Details of the model parameter, based on the studies focused on the analysis of the TiO$_2$ surfaces [24–26], are presented in Table 4.

However, as shown in Fig. 5a, such rate constants, predicted without considering the pollutant structure, do not follow the experimental results strictly. Furthermore, some series fit better to the initial model when grouped by the pollutant type, while ibuprofen and carbamazepine show the highest deviation (Fig. 5b). Although the exposed TiO$_2$ crystal facet primarily determines the overall activity, the prediction of the degradation rate without taking into account pollutant structure can lead to relatively high error, especially when comparing the degradation

Table 4
Detailed values introduce to the initial model, considering different TiO$_2$ facets.

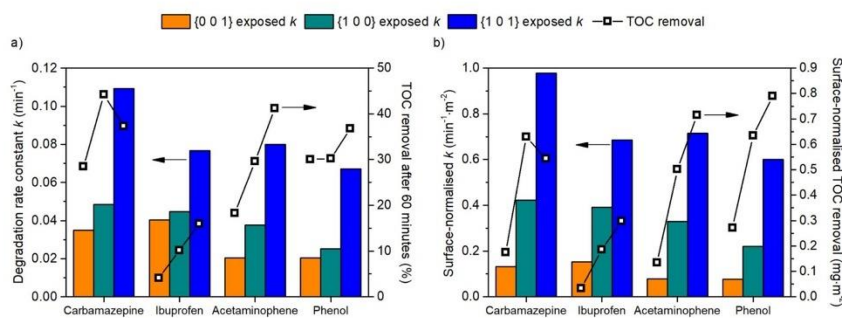| Facet	E_{surf} (J•m^{-2})	E_{trap} (J)	n_{trap} density (m^{-2})	A	B
{0 0 1}	0.90	0.77·10^{-19}	6.96•10^{18}	3.327•10^{-4}	0.02766
{1 0 0}	0.53	2.30·10^{-19}	9.25•10^{18}		
{1 0 1}	0.44	3.80·10^{-19}	1.03 •10^{19}		

Fig. 4. Calculated degradation rate constants and removal of the total organic carbon (TOC) for the investigated compounds in the presence of different TiO$_2$ nanostructures; (a) as observed and (b) after normalization with the surface area of the photocatalyst. Column order from left to right match the one in the legend.
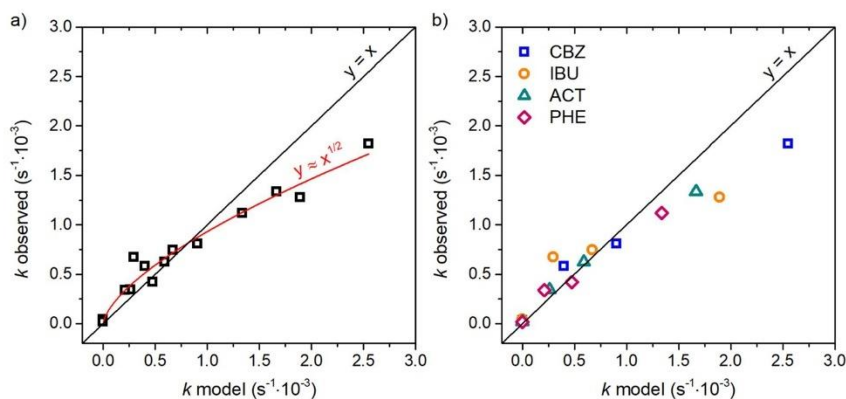
6

Fig. 5. Results of modeling the degradation rate constant based on a model developed for phenol degradation over different TiO$_2$ facets (a); as well as their further division with respect to the pollutant (b).

of different compounds. Therefore, identification of the pollutant-specific features that determine the observed activity might be desirable to better describe TiO$_2$-pollutant interactions.

In this regard, to describe the effect of the pollutant structure, the initial model (1) was rearranged to focus on the $n_{trap}/n_{pollutant}$ term since all others are either constant (k_0) or depend strictly on the photocatalyst nature and not on the pollutant (E_{surf} and E_{trap}). Therefore, the analyzed relation could be presented as described in Eq. (6).

$$\frac{k - k_0}{E_{surf} \cdot \left(e^{\frac{0.02766 \cdot E_{trap}}{kT}} - 1\right)} = A_1 \cdot \left(\frac{n_{trap}}{n_{pollutant}}\right)^C \qquad (6)$$

where the left side of the equation is known, while A_1 and C are new fitted factors. It should be noted that previously the C was found to be ½ in the case of phenol degradation, however it is not obvious if this will be true for other pollutants as well. Therefore, the analysis was started by considering $C = ½$; 1 and 2 and looking for possible A_1 values.

Fig. 6 presents the obtained relations, showing that overall the $C = 1$ gives the best accuracy between all pollutants. In this regard, the values

of A_1 fitted for this case ($C = 1$) and presented in Table 5 were taken for further analysis.

The actual pollutant structure-activity analysis was started with computational simulations of each pollutant under the DFT theory level with CMCP solvation model. The optimized structures of each molecule in their dominant aqueous form (ibuprofen as an anion) are presented in Fig. 7, together with their HOMO and LUMO maps and energies. Based on these results, a set of global reactivity predictors [49] was determined, as described in the experimental section. The exact values of each predictor are shown in Table 6. Based on the values presented in Table 6, the correlation between the predictors and A_1 value, determined as a slope from Fig. 6 for $C = 1$, was studied assuming simple

Table 5
Detailed values of the A_1 parameter obtained for $C = 1$.

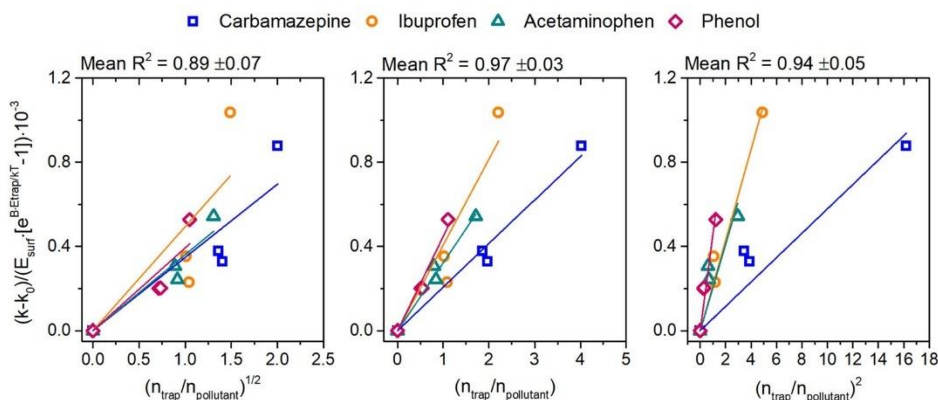|	Carbamazepine	Ibuprofen	Acetaminophen	Phenol
A_1	2.06889•10^{-4}	4.07053•10^{-4}	3.22663•10^{-4}	4.48345•10^{-4}

Fig. 6. Linear relations between the pollutant-independent part of the model (OY axis) and the ratio between the number of photocatalyst trapping sites and the number of pollutant molecules, including different C exponents.
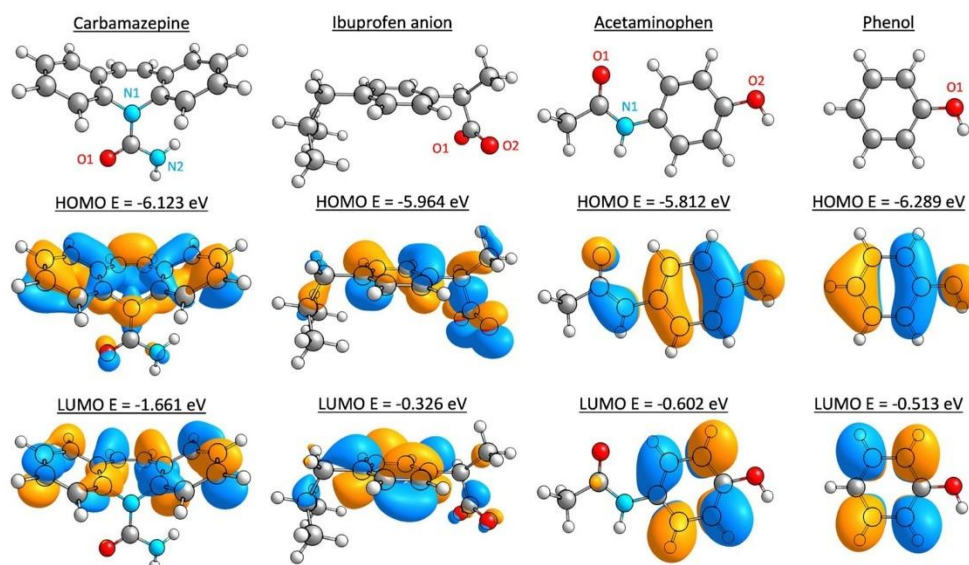
7

Fig. 7. Visualization of the optimized geometry for each pollutant, as well as their HOMO and LUMO maps and corresponding energies. Grey, white, cyan and red spheres are C, H, N and O atoms, respectively. In the case of ibuprofen, only the geometry of R enantiomer is shown since no significant difference was observed for the S structure, however the HOMO and LUMO energies are presented as mean.

Table 6
Detailed values of the reactivity predictors describing each of the analyzed molecules.

Compound	G (Ha)	d (D)	E_{HOMO} (eV)	E_{LUMO} (eV)	ΔE (eV)	μ (eV)	χ (eV)	η (eV)	S (eV)	ω (eV)
CBZ	763.22	6.09	6.123	1.661	4.462	3.892	3.892	2.046	0.489	3.702
ACT	-515.28	7.29	-5.812	-0.602	5.210	-3.207	3.207	2.475	0.404	2.077
PHE	-307.34	1.82	-6.289	-0.513	5.775	-3.401	3.401	2.766	0.362	2.091
[IBU]⁻ (mean)	-655.92	18.36	-5.964	-0.326	5.638	-3.145	3.145	2.653	0.377	1.864
[IBU]⁻ R	-655.92	18.28	-5.959	-0.327	5.632	-3.143	3.143	2.649	0.378	1.864
[IBU]⁻ S	-655.92	18.45	-5.970	-0.325	5.645	-3.147	3.147	2.657	0.376	1.864

linear relation.

The values of the observed R^2 parameters for different A_1 expressions, including single predictor or their combinations and squared values, are presented in Table 7. The full analysis included each predictor independently, as well as their interactions (multiplication of two predictors) and squared values. Obtained results have shown a very strong correlation between the fitted A_1 parameter and the chemical

softness/hardness, as well as the HOMO-LUMO energy difference (ΔE). At this point, it should be noted that these predictors are directly related (Eq. (3) in the experimental section), so similarities are not unexpected.

Concerning the hardness/softness relations, the softness value is an inverse of the hardness and the correlation is slightly more accurate for the hardness (η). As a result, it is observed that "harder" compounds react faster with the photocatalyst. The same relation is true for the

Table 7
Detailed values of the R^2 parameters describing the linear correlation between the determined predictors (independent and including 2-factor interactions) and observed A_1 values.

R^2 matrix	G	d	E_{HOMO}	E_{LUMO}	ΔE	μ	χ	η	S	ω
Single	0.56	0.02	0.05	0.81	**0.99**	0.54	0.54	**0.98**	**0.96**	0.76
G	0.59	< 0.01	0.57	0.85	0.23	0.73	0.73	0.20	0.77	0.83
d		0.09	0.02	0.75	0.04	< 0.01	< 0.01	0.05	< 0.01	0.06
E_{HOMO}			0.05	0.79	**0.97**	0.31	0.31	**0.97**	0.84	0.70
E_{LUMO}				0.79	0.78	0.79	0.79	0.77	0.83	0.79
ΔE					**0.99**	0.45	0.45	**0.99**	0.74	0.60
μ						0.56	0.56	0.61	0.83	0.72
χ							0.56	0.61	0.83	0.72
η								**0.99**	0.02	0.56
S									**0.95**	0.82
ω										0.76

8

higher HOMO-LUMO gap. In both cases, the best accuracy is observed for the squared values of η and ΔE, presented in Fig. 8.

Ultimately, we propose that within the investigated range of η and ΔE, A_1 can be described using both of these predictors (Eqs. (7) and (8)), considering their values in J:

$$A_1 = 2.73231\cdot 10^{33}\cdot \eta^2 - 9.21375\cdot 10^{-5} \tag{7}$$

$$A_1 = 6.86473\cdot 10^{32}\cdot \Delta E^2 - 1.48052\cdot 10^{-4} \tag{8}$$

For both of the possible A_1 equations, the final model might be visibly improved, as shown in Fig. 9 for the case of η^2 relation (combination of Eq. (7) with Eq. (1)). Here, the only point that visibly stands out is ibuprofen degradation over {1 0 1} sample. However, it can be noticed that this is a special case. As mentioned, in the neutral conditions, ibuprofen is present in its anionic form, while {1 0 1} facets are specifically reductive and prefer to accumulate electrons during the photocatalytic process, in contrast to both {0 0 1} and {1 0 0} [25]. In this regard, under UV light irradiation, electrostatic interactions might specifically hinder the process for this particular case, which is observed as k being visibly lower than predicted.

However, it should also be noted that for pollutants with possibly low values of η and ΔE, for example dyes, the introduction of Eqs. (7) and (8) could result in negative A_1 values, which is not reasonable. In this regard, for such compounds, modified relations (9) and (10) could be used.

$$A_1 = 1.9263\cdot 10^{33}\cdot \eta^2 \tag{9}$$

$$A_1 = 4.04836\cdot 10^{32}\cdot \Delta E^2 \tag{10}$$

This is further justified by control experiments of methyl orange (MO) degradation. MO is known to have a small HOMO-LUMO gap of 2.01 eV, which under the Koopman theorem, corresponds to the chemical hardness value of about 1.005 eV. Therefore, as shown in Table 8, the introduction of Eqs. (7) and (8) results in a negative value of A_1 and, in consequence, a negative value of k, which is meaningless. On the other hand, scaling the relation down to (0, 0) with Eqs. (9) and (10) results in the final predicted k being already close to the experimental results. Moreover, it is noteworthy that both predicted and observed rate constants are the order of magnitude lower than in the case of other compounds. This is in agreement with the general trend that lower η or ΔE should result in slower degradation.

3.4. Interpretation of the model

The final model shows that the observed photocatalytic degradation rate of different organic pollutants in water depends mostly on three factors: (i) the ratio between surface trapping centers of the photocatalyst and the number of pollutant molecules, (ii) the trapping energy of charge carriers on the photocatalyst surface and (iii) chemical hardness, or alternatively HOMO-LUMO energy gap, of the degrading pollutant. In each case, an increase in the numerical value of the factor results in an increase in the observed degradation rate constant. The first one of the factors is right now well understood during the photocatalytic processes, and an increase of the k with an increasing number of the surface active centers is expected. Furthermore, we have recently reported that for a faceted TiO$_2$, the probability of charge carriers trapping on the surface, defined with trapping energy, is crucial for the degradation of organic compounds. Therefore, the combination of factors (i) and (ii) describes the probability of charge carriers trapping at the surface and the actual number of possible trapping centers per number of reacting molecules, and their further interpretation seems unnecessary. However, to our best knowledge, factor (iii) is reported for the first time, and in this regard, we will discuss its interpretation further.

Firstly, it is noteworthy that compared to other studied reactivity predictors, both η and ΔE depend on the energetic stability of the pollutant when an electron is added or removed from the molecule. This is presented in Fig. 10, where additional calculations were performed for the molecules with a number of electrons $N + 1$ and all results are presented relative to the energy in the ground state. In this figure, higher points on the OY axis are less stable, indicating possibly fast subsequent transformation. Therefore, the relative stability of the investigated compounds in their N-1 state is ACT > IBU > CBZ > PHE, while in their $N + 1$ states, it goes CBZ > IBU $\approx$ ACT > PHE. This ordering leads to the observation that the stability of neither $N + 1$ or N-1 state correlates with the experimental degradation data. Under the Koopman theorem, this is further true for the HOMO and LUMO energies. Alternatively, η and ΔE describe the relative stability of both N-1 and $N + 1$ states together, specifically being the second derivative of the $E(N)$ function [33] or a difference between N-1 and $N + 1$ energies (please note that initially, all E values are negative and only in Fig. 10 for clarity they are presented with different signs). For example, low stability of both $N + 1$ and N-1 states for phenol results in the highest η and ΔE values, while for carbamazepine very stable $N + 1$ state decreases both predictors. In this regard, although it should be noted that the introduction of exact E values for the N-1, N, $N + 1$ states, HOMO and LUMO energies, chemical
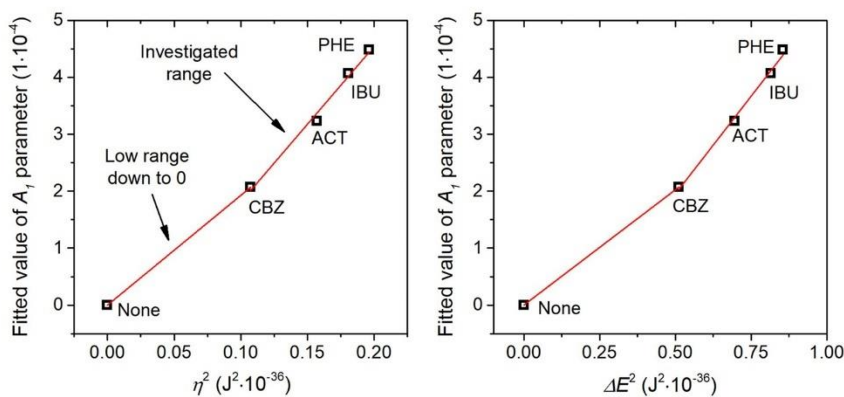

Fig. 8. Observed correlation between the fitted value of A_1 and calculated chemical hardness (η) or HOMO-LUMO energy gap (ΔE) of the pollutant.
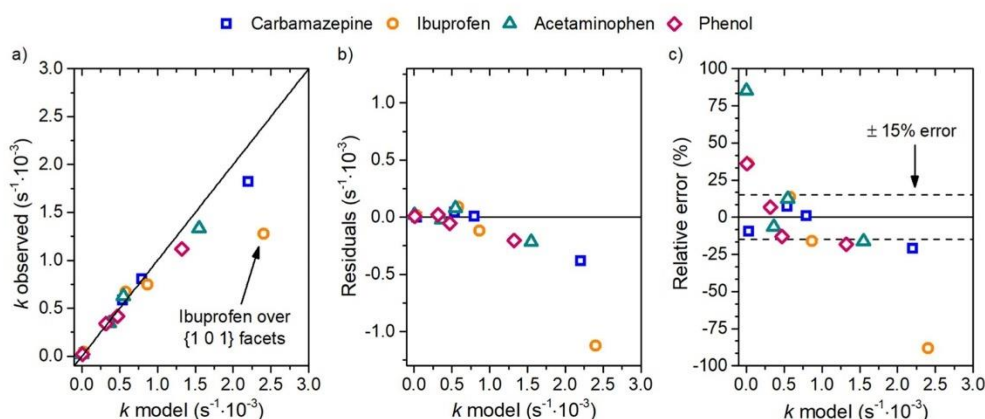
9

Fig. 9. Accuracy of the final model, after the introduction of the squared chemical hardness of each analyzed pollutant, presented as direct model-observation correlation (a), the absolute value of the residuals (b) and relative error (c).

Table 8
Validation of the model for methyl orange degradation. The experimental conditions were unchanged, the initial concentration of MO was about 200 μmol•dm^{-3}, similar to phenol.

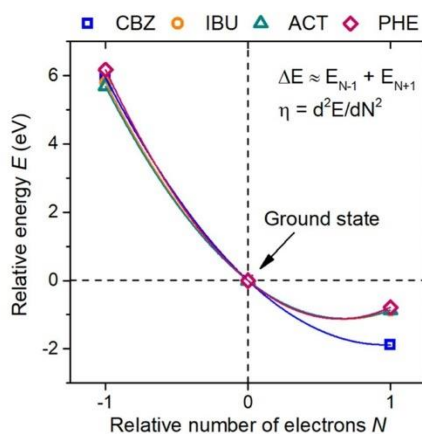| Facet	MO η (J•10^{-19})	MO ΔE (J•10^{-19})	A_I Eq. (7) η^2	A_I Eq. (8) ΔE^2	A_I Eq. (9) η^2	A_I Eq. (10) ΔE^2	$k_{model}\,\eta$ (s^{-1}•10^{-5})	$k_{model}\,\Delta E$ (s^{-1}•10^{-5})	$k_{observed}$ (s^{-1}•10^{-5})
{0 0 1}	1.61	3.22	-2.13•10^{-5}	-7.69•10^{-5}	4.99•10^{-5}	4.20•10^{-5}	3.43	2.89	2.81
{1 0 1}							14.7	12.4	10.05

Fig. 10. Detailed results of the energy change as the function of electron number (N) obtained from the DFT simulations for investigated compounds.

hardness calculated using Eq. (3) or as a derivative of the curve presented in Fig. 10 give a bit different results in each case, they always create a reasonable trend with the experimentally observed results. Therefore, only when the stability of both oxidized and reduced molecules is considered can the final rate constant be predicted with improved accuracy.

The observations are also in agreement with the degradation mechanisms reported for different organic compounds, which usually cannot distinguish a single, well-defined degradation pathway [50–52]. Although it is commonly accepted that such processes are initiated by the hole transfer from the photocatalyst to pollutant or direct attack of •OH [53–55], it is known that electron transfer is also important for the overall process efficiency. This is either due to the involvement of the •O$_2^-$, or other reduced species [56,57], in the process or due to the possible occurrence of the back reactions of organic radicals [58]. In this regard, the relative stability of the N-1 state for PHE, IBU and ACT agrees with the final degradation rate for these compounds, where less stable radical implies faster transformation. However, CBZ stands out from this simple relation. Based on the described results, this is correlated with the low position of the LUMO orbital and, therefore, the high stability of the $N+1$ state of CBZ. This suggests that, especially for carbamazepine, interactions with excited electrons might be responsible for slowing down the process, either by promoting back reactions of intermediate radicals or, hypothetically, as the result of increased interactions between e and CBZ itself. In this regard, a detailed study on the interactions between charge carriers on the TiO$_2$ surface and carbamazepine, or other pollutants with a low position of LUMO orbital, might give a better insight into how the degradation process differs compared to the phenolic compounds. The differences are expected since the simple position of the HOMO orbital, corresponding to the oxidized radical state in the initial part of the process, cannot explain the lower degradation rate of CBZ, observed independently for all three investigated TiO$_2$ facets.

3.5. Degradation of the pharmaceuticals mixture

Finally, obtained photocatalysts and TiO$_2$ P25 were studied in the degradation process of the pharmaceuticals mixture, including total pollutants concentrations of 50 mg·dm^{-3}, 13 mg·dm^{-3} and 5 mg·dm^{-3}

10

(the fraction of carbamazepine, ibuprofen, and acetaminophen was 1:1:0.5). Obtained results of the degradation rate for each individual pollutant are presented in Fig. 11a in comparison with the single-pollutant system. In the case of the 50 mg·dm^{-3} mixture, the initial concentration of each pharmaceutical is the same for individual degradation tests, and the degradation rates are decreased, which is expected due to the increased total concentration of pollutants [59].

Furthermore, two main effects can be noticed when all pollutants are present together. First of all, ibuprofen degradation is almost always in favor, showing a strong preference to react in the more complex system. This is especially visible for the {1 0 0} and {1 0 1} series, which are characterized by lower surface area. Secondly, the efficiency of acetaminophen degradation is different for each photocatalyst. Interestingly, despite lowering the total concentration, ACT degradation is not increased in the case of {1 0 0} and {1 0 1} samples between the 50 mg·dm^{-3} and 13 mg·dm^{-3} mixtures. A further increase is observed only when the total concentration decrease to 5 mg·dm^{-3}.

However, in the case of the {1 0 1} sample, the process is still hindered compared to the ACT alone. These results clearly showed that there is a preference about which pharmaceutical had a "priority" to be degraded during the process, and this follows the order of ibuprofen > carbamazepine > acetaminophen. Interestingly, acetaminophen degradation can be visibly enhanced for the {0 0 1} and {1 0 0} surfaces, but only when concentration is low enough. This relation is in agreement with the observed adsorption of the pollutants on the TiO$_2$ surfaces, which especially favors ibuprofen and acetaminophen the least. Therefore, pre-irradiation adsorption determines the observed degradation rate when multiple pollutants are present in the solution. This implies that a sufficiently high photocatalyst surface area should be desirable to enable the efficient degradation of all pharmaceuticals. In other cases, such as ACT degradation over the {1 0 0} and {1 0 1} facets for high total concentrations, the degradation rate of some compounds might be hindered due to the preference of other pollutants to react first. Similar observations are noticed for TiO$_2$ P25, which showed a significant increase in the degradation rate only for the lowest concentration of the pharmaceuticals mixture of 5 mg•dm^{-3}. Therefore, when the concentration of pollutants is relatively higher (50 mg·dm^{-3} or 13 mg·dm^{-3}), the sample exposing {1 0 1} facets generally revealed the
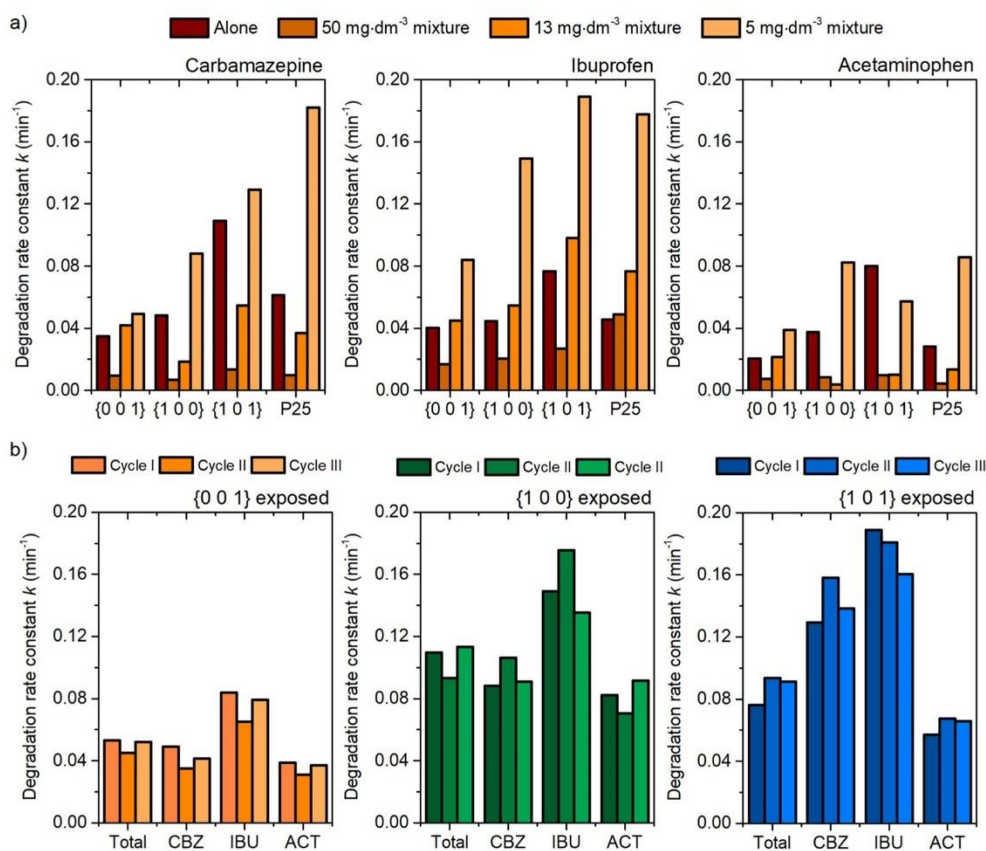

Fig. 11. Comparison of the degradation rate constants for the carbamazepine, ibuprofen and acetaminophen, over the TiO$_2$ photocatalysts: effect of the pharmaceuticals mixture and its concentration (a) and stability tests of the synthesized samples during degradation process of the 5 mg•dm^{-3} mixture (b). Column order from left to right match the one in the legend.

highest photocatalytic activity, especially when comparing the available surface area of samples.

Based on these results, it could also be suggested that during the actual process, a mixture of different photocatalysts might be optimized to obtain the best performance for the mixture of pollutants with the lowest concentration of 5 mg·dm^{-3}. For example, the {1 0 0} sample showed better ACT degradation than {1 0 1} with a similar surface area, but not for the CBZ and IBU. Moreover, as shown further in Fig. 11b, these photocatalytic activities are similar for all prepared samples during three subsequent cycles of degradation.

As presented in Table 9, these results are generally followed by the removal of total organic carbon (TOC), which achieved the highest values for the {1 0 1} exposing sample (18%, 31% and 51% of the removal after 1 h, depending on the concentration). Only in the case of the lowest concentration of pharmaceuticals, TiO$_2$ P25 achieved better TOC removal efficiency of 69%. However, after the third extended cycle of degradation (3 h), the sample exposing {1 0 1} facets achieved 83% of the TOC removal, which gives the residual value in the range of the pure water matrix (approximately 1 mg·dm^{-3}). However, it is also noteworthy that for the {0 0 1} and {1 0 0} exposing samples, higher differences were observed for the TOC removal during the cycling processes. This suggests that the final activity of these samples is more sensitive to the process conditions. Nevertheless, it doesn't influence the conclusions.

Furthermore, Fig. 12 shows observed degradation rates when specific scavengers of the active species are added to the reaction system (5 mg·dm^{-3} of pharmaceuticals). As observed, •OH, •O$_2$ and h$^+$ were found to be important for the degradation process. Nevertheless, some additional observations are noticeable. Interestingly, h$^+$ seems to be least important for carbamazepine degradation, especially over {0 0 1} and {1 0 0} facets. This is in agreement with the lack of correlation between CBZ degradation rate and stability of the [CBZ]$^+$ molecule, described in the previous section. On the other hand, h$^+$ are most important for ibuprofen removal, which also agrees with its preferred surface adsorption and negative charge. Therefore, direct h$^+$ transfer from the surface to the pollutant seems as a relatively important process for IBU. Finally, acetaminophen degradation is specifically sensitive to benzoquinone presence, which suggests the importance of the •O$_2$ radicals in its degradation process. In all cases, •OH is shown to play an important role in the photocatalytic reaction.

Finally, Fig. 13 shows the comparison between the degradation rates of the 5 mg·dm^{-3} mixture, obtained using a set-up with UV light and the alternative set-up, utilizing a lamp emitting UV–vis light. As observed, set-up with UV–vis light allowed to achieve of similar or higher degradation rates, especially affecting the transformation of CBZ and ACT over the {1 0 0} and {1 0 1} exposing samples. Noteworthy, relative degradation rates of the different pollutants over {1 0 1} sample under the UV–vis light irradiation match closely results obtained for the single compounds presented in Figs. 4 and 11a. As the nature of the photocatalyst and photogenerated active species is not expected to change depending on the pollutant, it is shown that preferred IBU degradation is sensitive to the parameters of the set-up itself. In this regard, two differences can be highlighted. First, utilized set-up 2 with a Xe lamp emitting UV–vis light possessed higher UVA photon flux (mW·cm^{-2}) than set-up with a UV lamp (15 mW·cm^{-2}), which

generally might stimulate reaction rates. However, in this case, the effect should be uniform for all samples, which is not consistent with the observed activity for the sample exposing {0 0 1} facets. On the other hand, both photocatalytic set-ups also differ in the reactor geometry, which mostly connects with the elongated profile and slightly shorter optical length of the UV lamp reactor. From these factors, the first one seems to have a possible effect, as the long profile of the reactor results in less homogeneous mixing between the bottom and the top of the solution (this could be observed during the stabilization period of the suspension). In this regard, more homogeneous mixing and mass transfer achieved in the reactor equipped with UV–vis light (xenon lamp) might be responsible for more uniform degradation rates observed for the samples with lower surface area, resulting in the relative degradation rates being more similar to the pure compounds. Ultimately, this allowed to achieve the highest photocatalytic activity of the {1 0 1}, with a 3-times faster TOC removal, compared to a set-up equipped with a UV lamp.

4. Conclusions

The overall results present important conclusions for further studies. First of all, photocatalytic degradation of all tested emerging pollutants occurs most efficiently for anatase octahedral particles exposing {1 0 1} facets when studied independently. This proves that the efficiency of such a process depends on the density of surface trapping sites of the TiO$_2$, which should be high for this facet rather than its surface energy. Therefore, it confirms our previous observations made for phenol degradation, this time for a bigger set of real water pollutants with diverse chemical structures. Furthermore, after taking into account the effect of exposed crystal facets, it is observed that pollutants with higher chemical hardness (or higher HOMO-LUMO energy gap) react faster with the photocatalyst. The same correlation was not observed for the simple HOMO energy level, which would correspond to the stability of the h$^+$ generated organic radical, since carbamazepine significantly stands out from such a relation. This is correlated with the very low position of the LUMO orbital for CBZ, which mathematically affects value only for the η and ΔE predictors. In this regard, it is expected that detailed interactions between CBZ (or other compounds with lower LUMO position) and charge carriers on the TiO$_2$ surface might be different than for phenolic compounds. For the remaining compounds, the energy of the oxidized molecule gives a reasonable trend, which is in agreement with a possible process initiation by h$^+$. However, based on the overall results, we propose that chemical hardness or energy gap are better predictors for a diverse set of organic pollutants with different electronic properties.

Furthermore, analysis of the photocatalytic degradation of the pharmaceuticals mixture has shown that for a more complex matrix final degradation rate starts to depend on both total concentration, the pollutant type and the exposed crystal facet and reactor/lamp configuration. Specifically, ibuprofen degradation was preferred, while acetaminophen degradation was hindered for the {1 0 0} and {1 0 1} facets. The preference for the degradation of ibuprofen is in agreement with the preferred adsorption during the pre-irradiation stabilization period. Therefore, the surface presence of the pollutant determines degradation efficiency, which suggests that all of the investigated pharmaceuticals

Table 9
Results of the TOC removal for the degradation of the pharmaceuticals mixtures.

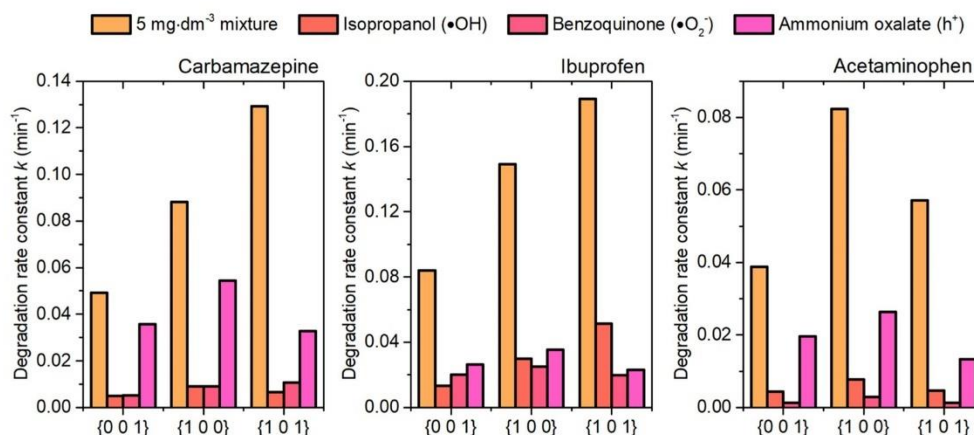| Sample	Total organic carbon removal (%) after 1 h of the process						
	Mixture 50 mg·dm^{-3}	Mixture 13 mg·dm^{-3}	Mixture 5 mg·dm^{-3}				
			Cycle I	Cycle II	Cycle III	Cycle III (3 h)	Xe lamp
{0 0 1}	3	20	41	9	41	62	17
{1 0 0}	14	26	24	51	25	37	48
{1 0 1}	18	31	51	62	55	83	81
P25	11	17	69	n.d.	n.d.	n.d.	n.d.

12

Fig. 12. Effect of the scavenger addition on the degradation rates observed for the 5 mg•dm^{-3} pharmaceuticals mixture. Column order from left to right match the one in the legend.
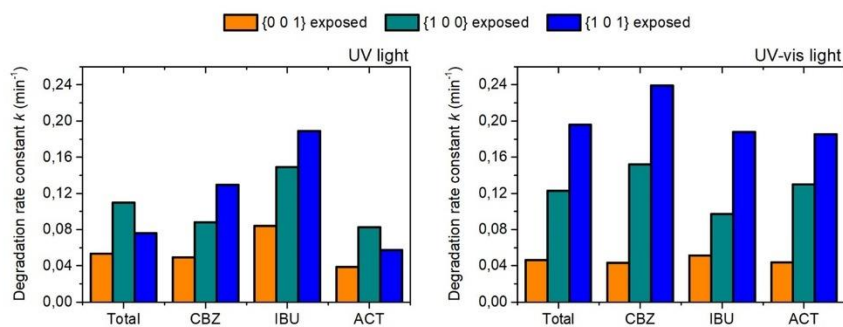

Fig. 13. Comparison of the degradation rates observed for the 5 mg•dm^{-3} using a different light sources (a), as well as scheme of the reaction set-up (b).

react strictly on the photocatalyst surface. The results imply that for specific processes with a complex matrix, a mixture of different photocatalysts might be possibly optimized to achieve higher degradation efficiencies. Alternatively, a sufficiently high surface area of the photocatalyst or optimized process conditions might be needed to effectively induce the degradation of all compounds over a single photocatalyst.

CRediT authorship contribution statement

Szymon Dudziak: designed and conducted the experiments, carried out the DFT calculations, analyzed the data and wrote the manuscript. **Agnieszka Fiszka Borzyszkowska**: contributed to photocatalytic activity analyses. **Anna Zielińska-Jurek**: contributed to conceptualization, methodology, supervised the work, manuscript writing and editing, fund-raising, and project administration.

Declaration of Competing Interest

The authors declare that they have no known competing financial interests or personal relationships that could have appeared to influence

the work reported in this paper.

Data availability

Data will be made available on request.

References

[1] P. Paíga, C. Delerue Matos, Sci. Total Environ. 569–570 (2016) 16.
[2] J. Liu, G. Lu, Z. Xie, Z. Zhang, S. Li, Z. Yan, Sci. Total Environ. 511 (2015) 54.
[3] E. Archer, B. Petrie, B. Kasprzyk-Hordern, G.M. Wolfaardt, Chemosphere 174 (2017) 437.
[4] M. Galus, N. Kirischian, S. Higgins, J. Purdy, J. Chow, S. Rangaranjan, H. Li, C. Metcalfe, J.Y. Wilson, Aquat. Toxicol. 132–133 (2013) 200.

13

[5] V. Contardo Jara, C. Lorenz, S. Pflugmacher, G. Nützmann, W. Kloas, C. Wiegand, Aquat. Toxicol. 105 (2011) 428.

[6] M. Parolini, A. Binelli, D. Cogni, A. Provini, Chemosphere 79 (2010) 489.

[7] X. Yuan, S. Li, J. Hu, M. Yu, Y. Li, Z. Wang, Sci. Total Environ. 655 (2019) 1125.

[8] E. Donner, T. Kosjek, S. Qualmann, K.O. Kusk, E. Heath, D.M. Revitt, A. Ledin, H. R. Andersen, Sci. Total Environ. 443 (2013) 870.

[9] Z. Bielan, S. Dudziak, A. Sulowska, D. Pelczarski, J. Ryl, A. Zielińska-Jurek, Materials 13 (2020) 1.

[10] P. García Muñoz, F. Fresno, C. Lefevre, D. Robert, N. Keller, ACS Appl. Mater. Interfaces 12 (2020) 57025.

[11] A. Grzegórska, P. Głuchowski, J. Karczewski, J. Ryl, I. Wysocka, K. Siuzdak, G. Trykowski, K. Grochowska, A. Zielińska-Jurek, Chem. Eng. J. 426 (2021), 130801.

[12] M. Kowalkińska, P. Głuchowski, T. Swebocki, T. Ossowski, A. Ostrowski, W. Bednarski, J. Karczewski, A. Zielińska-Jurek, J. Phys. Chem. C. 125 (2021) 25497.

[13] R. Mohammadzadeh Kakhki, R. Tayebee, S. Hedayat, Appl. Organomet. Chem. 32 (2018) 1.

[14] R. Tayebee, E. Esmaeili, B. Maleki, A. Khoshniat, M. Chahkandi, N. Mollania, J. Mol. Liq. 317 (2020), 113928.

[15] A. Mirzaei, L. Yerushalmi, Z. Chen, F. Haghighat, J. Hazard. Mater. 359 (2018) 516.

[16] S. Dudziak, Z. Bielan, P. Kubica, A. Zielinska-Jurek, J. Environ. Chem. Eng. 9 (2021), 105782.

[17] D. Wang, M.A. Mueses, J.A.C. Márquez, F. Machuca-Martínez, I. Grčić, R. Peralta, Muniz Moreira, and G. Li Puma, Water Res. (2021) 202.

[18] K.P. Sundar, S. Kanmani, Chem. Eng. Res. Des. 154 (2020) 135.

[19] M. Kowalkińska, S. Dudziak, J. Karczewski, J. Ryl, G. Trykowski, A. Zielińska-Jurek, Chem. Eng. J. 404 (2021), 126493.

[20] S. Dudziak, M. Kowalkińska, J. Karczewski, M. Pisarek, K. Siuzdak, A. Kubiak, K. Siwińska-Ciesielczyk, A. Zielińska-Jurek, Appl. Surf. Sci. 563 (2021), 150360.

[21] J. Chen, Y.F. Li, P. Sit, A. Selloni, J. Am. Chem. Soc. 135 (2013) 18774.

[22] M. Setvin, U. Aschauer, J. Hulva, T. Simschitz, B. Daniel, M. Schmid, A. Selloni, U. Diebold, J. Am. Chem. Soc. 138 (2016) 9565.

[23] Y.F. Li, A. Selloni, ACS Catal. 6 (2016) 4769.

[24] S. Dudziak, M. Kowalkińska, J. Karczewski, M. Pisarek, J.D. Gouveia, J.R. B. Gomes, A. Zielińska-Jurek, J. Phys. Chem. C. 126 (2022) 14859.

[25] X. Ma, Y. Dai, M. Guo, B. Huang, Langmuir 29 (2013) 13647.

[26] M. Lazzeri, A. Vittadini, A. Selloni, Phys. Rev. B - Condens. Matter Mater. Phys. 63 (2001) 1554091.

[27] F. Amano, T. Yasumoto, O.O. Prieto-Mahaney, S. Uchida, T. Shibayama, B. Ohtani, Chem. Commun. (2009) 2311.

[28] J. Li, D. Xu, Chem. Commun. 46 (2010) 2301.

[29] F. Neese, Wiley Interdiscip. Rev.: Comput. Mol. Sci. (2022) 1.

[30] F. Neese, Wiley Interdiscip. Rev.: Comput. Mol. Sci. 2 (2012) 73.

[31] A.D. Becke, J. Chem. Phys. 98 (1993) 5648.

[32] J.C. Zapata, L.K. McKemmish, J. Phys. Chem. A 124 (2020) 7538.

[33] R.G. Parr, R.G. Pearson, J. Am. Chem. Soc. 105 (1983) 7512.

[34] R.G. Parr, L. von Szentpaly, S. Liu, J. Am. Chem. Soc. 121 (1999) 1922.

[35] T. Koopmans, Physica 1 (1934) 104.

[36] D.J. Tozer, F. De Proft, J. Phys. Chem. A 109 (2005) 8923.

[37] X. Wang, L. Sø, R. Su, S. Wendt, P. Hald, A. Mamakhel, C. Yang, Y. Huang, B. B. Iversen, F. Besenbacher, J. Catal. 310 (2014) 100.

[38] A. El Mragui, I. Daou, O. Zegaoui, Catal. Today 321–322 (2019) 41.

[39] X. Guo, H. Yuan, T. Xiao, Y. Wu, Int. J. Biol. Macromol. 131 (2019) 1038.

[40] A.S. Barnard, L.A. Curtiss, Nano Lett. 5 (2005) 1261.

[41] J.J. Murcia, M.C. Hidalgo, J.A. Navío, J. Araña, J.M. Doña Rodríguez, Appl. Catal. B: Environ. 179 (2015) 305.

[42] Q. Xiang, K. Lv, J. Yu, Appl. Catal. B: Environ. 96 (2010) 557.

[43] M. Maisano, M.V. Dozzi, M. Coduri, L. Artiglia, G. Granozzi, E. Selli, ACS Appl. Mater. Interfaces 8 (2016) 9745.

[44] L. Mino, F. Pellegrino, S. Rades, J. Radnik, V.D. Hodoroaba, G. Spoto, V. Maurino, G. Martra, ACS Appl. Nano Mater. 1 (2018) 5355.

[45] J. Zhang, Y. Nosaka, Appl. Catal. B: Environ. 166–167 (2015) 32.

[46] H. Gong, W. Chu, Y. Huang, L. Xu, M. Chen, M. Yan, Environ. Pollut. 276 (2021), 116691.

[47] J.C.C. Da Silva, J.A.R. Teodoro, R.J.D.C.F. Afonso, S.F. Aquino, R. Augusti, J. Mass Spectrom. 49 (2014) 145.

[48] K.H. Hama Aziz, H. Miessner, S. Mueller, D. Kalass, D. Moeller, I. Khorshid, M.A. M. Rashid, Chem. Eng. J. 313 (2017) 1033.

[49] N. Flores-Holguín, J. Frau, D. Glossman-Mitnik, Molecules (2019) 24.

[50] T. Hathway, W.S. Jenks, J. Photochem. Photobiol. A: Chem. 200 (2008) 216.

[51] S. Moradi, A.A. Isari, F. Hayati, R. Rezaei Kalantary, B. Kakavandi, Chem. Eng. J. 414 (2021), 128618.

[52] C. Minero, G. Mariella, V. Maurino, D. Vione, E. Pelizzetti, Langmuir 16 (2000) 8964.

[53] A.G. Agrios, P. Pichat, J. Photochem. Photobiol. A: Chem. 180 (2006) 130.

[54] K. Lv, X. Guo, X. Wu, Q. Li, W. Ho, M. Li, H. Ye, D. Du, Appl. Catal. B: Environ. 199 (2016) 405.

[55] Y. Sun, J.J. Pignatello, Environ. Sci. Technol. 29 (1995) 2065.

[56] C.S.A. Antunes, M. Bietti, M. Salamone, N. Scione, J. Photochem. Photobiol. A: Chem. 163 (2004) 453.

[57] J.Y. Hwang, G. hee Moon, B. Kim, T. Tachikawa, T. Majima, S. Hong, K. Cho, W. Kim, W. Choi, Appl. Catal. B: Environ. 286 (2021), 119905.

[58] S. Valencia, F. Cataño, L. Rios, G. Restrepo, J. Marín, Appl. Catal. B: Environ. 104 (2011) 300.

[59] F. Amano, K. Nogami, M. Tanaka, B. Ohtani, Langmuir 26 (2010) 7174.

14

ACS **APPLIED** MATERIALS & INTERFACES

www.acsami.org

Research Article

Insight into (Electro)magnetic Interactions within Facet-Engineered BaFe$_{12}$O$_{19}$/TiO$_2$ Magnetic Photocatalysts

Szymon Dudziak,* Cristina Gómez-Polo, Jakub Karczewski, Kostiantyn Nikiforow, and Anna Zielińska-Jurek*

Cite This: https://doi.org/10.1021/acsami.3c13380

Read Online

ACCESS | Metrics & More | Article Recommendations | Supporting Information

ABSTRACT: A series of facet-engineered TiO$_2$/BaFe$_{12}$O$_{19}$ composites were synthesized through hydrothermal growth of both phases and subsequent deposition of the different, faceted TiO$_2$ nanoparticles onto BaFe$_{12}$O$_{19}$ microplates. The well-defined geometry of the composite and uniaxial magnetic anisotropy of the ferrite allowed alternate interfaces between both phases and fixed the orientation between the TiO$_2$ crystal structure and the remanent magnetic field within BaFe$_{12}$O$_{19}$. The morphology and crystal structure of the composites were confirmed by a combination of scanning electron microscopy (SEM) and X-ray diffraction (XRD) analyses together with the detailed study of BaFe$_{12}$O$_{19}$ electronic and magnetic properties. The photocatalytic activity and magnetic field effect were studied in the reaction of phenol degradation for TiO$_2$/BaFe$_{12}$O$_{19}$ and composites of BaFe$_{12}$O$_{19}$ covered with a SiO$_2$ protective layer and TiO$_2$. The observed differences in phenol degradation are associated with electron transfer and the contribution of the magnetic field. All obtained magnetic composite materials can be easily separated in an external magnetic field, with efficiencies exceeding 95%, and recycled without significant loss of photocatalytic activity. The highest activity was observed for the composite of BaFe$_{12}$O$_{19}$ with TiO$_2$ exposing {1 0 1} facets. However, to prevent electron transfer within the composite structure, this photocatalyst material was additionally coated with a protective SiO$_2$ layer. Furthermore, TiO$_2$ exposing {1 0 0} facets exhibited significant synergy with the BaFe$_{12}$O$_{19}$ magnetic field, leading to 2 times higher photocatalytic activity when ferrite was magnetized before the process. The photoluminescence emission study suggests that for this particular combination, the built-in magnetic field of the ferrite suppressed the recombination of the photogenerated charge carriers. Ultimately, possible effects of complex electro/magnetic interactions within the magnetic photocatalyst are shown and discussed for the first time, including the anisotropic properties of both phases.

KEYWORDS: BaFe$_{12}$O$_{19}$, TiO$_2$, magnetic photocatalyst, magnetic field, crystal facets
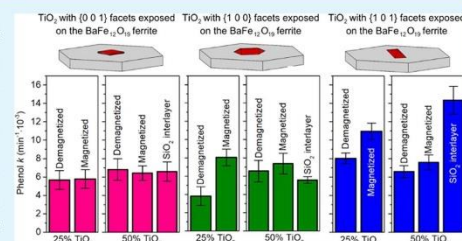
1. INTRODUCTION

Photocatalysis presents a promising but challenging solution for various environmentally relevant processes, such as the generation of solar fuels and the purification of water and gas streams.[1−3] However, large-scale application of heterogeneous photocatalysis still requires solving some challenges related to enhancing semiconductor activity and decreasing the recombination of photogenerated charge carriers participating in the redox reactions on the photocatalyst surface. In recent years, this has led to great attention focused on improving photocatalytic activity by designing and synthesizing different photocatalytic materials.[4−7] More recently, studies have shown that photocatalytic processes might be optimized by alternating the exposition of the specific crystal planes.[8−10] This is strictly connected with the anisotropy of the photocatalyst electronic structure, which depends on the direction inside the crystal structure, the specific arrangement of atoms at the interface, and the nature of the interface itself.[11−13] Ultimately, the alternation of the photocatalyst morphology and exposed crystal facet is recognized as the state-of-the-art approach to optimize the performance in photocatalytic reactions. Another important technological issue in the application of such photocatalytic nanostructures is their separation after the reaction, which is especially important for water treatment processes. An interesting and promising strategy to overcome this challenge is to design a photocatalyst that can be separated in an external magnetic field. However, since the material that would be both ferromagnetic and highly photocatalytic active has not been found so far, this approach usually requires

A

combining ferromagnetic/photocatalytic materials in the form of composites.[14−16] While this approach seems generally straightforward, it creates a complex problem of possible interactions between both phases, which is especially important in the highlighted approach of photocatalyst shape engineering. Noteworthy, these interactions include not only possible electron transfer, which is a well-described phenomenon, but also possible interactions with the inner magnetic field that can be built-in within the ferromagnetic phase. At present, it is known that the introduction of the magnetic field can influence the photocatalytic activity and behavior of the photogenerated charge carriers.[17−19] However, these studies generally do not include a possible anisotropy of the TiO_2 electronic structure. In order to discuss such effects, it would be beneficial to achieve strict orientation between an external magnetic field and suspended particles, which is impossible due to the dispersed particles' random orientation. As a consequence, at present, the possible effect of the magnetic field on TiO_2 activity is limited only to general observations that are difficult to discuss with respect to the detailed photocatalyst structure. However, a well-defined orientation between two shape-engineered particles could lead to a fixed orientation between a built-in magnetic field and a combined photocatalyst. This possibility has inspired us to design a ferromagnet/photocatalyst composite with defined morphology to study both electronic and magnetic interactions that can be designed through their mutual shape engineering.

In this regard, the aim of the present study is to explain the following: (i) How changing the exposed crystal facets will influence the ferromagnet/photocatalyst interface and resulting performance? (ii) To what extent this interface can be optimized? (iii) Is the observed effect associated only with charge carrier transport or also with the built-in magnetic field? (iv) Does the magnetic/electronic interactions differ, depending on the system shape and orientation? To find answers to these questions, faceted anatase nanoparticles were prepared and used as the photocatalytic part of the composite due to their well-documented properties and performance.[20−22] For the ferromagnetic phase, hexagonal $BaFe_{12}O_{19}$ was selected due to its high remanent magnetization, uniaxial magnetic anisotropy, relatively low Curie point, and preferred growth into two-dimensional (2D) microplates under hydrothermal conditions.[23,24] Such a combination allows for the deposition of TiO_2 with exposed {1 0 1}, {1 0 0}, and {0 0 1} crystal facets onto the same, preferentially exposed crystal facet of the ferrite, resulting in good control over both the interface and orientation between TiO_2 and the vector of a built-in magnetic field, which is pointing at the specific direction, according to the uniaxial anisotropy. Furthermore, the relatively low Curie point of $BaFe_{12}O_{19}$ (about 450 °C) allows for demagnetization of the composite through calcination at temperatures that should not induce significant phase transformation of both materials. Finally, coating magnetic particles with a SiO_2 layer to prevent electron transfer within the composite structure was also studied as a control to the samples in direct contact.

2. METHODS

2.1. Synthesis of $BaFe_{12}O_{19}$ and $BaFe_{12}O_{19}@SiO_2$.
The synthesis of unmodified $BaFe_{12}O_{19}$ microplates was performed hydrothermally.[25] Furthermore, purification of the NaOH solution from CO_3^{2-} presence was performed based on the CaO-assisted procedure suggested by Sipos et al.[26] Briefly, 100 cm^3 of NaOH solution with a nominal concentration of 5 mol·dm^{-3} was mixed with

1 g of CaO, freshly calcined at 900 °C for 2 h, and ground to remove possible impurities. The mixture was sealed and left to react for 2 h under magnetic stirring, after which it was left for a few minutes to sediment most of the powder. Simultaneously, 4.5 g of $Fe(NO_3)_3$·$9H_2O$ and 0.4 g of $Ba(NO_3)_2$ were dissolved in 80 cm^3 of deionized water with the addition of 0.5 g of poly(ethylene glycol) (PEG) inside the 200 cm^3 lining of a hydrothermal reactor. The mixture was sealed with Al foil and magnetically stirred under a constant N_2 flow for 20 min. After this time, a part of the sealing was opened, and 45 cm^3 of the purified NaOH solution was immediately introduced to the mixture, passing through the two subsequent silica gel filters to help remove the last of the dispersed Ca particles. After precipitation, the magnetic stirrer and Al foils were removed, and the reactor was immediately closed and left to react at 250 °C for 24 h. After the reaction, the prepared powder was magnetically separated and washed with 10% (wt) CH_3COOH and water. Finally, it was dried at 80 °C and calcined at 500 °C for 2 h before further characterization and modification.

Furthermore, surface coating of the prepared $BaFe_{12}O_{19}$ with SiO_2 was achieved through a two-step condensation of tetraethyl orthosilicate (TEOS) in the presence of the ferrite particles. Specifically, 0.25 g of the ferrite was dispersed in the mixture of 100 cm^3 of water with 5 cm^3 of a 25% (wt) NH_4OH solution, followed by the addition of 10 μL of TEOS under mechanical stirring. After 1 h of the initial reaction, magnetic particles were separated with a magnet. Further growth of the SiO_2 layer was continued in the second dispersion using 20 cm^3 of water and 100 cm^3 of ethanol. During this step, two parts of 30 μL of TEOS were added with a 1 h interval and finally left to react for an additional 2 h. The final modified ferrite was separated with a magnet, washed with water, dried at 80 °C, and calcined at 500 °C for 2 h before further characterization and modification.

2.2. Synthesis of Faceted TiO_2.
The synthesis of the faceted TiO_2 particles, exposing the majority of the {0 0 1}, {1 0 0}, or {1 0 1} facets, was performed hydrothermally, following previously described procedures.[27−29] Briefly, a mixture of 17 cm^3 of titanium tert-butoxide, 30 cm^3 of n-butanol, and 3.4 cm^3 of a 50% (wt) HF solution was reacted at 210 °C for 18 h to achieve dominant exposition of the {0 0 1} facets. Furthermore, 1 g of commercial TiO_2 P25 (Evonik) was treated either with 40 cm^3 of a 10 mol·dm^{-3} NaOH solution at 120 °C for 20 h or with 40 cm^3 of a 8.5 mol·dm^{-3} KOH solution at 200 °C for 16 h to obtain corresponding Na/K titanates as the precursors for the remaining samples. Dominant exposition of the {1 0 0} facets was achieved by reacting half of the obtained Na titanate with 100 cm^3 of water at 210 °C for 24 h. For this reaction, the Na precursor was used directly after its formation without drying, only after washing it to a pH between 10 and 11. Finally, exposition of the {1 0 1} facets was achieved by washing the obtained K titanate precursor to the pH between 7 and 8, drying it at 80 °C and reacting 0.4 g of the dried powder with 100 cm^3 of NH_4OH/NH_4Cl (0.3/0.3 mol·dm^{-3}) buffer at 210 °C for 16 h.

All TiO_2 samples were washed with water several times and dried at 80 °C prior to initial characterization and further combination with the ferrite. Control samples of pure TiO_2 were also calcined at 500 °C for 2 h, similar to the case for the composites.

2.3. Preparation of the $BaFe_{12}O_{19}/TiO_2$ and $BaFe_{12}O_{19}@SiO_2/TiO_2$ Composites.
The preparation of magnetic composites with platelet $BaFe_{12}O_{19}$ combined with the prepared TiO_2 with different morphologies was achieved based on attractive interactions between both suspended phases based on the performed ζ potential analyses. A typical procedure included individual dispersion of both materials in water under mechanical stirring and a further combination of the prepared suspensions at pH between 5 and 6. The final amount of the combined material was designed to be 0.1 g in each case and was suspended in a total volume of 200 cm^3 of water, while specific amounts of $BaFe_{12}O_{19}$ and TiO_2 varied. Furthermore, the pH of the suspension was controlled by using HCl and NH_4OH. After stabilization, the prepared suspension was slowly evaporated under constant mechanical stirring, and the resulting powder was collected
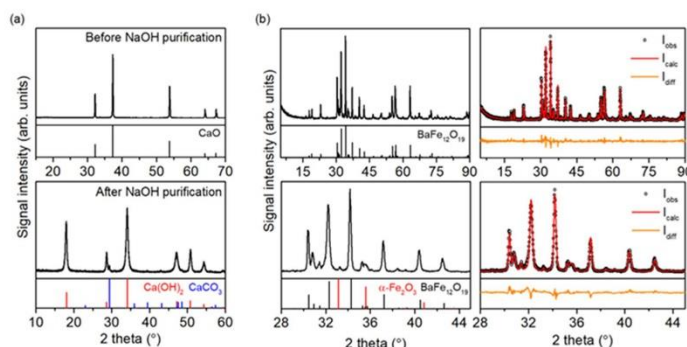
B

Figure 1. X-ray diffraction patterns of (a) CaO used for purification of the NaOH solution before and after the reaction and (b) final obtained $BaFe_{12}O_{19}$ sample after calcination at 500 °C for 2 h. Panel (b) shows patterns itself and Rietveld-refined profiles with calculated residuals.

and calcined at 500 °C for 2 h. Modification with TiO_2 of both unmodified $BaFe_{12}O_{19}$ and $BaFe_{12}O_{19}@SiO_2$ was performed similarly.

2.4. Characterization of the Materials. The crystalline structure of the prepared materials was characterized by using a Rigaku Mini Flex powder X-ray diffractometer (XRD) with a Cu Kα radiation source. The morphology and elemental composition of the samples were analyzed by using an FEI Quanta FEG 250 scanning electron microscope (SEM) combined with an Apollo-X SDD energy-dispersive X-ray spectroscopy detector (EDS). For the SEM/EDS analysis, samples were coated with a thin layer of Au to remove excess charge. Surface composition and oxidation states of the elements were analyzed based on the X-ray photoelectron spectroscopy (XPS) measurements using a PHI 5000 Versa Probe spectrometer with monochromatic Al Kα radiation. The high-resolution (HR) XPS spectra were collected with the hemispherical analyzer at a pass energy of 117.4 eV and an energy step size of 0.1 eV. Deconvolution of the spectra was performed using a Shirley background and a Gaussian peak shape with 30% Lorentzian character by using Casa XPS 2.3 software. Magnetic properties of the materials were analyzed using a Quantum Design MPMS XL7 SQUID magnetometer in the temperature range between 5 and 300 K. Absorption properties of the samples were determined using a Thermo Fisher Evolution 220 spectrophotometer for the wavelengths between 200 and 1100 nm, using $BaSO_4$ as a diffusive reflectance standard (DR UV–vis), as well as a Nicolet Avatar 360 FTIR spectrometer for the wavenumbers between 400 and 4000 cm^{-1} (FTIR). For the FTIR measurements, approximately 0.5 mg of the sample was mixed with 200 mg of KBr and pressed into the pellet, which was further pretreated at 150 °C for 2 h under reduced pressure to minimize the amount of adsorbed water. The ζ potential of the samples was analyzed using Malvern Instruments Zetasizer 3000 apparatuses and HCl/NH_4OH solutions for pH control. Electrochemical tests were performed using an Autolab PGSTAT204 potentiostat–galvanostat equipped with the FRA32 M module and using a 0.5 $mol \cdot dm^{-3}$ Na_2SO_4 solution as an electrolyte. Screen-printed electrodes were used during the measurements, with working and counter electrodes made of carbon and the reference electrode being Ag/AgCl. Prior to measurements, prepared samples were dispersed in a 1:1 vol. ethanol/water mixture and were drop-casted on the surface of the working electrode. After drying, the prepared layer was blocked with 2 μL of Nafion solution (1% in ethanol) and dried for final measurements. The Mott–Schottky analysis of the samples was performed based on the electrochemical impedance spectroscopy measurements, collected using 10 mV amplitude of the AC signal and 1000 Hz frequency. The space charge capacitance (C) was calculated using the relation $C = -(2\pi \cdot f \cdot Z_{im})^{-1}$, where f is the frequency and Z_{im} is the imaginary part of the impedance.[30] The flatband potential position was determined as the zero point of the fitted linear jump on the C^{2-} versus E graph. Photoluminescence

spectra (PL) of the obtained samples were recorded using a Shimadzu RF-6000 spectrophotometer.

2.5. Computational Details. The electronic structure of the $BaFe_{12}O_{19}$ phase was simulated at the density functional theory (DFT) level using the projector augmented wave method (PAW) and Perdew–Burke–Ernzerhof (PBE) functionals with an energy cutoff of 500 eV, as implemented in the Quantum Espresso software package.[31–34] During the calculations, the crystal structure was relaxed to the threshold of 10^{-3} Ry·Bohr^{-1} using $4 \times 4 \times 2$ k-point sampling of the Brillouin zone. The simulation of the electronic structure was performed for the optimized geometry, including density of states (DOS) calculation for the $5 \times 5 \times 2$ k-point grind and band structure calculation with 20 points between each high-symmetry point on the K-path.[35] To get the best description of the electronic structure, calculations were repeated using different values of the Hubbard U parameter applied for Fe ions in order to take into account Coulombic interactions between different sites (U_{Fe} = 0, 3, 6, 9, 10, and 12 eV). The final structure is presented for the simulation that gave the best fit with the experimental results.

2.6. Photocatalytic Activity. The photocatalytic activity of the prepared materials was investigated in the reaction of phenol degradation. Typically, 25 mg of the sample was dispersed in the 25 cm^3 of phenol solution with a concentration of 200 $\mu mol \cdot dm^{-3}$ inside the photoreactor, equipped with a quartz window. The prepared suspension was stirred mechanically and was aerated with a 4 $dm \cdot h^{-1}$ airflow for 30 min to achieve adsorption–desorption equilibrium. After this time, the reactor was irradiated with a 300 W Xe lamp located 60 cm from the reactor border. During the process, samples were collected before the stabilization, at the start of irradiation, and then every 5 min for a total of 30 min. Phenol concentration was estimated based on the conjugation reaction with 4-nitroaniline and colorimetric quantification for λ = 480 nm.

3. RESULTS AND DISCUSSION

3.1. Structure and Morphology of the Prepared $BaFe_{12}O_{19}$ and $BaFe_{12}O_{19}@SiO_2$. Preparation of single-phase $BaFe_{12}O_{19}$ usually requires either high calcination temperatures or a high excess of Ba introduced to the hydrothermal reaction. This is mostly associated with the problem of the Ba^{2+} reaction with CO_2/CO_3^{2-}, which results in the formation of $BaCO_3$, leading to limited incorporation of barium into the hexaferrite structure and simultaneous cocreation of hematite α-Fe_2O_3. The further reaction between $BaCO_3$ and α-Fe_2O_3 requires at least 600 °C to complete the formation of $BaFe_{12}O_{19}$.[36] However, temperatures exceeding 800 °C are commonly needed to obtain single-phase ferrite.[37]
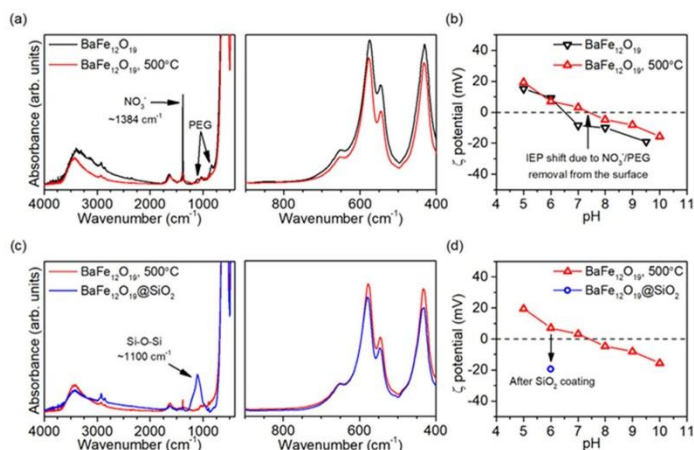
Figure 2. Comparison of the FTIR spectra (a, c) and ζ potential change with pH (b, d) of the prepared $BaFe_{12}O_{19}$ samples directly after the synthesis and calcination at 500 °C for 2 h and after modification with SiO_2.
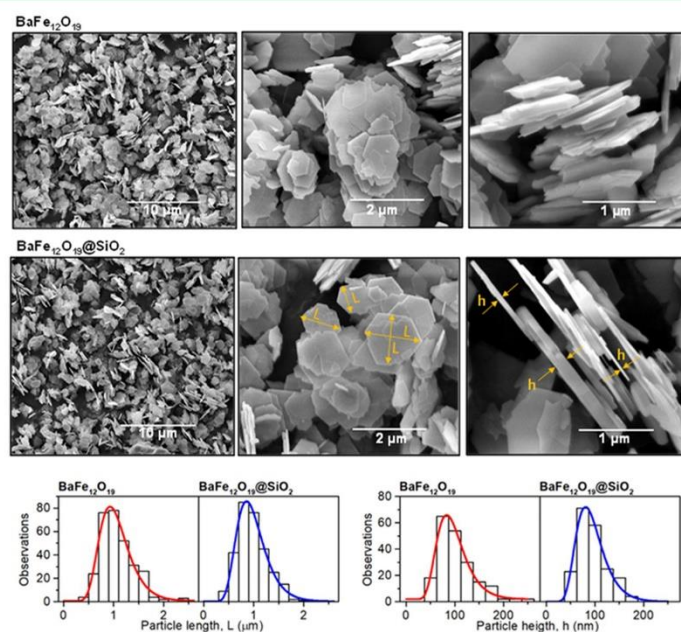
Figure 3. SEM images of the final calcined $BaFe_{12}O_{19}$ sample, before and after modification with SiO_2, together with the statistical distribution of the observed dimensions L (300 counts per sample) and h (200 counts). Exemplary dimensions are highlighted for the $BaFe_{12}O_{19}@SiO_2$ sample.

Focusing on the possible application of $BaFe_{12}O_{19}$ in photocatalytic processes, calcination at such temperatures is not desired, as it can lead to significant aggregation and sintering of the particles, reducing their surface area and limiting control over their further modification. On the other hand, the hydrothermal approach in Ba-rich solutions generally leads to the formation of very elongated $BaFe_{12}O_{19}$ microplates with visibly decreased coercivity, magnetic saturation, and remanence.[38] As this study aims to analyze the potential impact of the $BaFe_{12}O_{19}$ inner magnetic field on the

D

Page | 163

Table 1. Mean Observed Dimensions of the $BaFe_{12}O_{19}$ Plates and Summation of the Elemental Analysis

sample	particle length (μm)	particle height (nm)	particle volume[a] (μm^3)	EDS Fe/Ba (at.)	EDS Si (atom %)	XPS Si (atom %)
$BaFe_{12}O_{19}$	1.06 ± 0.32	97 ± 32	9.441×10^{-2}	11.0 ± 0.6	n.d.	n.d.
$BaFe_{12}O_{19}@SiO_2$	0.99 ± 0.31	95 ± 31	7.971×10^{-2}	10.9 ± 0.6	n.d.	8.1

[a]Calculated assuming the length of the particle as double apothem of the regular hexagon.
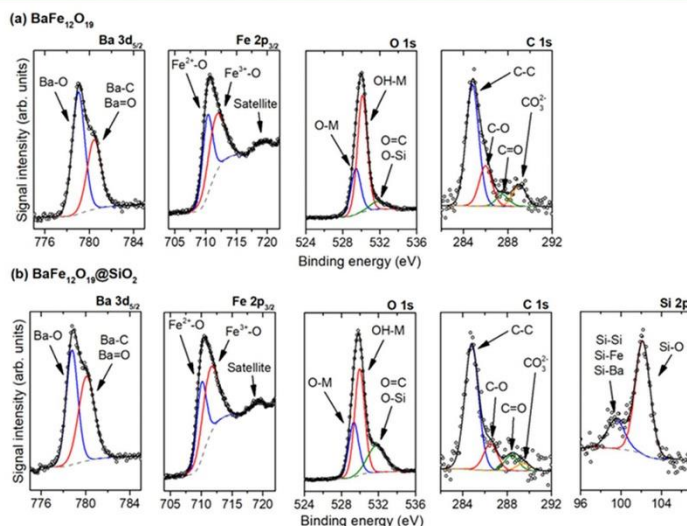

Figure 4. Deconvolution of the observed XPS signals for both unmodified (a) and SiO_2-modified (b) $BaFe_{12}O_{19}$ samples. Deconvolution of the Ba $3d_{5/2}$ peak is presented after the extraction of the $Fe_{L,MM}$ signal.

photocatalytic activity, softening its properties is also not desired. In this regard, it is necessary to eliminate CO_2/CO_3^{2-} from the synthesis by purifying NaOH solution from Na_2CO_3 presence through the reaction with freshly calcined CaO, as suggested by Sipos et al.[26] As shown in Figure 1a, this process resulted in precipitation of about 3.6% (wt) calcite $CaCO_3$, showing successful solution purification. However, most CaO was simultaneously transformed to $Ca(OH)_2$, affecting the actual concentration of the OH^- ions introduced to the synthesis and influencing $BaFe_{12}O_{19}$ nucleation. In this regard, in the present study, the optimal amount of the purified NaOH was determined experimentally to be around 45 cm^3, while especially lower amounts resulted in the clear presence of α-Fe_2O_3 (>5% wt). Ultimately, $BaFe_{12}O_{19}$ prepared under such conditions and further calcined at 500 °C for 2 h showed high purity, as presented in Figure 1b, with the presence of α-Fe_2O_3 reduced to 1.8% (wt), as determined through Rietveld refinement of the whole pattern ($\chi^2 = 1.53$). This amount of α-Fe_2O_3 resulted from capturing atmospheric CO_2 during the precipitation, which is likely impossible to avoid completely. Nevertheless, the amount of α-Fe_2O_3 is very small and will not influence, e.g., the overall magnetic properties, as shown later. Modification of obtained $BaFe_{12}O_{19}$ with SiO_2 resulted in no change in its diffraction pattern, which is in accordance with the expected amorphous nature of the obtained silica particles.

Furthermore, calcination of the synthesized $BaFe_{12}O_{19}$ was necessary to purify its surface from residual NO_3^- and PEG

molecules that were left after the synthesis. This was controlled by a combination of FTIR and zeta (ζ) potential measurements, as shown in Figure 2. The NO_3^- presence after the synthesis is observed as a sharp peak at ~1384 cm^{-1},[39] and the residual PEG molecules are noticed due to weak bands at 840−860 and ~1100 cm^{-1}, characteristic for C−O and C−C vibrations, respectively, observed previously for PEG.[40] Both of these signals are mostly hindered after the calcination, which is accompanied by the shift of the observed isoelectric point (IEP) to the higher pH value, similar to the one reported previously for the $BaFe_{12}O_{19}$ prepared by calcination at 1000 °C.[41] Both of these observations prove successful purification of the ferrite surface before further investigation.

Moreover, after coating with SiO_2, a broad, asymmetric signal centered at 1100 cm^{-1} appeared, which is in very good agreement with the known signals for the analogical silica structures.[42,43] A simultaneous shift of the measured ζ potential at a pH of 6 to a strongly negative value further proves successful modification with SiO_2. During both described procedures, no significant changes in the absorbance characteristic for metal oxides (<700 cm^{-1}) are noticed, suggesting that their effect on the structure of $BaFe_{12}O_{19}$ itself is limited.

The morphology of the final calcined $BaFe_{12}O_{19}$ sample was observed in detail before and after modification with SiO_2. As shown in Figure 3, almost no difference was visible between both materials, and hexagonal-shaped microplates with clean
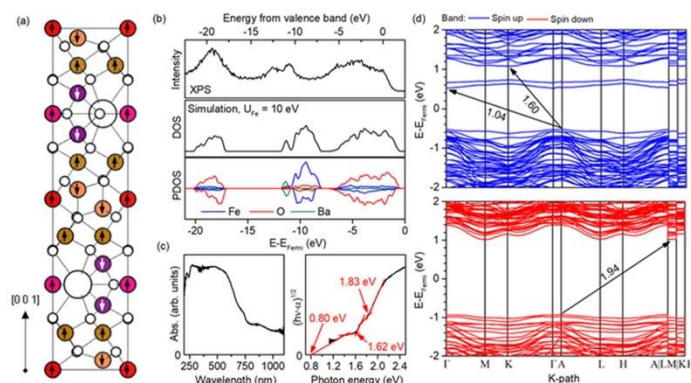
E

Figure 5. Summation of the $BaFe_{12}O_{19}$ electronic structure with a minimum-energy spin configuration of the Fe atoms, as shown in panel (a), where Fe sites with the same coordination are marked with the same color (big white spheres are Ba and small white spheres are O atoms). The simulated density of states distribution, compared to the observed density of occupied states below valence band top (b), band gap determination from absorbance results (c), and detailed band structure (d).

facets were systematically observed in all images. Based on the statistical distribution of the observed dimensions, the mean length and height of the plates were about 1000 mm × 95 nm. Detailed values are shown in Table 1, with errors presented as standard deviations of the fitted log-normal distributions. Such morphology is in agreement with previous studies on the preparation of $BaFe_{12}O_{19}$, which shows that large facets are oriented perpendicularly to the [0 0 1] vector of the ferrite crystal structure.[38] Although the atomic geometries of these facets are not known at the moment, it is important to notice that they are also perpendicular to the easy magnetization axis of $BaFe_{12}O_{19}$,[23] and therefore, the vector of ferrite inner magnetic field will tend to point at the exposed surface.

Furthermore, the consistency of the observed morphology and exposition of the clean facets in both cases suggests that SiO_2 forms a very thin layer on the surface without significant aggregation into bigger entities. This was further confirmed with the EDS analysis, performed over approximately 65 μm^2 of the sample, which showed no Si enrichment for the SiO_2-coated sample. As the EDS analysis has low sensitivity for the detection of surface species, this suggests that Si—O—Si structures observed in the FTIR spectrum are predominantly present on the surface.

Finally, the detailed surface composition of both samples was analyzed based on the XPS results, as shown in Figure 4. For the $BaFe_{12}O_{19}@SiO_2$ sample, the presence of 8.1% (at.) silicon was observed, ultimately proving its surface presence. Deconvolution of the Si peak in Figure 4b has shown that Si exists mostly as the nonstoichiometric oxide, which is further confirmed with the increased O 1s signal for the binding energy of ~532 eV. Noteworthy, some of the Si exist in the metallic form, originating from the Si—Si bonds within the SiO_x structure or Si—Ba/Si—Fe that could be formed between the ferrite surface and the growing SiO_2 layer. Assuming that the silica layer forms a very thin structure, which is in accordance with its presence not observed during the SEM/EDS studies, the appearance of a relatively strong signal originating from the Fe/Ba—Si bonds formed at the interface

seems reasonable. No presence of Si was observed in the case of the unmodified sample.

Besides, both materials are fairly similar, showing no significant differences. In both cases, surface enrichment with barium is observed, connected to the existence of two different Ba states. Especially, the second state at higher binding energy (780.5 eV) is not related to the $BaFe_{12}O_{19}$ structure[44−46] and shows $BaCO_3$ presence. This is especially visible for the unmodified sample, clearly confirmed with the C 1s signal at ~289 eV and the O 1s signal at ~532 eV that give an almost stoichiometric ratio of all elements (calculated Ba/C/O for these states is 1:0.92:3, after correction for the C=O bonds with the C 1s signal at ~287.5 eV). As already mentioned, the formation of $BaCO_3$ results probably from the capture of atmospheric CO_2 during precipitation with NaOH, despite its previous purification, and is in agreement with the trace amount of α-Fe_2O_3 observed in the XRD pattern. Nevertheless, the absolute presence of Ba species associated with the carbonate is only ~1.3% (at.), showing that the vast majority of the sample surface results strictly from the $BaFe_{12}O_{19}$ structure. Moreover, for both samples, a detailed analysis of the Fe $2p_{3/2}$ signal suggests the existence of two different Fe states with lower and higher oxidations in the oxide structure. However, this is probably the effect of different Fe^{3+} coordination inside the $BaFe_{12}O_{19}$ crystal lattice (octahedral, tetrahedral, and bipyramidal Fe^{3+} sites are present in the bulk structure[14]), which are known to affect Fe $2p_{3/2}$ peak shape.[47] In this regard, the dominant presence of Fe^{3+} is confirmed with a satellite peak separated from the main Fe $2p_{3/2}$ signal, which is not observed for the Fe^{2+} ions.[48] Therefore, the Fe signal is in agreement with the expected $BaFe_{12}O_{19}$ structure. For the SiO_2-modified sample, a slight increase in the Ba and Fe states with higher binding energy results probably from the additional calcination of the sample, forming more oxidized species at the surface.

3.2. Magnetic and Electronic Properties of the Prepared $BaFe_{12}O_{19}$ and $BaFe_{12}O_{19}@SiO_2$. Due to the relatively low amount of information about $BaFe_{12}O_{19}$ application in the photocatalysis process, its electronic

F

structure was investigated in detail before combining it with TiO_2. It was started by simulating the density of state distribution and band structure, assuming minimum-energy spin configuration between the subsequent Fe layers,[49] as shown in Figure 5a. During these studies, different values of the Hubbard parameter U were applied for the Fe atoms to achieve a possibly good correlation between the simulated structure and experimental results obtained from the XPS and DR/UV−vis analyses (U_{Fe} = 0, 3, 6, 9, 10, and 12 eV). Ultimately, the best agreement was obtained for U_{Fe} = 10 eV. Specifically, as shown in Figure 5b, the simulated band structure down to $E − E_{Fermi}$ = −21 eV is in good agreement with the XPS results, showing three subsequent bands, in accordance with, e.g., a previous study by Atuchin et al.[46] Interestingly, the detailed band gap analysis presented in Figure 5c suggests the existence of up to three electron transitions, which was further supported by band structure calculations (Figure 5d). The lowest energy transition occurs between the A/Γ symmetry points in the spin-up component, with a computed energy of about 1 eV. Interestingly, this is in agreement with the absorbance studies, which show visible absorption down to the full measurement range of the apparatus (~1.1 eV). Extrapolation of this trend beyond experimental data suggests that the minimum excitation energy can be as low as 0.80 eV, which is a bit lower than a value obtained from the simulation. However, it should be pointed out that in this case, a detailed comparison of these values is difficult due to the various factors present in both measurements (arbitrary applied U value during the simulation, which affected the exact position of the band, the possible presence of some defect states in the analyzed sample, and extrapolation of the experimental value). Nevertheless, both absorbance and DFT studies agree that this low-energy transition can be distinguished for $BaFe_{12}O_{19}$, which might affect its photocatalytic performance. Furthermore, the second signal observed in the absorbance spectra, with a minimum energy of 1.62 eV, belongs to the indirect excitation between the A and K high-symmetry points, also in the spin-up part of the structure. As shown, the analogous transition in the spin-down component is associated with a bit higher energy (1.94 eV from simulations, between the A and minimum at the L → M path), in accordance with the absorption spectra (third transition at 1.83 eV). However, it should be noted that above ~1.8 eV, direct excitation of the electrons with the up-spin might also occur, which will cause overlapping of these signals.

Furthermore, band structure studies were followed with Mott−Schottky analysis to determine the ferrite position of the conduction band (CB) based on the determined flatband potential. As shown in Figure 6, the conduction band edge for $BaFe_{12}O_{19}$ is estimated at 0.688 V relative to the standard hydrogen electrode. This value is in good agreement with the CB position of, e.g., α-Fe_2O_3, being approximately 0.6−0.8 V, as reported in the literature.[50,51] Noteworthy, when $BaFe_{12}O_{19}$ was modified with the SiO_2 layer, the effective CB edge was shifted to the significantly lower potential of −0.822 V. While it is unlikely that this value represents the conduction band of SiO_2 itself and is probably influenced by both silica nonstoichiometry and creation of the interface between SiO_2 and other surface species observed during XPS studies, it does show that effective potential of the electrons present at the $BaFe_{12}O_{19}$@SiO_2 surface is significantly lowered. Above all, this will be used to hinder electron transfer from TiO_2 to
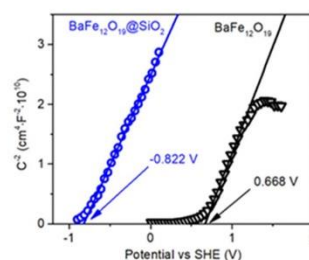

Figure 6. Mott−Schottky plot and determined flatband potentials for the $BaFe_{12}O_{19}$ and $BaFe_{12}O_{19}$@SiO_2 samples.

$BaFe_{12}O_{19}$, as shown in the further sections of the present study.

The analysis of the electronic properties was followed with magnetization studies, and the results are summarized in Figure 7. Depending on the analysis details, the obtained mass magnetization ($Am^2 \cdot kg^{-1}$) was recalculated to volume magnetization ($A \cdot m^{-1}$) using the density of the $BaFe_{12}O_{19}$ crystal phase obtained from the XRD pattern (~5200 $kg \cdot m^{-3}$). As shown in panels a−c, magnetization of the obtained sample occurs smoothly, without noticeable steps, proving that formation and reversal of the magnetic field are uniform within the material. The sample showed semihard ferromagnetic-type hysteresis with relatively large values of remanent magnetization (M_r) and coercivity (H_c). This is followed by the magnetization saturation (M_s) value, as determined from the fitted law of approach to saturation (LAS),[52] presented in Figure 7d for the reversible part of the hysteresis in the first quadrant. Based on the fitted LAS function, the effective magnetic anisotropy of the synthesized sample (K_{eff}) was calculated from parameter b, according to the known relation for materials with hexagonal symmetry.[53]

$$b = \frac{4}{15} \cdot \left(\frac{K_{eff}}{M_s} \right)^2$$

A summary of these values is presented in Table 2. However, all of them fit the expected behavior of $BaFe_{12}O_{19}$ compared to, e.g., spinel-type ferrites. Notably, they are generally lower than values reported previously for the high-quality samples.[54] In the case of the H_c and K_{eff} values, the reason for this could be connected with the synthesized plates being elongated in a direction perpendicular to the easy magnetization axis of the ferrite, resulting in a competition between magnetocrystalline and shape anisotropy of the final material. Therefore, magnetization reversal should require a lower energy barrier than for the bulk structure, effectively lowering values of the determined parameters, especially K_{eff} and H_c.[55] Furthermore, analysis of the $M(T)$ relation was also performed in the temperature range between 5 and 300 K.

Following the measurement, obtained data were fitted to the Bloch law $M = M_0 \cdot (1 − \beta \cdot T^{3/2})$ for 75 K ≤ T ≤ 300 K, giving parameter $\beta = 6.015 \times 10^{-5}$ $K^{-3/2}$, as shown in Figure 7e. The magnetization plateau for $T < 75$ K would indicate the occurrence of magnetic frustration at this low-temperature range. Noteworthy, the β coefficient is known to be inversely proportional to the exchange interactions, influencing the Curie temperature (T_C) of the material. In this regard,
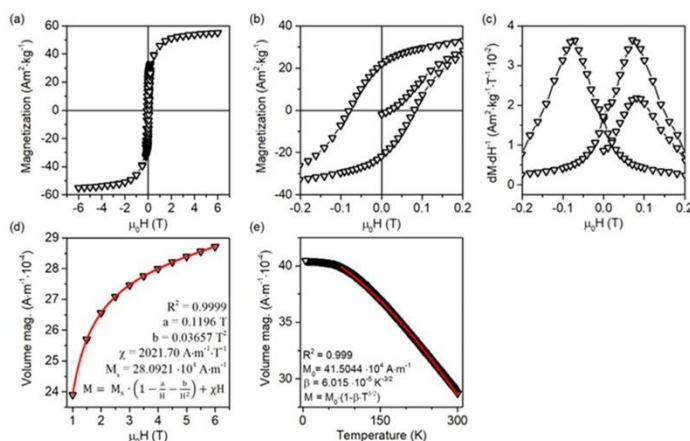
Figure 7. Summation of the magnetization studies for the prepared $BaFe_{12}O_{19}$ sample: (a, b) magnetization hysteresis with (c) calculated dM/dH derivative, (d) results of the high-field magnetization fitting to the LAS equation, and (e) high-field M versus T data.

Table 2. Summation of the Magnetic Properties Obtained for the Parred $BaFe_{12}O_{19}$ Sample

sample	M_s ($Am^2 \cdot kg^{-1}$)	H_c (T)	M_r ($Am^2 \cdot kg^{-1}$)	K_{eff} ($MJ \cdot m^{-3}$)	β ($K^{-3/2} \times 10^{-5}$)	refs
$BaFe_{12}O_{19}$	54	0.08	22	0.104	6.015	in this work
	72	Up to 0.7	n.d.	0.330	4.859–6.210	23,56–58

comparing obtained β to other studies shows that its value is similar,[56] suggesting that no significant differences in the T_C are expected in the case of the analyzed sample.

Finally, performed analysis of the magnetic properties indicated that the prepared material does not follow its expected bulk structure behavior in a strict way, which might be connected with reduction dimensions along the *c*-axis. Nevertheless, after the magnetization, the sample clearly preserves its magnetization in the absence of an external field ($M_r = 22$ $Am^2 \cdot kg^{-1}$), which should allow us to create an in situ magnetic field around its particles and study its effect on the photocatalytic reaction. Moreover, the obtained β value suggests that no significant increase of T_C occurs with respect to the reported bulk values (~450 °C) and that simple calcination above this temperature should demagnetize its microscopic structure. In this regard, it was found suitable for the further preparation of the composites.

3.3. Characterization of the Magnetic Composite Materials. Prepared $BaFe_{12}O_{19}$ samples were combined with three different TiO_2 morphologies, resulting in composites where TiO_2 exposed the majority of {0 0 1}, {1 0 0}, or {1 0 1} crystal facets analogically to other recent studies.[11,59,60] The change of the TiO_2 surface charge, depending on pH and exposed crystal facet, is presented in Figure 8.

The presence of both phases in the final composite samples with the designed TiO_2 contents of 25% and 50% (wt) was confirmed by the XRD analysis and SEM observations. In each case, only $BaFe_{12}O_{19}$ and anatase TiO_2 reflections were observed in the XRD patterns, presented in detail in Figures S1 and S2 in the Supporting Information (absence of the α-Fe_2O_3 signals results probably from decreasing its amount below the detection limit, as well as reduction of the sample amount taken for analysis, comparing with pure ferrite). As
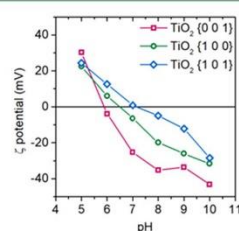
Figure 8. ζ potential analyses for the TiO_2 samples before combining with $BaFe_{12}O_{19}$ as a function of pH and exposed crystal facet.

shown in Figure 9, the deposition of the TiO_2 nanoparticles on the $BaFe_{12}O_{19}$ plates is observed, with their morphology depending on the exposed facet. Furthermore, the increased TiO_2 content resulted in the particles being distributed more densely on the ferrite surface. Noteworthy, this also leads to increased aggregation of TiO_2, especially noticeable for the {1 0 0} structures. This is a logical consequence of increasing the amount of TiO_2 with a limited $BaFe_{12}O_{19}$ surface left to create the interface. In this regard, composites with higher amounts of TiO_2 were not investigated in this study, since the limitation of the possible $BaFe_{12}O_{19}/TiO_2$ interface will also limit the effect of their interactions on the final activity of the composite (that is, for high amounts of aggregated TiO_2, not connected to the ferrite, final properties will start to depend more on the properties of TiO_2 itself, rather than the $TiO_2/BaFe_{12}O_{19}$ interface).

A detailed analysis of the morphology of deposited TiO_2 is presented in Figure 10a. As observed, rectangular platelets, rods, and octahedrons are formed in each case, which match

H

Figure 9. SEM images of the prepared composites, together with the scheme of the idealized orientation between $BaFe_{12}O_{19}$ and anatase crystal structures (ferrite as gray plates and TiO_2 as red particles).

the expected shape of the nanocrystals. In the case of the $\{0\ 0\ 1\}$ facets, the formation of the 2D plates results from the exposition of the 2 equiv planes (the $(0\ 0\ 1)$ and $(0\ 0\ \bar{1})$), thermodynamically stabilized by the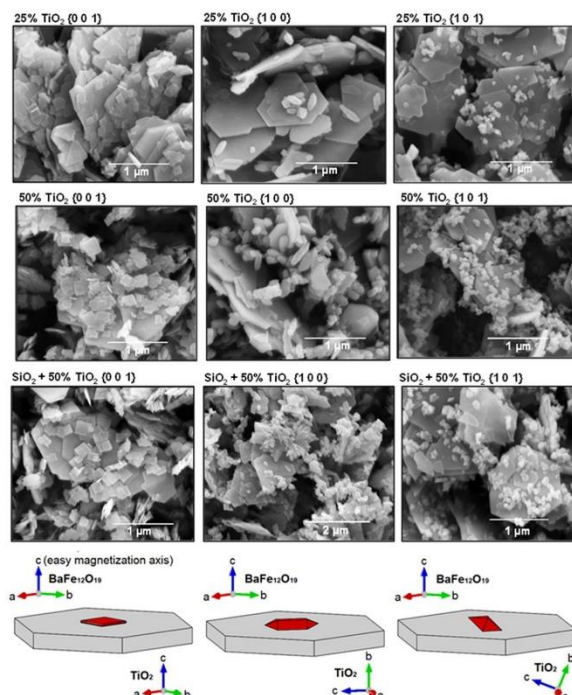 coadsorption of HF and *n*-butanol during the synthesis.[61] Additional analysis of the XRD reflections for the control TiO_2 samples showed that for this nanostructure, selective broadening of the $(0\ 0\ 4)$ and $(1\ 0\ 5)$ reflections occurs, which is in agreement with the reduction of the crystal structure along the $[0\ 0\ 1]$ direction (Figure 10b). In the case of $\{1\ 0\ 0\}$ facets, four sides of the rods correspond to the four equivalent planes that adopt the $(1\ 0\ 0)$ structure. Although it might be noticed that in the case of this sample, the symmetry of the particles is occasionally broken, possibly due to the calcination, elongated particles with parallel sides are systematically observed on the surface of the ferrite, which matches preferred growth along the $[0\ 0\ 1]$ direction and resulting exposure of the $\{1\ 0\ 0\}$ facets. This is also in accordance with the thermodynamic stabilization of the $\{1\ 0\ 0\}$ planes due to the oxygenation of the surface,[62] occurring due to the highly basic conditions during the preparation. Finally, in the case of the $\{1\ 0\ 1\}$ facets exposed, octahedral nanocrystals are systematically observed, resulting from the exposition of the 8 equiv $\{1\ 0\ 1\}$ planes. Moreover, the neighboring facets form an angle close to $136.6°$, as highlighted in Figure 10a, which is a theoretical value of the angle between the $(1\ 0\ 1)$ and $(1\ 0\ \bar{1})$ planes of the anatase crystal structure.

Also, a slightly higher intensity of the $(1\ 0\ 5)$ reflection than the $(2\ 1\ 1)$ one is noticed in the XRD pattern of this sample, which is a characteristic feature of the $\{1\ 0\ 1\}$ exposition.[63] In this regard, the successful formation of all of the described nanostructures is concluded.

3.4. Photocatalytic Degradation of Phenol. Ultimately, the prepared magnetic nanocomposites were studied in the reaction with phenol degradation. During these studies, dispersed composites were mixed with a three-dimensional (3D)-printed stirrer mounted to an overhead motor to ensure that no magnetic field was present during the reaction. After each process, composites were separated using a lab magnet, dried, and weighed to calculate the recovery of the material after the process. Figure 11 shows the rate constants of phenol removal, calculated for the first-order reaction, together with the estimated photocatalysts recovery. The fitting of the observed phenol concentration to the first-reaction model is presented in detail in Figure S3 in the Supporting Information. As observed, pure $BaFe_{12}O_{19}$ shows relatively low activity, actually being close to the value of spontaneous phenol photolysis under the experimental conditions (0.1×10^{-2} min^{-1}). On the other hand, the activity of the TiO_2 structures was at least a few times higher, proving their high phenol degradation efficiency. Noteworthy, the relative activity of the pure TiO_2 photocatalysts is in agreement with the previous reports on their ability to degrade organic pollutants,[10,20,64]
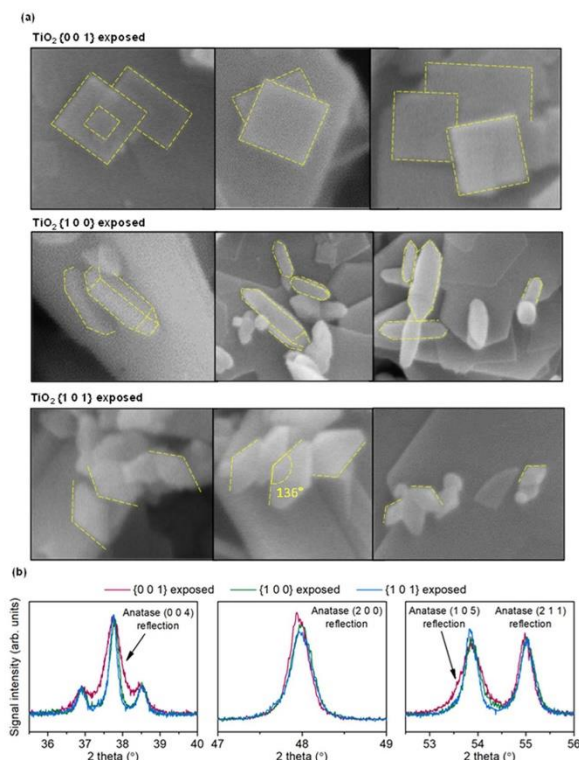
www.acsami.org

Figure 10. SEM images showing a detailed morphology of the deposited TiO_2 (a) together with the closeup of the selected XRD reflections of the control TiO_2 samples (b).

showing high activity of the $\{1\ 0\ 1\}$ facets. Following the observed rate constants for pure compounds, the performance of the prepared composites can be compared with the results expected from their fraction, as presented in Figure 11 as solid lines. Any deviation from this trend might be seen as the result of interactions between both phases. Interestingly, depending on the system details, different effects might be noticed. For a simple $BaFe_{12}O_{19}/TiO_2$ combination, the activity of the composites changed fairly linearly, with the exception of the 50% $TiO_2\{1\ 0\ 1\}$ sample, whose activity was significantly reduced. On the other hand, a slightly positive effect can be observed for the composite containing 25% TiO_2, exposing the majority of the $\{0\ 0\ 1\}$ crystal facet. However, this change is relatively small, and the effect of possible random error cannot be completely ruled out.

Following the results obtained for the composite in direct contact with demagnetized ferrite, further analyses after magnetization of the ferrite or after the introduction of the SiO_2 layer induce significant changes only in two cases. First of all, the magnetization of the ferrite resulted in more than 2 times higher activity of the 25% $TiO_2\{1\ 0\ 0\}$ sample compared to the demagnetized state. Noteworthy, the same trend was noticed for the 50% $TiO_2\{1\ 0\ 0\}$ composite. The higher effect

observed for 25% $TiO_2\{1\ 0\ 0\}$ than 50% $TiO_2\{1\ 0\ 0\}$ might especially result from better TiO_2 dispersion on the $BaFe_{12}O_{19}$ surface observed in SEM images. Finally, the introduction of the SiO_2 layer increased the activity of the sample 50% $TiO_2\{1\ 0\ 1\}$ back to the expected level, while no change was observed for other structures.

Recovered particles were analyzed with XRD to check for the possible change in composition. Qualitatively, no changes were observed for all samples, as shown in Figure S1 in the Supporting Information. Moreover, Table 3 shows the results of the quantitative analysis of the presence of TiO_2 in all prepared composites. As presented, the prepared composites are generally within ±5% error to their designed composition, which is reasonable due to unavoidable imperfections of the deposition process and measurement errors. Moreover, the composition of the prepared materials is not changed due to the reaction, showing variance mostly within ±2% of the TiO_2 content. These results confirmed the successful separation of the composites as well as their stability during the reaction. Nevertheless, it can be noted that in the case of the 50% $TiO_2\{0\ 0\ 1\}$ sample, some loss of the TiO_2 was observed during the separation process, as shown in Figures S4 and S5 in the Supporting Information. It can result from the large
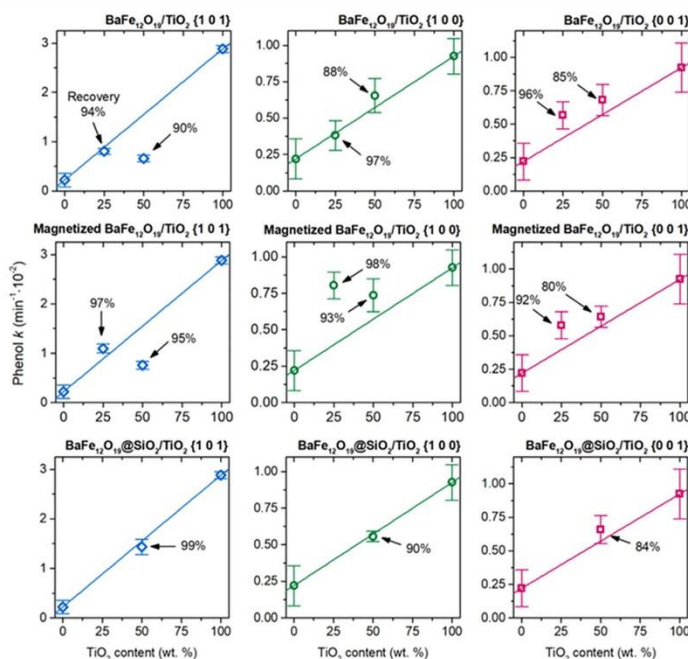
Figure 11. Results of the observed phenol degradation over prepared samples, presented as the calculated rate constant (k) of the I-order reaction. The solid lines represent the activity level expected when effectively no interactions are present between both phases.

Table 3. Summation of the XRD Quantitative Analysis of the Refined Composite Patterns, Performed before and after the Photocatalysis Process

sample	TiO$_2${1 0 1} facets			TiO$_2${1 0 0} facets			TiO$_2${0 0 1} facets		
	25%	50%	50% SiO$_2$	25%	50%	50% SiO$_2$	25%	50%	50% SiO$_2$
TiO$_2$ % before	28.2	51.4	53.4	22.8	44.7	48.5	24.9	52.1	54.0
TiO$_2$ % after	27.7	49.9	55.9	23.2	44.9	48.1	23.6	51.9	56.2
χ^2 before	1.22	1.29	1.39	1.29	1.18	1.48	1.12	1.15	1.21
χ^2 after	1.18	1.20	1.29	1.19	1.42	1.13	1.06	1.04	1.20
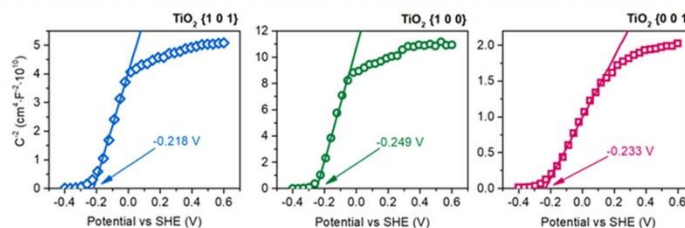
Figure 12. Mott−Schottky plots for the calcined TiO$_2$ samples exposing the majority of different crystal facets.

scattering and absorption coefficients of these particles, reported previously.[11]

3.5. Mechanism Discussion. Ultimately, comparing the results obtained for different composite systems (magnetized, demagnetized, and SiO$_2$-covered ferrite) enables the discussion

of the possible effect of complex interactions between both components concerning different orientations between both phases and possible anisotropy of their properties as well as the effect of the BaFe$_{12}$O$_{19}$ inner magnetic field. Noteworthy, the combination of TiO$_2$ with BaFe$_{12}$O$_{19}$ always reduces its

K
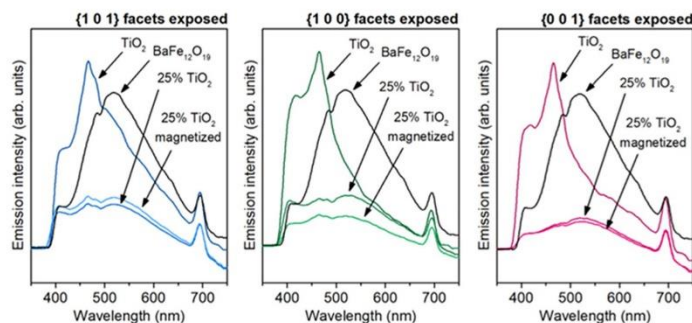
Figure 13. Photoluminescence emission spectra of the pure compounds and 25% TiO$_2$ composites in the magnetized and demagnetized states of the ferrite.

activity, which is connected with the negligible activity of BaFe$_{12}$O$_{19}$ itself, resulting from the location of conduction and valence bands (calculated from Mott−Schottky analysis and band gap), as both these values suggest that charge transfer to oxygen and water to form reactive species should be hindered (the potentials for H$_2$O/$^\bullet$OH and O$_{2(aq)}$/$^\bullet$O$_2^-$ are approximately 2.31 and −0.16 V, respectively[65]). However, the exact activity change when both phases are combined starts to depend on the investigated details, proving their influence on the process. First of all, a significant reduction of the {1 0 1} activity when combined with the ferrite can be especially connected to the electron transfer from TiO$_2$ to BaFe$_{12}$O$_{19}$. This was further confirmed with the Mott−Schottky analysis of the calcined TiO$_2$ samples, as presented in Figure 12. As shown, the potential of the conduction band edge of all TiO$_2$ nanostructures is fairly similar and is approximately 0.8 V lower than that for BaFe$_{12}$O$_{19}$, confirming the preferred electron transfer from anatase to ferrite. This process is especially undesired for the nanoparticles exposing {1 0 1} facets, which are known to be reductive in nature, and electrons play a crucial role in their ability to generate reactive oxygen species.[66,67] Therefore, direct electric contact between inactive BaFe$_{12}$O$_{19}$ and TiO$_2$ exposing {1 0 1} facets is especially unfavorable. The introduction of SiO$_2$ prevents electron transfer, resulting in higher photocatalytic activity observed for the composite material. This material shows the highest activity within prepared composites, in accordance with {1 0 1} being exceptionally suitable for phenol degradation, as shown before when compared to the TiO$_2$ P25 standard.[11] However, such significantly negative electronic interactions with BaFe$_{12}$O$_{19}$ imply that other composite systems, with maximized {1 0 1} content and minimized electron transfer, might be better suited for practical application. Interestingly, the same effect was not observed for the composites exposing {1 0 0} and {0 0 1} TiO$_2$ facets. It might be connected to the fact that these facets are preferentially oxidative, and partial transfer of electrons to the ferrite might not be decisive for their ability to generate reactive species and induce a degradation process.[12,68]

Furthermore, the most interesting finding is a significant change of observed activity for the 25% TiO$_2${1 0 0} composite, simply as the result of BaFe$_{12}$O$_{19}$ magnetization. This observation is unique for the TiO$_2$ exposing {1 0 0} facets, and the effect is too strong to result from the random

error (the activity of this sample is actually comparable to pure TiO$_2$, despite its 4 times lower content). The photo-luminescence measurements showed that the improved activity of the magnetized composite sample resulted from the effect of the inner magnetic field. As shown in Figure 13, the composite with 25% TiO$_2$ exposing {1 0 0} facets showed a significant change in the emission intensity, suggesting that the BaFe$_{12}$O$_{19}$ inner magnetic field suppressed the recombination of charge carriers. Noteworthy, these results showed that interactions between the magnetic field and TiO$_2$ are anisotropic and depend on their mutual orientation. However, at this point, it is not possible to distinguish to what extent this anisotropy results from bulk properties (e.g., different mobility of charge carriers in different directions[69]) or from the properties of the exposed facet itself. The obtained results indicate that under the magnetic field, the electronic structure of {1 0 0} is changed toward lower energies, forming more stable states at the surface. Increased stability of such surface states might both reduce the energy of the facet and promote the trapping of long-lived charge carriers at the surface, ultimately leading to reduced recombination and increased activity.

4. CONCLUSIONS

In the present work, detailed insights into complex electronic and magnetic interactions that can be designed within multicomponent, facet-engineered magnetic photocatalysts are described for the first time. Deposition of faceted TiO$_2$ on the surface of single-crystalline BaFe$_{12}$O$_{19}$ microplates allowed for in situ fixing of the orientation between both phases, resulting in different interfaces and different orientations between the faceted TiO$_2$ and uniaxial inner magnetic field of the ferrite. Based on the photocatalytic activity analyses, it was noticed that both positive and negative interactions are possible, depending on the system details. Specifically, electron transfer from the {1 0 1} anatase facets to the ferrite phase significantly reduced the final photocatalytic activity. This is in accordance with recent reports showing the importance of the reduction process on the generation of reactive species on {1 0 1} surfaces. For such composites, the introduction of insulating SiO$_2$ is especially desired, leading to their high activity when no charge transfer to ferrite occurs. Simultaneously, the analogical electron transfer less influenced the activity of {1 0 0} and {0 0 1} facets, confirming that different effects of the same junction can be expected,

depending on the exposed crystal facet. Furthermore, the inner magnetic field of $BaFe_{12}O_{19}$ was found to increase the activity of the composites over 2 times for the TiO_2 sample, exposing {1 0 0} crystal facets. It suggests that the interactions between a magnetic field and TiO_2 are anisotropic and depend on either their mutual orientation or the electronic structure of the exposed surface. A sharp distinction between bulk and surface effects would require further studies; nevertheless, these results show for the first time that a remarkable activity increase might be achieved due to the action of a magnetic field created in situ within the ferromagnet–photocatalyst composite. However, to observe such an effect, it require a system to be carefully designed. In this regard, further studies in this direction might be desired to help increase the activity of different photocatalytic systems.

■ ASSOCIATED CONTENT

ⓢ Supporting Information

The Supporting Information is available free of charge at https://pubs.acs.org/doi/10.1021/acsami.3c13380.

> Detailed XRD patterns; results of the Rietveld refinement; observed kinetics of phenol degradation; and snapshots of the performed magnetic separation (PDF)

■ AUTHOR INFORMATION

Corresponding Authors

Szymon Dudziak – *Department of Process Engineering and Chemical Technology, Gdansk University of Technology, 80-233 Gdansk, Poland;* ⓞ orcid.org/0000-0002-9225-7748; Email: dudziakszy@gmail.com

Anna Zielińska-Jurek – *Department of Process Engineering and Chemical Technology, Gdansk University of Technology, 80-233 Gdansk, Poland;* ⓞ orcid.org/0000-0002-9830-1797; Email: annjurek@pg.edu.pl

Authors

Cristina Gómez-Polo – *Institute for Advanced Materials and Mathematics, INAMAT2, Public University of Navarre, 31006 Pamplona, Pamplona, Spain*

Jakub Karczewski – *Institute of Nanotechnology and Materials Engineering, Gdansk University of Technology, 80-233 Gdansk, Poland*

Kostiantyn Nikiforow – *Institute of Physical Chemistry, Polish Academy of Sciences, 01-224 Warsaw, Poland*

Complete contact information is available at:
https://pubs.acs.org/10.1021/acsami.3c13380

Notes

The authors declare no competing financial interest.

■ ACKNOWLEDGMENTS

■ REFERENCES

(1) Grzegórska, A.; Głuchowski, P.; Karczewski, J.; Ryl, J.; Wysocka, I.; Siuzdak, K.; Trykowski, G.; Grochowska, K.; Zielińska-Jurek, A. Enhanced Photocatalytic Activity of Accordion-like Layered Ti_3C_2 (MXene) Coupled with Fe-Modified Decahedral Anatase Particles Exposing {1 0 1} and {0 0 1} Facets. *Chem. Eng. J.* **2021**, *426*, No. 130801.

(2) Ji, S.; Qu, Y.; Wang, T.; Chen, Y.; Wang, G.; Li, X.; Dong, J.; Chen, Q. Y.; Zhang, W.; Zhang, Z.; Liang, S.; Yu, R.; Wang, Y.; Wang, D.; Li, Y. Rare-Earth Single Erbium Atoms for Enhanced Photocatalytic CO_2 Reduction. *Adv. Mater.* **2020**, *59* (26), 10738–10744.

(3) Kubiak, A.; Żółtowska, S.; Gabała, E.; Szybowicz, M.; Siwińska-Ciesielczyk, K.; Jesionowski, T. Controlled Microwave-Assisted and PH-Affected Growth of ZnO Structures and Their Photocatalytic Performance. *Powder Technol.* **2021**, *386*, 221–235.

(4) Kowalkińska, M.; Głuchowski, P.; Swebocki, T.; Ossowski, T.; Ostrowski, A.; Bednarski, W.; Karczewski, J.; Zielińska-Jurek, A. Scheelite-Type Wide-Bandgap ABO_4 Compounds (A = Ca, Sr, and Ba; B = Mo and W) as Potential Photocatalysts for Water Treatment. *J. Phys. Chem. C* **2021**, *125* (46), 25497–25513.

(5) Mazheika, A.; Wang, Y. G.; Valero, R.; Viñes, F.; Illas, F.; Ghiringhelli, L. M.; Levchenko, S. V.; Scheffler, M. Artificial-Intelligence-Driven Discovery of Catalyst Genes with Application to CO_2 Activation on Semiconductor Oxides. *Nat. Commun.* **2022**, *13* (1), No. 419.

(6) Deng, Y.; Zhou, H.; Zhao, Y.; Yang, B.; Shi, M.; Tao, X.; Yang, S.; Li, R.; Li, C. Spatial Separation of Photogenerated Charges on Well-Defined Bismuth Vanadate Square Nanocrystals. *Small* **2022**, *18* (5), 1–9.

(7) Zhou, P.; Navid, I. A.; Ma, Y.; Xiao, Y.; Wang, P.; Ye, Z.; Zhou, B.; Sun, K.; Mi, Z. Solar-to-Hydrogen Efficiency of More than 9% in Photocatalytic Water Splitting. *Nature* **2023**, *613* (7942), 66–70.

(8) Takata, T.; Jiang, J.; Sakata, Y.; Nakabayashi, M.; Shibata, N.; Nandal, V.; Seki, K.; Hisatomi, T.; Domen, K. Photocatalytic Water Splitting with a Quantum Efficiency of Almost Unity. *Nature* **2020**, *581* (7809), 411–414.

(9) Meng, J.; Duan, Y.; Jing, S.; Ma, J.; Wang, K.; Zhou, K.; Ban, C.; Wang, Y.; Hu, B.; Yu, D.; Gan, L.; Zhou, X. Facet Junction of BiOBr Nanosheets Boosting Spatial Charge Separation for CO_2 Photoreduction. *Nano Energy* **2022**, *92*, No. 106671.

(10) Dudziak, S.; Fiszka Borzyszkowska, A.; Zielińska-Jurek, A. Photocatalytic Degradation and Pollutant-Oriented Structure-Activity Analysis of Carbamazepine, Ibuprofen and Acetaminophen over Faceted TiO_2. *J. Environ. Chem. Eng.* **2023**, *11*, No. 1095533.

(11) Dudziak, S.; Kowalska, E.; Wang, K.; Karczewski, J.; Sawczak, M.; Ohtani, B.; Zielińska-Jurek, A. The Interplay between Dopant and a Surface Structure of the Photocatalyst – The Case Study of Nb-Doped Faceted TiO_2. *Appl. Catal., B* **2023**, *328*, No. 122448, DOI: 10.1016/j.apcatb.2023.122448.

(12) Selcuk, S.; Selloni, A. Facet-Dependent Trapping and Dynamics of Excess Electrons at Anatase TiO_2 Surfaces and Aqueous Interfaces. *Nat. Mater.* **2016**, *15* (10), 1107–1112.

(13) Shirai, K.; Fazio, G.; Sugimoto, T.; Selli, D.; Ferraro, L.; Watanabe, K.; Haruta, M.; Ohtani, B.; Kurata, H.; Di Valentin, C.; Matsumoto, Y. Water-Assisted Hole Trapping at the Highly Curved Surface of Nano-TiO_2 Photocatalyst. *J. Am. Chem. Soc.* **2018**, *140* (4), 1415–1422.

(14) Bielan, Z.; Dudziak, S.; Kubiak, A.; Kowalska, E. Application of Spinel and Hexagonal Ferrites in Heterogeneous Photocatalysis. *Appl. Sci.* **2021**, *11* (21), No. 10160.

(15) Abd Aziz, A.; Yau, Y. H.; Puma, G. L.; Fischer, C.; Ibrahim, S.; Pichiah, S. Highly Efficient Magnetically Separable TiO_2-Graphene Oxide Supported $SrFe_{12}O_{19}$ for Direct Sunlight-Driven Photoactivity. *Chem. Eng. J.* **2014**, *235*, 264–274.

(16) Xie, M.; Wang, D.; Jing, L.; Wei, W.; Xu, Y.; Xu, H.; Li, H.; Xie, J. Preparation of Magnetically Recoverable and Z-Scheme BaFe12O19/AgBr Composite for Degradation of 2-Mercaptobenzothiazole and Methyl Orange under Visible Light. *Appl. Surf. Sci.* **2020**, *521*, No. 146343.

(17) Gao, W.; Lu, J.; Zhang, S.; Zhang, X.; Wang, Z.; Qin, W.; Wang, J.; Zhou, W.; Liu, H.; Sang, Y. Suppressing Photoinduced Charge Recombination via the Lorentz Force in a Photocatalytic System. *Adv. Sci.* **2019**, *6* (18), No. 1901244.

Page | 172

(18) Okumura, H.; Endo, S.; Joonwichien, S.; Yamasue, E.; Ishihara, K. N. Magnetic Field Effect on Heterogeneous Photocatalysis. *Catal. Today* **2015**, *258*, 634−647.

(19) Wang, Y. H.; Zhao, J. L.; Liang, Y. Degradation Kinetics of Phenol by a Titanium Dioxide Photocatalyst Coupled with a Magnetic Field. *React. Kinet., Mech. Catal.* **2013**, *109* (1), 273−283.

(20) Mino, L.; Pellegrino, F.; Rades, S.; Radnik, J.; Hodoroaba, V. D.; Spoto, G.; Maurino, V.; Martra, G. Beyond Shape Engineering of TiO2 Nanoparticles: Post-Synthesis Treatment Dependence of Surface Hydration, Hydroxylation, Lewis Acidity and Photocatalytic Activity of TiO$_2$ Anatase Nanoparticles with Dominant {001} or {101} Facets. *ACS Appl. Nano Mater.* **2018**, *1* (9), 5355−5365.

(21) Li, J.; Yu, Y.; Chen, Q.; Li, J.; Xu, D. Controllable Synthesis of TiO$_2$ Single Crystals with Tunable Shapes Using Ammonium-Exchanged Titanate Nanowires as Precursors. *Cryst. Growth Des.* **2010**, *10* (5), 2111−2115.

(22) Mikrut, P.; Kobielusz, M.; Macyk, W. Spectroelectrochemical Characterization of Euhedral Anatase TiO$_2$ Crystals − Implications for Photoelectrochemical and Photocatalytic Properties of {001} {100} and {101} Facets. *Electrochim. Acta* **2019**, *310*, 256−265.

(23) Pullar, R. C. Hexagonal Ferrites: A Review of the Synthesis, Properties and Applications of Hexaferrite Ceramics. *Prog. Mater. Sci.* **2012**, *57* (7), 1191−1334.

(24) Lisjak, D.; Drofenik, M. Chemical Substitution-an Alternative Strategy for Controlling the Particle Size of Barium Ferrite. *Cryst. Growth Des.* **2012**, *12* (11), 5174−5179.

(25) Cao, L.; Zeng, Y.; Ding, C.; Li, R.; Li, C.; Zhang, C. One-Step Synthesis of Single Phase Micro-Sized BaFe$_{12}$O$_{19}$ Hexaplates via a Modified Hydrothermal Approach. *Mater. Chem. Phys.* **2016**, *184*, 241−249.

(26) Sipos, P.; May, P. M.; Hefter, G. T. Carbonate Removal from Concentrated Hydroxide Solutions. *Analyst* **2000**, *125* (5), 955−958.

(27) Dudziak, S.; Kowalkińska, M.; Karczewski, J.; Pisarek, M.; Siuzdak, K.; Kubiak, A.; Siwińska-Ciesielczyk, K.; Zielińska-Jurek, A. Solvothermal Growth of {0 0 1} Exposed Anatase Nanosheets and Their Ability to Mineralize Organic Pollutants. The Effect of Alcohol Type and Content on the Nucleation and Growth of TiO$_2$ Nanostructures. *Appl. Surf. Sci.* **2021**, *563*, No. 150360.

(28) Amano, F.; Yasumoto, T.; Prieto-Mahaney, O. O.; Uchida, S.; Shibayama, T.; Ohtani, B. Photocatalytic Activity of Octahedral Single-Crystalline Mesoparticles of Anatase Titanium(IV) Oxide. *Chem. Commun.* **2009**, No. No. 17, 2311−2313.

(29) Li, J.; Xu, D. Tetragonal Faceted-Nanorods of Anatase TiO2 Single Crystals with a Large Percentage of Active {100} Facets. *Chem. Commun.* **2010**, *46* (13), 2301−2303.

(30) Beranek, R. Photo)Electrochemical Methods for the Determination of the Band Edge Positions of TiO$_2$-Based Nanomaterials. *Adv. Phys. Chem.* **2011**, *2011*, 80−83.

(31) Giannozzi, P.; Andreussi, O.; Brumme, T.; Bunau, O.; Buongiorno Nardelli, M.; Calandra, M.; Car, R.; Cavazzoni, C.; Ceresoli, D.; Cococcioni, M.; Colonna, N.; Carnimeo, I.; Dal Corso, A.; De Gironcoli, S.; Delugas, P.; DiStasio, R. A., Jr; Ferretii, A.; Floris, A.; Fratesi, G.; Fugallo, G.; Gebauer, R.; Gerstmann, U.; Giustino, F.; Gorni, T.; Jia, J.; Kawamura, M.; Ko, H.-Y.; Kokalj, A.; Küçükbenli, E.; Lazzeri, M.; Marsili, M.; Marzani, N.; Mauri, F.; Nguyen, N. L.; Nguyen, H.-V.; Otero-de-la-Roza, A.; Paulatto, L.; Poncé, S.; Rocca, D.; Sabatini, R.; Santra, B.; Schlipf, M.; Seitsonen, A. P.; Smogunov, A.; Timrov, I.; Thonhauser, T.; Umari, P.; Vast, N.; Wu, X.; Baroni, S. Advanced Capabilities for Materials Modelling with Quantum Espresso. *J. Phys.: Condens. Matter* **2017**, *29*, No. 465901.

(32) Giannozzi, P.; Baroni, S.; Bonini, N.; Calandra, M.; Car, R.; Cavazzoni, C.; Ceresoli, D.; Chiarotti, G. L.; Cococcioni, M.; Dabo, I.; Dal Corso, A.; De Gironcoli, S.; Fabris, S.; Fratesi, G.; Gebauer, R.; Gerstmann, U.; Gougoussis, C.; Kokalj, A.; Lazzeri, M.; Martin-Samos, L.; Marzari, N.; Mauri, F.; Mazzarello, R.; Paolini, S.; Pasquarello, A.; Paulatto, L.; Sbraccia, C.; Scandolo, S.; Sclauzero, G.; Seitsonen, A. P.; Smogunov, A.; Umari, P.; Wentzcovitch, R. M. QUANTUM ESPRESSO: A Modular and Open-Source Software

Project for Quantum Simulations of Materials. *J. Phys.: Condens. Matter* **2009**, *21* (39), No. 395502.

(33) Perdew, J. P.; Burke, K.; Ernzerhof, M. Generalized Gradient Approximation Made Simple. *Phys. Rev. Lett.* **1996**, *77* (18), 3865−3868.

(34) Perdew, J. P.; Ernzerhof, M.; Burke, K. Rationale for Mixing Exact Exchange with Density Functional Approximations Rationale for Mixing Exact Exchange with Density Functional Approximations. *J. Phys. Chem. A* **1996**, *105* (22), 9982−9985.

(35) Setyawan, W.; Curtarolo, S. High-Throughput Electronic Band Structure Calculations: Challenges and Tools. *Comput. Mater. Sci.* **2010**, *49* (2), 299−312.

(36) Lisjak, D.; Drofenik, M. The Mechanism of the Low-Temperature Formation of Barium Hexaferrite. *J. Eur. Ceram. Soc.* **2007**, *27* (16), 4515−4520.

(37) Huang, J.; Zhuang, H.; Li, W. Synthesis and Characterization of Nano Crystalline BaFe12O19 Powders by Low Temperature Combustion. *Mater. Res. Bull.* **2003**, *38*, 149−159.

(38) Primc, D.; Makovec, D.; Lisjak, D.; Drofenik, M. Hydrothermal Synthesis of Ultrafine Barium Hexaferrite Nanoparticles and the Preparation of Their Stable Suspensions. *Nanotechnology* **2009**, *20* (31), No. 315605.

(39) Jaworski, M. A.; Flores, F. M.; Fernández, M. A.; Casella, M.; Torres Sánchez, R. M. Use of Organo-Montmorillonite for the Nitrate Retention in Water: Influence of Alkyl Length of Loaded Surfactants. *SN Appl. Sci.* **2019**, *1* (11), 1−9.

(40) Tunç, S.; Duman, O. The Effect of Different Molecular Weight of Poly(Ethylene Glycol) on the Electrokinetic and Rheological Properties of Na-Bentonite Suspensions. *Colloids Surf., A* **2008**, *317* (1−3), 93−99.

(41) Zielińska-Jurek, A.; Bielan, Z.; Dudziak, S.; Wolak, I.; Sobczak, Z.; Klimczuk, T.; Nowaczyk, G.; Hupka, J. Design and Application of Magnetic Photocatalysts for Water Treatment. The Effect of Particle Charge on Surface Functionality. *Catalysts* **2017**, *7*, No. 360.

(42) Dong, R.; Wang, L.; Zhu, J.; Liu, L.; Qian, Y. A Novel SiO$_2$−GO/Acrylic Resin Nanocomposite: Fabrication, Characterization and Properties. *Appl. Phys., A: Mater. Sci. Process* **2019**, *125* (8), 1−11.

(43) Djaniš, J. P.; Prinčič, G. G.; Mavrič, A.; Mertelj, A.; Iskra, J.; Lisjak, D. New Insights into Amino-Functionalization of Magnetic Nanoplatelets with Silanes and Phosphonates. *Nanomaterials* **2022**, *12* (12), No. 2123, DOI: 10.3390/nano12122123.

(44) Wang, L.; Zhang, J.; Zhang, Q.; Xu, N.; Song, J. XAFS and XPS Studies on Site Occupation of Sm3+ Ions in Sm Doped M-Type BaFe$_{12}$O$_{19}$. *J. Magn. Magn. Mater.* **2015**, *377*, 362−367.

(45) Lisjak, D.; Ovtar, S.; Kovač, J.; Gregoratti, L.; Aleman, B.; Amati, M.; Fanetti, M.; Makovec, D. A Surface-Chemistry Study of Barium Ferrite Nanoplates with DBSa-Modified Surfaces. *Appl. Surf. Sci.* **2014**, *305*, 366−374.

(46) Atuchin, V. V.; Vinnik, D. A.; Gavrilova, T. A.; Gudkova, S. A.; Isaenko, L. I; Jiang, X.; Pokrovsky, L. D.; Prosvirin, I. P.; Mashkovtseva, L. S.; Lin, Z. Flux Crystal Growth and the Electronic Structure of BaFe$_{12}$O$_{19}$ Hexaferrite. *J. Phys. Chem. C* **2016**, *120* (9), 5114−5123.

(47) Grosvenor, A. P.; Kobe, B. A.; Biesinger, M. C.; McIntyre, N. S. Investigation of Multiplet Splitting of Fe 2p XPS Spectra and Bonding in Iron Compounds. *Surf. Interface Anal.* **2004**, *36* (12), 1564−1574.

(48) Yamashita, T.; Hayes, P. Analysis of XPS Spectra of Fe^{2+} and Fe^{3+} Ions in Oxide Materials. *Appl. Surf. Sci.* **2008**, *254* (8), 2441−2449.

(49) Novák, P.; Rusz, J. Exchange Interactions in Barium Hexaferrite. *Phys. Rev. B:* **2005**, *71* (18), No. 184433, DOI: 10.1103/PhysRevB.71.184433.

(50) Hu, J.; Zhao, X.; Chen, W.; Chen, Z. Enhanced Charge Transport and Increased Active Sites on α-Fe$_2$O$_3$ (110) Nanorod Surface Containing Oxygen Vacancies for Improved Solar Water Oxidation Performance. *ACS Omega* **2018**, *3* (11), 14973−14980.

(51) Ramachandran, K.; Geerthana, M.; Maadeswaran, P.; Navaneethan, M.; Harish, S.; Ramesh, R. α-Fe$_2$O$_3$/AmTiO$_2$ Heterojunction-Based Photoanode with Improved Interfacial Charge

Transport Properties for Enhanced Photoelectrochemical Water Splitting. *J. Mater. Sci.: Mater. Electron.* **2022**, 33 (11), 8318–8326.

(52) Sung Lee, J.; Cha, J. M.; Yoon, H. Y.; Lee, J. K.; Kim, Y. K. Magnetic Multi-Granule Nanoclusters: A Model System That Exhibits Universal Size Effect of Magnetic Coercivity. *Sci. Rep.* **2015**, 5, No. 12135.

(53) Fang, H. C.; Yang, Z.; Ong, C. K.; Li, Y.; Wang, C. S. Preparation and Magnetic Properties of (Zn-Sn) Substituted Barium Hexaferrite Nanoparticles for Magnetic Recording. *J. Magn. Magn. Mater.* **1998**, 187 (1), 129–135.

(54) Kojima, H. Chapter 5 Fundamental Properties of Hexagonal Ferrites with Magnetoplumbite Structure. In *Handbook of Ferromagnetic Materials*; Wohlfarth, E. P., Ed.; North-Holland Publishing Company, 1982; Vol. 3, pp 305–391.

(55) Golubenko, Z. V.; Ol'khovik, L. P.; Popkov, Y. A.; Sizova, Z. I. Magnetic Anisotropy of a System of Nanocrystalline BaO−6Fe2O3 Particles. *Phys. Solid State* **1998**, 40 (10), 1718–1720.

(56) Karnajit Singh, H.; Mohapatra, P. P.; Sahu, S.; Dobbidi, P. Dielectric and Temperature Dependent Magnetic Studies of Al3+ Substituted Ba0.4La0.1Sr0.5AlxFe12-XO19 Hexaferrite for Microwave Application. *Mater. Sci. Eng., B* **2022**, 284, No. 115876.

(57) Carosella, C. A.; Chrisey, D. B.; Lubitz, P.; Horwitz, J. S.; et al. Pulsed Laser Deposition of Epitaxial BaFe12O19 Thin Films. *J. Appl. Phys.* **1992**, 71, 5107–5110.

(58) Li, P.; Kally, J.; Zhang, S. S. L.; Pillsbury, T.; Ding, J.; Csaba, G.; Ding, J.; Jiang, J. S.; Liu, Y.; Sinclair, R.; Bi, C.; DeMann, A.; Rimal, G.; Zhang, W.; Field, S. B.; Tang, J.; Wang, W.; Heinonen, O. G.; Novosad, V.; Hoffmann, A.; Samarth, N.; Wu, M. Magnetization Switching Using Topological Surface States. *Sci. Adv.* **2019**, 5 (8), No. eaaw3415, DOI: 10.1126/sciadv.aaw3415.

(59) Wang, Y.; Mino, L.; Pellegrino, F.; Homs, N.; Ramírez de la Piscina, P. Engineered Mo$_x$C/TiO$_2$ Interfaces for Efficient Noble Metal-Free Photocatalytic Hydrogen Production. *Appl. Catal., B* **2022**, 318, No. 121783.

(60) Dudziak, S.; Kowalkińska, M.; Karczewski, J.; Pisarek, M.; Gouveia, J. D.; Gomes, J. R. B.; Zielińska-Jurek, A. Surface and Trapping Energies as Predictors for the Photocatalytic Degradation of Aromatic Organic Pollutants. *J. Phys. Chem. C* **2022**, 126, 14859–14877.

(61) Yang, H. G.; Liu, G.; Qiao, S. Z.; Sun, C. H.; Jin, Y. G.; Smith, S. C.; Zou, J.; Cheng, H. M.; Lu, G. Q. Solvothermal Synthesis and Photoreactivity of Anatase TiO$_2$ Nanosheets with Dominant {001} Facets. *J. Am. Chem. Soc.* **2009**, 131 (11), 4078–4083.

(62) Barnard, A. S.; Zapol, P.; Curtiss, L. A. Anatase and Rutile Surfaces with Adsorbates Representative of Acidic and Basic Conditions. *Surf. Sci.* **2005**, 582 (1–3), 173–188.

(63) Gordon, T. R.; Cargnello, M.; Paik, T.; Mangolini, F.; Weber, R. T.; Fornasiero, P.; Murray, C. B. Nonaqueous Synthesis of TiO$_2$ Nanocrystals Using TiF 4 to Engineer Morphology, Oxygen Vacancy Concentration, and Photocatalytic Activity. *J. Am. Chem. Soc.* **2012**, 134 (15), 6751–6761.

(64) Kowalkińska, M.; Sikora, K.; Łapiński, M.; Karczewski, J.; Zielińska-Jurek, A. Non-Toxic Fluorine-Doped TiO$_2$ Nanocrystals from TiOF$_2$ for Facet-Dependent Naproxen Degradation. *Catal. Today* **2023**, 413–415, No. 113959.

(65) Koppenol, W. H.; Stanbury, D. M.; Bounds, P. L. Electrode Potentials of Partially Reduced Oxygen Species, from Dioxygen to Water. *Free Radical Biol. Med.* **2010**, 49 (3), 317–322.

(66) Hwang, J. Y.; Moon, G. h.; Kim, B.; Tachikawa, T.; Majima, T.; Hong, S.; Cho, K.; Kim, W.; Choi, W. Crystal Phase-Dependent Generation of Mobile OH Radicals on TiO$_2$: Revisiting the Photocatalytic Oxidation Mechanism of Anatase and Rutile. *Appl. Catal., B* **2021**, 286, No. 119905.

(67) Setvin, M.; Aschauer, U.; Hulva, J.; Simschitz, T.; Daniel, B.; Schmid, M.; Selloni, A.; Diebold, U. Following the Reduction of Oxygen on TiO$_2$ Anatase (101) Step by Step. *J. Am. Chem. Soc.* **2016**, 138 (30), 9565–9571.

(68) Carey, J. J.; McKenna, K. P. Does Polaronic Self-Trapping Occur at Anatase TiO$_2$ Surfaces? *J. Phys. Chem. C* **2018**, 122 (48), 27540–27553.

(69) Liu, G.; Yin, L. C.; Pan, J.; Li, F.; Wen, L.; Zhen, C.; Cheng, H. M. Greatly Enhanced Electronic Conduction and Lithium Storage of Faceted TiO$_2$ Crystals Supported on Metallic Substrates by Tuning Crystallographic Orientation of TiO$_2$. *Adv. Mater.* **2015**, 27 (23), 3507–3512.

O

PUBLICATION [P6]

The interplay between dopant and a surface structure of the photocatalyst – The case study of Nb-doped faceted TiO$_2$

Szymon Dudziak [a],[*], Ewa Kowalska [b],[c], Kunlei Wang [b], Jakub Karczewski [d], Mirosław Sawczak [e], Bunsho Ohtani [b], Anna Zielińska-Jurek [a],[*]

[a] Department of Process Engineering and Chemical Technology, Gdansk University of Technology, G. Narutowicza 11/12, 80-233 Gdansk, Poland
[b] Institute for Catalysis, Hokkaido University, N21, W10, Sapporo 001-0021, Japan
[c] Faculty of Chemistry, Jagiellonian University, Gronostajowa 2, 30 387 Kraków, Poland
[d] Department of Solid State Physics, Gdansk University of Technology, G. Narutowicza 11/12, 80-233 Gdansk, Poland
[e] Szewalski Institute of Fluid Flow Machinery, Polish Academy of Sciences, Fiszera 14, Gdansk, Poland

ARTICLE INFO

Keywords:
Anatase
Doping
Electron trapping
Crystal facets
Reduction

ABSTRACT

Anatase nanoparticles, exposing the majority of the {0 0 1}, {1 0 0} and {1 0 1} facets were synthesized and doped with different niobium amount to investigate the self-trapping of the excess electrons and resulting photocatalytic activity. Photocatalyst structure and presence of excess electrons inside the obtained Nb-doped anatase samples was confirmed by the combination of structural and spectroscopic analyses. Only for the {1 0 1} facets, introduced electrons were found to localize on the surface titanium sites, as long as the analysis was performed in the ambient environment. The photocatalytic activity data, studied in the reaction of 4-nitrophenol reduction and phenol oxidation, show that the dopant-introduced electrons might increase photocatalytic activity only for the anatase structures exposing {0 0 1} and {1 0 0} facets. Ultimately, the dopant effect on the photocatalytic activity depends on the exposed facet, which might be investigated for other systems to increase their applicability.

1. Introduction

Semiconductor-based technologies, such as the photocatalytic degradation process, are one of the most important areas of science and technology with a wide range of possible applications. An induced photoexcitation of an electron from the valence band to the conduction band of a semiconductor material can be seen as a mutual starting point for any further physicochemical phenomena. However, the post-excitation fate of charge carriers often defines the efficiency of a specific process. Focusing on the photocatalytic reactions, their occurrence is directly dependent on the charge transfer between the excited photocatalyst and reacting species present in a medium. This transfer is specifically a surface process, and therefore, the differences in the reaction rate might depend on the atoms' arrangement at the interface. This problem was the subject of numerous studies presented in recent years [1–18], which have both predicted and proved the significance of the photocatalyst surface structure on the efficiency of the photocatalytic reactions. Especially, the preferential localization of photogenerated holes and electrons on the outmost atoms has been deeply

analyzed by computational methods [19–24]. The recent studies described in detail the self-trapping phenomena of both charge carriers on a variety of possible TiO$_2$ surfaces. However, some concerns remain in the interpretation of the reported results. First of all, there is no consensus on the possible surface trapping of the electrons for the low-index anatase facets. Initially, Ma et al. had reported that e$^-$ should be trapped on the (1 0 1) and (1 0 0) surfaces [19], but further study by Carey and McKenna showed that such trapping could occur only for the high index surfaces, such as (1 0 3), (1 0 5) or (1 0 7) [20]. Furthermore, Selcuk and Selloni presented a more detailed analysis, in which it was found that the experimental conditions influence trapping, i.e., electrons are not trapped on the (1 0 1) surface when analyzed in vacuum, but electron trapping occurs when experiments are performed in the presence of water at the interface [21]. It should be pointed out that photocatalytic processes are not performed in a vacuum, and thus, the last finding might be especially important. Nevertheless, experimental verification is still important to discuss these predictions. The other problem with strict interpretation of these studies is that the e$^-$ and h$^+$ are usually modelled by arbitrarily introducing or withdrawing excess

electrons from the model. Although obtained results are still useful, closely representing the energy states of the photogenerated charge carriers, this is different from the actual photocatalytic reaction where both e^- and h^+ are generated simultaneously. On the other hand, this is similar to the case of modified semiconductor structure, where point defects should result in a change of the charge carriers number at the ground state. At present, doping of the TiO_2 structure with both metals and non-metals is constantly studied as one of the methods to increase its light absorption properties [25–31]. However, these studies usually do not discuss the dopant effect on the charge carriers' density and how they behave on the surface, while theoretical findings predict that surface dependence could also be expected in that case.

In this regard, the study on the interplay between electron-donating dopant and the surface structure of the anatase TiO_2 photocatalyst is especially desired. First of all, it might help to confirm the possible electron trapping on the commonly observed crystal facets, {0 0 1}, {1 0 0} and {1 0 1}, which might be questionable due to some conflicting results presented in the computational studies. Moreover, verifying the surface-dependent effect of the dopant for TiO_2 would imply that similar behavior might be expected for other photocatalysts and dopants. Therefore, it would define a new approach to the problem of photocatalyst doping in general. Finally, it would be helpful to evaluate how possible surface trapping affects the photocatalytic activity of the prepared materials since the available simulations do not predict it directly.

In view of this, a shallow donor introduced to the anatase lattice is desired to avoid the creation of the deep-trapping states of the dopant. For the anatase TiO_2, Nb can be beneficial as a donor since its shallow character is well-defined, and niobium can be easily incorporated into the anatase structure. Wang et al. reported the introduction of 20 % Nb into the TiO_2 structure without the formation of any secondary phase and only with a limited effect on their absorption properties [32]. The previous studies also predict that for the bulk anatase, a relatively low amount of Nb substituting Ti should not form any additional energy levels [33–36]. Finally, Nb was an element introduced to the anatase models, analyzed by Selcuk and Selloni [21].

In this regard, in the present study, well-defined anatase nanoparticles exposing the majority of the {0 0 1}, {1 0 0} and {1 0 1} facets were prepared and further doped with a low amount of Nb (designed Ti/Nb atomic ratios were 0.5 %, 1.0 % and 1.5 % for each structure) to study the effect of excess electrons on the photocatalytic oxidation of phenol and photoreduction of 4-nitrophenol to 4-aminophenol under simulated solar light. Performed syntheses were based on the reported HF-mediated stabilization of the {0 0 1} facets, as well as pH-controlled growth of the {1 0 0} and {1 0 1} structures via two-step etching-rebuilding process in alkaline conditions [37–39].

2. Experimental

2.1. Preparation of the photocatalysts

Nb-doped anatase nanoparticles with dominant {1 0 1}, {1 0 0} and {0 0 1} exposed facets were prepared hydrothermally. In this regard, commercial TiO_2 P25 (Evonik), potassium hydroxide, sodium hydroxide, 25 % ammonia solution, ammonium chloride, titanium tert-butoxide, n-butanol, 45 % hydrofluoric acid, and niobium(V) ethoxide were used as received. Each nanostructure was synthesized in its non-doped form, as well as with designed Nb contents of 0.5 %, 1.0 %, and 1.5 %, calculated as an atomic percent relative to Ti.

For the synthesis of {1 0 1} exposing nanoparticles, 1 g of TiO_2 P25 was treated with 40 cm^3 of 8.5 M potassium hydroxide solution for the 16 h at the temperature of 200 °C in a 100 cm^3 Teflon-lined autoclave. To obtain desired doping concentration, a corresponding amount of niobium(V) ethoxide was added to the reaction suspension prior to thermal treatment. The obtained products were centrifuged, washed with water to the neutral pH, and dried at 80 °C. Subsequently, 0.4 g of each precursor was further converted to TiO_2 using 100 cm^3 of $NH_4OH/$

NH_4Cl buffer adjusted to pH = 9 (0.3/0.3 M) inside the 200 cm^3 Teflon-lined autoclave at the 210 °C for 16 h. The final products were centrifuged, washed with water five times, and dried at 80 °C.

Synthesis of the {1 0 0} exposing nanoparticles was carried out analogically to the {1 0 1} ones, except that 10 M sodium hydroxide solution was used and the first step was carried out at 120 °C for 24 h. Obtained products were washed with water to the pH of about 10.5 and treated in a Teflon-lined autoclave with 120 cm^3 of pure water at 200 °C for 24 h.

Synthesis of the {0 0 1} exposing nanoparticles was performed in one step, starting from the 17 cm^3 of titanium tert-butoxide, mixed with 30 cm^3 of n-butanol, 3.4 cm^3 of HF solution, and a corresponding amount of niobium(V) ethoxide. The mixtures were kept in the 200 cm^3 Teflon-lined autoclave at 180 °C for 18 h. Obtained products were centrifuged and washed three times with ethanol and further with water as well as 2.5 % NH_4OH solution to obtain neutral pH. After the pH correction, obtained materials were washed with pure water five times and finally dried at 80 °C.

2.2. Phase structure, morphology and elemental composition

The phase structure of the obtained materials was analyzed with the powder X-ray diffraction (XRD) method, using Rigaku MiniFlex 600 instrument. The scan speed during the measurements was $0.75° \cdot min^{-1}$ with the step of 0.05°. Rietveld refinement of obtained patterns was performed using PANanalytical X'Per HighScore Plus 2006 software, based on the Crystallography Open Database data of anatase crystal structure [40]. Profile fitting was based on the pseudo-Voigt function. Specimen displacement, coefficients for background function, lattice parameters a and c, as well as profile parameters including anisotropic peak broadening were refined. The morphology and elemental composition of the materials were analyzed using FEI Quanta FEG 250 scanning electron microscope (SEM), combined with an Apollo-X SDD energy-dispersive spectrometer (EDS). The EDS data was obtained using accelerating voltage of 30 kV with a scanning resolution of 132 eV and the composition was determined as the average over the large sample area (approx. 2000–4000 μm^2, depending on the samples). Detection level for the analyzed elements, except of oxygen, was determined as 0.1 at %. Obtained data was analyzed using the EDAX Genesis APEX 2i software. Additional elemental analysis was performed for the selected samples using inductively coupled plasma optical emission spectroscopy method (ICP-OES) for the titanium and niobium presence. Development of the surface area for the obtained samples was analyzed with the Brunauer-Emmett-Teller adsorption isotherm method (BET), measured at the 10 points with the N_2 sorption within the p/p_0 range between 0.05 and 0.98 and at the 77.15 K temperature, using Micromeritics Gemini V instrument. Prior to the BET measurements, all samples were degassed at 200 °C for 2 h under the N_2 flow.

2.3. Spectroscopic analyses

The optical absorption of the obtained samples was analyzed via diffuse reflectance spectroscopy (DR/UV–vis) using the Thermo Fisher Scientific Evolution 220 spectrophotometer. Prior to measurements, $BaSO_4$ was used as a reference material in the wavelength range between 190 and 1100 nm. Electron paramagnetic spectroscopy analysis (EPR) was performed at the temperature of liquid N_2, using a Radiopan SE/X-2547 spectrometer with a frequency in the range between 8.911490 and 8.91494 GHz. Modulation amplitude was 5 Gs, for the samples of the {0 0 1} and {1 0 0} series, and 10 Gs for the {1 0 1} ones. The surface properties were analyzed by X-ray photoelectron spectroscopy (XPS, JEOL, JP-9010MC) for 50 scans to estimate the oxidation state of titanium, oxygen and niobium. For the estimation of energy distribution of the electron traps, the photoacoustic spectroscopy (PAS) and reversed double beam photoacoustic spectroscopy (RDB-PAS) with a laboratory-made equipment was performed, as described in the previous paper

[41].

Optical properties of the photocatalyst suspension in water and methanol were performed based on the procedure proposed by Cabrera et al. [42] Briefly, transmittance and diffusive transmittance measurements for the suspensions of the non-modified samples were performed with powder concentration up to 1 g•dm^{-3} in the spectral range of 300–40 nm. Then, specific mass extinction (β) and absorption (κ) coefficients were determined as the slope of the change in the linear region of this relation. The final values are determined as spectral-average and were used to determine mass scattering coefficient (σ), using relation β = σ + κ, as well as scattering albedo ω = σ•β^{-1}.

2.4. Photocatalytic activity tests

Obtained materials were studied in two different photocatalytic reactions: photooxidation of phenol in water and photoreduction of 4-nitrophenol to 4-aminophenol in methanol. All reactions were performed inside the same glass reactor with a quartz window for the light entry, working volume of 25 cm^3, equipped with a magnetic stirrer, cooling jacket and additional hoses for the samples collection and possible introduction of the airflow. The reactor is approximately 3.6 cm in diameter and 2.5 cm thick. For each reaction, prepared photocatalyst suspension was stabilized for 30 or 20 min (details in Table 1) and was immediately introduced to the beam of concentrated 300 W Xe lamp light. During all experiments, reactor position in the light beam was monitored to always be in the centre of the light's intensity, perpendicular to the beam. The measured maximum of the UVA flux intensity at the reactor border was set to be 30 ± 1 mW•cm^{-2} and was controlled directly before and after the reaction. Shimadzu high-pressure liquid chromatography system, equipped with a diode array detector and C18 column (Phenomenex), was used to detect dissolved products (HPLC-DAD). Quantitative analyses, including phenol, para-hydroxyphenol, ortho-hydroxyphenol, benzoquinone, 4-nitrophenol, and 4-aminophenol, were performed after calibration with standard compounds provided by Merck. Summation and some further details on each reaction are presented in Table 1. The detailed scheme, dimensions of the setup, emission spectrum of the utilized xenon lamp and approximate distribution of the light's intensity over the reactor area are presented in Supporting Information (SI). Based on these data, molar flux of photon possible to excite photocatalyst was calculated and compared to the reaction efficiency to achieve apparent quantum efficiency. During these calculations, 6 electrons (6 photons) are needed to reduce one molecule of 4-nitrophenol, while every photon is assumed to possibly induce transformation of phenol. However, since phenol degradation is a step-by-step process, which will include reactions with the formed by-products in the further parts of the process, only an initial rate (5 min) was taken for the calculations.

3. Results and discussion

3.1. Morphology, crystal structure, and composition of the photocatalysts

Morphologies of the synthesized nanocrystals and Nb presence were confirmed by SEM observations and EDS elemental analysis,

respectively. As presented in Fig. 1, unique morphology is obtained for each series with only slight impact of the Nb presence on the size of the formed particles.

Furthermore, the shapes of the TiO$_2$ nanocrystals with exposed facets can be identified based on the Wulff construction of anatase [43]. As presented in Fig. 1a and b, despite the formation of fine nanoparticles, their platelet character can be noticed, which is in accordance with the expected exposition of the {0 0 1} facets. The stabilization of these facet results from the HF presence, as already reported [44–47]. The four elongated sides of the rectangular rods, presented in Fig. 1c and d, correspond to the {1 0 0} facet, which is further topped off with other crystal facets. Finally, octahedral particles, shown in Fig. 1e and f, are almost exclusively enclosed by the {1 0 1} facets, with observed angles between specific crystal sides being very close to the theoretical values (136.6° and 43.4° for the obtuse and the acute ones, respectively). The formation of particles exposing {1 0 0} and {1 0 1} facets depends on the pH value during the second stage of the process, and is directly controlled by the selection of the etching agent (NaOH or KOH), as well as the washing of the obtained precursor and buffer introduction. For these samples, stabilization of both desired facets resulted from the increased alkaline conditions, hydration and oxygenation of the surface [37,48]. Moreover, no clear evidence of other particles than titania (e.g., deposited on the surface of faceted anatase) suggests that secondary phase (e.g., niobium oxide) has not been formed.

Furthermore, EDS analysis confirmed Nb presence in all modified samples, with Nb/Ti ratio consequently increasing with an increase in niobium content during synthesis. The introduction of Nb results from either direct co-crystallization of Ti and Nb from organic precursors or Nb crystallization and diffusion during the two-step etching and rebuilding of the TiO$_2$ structure [49]. These results are consistent with the additional ICP-OES analysis, however the latter have shown Nb concentrations closer to designed ones for samples from the {0 0 1} and {1 0 1} series. This suggests that for these nanostructures, some preference for Nb to localise near surface might exist, which might influence EDS results. In addition, EDS analysis indicates some differences in the stoichiometry of the prepared samples, which correlates well with the accepted preparation procedures. The {0 0 1} series, synthesized in the H$^+$ rich environment of n-butanol, is slightly deficient in oxygen, whereas {1 0 0} and {1 0 1} series, prepared in the OH$^-$ rich water solutions, showed no clear signs of O deficiency, when taking into account possible analysis error.

Finally, since slight differences in the size of the particles are observed during SEM analysis, additional measurements of the specific surface area (SSA) were performed. However, no dependence of the SSA on the Nb amount for the prepared samples was noticed. Detailed results of the elemental composition and BET surface area analysis are presented in Table 2.

Furthermore, XRD analysis confirmed that all obtained materials were composed of pure anatase, without any additional crystalline phases, as shown in Fig. 2a. Nevertheless, some differences in the XRD patterns between series are noticeable, especially for samples with exposed {0 0 1} facets. It is known that the morphology of the nanocrystals can affect the width and intensity of the specific XRD reflections and for this series, broadening of the (0 0 4) and (1 0 5) signals at 2θ

Table 1
Details of the performed photocatalytic tests and analytical procedures.

Reaction	Light source and UVA flux int. (mW•cm^{-2})	Setup details	Pre-treatment	Detection method	Mobile phase (volume %)
Phenol degradation	Xe lamp, 30 ± 1	0.2 mM solution, 25 cm^3 reactor, 20 ± 1 °C, 4 dm^3•h^{-1} airflow, in water	30 min stabilization	HPLC-DAD	Acetonitrile – 70 Water – 29.5 H$_3$PO$_4$[a] – 0.5
4-nitrophenol reduction		0.5 mM solution, 25 cm^3 reactor, 20 ± 1 °C, in methanol	20 min purging with Ar		Acetonitrile – 39.5 Water – 60 H$_3$PO$_4$[a] – 0.5

[a] given fraction corresponds to the 85 % solution (w/w).
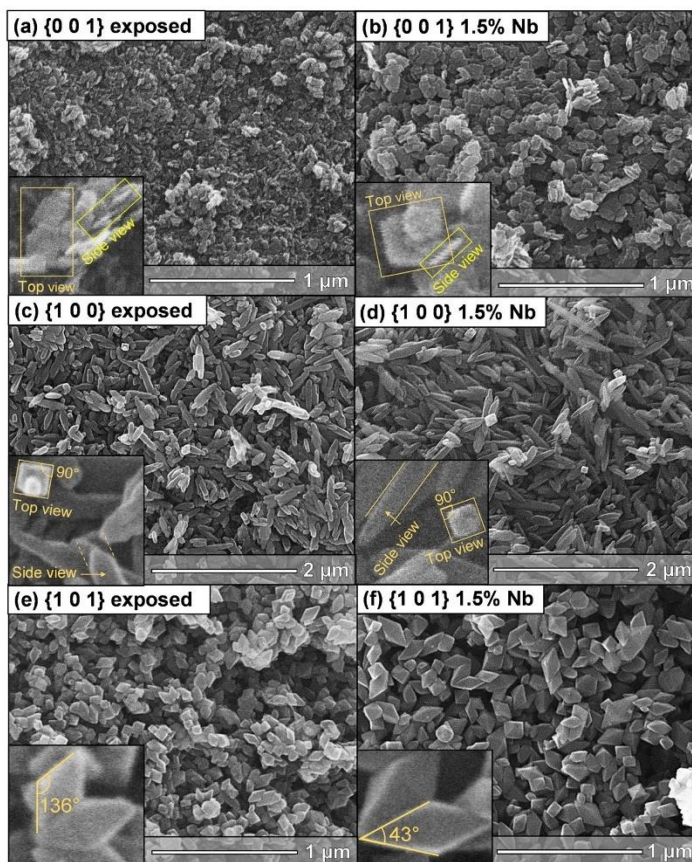
<center>3</center>

Fig. 1. SEM images of the obtained bare and 1.5 % Nb-modified samples for each series. For images a,b,c and d the "top" and "side" correspond to the views along with and perpendicular to the [0 0 1] crystallographic direction, respectively.

$\approx 37°$ and $54°$ is in agreement with expected size reduction along with the [0 0 1] crystallographic direction [50]. Therefore, dominant exposition of the {0 0 1} facet can be proven, based on both their morphology and broadening of these reflections. For other series, similar behavior is not observed and XRD patterns resemble typical anatase standard. Nevertheless, an overall consistency of XRD patterns within each series can be noticed, proving that introduced Nb did not influence the crystallization process of the final nanoparticles, which also in accordance with the SEM morphologies. Noteworthy, for the largest content of Nb (1.5 % at.), the possible mass fraction of Nb_2O_5 could reach ca. 3–4 %, and thus it should be relatively high to be detected by XRD. In this regard, it might be proposed that the successful Nb doping is more probable rather than the formation of the heterojunction between TiO_2 and NbO_x secondary phase.

The detailed effect of the Nb introduction on the crystal structure of each nanostructure was further examined including Rietveld refinement of the obtained patterns. Exemplary refined profiles are shown in Fig. 2b for the 1.5 % Nb modified samples, while detailed data is presented in Tables S1 and S2, as well as in Fig. S3 in the Supporting Information. As

seen in Fig. 3a, for the {1 0 0} and {1 0 1} series increase of the niobium content linearly increase volume of the unit cell, which is also in accordance with the data reported for the other Nb-doped TiO_2 structures, [51–53]. This change is in a good accordance with possible substitution of Ti^{4+} by a slightly larger Nb^{5+}. Only in case of the {0 0 1} samples, the effect is not linear and generally does not follow any strict order. This might be especially due to some amount of O deficiency, which was suggested by the EDS results and could be expected due to the aggressive HF environment used during the synthesis [54]. Therefore, in this particular series, slight amount of O vacancies might also form along the Nb presence, which results in a "chaotic" evolution of the unit cell volume. Finally, calcination of the samples modified with 1.5 % Nb in each series at 600 °C for 2 h have not shown crystallization of any Nb phase, which suggest that no amorphous Nb species are present [55]. Noteworthy, this process also induce expansion of the unit cell in case of the {1 0 1} {1 0 0} samples and contraction in case of {0 0 1} one, as shown in Fig. 3b. These facts will be discussed in the further parts.

4

S. Dudziak et al.

Table 2
Summation of the EDS, ICP-OES and BET surface area analysis for all samples.

Sample name	Designed Nb/Ti (at.)	EDS Nb/Ti (at.)	ICP-OES Nb/Ti (at.)	EDS O/Ti (at.)	BET surface area (m²•g⁻¹)
{0 0 1}	0	0	n.d.	1.8 ± 0.50	84
{0 0 1} 0.5 % Nb	0.005	0.003 ± 0.002	0.0057 ± 0.0010	2.0 ± 0.50	79
{0 0 1} 1.0 % Nb	0.010	0.009 ± 0.002	n.d.	1.7 ± 0.50	81
{0 0 1} 1.5 % Nb	0.015	0.011 ± 0.002	0.0177 ± 0.0010	1.8 ± 0.50	92
{1 0 0}	0	0	n.d.	1.9 ± 0.50	17
{1 0 0} 0.5 % Nb	0.005	0.005 ± 0.002	0.0048 ± 0.0010	3.0 ± 0.50	16
{1 0 0} 1.0 % Nb	0.010	0.008 ± 0.002	0.0081 ± 0.0010	2.3 ± 0.50	14
{1 0 0} 1.5 % Nb	0.015	0.013 ± 0.002	n.d.	2.7 ± 0.50	16
{1 0 1}	0	0	n.d.	1.9 ± 0.50	23
{1 0 1} 0.5 % Nb	0.005	0.003 ± 0.002	n.d.	2.2 ± 0.50	15
{1 0 1} 1.0 % Nb	0.010	0.005 ± 0.002	0.0110 ± 0.0010	2.3 ± 0.50	14
{1 0 1} 1.5 % Nb	0.015	0.011 ± 0.002	n.d.	2.3 ± 0.50	16

3.2. XPS and DR/UV–vis spectroscopy

To study the surface composition and oxidation state of elements, XPS analyses were performed and obtained data are summarized in Table 3, as well as exemplary spectra are presented in Fig. 4. For the {0 0 1} and {1 0 1} samples, niobium content correlates with used precursor, i.e., the higher the Nb amount used for the synthesis was, the higher was its content in the resultant samples, reaching 1.5 %, 2.5 % and 3.2–3.6 % (in respect to titanium) for 0.5, 1.0 and 1.5 samples, respectively. These data indicate the enrichment of {1 0 1} and {0 0 1} surfaces with niobium, which is also in accordance with the comparison of EDS and ICP-OES results. Thus, some preference for surface modification rather than uniform bulk doping is expected for these samples. However, in the case of {1 0 0} sample, an increase in niobium content does not result in an increase in its content on the surface. Moreover, a decrease in niobium content from 2.1 % to 1.0 % and 0.05 % (for 0.5, 1.0 and 1.5 samples, respectively) has been observed, which means that either there is some limit of titania "doping/modification" with niobium (at ca. 0.5 at %) or niobium is mainly doped in the bulk. Similar doping limits have already been reported for other materials, e.g., Rh-doped titania [56]. However, the former does not explain a decrease in niobium content, and thus Nb-doping in the bulk is rather proposed for {1 0 0}-based samples All samples are highly enriched with oxygen on the surface, where oxygen to titanium ratio exceeds stoichiometric 2.0, reaching even ca. 4.0, which is typical for titania sample, being caused by the presence of hydroxyl groups and adsorbed water. Interestingly, the modification of samples with niobium causes different effect, i.e., an increase and a decrease in oxygen content. In contrast, in the case of titania modification with deposits of noble, rare-earth metals and ruthenium complexes, a decrease in oxygen content has been commonly observed, resulting from the replacement of hydroxyl groups by metal, and thus even lower O/Ti ratio than 2.0 [57]. Here, lack of strict

correlation between low O/Ti ratio and niobium content suggest that similar -OH replacement is not occurring and Ti-Nb bonds probably do not form. This is also in agreement with the used Nb precursor (eth-oxide), which already introduced oxidized Nb form with attached oxygens.

Titanium, oxygen and niobium peaks have been deconvoluted, as exemplary shown in Fig. 4. Titanium exists mainly in Ti^{4+} form as it is in TiO_2, but slight content of reduced Ti^{3+} was also noticed, which is typical for various titania samples. For example, for O/Ti ratio data, there is no clear correlation between niobium amount and the content of Ti^{3+}. On the contrary, niobium exists mainly in four-valence state, reaching 72–96 %. This could suggest the formation of the fine NbO_2 on the surface, however reduction of the Nb^{5+} to Nb^{4+} during the synthesis procedure is not expected, as well as the presence of stable NbO_2 will not be supported by the UV–vis analysis, especially for the {0 0 1} and {1 0 0} samples. On the other hand, it is known that Nb competes with the Ti as the trapping site for excess electrons when considered as a dopant and the localization of the charge on Ti is specifically stabilized by the environment [21]. In this regard, under the XPS vacuum conditions, a preference to trap electrons on the Nb might be expected, which causes its reduction to Nb^{4+}. Nevertheless, the minority of the Nb^{5+} states is also always present, with no clear correlation with the amount of introduced Nb. This suggests that some competition between Nb doping and the formation of other Nb structures (e.g. oxides) might still happen, however the latter seems to be limited.

Furthermore, the XPS studies were followed by the DR/UV–vis absorbance analysis. The effect of the photocatalyst morphology can be observed, with {1 0 1} enclosed anatase particles exhibiting a significant absorption increase in the Vis and NIR regions (see in Fig. 5). Similar, but much smaller effect is also observed for the {0 0 1} samples. Therefore, additional energy states are created within the material, especially for this series.

This effect for the {1 0 1} series cannot originate from the possible Nb_2O_5 presence, since its bandgap is almost the same as that of anatase TiO_2, and no mid-gap states should be visible in the spectrum [58–62]. Furthermore, such effect could result from the presence of the stable NbO_2 phase, but this is not supported by XRD and SEM analysis. Moreover, additional treatment of the 1.5 % Nb sample with H_2O_2 (30 min, with high excess of molar H_2O_2 relative to Ti) resulted in no change in the absorbance as shown in the Fig. S4 in the Supporting Information. Similar effect was also observed for the O_3 treatment. Therefore, formation of any oxidizable species on the surface of this sample cannot be responsible for the formation of these additional states. This includes possible reduced Nb species, as well as surface oxygen vacancies and possible carbon species. Furthermore, the XPS results have shown that Nb^{4+} cations are present in all TiO_2 nano-structures with similar content, which cannot explain differences in the absorbance between the series. In this regard, it is expected that this effect results from different localization of the electrons introduced to the TiO_2 lattice with the Nb dopant, which should depend on both the surface structure and the environment. Especially, transfer of e from Nb site to the surface Ti is suggested for the {1 0 1} facets, based on the simulations performed at the interface with water [21]. Therefore, especially for this series, the formation of the Ti^{3+} defects might be preferred under the ambient conditions, which is also in agreement with increased Vis-NIR absorbance. Similar effect is also a well-known phenomenon for the oxygen-deficient TiO_2, which ultimately causes the blue coloration of the powder [63–66]. However, especially in the case of anatase samples exposing {1 0 0} and {1 0 1}, no presence of oxygen vacancies is expected since these samples were prepared in relatively oxygen-rich conditions under high pH values. Moreover, both EDS and XPS measurements have not indicated any oxygen deficiency for these series. The fact that Vis-NIR absorbance of the {1 0 1} is not related to the oxygen vacancies is also in accordance with the performed calcination of the 1.5 % Nb sample, which resulted in the expansion of the unit cell. As the oxygen deficiency results in the formation of Ti^{3+}, the

5
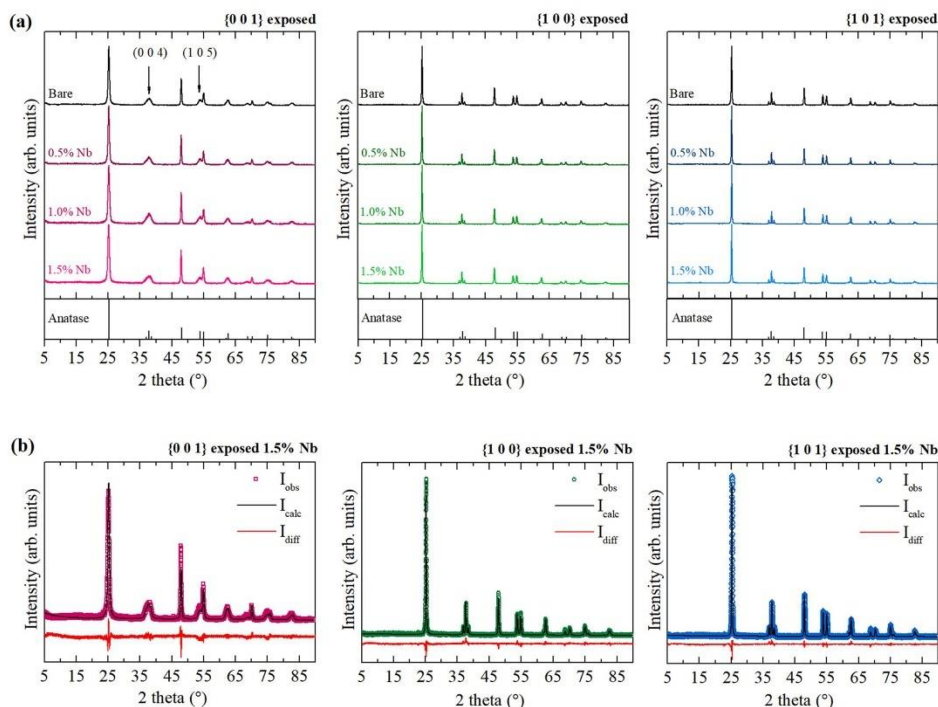
Fig. 2. XRD patterns of the obtained TiO$_2$ photocatalysts (exposing different crystal facets) modified with Nb (a) and exemplary Rietveld refined patterns for the most modified samples in each series (b).
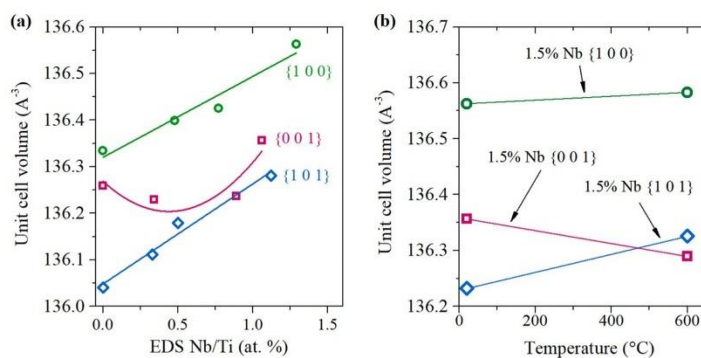
Fig. 3. Effect of Nb presence on the unit cell volume obtained from the refined XRD patterns (a) and calcination effect on the unit cell volume of the most modified sample in each series (b).

unit cell of the reduced TiO$_2$ is also know to expand similarly to the Nb^{5+} doping [67]. However, in consequence, if vacancies are removed from the structure, contraction might be expected as the source of the excess electrons disappears from the structure. In fact, this is observed for the calcined {0 0 1} 1.5 % Nb sample, where some V$_O$ might be present due to the accepted preparation procedure. In the case of the 1.5 % {1 0 1}

the unit cell expands which, interestingly, is also accompanied by the diminishing of the Vis-NIR absorbance, as shown in Fig. S5 in Supporting Information. Instead, a slight new absorbance band appear down to the ~2.4 eV. Noteworthy, such behavior is in a very good agreement with possible incorporation of the excess oxygens into the TiO$_2$ structure, which can form absorbance states at similar energy levels [35].

6

Page | 180

S. Dudziak et al.

Table 3
Summation of the XPS data for the obtained samples.

Sample name	XPS Nb/Ti (at.)	XPS O/Ti (at.)	Ti species (at %)		Nb species (at %)	
			4 +	3 +	5 +	4 +
{0 0 1}	0	3.03	94.3	5.7	-	-
{0 0 1} 0.5 % Nb	0.015	2.35	95.0	5.0	23.9	76.1
{0 0 1} 1.0 % Nb	0.025	4.25	93.7	6.3	3.5	96.5
{0 0 1} 1.5 % Nb	0.036	3.02	93.7	6.3	11.4	88.6
{1 0 0}	0	3.65	95.69	4.3	-	-
{1 0 0} 0.5 % Nb	0.021	3.76	93.3	6.7	28.2	71.8
{1 0 0} 1.0 % Nb	0.010	2.16	95.2	4.8	3.7	96.3
{1 0 0} 1.5 % Nb	0.005	2.34	96.1	3.9	22.6	77.4
{1 0 1}	0	2.30	95.7	4.3	-	-
{1 0 1} 0.5 % Nb	0.015	2.29	95.6	4.4	17.9	82.1
{1 0 1} 1.0 % Nb	0.025	2.33	94.6	5.4	29.5	70.5
{1 0 1} 1.5 % Nb	0.032	2.16	95.9	4.1	7.5	92.4

Moreover, introduction of excess atoms would explain well expansion of the unit cell. Formation of such O rich structure is also in agreement with possible passivation of the Nb-doping, which was discussed in the literature [34,68].

As for the {0 0 1} and {1 0 0} samples, the relatively low absorption suggest that similar electron trapping (on the surface or in the bulk) is less prominent, which indicates that introduced electrons became delocalized over different sites. This is in agreement with the general predictions for the bulk anatase doped with Nb, proving that this phenomenon depends on the surface structure [34–36].

Furthermore, DR/UV–vis analysis could be discussed in terms of the possible formation of O-rich anatase structures for the {1 0 0} series, which might be suggested, since it was characterized by the high O/Ti ration during the EDS analysis and no absorbance increase characteristic for the excess electrons was observed. However, as shown for calcined 1.5 % {1 0 1} sample, combination of Nb and O_I defects inside the anatase crystal structure, as well as Nb with surface peroxo complexes, should create additional energy states above the valence band edge (yellow coloration) [34,68]. This effect was also reported for other point defects related to the oxygen excess inside the TiO_2 structure, such as a simple O excess [69,70], Ti vacancy, or interstitial Ti [30,71]. In this regard, the almost perfect alignment of the absorbance edge for the {1 0 0} samples cannot support the formation of such O-rich structures. Therefore, the high oxygen amount observed for these samples could result from high surface hydroxylation, which might be connected with highly alkaline preparation conditions.

In this regard, DR/UV–vis spectroscopy has revealed possible surface trapping of the Nb-originating excess electrons on the titanium sites of {1 0 1} facets, as predicted by the computational studies. However, since this trapping depends on the interface character and is not preferred in a vacuum, XPS was found to be not reliable in the determination of the possible surface Ti reduction. Instead, excess electrons are preferred to trap on the Nb atoms, causing the appearance of dominant Nb^{4+} signals. Therefore, to further prove the differences between the samples, additional analyses were performed based on the low-temperature EPR and RDB-PAS measurements, as both of these techniques are surface-sensitive and do not require vacuum conditions.

3.3. EPR spectroscopy and RDB-PAS

The EPR spectra of the pure and 1.5 % Nb samples for each series, in which three main signals can be identified, are presented in Fig. 6. The signals located at g ≈ 1.989 and g ≈ 1.955 are well-known to originate from the electrons trapped at the bulk Ti sites (bulk Ti^{3+}) and are the only signals observed for the {0 0 1} exposed nanoparticles [72–74]. Moreover, existence of some bulk Ti^{3+} defects in these samples is in agreement with a discussed presence of O vacancies for these nanoparticles. Nevertheless, although precise quantification was not possible during this analysis, a higher signal-to-noise ratio is observed for the 1.5 % Nb-TiO_2 sample, suggesting that a higher number of Ti^{3+} states were formed when Nb was introduced to the photocatalyst, under otherwise identical synthesis conditions. An increase of the bulk Ti^{3+} states is especially connected with excess electrons present inside the TiO_2 lattice, which further prove the doping behavior of the introduced Nb. It could also be noted that both bare and 1.5 % Nb {0 0 1} samples were characterized by almost identical O-stoichiometry both during the EDS and XPS analyses. Furthermore, for other samples, the additional signal at g ≈ 2.003 is observed, especially for the unmodified structures. The signal in this region is often observed due to the electrons trapped at the oxygen vacancies. However, it is generally observed as a sharp and symmetrical peak in both high and low fields of the spectrum, which is not the case here. Moreover, both EDS and XPS analyses have not revealed any meaningful oxygen deficiency for these series. Therefore, these signals' appearance might be connected with possible charge carriers trapping at the different oxygen species. This might include the formation of the lattice O^-, as well as •O_2 at the surface since both of these species are characterized by signals with similar g values [75–78]. Although their precise identification seems to be impossible for obtained results, they do not correlate with the observed absorbance increase for the {1 0 1} series, nor the Nb presence. Therefore, it can be assumed that their appearance results from the features specific to each facet type, and they should not contribute to the differences observed within the series. On the other hand, the introduction of Nb further causes the appearance of different features in the spectrum of both {1 0 0} and {1 0 1} samples. For nanoparticles enclosed with the {1 0 0} facets, Nb presence creates additional bulk Ti^{3+} states, similar to the {0 0 1} samples. However, this signal is relatively low compared to the possible O⁻/•O_2 formation, which is dominant for this sample. This is in agreement with the absorption studies, which have shown that the formation of the Ti^{3+} states at room temperature is not observed by the UV–vis spectroscopy. Therefore, their delocalization should be preferred in the room conditions for the {1 0 0} structure. Finally, in the case of the {1 0 1} sample, Nb presence results in the clear distortion of the EPR signal for the g < 1.99. The overlapping of the low-intensity signals in this region originates from the electron trapping on the surface Ti sites (surface Ti^{3+}). In this case, the lack of a strictly defined peak results from the differences between the various surface sites, forming a broad distortion-like signal in this region. This behavior is well-observed only in the spectrum of the Nb-modified {1 0 1} sample. Since, in this spectrum, no other high-intensity signals are observed, the formation of the surface Ti^{3+} seems to be the only possible explanation for the combined EPR and DR/UV–vis results, and thus proving the surface trapping of the excess electrons only for the {1 0 1} facets.

Finally, RDB-PAS analysis was performed to obtain the energy distribution of the electron traps within the materials. During these analyses, valence band electrons are excited directly to the trapping sites of the semiconductor using wavelength scanned continuous light irradiation in the presence of methanol as the scavenger of photogenerated holes. This method was designed specifically to investigate photocatalyst powders allowing analysis of their surface traps, identification of the specific materials as well as observing possible interphase charge transfer [79–81]. Fig. 7 shows obtained distributions of trap density for pristine and Nb-doped samples (total densities are given in chevrons). As shown, niobium presence contributed differently to the trap density, depending on the nature of the exposed facets. Especially, for the {1 0 1} samples, systematic reduction of the trapping sites' density is observed together with the increase of the Nb content. As reported before,

7
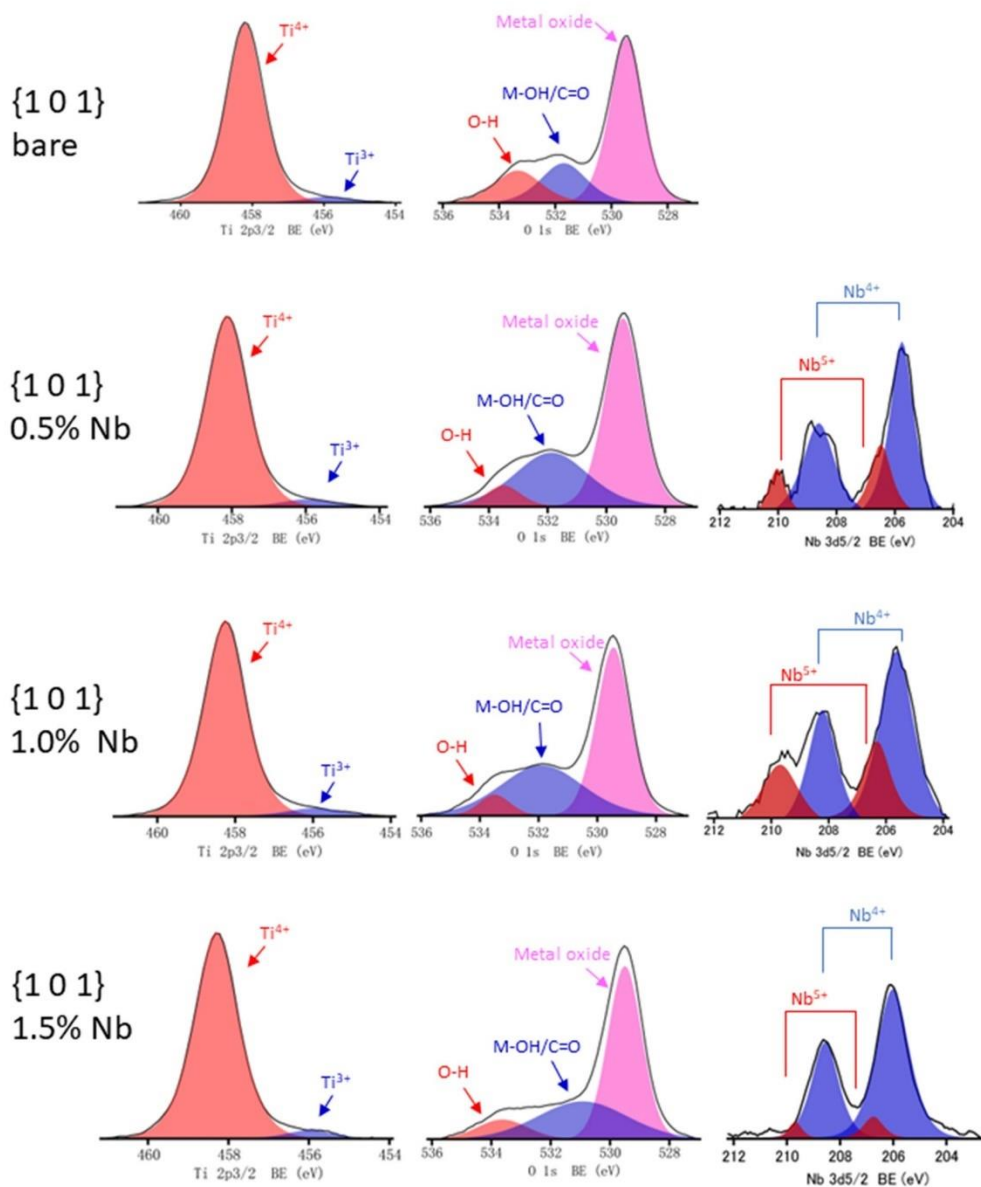
Fig. 4. Exemplary XPS results for {1 0 1} samples of Ti $2p_{3/2}$, O 1 s and Nb $3d_{5/2}$.

RDB-PAS analyses are specifically sensitive towards the surface electron traps, showing a clear trend of the determined trap density, together with the surface area of the photocatalyst [79]. Therefore, a decrease of the trap density for the {1 0 1} samples should especially result from filling of these surface states with excess electrons, introduced together with the Nb. This is not observed for the {0 0 1} and {1 0 0} samples, where Nb presence does not affect total densities in a significant way. This agrees with the EPR results, which showed the appearance of the bulk Ti^{3+} states for these samples, when Nb was introduced. Ultimately, this further proves that only in the case of Nb-doped {1 0 1} samples

8
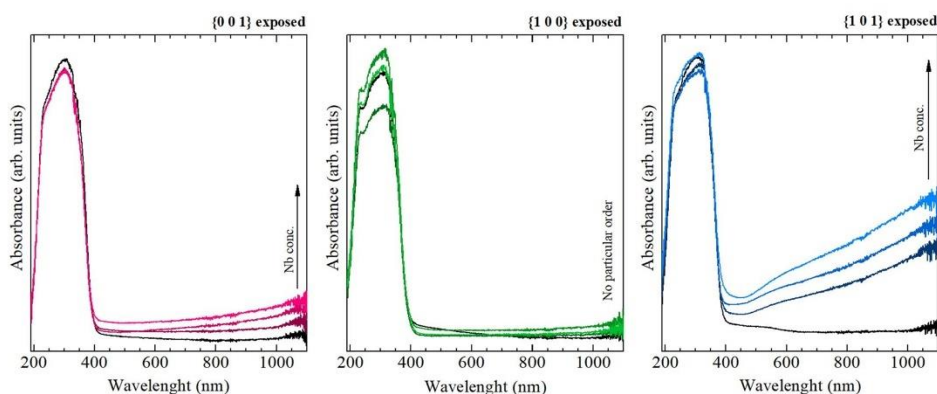
Fig. 5. DR/UV–vis absorption analysis for the obtained TiO₂ photocatalysts doped with Nb and exposed with different crystal facets.
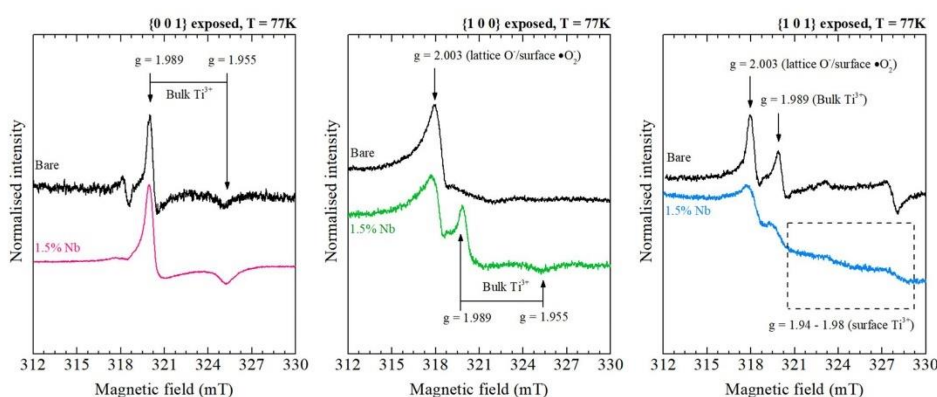
Fig. 6. Low temperature (77 K), min-max normalized EPR spectra of the bare and most Nb-modified TiO₂ samples in each series.
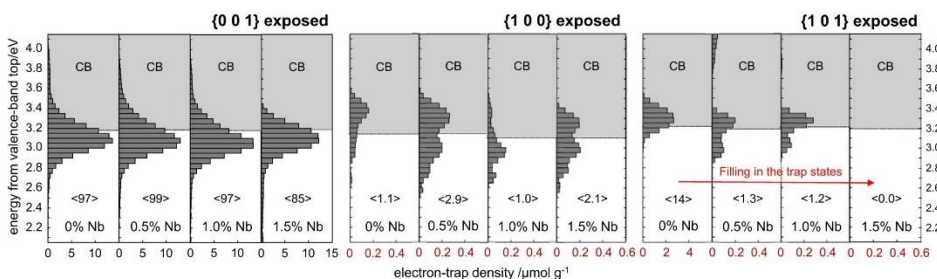
Fig. 7. Energy distributions of the electron trap density present in the prepared TiO₂ samples, as obtained from the RBD-PAS measurements. Total densities are given in chevrons. Please note different X scale between the samples.

additional electrons should trap at the surface sites.

Furthermore, in the case of samples {1 0 0} the density of electron traps is overall very low, which might be due to the preferred hole

trapping, reported previously for this surface [19], as well as possible capping of the trapping sites with i.e. -OH groups. The second might be especially reasonable due to the alkaline conditions present during the

9

synthesis and generally high oxygen presence observed for these series. Similar effect might also be suggested for the {1 0 1} exposing sample, where electron traps might be hypothetically capped with both -OH and ammonia, however further reduction of their density, together with Nb is still noticeable for these samples. Finally, especially for the {1 0 0} facets, the introduction of the Nb promotes the appearance of the additional trapping sites, approx. 0.2 eV below the conduction band edge. This is also observed for the 0.5 % and 1.0 % Nb-modified {1 0 1} samples, however, the effect disappeared together with the reduction of the trapping sites amount. The appearance of these states may result from the formation of the secondary phase inside the photocatalyst, with its valence band edge having lover potential than the primary material. In such a case, electrons from the secondary phase could be excited to the trap states of the primary material with lower energy [81]. The same can result if additional energy states are created above the valence band edge of the anatase. However, especially for the {1 0 0} samples, this is not supported since no difference in the absorption spectra was observed, as well as XPS/EDS analysis revealed that Nb localizes in the bulk of the material for the higher concentrations. On the other hand, a similar maximum of the trap density below the conduction band is always present for the {0 0 1} samples, which are especially characterized by the bulk Ti^{3+} defects. In this regard, for the {1 0 0} structures, these states also appear as a consequence of the increased number of bulk defects, as shown by the EPR analysis.

Ultimately, based on the combined structural, morphological, and spectroscopy analyses, Nb is expected to act as the electron-donating dopant in the prepared anatase TiO_2 samples, which resulted in the presence of excess electrons inside its crystal lattice. The self-trapping of these electrons on the Ti centres could be observed under the non-vacuum conditions, showing their preferred surface localization only for the {1 0 1} facets. These results are in good agreement with some of the computational predictions, simultaneously proving that such trapping can occur for the low-index TiO_2 facets under the ambient conditions [21]. Therefore, similar phenomena might also be expected for the other semiconductor/dopant combinations. It should also be noted that different effects could be expected for the commonly obtained non-faceted, spherical particles, since it is known that charge carriers trapping is different in such structures [23]. Finally, to verify how this self-trapping at the ground states affects the photocatalytic activity of the prepared samples, photoreduction of the 4-nitrophenol, as well as photooxidation of phenol were studied in the presence of the obtained Nb-doped anatase structures.

3.4. Determination of the optimal photocatalyst concentrations

Prior to the actual analysis of the photocatalytic activity, photocatalyst concentration was optimized for both reactions (phenol degradation in water and 4-nitrophenol reduction in methanol) to account for the possible effect of different optical properties of the suspensions. For the phenol degradation, procedure was performed experimentally, following suggested protocol with P25 as an internal standard [82]. As shown in Fig. 8, all samples show a bit different increase of the observed rate constant, however in each case they achieve maximum activity around 2 g·dm^{-3}, which was adapted as optimal for this reaction.

Furthermore, due to the different environment used, performance might be different in case of 4-nitrophenol reduction. Therefore experimental results of phenol degradation were followed with determination of optical properties for each sample (both in the water and methanol), as specified in the experimental section. Summation of the obtained parameters is shown in Table 4, together with the resulting apparent optical thickness of the reactor, calculated based on the six-flux model (SFM) as $\tau_{app} = \beta \cdot C \cdot L \cdot A \cdot (1- \omega_{corr}^2)^{1/2}$ [83], where C is photocatalyst concentration, L is reactor length (2.5 cm), ω_{corr} is corrected scattering albedo and A is SFM parameter [84]. Noteworthy, obtained values are quite consistent with the parameters reported for other TiO_2 materials [85,86], including P25 ($\beta = 14705$ cm^2·g^{-1}, $\kappa = 3088$ cm^2·g^{-1},
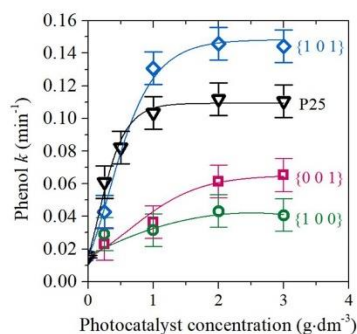

Fig. 8. Change of the observed phenol degradation rate as the function of photocatalyst concentration for each of the unmodified samples and P25 control. Experimental error based on the variance of P25 at the optimal concentration of 2 g·dm^{-3}. Rate constant determination is presented in Figs. S6 and S8 in Supporting Information.

$\omega = 0.79$ in water [87]).

Based on these calculated parameters two observations can be made. Firstly, the experimentally determined optimal concentrations from Fig. 8 achieve quite larger values of τ_{app}, comparing to the optimal ones reported in the literature (approx. 3–4 [87,88]). In general, as shown in Fig. S7 using P25 as an example, the experimental degradation rate increase slower than photon absorption predicted with SFM. This effect is systematic for all samples, suggesting its dependence on the experimental setup, rather than photocatalyst itself. In this regard, it could be highlighted that the reactor used does not follow some of the SFM assumptions [84]. This includes mostly non-uniform photocatalyst distribution (especially under high concentrations and due to intensive stirring directly inside the reactor space), as well as limited size of the reactor in all directions with significant flux changes at the reactor border (see Figs. S1 and S2b). In this regard, differences between experimental and SFM results seems reasonable, leading to experimentally best conditions at 2 g·dm^{-3}.

Secondly, the optical properties in methanol are different than in water and are actually similar between all samples. This fits quite well observations by Delforce et al., who have shown that isoelectric point of TiO_2 in methanol is significantly shifted to the basic conditions (approx. pH = 11), compared to the water (close to the neutral conditions) [89]. Therefore, stabilization of the photocatalysts suspension in methanol might be expected due to the relatively strong surface charge regardless of the sample, resulting in a similar optical properties of the suspensions. Furthermore, following calculated τ_{app} it was suggested that optimal conditions for 4-nitrophenol reduction might have been achieved at 1 g·dm^{-3}, due to the similarities with the results obtained for phenol. However, as shown in Fig. S9 in the SI, further increase of the photocatalyst concentration up to 2 g·dm^{-3} resulted in a systematic increase of the reduction efficiency, independently of the optimal τ_{app} observed for water reaction. As this reaction is fundamentally different from phenol degradation, this shown that optimal conditions are probably not the same for these two systems. Nevertheless, the relative differences observed between 1 and 2 g·dm^{-3} are similar for all tested samples, which agrees with similar optical properties of methanol suspensions. In this regard, comparison at the same concentration should be reasonable to determine the Nb effect, independently on the strictly optimal conditions. Therefore, results obtained at the 1 g·dm^{-3} were taken for further discussion.

10

Table 4
Summation of the calculated optical properties in water and methanol.

Water				Apparent optical thickness τ_{app}			
Sample	β (cm$^2 \bullet$g^{-1})	κ (cm$^2 \bullet$g^{-1})	σ (cm$^2 \bullet$g^{-1})	ω	0.25 g$\bullet$dm^{-3}	1 g$\bullet$dm^{-3}	2 g$\bullet$dm^{-3}	3 g$\bullet$dm^{-3}
{0 0 1}	38837	9339	29499	0.76	10	39	78	118
{1 0 0}	13011	3545	9466	0.73	3.5	14	28	42
{1 0 1}	11484	3404	8080	0.70	3	13	26	39

Methanol				Apparent optical thickness τ_{app}			
Sample	β (cm$^2 \bullet$g^{-1})	κ (cm$^2 \bullet$g^{-1})	σ (cm$^2 \bullet$g^{-1})	ω	0.25 g$\bullet$dm^{-3}	1 g$\bullet$dm^{-3}	2 g$\bullet$dm^{-3}	3 g$\bullet$dm^{-3}
{0 0 1}	29062	4071	24991	0.86	6	23	46	68
{1 0 0}	30352	5517	24836	0.82	7	27	53	80
{1 0 1}	27706	5996	21710	0.78	7	27	53	80

3.5. Photocatalytic activity

The effect of Nb-introduced excess electrons in anatase structure with exposed different crystal facets on photocatalytic reduction of 4-nitrophenol to 4-aminophenol in methanol is presented in Fig. 9, while detailed kinetics are presented in Supporting Information. Moreover, selectivity of the reduction process was calculated as the ratio between produced 4-aminophenol and the number of disappeared 4-nitrophenol molecules (mean over time). From these results, a clear effect of the exposed facet, as well as Nb presence, can be observed. For the bare TiO$_2$ materials, both directly observed and per-surface reduction activity order is {1 0 1} > {0 0 1} > {1 0 0}, which is in agreement with preferred photoreduction character of these surfaces [19]. Furthermore, for the {1 0 1} samples introduction of the Nb resulted in visible decrease in their reduction ability, although excess electrons localize on the surface and the calculated selectivity was significantly increased for this series. This decrease is observed independently of the surface normalization and is linear after normalization. In this regard, the introduction of the additional electrons could not support the reduction ability of the {1 0 1} facets. This might result from two possible effects. Firstly, a significant amount of surface defects, such as Ti^{3+}, might increase the recombination rate at the surface, therefore decreasing the total amount of reacting charge carriers for these structures. Secondly, it might be expected that a large number of excess electrons localized on the surface would inhibit the photooxidation reaction, which must also occur to counter the reduction process. In such a case, the process might start to be limited by lowering the photooxidation potential of these materials. On the other hand, both for the {0 0 1} and {1 0 0} samples, the introduction of the Nb increased their reduction ability, with some maximum observed somewhere up to the ~0.7 at % of Nb/Ti ratio. Again, the Nb effect is observed both without and after considering possible effect of the surface development. Noteworthy, for the modified structures, the {0 0 1} samples achieve the highest reduction ability as a combination of positive Nb effect and high surface area. Furthermore, from the three investigated facets, only the {1 0 1} ones are expected to preferably trap electrons over the photogenerated holes [19]. In this regard, positive Nb effect also correlates with the "oxidative" character of both {0 0 1} and {1 0 0} surfaces. For the surface-normalized results, the highest increase of the reduction ability is observed for the {1 0 0} series, which would create precisely opposite trend to the reduction ability of the non-modified facets (highest increase for the most oxidative facet and a decrease for a reductive one). However, it must be noted that the exact relation between the surface development of the specific facet and observed nitrophenol reduction is not proved so far, therefore it is not obvious if activity would increase linearly with the photocatalyst surface area. In this regard, such observation would need further investigation. On the other hand, for the non-normalized results, the highest reduction enhancement by Nb presence is observed for the {0 0 1} facets, which would also correlate with the highest electron trap density. For both {0 0 1} and {1 0 0} samples Nb presence increase reduction selectivity, the same as for the {1 0 1}, however the effect is visibly lower for the {0 0 1} ones.

Furthermore, degradation of phenolic compounds occurs through photogenerated reactive oxygen species, which are created through reduction and oxidation reactions [90]. As shown in Fig. 10, the effect of the exposed facet and Nb presence can also be noticed, especially for the {1 0 1} samples, however differences are less noticeable than for nitrophenol reduction. The per-surface activity for the bare anatase
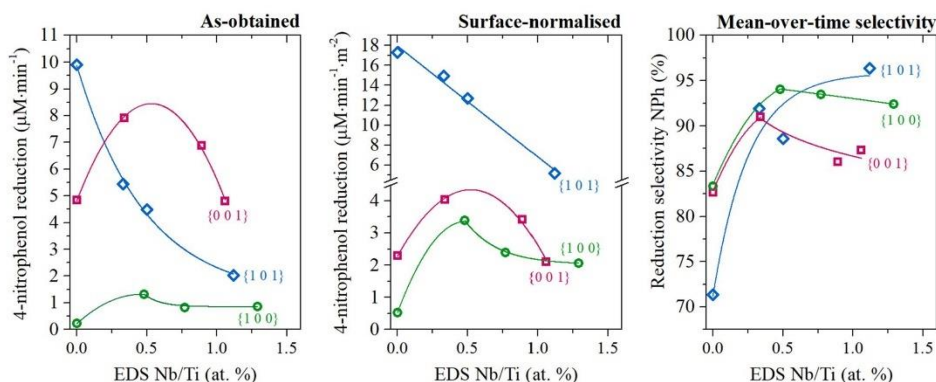

Fig. 9. As-obtained and surface-normalized efficiency of the photocatalytic 4-nitrophenol reduction to 4-aminophenol after a 30 min process, together with the calculated selectivity as the function of exposed crystal facet and Nb concentration. Lines are added as guides.
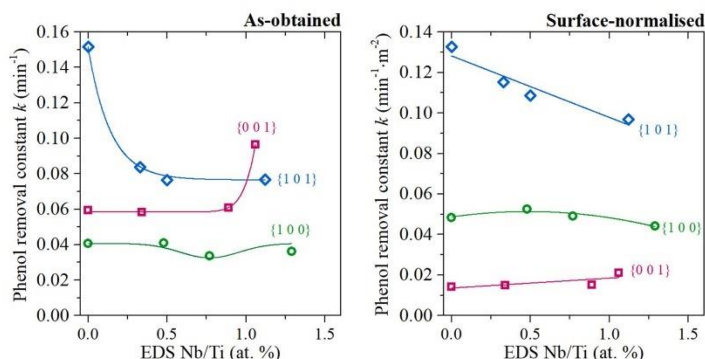
11

Fig. 10. As-obtained and surface-normalized rate constants of the photocatalytic phenol degradation as the function of exposed crystal facet and Nb concentration. Lines are added as guides. Detailed data is shown in Fig. S10 in the SI.

structures is {1 0 1} > {1 0 0} > {0 0 1}, which especially correlated with the high surface trapping of both electrons and holes on the {1 0 1} facets resulting in their high activity [19,91,92]. However, similarly to the 4-nitrophneol reduction, Nb presence decreased the observed rate constant for these samples, again independently on the surface development. For the remaining two series, niobium introduction affected their activity very slightly and no clear negative effect was observed. On the other hand, some positive effect might be seen, depending if surface normalization was considered. Specifically, {0 0 1} sample modified with the largest amount of Nb showed visible activity enhancement when its surface area was not considered. However, we have previously noted that high phenol degradation rates over these particular facets show general dependence on the high surface area, when synthesis was performed in the same environment [93]. Therefore, some effect of the surface area development might be expected in this case. Independently of the surface area, the Nb effect on phenol degradation is the lowest for the {1 0 0} facets.

Ultimately, it was found that the Nb effect is quite similar for both photoreduction and photodegradation processes. However, the reduction is more sensitive to its presence. The overall results suggest that excess electrons introduced to the TiO_2 photocatalyst can enhance its activity, but only when it does not compromise the reactivity of the co-generated holes. In this case, it is expected only for the {0 0 1} and {1 0 0} facets, which show oxidative character and prefer to trap h^+ in their non-modified form. Finally, calculated apparent quantum efficiencies for the presented results are summarized in the Table 5.

4. Conclusions

Three anatase nanostructures, exposing the majority of the {0 0 1}, {1 0 0}, and {1 0 1} facets were successfully prepared by different conditions of the hydrothermal method. Moreover, the faceted TiO_2 samples were doped with Nb, which allowed us to study the self-trapping of the excess electrons in the photocatalyst structure in the ground state. Based on the performed structural, morphological, and

elemental analysis, the formation of a single-phase anatase was confirmed with no secondary Nb-phase. The surface trapping at the Ti sites was observed only for the {1 0 1} facets under the non-vacuum conditions, which resulted in the visible absorption increase in the vis-NIR region (blue coloration), distortion of the EPR signal for the g < 1.99, as well as the disappearance of the "empty" surface electron traps during the RDB-PAS analysis. Simultaneously, no oxygen deficiency was noticed in these samples. For the {0 0 1} facets, introduced electrons localize strictly on the bulk Ti, while for the {1 0 0} ones, they either delocalized over the conduction band states or became trapped at the bulk Ti. The highest activity was observed for the anatase exposing {1 0 1} facets. However, for such octahedral anatase particles exposing {1 0 1} facets, Nb presence decreased activity in both phenol oxidation and 4-nitrophenol reduction reactions. On the other hand, for the {0 0 1} and {1 0 0} series, the introduction of Nb promoted their reactivity, with a maximum depending on the Nb amount. For all samples, the Nb effect is more clear in the reaction of 4-nitrophenol reduction than in phenol photodegradation.

Described results present two important conclusions for further studies. First of all, it experimentally confirms that possible localisation of excess electrons in the photocatalyst structure depend both on the surface structure and the presence of interface species. Especially, results obtained under the vacuum and non-vacuum conditions are different, showing competition between e⁻ trapping on Nb or Ti sites. With respect to the photocatalyst preparation, it proves that the observed doping effect on the activity might be connected with the photocatalyst surface structure and the charge carriers introduced with the dopant. Empirically, it shows that the positive effect of the electron-donating dopant on the photoreduction process can be obtained for the oxidative TiO_2 facets. Therefore, these findings might be introduced to other photocatalysts/dopants systems to tailor their properties and increase application potential.

CRediT authorship contribution statement

Szymon Dudziak: Conceptualization, Methodology, Investigation, Formal analysis, Draft preparation, Writing – Review & Editing, Visualization, Funding acquisition. **Ewa Kowalska:** Formal analysis, Draft preparation, Writing – Review & Editing. **Kunlei Wang:** Investigation, Formal Analysis, Visualization. **Jakub Karczewski:** Investigation, Writing – Review & Editing. **Mirosław Sawczak:** Investigation. **Bunsho Ohtani:** Methodology, Investigation, Formal analysis, Writing – Review & Editing, Visualization. **Anna Zielińska-Jurek:** Methodology, Writing – Review & Editing, Supervision, Project administration, Funding

Table 5
Calculated apparent quantum efficiencies (%) for the analyzed samples.

Sample	4-nitrophenol reduction 30 min			Phenol degradation 5 min		
	{0 0 1}	{1 0 0}	{1 0 1}	{0 0 1}	{1 0 0}	{1 0 1}
Bare	2.90	0.13	5.94	1.09	0.72	1.85
0.5 % Nb	4.75	0.79	3.27	0.97	0.84	1.10
1.0 % Nb	4.13	0.49	2.69	1.15	0.55	1.39
1.5 % Nb	2.88	0.51	1.22	1.83	0.63	1.28

acquisition.

Declaration of Competing Interest

Data availability

Data will be made available on request.

Acknowledgements

Appendix A. Supporting information

Supplementary data associated with this article can be found in the online version at doi:10.1016/j.apcatb.2023.122448.

References

[1] J. Pan, G. Liu, G.Q. Lu, H.M. Cheng, On the true photoreactivity order of {001}, {010}, and {101} facets of anatase TiO₂ crystals, Angew. Chem. - Int. Ed. 50 (2011) 2133–2137.

[2] M. Lazzeri, A. Vittadini, A. Selloni, Structure and energetics of stoichiometric TiO₂ anatase surfaces, Phys. Rev. B - Condens. Matter Mater. Phys. 63 (2001) 1554091–1554099.

[3] Y. Cao, Q. Li, C. Li, J. Li, J. Yang, Surface heterojunction between {001} and {101} facets of ultrafine anatase TiO₂ nanocrystals for highly efficient photoreduction CO₂ to CH₄, Appl. Catal. B Environ. 198 (2016) 378–388.

[4] P. Mikrut, M. Kobielusz, W. Macyk, Spectroelectrochemical characterization of euhedral anatase TiO₂ crystals – implications for photoelectrochemical and photocatalytic properties of {001} {100} and {101} facets, Electrochim. Acta 310 (2019) 256–265.

[5] D. Zhang, S. Wang, J. Zhu, H. Li, Y. Lu, WO₃ nanocrystals with tunable percentage of {001}-facet exposure, Appl. Catal. B Environ. 123–124 (2012) 398–404.

[6] M. Huang, Y. Yan, W. Feng, S. Weng, Z. Zheng, X. Fu, P. Liu, Controllable tuning various ratios of ZnO polar facets by crystal seed-assisted growth and their photocatalytic activity, Cryst. Growth Des. 14 (2014) 2179–2186.

[7] H.B. Jiang, Q. Cuan, C.Z. Wen, J. Xing, D. Wu, X.Q. Gong, C. Li, H.G. Yang, Anatase TiO₂ crystals with exposed high index facets, Angew. Chem. - Int. Ed. 50 (2011) 3764–3768.

[8] M. Kowalkińska, S. Dudziak, J. Karczewski, J. Ryl, G. Trykowski, A. Zielińska-Jurek, Facet effect of TiO₂ nanostructures from TiOF₂ and their photocatalytic activity, Chem. Eng. J. 404 (2021), 126493.

[9] A. Grzegórska, P. Głuchowski, J. Karczewski, J. Ryl, I. Wysocka, K. Siuzdak, G. Trykowski, K. Grochowska, A. Zielińska-Jurek, Enhanced photocatalytic activity of accordion-like layered Ti₃C₂ (MXene) coupled with Fe-modified decahedral anatase particles exposing {1 0 1} and {0 0 1} facets, Chem. Eng. J. 426 (2021), 130801.

[10] T. Takata, J. Jiang, Y. Sakata, M. Nakabayashi, N. Shibata, V. Nandal, K. Seki, T. Hisatomi, K. Domen, Photocatalytic water splitting with a quantum efficiency of almost unity, Nature 581 (2020) 411–414.

[11] X.H. Yang, Z. Li, C. Sun, H.G. Yang, C. Li, Hydrothermal stability of {001} faceted anatase TiO2, Chem. Mater. 23 (2011) 3486–3494.

[12] A. Ballestas-Barrientos, X. Li, S. Yick, A.F. Masters, T. Maschmeyer, Optimised heterojunctions between [100]-oriented rutile TiO₂ arrays and {001} faceted anatase nanodomains for enhanced photoelectrochemical activity, Sustain. Energy Fuels 2 (2018) 1463–1473.

[13] Q.D. Truong, H.T. Hoa, T.S. Le, Rutile TiO₂ nanocrystals with exposed {3 3 1} facets for enhanced photocatalytic CO₂ reduction activity, J. Colloid Interface Sci. 504 (2017) 223–229.

[14] J. Mao, L. Ye, K. Li, X. Zhang, J. Liu, T. Peng, L. Zan, Pt-loading reverses the photocatalytic activity order of anatase TiO₂ {001} and {010} facets for photoreduction of CO₂ to CH₄, Appl. Catal. B Environ. 144 (2014) 855–862.

[15] Q. Chen, H. Wang, C. Wang, R. Guan, R. Duan, Y. Fang, X. Hu, Activation of molecular oxygen in selectively photocatalytic organic conversion upon defective TiO₂ nanosheets with boosted separation of charge carriers, Appl. Catal. B Environ. 262 (2020), 118258.

[16] Y.K. Peng, Y. Hu, H.L. Chou, Y. Fu, I.F. Teixeira, L. Zhang, H. He, S.C.E. Tsang, Mapping surface-modified titania nanoparticles with implications for activity and facet control, Nat. Commun. 8 (2017) 1–13.

[17] Y. Zhou, D.E. Doronkin, M. Chen, S. Wei, J.D. Grunwaldt, Interplay of Pt and crystal facets of TiO₂: CO oxidation activity and operando XAS/DRIFTS studies, ACS Catal. 6 (2016) 7799–7809.

[18] Y. Bi, S. Ouyang, N. Umezawa, J. Cao, J. Ye, Facet effect of single crystalline Ag₃PO₄ sub-microcrystals on photocatalytic properties, J. Am. Chem. Soc. 133 (2011) 6490–6492.

[19] X. Ma, Y. Dai, M. Guo, B. Huang, Relative photooxidation and photoreduction activities of the {100}, {101}, and {001} surfaces of anatase TiO₂, Langmuir 29 (2013) 13647–13654.

[20] J.J. Carey, K.P. McKenna, Does polaronic self-trapping occur at anatase TiO₂ surfaces? J. Phys. Chem. C. 122 (2018) 27540–27553.

[21] S. Selcuk, A. Selloni, Facet-dependent trapping and dynamics of excess electrons at anatase TiO₂ surfaces and aqueous interfaces, Nat. Mater. 15 (2016) 1107–1112.

[22] S.K. Wallace, K.P. Mckenna, Facet-dependent electron trapping in TiO₂ nanocrystals, J. Phys. Chem. C. 119 (2015) 1913–1920.

[23] G. Fazio, L. Ferrighi, C. Di Valentin, Photoexcited carriers recombination and trapping in spherical vs faceted TiO₂ nanoparticles, Nano Energy 27 (2016) 673–689.

[24] D. Selli, G. Fazio, C. Di Valentin, Using density functional theory to model realistic TiO₂ nanoparticles, their photoactivation and interaction with water, Catalysts 7 (2017) 357.

[25] O. Avilés-García, J. Espino-Valencia, R. Romero, J.L. Rico-Cerda, M. Arroyo-Albiter, R. Natividad, W and Mo doped TiO₂: synthesis, characterization and photocatalytic activity, Fuel 198 (2017) 31–41.

[26] G. Xiang, Z. Yu, Y. Hou, Y. Chen, Z. Peng, L. Sun, L. Sun, Simulated solar-light induced photoelectrocatalytic degradation of bisphenol-A using Fe³⁺-doped TiO₂ nanotube arrays as a photoanode with simultaneous aeration, Sep. Purif. Technol. 161 (2016) 144–151.

[27] N. Bao, Z. Wei, Z. Ma, F. Liu, G. Yin, Si doped mesoporous TiO₂ continuous fibers: preparation by centrifugal spinning and photocatalytic properties, J. Hazard. Mater. 174 (2010) 129–136.

[28] T. Simon, M.T. Carlson, J.K. Stolarczyk, J. Feldmann, Electron transfer rate vs recombination losses in photocatalytic H₂ generation on Pt- decorated CdS nanorods, ACS Energy Lett. 1 (2016) 1137–1142.

[29] A. Zielińska-Jurek, M. Klein, J. Hupka, Enhanced visible light photocatalytic activity of Pt/I-TiO₂ in a slurry system and supported on glass packing, Sep. Purif. Technol. 189 (2017) 246–252.

[30] Z. Bielan, S. Dudziak, A. Sulowska, D. Pełczarski, J. Ryl, A. Zielińska-Jurek, Preparation and characterization of defective TiO₂. the effect of the reaction environment on titanium vacancies formation, Materials 13 (2020) 1–25.

[31] P. Mazierski, P.N. Arellano Caicedo, T. Grzyb, A. Mikolajczyk, J.K. Roy, E. Wyrzykowska, Z. Wei, E. Kowalska, T. Puzyn, A. Zaleska-Medynska, J. Nadolna, Experimental and computational study of Tm-doped TiO₂: the effect of Li⁺ on vis-response photocatalysis and luminescence, Appl. Catal. B Environ. 252 (2019) 138–151.

[32] H.Y. Wang, J. Chen, F.X. Xiao, J. Zheng, B. Liu, Doping-induced structural evolution from rutile to anatase: formation of Nb-doped anatase TiO₂ nanosheets with high photocatalytic activity, J. Mater. Chem. A 4 (2016) 6926–6932.

[33] X. Han, K. Song, L. Lu, Q. Deng, X. Xia, G. Shao, Limitation and extrapolation correction of the GGA + U formalism: a case study of Nb-doped anatase TiO₂, J. Mater. Chem. C. 1 (2013) 3736–3746.

[34] H.Y. Lee, J. Robertson, Doping and compensation in Nb Doped anatase and rutile TiO₂, J. Appl. Phys. 113 (2013).

[35] S. Khan, H. Cho, D. Kim, S.S. Han, K.H. Lee, S.H. Cho, T. Song, H. Choi, Defect engineering toward strong photocatalysis of Nb-doped anatase TiO₂: computational predictions and experimental verifications, Appl. Catal. B Environ. 206 (2017) 520–530.

[36] H. Kamisaka, T. Hitosugi, T. Suenaga, T. Hasegawa, K. Yamashita, Density functional theory based first-principle calculation of Nb-doped anatase TiO₂ and its interactions with oxygen vacancies and interstitial oxygen, J. Chem. Phys. (2009) 131.

[37] A.S. Barnard, L.A. Curtiss, Prediction of TiO₂ nanoparticle phase and shape transitions controlled by surface chemistry, Nano Lett. 5 (2005) 1261–1266.

[38] F. Amano, T. Yasumoto, O.O. Prieto Mahaney, S. Uchida, T. Shibayama, B. Ohtani, Photocatalytic activity of octahedral single-crystalline mesoparticles of anatase titanium(IV) oxide, Chem. Commun. (No. 17) (2009) 2311–2313.

[39] J. Li, D. Xu, Tetragonal faceted-nanorods of anatase TiO₂ single crystals with a large percentage of active {100} facets, Chem. Commun. 46 (2010) 2301–2303.

[40] C.J. Howard, T.M. Sabine, F. Dickson, Structural and thermal parameters for rutile and anatase, Acta Cryst. B47 (1991) 462–468.

[41] B. Ohtani, Photoacoustic Spectroscopy, in: D.W. Bahnemann, A.O. Patrocinio, C. Colbeau Justin (Eds.), Springer Handbook of Inorganic Photochemistry, Springer-Nature, 2022, pp. 303–313 (Section B).

[42] M.I. Cabrera, O.M. Alfano, A.E. Cassano, Absorption and scattering coefficients of titanium dioxide participate suspensions in water, J. Phys. Chem. 100 (1996) 20043.

[43] R. Li, X. Zhang, H. Dong, Q. Li, Z. Shuai, W. Hu, Gibbs-Curie-Wulff theorem in organic materials: a case study on the relationship between surface energy and crystal growth, Adv. Mater. 28 (2016) 1697–1702.

[44] M. Zhang, X. Xiao, X. Wang, M. Chen, Y. Lu, M. Liu, L. Chen, Excellent catalysis of TiO₂ nanosheets with high-surface-energy {001} facets on the hydrogen storage properties of MgH₂, Nanoscale 11 (2019) 7465–7473.

[45] X. Han, Q. Kuang, M. Jin, Z. Xie, L. Zheng, Synthesis of titania nanosheets with high percentage of exposed (001) facets and related photocatalytic properties, J. Am. Chem. Soc. 131 (2009) 3152–3153.

[46] M. Maisano, M. Dozzi, M. Coduri, L. Artiglia, Q. Granozzi, E. Selli, Unraveling the multiple effects originating the increased oxidative photoactivity of {001}-facet enriched anatase TiO₂, ACS Appl. Mater. Interfaces 8 (2016) 9745–9754.

[47] Y.J. Yuan, Z.J. Ye, H.W. Lu, B. Hu, Y.H. Li, D.Q. Chen, J.S. Zhong, Z.T. Yu, Z. G. Zou, Constructing anatase TiO₂ nanosheets with exposed (001) facets/layered MoS₂ two-dimensional nanojunctions for enhanced solar hydrogen generation, ACS Catal. 6 (2016) 532–541.

[48] A.S. Barnard, P. Zapol, L.A. Curtiss, Anatase and rutile surfaces with adsorbates representative of acidic and basic conditions, Surf. Sci. 582 (2005) 173–188.

[49] Y. Zhang, C. Li, C. Pan, N + Ni codoped anatase TiO 2 nanocrystals with exposed {001} facets through two-step hydrothermal route, J. Am. Ceram. Soc. 95 (2012) 2951–2956.

[50] T.R. Gordon, M. Cargnello, T. Paik, F. Mangolini, R.T. Weber, P. Fornasiero, C. B. Murray, Nonaqueous synthesis of TiO₂ nanocrystals using TiF₄ to engineer morphology, oxygen vacancy concentration, and photocatalytic activity, J. Am. Chem. Soc. 134 (2012) 6751–6761.

[51] D.S. Bhachu, S. Sathasivam, G. Sankar, D.O. Scanlon, G. Cibin, C.J. Carmalt, I. P. Parkin, G.W. Watson, S.M. Bawaked, A.Y. Obaid, S. Al Thabaiti, S.N. Basahel, Solution processing route to multifunctional titania thin films: highly conductive and photcatalytically active Nb:TiO₂, Adv. Funct. Mater. 24 (2014) 5075.

[52] X. Lü, W. Yang, Z. Quan, T. Lin, L. Bai, L. Wang, F. Huang, Y. Zhao, Enhanced electron transport in Nb-doped TiO₂ nanoparticles via pressure induced phase transitions, J. Am. Chem. Soc. 136 (2014) 419.

[53] F. Zhao, B. Wang, Y. Tang, H. Ge, Z. Huang, H.K. Liu, Niobium doped anatase TiO₂ as an effective anode material for sodium-ion batteries, J. Mater. Chem. A 3 (2015) 22969.

[54] Y. Wang, H. Zhang, Y. Han, P. Liu, X. Yao, H. Zhao, A selective etching phenomenon on (001) faceted anatase titanium dioxide single crystal surfaces by hydrofluoric acid, Chem. Comm. 47 (2011) 2829.

[55] K. Morawa Eblagon, A. Malaika, K. Ptaszynska, M.F.R. Pereira, J.L. Figueiredo, Impact of thermal treatment of Nb₂O₅ on its performance in glucose dehydration to 5 hydroxymethylfurfural in water, Nanomaterials 10 (2020) 1685.

[56] J. Kuncewicz, B. Ohtani, Titania photocatalysis through two-photon band-gap excitation with built in rhodium redox mediator, Chem. Commun. 51 (2015) 298–301.

[57] S. Zheng, Z. Wei, K. Yoshiiri, M. Braunmüller, B. Ohtani, S. Rau, E. Kowalska, Titania modification with a ruthenium(II) complex and gold nanoparticles for photocatalytic degradation of organic compounds, Photochem. Photobiol. Sci. 15 (2016) 69–79.

[58] L.A. Morais, C. Adán, A.S. Araujo, A.P.M.A. Guedes, J. Marugán, Synthesis, characterization, and photonic efficiency of novel photocatalytic niobium oxide materials, Glob. Chall. 1 (2017) 1700066.

[59] N.P. Ferraz, F.C.D. Marcos, A.E. Nogueira, A.S. Martins, M.R.V. Lanza, E.M. Assaf, Y.J.O. Asencios, Hexagonal Nb₂O₅/anatase TiO₂ mixtures and their applications in the removal of methylene blue dye under various conditions, Mater. Chem. Phys. 198 (2017) 331–340.

[60] A.M. Raba, J. Bautista Ruíz, M.R. Joya, Synthesis and structural properties of niobium pentoxide powders: a comparative study of the growth process, Mater. Res. 19 (2016) 1381–1387.

[61] J. Yan, G. Wu, N. Guan, L. Li, Nb₂O₅/TiO₂ heterojunctions: synthesis strategy and photocatalytic activity, Appl. Catal. B Environ. 152–153 (2014) 280–288.

[62] X. Bi, G. Du, A. Kalam, D. Sun, W. Zhao, Y. Yu, Q. Su, B. Xu, A.G. Al-Sehemi, Constructing anatase TiO₂/amorphous Nb₂O₅ heterostructures to enhance photocatalytic degradation of acetaminophen and nitrogen oxide, J. Colloid Interface Sci. 601 (2021) 346–354.

[63] S. Zhang, S. Cao, T. Zhang, J.Y. Lee, Plasmonic oxygen-deficient TiO₂₋ₓ nanocrystals for dual-band electrochromic smart windows with efficient energy recycling, Adv. Mater. (2020) 32.

[64] G. Liu, H.G. Yang, X. Wang, L. Cheng, H. Lu, L. Wang, G.Q. Lu, H.M. Cheng, Enhanced photoactivity of oxygen-deficient anatase TiO₂ sheets with dominant {001} facets, J. Phys. Chem. C 113 (2009) 21784–21788.

[65] L. Liu, Y. Jiang, H. Zhao, J. Chen, J. Cheng, K. Yang, Y. Li, Engineering coexposed {001} and {101} facets in oxygen deficient TiO₂ nanocrystals for enhanced CO₂ photoreduction under visible light, ACS Catal. 6 (2016) 1097–1108.

[66] G. Zhu, Y. Shan, T. Lin, W. Zhao, J. Xu, T. Tian, H. Zhang, C. Zheng, F. Huang, Hydrogenated blue titania with high solar absorption and greatly improved photocatalysis, Nanoscale 8 (2016) 4705–4712.

[67] S.T. Myung, M. Kikuchi, C.S. Yoon, H. Yashiro, S.J. Kim, Y.K. Sun, B. Scrosati, Black anatase titania enabling ultra high cycling rates for rechargeable lithium batteries, Energy Environ. Sci. 6 (2013) 2609.

[68] H. Nogawa, T. Hitosugi, A. Chikamatsu, S. Nakao, Y. Hirose, T. Shimada, H. Kumigashira, M. Oshima, T. Hasegawa, Carrier compensation by excess oxygen atoms in Ti₀.₉₄Nb₀.₀₆O₂₋δ epitaxial thin films, Jpn. J. Appl. Phys. 49 (2010), 041102.

[69] L. Kong, C. Wang, H. Zheng, X. Zhang, Y. Liu, Defect induced yellow color in Nb doped TiO₂ and its impact on visible-light photocatalysis, J. Phys. Chem. C 119 (2015) 16623–16632.

[70] V. Etacheri, M.K. Seery, S.J. Hinder, S.C. Pillai, Oxygen rich titania: a dopant free, high temperature stable, and visible-light active anatase photocatalyst, Adv. Funct. Mater. 21 (2011) 3744–3752.

[71] Q. Wu, F. Huang, M. Zhao, J. Xu, J. Zhou, Y. Wang, Ultra-small yellow defective TiO₂ nanoparticles for co catalyst free photocatalytic hydrogen production, Nano Energy 24 (2016) 63–71.

[72] F. Pellegrino, E. Morra, L. Mino, G. Martra, M. Chiesa, V. Maurino, Surface and bulk distribution of fluorides and Ti³⁺ species in TiO₂ nanosheets: implications on charge carrier dynamics and photocatalysis, J. Phys. Chem. C 124 (2020) 3141–3149.

[73] J. Biedrzycki, S. Livraghi, E. Giamello, S. Agnoli, G. Granozzi, Fluorine- and niobium-doped TiO₂: chemical and spectroscopic properties of polycrystalline n-type doped anatase, J. Phys. Chem. C 118 (2014) 8462–8473.

[74] M. Chiesa, M.C. Paganini, S. Livraghi, E. Giamello, Charge trapping in TiO₂ polymorphs as seen by electron paramagnetic resonance spectroscopy, Phys. Chem. Chem. Phys. 15 (2013) 9435–9447.

[75] T. Li, Z. Shen, Y. Shu, X. Li, C. Jiang, W. Chen, Facet-dependent evolution of surface defects in anatase TiO₂ by thermal treatment: implications for environmental applications of photocatalysis, Environ. Sci. Nano 6 (2019) 1740–1753.

[76] V. Polliotto, S. Livraghi, E. Giamello, Electron magnetic resonance as a tool to monitor charge separation and reactivity in photocatalytic materials, Res. Chem. Intermed. 44 (2018) 3905–3921.

[77] J.B. Priebe, J. Radnik, A.J.J. Lennox, M.M. Pohl, M. Karnahl, D. Hollmann, K. Grabow, U. Bentrup, H. Junge, M. Beller, A. Brückner, Solar hydrogen production by plasmonic Au-TiO₂ catalysts: impact of synthesis protocol and TiO₂ phase on charge transfer efficiency and H₂ evolution rates, ACS Catal. 5 (2015) 2137–2148.

[78] C.P. Kumar, N.O. Gopal, T.C. Wang, EPR investigation of TiO₂ nanoparticles with temperature dependent properties, J. Phys. Chem. B 110 (2006) 5223–5229.

[79] A. Nitta, M. Takashima, N. Murakami, M. Takase, B. Ohtani, Reversed double-beam photoacoustic spectroscopy of metal oxide powders for estimation of their energy-resolved distribution of electron traps and electronic-band structure, Electrochim. Acta 264 (2018) 83–90.

[80] A. Nitta, M. Takashima, M. Takase, B. Ohtani, Identification and characterization of titania photocatalyst powders using their energy-resolved distribution of electron traps as a fingerprint, Catal. Today 321–322 (2019) 2–8.

[81] Y. Shen, A. Nitta, M. Takashima, B. Ohtani, Do particles interact electronically? Proof of interparticle charge-transfer excitation between adjoined anatase and rutile particles, Chem. Lett. 50 (2021) 80–83.

[82] N. Serpone, A. Salinaro, Terminology, relative photonic efficiencies and quantum yields in heterogeneous photocatalysis. Part I: suggested protocol (technical report), Pure Appl. Chem. 71 (1999) 303.

[83] J. Colina-Márquez, F. Machuca-Martínez, G. Li Puma, Radiation absorption and optimization of solar photocatalytic reactors for environmental applications, Environ. Sci. Technol. 44 (2010) 5112–5120.

[84] A. Brucato, A.E. Cassano, F. Grisafi, G. Montante, L. Rizzuti, G. Vella, Estimating radiant fields in flat heterogeneous photoreactors by the six-flux model, AIChE J. 52 (2006) 3882–3890.

[85] S. Yurdakal, V. Loddo, B.B. Ferrer, G. Palmisano, V. Augugliaro, J.G. Farreras, L. Palmisano, Optical properties of TiO₂ suspensions: influence of pH and powder concentration on mean particle size, Ind. Eng. Chem. Res. 46 (2007) 7620.

[86] M.L. Satuf, R.J. Brandi, A.E. Cassano, O.M. Alfano, Experimental method to evaluate the optical properties of aqueous titanium dioxide suspensions, Ind. Eng. Chem. Res. 44 (2005) 6643.

[87] R. Acosta-Herazo, M.A. Mueses, G. Li Puma, F. Machuca-Martínez, Impact of photocatalyst optical properties on the efficiency of solar photocatalytic reactors rationalized by the concepts of initial rate of photon absorption (IRPA) dimensionless boundary layer of photon absorption and apparent optical thickness, Chem. Eng. J. 356 (2019) 839–849.

[88] G. Li Puma, A. Brucato, Dimensionless analysis of slurry photocatalytic reactors using two-flux and six-flux radiation absorption-scattering models, Cat. Today 122 (2007) 78–90.

[89] L. Delforce, E. Hofmann, V. Nardello-Rataj, J.M. Aubry, TiO₂ nanoparticle dispersions in water and nonaqueous solvents studied by gravitational sedimentation analysis: complementarity of hansen parameters and DLVO interpretations, Colloids Surf. A: Physicochem. Eng. Asp. 628 (2021), 127333.

[90] Y. Nosaka, A.Y. Nosaka, Generation and detection of reactive oxygen species in photocatalysis, Chem. Rev. 117 (2017) 11302–11336.

[91] S. Dudziak, M. Kowalkińska, J. Karczewski, M. Pisarek, J.D. Gouveia, J.R. B. Gomes, A. Zielińska-Jurek, Surface and trapping energies as predictors for the photocatalytic degradation of aromatic organic pollutants, J. Phys. Chem. C 126 (2022) 14859–14877.

[92] M. Kowalkińska, K. Sikora, M. Łapiński, J. Karczewski, A. Zielińska-Jurek, Non-toxic fluorine-doped TiO₂ nanocrystals from TiOF₂ for facet-dependent naproxen degradation, Catal. Today, DOI: ⟨https://doi.org/10.1016/j.cattod.2022.11.020⟩.

[93] S. Dudziak, M. Kowalkińska, J. Karczewski, M. Pisarek, A. Kubiak, K. Siwińska-Ciesielczyk, A. Zielińska-Jurek, Solvothermal growth of {0 0 1} exposed anatase nanosheets and their ability to mineralize organic pollutants. the effect of alcohol type and content on the nucleation and growth of TiO₂ nanostructures, Appl. Surf. Sci. 563 (2021), 150360.

CO-AUTHORS STATEMENTS OF CONTRIBUTION

Szymon Dudziak, MSc. Eng.   Gdańsk, 14.12.2023
Department of Process Engineering and Chemical Technology,
Faculty of Chemistry,
Gdańsk University of Technology,
Gabriela Narutowicza 11/12,
80-233, Gdańsk, Poland

Statement of Contribution

I have contributed to the publications which constitute a part of my PhD dissertation in the following way:

- o M. Kowalkińska, S. Dudziak, J. Karczewski, J. Ryl, G. Trykowski, A. Zielińska-Jurek, *„Facet effect of TiO_2 nanostructures from $TiOF_2$ and their photocatalytic activity"*, Chem. Eng. J., vol. 404 (2021), no. 126493, P1

In the above study I was co-responsible for conceiving the concept of studying different crystal facets of TiO_2 for phenol degradation and mineralisation. I was also co-responsible for the preparation of all materials, measurements and analysis of their crystal structure, optical properties, BET surface areas and morphologies, as well as for writing the manuscript. I was mainly responsible for discussing photocatalytic activity of the obtained materials and for the nudged elastic band calculations.

- o S. Dudziak, M. Kowalkińska, J. Karczewski, M. Pisarek, K. Siuzdak, A. Kubiak, K. Siwińska-Ciesielczyk, A. Zielińska-Jurek, *„Solvothermal growth of {0 0 1} exposed anatase nanosheets and their ability to mineralize organic pollutants. The effect of alcohol type and content on the nucleation and growth of TiO_2 nanostructures."*, Appl. Surf. Sci., vol. 563 (2021), no. 150360, P2

In the above study I was co-responsible for the concept of the study, as well as for the preparation and characterization of all the materials, including crystal structure, optical properties, morphology analysis, photocatalytic activity and writing the manuscript. I was mainly responsible for discussing growth of the obtained materials and density functional theory calculations.

- o S. Dudziak, M. Kowalkińska, J. Karczewski, M. Pisarek, J. D. Gouveia, J. R. B. Gomes, A. Zielińska-Jurek *„Surface and Trapping Energies as Predictors for the Photocatalytic Degradation of Aromatic Organic Pollutants"*, J. Phys. Chem. C, vol. 126 (2022), p. 14859-14877, P3

- o S. Dudziak, A. Fiszka Borzyszkowska, A. Zielińska-Jurek, *"Photocatalytic degradation and pollutant-oriented structure-activity analysis of carbamazepine, ibuprofen and acetaminophen over faceted TiO_2"*, J. Environ. Chem. Eng., vol. 11 (2023), no. 109553, P4

In the above studies I was mainly responsible for their concept, workplan, preparation and characterization of all materials, including crystal structure, morphology, optical properties and BET surface areas, as well as for the analysis of the photocatalytic activity data, development and discussion of the correlation models and writing the manuscripts.

In case of the publication P3, I was additionally responsible for the photocatalytic studies in the aqueous phase. In case of the publication P4, I was additionally responsible for the density functional theory calculations of the molecular predictors.

- o S. Dudziak, C. Gómez-Polo, J. Karczewski, K. Nikiforow, , A. Zielińska-Jurek "*Insight into (Electro)magnetic Interactions within Facet-Engineered BaFe$_{12}$O$_{19}$/TiO$_2$ Magnetic Photocatalysts*", ACS Appl. Mater. Interfaces, vol. 15 (2023), p. 56511-56525, P5

In the above study I was co-responsible for the concept of the study. I was mainly responsible for the workplan, preparation and characterization of the materials, including crystal structure, ζ potential, morphology analysis, optical properties, density functional theory calculations, electrochemical and photocatalytic studies, as well as writing the manuscript.

- o S. Dudziak, E. Kowalska, J. Karczewski, K. Wang, M. Sawczak, B. Ohtani, A. Zielińska-Jurek "*The interplay between dopant and a surface structure of the photocatalyst – The case study of Nb-doped faceted TiO$_2$*", Appl. Catal. B: Environ. vol. 328 (2023), no. 122448, P6

In the above study I was mainly responsible for the concept of the study, overall workplan, preparation and characterization of all the materials, including crystal structure, optical properties, BET surface areas, analysis of morphology and EPR data, photocatalytic studies and writing of the manuscript. I was additionally responsible for the local volume rate of photon absorption analysis of the studied dispersions.

_____

Szymon Dudziak, MSc. Eng.

FACULTY OF CHEMISTRY

GDAŃSK UNIVERSITY OF TECHNOLOGY

Assoc. Prof. Anna Zielińska-Jurek, PhD. DSc. Eng.   Gdańsk, 28.12.2023
Department of Process Engineering and Chemical Technology,
Faculty of Chemistry,
Gdańsk University of Technology,
Gabriela Narutowicza 11/12,
80-233, Gdańsk, Poland

Statement of Contribution

I have contributed to the publications which constitute a part of PhD dissertation of mgr inż. Szymon Dudziak in the following way:

o M. Kowalkińska, S. Dudziak, J. Karczewski, J. Ryl, G. Trykowski, A. Zielińska-Jurek, *Facet effect of TiO$_2$ nanostructures from TiOF$_2$ and their photocatalytic activity*, Chem. Eng. J., 404 (2021) 126493. doi:10.1016/j.cej.2020.126493

o S. Dudziak, M. Kowalkińska, J. Karczewski, M. Pisarek, K. Siuzdak, A. Kubiak, K. Siwińska-Ciesielczyk, A. Zielińska-Jurek, *Solvothermal growth of {0 0 1} exposed anatase nanosheets and their ability to mineralize organic pollutants. The effect of alcohol type and content on the nucleation and growth of TiO$_2$ nanostructures*, Appl. Surf. Sci., 563 (2021) 150360. doi.org/10.1016/j.apsusc.2021.150360

o S. Dudziak, A. Fiszka Borzyszkowska, A. Zielińska-Jurek, *Photocatalytic degradation and pollutant-oriented structure-activity analysis of carbamazepine, ibuprofen and acetaminophen over faceted TiO$_2$*, J. Environ. Chem. Eng., 11 (2023) 109553. doi.org/10.1016/j.jece.2023.109553

In the above studies I initiated the research topic, conceived the concept, prepared responses for reviewers, contributed to the draft and final versions of the manuscripts.

o S. Dudziak, M. Kowalkińska, J. Karczewski, M. Pisarek, J. D. Gouveia, J. R. B. Gomes, A. Zielińska-Jurek „*Surface and Trapping Energies as Predictors for the Photocatalytic Degradation of Aromatic Organic Pollutants*", J. Phys. Chem. C, vol. 126 (2022), p. 14859-14877,

o S. Dudziak, C. Gómez-Polo, J. Karczewski, K. Nikiforow, A. Zielińska-Jurek, *Insight into (Electro)magnetic Interactions within Facet-Engineered BaFe$_{12}$O$_{19}$/TiO$_2$ Magnetic Photocatalysts*, ACS Appl. Mater. Interfaces, 15 (2023) 56511-56525. doi.org/10.1021/acsami.3c13380

o S. Dudziak, E. Kowalska, J. Karczewski, K. Wang, M. Sawczak, B. Ohtani, A. Zielińska-Jurek "*The interplay between dopant and a surface structure of the photocatalyst – The case study*

GDAŃSK UNIVERSITY
OF TECHNOLOGY
G. Narutowicza 11/12
80-233 Gdańsk, Poland

tel +48 58 347 23 52
fax +48 58 347 20 65
e-mail: annjurek@pg.edu.pl
www.pg.edu.pl

GDAŃSK UNIVERSITY
OF TECHNOLOGY

GDAŃSK UNIVERSITY
OF TECHNOLOGY

FACULTY OF
CHEMISTRY

of Nb-doped faceted TiO₂", Appl. Catal. B: Environ. 328 (2023), 122448. doi:10.1016/j.apcatb.2023.122448

In the above studies I initiated the research topic. I took part in discussion of the results and general comments at the stage of preparation of the manuscripts for publication. I helped in the preparation of draft versions of the manuscripts and contributed to the final versions of the manuscripts.

_____

Assoc. Prof. Anna Zielińska-Jurek, PhD. DSc. Eng.

Assoc. Prof. Jakub Karczewski, PhD. DSc. Eng.   Gdańsk, 12.12.2023
Institute of Nanotechnology and Materials Science,
Faculty of Physics and Applied Mathematics,
Gdańsk University of Technology,
Gabriela Narutowicza 11/12,
80-233, Gdańsk, Poland

Statement of Contribution

I have contributed to the publications which constitute a part of PhD dissertation of Szymon Dudziak in the following way:

- M. Kowalkińska, S. Dudziak, J. Karczewski, J. Ryl, G. Trykowski, A. Zielińska-Jurek, „*Facet effect of TiO_2 nanostructures from $TiOF_2$ and their photocatalytic activity*", Chem. Eng. J., vol. 404 (2021), no. 126493, P1

- S. Dudziak, M. Kowalkińska, J. Karczewski, M. Pisarek, K. Siuzdak, A. Kubiak, K. Siwińska-Ciesielczyk, A. Zielińska-Jurek, „*Solvothermal growth of {0 0 1} exposed anatase nanosheets and their ability to mineralize organic pollutants. The effect of alcohol type and content on the nucleation and growth of TiO_2 nanostructures.*", Appl. Surf. Sci., vol. 563 (2021), no. 150360, P2

- S. Dudziak, M. Kowalkińska, J. Karczewski, M. Pisarek, J. D. Gouveia, J. R. B. Gomes, A. Zielińska-Jurek „*Surface and Trapping Energies as Predictors for the Photocatalytic Degradation of Aromatic Organic Pollutants*", J. Phys. Chem. C, vol. 126 (2022), p. 14859-14877, P3

- S. Dudziak, C. Gómez-Polo, J. Karczewski, K. Nikiforow, , A. Zielińska-Jurek "*Insight into (Electro)magnetic Interactions within Facet-Engineered $BaFe_{12}O_{19}/TiO_2$ Magnetic Photocatalysts*", ACS Appl. Mater. Interfaces, vol. 15 (2023), no. 56511-56525, P5

- S. Dudziak, E. Kowalska, J. Karczewski, K. Wang, M. Sawczak, B. Ohtani, A. Zielińska-Jurek "*The interplay between dopant and a surface structure of the photocatalyst – The case study of Nb-doped faceted TiO_2*", Appl. Catal. B: Environ. vol. 328 (2023), no. 122448, P6

In the above studies I have performed scanning electron microscope studies, including sample preparation, and energy-dispersive X-ray spectroscopy analyses.

Assoc Prof. Jakub Karczewski, PhD. DSc. Eng.

Marta Kowalkińska, MSc. Eng. Gdańsk, 12.12.2023
Department of Process Engineering and Chemical Technology,
Faculty of Chemistry,
Gdańsk University of Technology,
Gabriela Narutowicza 11/12,
80-233, Gdańsk, Poland

Statement of Contribution

I have contributed to the publications which constitute a part of PhD dissertation of Szymon Dudziak in the following way:

- M. Kowalkińska, S. Dudziak, J. Karczewski, J. Ryl, G. Trykowski, A. Zielińska-Jurek, „Facet effect of TiO2 nanostructures from TiOF2 and their photocatalytic activity", Chem. Eng. J., vol. 404 (2021), no. 126493, P1

In the above study I was mainly responsible for the concept of using $TiOF_2$ as a universal precursor for obtaining TiO_2 particles with different morphologies. I was co-responsible for the preparation and characterization of all materials, as well as for writing the manuscript

- S. Dudziak, M. Kowalkińska, J. Karczewski, M. Pisarek, K. Siuzdak, A. Kubiak, K. Siwińska-Ciesielczyk, A. Zielińska-Jurek, „Solvothermal growth of {0 0 1} exposed anatase nanosheets and their ability to mineralize organic pollutants. The effect of alcohol type and content on the nucleation and growth of TiO2 nanostructures.", Appl. Surf. Sci., vol. 563 (2021), no. 150360, P2

In the above study I was co-responsible for the and initial choice of the studied preparation variables, workplan of the study, as well as for the preparation, characterization of all the materials and writing the manuscript.

- S. Dudziak, M. Kowalkińska, J. Karczewski, M. Pisarek, J. D. Gouveia, J. R. B. Gomes, A. Zielińska-Jurek „Surface and Trapping Energies as Predictors for the Photocatalytic Degradation of Aromatic Organic Pollutants", J. Phys. Chem. C, vol. 126 (2022), p. 14859-14877, P3

In the above study I have performed gas-phase toluene degradation and prepared corresponding data for the correlation analysis.

Marta Kowalkińska, MSc. Eng.

Page | 194

Assoc. Prof. Marcin Pisarek, PhD. DSc. Eng.   Warsaw, 12.12.2023
Institute of Physical Chemistry,
Polish Academy of Sciences,
Kasprzaka 44/52,
01-224, Warsaw, Poland

Statement of Contribution

I have contributed to the publications which constitute a part of PhD dissertation of Szymon Dudziak in the following way:

- S. Dudziak, M. Kowalkińska, J. Karczewski, M. Pisarek, K. Siuzdak, A. Kubiak, K. Siwińska-Ciesielczyk, A. Zielińska-Jurek, *„Solvothermal growth of {0 0 1} exposed anatase nanosheets and their ability to mineralize organic pollutants. The effect of alcohol type and content on the nucleation and growth of TiO_2 nanostructures."*, Appl. Surf. Sci., vol. 563 (2021), no. 150360, P2

- S. Dudziak, M. Kowalkińska, J. Karczewski, M. Pisarek, J. D. Gouveia, J. R. B. Gomes, A. Zielińska-Jurek *„Surface and Trapping Energies as Predictors for the Photocatalytic Degradation of Aromatic Organic Pollutants"*, J. Phys. Chem. C, vol. 126 (2022), p. 14859-14877, P3

In the above studies I have performed X-ray photoelectron spectroscopy measurements, deconvoluted the signals and helped interpret chemical nature of the observed states.

Marcin Pisarek

_____

Assoc. Prof. Marcin Pisarek, PhD. DSc. Eng.

Assoc. Prof. Jacek Ryl, PhD. DSc. Eng.   Gdańsk, 12.12.2023
Institute of Nanotechnology and Materials Science,
Faculty of Physics and Applied Mathematics,
Gdańsk University of Technology,
Gabriela Narutowicza 11/12,
80-233, Gdańsk, Poland

Statement of Contribution

I have contributed to the publications which constitute a part of PhD dissertation of Szymon Dudziak in the following way:

o M. Kowalkińska, S. Dudziak, J. Karczewski, J. Ryl, G. Trykowski, A. Zielińska-Jurek, *„Facet effect of TiO$_2$ nanostructures from TiOF$_2$ and their photocatalytic activity"*, Chem. Eng. J., vol. 404 (2021), no. 126493, P1

In the above study I have performed X-ray photoelectron spectroscopy measurements, deconvoluted the signals and helped interpret chemical nature of the observed states.

Assoc. Prof. Jacek Ryl, PhD. DSc. Eng.

**NICOLAUS COPERNICUS
UNIVERSITY
IN TORUŃ**
Faculty of Chemistry

**RESEARCH
UNIVERSITY**
EXCELLENCE INITIATIVE

Toruń, 12.12.2023

Grzegorz Trykowski, PhD
Department of Chemistry of Materials, Adsorption and Catalysis,
Faculty of Chemistry,
Nicolaus Copernicus University in Toruń,
Gagarina 7, 87-100, Toruń, Poland

Statement of Contribution

I have contributed to the publications

M. Kowalkińska, S. Dudziak, J. Karczewski, J. Ryl, G. Trykowski, A. Zielińska-Jurek,

„Facet effect of TiO₂ nanostructures from TiOF₂ and their photocatalytic activity",

Chem. Eng. J., vol. 404 (2021), no. 126493, P1,

which constitute a part of **PhD dissertation of Szymon Dudziak** in the following way.

I have performed transmission electron microscope studies, selected-area electron

diffraction measurements and participated in the process of publishing this results.

12.12.2023

Assoc. Prof. Katarzyna Siuzdak, PhD. DSc. Eng.   Gdańsk, 16.12.2023
Institute of Fluid-Flow Machinery,
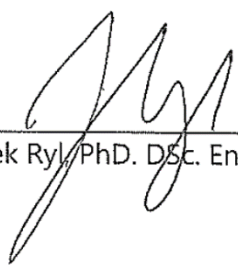Polish Academy of Sciences,
Fiszera 14,
80-231, Gdańsk, Poland

Statement of Contribution

I have contributed to the publications which constitute a part of PhD dissertation of Szymon Dudziak in the following way:

- o S. Dudziak, M. Kowalkińska, J. Karczewski, M. Pisarek, K. Siuzdak, A. Kubiak, K. Siwińska-Ciesielczyk, A. Zielińska-Jurek, „*Solvothermal growth of {0 0 1} exposed anatase nanosheets and their ability to mineralize organic pollutants. The effect of alcohol type and content on the nucleation and growth of TiO$_2$ nanostructures.*", Appl. Surf. Sci., vol. 563 (2021), no. 150360, P2

In the above study I have performed electrochemical measurements, as well as helped with analysis and interpretation of those results.

dr hab. inż. Katarzyna Siuzdak
prof. IMP PAN

Kierownik
Pracowni Materiałów Funkcjonalnych

_____
Assoc. Prof. Katarzyna Siuzdak, PhD. DSc. Eng.

Adam Kubiak, PhD. Eng.   Poznań, 12.12.2023
Faculty of Chemistry,
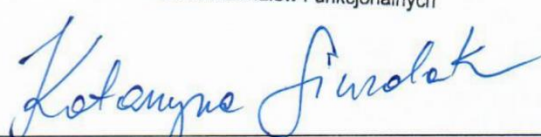Adam Mickiewicz University,
Uniwersytetu Poznańskiego 8,
61-614, Poznań, Poland

Statement of Contribution

I have contributed to the publications which constitute a part of PhD dissertation of Szymon Dudziak in the following way:

o   S. Dudziak, M. Kowalkińska, J. Karczewski, M. Pisarek, K. Siuzdak, A. Kubiak, K. Siwińska-Ciesielczyk, A. Zielińska-Jurek, *„Solvothermal growth of {0 0 1} exposed anatase nanosheets and their ability to mineralize organic pollutants. The effect of alcohol type and content on the nucleation and growth of TiO_2 nanostructures."*, Appl. Surf. Sci., vol. 563 (2021), no. 150360, P2

In the above study I was responsible for the adsorption isotherms measurements and I have revised the final manuscript.

Adam Kubiak, PhD. Eng.

Katarzyna Siwińska-Ciesielczyk, Associate Professor   Poznań, 16.12.2023
Institute of Chemical Technology and Engineering,
Faculty of Chemical technology,
Poznań University of Technology,
Berdychowo 4,
60-965, Poznań, Poland

Statement of Contribution

I have contributed to the publications which constitute a part of PhD dissertation of Szymon Dudziak in the following way:

o S. Dudziak, M. Kowalkińska, J. Karczewski, M. Pisarek, K. Siuzdak, A. Kubiak, K. Siwińska-Ciesielczyk, A. Zielińska-Jurek, „*Solvothermal growth of {0 0 1} exposed anatase nanosheets and their ability to mineralize organic pollutants. The effect of alcohol type and content on the nucleation and growth of TiO$_2$ nanostructures.*", Appl. Surf. Sci., vol. 563 (2021), no. 150360, P2

In the above study, I have performed the adsorption isotherms measurements.

Katarzyna Siwińska- Ciesielczyk

—————————————————————————
Katarzyna Siwińska-Ciesielczyk, Associate Professor

José D. Gouveia, PhD.   Aveiro, 15.12.2023
CICECO - Aveiro Institute of Materials,
Department of Chemistry,
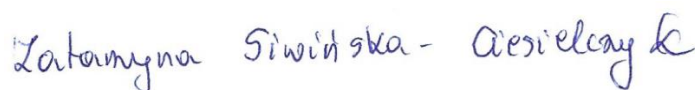University of Aveiro,
Campus Universitário de Santiago,
3810-193, Aveiro, Portugal

Statement of Contribution

I have contributed to the publications which constitute a part of PhD dissertation of Szymon Dudziak in the following way:

o   S. Dudziak, M. Kowalkińska, J. Karczewski, M. Pisarek, J. D. Gouveia, J. R. B. Gomes, A. Zielińska-Jurek „*Surface and Trapping Energies as Predictors for the Photocatalytic Degradation of Aromatic Organic Pollutants*", J. Phys. Chem. C, vol. 126 (2022), p. 14859-14877, P3

In the above study I have performed density functional theory calculations of the electron localisation on the fluorinated (0 0 1) surface of anatase TiO_2, as well as analysed and helped with interpretation of those results, and written the report on the computational results.

José Daniel Gouveia

José D. Gouveia, PhD.

Dr. José R. B. Gomes,   Aveiro, 12.12.2023
Principal Researcher,
CICECO - Aveiro Institute of Materials,
Department of Chemistry,
University of Aveiro,
Campus Universitário de Santiago,
3810-193, Aveiro, Portugal

Statement of Contribution

I have contributed to the publications which constitute a part of PhD dissertation of Szymon Dudziak in the following way:

o S. Dudziak, M. Kowalkińska, J. Karczewski, M. Pisarek, J. D. Gouveia, J. R. B. Gomes, A. Zielińska-Jurek „*Surface and Trapping Energies as Predictors for the Photocatalytic Degradation of Aromatic Organic Pollutants*", J. Phys. Chem. C, vol. 126 (2022), p. 14859-14877, P3

In the above study I have supervised density functional theory calculations of the electron localisation on the fluorinated (0 0 1) surface of anatase TiO_2, as well as revised the final version of manuscript.

Dr. José R. B. Gomes

Agnieszka Fiszka Borzyszkowska, PhD. Eng.   Gdańsk, 28.12.2023
Department of Process Engineering and Chemical Technology,
Faculty of Chemistry,
Gdańsk University of Technology,
Gabriela Narutowicza 11/12,
80-233, Gdańsk, Poland

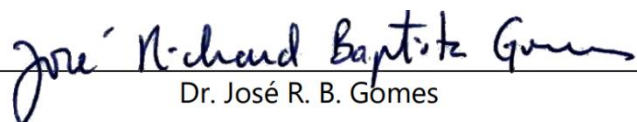## Statement of Contribution

I have contributed to the publications which constitute a part of PhD dissertation of Szymon Dudziak in the following way:

o   S. Dudziak, A. Fiszka Borzyszkowska, A. Zielińska-Jurek, "*Photocatalytic degradation and pollutant-oriented structure-activity analysis of carbamazepine, ibuprofen and acetaminophen over faceted TiO$_2$*", J. Environ. Chem. Eng., vol. 11 (2023), no. 109553, P4

In the above study I have performed photocatalytic activity tests, prepared the data for further analysis and performed Fourier-transform infrared spectroscopy measurements.

Agnieszka Fiszka Borzyszkowska
Agnieszka Fiszka Borzyszkowska, PhD. Eng.

Prof. Cristina Gómez-Polo, PhD.   Pamplona, 12.12.2023
Institute for Advanced Materials and Mathematics. Science
Department.
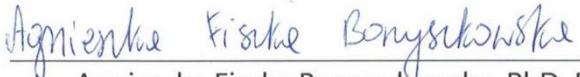Universidad Pública de Navarra,
Campus de Arrosadia,
31006, Pamplona, Spain

Statement of Contribution

I have contributed to the publications which constitute a part of PhD dissertation of Szymon Dudziak in the following way:

- S. Dudziak, C. Gómez-Polo, J. Karczewski, K. Nikiforow, , A. Zielińska-Jurek *"Insight into (Electro)magnetic Interactions within Facet-Engineered $BaFe_{12}O_{19}/TiO_2$ Magnetic Photocatalysts"*, ACS Appl. Mater. Interfaces, vol. 15 (2023), no. 56511-56525, P5

In the above study I have supervised the experiments taking place at the Public University of Navarre, helped to analyse and interpret measurements of the magnetic properties and revised the final version of the manuscript.

_____
Prof. Cristina Gómez-Polo, PhD.

Kostiantyn Nikiforow, PhD. Warsaw, 12.12.2023
Institute of Physical Chemistry,
Polish Academy of Sciences,
Kasprzaka 44/52,
01-224, Warsaw, Poland
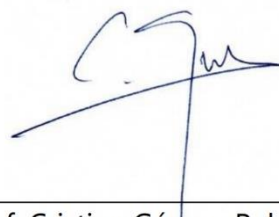
Statement of Contribution

I have contributed to the publications which constitute a part of PhD dissertation of Szymon Dudziak in the following way:

○ S. Dudziak, C. Gómez-Polo, J. Karczewski, K. Nikiforow, , A. Zielińska-Jurek "*Insight into (Electro)magnetic Interactions within Facet-Engineered BaFe$_{12}$O$_{19}$/TiO$_2$ Magnetic Photocatalysts*", ACS Appl. Mater. Interfaces, vol. 15 (2023), no. 56511-56525, P5

In the above study I have performed X-ray photoelectron spectroscopy measurements, deconvoluted the signals and helped interpret chemical nature of the observed states.

Kostiantyn Nikiforow, PhD.

Faculty of Chemistry
Jagiellonian University
https://chemia.uj.edu.pl/en_GB/

Krakow, 13.12.2023

Statement of Contribution

I have contributed to the publication that constitutes a part of PhD dissertation of Szymon Dudziak in the following way:

o   S. Dudziak, E. Kowalska, J. Karczewski, K. Wang, M. Sawczak, B. Ohtani, A. Zielińska-Jurek "The interplay between dopant and a surface structure of the photocatalyst – The case study of Nb-doped faceted TiO2", Appl. Catal. B: Environ. vol. 328 (2023), no. 122448, P6

In the above study, I have supervised X-ray photoelectron spectroscopy measurements, helped with interpretation of the chemical nature of the observed states and revised the final version of manuscript.

Ewa Kowalska, PhD
Professor U.J.
Faculty of Chemistry, Jagiellonian University
ewa.k.kowalska@uj.edu.pl
https://ewakowalskasapporo.wixsite.com/ewa-kowalska

Kunlei Wang, PhD.   Sapporo, 14.12.2023
Institute for Catalysis,
Hokkaido University,
North 21, West 10,
001-0021, Sapporo, Japan

Statement of Contribution

I have contributed to the publications which constitute a part of PhD dissertation of Szymon Dudziak in the following way:

o   S. Dudziak, E. Kowalska, J. Karczewski, K. Wang, M. Sawczak, B. Ohtani, A. Zielińska-Jurek "*The interplay between dopant and a surface structure of the photocatalyst – The case study of Nb-doped faceted TiO$_2$*", Appl. Catal. B: Environ. vol. 328 (2023), no. 122448, P6

In the above study I have performed X-ray photoelectron spectroscopy measurements, deconvoluted the signals, prepared the graphs and helped to interpret chemical nature of the observed states.

Kunlei Wang, PhD.

Assoc. Prof. Mirosław Sawczak, PhD. DSc. Eng.   Gdańsk, 16.12.2023
Institute of Fluid-Flow Machinery,
Polish Academy of Sciences,
Fiszera 14,
80-231, Gdańsk, Poland

Statement of Contribution

I have contributed to the publications which constitute a part of PhD dissertation of Szymon Dudziak in the following way:

- o S. Dudziak, E. Kowalska, J. Karczewski, K. Wang, M. Sawczak, B. Ohtani, A. Zielińska-Jurek "*The interplay between dopant and a surface structure of the photocatalyst – The case study of Nb-doped faceted TiO₂*", Appl. Catal. B: Environ. vol. 328 (2023), no. 122448, P6

In the above study I have helped with performing scattered absorbance and scattered transmittance measurements of the TiO_2 suspensions.

M. Sawczak

Assoc. Prof. Mirosław Sawczak, PhD. DSc. Eng.

Prof. Bunsho Ohtani, PhD.   Sapporo, 16.12.2023
Institute for Catalysis,
Hokkaido University,
North 21, West 10,
001-0021, Sapporo, Japan

Statement of Contribution

I have contributed to the publications which constitute a part of PhD dissertation of Szymon Dudziak in the following way:

o   S. Dudziak, E. Kowalska, J. Karczewski, K. Wang, M. Sawczak, B. Ohtani, A. Zielińska-Jurek "*The interplay between dopant and a surface structure of the photocatalyst – The case study of Nb-doped faceted TiO$_2$*", Appl. Catal. B: Environ. vol. 328 (2023), no. 122448, P6

In the above study I have performed reversed double beam photoacoustic spectroscopy measurements, analysed the data, prepared the graphs, helped to interpret those results and revised the final version of manuscript.

_____
                                      Prof. Bunsho Ohtani, PhD.

LIST OF SCIENTIFIC ACHIEVEMENTS

15. PUBLICATIONS

1. Zielińska-Jurek, Z. Bielan, <u>S. Dudziak</u>, I. Wolak, Z. Sobczak, T. Klimczuk, G. Nowaczyk, J. Hupka, "*Design and application of magnetic photocatalysts for water treatment. The effect of particle charge on surface functionality*", Catalysts vol. 7 (2017), no. 360,

    IF = 3.465, MNiSW = 100 pts, Citations = 60

2. E. Mrotek, <u>S. Dudziak</u>, I. Malinowska, D. Pelczarski, Z. Ryżyńska, A. Zielińska-Jurek, „*Improved degradation of etodolac in the presence of core-shell $ZnFe_2O_4/SiO_2/TiO_2$ magnetic photocatalyst*", Sci. Total Environ., vol. 724 (2020), no. 138167,

    IF = 7.963, MNiSW = 200 pts, Citations = 37

3. Z. Bielan, E. Kowalska, <u>S. Dudziak</u>, K. Wang, B. Ohtani, A. Zielińska-Jurek, „*Mono- and bimetallic (Pt/Cu) titanium(IV) oxide core-shell photocatalysts with UV/Vis light activity and magnetic separability*", Catal. Today, vol. 361 (2021), no. 198,

    IF = 6.562, MNiSW = 140 pts, Citations = 23

4. <u>S. Dudziak</u>, Z. Ryżyńska, Z. Bielan, J. Ryl, T. Klimczuk, A. Zielińska-Jurek, „*Pseudo-superparamagnetic behaviour of barium hexaferrite particles*", RSC Adv., vol. 10 (2020), no. 18784,

    IF = 3.361, MNiSW = 100 pts, Citations = 22

5. Z. Bielan, E. Kowalska, <u>S. Dudziak</u>, K. Wang, B. Ohtani, A. Zielińska-Jurek, „*Mono- and bimetallic (Pt/Cu) titanium(IV) oxide photocatalysts. Physicochemical and photocatalytic data of magnetic nanocomposites' she*ll", Data Brief, vol. 31 (2020), no. 15814,

    MNiSW = 40 pts, Citations = 3

6. Z. Bielan, A. Sulowska, <u>S. Dudziak</u>, K. Siuzdak, J. Ryl, A. Zielińska-Jurek, „*Defective TiO_2 core-shell magnetic photocatalyst modified with plasmonic nanoparticles for visible light-induced photocatalytic activity*", Catalysts, vol 10 (2020), no. 672,

    IF = 4.146, MNiSW = 100 pts, Citations = 18

7. Z. Bielan, <u>S. Dudziak</u>, A. Sulowska, D. Pelczarski, J. Ryl, A. Zielińska-Jurek, „*Preparation and characterization of defective TiO_2. The effect of the reaction environment on titanium vacancies formation*", Materials, vol. 13 (2020), no. 2763,

    IF = 3.623, MNiSW = 140 pts, Citations = 17

8. M. Kowalkińska, <u>S. Dudziak</u>, J. Karczewski, J. Ryl, G. Trykowski, A. Zielińska-Jurek, „*Facet effect of TiO_2 nanostructures from $TiOF_2$ and their photocatalytic activity*", Chem. Eng. J., vol. 404 (2021), no. 126493,

    IF = 16.744, MNiSW = 200 pts, Citations = 36 (Publication P1)

9. S. Dudziak, Z. Bielan, P. Kubica, A. Zielińska-Jurek, „*Optimization of carbamazepine photodegradation on defective TiO$_2$-based magnetic photocatalyst*", J. Environ. Chem. Eng., vol. 9 (2021), no. 105782,

   IF = 7.968, MNiSW = 100 pts, Citations = 17

10. S. Dudziak, M. Kowalkińska, J. Karczewski, M. Pisarek, K. Siuzdak, A. Kubiak, K. Siwińska-Ciesielczyk, A. Zielińska-Jurek, „*Solvothermal growth of {0 0 1} exposed anatase nanosheets and their ability to mineralize organic pollutants. The effect of alcohol type and content on the nucleation and growth of TiO$_2$ nanostructures.*", Appl. Surf. Sci., vol. 563 (2021), no. 150360,

   IF = 7.392, MNiSW = 140 pts, Citations = 22 (Publication P2)

11. Z. Bielan, S. Dudziak, A. Kubiak, E. Kowalska, "*Application of spinel and hexagonal ferrites in heterogeneous photocatalysis*", Appl. Sci., vol. 11 (2021), no. 10160,

   IF = 2.838, MNiSW = 100 pts, Citations = 13

12. N. Czaplicka, D. Dobrzyniewski, S. Dudziak, C. Jiang, D. Konopacka-Łyskawa, „*Improvement of CO$_2$ absorption and inhibition of NH$_3$ escape during CaCO$_3$ precipitation in the presence of selected alcohols and polyols*", J. CO2 Util., vol. 62 (2022), no. 102085,

   IF = 8.321, MNiSW = 140 pts, Citations = 0

13. S. Dudziak, M. Kowalkińska, J. Karczewski, M. Pisarek, J. D. Gouveia, J. R. B. Gomes, A. Zielińska-Jurek „*Surface and Trapping Energies as Predictors for the Photocatalytic Degradation of Aromatic Organic Pollutants*", J. Phys. Chem. C, vol. 126 (2022), p. 14859-14877,

   IF = 4.177, MNiSW = 140 pts, Citations = 6 (Publication P3)

14. E. Cako, S. Dudziak, P. Głuchowski, G. Trykowski, M. Pisarek, A. Fiszka Borzyszkowska, K. Sikora, A. Zielińska-Jurek "*Heterojunction of (P, S) co-doped g-C$_3$N$_4$ and 2D TiO$_2$ for improved carbamazepine and acetaminophen photocatalytic degradation*", Sep. Purif. Technol. vol. 311 (2023), no. 123320,

   IF = 9.136, MNiSW = 140 pts, Citations = 5

15. S. Dudziak, A. Fiszka Borzyszkowska, A. Zielińska-Jurek, "*Photocatalytic degradation and pollutant-oriented structure-activity analysis of carbamazepine, ibuprofen and acetaminophen over faceted TiO$_2$*", J. Environ. Chem. Eng., vol. 11 (2023), no. 109553,

   IF = 7.968, MNiSW = 100 pts, Citations = 4 (Publication P4)

16. S. Dudziak, E. Kowalska, J. Karczewski, K. Wang, M. Sawczak, B. Ohtani, A. Zielińska-Jurek "*The interplay between dopant and a surface structure of the photocatalyst – The case study of Nb-doped faceted TiO$_2$*", Appl. Catal. B: Environ. vol. 328 (2023), no. 122448,

   IF = 22.100, MNiSW = 200 pts, Citations = 4 (Publication P6)

17. <u>S. Dudziak</u>, C. Gómez-Polo, J. Karczewski, K. Nikiforow, , A. Zielińska-Jurek "*Insight into (Electro)magnetic Interactions within Facet-Engineered $BaFe_{12}O_{19}/TiO_2$ Magnetic Photocatalysts*", ACS Appl. Mater. Interfaces, vol. 15 (2023), no. 56511-56525,

<div align="center">IF = 9.500, MNiSW = 200 pts, Citations = 0 (Publication P5)</div>

Overall: Σ_{IF} = 127.483 Σ_{MNiSW} = 2300 pts $\Sigma_{Citations}$ = 287   h-index = 10

P1-P6: Σ_{IF} = 67.881 Σ_{MNiSW} = 980 pts $\Sigma_{Citations}$ = 72

16. BOOK CHAPTERS

1. <u>S. Dudziak</u>, M. Kowalkińska, A. Zielińska-Jurek, "*Crystal Facet Engineering of TiO_2 from Theory to Application*", from "*Updates on Titanium Dioxide*" (ed. Bochra Bejaoui), 2023 IntechOpen.

17. REVIEWER ACTIVITIY

1. Scientific Reports,

2. Journal of Environmental Chemical Engineering,

3. Materials Science in Semiconductor Processing,

4. Chemical Papers,

5. Crystals,

6. Molecules

18. CONFERENCE PRESENTATIONS

1. <u>S. Dudziak</u>, Z. Bielan, A. Zielińska-Jurek, „*Characterization of hexagonal ferrites modified with TiO_2 and their application in heterogeneous photocatalysis*", Interfacial phenomena in theory and practice, The XIIth summer school for postgraduate students and young researchers, 25-30.06.2017, Sudomie,

2. A. Zielińska-Jurek, Z. Bielan, I. Wysocka, <u>S. Dudziak</u>, I. Wolak, „*Magnetic photocatalysts for water treatment*", Symposium on nanomaterials for environmental purification and energy conversion, 20 21.02.2018, Sapporo,

3. <u>S. Dudziak</u>, Z. Sobczak, A. Zielińska-Jurek, „*Impurities and optimal ratio of Fe^{3+}/Ba^{2+} in barium hexaferrite particles. The effect of reagents concentration and reaction dynamics*", 3rd International symposium on energy and environmental photocatalytic materials, 15-19.05.2018, Kraków,

4. A. Zielińska-Jurek, Z. Bielan, <u>S. Dudziak</u>, I. Wolak, J. Hupka, "*Design, preparation and characterization of magnetic photocatalysts*", 3rd International symposium on energy and environmental photocatalytic materials, 15-19.05.2018, Kraków,

5. S. Dudziak, Z. Sobczak, A. Zielińska-Jurek, „*A study over controllable synthesis of BaFe$_{12}$O$_{19}$ nanoparticles and their further modification for preparation of core shell type magnetic photocatalysts*", Interfacial phenomena in theory and practice, The XIIIth summer school for postgraduate students and young researchers, 25-29.06.2018, Sudomie.

6. Z. Bielan, S. Dudziak, I. Wolak, Z. Sobczak, A. Zielińska-Jurek, „*A magnetically recoverable photocatalyst prepared by supporting TiO$_2$ nanoparticles on a ferromagnetic oxide core@silica shell composite*", The XIIIth summer school for postgraduate students and young researchers, 25-29.06.2018, Sudomie,

7. S. Dudziak, Z. Bielan, A. Sulowska, A. Zielińska-Jurek, „*Kinetics and degradation pathways of carbamazepine. A comparative study using visible light active TiO$_2$ photocatalysts*", 6th European conference on environmental applications of advanced oxidation processes, 26-30.06.2019, Portorose,

8. A. Zielińska-Jurek, S. Dudziak, Z. Bielan, A. Sulowska, I. Malinowska, I. Wysocka, „*Magnetic photocatalysts for water treatment*", 6th European conference on environmental applications of advanced oxidation processes, 26-30.06.2019, Portorose,

9. M. Kowalkińska, S. Dudziak, J. Karczewski, A. Zielińska-Jurek, "*Fluorine ions in photocatalysts' synthesis: an obstacle or an ally? The investigation of photocatalysts in Ti-O-F system*", The 2nd international electronic conference on catalysis sciences – a celebration of Catalysts 10th anniversary, 15-30.10.2021, online,

10. S. Dudziak, A. Zielińska-Jurek, „*The interplay between TiO$_2$ surface structure and the Nb/Gd dopants towards efficient phenol degradation*", The 6th international conference on new photocatalytic materials for environment, energy and sustainability & The 7th international conference on photocatalytic and advanced oxidation technologies for treatment of water, air, soil and surfaces, 5-6.04.2022, Ljubljana, Slovenia,

11. A. Zielińska-Jurek, S. Dudziak, A. Grzegórska, E. Cako, I. Malinowska, "*Development of new hybrid photocatalysts with exposed crystal facets for degradation of pharmaceutically active compounds*", 11th European Meeting on Solar Chemistry and Photocatalysis: Environmental Applications, 6 10.06.2022, Turin, Italy,

12. S. Dudziak, A Fiszka Borzyszkowska, A. Zielińska-Jurek, „*Identification of the main features affecting degradation of organic compounds over faceted TiO$_2$ photocatalysts*", 15th Pannonian international symposium on catalysis, 4-8.09.2022, Jastrzębia Góra, Poland,

13. S. Dudziak, J. Smoliński, A. Zielińska-Jurek, „*Modification of the {1 0 1} exposed anatase nanoparticles for water treatment from organic pollutants*", 8th *International Conference on Semiconductor Photochemistry,* 11-15.09.2023, Strasburg, France.

19. AWARDED PROJECTS

1. 02.2022-02.2025 – Polish National Science Centre (NCN) project no. 2021/41/N/ST5/03447 from the Preludium call, entitled "*Facet-dependent photocatalysts design towards efficient water treatment*". Principal Investigator: Szymon Dudziak.

20. ACTIVITY IN OTHER SCIENTIFIC PROJECTS

1. Polish National Science Centre (NCN) project no. 2016/23/D/ST5/01021 from the Sonata call, entitled „*Studies on preparation, physicochemical characterization of TiO$_2$ nanocomposites based on spinel and hexagonal ferrites for oxidation of organic compounds in the aqueous phase*". Principal Investigator: Anna Zielińska-Jurek, PhD. DSc. Eng.

2. Polish National Science Centre (NCN) project no. 2018/30/E/ST5/00845 from the Sonata-bis call, entitled „*Design, synthesis, and physicochemical characterization of 2D nanosheet-based hybrid photocatalysts for degradation of pharmaceuticals*". Principal Investigator" Anna Zielińska-Jurek, PhD. DSc. Eng.

3. Polish National Science Centre (NCN) project no. 2021/43/B/ST5/02983 from the Opus call, entitled "*Design and synthesis of multifunctional materials for thermo-photocatalytic reduction of carbon dioxide and photodegradation of persistent organic pollutants*". Principal Investigator: Anna Zielińska-Jurek, PhD. DSc. Eng.

21. INTERNSHIPS

1. 1.05.2022-30.06.2022 – Internship at the Public University of Navarre (Universidad Publica de Navarra), in Pamplona, Spain, under the supervision of prof. Cristina Gómez-Polo. Internship included studying electronic and magnetic interactions between faceted TiO$_2$ photocatalysts and ferrimagnetic BaFe$_{12}$O$_{19}$.

22. AWARDS

1. "*Diploma of the Year*" award from the Faculty of Chemistry of Gdańsk University of Technology for the best diploma thesis in the year 2018,

2. „*Best Paper Award*" from The 2nd International Electronic Conference on Catalysis Sciences – A Celebration of Catalysts 10th Anniversary, for the publication „*Fluorine Ions in Photocatalysts' Synthesis: An Obstacle or An Ally? The Investigation of Photocatalysts in Ti-O-F System*".